Structural and hydrothermal evolution of the Mount Painter Inlier, South Australia

Dissertation

der Mathematisch-Naturwissenschaftlichen Fakultät

der Eberhard Karls Universität Tübingen

zur Erlangung des Grades eines

Doktors der Naturwissenschaften

(Dr. rer. nat.)

vorgelegt von

Dipl. Geol. Anett Weisheit

aus Schmalkalden

Tübingen

2013

Tag der mündlichen Qualifikation:	19.09.2013
Dekan:	Prof. Dr. Wolfgang Rosenstiel
1. Berichterstatter:	Prof. Dr. Paul D. Bons
2. Berichterstatter:	Prof. Dr. Marlina A. Elburg

Ich erkläre hiermit, dass ich die zur Promotion eingereichte Arbeit selbständig verfasst, nur die angegebenen Quellen und Hilfsmittel benutzt und wörtlich oder inhaltlich übernommene Stellen als solche gekennzeichnet habe. Ich erkläre, dass die Richtlinien zur Sicherung guter wissenschaftlicher Praxis der Universität Tübingen (Beschluss des Senats vom 25.5.2000) beachtet wurden. Ich versichere an Eides statt, dass diese Angaben wahr sind und dass ich nichts verschwiegen habe. Mir ist bekannt, dass die falsche Abgabe einer Versicherung an Eides statt mit Freiheitsstrafe bis zu drei Jahren oder mit Geldstrafe bestraft wird.

Tübingen,

Ort, Datum Unterschrift

Not all those who wander are lost

J.R.R. Tolkien, 1954, The Lord of the Rings,

The Fellowship of the Ring, George Allen & Unwin

---------- DANKSAGUNG ----------

Ursprünglich hatte ich nicht vor eine Danksagung zu schreiben. Es kam mir vor, als würde ich sonst Worte, die schon hunderte Mal am Beginn von Doktorarbeiten geschrieben wurden, einfach nur wieder daher leiern. Aber ein sehr, sehr guter Freund hat mich überzeugt meine eigenen Gedanken doch in einer Danksagung zusammen zu fassen; und mit ihm möchte ich auch beginnen. Er war derjenige, der mich von Anfang an begleitet hat, vom ersten Jahr meines Studiums in Tübingen – bis hin zu dieser Danksagung. Wie kein anderer hat er es verstanden mich zu motivieren, aufzumuntern, weiter zu führen, mich in die Zukunft, anstatt in die Vergangenheit blicken zu lassen. Durch ihn habe ich Wege beschritten (we boldly go…), von denen ich vorher nicht wusste, dass es sie gibt (…where no man has gone before.). Ich danke dir, Martin, dafür, dass du für mich in allen Lebenslagen da warst und letztendlich, aber nicht ausschließlich, auch diese Danksagung ermöglicht hast!

Nun, standardmäßig sagt man, dass diese Arbeit nicht ohne die zwei Supervisors hätte stattfinden können. Das ist auch richtig, aber es ist noch viel mehr. Paul, dein Einsatz und dein Ideenreichtum für das Projekt haben es immer wieder vorangetrieben. Vor allem im Gelände waren unsere Möglichkeiten fast unerschöpflich; Ideen und Ziele kamen auch noch nachts am Lagerfeuer. Doch Büro- und Laborrealitäten zeigten ein Eigenleben und das Lagerfeuer war dann fern. Du hast uns auf neue Ziele gelenkt, wenn die Sackgassen enger wurden. Auch habe ich durch deine Hilfe viele wichtige Ansätze für ein gutes Wissenschaftsenglisch verinnerlicht, was sicher einer der wichtigsten Punkte für diese kumulative Dissertation ist. Gerade weil der Weg dahin für beide Seiten sehr lang und anstrengend war danke ich dir für deine Geduld und Unterstützung.

Marlina, we met only a few times during my PhD thesis, but you found a way to guide and drive the research forward during the entire project. We could discuss ideas and possibilities via e-mail contact and improve the interpretations of a rather challenging geochemistry. I thank you for your help and supervision.

Wie schon oben angesprochen sind Freunde die wichtigste Motivation, die man während einer solchen Arbeit hat. Mit Jens (und für den wahrscheinlichen Fall, dass sich mehrere angesprochen fühlen füge ich noch hinzu:), meinem Büro-„Mitinsassen“, habe ich über viele Jahre die Höhen und Tiefen zweier Doktorarbeiten mitgemacht. Wir haben uns gegenseitig aufgebaut, geholfen, motiviert – es war unser Büro! Aber gemeinsame Ziele, Interessen und Vorstellungen führten uns immer wieder raus, aus dem Alltag und der Welt. Oz oder Schwabenland – die Zeit war schön und ich danke dir dafür!

Es gibt einen weiteren Jens, der mich immer wieder unterstützt hat, die ganzen Jahre; trotz allem, was passierte. Für deine offenen Ohren, deine Ratschläge und deine Hilfe bei vielen Fragen, ob zu Hause oder in Tübingen, Jens, möchte ich dir von ganzem Herzen danken!

Horst, du warst mir von Beginn meines Studiums an ein Mentor und ein guter Freund. Ich hatte immer das Ziel (und werde es immer haben) dich nicht zu enttäuschen. Ich hoffe sehr, dass ich es geschafft habe.

Am Ende einer Doktorarbeit kann die Liste an Freunden sehr lang sein und den Rahmen einer Danksagung sprengen. Auch wenn die folgenden Danksagungen kompakter ausfallen als die vorherigen, hat dies nichts mit der Wichtigkeit zu tun, sondern nur weil mir der Platz ausgeht. ;)

Anke, Ursina und Viktoria! Ihr seid die besten! Ich danke euch für eure langjährige Freundschaft, dass ihr zu mir haltet, mich unterstützt, aufmuntert und nach vorne bringt. Macht weiter so! :)

Auch Wolfgang hat mir viele Ratschläge gegeben und mich mit vielen interessanten Gesprächen in eine andere Welt versetzt – danke sehr! Simon, Jürgen, Elena, Iwan, Sarah, Sümeyya und Zhong Bao, ihr habt mich vor allem über die letzten Jahre erfolgreich begleitet, unterstützt; und abgelenkt. ;)

Viel mehr als alle Freunde konnte natürlich der EINE Freund mit so vielen Möglichkeiten zur Seite stehen und den Rücken frei halten, aufbauen und Kraft und Energie spenden. Klaus, du zeigtest mir die Zukunft mit Freude zu sehen; und sie heute zu beschreiten. Mal sehen, was sie bringt.

Auch wenn die Familie traditionell als letztes bei solchen Danksagungen genannt wird, nimmt sie doch einen viel wichtigeren Stellenwert ein. Meine Eltern haben mich von Anfang an unterstützt, waren immer interessiert an meinen Fortschritten (und Rückschlägen) und, das aller-aller-wichtigste, sie haben mir immer das Gefühl von zu Hause vermittelt. Die Worte „Familie“ und „zu Hause“ beinhalten viel mehr, als diese Danksagung fassen kann. Es gibt einen Ort zu dem ich gehöre – egal was anderswo geschieht. Dafür danke ich euch und meinen Brüdern, aus tiefstem Herzen.

Es geht weiter.

Eure Anett.

---------- ZUSAMMENFASSUNG ----------

Der mesoproterozoische Mount Painter Inlier ist im nördlichen Adelaide Falten- und Überschiebungsgürtel in Südaustralien als Grundgebirge im Kern einer 10 km großen Antiklinale aufgeschlossen. Im südlichen und zentralen Inlier erstreckt sich ein hydrothermales Alterationssystem aus massiven Kalifeldspat-Quarz Gesteinen und verschiedenen Brekzien Zonen. Ihre geologische Bedeutung für die Entwicklung des Mount Painter Inliers wurde von der Doktorandin, Mitarbeitern und Studenten der Universitäten Tübingen und Ghent in Zusammenarbeit mit anderen Universitäten und dem Geologischen Dienst von Südaustralien erforscht. Hervorragende Aufschlussbedingungen und die Nähe zum Arkaroola Sanctuary ermöglichten intensive und detaillierte geologische Kartierung, Probennahme und Fernerkundungsanalysen des deformierten und alterierten Grund- und neoproterozoischen Deckgebirges. Die Kartierungen, wie auch die Daten von publizierten Karten und Probenlokationen wurden in eine umfassende GIS/MapInfo Datenbank integriert und in einem Kartierbericht erläutert (Chapter 2).

Ein Fokus des Forschungsprojektes lag auf der Kalifeldspat Alteration und Brekziierung, die ein Gebiet von ~60 km² umfasst und alle Ausgangsgesteine überprägt. Das Alterationsgebiet ist an Hauptstrukturen wie Schieferungsebenen, Störungszonen und die antiklinale Faltenachsenebene gebunden. Eine ungerichtete Blastese von Kalifeldspat ging mit dem Zerfall von Glimmern (Freisetzen von Wasser) und dem Wachstum von Eisenoxiden einher. Diese Alteration fand in der Regel vor einer Chloritisierung und einer Silizifizierung statt. Diopsid-Titanit Adern, Eisenerzbrekzien und Phlogopitisierung treten im Grundgebirge auf, während Verskarnung das Deckgebirge alterierte (Chapter 3).

Im Grund- und Deckgebirge bildeten sich vereinzelt besondere Brekzienzonen die eine umfassende Durchmischung von Lithologien und einen kontinuierlichen Bereich an Klastengrößen vom mm bis zum 100 m-Maßstab aufweisen (Appendix 2). Im Hidden Valley Gebiet erreicht diese Brekzie eine Größe von 10 km² und enthält Grund- und Deckgebirgsklasten die ursprünglich stratigraphisch mehrere Kilometer voneinander entfernt waren. Die Hidden Valley Brekzie bildete sich durch den Durchlauf eines fokussierten Fluidvolumens von ~5-30 km³ entlang der Hauptstrukturen, nachdem die weitläufige Kalifeldspat Alteration stattfand.

Die Kalifeldspat Alteration überprägte einen Pegmatit, der um ~478 Ma in das Grundgebirge intrudierte (Rb-Sr Gesamtgestein und Muskovit, Chapter 3). Andere Pegmatite wie auch die Diopsid-Titanit Adern, die um ~450/440 Ma gebildet wurden, intrudierten in bereits alterierte Gesteine und wurden selber durch Kalifeldspatblastese überprägt. Phlogopitisierung fand vermutlich um ~455 Ma statt (Appendix 4). ~355 Ma alte Eisenerze (Monazit U-Pb) sind die soweit jüngsten Gesteine des Alterationssystems (Appendix 3), das demnach örtlich zwischen ≤478 Ma und ≤355 Ma während pulshaftem oder konstantem Fluidfluss aktiv war.

Strukturgeologische Rekonstruktionen und eine Re-Interpretation von publizierten K-Ar Daten zeigen, dass das Alterationssystem während eines lang-anhaltenden Deformationsereignisses zwischen ~500/450 Ma und ~300 Ma aktiv war (Appendix 1). Der Inlier exhumierte während dieses Zeitraumes, der die Delamerische und die Alice Springs Orogeny umfasst, im wachsenden Kern der krustalen Antikline. Die Antikline bildete sich im Hangenden der östlich angrenzenden Paralana Störungszone durch ostwärts gerichtete Rampenverschiebung.

Deformation, Exhumierung und Alteration im Paläozoikum sind vermutlich miteinander verbunden. Reaktive Formationswässer dekomprimierten während der Exhumierung des Grundgebirges, stiegen auf, fokussierten und verursachten Alterationsreaktionen und Brekziierung in bestimmten Krustenniveaus der mittleren und oberen Kruste. Die Glimmeralteration setzte zusätzliches Wasser frei, das verschiedene Mineralreaktionen und zusätzliche Brekziirung verursachte (Appendix 2). Die komplexe Architektur des Alterationssystems und großräumige Brekzienzonen entwickelten sich während der Exhumierung des Inliers durch diese einzelnen Niveaus. Das hydrothermale System wurde spätestens mit der endgültigen Exhumierung des Inliers an die Oberfläche inaktiv und von einem oberflächennahen Quarz-Hämatit Sinter überprägt. Das Alter dieses Sinters wurde auf 290 Ma datiert, aber neue Niedrigtemperatur-Thermochronologie Daten zeigen, dass die Sinteraktivität das Gebiet für etwa 100 Myr beeinflusste (Appendix 1).

---------- **ABSTRACT** ----------

The Mesoproterozoic Mount Painter Inlier in the northern Adelaide Fold and Thrust Belt in South Australia comprises an exceptionally large area of massive metasomatic/hydrothermal K-feldspar-quartz-rich rocks and diverse breccia zones. Their geological importance to the evolution of the Mount Painter Inlier was studied by the PhD candidate, staff and students of the University of Tuebingen and Ghent in collaboration with other Universities and the Geological Survey of South Australia. Excellent outcrop conditions and the proximity to the Arkaroola Sanctuary enabled extensive, detailed geological mapping, sampling, as well as remote sensing analyses of the deformed and altered basement inlier and the Neoproterozoic Adelaidean cover sediments. Mapping results and data from published maps and sampling localities were included in a comprehensive GIS/MapInfo database and a corresponding mapping report (Chapter 2).

One focus of the study was the K-feldspar alteration and brecciation that comprises an area of about 60 km², affecting any host rock. Alteration is focussed along major structures including foliation planes, fault zones and the hinge of a 10 km-scale, thick-skinned anticline. Hydrothermal K-feldspar blastesis accompanies the breakdown of micas (hence the release of water) and the growth of iron oxides, while chloritisation and silicification usually post-date the alkali-metasomatism. Diopside-titanite veins, iron-oxide breccia ores and phlogopitisation can be found in basement rocks, and skarning affected Adelaidean sediments (Chapter 3).

Special breccia zones with thorough mixing of lithologies and a continuous range in clast sizes from the mm to the 100 m-scale developed in basement and cover rocks (Appendix 2). In Hidden Valley this breccia reaches an area of 10 km², incorporating basement and Adelaidean rocks that were originally km apart stratigraphically. A fluid volume of ~5-30 km³ caused the extensive brecciation that postdates K-feldspar metasomatism.

K-feldspar alteration affected a pegmatite that intruded at ~478 Ma (Rb-Sr whole rock and muscovite, Chapter 3). Pegmatites and diopside-titanite veins that formed at ~450/440 Ma intrude K-feldspar altered rocks, but are also overprinted by K-feldspar blasts. Phlogopitisation probably occurred at ~455 Ma (Appendix 4). The so far youngest rocks that are possibly related to the complex alteration system are iron-oxide breccia ores that reveal a monazite U-Pb of ~355 Ma (Appendix 3). Alteration and brecciation was hence active in places between ≤478 Ma and ≤355 Ma either in pulses or during constant fluid release.

A structural reconstruction of the evolution of the Mount Painter Inlier and a reinterpretation of published K-Ar ages show that this alteration system was active during a long-lived deformation event that folded and exhumed inlier and cover between ~500/450 Ma and ~300 Ma, spanning the Delamerian and Alice Springs Orogenies (Appendix 1). Crustal-scale anticlinal folding occurred during an eastward ramping in the hanging wall of the major Paralana Fault System that bounds the Mount Painter Inlier to the east.

Deformation, exhumation and alteration in the Palaeozoic are possibly liked. Reactive pore fluids were released and ascended during decompression, causing alteration and brecciation at certain levels in the middle and upper crust (Appendix 2). Additional water arose from the hydrothermal breakdown of micas that resulted in various mineral reactions and brecciation at zones of structural focussing. The complex architecture of the alteration system and the large-scale breccia zones developed during the exhumation of the inlier through the crustal levels of alteration and brecciation. This extensive fluid flow system stopped at the latest when the

inlier reached the surface and was overprinted by a sub-surface hematite-quartz sinter event. This event is known to have started at ~290 Ma and possibly lasted for ~100 Myr (low-temperature thermochronology, Appendix 1).

---------- **TABLE OF CONTENTS** ----------

---------- STRUCTURE OF THE CUMULATIVE DOCTORAL THESIS AND LIST OF PUBLICATIONS ----------

This thesis is a cumulative doctoral thesis that includes two published first-author, two published co-author research articles, one unpublished mapping report for the Geological Survey of South Australia and one chapter that presents and discusses the results of geochemical analyses that were conducted in the framework of the PhD project. To maintain the logical order of the scientific contents this thesis is structured in a general introduction, overview and results of the project (Chapter 1), followed by the unpublished mapping report (Chapter 2) and the analytical Chapter 3. The Appendices 1-4 include the published papers. The general reference to the first-author papers is Weisheit et al. (2013a) (Appendix 2) and Weisheit et al. (2013b) (Appendix 1). Co-authorship papers are generally referred to as Elburg et al. (2013) (Appendix 3) and Elburg et al. (2012) (Appendix 4) in the different sections of this PhD-thesis.

The author's contributions to the various papers and chapters are as follows:

Chapter 2: Mapping report

Title:	Geological mapping of the southern Mount Painter Inlier, South Australia
Authors:	Anett Weisheit, Paul D. Bons
Status:	unpublished mapping report for the Geological Survey of South Australia (DMITRE)

Declaration:	contribution by author
Position in list of authors:	1
Scientific ideas:	50 %
Data generation:	40 %
Analysis and interpretation:	70 %
Report writing:	90 %

Chapter 3: Geochemical analyses

Title:	Crustal-scale fluid flow and a long-lived Palaeozoic hydrothermal system in the Mount Painter Inlier, South Australia
Author:	Anett Weisheit
Contributions:	Marlina A. Elburg, Paul D. Bons, Ronald Bakker, Alvar Soesoo, Wolfgang Siebel, Thomas Wenzel, Heiner Taubald, Tom Andersen

Declaration: contribution by author

Position in list of authors: 1

Scientific ideas: 40 %

Data generation: 80 %

Analysis and interpretation: 70 %

Writing: 90 %

Appendix 1: Published paper - folding

Title: Crustal-scale folding: Palaeozoic deformation of the Mt. Painter Inlier, South Australia

Authors: Anett Weisheit, Paul D. Bons, Martin Danišík, Marlina A. Elburg

Status: Accepted for publication in Geol Soc. London Spec. Publ. "Deformation Structures and Processes within the Continental Crust."

DOI: not yet available

Reference: Weisheit et al. (2013b)

Declaration: contribution by author

Position in list of authors: 1

Scientific ideas: 40 %

Data generation: 70 %

Analysis and interpretation: 80 %

Paper writing: 70 %

Appendix 2: Published paper - brecciation

Title: Long-lived crustal-scale fluid flow: the hydrothermal mega-breccia of Hidden Valley, Mt. Painter Inlier, South Australia

Authors: Anett Weisheit, Paul D. Bons, Marlina A. Elburg

Status: published in International Journal of Earth Sciences 102 (2013), 1219-1236

DOI: 10.1007/s00531-013-0875-7

Reference: Weisheit et al. (2013a)

Declaration: contribution by author

Position in list of authors: 1

Scientific ideas: 40 %

Data generation: 80 %

Analysis and interpretation: 70 %

Paper writing: 60 %

Appendix 3: Published paper – Phanerozoic magmatism and alteration

Title: New constraints on Phanerozoic magmatic and hydrothermal events in the Mt Painter Province, South Australia

Authors: Marlina A. Elburg, Tom Andersen, Paul D. Bons, Siri L. Simonsen, Anett Weisheit

Status: published in Gondwana Research 24 (2013), 700-712

DOI: 10.1016/j.gr.2012.12.017

Reference: Elburg et al. (2013)

Declaration: contribution by author

Position in list of authors: 5

Scientific ideas: 10 %

Data generation: 10 %

Analysis and interpretation: 20 %

Paper writing: 10 %

Appendix 4: Published paper – Proterozoic magmatism and alteration

Title: Metasomatism and metallogeny of A-type granites of the Mt Painter-Mt Babbage Inliers, South Australia

Authors: Marlina A. Elburg, Tom Andersen, Paul D. Bons, Anett Weisheit, Siri L. Simonsen, Ingrid Smet

Status: published in Lithos 181 (2012), 83-1074

DOI: 10.1016/j.lithos.2011.09.009

Reference: Elburg et al. (2012)

Declaration: Share in the publication done in team work

Position in list of authors: 4

Scientific ideas: 5 %

Data generation: 0 %

Analysis and interpretation: 10 %

Paper writing: 10 %

---------- **CHAPTER 1 (OVERVIEW)** ----------

Introduction

Studying hydrothermal fluid flow and mineral alteration processes in crustal rocks demands a large variety of geoscientific approaches, usually including a series of geochemical, mechanical and/or geochronological analyses of host rocks and alteration products based on detailed geological mapping (e.g. Plümper and Putnis, 2009; Sandström et al., 2010; Rohrmeier et al., 2013). Complex, large-scale hydrothermal systems with multiple overprints of the host rocks usually lack in clear analytical trends, forcing different situational concepts to give interpretations and scientific models of formation and evolution of the systems (e.g. Raimondo et al., 2011). The main questions that are usually addressed to major fluid flow events are (a) where did the fluids come from, (b) what are the major fluid pathways, (c) which dynamic processes may affect the fluid system and vice versa and (d) what was the effect on the local geology? A detailed investigation of the mineralogical and structural architecture of the hydrothermal system is a requirement to address these questions in complex and large-scale alteration zones. The Mount Painter region in arid South Australia is host to such a large-scale hydrothermal-metasomatic alteration system that is well exposed at almost continuous outcrops (Coats and Blissett, 1971; Brugger et al., 2011; Elburg et al., 2012). Because of the excellent conditions for detailed mapping and sampling, the Mount Painter Inlier was chosen for the analysis of its complex hydrothermal system and for a comparison with published hydrothermal studies worldwide. This PhD- and various related students projects were funded by the DFG grand BO-1776/8-1.

A brief introduction to the regional geology of the Mount Painter Inlier is given in the following section. This topic is discussed in greater detail in the mapping report of Chapter 2.

Regional Geology and questions to the project

The Mount Painter Inlier (MPI) is an approximately 15x60 km large basement structure that is, together with the smaller Mount Babbage Inlier, exposed in the core of a 10 km-scale, thick-skinned anticlinal structure (Yankaninna Anticline) in the northernmost exposure of the Adelaide Fold and Thrust Belt in South Australia (Fig.1; Coats and Blissett, 1971; Paul et al. 1999; Preiss, 2000). The Mesoproterozoic basement consists of metasediments (Radium Creek Group; Coats and Blissett, 1971; Cowley et al. 2012) that were deposited at ~1590 Ma (Fraser and Neumann, 2010), probably at the eastern coast of the Archaean-Palaeoproterozoic Gawler Craton (Fig.1A; Kositcin, 2010). Two

suites of granitoids intruded after the deposition and deformation of the metasediments. The Coulthard Suite formed at ~1585 Ma, and was affected by albitisation and biotitisation during the intrusion of the Moolawatana Suite at ~1555 Ma (Fig.1B, Fig.2; Stewart and Foden, 2003; McLaren et al., 2006; Elburg et al., 2001, 2012). A regional deformation event (or events?) affected these basement rocks prior to Proterozoic exhumation, erosion and the deposition of the Adelaidean cover sediments (Paul et al., 1999; Elburg et al., 2001; Armit et al., 2012). The early Adelaidean sedimentation started at ~800 Ma and filled km-scale graben structures at the MPI (Preiss, 2000). These grabens were later buried in a 100 km-scale sedimentary basin that formed between the Gawler Craton and the Palaeoproterozoic Curnamona Province. Sedimentation in the Adelaidean basin lasted until ~500 Ma (Preiss, 2000).

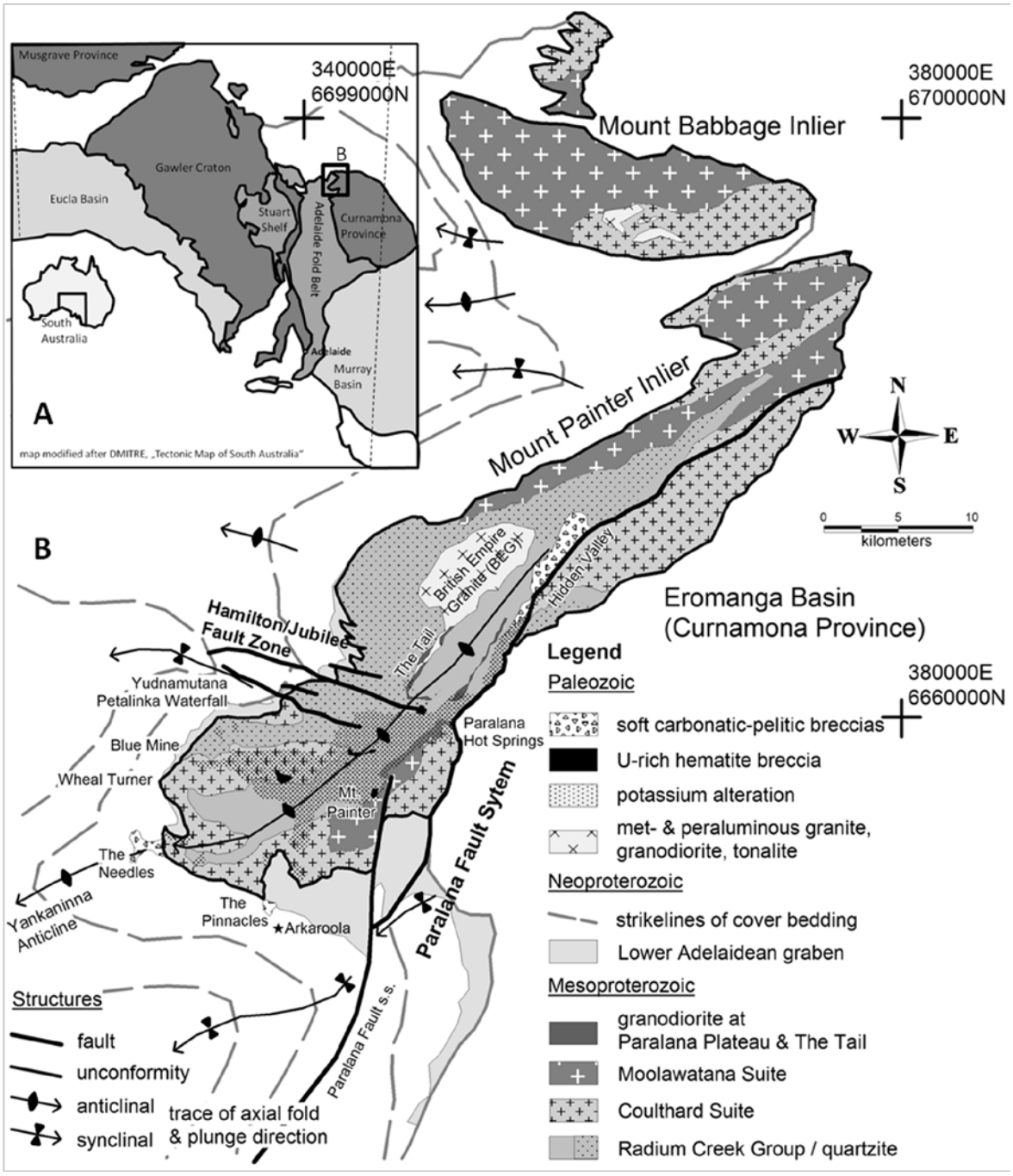

Fig.1: Location and geological map of the Mount Painter region in South Australia. A) The region is located at the northernmost extent of the Neoproterozoic Adelaide Fold and Thrust Belt between the Archaean-Palaeoproterozoic Gawler Craton and the Palaeoproterozoic Curnamona Province. B) Mesoproterozoic metasediments and metagranitic basement rocks are exposed in the core of the 10 km-scale Yankaninna Anticline at the hanging wall of the Paralana Fault System. Magmatism and extensive alteration affected basement and Neoproterozoic cover in Palaeozoic times. Map adapted from Coats and Blissett (1971).

The basement rocks at the MPI were covered by ~12 km at the time of the cessation of the sedimentary deposition (Fig.2; Paul et al., 1999). Regional folding, faulting and metamorphism

between the major Gawler Craton and the Curnamona Province resulted in the formation of the Adelaide Fold and Thrust Belt (Fig.1A). Geochronological analyses in the southern Adelaide Fold Belt revealed a short-term orogenic event at ~500 Ma (e.g. Foden et al., 2006). This Delamerian Orogeny was interpreted to have formed the whole belt, including the folding and faulting of the Mount Painter region at the hanging wall of the major Paralana Fault System (Fig.1B; e.g. Paul et al., 1999; McLaren et al., 2002).

According to the K-Ar study of McLaren et al. (2002), the Mount Painter region was exhumed in steps during Palaeozoic times. In their model, the Yankaninna Anticline first formed during the Delamerian Orogeny and was then subsequently passively exhumed. During exhumation, the peraluminous and metaluminous British Empire Granite and related pegmatites intruded in the core of the anticline at ~450 Ma (Fig.1B, Fig.2; Elburg et al., 2003, 2013; McLaren et al., 2006). However, there are structural problems with the interpretation of a Delamerian anticline, Palaeozoic exhumation and mid-crustal magmatic intrusion at the MPI at this time. Basement rocks that have been in depth of ~15 km are exposed in the core of the Yankaninna Anticline, according to the structural reconstructions of Paul et al. (1999). In contrast Adelaidean sediments in the core of the adjacent synclines did not exhume much. Hence, a Delamerian-aged anticline would have formed a large mountain range, which must have been covered again prior to the measured Palaeozoic exhumation from mid-crustal levels and the intrusion of the granite. A revision of the study by McLaren et al. (2002) in the scope of this PhD-project resulted in a structurally more plausible reinterpretation. It is shown here that the exhumation of the MPI occurred during the crustal-scale folding that occurred during almost the whole Palaeozoic (Fig.2; Weisheit et al., 2013b; Appendix 1).

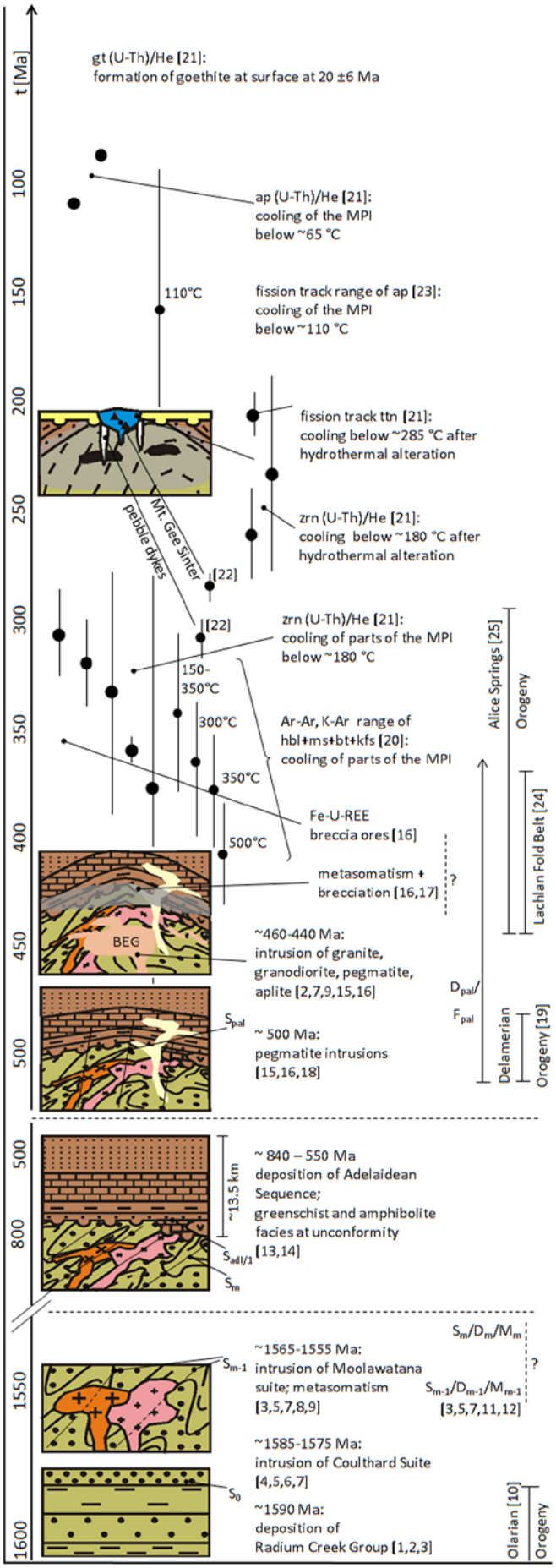

Fig. 2: Schematic summary of the geological and structural evolution of the Mount Painter region. A deformation event during Mesoproterozoic times formed a main foliation S_m in the metasediments and granites of the basement prior to the deposition of ~12 km thick Neoproterozoic Adelaidean basin sediments. Anticlinal folding that caused exhumation (published cooling ages and low-temperature thermochronology given in Weisheit et al. 2013b) of basement and cover occurred during the Palaeozoic and resulted in the formation of a Palaeozoic foliation S_{pal}. Magmatism and hydrothermal fluid flow affected the province during that time. The inlier reached the surface at ~300 Ma. Mineral abbreviations after Kretz 1983. Figure from Weisheit et al. (2013b). MPI: Mount Painter Inlier; BEG: British Empire Granite. 1. Fanning et al. (2003); 2. Wülser (2009); 3. Fraser & Neumann (2010); 4. Neumann (2001); 5. Elburg et al. (2001); 6. Steward & Foden (2003); 7. Elburg et al. (2012); 8. Sheard & Cockshell (1992); 9. McLaren et al. (2006); 10. Rutherford et al. (2007); 11. Paul et al. (1999); 12. Armit et al. (2012); 13. Wingate et al. (1998); 14. Preiss (2000); 15. Elburg et al. (2003); 16. Elburg et al. (2013); 17. Weisheit et al. (2013a); 18. Wülser et al. (2011); 19. Foden et al. (2006); 20. McLaren et al. (2002); 21. Weisheit et al. (2013b); 22. Brugger et al. (2011); 23. Mitchell et al. (2002); 24. Gray & Forster (2004); 25. Buick et al. (2008).

The activity of a large-scale hydrothermal fluid-flow system is indicated by a variety of metasomatic rock types that formed in the southern and central MPI during the Palaeozoic.

(a) Pegmatitic diopside-titanite veins intruded at ~440 Ma (Bakker and Elburg, 2006) and

(b) local phlogopitisation occurred at about the same time (Elburg et al., 2012).

(c) Uranium-rich hematite breccia ores formed at ~355 Ma as 100 m-scale sheets and lenses (Fig.1B; Elburg et al., 2013), while

(d) a quartz-hematite sinter (Mount Gee Sinter) overprinted all rock types locally. This sinter formed at the near-surface at ~290 Ma (Brugger et al., 2011) and was interpreted as a late stage of the magmatic-hydrothermal diopside-titanite veins (Bakker and Elburg, 2006).

(e) Soft, well weathered breccias of Adelaidean sediments and basement lithologies are located around the unconformity of the southern MPI (Fig.1B). The largest occurrences of these sedimentary breccias formed along the Paralana Fault Zone in basement rocks (Hidden Valley, Fig.1B; Weisheit et al., 2013a).

(f) Concentrated in the southern and central MPI is a large-scale K-feldspar metasomatism and brecciation (Fig.1B) that comes along with the breakdown of micas and the loss of original textures (Chapter 3). Potassium metasomatism and silicification in this area was already briefly discussed in the early literature by Coats and Blissett (1971) and Drexel and Major (1987).

These various hydrothermal rocks and breccias are found along the same structures with indicative overprinting relationships. However, only little was known about the Palaeozoic alteration system and detailed studies were missing at the beginning of this PhD-project.

Most metasomatic-hydrothermal rocks that have been found in the MPI formed after the deposition of the lower Adelaidean strata, which is locally affected by veins, brecciation and overprinting. Tectonic deformation structures are missing in the alteration products, but their major occurrence is along the hinge-zone of the anticlinal structure (Fig.1B; Chapter 3). Overprinting relationships suggest a particular geochemical evolution and focussing of the fluids during ascent in the crust (Chapter 3 and 5). The probably mid-crustal Palaeozoic alteration is, however, separated from the overprinting, near-surface Mount Gee Sinter event (Elburg et al., 2013). This conclusion is based on the observation that near-surface diamictitic pebble dykes (~315 Ma; Brugger et al., 2011) cut through K-feldspar altered rocks, but are overprinted by veins of the sinter event (Fig.2).

The recent landscape of the Mount Painter region formed during Neogene movement along the Paralana Fault System after a slight burial in Mesozoic times (Krieg et al., 1995; Célérier et al., 2005). The hydrothermal fluid flow stayed active up to recent times, as indicated by the activity of a hot spring in the region (Brugger et al., 2005; Weisheit et al., 2013b).

Scope of the project

As shown in the previous section, the hydrothermal evolution of the MPI, especially in Palaeozoic times, was poorly known and only individual hydrothermal rock types were studied prior to the start of this PhD-project. The Proterozoic and Palaeozoic tectonic evolution of the inlier was also ambiguous. Various published studies presented a variety of different interpretations, depending on the structural location and lithological properties of the study areas. To address the questions related to the mineralogical and structural evolution of the complex hydrothermal system in the MPI, a general model for the regional structural evolution of the Mount Painter region had to be found, with special attention on the Palaeozoic event(s).

The PhD-project thus focussed on several basic topics to interpret the dynamic evolution of the hydrothermal system. (a) Detailed hydrothermal and structural mapping and selected sampling of the major alteration zones, (b) analyses and interpretation of the various host rocks and (c) a model of the structural evolution of the inlier during the active fluid-flow.

(a) Detailed mapping of the (3D) architecture of the alteration area aimed to find the major fluid pathways and hence the probable source of the single fluid or the sources of several fluid-flow events (Chapter 2).

(b) Comprehensive petrological and geochemical analyses of various host rocks and alteration products were the base to identify the conditions and the properties of the fluids (Chapter 3). A detailed study of the Mesoproterozoic and the Palaeozoic magmatic host rocks was mainly done by M. Elburg and published in Elburg et al. (2013) and (2012) (Appendix 3 and 4).

(c) An interpretation of the regional tectonic activity during the fluid flow event gave the background to address the questions why the fluids moved (Appendix 1) and how breccias formed during fluid focussing (Appendix 2).

Methodology

The study of the hydrothermal system in the MPI in the framework of this PhD project is based on detailed geological mapping in the southern and central MPI and adjacent Adelaidean cover that were conducted during several field trips. The results of ten students mapping projects, mappings by the two supervisors and own mappings of the PhD candidate were used to reveal the structural and mineralogical architecture of the alteration area. Focuses of the geological maps were the extent and the character of the major alteration, as well as key areas in basement and cover to reconstruct the regional deformation history. The results are summarised in an extensive MapInfo/ArcGIS database

that includes new and published lithological, structural, geochemical, geochronological and airborne/satellite data. A detailed review of the mapping results is presented in Chapter 2.

Rock samples of host rocks and alteration products, as well as samples for microstructural analyses were taken at key outcrops in the field. After the preparation and the study of the thin sections, samples were selected for various geochemical (EMPA, ICPOES, XRD, $\delta^{18}O$, fluid inclusions, Lu-Hf) and geochronological (Rb-Sr, U-Pb, fission track, (U-Th)/He) analyses. Whole rock ICPOES measurements were conducted at the University of Ghent (under the supervision of M. Elburg). U-Pb and Lu-Hf analyses were done at the University of Oslo by M. Elburg and T. Andersen. The low temperature thermochronology was done in collaboration with M. Danišík (Curtin University, Perth) and E. Enkelmann (University of Tübingen). Fluid inclusion measurements with raman spectroscopy was conducted at the Montan-University of Leoben under the supervision of R. Bakker and the microthermometric analyses of the inclusions was done at the University of Tübingen. The electron microprobe in Tübingen was used for detailed spot analyses of doubly polished thin sections under the supervision of T. Wenzel. XRD, $\delta^{18}O$ and Rb-Sr measurements were done by the laboratory technician at the University of Tübingen under the supervision of H. Taubald (XRD, $\delta^{18}O$) and W. Siebel (Rb-Sr). Geostatistical analyses were done with the help of A. Soesoo (University of Tallin). A detailed description of the used methods and analysis software is given in Chapter 3 and 4. Geochemical analyses that are presented in the Appendix 3 and 4 were done by M. Elburg and others and discussed in detail in these publications.

Structural analyses and interpretations were conducted with diverse stereo-plot software and the 3D-drawing of the Yankaninna Anticline was conducted with the program move^{TM}2010 in the scope of a student project (K. Warber) under the supervision of P. Bons, University of Tübingen (Appendix 1). The presented structural reconstructions of the Mount Painter region are based on statistical measurements of foliation planes, lineations, faults and folds in the field and the relationships of various rock types to the observed deformation in the region.

Results and Discussion

Each following chapter of the PhD-thesis focuses on different research topics that are related to the study of the hydrothermal system in the MPI. A short summary of the main results and their discussion is given in the next sections.

Geological mapping (details in Chapter 2)

Several detailed geological maps were compiled during field trips between 2007 and 2011 by students of the University of Tübingen and the PhD candidate (2009-2011), supervised by P. Bons and M. Elburg. The mapping areas are concentrated along the extent of the K-feldspar metasomatism and related hydrothermal alteration in the southern and central MPI (Fig.3). Their size and scale vary with the major topic of the map, while important outcrops are mapped in greater detail and discussed in the students' mapping reports and in Chapter 2. Areas that include original, unaltered rocks are especially studied for their structures with special attention on the relationship between basement and cover lithologies. The detailed geological maps are connected by zones that are mapped in less detail to maintain an overview to the whole study area.

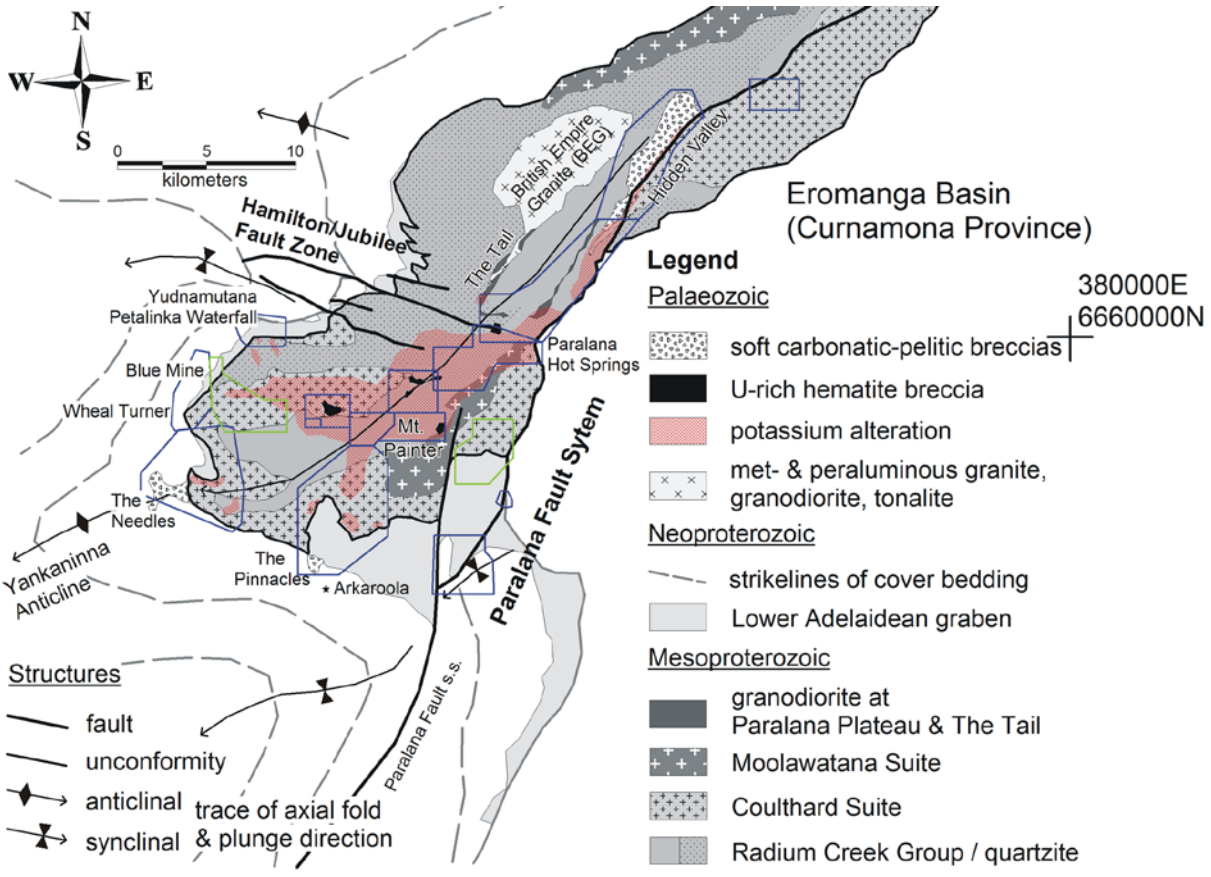

Fig.3: Main study area of the southern and central MPI with the location of the detailed geological maps (blue lines). Mapping is concentrated along the extent of the alteration zones and breccias and in areas that show the structural relation between basement units and cover. Green students' mapping areas are included in the discussion of Chapter 2 as overview areas.

The architecture of the alteration system and its relationship to the various host rocks could be resolved at the end of the comprehensive mapping project. An area of about 60 km² with outcrop depths exceeding ~500 m is altered into pinkish, K-feldspar-quartz-rich rocks and breccias in the southern and central MPI. The alteration is concentrated along the core of the Yankaninna Anticline and the Paralana Fault Zone, and it extends into adjacent cover rocks (Fig.3). Transitions from any unaltered, deformed host rock into a massive K-feldspar-quartz metasomatite are characteristic of the border areas at the alteration zone (Fig.4A+B). No macroscopic signature of the host rock may remain in the centre of the alteration and the metasomatites may be mistaken for granitic rocks ("granitisation" according to Coats and Blissett, 1971).

Observed metasomatites and breccias in the alteration zone vary in their mineralogy and texture and show various overprinting relationships to each other. K-feldspar-quartz cemented breccias for instance overprint the massive K-feldspar-quartz impregnated rocks (Fig.4C). Uranium-rich hematite breccias always overprint K-feldspar-quartz cemented breccias and are associated with chloritic-goethitic breccias. Chloritic breccias, however, may also be overprinted by K-feldspar-quartz breccias (Fig.4D). Hidden Valley type breccias overprint silicified breccias and both post-date the K-feldspar-quartz breccias and the hematite breccias. Details of the complex relationships of the massive metasomatites and the various breccias are given in Chapter 2.

The identified overprinting relationships indicate that fluid flow varied temporally and spatially and was guided by the regional structures in the MPI. Potassium alteration was active before and after the mantle-involved magmatic activity that resulted in the formation of the British Empire Granite, granodiorites, leuco-pegmatites and aplites at ~460/450 Ma (Elburg et al., 2003, 2013; McLaren et al., 2006) and the pegmatitic diopside-titanite veins at ~440 Ma (Bakker and Elburg, 2006). The uranium-rich hematite breccias formed at ~355 Ma (Elburg et al., 2013), probably from a fluid that transported the dissolved iron from the breakdown of the micas in the K-feldspar alteration zone (fluid properties and evolution is discussed in Chapter 3). These hematite breccias are in places overprinted by silicified breccias, indicating that fluid flow may have been active between ~460 and ~355 Ma, for possibly more than ~100 Myr. The near-surface sedimentary pebble dykes cut through the zone of K-feldspar alteration and brecciation. K-feldspar alteration thus formed before ~315 Ma (detrital zircon age of the pebble dyke, Brugger et al., 2011). The ~290 Ma, sub-surface quartz-hematite Mount Gee Sinter post-dates the pebble dykes (Brugger et al., 2011). It forms a large breccia zone building Mount Painter and the adjacent Mount Gee and can be found as veins and

breccias that are distributed in the southern and central MPI. The mineralogy and texture of the sub-surface Mount Gee Sinter is distinct from the K-feldspar alteration, indicating that at least two fluid flow systems were active after the deposition of the Adelaidean cover. Structural reconstructions of basement and cover in the MPI (Weisheit et al., 2013b) revealed a 200 Myr lasting period of exhumation from mid-crustal levels in Palaeozoic times. It is well possible that the fluid system that caused the extensive K-feldspar alteration and brecciation (prior to the Mount Gee Sinter) was also active during the exhumation.

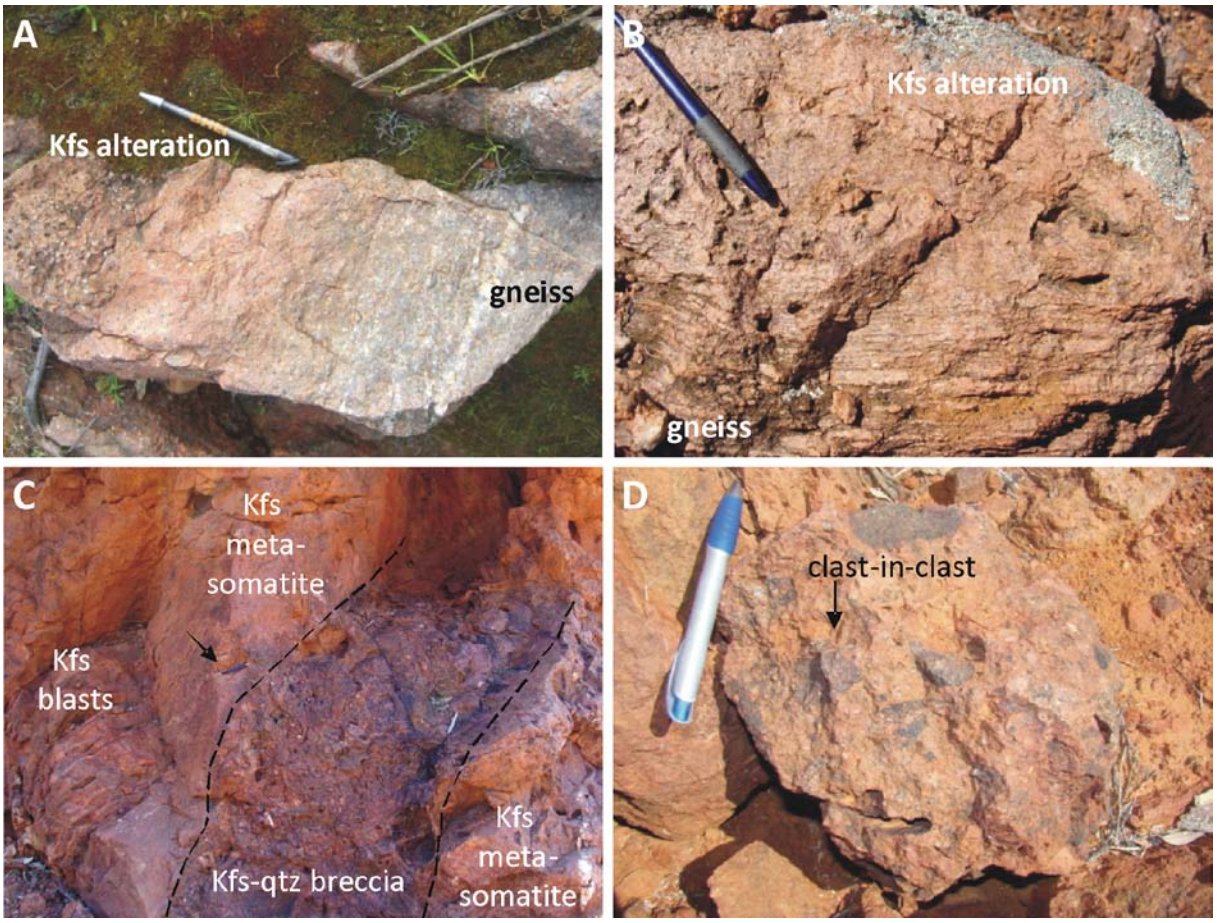

Fig.4: A) A deformed orthogneiss with quartz-augen is altered into a massive, pink K-feldspar-quartz-rich rock. K-feldspar blastesis is gradational and the quartz-augen remain in the less altered zones, indicating a hydrothermal alteration process instead of a leuco-granitic intrusion. B) K-feldspar alteration of a gneissic metapelite, resulting in the loss of texture and structure. Micas disappear and K-feldspar and quartz grow with increasing alteration. C) Overprinting relationships in the K-feldspar alteration zone. K-feldspar blasts grow parallel to the main foliation in a metapelite that gradually changes into a massive K-feldspar-quartz rock (Kfs metasomatite; arrow indicates pen for scale). This metasomatite is overprinted by a K-feldspar-quartz±hematite cemented breccia zone. D) K-feldspar-quartz breccias postdate chloritic breccias at some localities.

The study of the deformation in basement and cover rocks was focussed only on dominating structures that occur in most mapping areas and hence represent regional tectonics. After the end of the mapping project the following general sequence of deformation events could be defined (Fig.2).

Greenschist to amphibolite facies metamorphism and the formation of a foliation that is sub-parallel to the bedding of the metasediments in the basement (D1, M1, S_1 or S_{m-1}). A relict S_1 foliation is only recognisable in thin-sections of D2-deformed rocks.

The second deformation D2 affected all basement rocks and produced isoclinals folds (F2) at metamorphic conditions up to migmatitisation (M2). The foliation parallel to the axial plane of F2 is the main foliation in the basement and locally forms a shear fabric with a dextral sense of shear (S_m). S_m is cut by the unconformity between basement and Adelaidean cover sediments at an angle of ~10° and with a higher angle along local graben faults.

The last deformation of basement and cover occurred during the Palaeozoic (D_{pal}) and resulted in the formation of 10 km-scale open folds and a foliation or crenulation (S_{pal}) in suitable, mica-rich rocks. Continuing deformation in the Palaeozoic resulted in the successive overprinting of the folds and the formation of now NE-SW and E-W running anticlines and synclines (F_{pal}). Metamorphism in the early Palaeozoic was caused only by the passive burial of basement rocks below the basin sediments. Details on the structural reconstruction are given in Appendix 1.

Geochemical/geochronological analyses (details in Chapter 3)

A range of representative samples were taken for thin section, geochemical and geochronological analyses with special attention to the architecture of the mapped alteration system. The aim was to find geochemical variability on the thin section scale (using EMPA) between original, altered and new-grown minerals. Whole rock analyses (XRF and ICPOES) were aimed to determine element transport between host rocks and alteration products with various stages of overprinting. Fluid inclusion analyses and oxygen isotope measurements of selected samples were chosen to define the fluid properties and temperature/pressure conditions during alteration. Age and nature of zircons in totally altered rocks were analysed with U-Pb and Lu-Hf measurements and compared with results of published analyses of host rocks in the MPI. Finally Rb-Sr analyses of an altered and unaltered pegmatite were used to determine the age of the K-feldspar alteration at the edge of the alteration zone. The results of these measurements are summarised in detail in Chapter 3.

Potassium-altered rocks are mainly characterised by the breakdown of biotite and muscovite and the growth of K-feldspar and iron-oxides (Fig.5A). Other common reactions that are well visible in the thin section scale are muscovitisation (Fig.5B) and to a lesser extent chloritisation of biotite. The

alteration of plagioclase into microcline and the extensive new-growth of microcline may occur independently from the biotite breakdown. Altered biotite minerals are rich in magnesium (phlogopite) and the new-grown feldspars have an almost pure end-member composition (microcline and some albite; Fig.5C+D). Texture, composition and feldspar parageneses indicate that the alteration of the samples occurred during 200-300 °C hydrothermal alteration conditions.

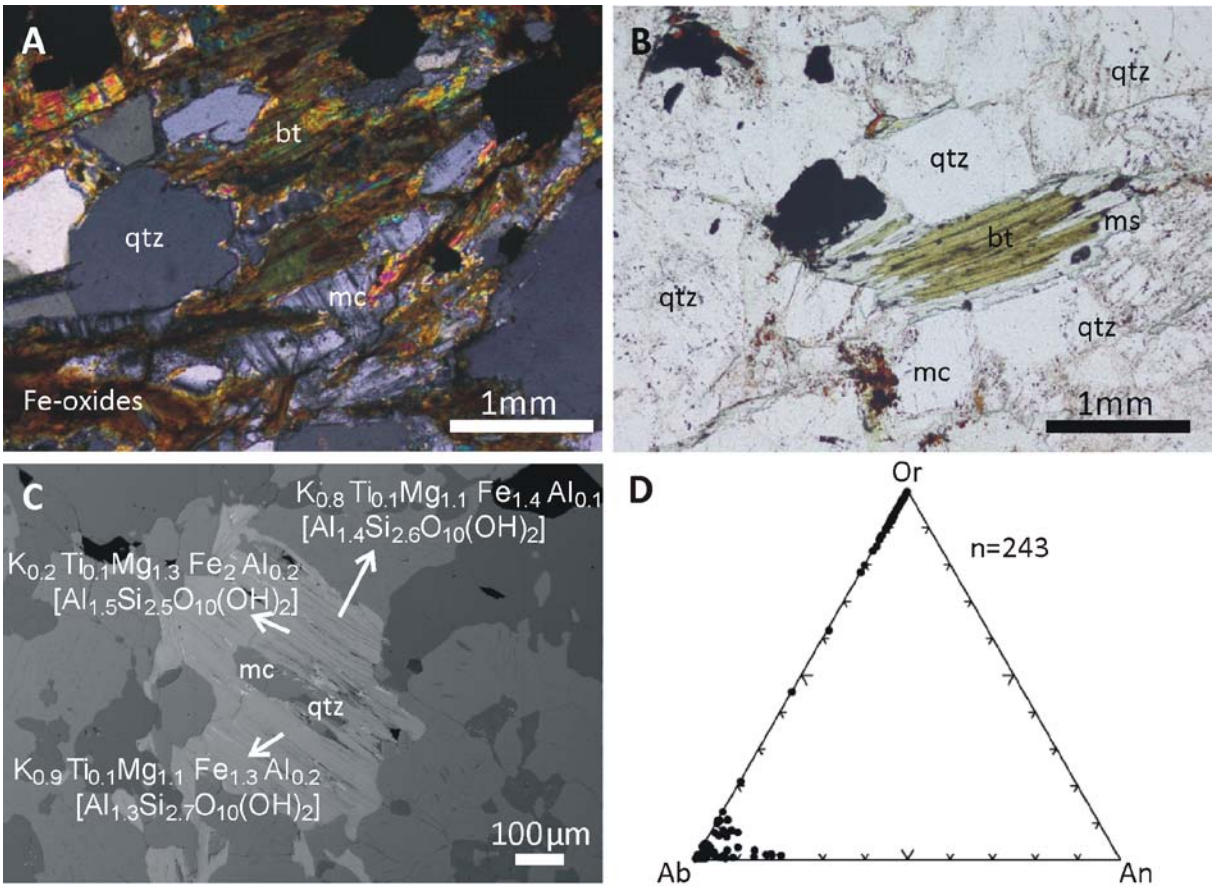

Fig.5: A) Characteristic reaction of a K-feldspar altered gneiss with quartz-augen. Biotite breaks down into microcline and iron-oxide. B) Biotite alters into muscovite in a gneiss at the K-feldspar alteration zone. C) Microprobe measurements of an altered biotite with inclusions of quartz and microcline reveal magnesium-, iron- and aluminium-rich compositions. D) Altered and new-grown feldspars in the K-feldspar alteration zone are of an almost end-member composition.

Whole rock analyses resulted in mainly scattered, overlapping signals between alteration products and host rocks due to a wide diversity of the host lithologies. Depletion in the MgO-content in altered samples is the only clear trend that is related to the breakdown of all mafic minerals (Fig.6A). A negative correlation between K_2O and Na_2O in all samples indicates a correlation between potassium and sodium mobility, which is independent from host rocks or alteration products (Fig.6B). A correlation between TiO_2 and Fe_2O_3 that is independent from the kind of the sample shows that the formation of iron-titanium-oxides and the breakdown of micas occurred at all levels of alteration

stages (Fig.6C). Only one pair of host rock and alteration product revealed an isocon plot that clearly shows an enrichment in K_2O and Rb, while Na_2O and CaO are depleted in the K-feldspar-enriched, altered sample (Fig.6D). The scattered signal in the whole rock analyses of most samples and sample pairs is a result of multiple alteration stages (albitisation, microclinisation, biotite breakdown, muscovitisation, muscovite breakdown, iron-titanium-oxide formation) and their spatial occurrences.

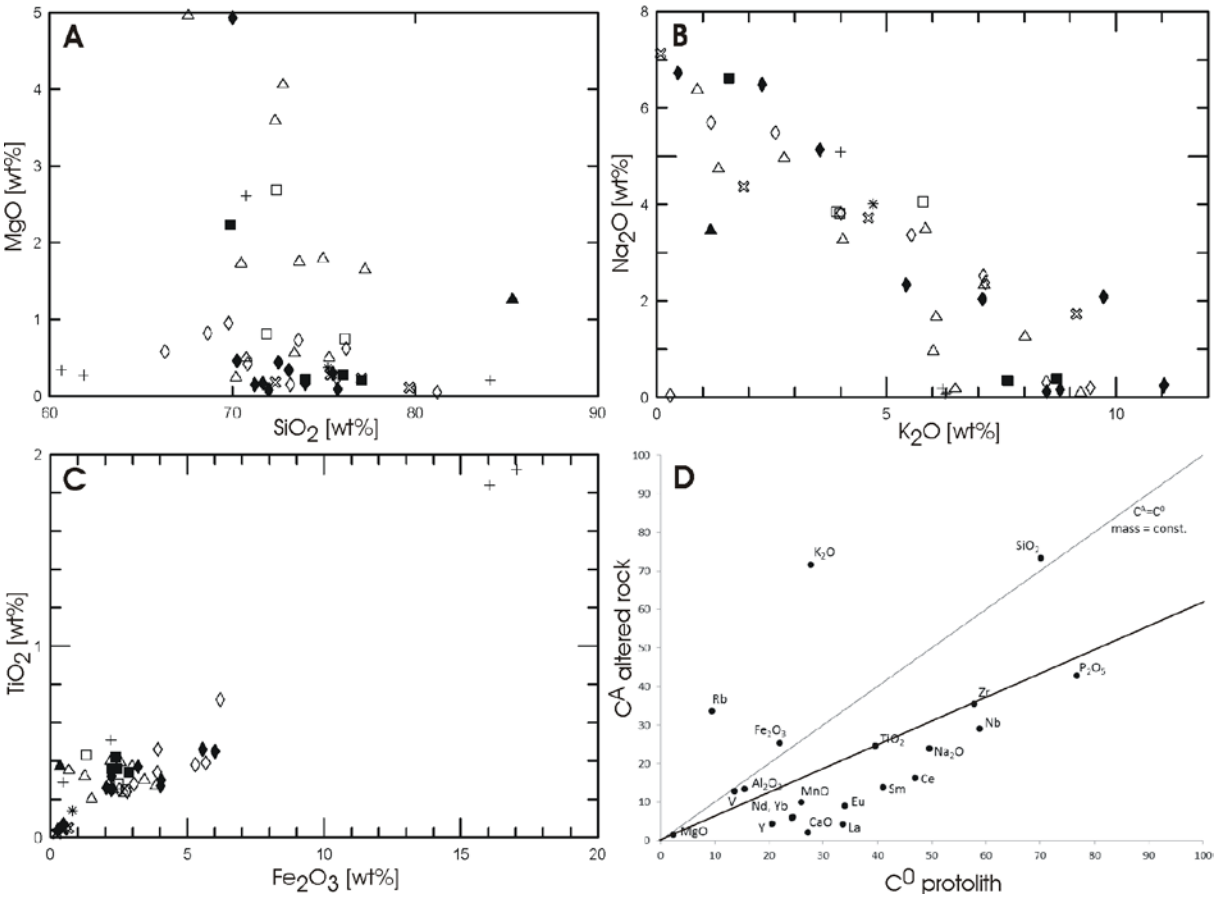

Fig.6: Results of whole rock analyses (details given in Chapter 3). A) K-feldspar altered rocks (square, diamond, plus) are depleted in MgO relative to original rocks (triangles). B) A negative correlation between Na_2O and K_2O and C) the positive correlation between TiO_2 and Fe_2O_3 are independent from the alteration. D) Isocon plot of a protolith and altered product that shows enrichment in K_2O + Rb (microclinisation) and depletion in CaO + Na_2O (breakdown of plagioclase). Fe_2O_3 (iron-oxides) is enriched, if the isocon is plotted through the immobile element Zr.

Data from fluid-inclusion measurements of quartz in altered samples and oxygen-isotope analyses of a K-feldspar-hematite and a quartz vein were highly scattered and could therefore not be used for general interpretations of the fluid properties.

U-Pb and Lu-Hf measurements of zircons that were extracted from totally altered samples resulted in signals that resemble the characteristic signals of granitoids in the basement. This result may be interpreted such that the measured samples represent magmatic leuco-pegmatites that

intruded either contemporaneous with the host granitoids or intruded later and were contaminated with the host's zircons. The observation of gradual mineralogical changes between altered samples and host rocks and the missing intrusive contacts indicate that these zircons are instead the relicts that remained after an extensive alteration of a host rock.

An undeformed pegmatite was chosen for whole-rock and muscovite Rb-Sr analyses of an unaltered and a K-feldspar-altered variety. Both samples revealed the same age (within error) of ~478 Ma. Variability between the initial $^{87}Sr/^{86}Sr$ ratios and the Rb-Sr ages indicate that the system stayed open during alteration processes after the formation of the pegmatite. Both analyses represent the crystallisation age of the pegmatite, which was only slightly disturbed by alteration. Potassium alteration hence occurred after ~478 Ma at this locality.

The complex overprinting relationships of mineral impregnations and brecciation in thin sections and the scattered signals in the geochemical analyses indicate that the alteration fluid evolved with time and interaction with the host rocks. A detailed model of the alteration system is presented in Chapter 3. Fluids likely derived from mid-crustal levels and were focused during their ascent, resulting in a spatial distribution of various alteration stages. The fluid sources are discussed in detail in Appendix 2, which concludes that fluids probably derived from trapped pore water that was released during decompression when the inlier was exhumed. Alteration occurred during ascent of the fluids causing a general sequence of mineral reactions (Fig.7). Biotite breakdown occurred at the lowermost level, possibly when pore-water fluids were released. This is followed by a level of alkali metasomatism and a stage of brecciation at increasing fluid focussing. Chloritisation, the formation of iron-oxide breccias and silicification occurred at lower temperature and pressure conditions. The proposed model incorporates the successive Palaeozoic exhumation of basement and cover rocks through the levels of alteration and brecciation. A decompression in the core of the Yankaninna Anticline resulted in the concentration of the main alteration in this area. The long-lived folding and exhumation of the inlier (discussed in the next section) probably caused a long-lived hydrothermal fluid flow that is expressed in the complex macroscopic and microscopic overprinting relationships.

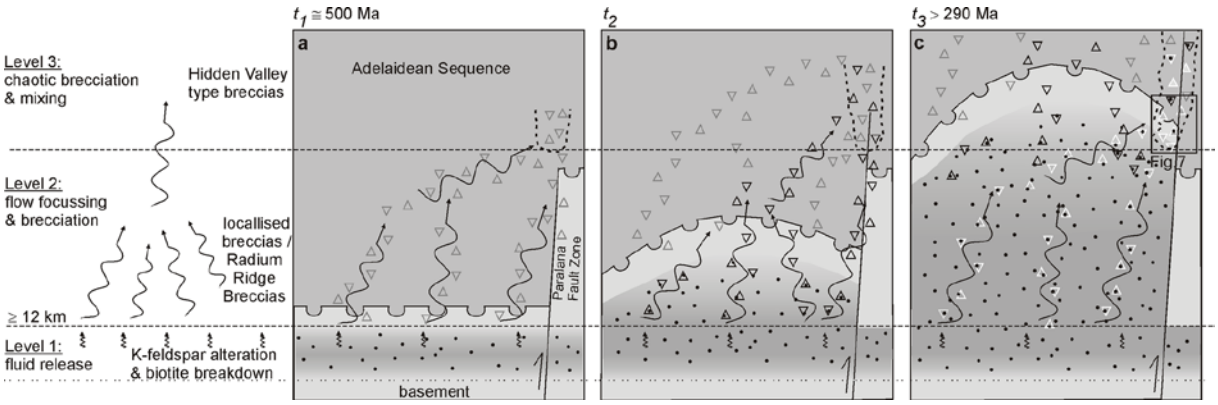

Fig.7: Model of the alteration system, folding and exhumation of the MPI in the Palaeozoic. Fluids that derived from trapped pore water fluids and/or biotite dehydration were released at mid-crustal levels in the core of the anticline. These fluids evolved in different levels of alteration (points), fluid focussing and brecciation (triangles). The Mount Painter rocks moved through the different levels during exhumation (a-c). As a result several stages of overprinting developed spatially and caused the formation of a complex alteration and brecciation system in the core of the anticline. Figure from Weisheit et al. (2013a).

Model of Palaeozoic tectonic evolution (details in Appendix 1)

The tectonic evolution of the Mount Painter region in the Palaeozoic is a key factor that controlled the hydrothermal system in the inlier, as indicated in the previous section. A comprehensive structural dataset of the mapping areas and additional published K-Ar cooling ages by McLaren et al. (2002) were used to reconstruct the timing of the prominent 10 km-scale folding in the region (Fig.1; Weisheit et al., 2013b). This thick-skinned folding was attributed to the Delamerian Orogeny at around 500 Ma (e.g. Paul et al., 1999). The exhumation of the fold belt subsequently occurred in steps during the Palaeozoic (McLaren et al., 2002).

McLaren et al. (2002) reported K-Ar and Ar-Ar hornblende, mica and K-feldspar analyses of basement and cover rocks. The cooling ages of the samples vary relative to their structural position in the major Yankaninna Anticline. Basement samples that derive from the core of the fold are significantly younger than samples from cover-sequence rocks at the anticline's limbs. The cooling ages can be understood if the situation at maximum burial depth (500 Ma) is known, as well as the shape of the current fold.

The lower Adelaidean sediments were deposited at ~800 Ma in half graben structures that ran about NW-SE above the MPI. This graben system was filled with flood basalts and sediments and deepened to ~2 km depth in the SE. Today this graben system crops out at the north-western and the south-eastern limb of the Yankaninna Anticline (Fig.1). Ongoing extension and regional subsidence resulted in the formation of the Adelaidean basin and the deposition of ~11 km upper Adelaidean sediments above the MPI until ~500 Ma. The westwards dipping Paralana Fault s.s. that strikes about

N-S east of Arkaroola (Fig.1) was active as a normal fault during the deposition of the Adelaidean sediments. Basement rocks were buried deepest west of the fault to ~13 km depth, while only ~9 km sediments were deposited east of it. The static metamorphism at the unconformity reached amphibolite facies conditions in the west and greenschist facies conditions in the east of the fault, at an assumed geothermal gradient of ~40 °C/km (based on studies by Mildren and Sandiford (1995) and Sandiford et al. (1998)).

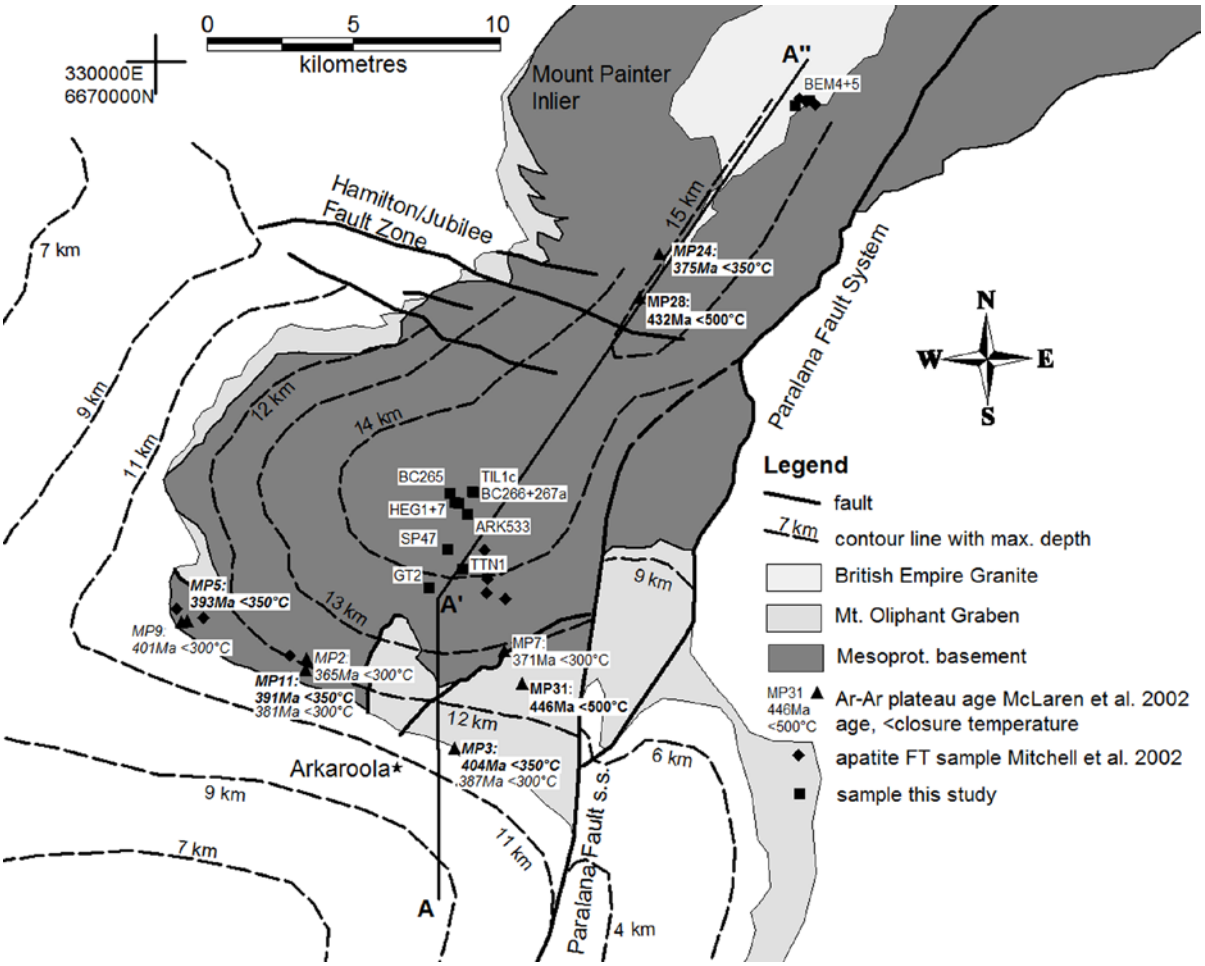

Fig.8: Simplified map of the southern MPI with contour lines of maximum burial depth after the deposition of the whole Adelaidean succession. The central MPI was buried deepest, down to ~15 km in the core of the anticline. K-Ar samples by McLaren et al. (2002) are located at various structural levels in the Yankaninna Anticline. Sample locations of low-temperature thermochronology analyses are also shown. See Fig.9 for profile A-A'-A''. Figure from Weisheit et al. (2013b).

Figure 8 illustrates the reconstructed contour lines of maximum burial depth of basement and cover rocks after the deposition of the whole Adelaidean strata. The deepest and youngest K-Ar samples of McLaren et al. (2002) were buried to ~ 15 km depth. Samples from the unconformity and the lower Adelaidean sediments reveal older cooling ages (Fig.8). These differences can be explained

with the structural position of the samples in the anticline and hence reflect the formation of the fold (Fig.9). Folding started between about 500 and 450 Ma and lasted until the formation of the sub-surface Mount Gee Sinter at ~290 Ma (Brugger et al., 2011). The average exhumation rate was low with ~0.1 km/Myr; however potential pulses of exhumation cannot be resolved in this study.

The crustal-scale folding at the MPI possibly started during the Delamerian Orogeny and lasted during the tectonic activities of the Alice Springs and the Lachlan Orogenies for ~200 Myr (Fig.2). Folding occurred during a long-lasting N-S compression in a wedge between the rigid Gawler Craton and the Curnamona Province. The Paralana Fault System acted as an oblique and lateral ramp onto the Curnamona Craton. The hanging wall became successively folded, tilted and re-folded, resulting in a major NE-SW striking anticline and smaller, E-W striking overprinting folds (Fig.1).

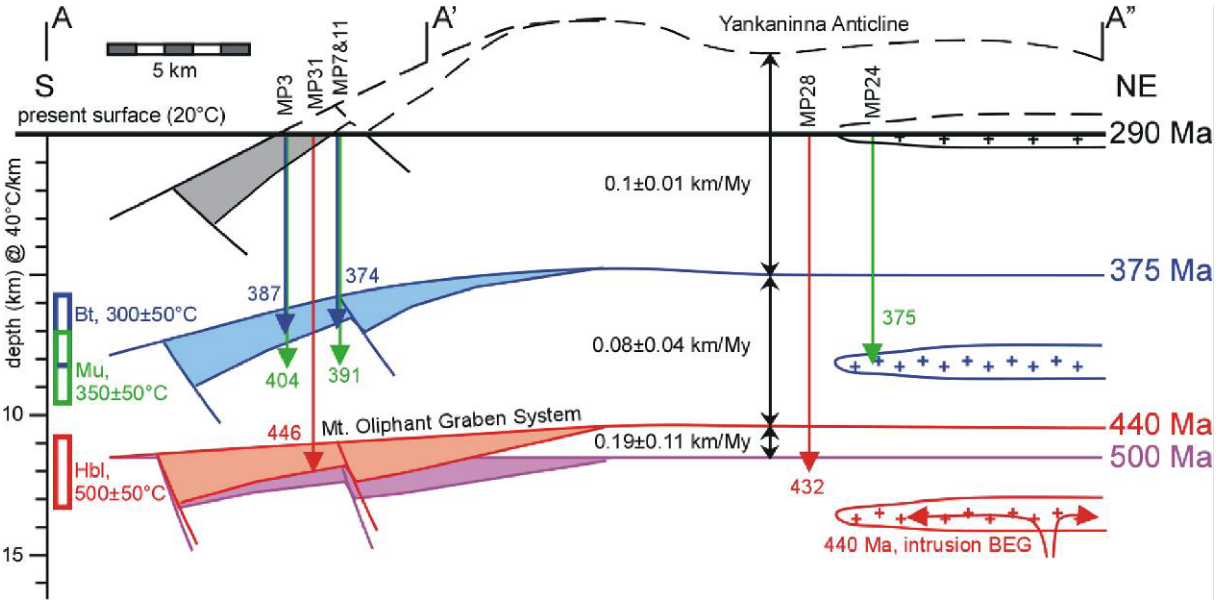

Fig.9: Time profile A-A'-A'' from the southern limb into the core of the Yankaninna Anticline (see Fig.8). The K-Ar cooling ages (McLaren et al., 2002) of samples that derive from various structural levels in the fold result from the crustal-scale folding and do not resemble a passive exhumation of an existing fold. Folding in the core of the anticline occurred with an average rate of ~0.1 km/Myr. Figure from Weisheit et al. (2013b).

Various samples from basement rocks in the southern MPI were selected for low-temperature thermochronology analyses to study the final exhumation of the inlier and the effect of a hydrothermal overprint by the Mount Gee Sinter event. A range of samples are younger than the general exhumation trend. They were probably reset by hot fluids of the sinter event, which was hence active for ~100 Myr. Details on the thermochronology study are given in Appendix 1.

Model of fluid-flow and brecciation processes (details in Appendix 2)

Long-lived Palaeozoic exhumation and the alteration system in the Mount Painter region are linked, as highlighted in the previous sections. Alteration is concentrated in the hinge of the rising Yankaninna Anticline and along the Paralana Fault System. Focussing of the alteration fluid in upper crustal levels resulted in the formation of large-scale K-feldspar-quartz cemented and silicified breccia zones in altered and non-altered rocks. But what happened with the fluids with further ascent through the crust? Are the Hidden Valley type breccias (Fig.1) that formed along fault zones and that include rounded clasts of basement and cover units related to this fluid flow system?

The results of statistical analyses of various breccia types in the MPI are presented and discussed in detail in Appendix 2. Clast shape and size distribution of the Hidden Valley type breccias (Fig.1; including breccias at The Pinnacles and at The Needles) were measured in micrographs, field images and on the map-scale, and compared with measurements on photographs of other MPI breccia types. All measurements are plotted in a log-log plot of the number of clasts larger than a certain area ($N_{\geq A}$) against that area (A). A straight line in this plot represents a fractal clast area distribution with a 2D fractal dimension D_{2D} according to the equation $N_{\geq A} = k*A^{-D2D}$ (e.g. Epstein 1947; Jébrak, 1997). The measured samples plot on a straight line with a fractal dimension of $D_{2D} = 1.03$ (Fig.10), implying that a single brecciation process formed the breccias in the alteration system. Exceptional is the fact that the fractal dimension is constant over 6 orders of magnitude from the 100 m-scale to <mm clast size of samples from the ~10 km² large Hidden Valley breccia. The Hidden Valley type breccias consist of almost 100 % clasts without a mineral cement. Clast shape parameters like circularity or ellipticity are similar for the various breccia types (Weisheit et al., 2013a).

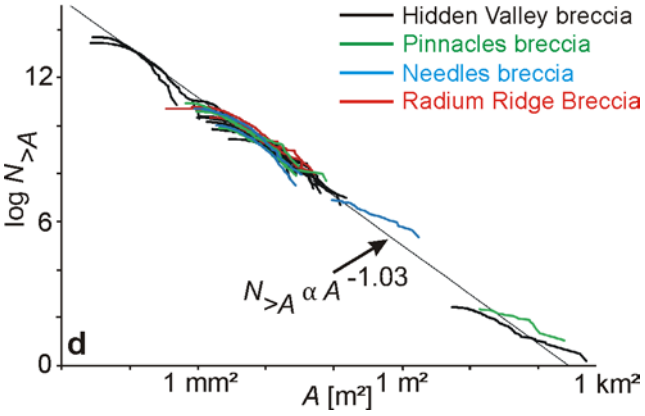

Fig.10: Fractal clast size distribution of all measured breccias in a log-log plot of number of clasts larger than a certain area ($N_{\geq A}$) against that area (A). $N_{>A}$ of all individual analyses was adjusted for a 3.2 km² area, to allow comparison between the different measurements. A straight line fits through all samples with a 2D fractal dimension of 1.03. The brecciation of Hidden Valley type breccias (Needles and Pinnacles) range from the 100 m down to the mm-scale. K-feldspar-quartz cemented Radium Ridge Breccias formed during a mechanically similar brecciation process. Figure from Weisheit et al. (2013a).

The characteristics of the breccias exclude chemical abrasion (no corrosive surfaces) and tectonic wear (no shear indicators) as major brecciation processes. The Hidden Valley type breccias formed during hydraulic fracturing and collapse/fluidisation. Fluids were focussed at the junction between the major Paralana Fault Zone and the hinge of the Yankaninna Anticline (Fig.1). Lower Adelaidean lithologies were brecciated together with basement rocks and both crop out together within basement units. The amount of fluids that is necessary to form the ~10 km² large Hidden Valley breccia is estimated to be ~5-30 km^3 in this study, assuming that the Adelaidean unconformity lies between 0.5 and 3 km above the present surface. Several potential fluid sources were considered. Fluid release from the British Empire Granite, as well as release of fluids in the thermal aureole of this intrusion (Staude et al., 2009) could potentially have provided up to ~ 6-12 km³. Biotite dehydration during the K-feldspar alteration could have produced ~10 km^3 of fluid, or more if the same alteration occurred east of the Paralana Fault system. Another fluid reservoir are pore fluids that were trapped in basement rocks prior to the deposition of the Adelaidean sediments. Decompression during the Palaeozoic may release ~5-10 km³ of these fluids (Staude et al., 2009), which can be focussed along major structures together with the other possible fluid sources (Weisheit et al., 2013a).

The model of alteration and brecciation in the Palaeozoic Mount Painter region (Fig.7) can now be extended to the formation of the Hidden Valley type breccias. Fluid focussing continued in the upper crust above the levels of K-feldspar alteration and brecciation. Single fluid batches (Bons, 2001) ascended and converged through zones of structural weakness like fault zones and fold hinges. At relative shallow levels, where the Hidden Valley type breccia formed, passage of fluid batches was dilatant and the fluid could lift clasts. These clasts moved down or up a certain distance after passage of the fluid batches and more material became brecciated and mixed (Fig.11). This process led to a single fractal size and shape distribution from the 100 m down to the mm-scale. The thorough mixing of lithologies in the breccia that have been originally kilometres apart stratigraphically is a result of contemporaneous brecciation at a certain level in the crust and exhumation of cover and basement rocks through this level (Fig.7).

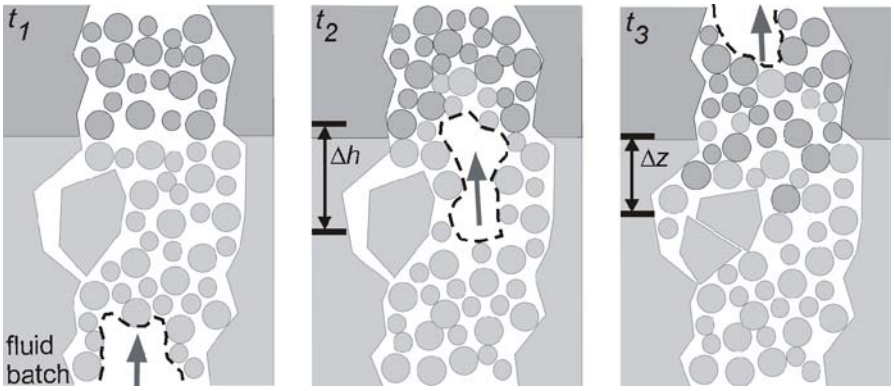

Fig.11: Schematic sketch of Hidden Valley type brecciation. Single fluid batches with a height Δh move through the zone of brecciation. Lifted clasts fall a distance Δz and brecciation continues after passage of the fluid. Figure from Weisheit et al. (2013a).

Timing of the hydrothermal system (details in Appendix 3)

The age of the extensive hydrothermal system in the MPI could be set between ≥ ~440 Ma (formation of a diopside-titanite vein in K-feldspar altered rocks; Bakker and Elburg, 2006) and >~290 Ma (detrital zircon age of a near-surface pebble dyke within K-feldspar altered rocks; Brugger et al., 2011). Additional geochronological analyses have been carried out parallel to this PhD project to further evaluate the timing of the hydrothermal system. Zircon U-Pb analyses of pegmatitic/granitic samples from a dyke-swarm in the southern MPI revealed weighted average intrusion ages of 462 and 455 Ma. These pegmatites partly intrude K-feldspar altered rocks and are overprinted by K-feldspar blasts. The K-feldspar alteration was hence active at least between ≥ ~460 Ma and ≤ ~440 Ma during the Ordovician magmatic activity. A missing aureole of K-feldspar altered rocks around the British Empire Granite body indicates that alteration occurred independently from that magmatism. Hf isotopic ratios and Nd isotopic characteristics (Elburg et al., 2012) point towards a mantle input during the pegmatitic/granitic intrusions between ~500 and ~440 Ma in the MPI, suggesting that folding of the Yankaninna Anticline, exhumation of the mantle and hydrothermal activity are linked.

Monazite U-Pb analyses of samples from U-rich iron-ore breccias resulted in a weighted average formation age of 355 Ma (Elburg et al., 2012). These magnetite-hematite breccias formed as lenses on the 100 m-scale within K-feldspar altered rocks and breccias, but they predate chloritisation and silicification in the southern and central MPI. The (sub-economic) iron-ore breccias are a result of purely intracrustal reworking (whole rock Sm-Nd systematics) and were formed during the evolution of the Palaeozoic hydrothermal system (Chapter 3). Fluid flow was hence active between ≥ 460 Ma and ~355 Ma either during a constant release of fluids while the inlier exhumed or during separate pulses.

Hyperaluminous rocks (details in Appendix 4)

Basement rocks in the southern and central MPI can be locally altered into light-coloured, undeformed phlogopitites that may include corundum, spinel, sapphirine and/or sillimanite. These hyperaluminous rocks postdate the strong Mesoproterozoic deformation events and are probably related to the Palaeozoic alteration system. Other, darker biotite schists have biotites that form the main Proterozoic foliation S_m and refolded in the style of the Palaeozoic folding. Biotitisation hence already occurred in the Mesoproterozoic after the formation of the Moolawatana Suite, independent of the much younger phlogopitites.

Geochemistry, Hf isotopic composition and U-Pb age of zircon cores from the hyperaluminous samples and the whole rock Nd isotopic ratios (carried out mainly by M. Elburg) are indistinguishable from samples of the host basement granites. The phlogopitites are hence an alteration product that formed during progressive Mg-metasomatism and desilicification. Zircon rims from two measured samples yield a plateau age of ~455 Ma, which is contemporaneous with the activity of the British Empire Granite/pegmatite magmatism and with the major K-feldspar alteration (Elburg et al., 2013).

The hyperaluminous rocks are not included in detail in the interpretation of the Palaeozoic hydrothermal system (Chapter 3). A mobilisation of magnesium during the breakdown of the micas and a change in the fluid properties during the fluid-rock interactions are, however, likely to result in local Mg-metasomatism and desilicification. The combination of fluid release, fluid focussing and contemporaneous exhumation was an effective recipe to kindle temporally and spatially dependent mineral reactions. That resulted in a large variety of metasomatites and breccias; a complex system, which required a combination of various structural, geochemical and geochronological methods in this study.

Open questions and future work

The model resulting from this research shows that tectonics and hydrothermal evolution of the Mount Painter region in the Palaeozoic are linked. A long-lived exhumation during ramping along the major Paralana Fault System resulted in ongoing release of fluids at a certain level in the middle crust. Alteration occurred in upper crustal levels at conditions, where elements like alkalis, iron and magnesium were mobile. Fluids were focussed during ascent along major structures, and a complex architecture of alteration and brecciation developed in basement and cover rocks as the inlier exhumed either constantly or in pulses through the zones of hydrothermal overprinting. The conditions of the fluid or the parameters of the various mineral reactions that took place within the alteration system could not yet be resolved. Samples were usually affected by several overprints that probably occurred at different points in space and time in the evolving system. Additionally, original, unaffected samples are rare and specific enrichments or depletion in elements at certain reactions could not be differentiated. The dataset can be completed with more samples from the outer areas of the alteration zone. However, a large range of statistical analyses is necessary to reconstruct the complex and widespread system in detail.

The Palaeozoic geological setting of the Mount Painter region is likely not unique and similar crustal alteration, brecciation and mineralisation systems may have developed elsewhere. Structures in the northern Adelaide Fold and Thrust Belt resemble those at the MPI. Adelaidean cover rocks form 10 km-scale anticlines and synclines, suggesting that basement rocks south of the MPI were exhumed close to the surface. “Diapiric” structures brought clasts of lower Adelaidean and basement rocks at the surface at major faults and fold hinges (e.g. Backé et al., 2010). These zones are traditionally interpreted as salt diapirs that arise from lower Adelaidean stratigraphy, but their setting and texture is similar to the Hidden Valley type breccias in the MPI. Crustal-scale deformation in the northern Adelaide Fold and Thrust Belt is attributed to the short-term Delamerian Orogeny that lasted for ~20 Myr in the southern Adelaide Fold and Thrust Belt. Detailed mapping at key structures and geochronological analyses of samples from different structural positions in the folds have to be conducted to possibly extend the proposed model of the Palaeozoic evolution of the Mount Painter region to the Northern Adelaide Fold and Thrust Belt.

A comparison of areas with similar geological setting to the MPI worldwide can help to improve and generalise the model of contemporaneous exhumation and hydrothermal fluid flow. The research on alterations and mineralisations that are bound on such settings is of economic interest and may lead to the discovery of economic ore deposits in the case of suitable host lithologies and fluid chemistry.

References

Armit, R.J., Betts, P.G., Schaefer, B.F., Ailleres, L., 2012. Constraints on long-lived Mesoproterozoic and Palaeozoic deformational events and crustal architecture in the northern Mount Painter Province, Australia. Gondwana Research, 22, 207–226.

Backé, G., Baines, G., Giles, D., Preiss, W., Alesci, A., 2010. Basin geometry and salt diapirs in the Flinders Ranges, South Australia: insights gained from geologically-constrained modeling of potential field data. Marine and Petroleum Geology, 27, 650–665.

Bakker, R.J., Elburg, M.A., 2006. A magmatic-hydrothermal transition in Arkaroola (Northern Flinders Ranges, South Australia): from diopside-titanite pegmatites to hematite-quartz growth. Contributions to Mineralogy and Petrology, 152, 541-569.

Brugger, J., Wülser, P.-A., Foden, J., 2011. Genesis and preservation of a uranium-rich Paleozoic epithermal system with a surface expression (Northern Flinders Ranges, South Australia): Radiogenic heat driving regional hydrothermal circulation over geological timescales. Astrobiology, 11, 499-508.

Brugger, J., Long, N., McPhail, D.C., Plimer, I., 2005. An active amagmatic hydrothermal system: The Paralana hot springs, Northern Flinders Ranges, South Australia. Chemical Geology, 222, 35-64.

Buick, I.S., Storkey, A., Williams, I.S., 2008. Timing relationships between pegmatite emplacement, metamorphism and deformation during the intra-plate Alice Springs Orogeny, central Australia. Journal of Metamorphic Geology, 26, 915-936.

Célérier, J., Sandiford, M., Lundbek Hansen, D., Quigley, M., 2005. Modes of active intraplate deformation, Flinders Ranges, Australia. Tectonics, 24.

Coats, R.P., Blissett, A.H., 1971. Regional and economic geology of the Mount Painter Province, South Australia. Geological Survey of South Australia, Bulletin 43, 425p.

Cowley, W.M., Hore, S.B., Preiss, W.V., Sheard, M.J., Wade C., 2012. A revised stratigraphic scheme for the Mount Painter and Mount Babbage Inliers. SAREIC 2012 Technical forum poster. published in the web http://minerals.dmitre.sa.gov.au/press_and_events/events/sareic_2012_technical_forum.

Drexel, J.F., Major, R.B., 1987. Geology of the uraniferous breccia near Mt Painter, South Australia and revision of rock nomenclature. Geological Survey of South Australia. Quarterly Notes, 104, 14-24.

Elburg, M.A., Andersen, T., Bons, P.D., Simonsen, S.L., Weisheit, A., 2013. New constraints on Phanerozoic magmatic and hydrothermal events in the Mt Painter Province, South Australia. Gondwana Research 24, 700-712. doi: 10.1016/j.gr.2012.12.017.

Elburg, M.A., Andersen, T., Bons, P.D., Weisheit, A., Simonsen, S.L., Smet, I., 2012. Metasomatism and metallogeny of A-type granites of the Mt Painter–Mt Babbage Inliers, South Australia. Lithos, 151, 83–104.

Elburg, M.A., Bons, P.D., Foden, J., Brugger, J., 2003. A newly defined Late Ordovician magmatic-thermal event in the Mt Painter Province, Northern Flinders Ranges, South Australia. Australian Journal of Earth Sciences, 50, 611-631.

Elburg, M.A., Bons, P.D., Dougherty-Page, J., Janka, C.E., Neumann, N., Schaefer, B., 2001. Age and metasomatic alteration of the Mt Neill Granite at Nooldoonooldoona Waterhole, Mt Painter Inlier, South Australia. Australian Journal of Earth Sciences, 48, 721-730.

Epstein, B., 1947. The mathematical description of certain breakage mechanism leading to the logarithmic-normal distribution. J. Franklin Institute, 244, 471-477.

Fanning, C.M., Teale, G.S., Robertson, R.S., 2003. Is there a Willyama Supergroup sequence in the Mount Painter Inlier? In: Peljo, M. (compiler) Broken Hill Exploration Initiative: Abstracts from the July 2003 conference. Geoscience Australia Record 2003/13, 38-41.

Foden, J., Elburg, M.A., Dougherty-Page, J., Burtt, A., 2006. The timing and duration of the Delamerian Orogeny: Correlation with the Ross Orogen and implications for Gondwana assembly. Journal of Geology, 114, 189-210.

Fraser, G.L., Neumann, N.L., 2010. New SHRIMP U-Pb zircon ages from the Gawler Craton and Curnamona Province, South Australia, 2008-2010. Geoscience Australia Record 2010/16, 192-254.

Gray, D.R., Foster, D.A., 2004. Tectonic evolution of the Lachlan Orogen, southeast Australia: historical review, data synthesis and modern perspectives. Australian Journal of Earth Sciences, 51, 773-817.

Jébrak, M., 1997. Hydrothermal breccias in vein-type ore deposits: A review of mechanisms, morphology and size distribution. Ore Geology Reviews, 12, 111-134.

Kositcin, N., 2010. Geodynamic synthesis of the Gawler Craton and Curnamona Province, Geoscience Australia, Record, 2010/27, 113p.

Krieg, G., Alexander, E.M., Rogers, P.A., 1995. Eromanga Basin, In: Drexel J. F., Preiss W. V. (eds) The geology of South Australia, vol. 2, The Phanerozoic. South Australia. Geological Survey, Bulletin 54, 101-105.

McLaren, S., Sandiford, M., Powell, R., Neumann, N., Woodhead, J., 2006. Palaeozoic intraplate crustal anatexis in the Mount Painter Province, South Australia; timing, thermal budgets and the role of crustal heat production. Journal of Petrology, 47, 2281-2302.

McLaren, S.N., Dunlap, W.J., Sandiford, M., McDougalln, I., 2002. Thermochronology of high heat-producing crust at Mount Painter, South Australia: Implications for tectonic reactivation of continental interiors. Tectonics, 21, doi. 10.1029/2000TC001275.

Mildren, S.D., Sandiford, M., 1995. Heat refraction and low-pressure metamorphism in the Northern Flinders Ranges, South Australia. Australian Journal of Earth Sciences, 42, 241-247.

Mitchell, M.M., Kohn, B.P., O'Sullivan, P.B., Hartley, M.J., Foster, D.A., 2002. Low-temperature thermochronology of the Mt Painter Province, South Australia. Australian Journal of Earth Sciences, 49, 551-563.

Neumann, N., 2001. Geochemical and isotopic characteristics of South Australian Proterozoic granites: implications for the origin and evolution of high heat-producing terrains. Department of Geology and Geophysics. PhD thesis University of Adelaide.

Paul, E., Flöttmann, T., Sandiford, M., 1999. Structural geometry and controls on basement-involved deformation in the northern Flinders Granges, Adelaide Fold Belt, South Australia. Australian Journal of Earth Sciences, 46, 343-354.

Plümper, O., Putnis, A., 2009. The complex hydrothermal history of granitic rocks: multiple feldspar replacement reactions under subsolidus conditions. Journal of Petrology, 50, 967-987.

Preiss, W.V., 2000. The Adelaide Geosyncline of South Australia and its significance in Neoproterozoic continental reconstruction. Precambrian Research, 100, 21–63.

Preiss, W.V., 1987. The Adelaide Geosyncline — Late Proterozoic stratigraphy, sedimentation, paleontology, and tectonics. South Australian Geological Survey Bulletin, 53, 438p.

Raimondo, T., Clark, C., Hand, M., Faure, K., 2011. Assessing the geochemical and tectonic impacts of fluid-rock interaction in mid-crustal shear zones: a case study from the intracontinental Alice Springs Orogen, central Australia. Journal of Metamorphic Geology, 29, 821-850.

Rohrmeier, M.K., von Quadt, A., Driesner, T., Heinrich, C.A., Handler, R., Ovtcharova, M., Ivanov, Z., Petrov, P., Sarov, S., Peytcheva, I., 2013. Post-Orogenic Extension and Hydrothermal Ore Formation: High-Precision Geochronology of the Central Rhodopian Metamorphic Core Complex (Bulgaria-Greece). Economic Geology, 108, 691-718.

Rutherford, L., Hand, M., Barovich, K., 2007. Timing of Proterozoic metamorphism in the southern Curnamona Province: implications for tectonic models and continental reconstructions. Australian Journal of Earth Sciences, 54, 65-81.

Sandiford, M., Hand, M., McLaren, S., 1998. High geothermal gradient metamorphism during thermal subsidence. Earth and Planetary Science Letters, 163, 149-165.

Sandström, B., Annersten, H., Tullborg, E.L., 2010. Fracture-related hydrothermal alteration of metagranitic rock and associated changes in mineralogy, geochemistry and degree of oxidation: a case study at Forsmark, central Sweden. International Journal of Earth Sciences, 99, 1-25.

Sheard, M., Cockshell, C.D., 1992. Seismic interpretation of Mt. Hopeless Line 1. Department of Energy and Science SA Report book 92/17, 176p.

Stewart, K., Foden, J., 2003. Mesoproterozoic granites of South Australia. Department of Primary Industries and Resources Report Book 2003/15, 142p.

Weisheit, A., Bons, P.D., Elburg, M.A., 2013a. Long-lived crustal fluid-flow: the hydrothermal mega-breccia of Hidden Valley, Mt. Painter Inlier, South Australia. International Journal of Earth Sciences, 102, 1219-1236, doi: 10.1007/s00531-013-0875-7.

Weisheit, A., Bons, P.D., Danišík, M., Elburg, M.A., 2013b. Crustal-scale folding: Palaeozoic deformation of the Mt. Painter Inlier, South Australia. Journal of the Geological Society, in press.

Wingate, M.T.D., Campbell, I.H., Compston, W., Gibson, G.M., 1998. Ion microprobe U–Pb ages for Neoproterozoic basaltic magmatism in south-central Australia and implications for the breakup of Rodinia. Precambrian Research, 87, 135–159.

Wülser, P.-A., Brugger, J., Foden, J., Pfeifer, H.-R., 2011. The sandstone-hosted Beverley uranium deposit, Lake Frome Basin, South Australia: Mineralogy, geochemistry, and a time-constrained model for its genesis. Economig Geology, 106, 835-867.

Wülser, P.-A., 2009. Uranium metallogeny in the Northern Flinders Ranges region of South Australia. Ph.D. thesis, University of Adelaide.

---------- **CHAPTER 2 (MAPPING REPORT)** ----------

Geological mapping

of the southern Mount Painter Inlier, South Australia

by

Anett Weisheit and Paul D. Bons,

Department of Geosciences, Eberhad Karls University Tübingen, Germany

August, 2013

Table of Contents

1. Abstract

Mesoproterozoic basement and Neoproterozoic to Cambrian cover rocks of the Mount Painter region in South Australia experienced an extensive, long-lived hydrothermal fluid flow event during the Palaeozoic. An area of ~60 km² is altered and brecciated along major pre-existing structures in the southern and central Mount Painter Inlier. Detailed geological maps with a focus on the hydrothermal overprint and deformation structures by Staff and students of the Universities of Tübingen and Ghent (now KwaZulu-Natal) during fieldtrips between 2007 and 2011 are compiled in this report. The maps are located along the extent of the metasomatic overprint. They introduce new hydrothermal lithologies and differentiate between several alteration rocks and breccias.

The most extensive and obvious alteration of any host rock in basement and cover of the southern Mount Painter Inlier is an extensive impregnation and overprint with K-feldspar and quartz. Host rocks may completely change into igneous-like leuco-pegmatitic rocks in the centre of the alteration. Relict biotites and microcline rims around alkali-feldspars and plagioclases in less altered areas are clear indications for a hydrothermal overprint. These metasomatites are often overprinted by K-feldspar-quartz cemented breccias that formed during focussing of the fluids along structurally preffered fluid pathways. The K-feldspar alteration follows foliation planes and fault zones in the basement and is concentrated along the axial plane of the 10 km-scale Yankaninna Anticline. Our structural reconstructions indicate that this fold formed during long-lasting deformation in Palaeozoic times. Age relationships of the K-feldspar alteration zone to pegmatites and iron-oxide-U-Cu ores indicate that fluid flow was active during the formation of the anticline at least between ~478 and ~355 Ma.

We propose a model where trapped, highly saline pore fluids, as well as fluids released by biotite breakdown were released during decompression in the core of the rising Yankaninna Anticline. The ascending fluids caused alteration and hydrothermal brecciation in certain levels of the crust. Basement and cover rocks moved through these levels during the exhumation in Palaeozoic times, resulting in a complex architecture of a large-scale alteration system. K-feldspar-quartz cemented breccias are overprinted by chloritic to hematitic (martite) breccia sheets that are host to uranium and copper mineralisations. The latter breccias formed at a late stage in the alteration system at certain redox-horizons and got overprinted by silicified rocks and breccias. When overprinted by the silica-fluid, the uranium-bearing hematite breccias got leached and therefore less prospective.

Silicification in the Mount Painter Inlier is partly a result of a sinter event that formed several generations of quartz-hematite sinter breccias and veins. This Mount Gee Sinter formed at ~290 Ma at the sub-surface and hence marks the time when the inlier exhumed to the surface at the latest. Low temperature thermochronology on apatites of host rocks adjacent to the sinter indicate a long-lived activity of the sinter fluids for over ~100 Myr.

Additional points of interest of this report are the origin of the Pepegoona “Porphyry” unit and the various granodiorites in the basement inlier. Geological mapping and geochemical analyses of the Pepegoona “Porphyry” at diverse outcrops in the inlier indicate that this unit describes areas of metasomatic overprints of various host rocks, including a porphyritic granite. The granodiorites in the inlier can be divided into deformed Mesoproterozoic and undeformed Palaeozoic varieties.

2. Introduction

The Mount Painter Inlier is a small tectonic window (approx. 600 km^2) in the far north of the Flinders Ranges in South Australia. Proterozoic metamorphic and (meta-) igneous rocks are exposed in a large anticline (Yankaninna Anticline; Coats and Blissett, 1971), surrounded by the mostly sedimentary Neoproterozoic (≤800-500 Ma; Preiss, 2000) Adelaidean succession, except to the east, where the inlier is fault-bound and in contact with recent sediments that cover the Curamona Province (Coats and Blissett, 1971). The Mount Painter Inlier has attracted ongoing exploration, in particular for its small copper deposits (late 19th century) and later for its U-bearing iron-oxide breccias. These are expressions of the major Palaeozoic hydrothermal activity in this area.

This report is a compilation of various mapping and sampling campaigns in and around the Mount Painter Inlier (MPI), carried out by Paul Bons and students from the Eberhard Karls University Tübingen, in collaboration with Marlina Elburg (now at the University of KwaZulu-Natal, South Africa) and Ronald Bakker (Montanuniversität Leoben, Austria). The main focus of the studies is the hydrothermal overprint of Mesoproterozoic basement and Neoproterozoic cover rocks and the structural control of fold axial planes, foliations and faults on the fluid flow. Areas most affected by hydrothermal activity were mapped in detail as student mapping projects. Surrounding areas were mapped and sampled in less detail, mostly by Weisheit, Bons and Elburg.

3. Regional geology of the Mount Painter region

The metasediments and the meta-igneous rocks of the Mount Painter Inlier (MPI) and the adjacent, smaller Mount Babbage Inlier (MBI), have been interpreted as part of the Palaeoproterozoic Curnamona Province (i.e. Moolawatana Domain) (e.g. Sheard, 1992; Teale, 1993a+b; Conor and Preiss, 2008), which include e.g. the Olary and Broken Hill Domains in New South Wales (Fig. 1). The Curnamona Province is separated from the Archaean Gawler Craton to the west by a folded, intercratonic sedimentary basin, the Neoproterozoic to Cambrian Adelaide "Geosyncline" (=Adelaide Fold and Thrust Belt; Preiss, 1987; Preiss, 2000). The MPI and the MBI form tectonic windows in the core of the Yankaninna Anticline at the northern-most end of exposures of the fold belt in the Flinders Ranges. An angular unconformity separates basement, with sheared and multiply deformed metamorphics and meta-igneous rocks, from ~ 12 km thick Adelaidean basin (meta-)sediments (Coats and Blissett, 1971). Several studies conclude that the thick-skinned folding of the basin in the northern Adelaide Fold and Thrust Belt is a result of the Delamerian Orogeny that formed the southern belt at ~500 Ma (Mildren and Sandiford, 1995; Paul, 1998; Elburg et al., 2003; Foden et al., 2006). McLaren et al. (2002, 2006) and Armit et al. (2012) discuss a re-folding effect on the Yankaninna Anticline by the Alice Springs Orogeny. This orogeny is most relevant in the centre of Australia at ~450-300 Ma (Buick et al., 2008). Based on the mapping of this study and K-Ar analyses by McLaren et al. (2002), Weisheit et al. (2013b) concluded that the anticline formed during a long-lived deformation event between ~500-300 Ma.

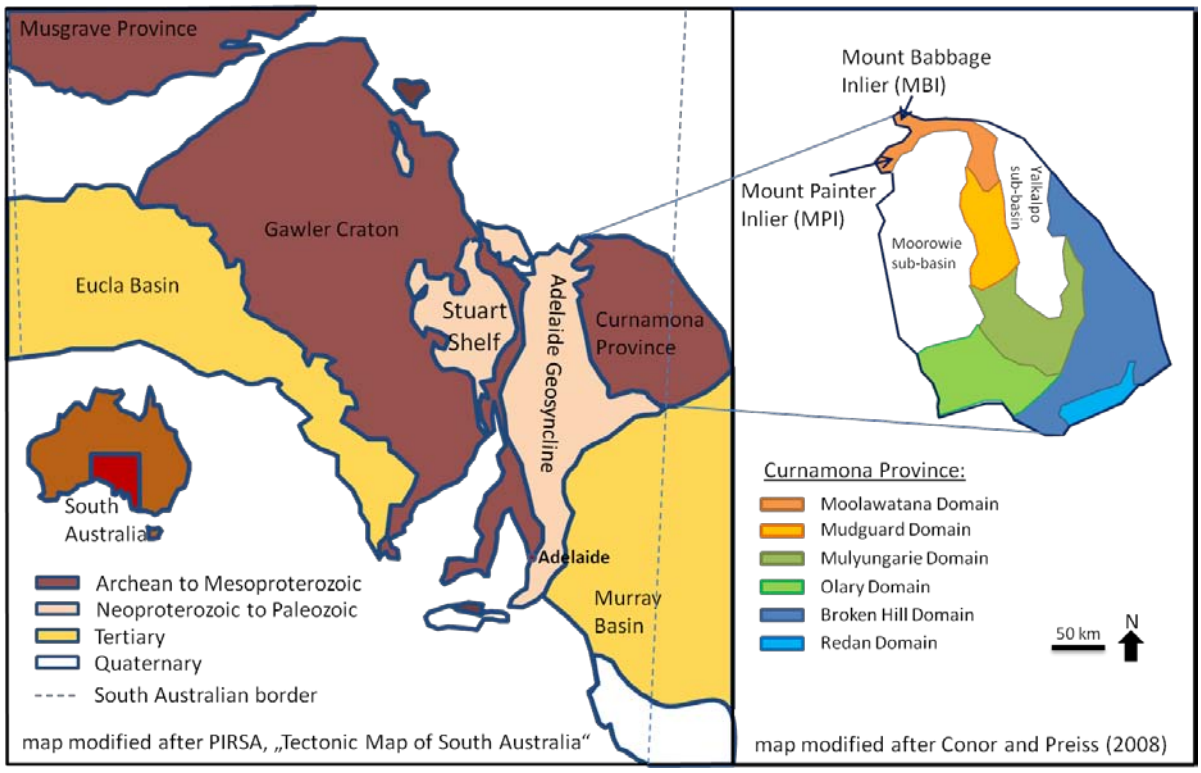

Fig. 1: Overview to the major geolocical provinces of South Australia and New South Wales. The Archaean Gawler Craton and the Proterozoic Curnamona Province are separated by the Neoproterozoic to Cambrian Adelaide "Geosyncline" (=Adelaide Fold and Thrust Belt). The Mount Painter Inlier (MPI) is traditionally assigned to the northernmost extent of the Curnamona Province as part of the Moolawatana Domain. Sketches adapted from the "Tectonic Map of South Australia", published by the Geological Survey of South Australia (PIRSA) and from Conor and Preiss (2008).

3.1 Mesoproterozoic: Metasediments, -granites, deformation & early hydrothermal activity

The oldest lithological units in the basement of the MPI are metasediments (Radium Creek Metamorphics; Coats and Blissett, 1971; "Radium Creek Group" by Cowley et al., 2012) that are intruded by several granitoid suites (Fig. 2). Coats and Blissett (1971), based on the research by e.g. Campana et al. (1961a-d), Mawson (1923) and Sprigg (1945), published a stratigraphic column of the deltaic or shoal-water metasedimentary succession of the Radium Creek Metamorphics (RCM). They consist of quartzites, phyllites, schists and migmatites. Detrital zircon ages on several quartzitic units yield a maximum deposition age between 1580 and 1590 Ma (Fanning, 2003; Wülser, 2008; Fraser and Neumann, 2010). These ages are significantly younger than the dominant Palaeoproterozoic Willyama Supergroup of the Curnamona Province (e.g. Conor and Preiss, 2008). Further studies on detrital zircons in the RCM of the MPI indicate a Gawler provenance rather than a Curnamona one (Fanning, 2003; Kositcin, 2010).

Coulthard Suite A-type plutonites (Cowley et al., 2012) intruded between ~ 1585 and 1575 Ma shortly after the deposition of the RCM sediments (Fanning, 1998; Neumann, 2001; Elburg et al., 2001; Stewart and Foden, 2003; McLaren et al., 2006; Neumann et al., 2009; Fraser and Neumann, 2010; Elburg et al., 2012). The Benagerie Volcanics extruded to the northeast of the MPI at about the same time (1585-1581 Ma; Fanning et al., 1998). The geochemical pattern of this early phase of the Older Granite Suite (Coats and Blissett, 1971; Fig. 2) is comparable with the geochemistry of the I- and A-Type granites and granodiorites of the Hiltaba Suite and the Gawler Range Volcanics (Barovich et al., 2006), which intruded into the Archaean Gawler Craton.

A-type granitoids of the Moolawatana Suite intruded between 1565 and 1555 Ma (Sheard, 1992; Sheard and Cockshell, 1992; Teale, 1995; Fanning et al. 1998; McLaren et al., 2006; Fraser and Neumann, 2010; Fig. 2). These younger granitoids are not albitised and may hence be the cause for a widespread albitisation of the early phase of the Older Granite Suite (Elburg et al., 2001; Elburg et al., 2012). The albitised metasomatic rocks were interpreted as stratigraphically younger trondhjemites (Teale, 1993). However, geochronological and geochemical data by Elburg et al. (2001) proved the trondhjemites to be an albitised granitoid of the first magmatic event.

The Moolawatana suite, as well as pelitic parts of the RCM are locally biotitised (Elburg et al., 2012). These metasomatic biotites show a mineral shape-preferred orientation parallel to a main foliation S_{main} in the basement with upright Palaeozoic crenulation cleavage. Therefore the biotitisation was active early in the MPI´s history.

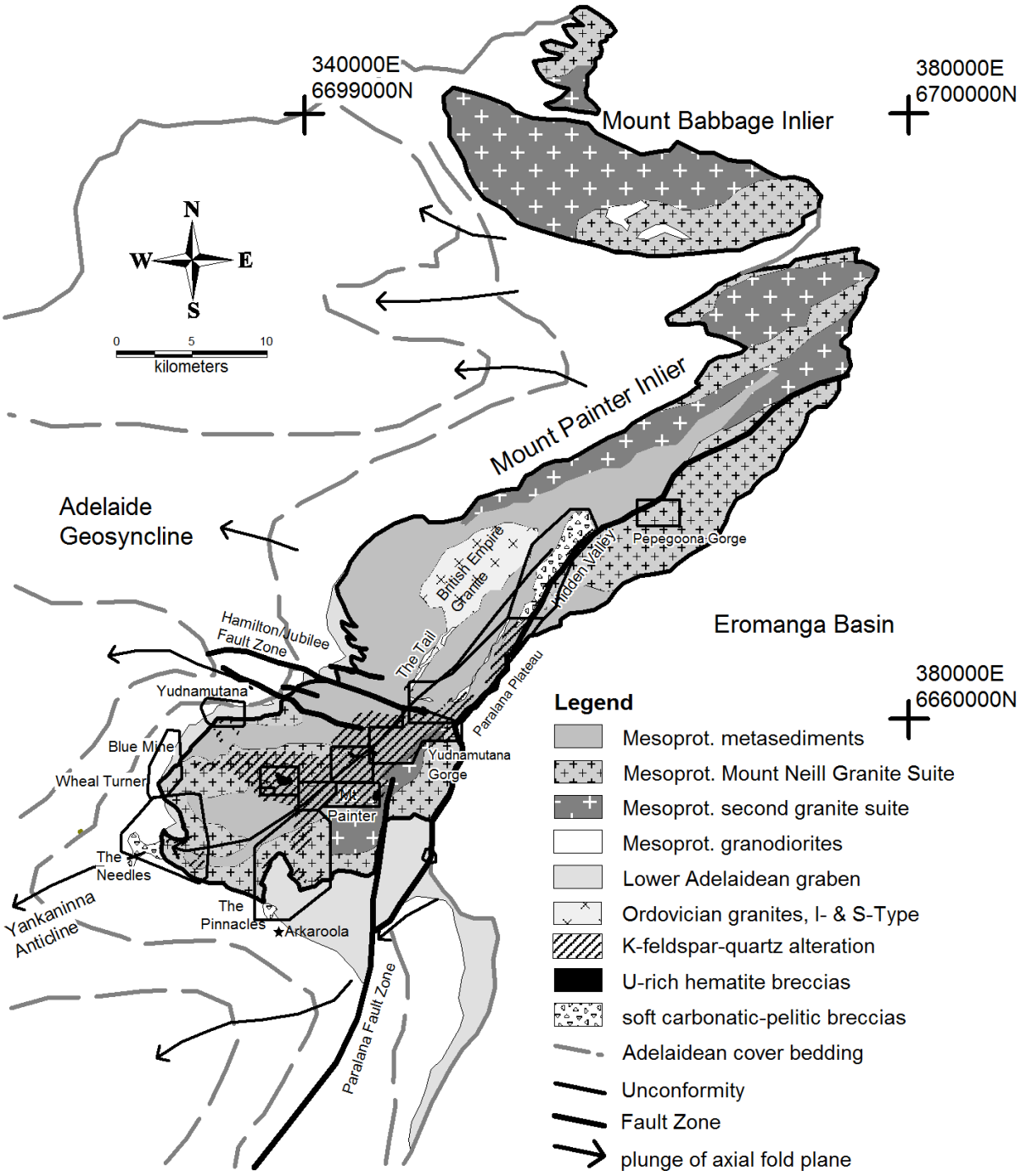

Fig. 2: Overview to the geology of the Mount Painter Inlier (MPI) and Mount Babbage Inlier (MBI) in South Australia. The definition of the units is adopted from Coats and Blissett (1971). Although some of their interpretation is now revised, the idea of one Proterozoic sedimentary succession (i.e. the Radium Creek Metamorphics, RCM) being intruded by Proterozoic granitoids is fundamental. After the deformation and exhumation of the basement, the Adelaidean sediments were deposited in Neoproterozoic and Cambrian times and subsequently folded and exhumed. Dashed lines indicate the folding pattern of the Adelaidean succession units. Palaeozoic exhumation is concentrated along the Paralana Fault Zone to the east of the MPI. The major Ordovician intrusion in the centre of the anticlinal structure is the British Empire Granite (BEG). Leucocratic rocks on the Paralana Plateau to the southeast of the BEG are now reinterpreted to be older than the Ordovician magmatic activity. The detailed mapping areas are indicated with black polygons.

The conditions of the Proterozoic deformation and metamorphism events in the MPI are interpreted diversely by several authors (Coats and Blissett, 1971; Teale, 1993; Paul, 1998; Elburg et

al., 2001; Armit et al., 2012). A reason for the discrepancy lies in the local variability of deformation. Due to strain localisation, the same lithology (especially the granitoids) may be strongly deformed in places, while remaining undeformed in others. The problem is compounded by the overprint of Palaeozoic folding and strong hydrothermal activity.

All Mesoproterozoic basement rocks show a variably strong main foliation (S_{main}), which is sub-parallel to the bedding in the metasediments, and is associated with isoclinal folds (Paul, 1998). Aligned biotite, sillimanite, cordierite, garnet and feldspar form the gneissic to migmatitic and schistose main foliation (Teale, 1993a+b; Paul, 1998; Armit et al., 2012). This mineral assemblage is interpreted to represent the peak metamorphic conditions in the MPI prior to the Palaeozoic deformation, locally reaching migmatitc conditions (Teale, 1993a+b). Several studies record at least one older deformation event, which is preserved as relictic mineral inclusion trails in porphyroblasts and as microlithons in S_m sheard rocks (Teale, 1993a+b; Elburg et al., 2003; Armit, 2012; see appendix 11.4: Summary of deformation and metamorphism studies). Elburg et al. (2001) found that the main foliation locally forms a crenulation cleavage itself. The metamorphic condition of these earlier event(s) was outranged by the peak metamorphism during S_{main}. Strike and dip of the main foliation roughly follow the large anticlinal structure that defines the current outcrop pattern of the MPI (Coats and Blissett, 1971; Paul et al., 1999). This, and the fact that S_{main} is truncated by the Adelaidean unconformity, is evidence that S_{main} is pre-Adelaidean in age. This issue will be further discussed below.

The age of the Proterozoic peak metamorphism and deformation is hardly preserved in the mineral record, because the rocks are overprinted by the Palaeozoic metamorphic event. Recent geochronological studies on migmatites and orthogneisses in the basement discuss a metamorphic recrystallisation at ~1550 Ma (Fraser and Neumann, 2010) or a metasomatic/metamorphic zircon-rim growth on detrital RCM zircons at ~1555 Ma (Armit et al., 2012). This age could, however, also be related to the hydrothermal activity during/after the second intrusion event in the Mesoproterozoic (Elburg et al., 2012). The timing of the metamorphism event remains enigmatic.

The only known inter-regional deformation and metamorphism events within the South Australian Craton (Myers et al., 1996) in the younger Mesoproterozoic are the Kararan Orogeny to the northwest (1570 – 1540 Ma; Daly et al., 1998), which resulted in the amalgamation of the Gawler Craton/Curnamona Province with the Musgrave Block; and the Coorabie Orogeny (Direen et al., 2005) in the Gawler Craton, which is predominantly related to reactivation of shear zones. The relation of the deformation and peak-metamorphism in the MPI to these distant deformation events is vague; therefore Paul (1998) introduced a separate “Mt. Painter event”. He interprets this event to be a result of extension in a continental rifting regime (Paul, 1998). Armit et al. (2012) link the MPI´s deformation to events recognised in the Northern and Southern Australian Cratons as far-field effects of extension and compression along distant plate margins.

Studies on seismic lines between the Gawler Craton and the Curnamona Province give further hints for the reconstruction of the palaeogeography of the MPI in relation to the other cratons. Korsch et al. (2010a) interpret the less-reflective deeper crust beneath the MPI to be connected to the Gawler Craton, not to the Curnamona Province. More studies are necessary to solve the inter-regional significance of the MPI and the MBI in Proterozoic times.

3.2 Neoproterozoic & Cambrian: Cover sedimentation

The metamorphosed and deformed basement of the MPI and the MBI reached the surface before ~800 Ma after a long hiatus without any record of ages between ~1550 and 830 Ma (= early rifting basalts: Wingate et al., 1998). Early NE-SW intra-cratonic extension led to the formation of grabens

and half-grabens at the inliers (Coats and Blissett, 1971) during the breakup of Rodinia. The grabens were filled with a few 100s meters to a few kilometres of terrestrial and marine sediments and early rifting basalts (Preiss, 1987; Preiss, 2000; Fig. 2). The Adelaide "Geosyncline" never developed to a real rift, but local erosion phases, followed by severval sag phases caused the formation of a deep basin until ~515 Ma (Preiss, 1987; Foden et al., 2006). Tillites were deposited with thicknesses of up to several hundreds of metres in the Sturtian and the Marinoan and erosion surfaces are recorded between several sequence horizons. The syn-sedimentary activity of the Paralana Fault Zone cause a drastic degrease in the thickness of the Adelaidean units east of one branch of the zone to the south of the MPI (Coats and Blissett, 1971; Fig. 2). About 12 km thick sediments were deposited west of the Paralana Fault *sensu strictu* (east of Arkaroola village), while the eastern basin only reached a depth of ~9 km (Coats and Blissett, 1971). This issue is discussed in Weisheit et al. (2013b).

The metamorphic isograde in the Adelaidean succession at the southern MPI are almost parallel to the basement outlines. The maximum metamorphic temperature at the unconformity is ~500 °C west of the Paralana Fault s.s., while it only reached ~200 °C east of it. The facies conditions change from amphibolite to greenschist facies at the fault. These metamorphic conditions are a result of the static burial of the inlier and an elevated geothermal gradient of 40-50 °C/km (Sandiford et al., 1998). This gradient is a result of the sedimentary cover blanketing of the high-heat producing uranium-rich granitoids in the basement (e.g. Sandiford et al., 1998; McLaren et al., 2002, 2006). The metamorphic conditions of the lower Adelaidean units are usually interpreted as an effect of the Delamerian Orogeny (see below), which is challenged in Weisheit et al. (2013b).

3.3 The Delamerian Orogeny

Compression started at ~514 Ma (first syntectonic granites) and lasted until ~492 Ma (first post-tectonic granites) in the southern Adelaide Fold and Thrust Belt (Foden et al., 2006). The metamorphism and deformation during the Delamerian Orogeny can be traced along the southern Adelaide Fold Belt down to Kangaroo Island (Preiss, 1987). Together with the Ross Orogen at Antarctica, South Africa and South America, the Delamerian Orogeny is part of the world-wide orogenic events that form Gondwana Land during the Palaeozoic (Foden et al., 2006). The similar structural elements in the whole Adelaide Fold and Thrust Belt resulted in the interpretation that the whole belt formed during Delamerian decompression. Nevertheless the belt has been differentiated from south to north into four structural domains, which experienced different amount and directions of deformation (Flöttmann et al., 1994). Whereas the southern parts are dominated by NE-SW trending open folds, the northern Flinders Ranges are marked by ~E-W trending folds, suggesting N-S shortening (Paul et al., 1999). Only at the MPI, the Adelaidean folds (e.g. the Yankaninna Anticline) trend ~NE-SW with a plunge of the fold axes to SW (Fig. 2). We show that the 10 km-scale folds in the northern Adelaide Fold and Thrust Belt formed during a long-lived N-S compression, almost independent from the Delamerian Orogeny to the south (Weisheit et al., 2013b).

Magmatic activity in the MPI during the Delamerian is restricted to small pegmatitic/aplitic intrusions. A deformed pegamtite in the MPI with a Rb-Sr age of 499 ±12 Ma is interpreted to be formed in the early stage of the Delamerian Orogeny (Elburg et al., 2003). Pegmatites and aplites within diverse breccias zones in the lower Adelaidean at the MPI (The Pinnacles, The Needles, Sitting Bull, Bob Knob, Tourmaline Hill, etc.) are also of mid-Cambrian age, although they appear to be undeformed (Elburg et al., 2003).

Metamorphic conditions in the lowermost Adelaidean sediments at the MPI were interpreteted as a result of the Delamerian Orogeny (Coats and Blissett, 1971; Mildren and Sandiford, 1995; Paul, 1998). We show that aligned andalusite/sillimanite, biotite and cordierite formed during static burial, that resulted in the observed lower amphibolite facies conditions (500 °C, 3 kbar) west of the

Paralana Fault s.s. (Weisheit et al., 2013b). McLaren et al. (2002) discuss a long-lived metamorphic evolution of the Delamerian Orogeny due to the heating blanket of Adelaidean sediments above the hot MPI. However, detailed studies on structures in the southern and central MPI (as presented in this report and in Elburg et al., 2003) and the regional geology do not support this interpretation. Palaeozoic structures are rare within the basement. Deformation is restricted to crenulation cleavage in schistose rocks and shear zones (Elburg et al., 2001; Elburg et al., 2012) during the development of the large-scale anticlines and synclines and parasitic folding.

3.4 Ordovician – Carboniferous: magmatic and hydrothermal events

Granites, leucogranites, granodiorites and pegmatites (Younger Granite Suite of Coats and Blissett, 1971, e.g. the British Empire Granite, BEG) intruded the basement and surrounding Adelaidean succession at ~440-460 Ma (Coats and Blissett, 1971; Elburg et al., 2003; McLaren et al., 2006; Wülser, 2008; Elburg et al., 2012; Fig. 2). The major igneous body, the BEG, consists of a S-type and an I-type phase (Elburg et al., 2003). The latter is suggested to represent a mantle component during the BEG-intrusion (Elburg et al., 2003), or as a separate older granodiorite intrusion (Neumann, 2001; McLaren et al., 2006; Fraser and Neumann, 2010). The intrusion depth of the BEG is interpreted to be at ~12-14 km depth, while the melts formed at ~15-16 km depth (McLaren et al., 2006). Undeformed pegmatites formed at the same time in dilatatant fractures in the southern MPI (as shown in this report), at brittle conditions below max. 500 °C. The same observation was documented by Bakker and Elburg (2006), who analysed a ~440 Ma old magmatic diopside-titanite pegmatite in the southern MPI. Fluid inclusions show a transition of magmatic conditions to hydrothermal ones of minerals within these veins.

Corundum-rich biotitites are documented in the MPI as a stratigraphic horizon within the Mesoproterozoic RCM (Coats and Blissett, 1971; Teale, 1993a). A recent study by Elburg et al. (2012) interprets these hyperaluminous rocks (phlogopitites) with corundum, spinel and tourmaline as alteration products of any host rock by post-deformational hydrothermal fluids. Monazite growth in these altered rocks is dated to ~455 Ma and slightly older (Elburg et al., 2012).

Other hydrothermal overprints are documented by a few authors. Coats and Blissett (1971) discuss a “granitisation” of basement rocks, which formed quatz-feldspar-rich lithologies. A successive development of these rocks into granitic and chloritic breccias is also discussed as an effect of hydrothermal activity (Drexel, 1980; Drexel and Major, 1987). Iron-oxide breccia sheets (with enrichments of Cu, Mn, U, and LREE) are dated to ~355 Ma (Pidgeon, 1980; Elburg et al., 2013).

Whether the processes in the MPI during the middle Palaeozoic are related to the ~450-300 Ma Alice Springs Orogeny ~800 km to the northwest, or to the subduction and terrane collisions in the Lachlan Fold Belt ~500 km to the southeast is a matter of debate. Magmatism, metamorphism and extensive ductile deformation are recorded in the Harts Ranges, as well as in the Lachlan Fold Belt (Bierlein et al., 2001; Lennox et al., 2005; Buick et al., 2008). Recorded Ordovician activities in the MPI are restricted to magmatic intrusions and alteration fluids, whereas no metamorphism and only minor shearing is known (Elburg et al., 2013).

A distinct hydrothermal event in the southern MPI formed large quartz-hematite breccias and veins that crosscut all basement units. Low-temperature and low-salinity fluids (Bakker and Elburg, 2006) caused silicification and sinter-formation close to the surface (Brugger et al., 2011). The age of this “Mt. Gee Event” was dated by Brugger at al. (2011) to ~290 Ma, but fluid flow may have been active for more than 100 Myr (Weisheit et al., 2013b).

3.5 Exhumation

McLaren et al. (2002) discuss their K-Ar, Ar-Ar cooling ages of K-feldspar, biotite, muscovite and hornblende samples in the MPI as hints for a long lived Delamerian Orogeny and rapid exhumation events at ~430 Ma, ~400 Ma and ~330-320 Ma (Fig. 3). K-A and Ar-Ar cooling ages of selected samples record the differential exhumation of the MPI during the Palaeozoic (Weisheit et al., 2013b).

The MPI has been close to the surface at least since the late Carboniferous / early Permian, suggested by the formation of diamictitic sedimentary dykes at ~315 Ma (Brugger et al., 2011) and several zircon (U-Th)/He analyses of metasediments and metagranites of the southern inlier (Weisheit et al., 2013b). Fission track models by Forster et al. (1994) and Mitchell (2002) conclude an earlier and more long lived exhumation, but they do not consider the widespread hydrothermal overprinting that potentially affected the data (Fig. 3).

By the time of breakup of Gondwana Land, the MPI and MBI were fully exhumed. Triassic and Cretaceous sediments cover the basement with a few 10s metres thickness today and are found in drill holes down to 600 m depth in the Eromanga Basin to the east (Sheared and Cockshell, 1992; Fig. 3). Palaeogene and Neogene horst and graben structures and ongoing seismic activity along the Paralana Fault Zone in the east of the MPI (Célérier et al., 2005) are an expression of continuous stress in the crust.

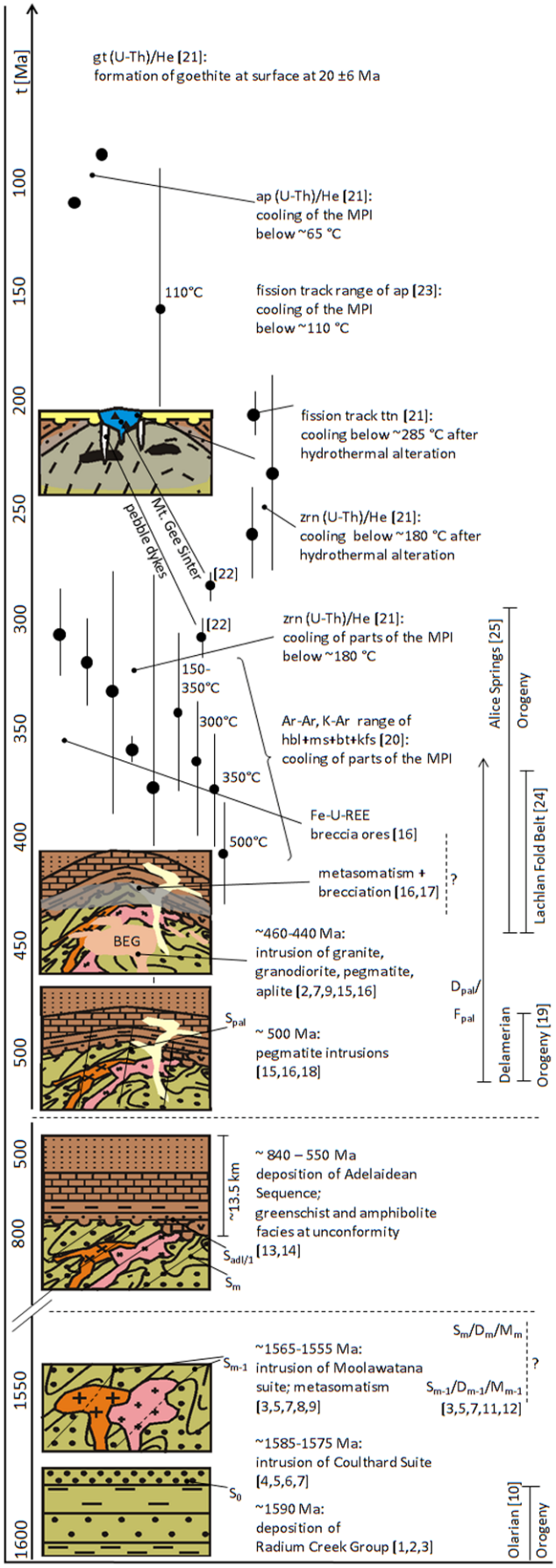

Fig. 3: Summary of all major geochronological studies in the MPI and proposed model of Palaeozoic deformation and fluid-flow. The Coulthard Suite and the Moolawatana Suite intruded shortly after the deposition of the Radium Creek Group (RCM). The second suite caused albitisation. Deformation and metamorphism of all basement units occurred contemporaneously or slightly after the intrusion of the second granite suite. Adelaidean sediments were deposited between ~800-500 Ma. Folding and exhumation of basement and cover occurred during the Palaeozoic. Hydrothermal fluid flow was dated with zircon and monazite rims at ~460-440 Ma. Phlogopitisation, pegmatite/granite intrusion and K-feldspar-quartz alteration occurred at the same time. Uranium-copper-rich iron-ores formed at redox horizons at ~355 Ma. The Mount Gee quartz-hematite sinter is the latest documented alteration in the MPI. Mineral abbreviations after Kretz 1983. MPI: Mount Painter Inlier; BEG: British Empire Granite. 1. Fanning et al. (2003); 2. Wülser (2009); 3. Fraser & Neumann (2010); 4. Neumann (2001); 5. Elburg et al. (2001); 6. Steward & Foden (2003); 7. Elburg et al. (2012); 8. Sheard & Cockshell (1992); 9. McLaren et al. (2006); 10. Rutherford et al. (2007); 11. Paul et al. (1999); 12. Armit et al. (2012); 13. Wingate et al. (1998); 14. Preiss (2000); 15. Elburg et al. (2003); 16. Elburg et al. (2013); 17. Weisheit et al. (2013b); 18. Wülser et al. (2011); 19. Foden et al. (2006); 20. McLaren et al. (2002); 21. this study; 22. Brugger et al. (2011); 23. Mitchell et al. (2002); 24. Gray & Forster (2004); 25. Buick et al. (2008).

The main focus of this report is to unravel the evolution of the hydrothermal activity during and after Palaeozoic deformation. We will give information on the extent and the kind of metasomatism in the MPI and the development of the fluids with ongoing exhumation of the basement. Detailed geochemical and mineralogical analyses on the fluid system(s) are given and discussed in Chapter 3 of the PhD thesis.

The fluids were guided mainly by pre-existing structures, such as foliation planes, faults and folds. Therefore the characterisation of the structural evolution of the MPI in a regional scale is also a focus of this report. Hence pre-Adelaidean structures in the basement, as well as the Palaeozoic deformation structures in basement and cover were mapped and analysed. A detailed structural reconstruction on the crustal folding and exhumation of basement and cover during the Palaeozoic is presented in Weisheit et al. (2013b).

4. Geological units and field observations

The first comprehensive study of the regional geology of the MPI and the MBI and the adjacent Adelaidean succession was published by Coats and Blissett (1971), who introduced a stratigraphic column of basement and cover. The lithological units, as well as the stratigraphical order of the basement was discussed and reworked by several authors in the following decades. The most striking modification was introduced by Teale (1993a and 1993b), who separated the basement rocks into deformed Palaeoproterozoic and undeformed Mesoproterozoic ones. The absence of deformation, however, is not an indication for the age of an unit (strain localisation, different rheologic properties), which was proven by later zircon studies that point to a single sedimentary sequence of the basement metasediments in the early Mesoproterozoic (Fanning et al., 2003; Wülser, 2009; Fraser and Neumann, 2010), as well as by the Mesoproterozoic ages of the Older Granite Suite (e.g. Elburg et al., 2001; Fraser and Neumann, 2010).

Due to the aforementioned reasons, the presented maps of this study are based on the stratigraphy of Coats and Blissett (1971). However, some minor changes and new lithologies, partly already introduced by other authors, complement the geology. The lithological description is based on the visual appearance of the rock in outcrop, hand specimen and thin section, taking structural and hydrothermal features into account. A geochemical differentiation of e.g. different granitoids is discussed in Chapter 3 of this PhD thesis, but not included in this report. The lithological units discussed in this section are, when possible, ordered by their age.

The provided mappings are digitalised using the GIS system MapInfo (Pitney Bowes Software) with separate layers for each lithology. The general projection of the maps is MGA, Zone 54, GDA94, unless otherwise noted. As the focus of the mappings lies on the metasomatic overprints in basement and cover, new hydrothermal units, veins and differentiated breccias (each as a layer in the GIS system) are introduced into the lithological description. Gradual changes of the mineralogical pattern of the rocks are typical for areas with intense hydrothermal overprinting. To do justice to this observation, this study introduces transparent alteration layers without boundaries into the GIS database, which lie on top of opaque layers of the host rock lithology. The transition to purely hydrothermally formed lithologies (opaque layers) is drawn when the dominant lithology changes. Small veins and structures are included in the database as points and polylines. Therefore they have to be located on top of all opaque units. The units are abbreviated generally with a three letter acronym for simplification. A table in the appendix summarises all used acronyms and suggests the optimal sequence of the layers in the GIS system from the top one at the beginning of the table to to lowermost one at the base of the table (appendix 11.2: Acronyms in the GIS database). Appendix 11.1 gives a snapshot of the whole geological mapping in MapInfo of the provided GIS database (state: April, 2012).

The single maps that were created by several students during this long-lasting project were combined in a cooperated map with the compilation of this report. This resulted in an aggregation of layers and the disappearance of units. This revision has to be considered while reading this report and the single theses that were compiled earlier by the students.

4.1 Mesoproterozoic metasediments and (meta-) igneous rocks

4.1.1 Radium Creek Metamorphics

The Radium Creek Metamorphics form a sequence of phyllites, quartzites and other impure gneissic to migmatitic metapsammites and metapelites, interpreted to been deposited in a shelf environment (Coats and Blisset, 1971). Their sedimentary layering S_0 (cm to >m scale) is often preserved, especially in quartzitic units with heavy mineral horizons or in alternating pelitic-quartzitic-feldspatic series. Quartzites are mapped as Radium Creek Metamorphics-Quartzite. More gneissic successions with clear sedimentary bedding are defined as Radium Creek Metamorphics-Gneiss, whereas the other metasediments are mapped as undifferentiated Radium Creek Metamorphics (Bons and Roessiger, 2008). Similarities to other common stratigraphic units defined by Paul (1999) and Neumann (2001) are discussed at the respective sections about the maps.

Calcsilicate lithologies, as described in literature (e.g. Paul, 1998; Wülser, 2008), were not encountered as mapable units in the study area.

Undifferentiated Radium Creek Metamorphics (RCM)

These quartzo-feldspathic schists and gneisses show variable biotite and sillimantite (fibrolite) content, with porphyroblasts and -clasts of feldspar and magnetite. A main foliation (S_{main}) is usually strongly developed (Fig. 4a+b). In some cases the porphyroblasts are accompanied by pressure shadows of sillimanite (fibrolite), indicating high-grade, amphibolite facies metamorphic conditions. The microstructure shows annealing in thin sections up to the formation of foam texture between quartz and feldspars (Roessiger, 2008). Sometimes aligned biotite is the only evidence of a former foliation. Often euhedral magnetites overgrow the host fabric unaffected, as well as large microclines with inclusions of the host rock. Their blastesis is probably related to hydrothermal mobilisation of iron and potassium, respectively, during the Palaeozoic hydrothermal events (see section 4.3 Palaeozoic deformation, magmatism and metasomatism).

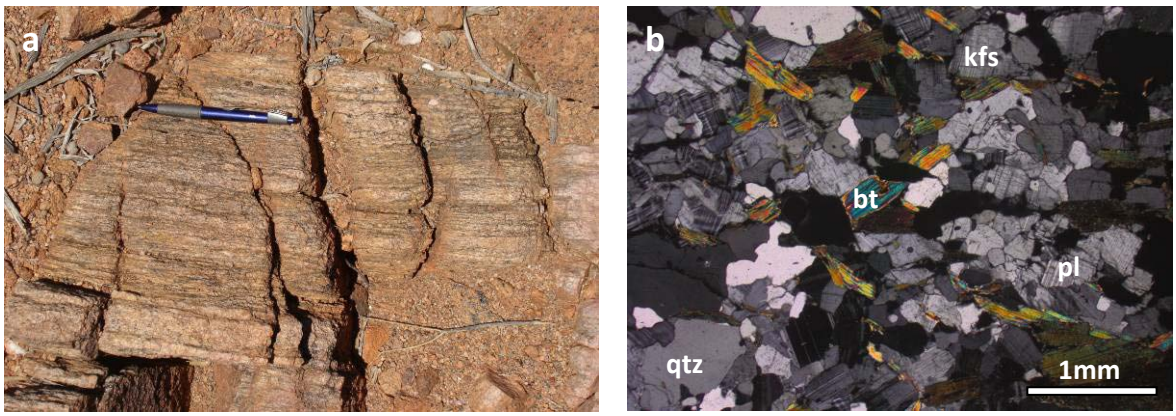

Fig. 4: Field photograph and thin section of the undifferentiated Radium Creek Metamorphics (RCM). a) The strike of the steep main foliation S_{main} of a quartzo-feldspatic biotitic gneiss at Radium Creek is NE-SW (340329E/ 6653154N). b) The RCM-gneises usually show a recrystallised texture of K-feldspar (kfs), plagioclase (pl) and quartz (qtz), while biotite (bt) displays often more than one relict foliation (339927E/ 6654922N).

A few lithologies of the RCM display partial melting by forming leucosome-like granitic/pegmatitic veins (Bons and Roessiger, 2008). This migmatitisation becomes dominant towards the east of the central MPI in the Paralana Hot Springs area (section 5.4 Map at Yudnamutana Gorge), whereas no

migmatitisation could be observed in the southwest at Wild Dog Creek (section 5.3 Map at Wild Dog Creek and The Needles). The SW-NE increase of the metamorphic conditions to anatexis has been discussed as a Delamerian effect (Teale, 1993a & b; Sandiford et al., 1998; Paul et al., 1999; Wülser, 2008). The formation of S_{main} by the orientation of biotite, fibrolite, quartz and feldspar is an indication that the amphibolite-facies metamorphism already occurred in the Mesoproterozoic. Recent U-Pb zircon dating on the migmatites in the Paralana Hot Springs area are interpreted as displaying a recrystallisation event at ~1560/1550 Ma (Fraser and Neumann, 2010).

Radium Creek Metamorphics – Gneiss (RCG)

Several tens to hundreds meters thick bands of orange-red Quartz-Feldspar Gneiss (QFG) are traceable over hundred of meters and could be mapped as a single lithology in the Mount Gee – Mount Painter maps (section 5.1 Mount Gee Map, Radium Ridge Map, East Painter Camp Map, Armchair - Streitberg Map; Fig. 5a+b). A meta-sedimentary or meta-igneous origin of the gneisses can in most cases not be determined with certainty in the field. In this case they were mapped as QFG in the Mount Gee - Mount Painter maps (Bons and Roessiger, 2008). When interbedded with undifferentiated RCM, the quartzo-feldspatic gneisses indicate a sedimentary origin. All feldspatic gneisses are mapped in the cooperated map as Radium Creek Metamorphics - Gneiss (RCG) to simplify the general nomenclature. Thin section analyses show that the QFG are mainly composed of quartz and microcline (±albite), with a grain size generally larger than in undifferentiated RCM. Their content of biotite and magnetite is also lower. Aligned biotite is the only mineral forming S_{main}, because the microstructure of quartz and feldspar is annealed (Bons and Roessiger, 2008).

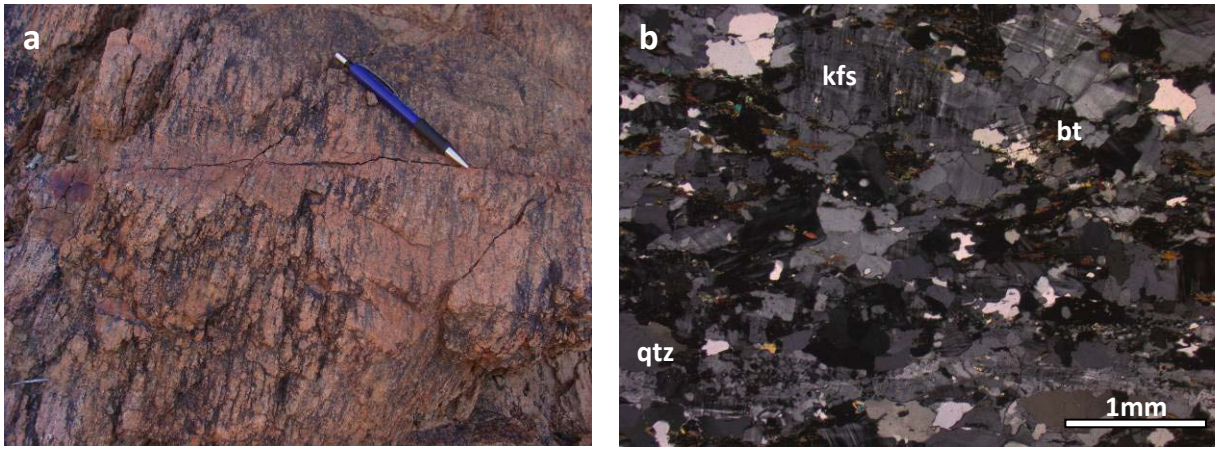

Fig. 5: Field photograph and thin section of a Quartz-Feldspar Gneiss (QFG). a) The QFG at East Painter Camp (344533E/6654429N) has a strong gneissic foliation S_{main} to 122/60. A hydrothermal quartz-feldspar vein crosscuts the foliation and causes a K-feldspar-impregnation. b) Recrystallised Quartz-Feldspar Gneiss (QFB) (33961E/6654811N). Quartz (qtz) and K-feldspar (kfs) are elongated and form augen between the aligned, altered biotite (bt).

Radium Creek Metamorphics – Quartzites (RCQ)

The quartz-dominated units of the RCM are mapped (when possible) as lithologies defined by Coats and Blissett (1971), such as the Freeling Heights Quartzite (FHQ) south of Yudnamutana and the Mount Adams Quartzite (MAQ) southeast of Hidden Valley (Fig. 6a). In cases where quartzites could not be assigned to any of these units, they were incorporated into the Radium Creek Metamorphics - Quartzites (RCQ) - layer.

The quartzites mainly consist of medium grained quartz and a few biotites with an annealed microstructure. S_0 bedding is usually well preserved with sedimentary cross-bedding and heavy mineral horizons. The quartz crystals are dynamically recrystallised and elongated in local shear zones, but in general, due to the relative competence of pure quartzites, no foliation is developed (Fig. 6b).

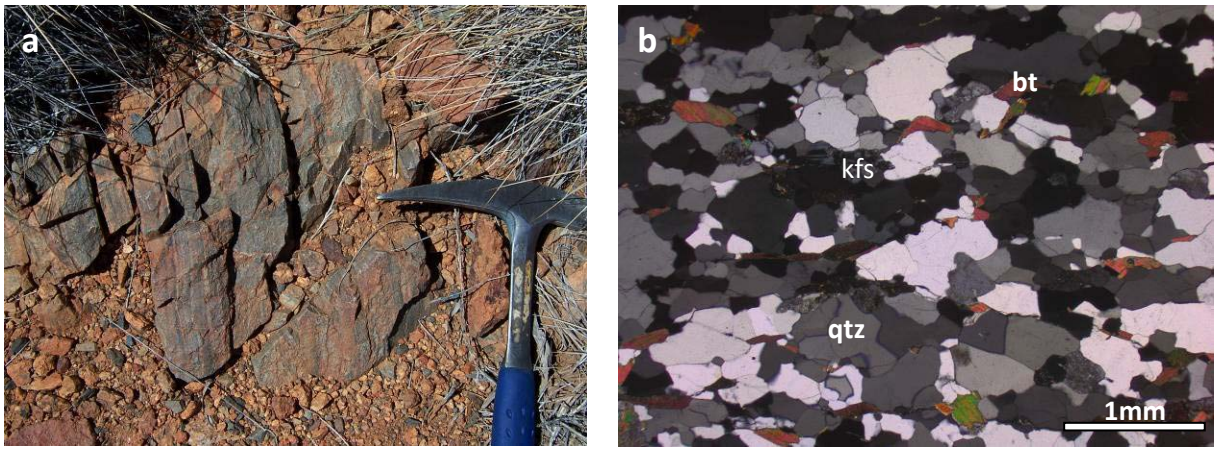

Fig. 6: Field photograph and thin section of quartzitic Radium Creek Metamorphics. a) There is no macroscopic tectonic foliation visible in the competent, layered Mount Adams Quartzite (MAQ) south of Hidden Valley (357650E/6667520N). b) Biotite and quartz (± feldspar) in quartzitic Radium Creek Metamorphics (RCQ) at Paralana Plateau are aligned (350576E/6661309N). Migrational recrystallisation causes serrate grain boundaries.

4.1.2 Intrusives: meta-igneous rocks and amphibolites

Mesoproterozoic igneous activity with mantle input (Elburg et al., 2012) caused the intrusion of alkaline A-type granitoids into the sedimentary succession of the RCM. Distinct differences in textural, petrological and geochemical properties have been used to define two distinct suits intruding between 1585-1575 Ma and 1565-1555 Ma (e.g. McLaren et al., 2006). The first one, the Mount Neill Suite (Coulthard Suite after Cowley et al., 2012), is partly altered by sodium-metasomatism into a secondary trondhjemite (Elburg et al., 2003). This alteration probably accompanied the intrusion of the second suite, the Moolawatana Suite (Terrapinna Granite and others; Coats and Blissett, 1971; Elburg et al., 2003; Elburg et al., 2012), which is not affected by a metasomatic enrichment of sodium and high field strength elements (HFSE) (Elburg et al., 2001; Neumann, 2001). Although the granitoids often appear massive and equigranular in the field, members of both intrusion suits locally developed the dominant S_{main} foliation (Fig. 7a+b).

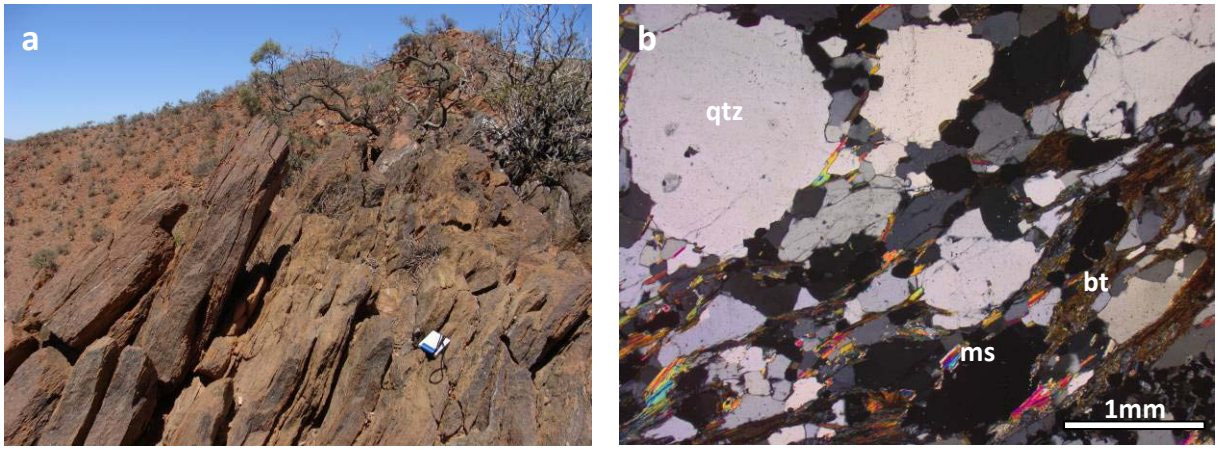

Fig. 7: Field photograph and thin section of Mount Neill Granite (MNG). a) The main foliation S_{main} in the MNG northwest of The Pinnacles (337211E/6648625N) varies from gneissic to shistose. D2 deformation occurs localised in the MPI. b) The MNG is characterised by cm-sized quartz augen (qtz) that appear blueish in the field. The magmatic augen remain after D2 shearing in a MNG north of The Pinnacles (337280E/ 6647968N). Biotite (bt) and muscovite (ms) for a S_{main} foliation.

There is an ongoing debate about the classification of the several granitoids in the basement into the defined lithological units, beacuse of their diverse mineralogical and structural appearance. Wülser (2009) discusses this problem in detail and summarises the relation of the different interpretations in his figure 3 (p. 83).

Amphibolites (AMP) and pegmatites (PEG) within the basement intruded contemporaneously or slightly after the granitoid (also prior to the formation of S_{main}). There are also amphibolite dykes related to Neoproterozoic rifting (i.e. feeding dykes to the Wooltana Volcanic basalts) and undeformed pegmatites, which intruded during Palaeozoic igneous activity (see below).

The Mount Neill suite: Mount Neill Granite (MNG) and related granitoids

The original granites of the Mount Neill Suite (i.e. the Mount Neill Granite (MNG) and its equivalents) are equigranular to porphyric in texture, locally with rapakivi-like K-feldspar ovoids (up to 5 cm in diameter; Fig. 8a) and omnipresent distinct blueish quartz augen (a few mm to cm in size). The MNG contains K-feldspar (mainly microcline) and plagioclase, as well as quartz, biotite, minor muscovite and accessory apatite, zircon and monazite (Fig. 7b). In outcrop it appears more pinkish in colour as the albitised equivalents (secondary trondjhemites; Elburg et al. 2001), which are distinctly grey. Deformation locally turned the granites and the albitised equivalentes into quartz-augen gneisses, with aligned micas and dynamically recrystallised feldspars and quartz augen forming S_{main}. Sometimes, in the case of heavy alteration, blue quartz augen are the only macroscopic evidence that the MNG is the host rock (Elburg et al., 2001) (Fig. 8b). As the Mount Neill Suite appears mineralogically and structurally diverse in outcrop, several sub-layers and information in the metadata table of the MNG are used to distinguish different alteration and deformation zones in the maps.

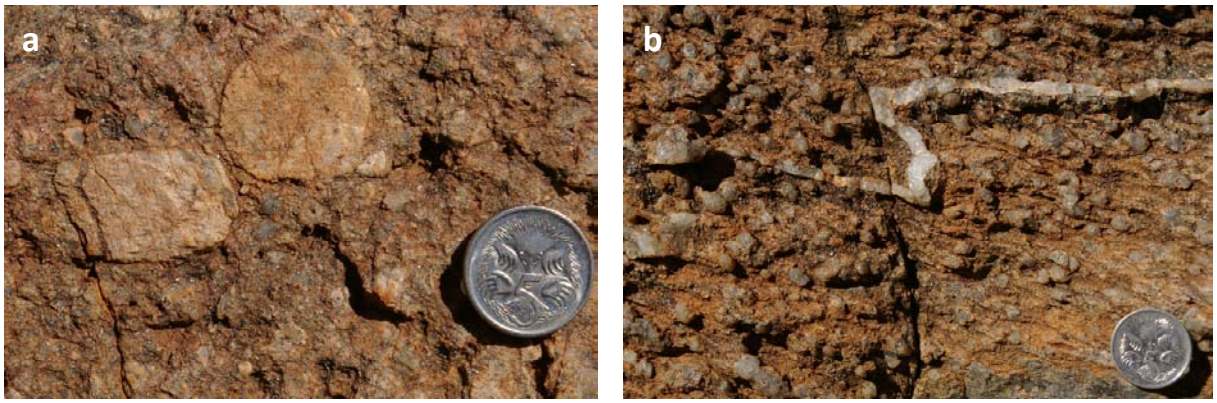

Fig. 8: Close-up photographs of massive and sheared Mount Neill Granite (MNG). a) Reddish MNG with K-feldspar ovoids and blue quartz augen at East Painter Gorge. Aligned biotites form a weak foliation. This rock is considered to be the original, unaltered MNG. b) Sheared MNG with distinct blueish quartz-augen close to Nooldoonooldoona Waterhole. Quartz-, feldspar-porphyroclasts and micas form the main foliation. A quartz-vein was folded during the formation of the axial planar S_{main}.

The MNG intruded as sills (with minor dykes) parallel to the bedding of the RCM in the south-western area of the MPI (section 5.3 Map at Wild Dog Creek and The Needles).

Coats and Blissett (1971) introduced the Pepegoona Porphyry (PEP) in Pepegoona Gorge and NE of Mt. Neill, as part of the RCM-stratigraphy. Rounded quartz and feldspars in a fine grained groundmass of feldspar, quartz and mica give these rocks a porphyritic appearance in the field. Phenocrysts of K-feldspars and idiomorphic quartz show irregular embayments in thin sections, indicating resorption processes (Fig. 9a). These embayments are typical for volcanic phenocrysts, but may also form in a hydrothermal environment (Chang and Meinert, 2004; Nicholl and Williams, 2006). The fine crystalline matrix consists of quartz, K-feldspar, some plagioclase and micas. In most cases this porphyry-looking rock is sheared (S_{main}) and its feldspars are altered to micas and clay-minerals (Fig. 9b). Sometimes there are clear indications, that silica has been mobile during the shearing event (Fig. 9c). The alteration of several host rocks (granodiorites, granites and porphyritic granites) results in a gradual change of the different lithologies in the Pepegoona Gorge area (Fig. 9d). Geochemical analyses of the Pepegoona Porphyry are discussed in section 6.1.

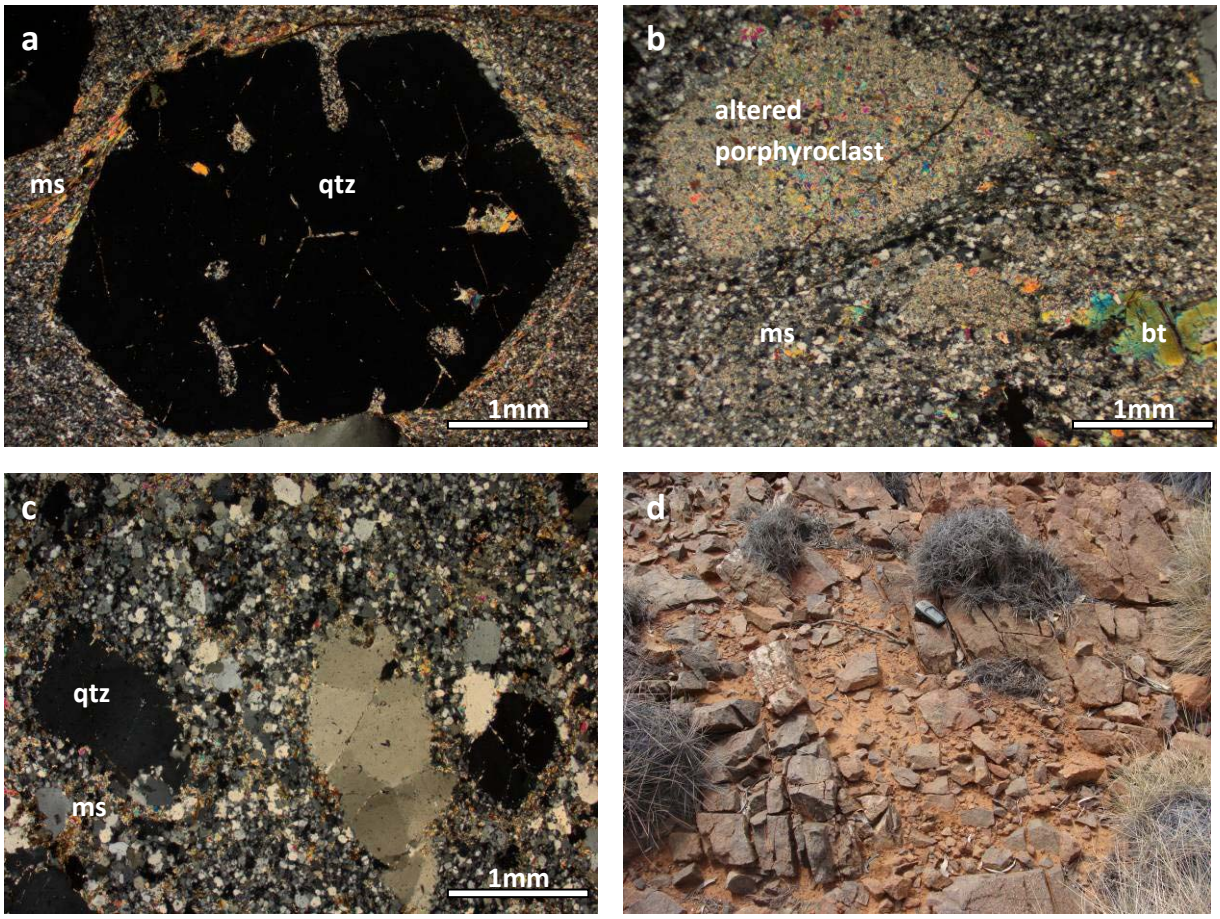

Fig. 9: Microphotographs and field picture of Pepegoona Porphyry (PEP). a) A quartz (qtz) phenocryst floating in a fine crystalline matrix of quartz, feldspar and muscovite (ms) in a PEP NW of Pepegoona Gorge (0363156E/ 6674237N). The irregular embayments and inclusions result from resorption during silica-disequilibrium. The alignment of phenocrysts and muscovite occurred during the formation of the regional main folaition S_{main}. b) Altered feldspar(?) porphyroclast in a matrix of quartz, feldspar and altered micas (PEP NW of Pepegoona Gorge: 0363533E/6673416N). Shearing of the rock occurred during the formation of the regional main folaition S_{main}. c) Quartz porphyroclasts in a sheared PEP NE of Pepegoona Gorge are aligned with S_{main} and show brittle fragmentation (363219E/6673195N). The formation of a pressure shadow and irregular grain-boundaries indicate silica-mobility during the dynamic recrystallisation. d) Various igneous host rocks at Pepegoona Gorge were altered and sho gradual transitions. A massive bluish-grey granodiorite (lower left corner) in this outcrop turns into an altered, reddish granodiorite with a porphyritic appearance (upper right corner) (0362777E/6673316N).

The PEP is interpreted as being a shallowly intruded, porphyritic variety of the MNG, because outcrops of PEP are associated with MNG occurences (Coats and Blissett, 1971; Teale, 1993; Neumann, 2001). This will be discussed in section 7.2: Deformed and undeformed granodiorites, migmatites and „porphyries“. Other occurrences of such a PEP-like igneous rock could be found in the basement SE of Yudnamutana and as a mylonite (MYL) in Hidden Valley.

The Moolawatana Suite: Terrapinna Granite (TPG) and other granitoids

The younger Terrapinna Granite (TPG) has a more pronounced rapakivi texture than the MNG, with pink-orange K-feldspar ovoids within a medium-grained groundmass of plagioclase, quartz and biotite (accessory zircon, apatite and monazite). Sometimes quartz and feldspar show graphic intergrowth. The TPG occurs as coarse-grained quartz-feldspar gneiss in large areas of the maps south and southwest of Paralana Hot Springs (section 5.1.3 East Painter Camp Map and section 5.4 Map at Yudnamutana Gorge). S_{main} is formed by biotite and elongated quartz and feldspars (Fig. 10). A contact between the TPG and the RCM can be observed in a few localities. Coats and Blissett (1971) describe it as always concordant. The definition of these rocks as being part of the TPG is taken over of Coats and Blissett´s map (1971), who were the first to define the TPG. A geochemical study of these rocks is briefly described in Chapter 3 of this PhD thesis.

Fig. 10: Field photograph of a sheared feldspar-quartz-biotite Terrapinna Granite (TPG) south of East Painter Camp (S_{main}=117/61). The transition to the Quartz-Feldspar Gneiss (QFG) in this area is gradational (344340E/ 6654252N).

Other granites of the Molawatana Suite are the Yerila Granite, the Wattleowie Granite, the Box Bore Granite, the Golden Pole Granite and the Con Bore Granite (Coats and Blissett, 1971; Sheard et al., 1992; Teale, 1993a+b; Neumann, 2001; Stewart and Foden, 2003). These studies could find clear intrusion relationships between the granitoids and therefore relative ages of the intrusion bodies. A summary of the literature to these granitoids is given in the Appendix 11.3: Overview to the granitoid studies in the MPI, because they do not appear within the maps of this study.

Special attention is given to the magmatic Hot Springs Gneisses (Neumann, 2001), with their main occurrence at the Paralana Hot Springs area, adjacent to paragneisses (Paralana Composite Gneiss of Neumann, 2001) and migmatites. A recent geochronological study gives evidence for a magmatic crystallisation age of ca. 1580 Ma and a metamorphic overgrowth at ~1550 Ma of a Hot Springs

Gneiss in the Hot Springs Creek (Fraser and Neumann, 2010). Coats and Blissett (1971) mapped rocks further to the south of Hot Springs Creek in the Hodgkinson area as Terrapinna Granite (TPG). This study, however, could not relate gneissic outcrops at the Hot Springs Creek to gneissic outcrops of the main occurrence of the Terrapinna Granite at the Hodgkinson area. A direct relation is therefore doubtful and due to the lack of geochemical and geochronological data the augen-gneisses in the Hodgkinson area are mapped as Terrapinna Granite (section 5.4 Map at Yudnamutana Gorge) and at the Hot Springs Creek only undifferentiated gneisses are defined as Radium Creek Metamorphics - Gneiss (RCG) (Fig. 11; section 5.5 Map at Paralana Plateau).

Fig. 11: Field photograph of undifferentiated gneiss (RCG) in the Paralana Hot Springs area. The main foliation dips to the SE (347463E/6662079N).

Granodiorites (GDT)

The occurrence of granodiorites all over the inlier is documented by several studies (Coats and Blissett, 1971; Teale, 1993a+b; Neumann, 2001; Fraser and Neumann, 2010), although there are uncertainties concerning the age and relative relationships of single outcrops of these rocks. These white granodiorites are in general medium to fine grained with plagioclase, quartz and biotite, accessory xenotime and zircon. The structure of the granodiorites varies from totally undeformed, massive magmatic, to a strong mineral shape-preferred orientation of micas and elongation of quartz and feldspar forming S_{main}, to an annealed structure of static recrystallised grains. This microscopic and macroscopic variety of the granodiorites results in age interpretations that vary from Mesoproterozoic to post-deformational Ordovician. Coats and Blissett (1971) mapped a massive white Granodiorite with a direct relationship to the MNG; Neumann (2001) defined the Paralana Granodiorite at the Paralana Plateau and at The Tail of the British Empire Granite as being pre-Delamerian in age; Elburg et al. (2003) gave evidence for an undeformed I-Type variety of the Ordovician British Empire Granite and Fraser and Neumann (2010) dated a Hodgkinson Granodiorite at the southern Tail and northeast of the Paralana Plateau as Mesoproterozoic in age. Only detailed geochemical studies and structural mappings might solve the problem of intermixed Mesoproterozoic and Ordovician granodiorites in the MPI. So far this study confines the definition of an undifferentiated Granodiorite (GDT) with details to structural features within the metadata table.

Mafics (MAF) and Pegmatites (PEG)

Small vein-like and lenticular outcrops of mafic dykes (MAF) can be found all over the inlier within metasediments as well as metagranitoids, metamorphosed to amphibolites. All observed amphibolites have medium to fine grained plagioclase and green hornblende aligned parallel to the foliation of the surrounding rocks (S_{main}). Large hornblende grains are sheared into porphyroclasts. Like in the metasediments the microstructure is well annealed.

The fine-grained mafic dykes (amphibolites) sometimes grade into Black Biotite Schists (BBS), as a result of an early hyperaluminous alteration event (Elburg et al., 2012).

Magnetite and martite with rutile/anatase overgrow the structure of the amphibolites, as well as retrograde chlorite, which sometimes appears in veins through the rock.

Mesoproterozoic pegmatites (PEG) can be found within metagranites and metasediments of the RCM. They intruded in dykes and sills, following the bedding in the RCM. Large graphic quartz and K-feldspars, with sizes up to a half a meter, are not well suited for the formation of a foliation. However, patches of up to 10 cm large muscovite are sometimes aligned parallel to the main foliation S_{main}; especially in zones where the strain became localised. However, the texture of pegmatites often prevents the formation of deformation structures. Hence boudinage within S_{main} is often the only hint that these pegmatites intruded prior or contemporaneous to the deformation that formed S_{main} (Fig. 12). Magmatic garnet (up to a half a centimetre in size) could be found in deformed pegmatites in a few outcrops in the Well Creek area.

Fig. 12: Photograph of a Mesoproterozoic pegmatite boudin in Freeling Heights Quartzite (FHQ) west of Hidden Valley (356508E/6672126N). The dextral sigma-clast displays a reverse movement of the NW-block. Note that despite the obvious intense deformation, the quartzite itself appears relatively undeformed.

There are also pegmatites in the basement that are dated to ~500 Ma (Elburg et al., 2003) and those associated with the Palaeozoic British Empire Granite, which is totally undeformed (Elburg et al., 2013). As these pegmatites are mineralogically or texturally not clearly distinct from their Mesoproterozoic counterparts, all occurrences are mapped as undifferentiated pegmatites (PEG); although the metadata table gives information about the relative age of outcrops, when possible.

Migmatites (MIG)

Migmatites (MIG) form the dominant lithology in the Paralana Hot Springs area (section 5.5 Map at Paralana Plateau). Orthogneisses, as well as paragneisses are the host rocks of metatexites to anatexites in lenses of several tens of meters. The recrystallisation age, and probably therefore the anatexis of the basement rocks is Mesoproterozoic at ~1550 Ma (Fraser and Neumann, 2010). This interpretation is supported by structural features in the biotitic melanosomes that are foliated with S_{main} and the occurrence of the anatectic lenses, which follow the limbs of the Palaeozoic fold (see section 5.5 Map at Paralana Plateau). Therefore S_{main} formed during or shortly after this anatectic event.

Leucosomes in the migmatites are composed of elongated quartz, large K-feldspars and plagioclases and biotite. Micrographic textures and inclusions of each mineral are common. Irregular grain-boundaties indicate migrational recrystallisation after the migmatite's formation. Aligned, medium-grained biotites with porphyroclasts of feldspar and quartz form the melanosomes, which sometimes grade into coarse-grained biotitites (Black Biotite Schists; Fig. 13). As the melanosomes are already enriched in aluminous minerals, they act as fertile hosts for the formation of metasomatic hyperaluminous rocks (biotitites; Elburg et al., 2012).

Fig. 13: Photograph of isoclinal folding of a migmatite (MIG) at Winters Creek. S_{main} forms the axial-planar cleavage. In adjacent outcrops the melanosomes may be concentrated and mapped as biotitite schists – BBS (352874E/ 6665602N).

Black Biotite Schists (BBS)

Biotite-rich layers with porphyroblasts of corundum, spinel and tourmaline within the RCM have been interpreted as distinct sedimentary beds (Coats and Blissett, 1971) and altered mafic tuffs (Teale, 1993a). Elburg et al. (2012) found biotite-rich layers also within meta-igneous rocks, sometimes with a gradational transition to the host rock (discussed as "hyperaluminous rocks"). The thickness of these Black Biotite Schists (BBS) varies between centimetres to metres. In some cases they are traceable over hundreds of meters, useable as marker horizons for large-scale folding in the RCM (section 5.1.1 Mount Gee Map). The coarse-grained biotite crystals are aligned within S_{main}; often with an overprint of one (sometimes two) pronounced crenulation cleavages that are formed during the Palaeozoic deformation (Fig. 14a+b). The growth of porphyroblasts of corundum, spinel and sapphirine occurred syn- to late tectonic, as they overgrow the foliation, but the foliation also wraps around them. White corundum (first generation) is rimmed by green spinel; blue corundum

grew associated with chlorite (Roessiger, 2008; Elburg et al., 2012). Green spinel turned into blue spinel at one stage of metasomatism associated with the exolution of magnetite/hematite (Roessiger, 2008). Sapphirine is rare compared to corundum and spinel and is inferred to have formed late, as it overgrows first and second generation porphyroblasts. It is probably contemporaneous with a static recrystallisation of biotite during the Palaeozoic. Tourmaline is very common in the biotite schists and invariably overgrows all existing foliations and shows no signs of any deformation post-dating tourmaline growth. Cordierite, randomly oriented sillimanite, rutil/anatas, monazite/xenotime and inherited zircon are also found within the BBS (Elburg et al., 2012), also högbomite and taafeeite minerals in a spinel-phlogopite layer were recorded by Teale (1980). The genetic relationship of these minerals is complex and not yet analysed in detail.

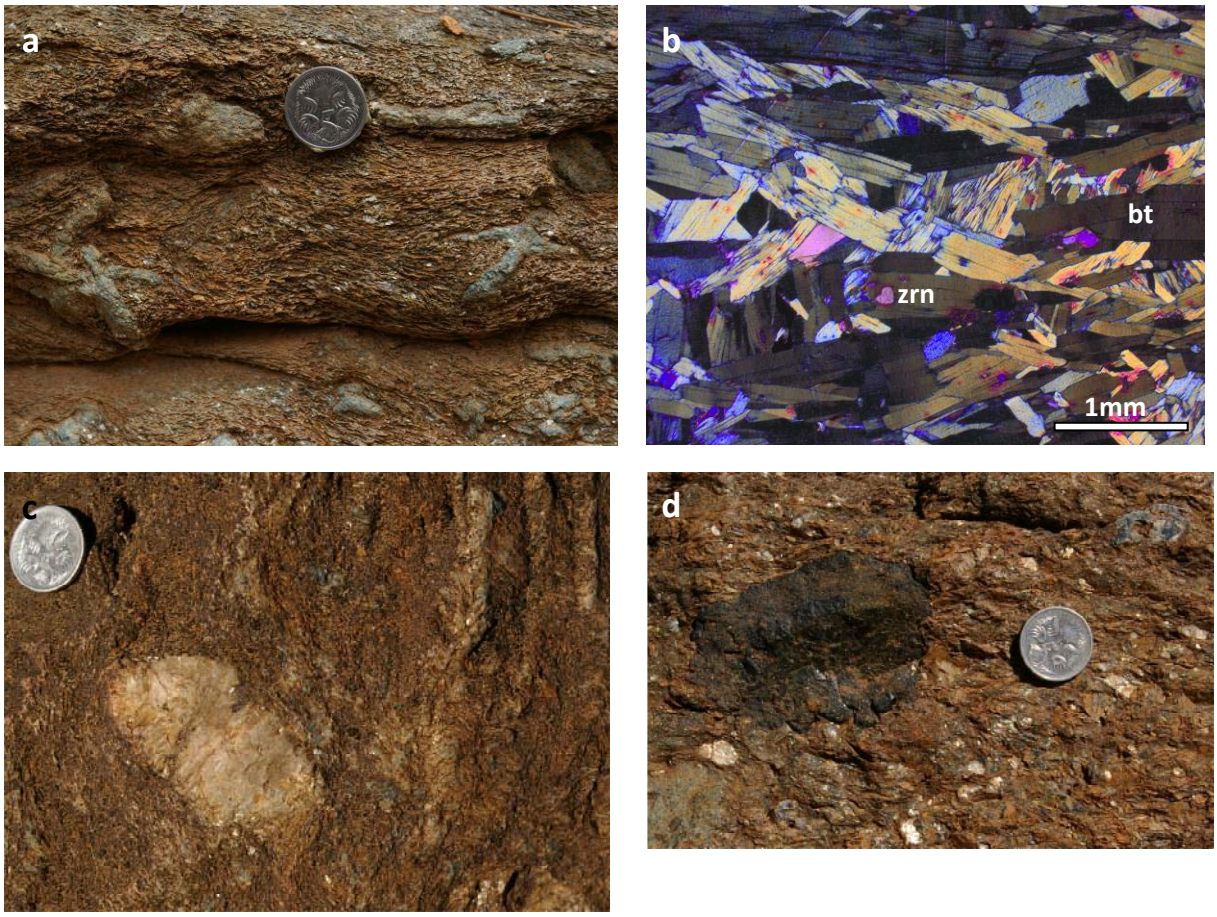

Fig. 14: Field photographs and thin section of Black Biotite Schist (BBS). a) Crenulated BBS with saphirine porphyroblasts. The saphirine overgrows the mica foliation. This strong foliation is unaffected by the presence of the sapphirine porphyroblasts, which therefore grew post-tectonically (340701E/ 6654070N). b) Microphotograph of a BBS. Biotite is mostly aligned along S_{main}, which is itself a crenulation cleavage (342074E/6655470N). c) Cm-sized white corundum porphyroblasts in biotite schist in former MNG in Arkaroola Creek, E of Nooldoonooldoona WH. S_{main} is crenulated in cm-scale kink folds, and wraps around the porphyroblast. Both may be related to a single (?Palaeozoic) deformation event. Small blue corundum crystals are scattered throughout the biotite schist. d) Large, completely post-tectonic tourmaline porphyroblast at same locality as Fig. 6c.

The formation of pure, iron-rich biotitites as distinct layers within the RCM and the granitoids is probably the result of an early Mesoproterozoic hydrothermal event, mobilising and concentrating aluminium (and other elements) of pelitic parts of the metasedimentary sequence and of mafic/granitoid intrusions within the metasediments and metagranites (Elburg et al., 2012).

Some BBS consist almost purely of phlogopite with randomly oriented crystals. This suggests that phlogopite replaced biotite after any significant deformation took place, and is therefore inferred to be related to a Palaeozoic hydrothermal activity (section 4.3 Palaeozoic deformation, magmatism and metasomatism). As the phlogopitites are likely to be altered Proterozoic Fe-rich biotitites, they are mapped as BBS.

4.2 Neoproterozoic Adelaidean succession

The deformed and metamorphosed basement was exhumed and eroded in the late Neoproterozoic. The extrusion of basalts onto the Curnamona and Gawler Cratons at ~827 Ma (Wingate et al., 1998) marks the onset of an intracontinental rifting in South Australia during the world-wide break-up of Rodinia. Several, a few km wide horst and graben structures around the MPI were filled with terrestrial and marine Willouran sediments and volcanics and are evidence of an extensional regime, causing listric normal faults in the basement. These graben faults provide pathways for later hydrothermal fluid flow (section 5.2 Map of Sunshine Pound, Arkaroola Creek and The Pinnacles, section 5.3 Map at Wild Dog Creek and The Needles, section 5.7.2 Wheal Turner and Blue Mine Map, section 5.7.3 Yudnamutana Map). Rift and sag phases, with several transgression-regression cycles and two major glaciations events alternate for more than 300 million years (Preiss, 2000). A hundreds of km wide basin, filled with marine and terrestrial sediments, covers the small Willouran grabens until syntectonic granites at ~514 Ma (Foden at al., 2006) mark the onset of the thick skinned Delamerian Orogeny in the southern Adelaide Fold Belt. A detailed description of the sediments and volcanics of the Adelaide “Geosyncline” is provided in Preiss (1987) and Preiss (2000) and will not be repeated here. Special issues on the lithology and deformation will be discussed in the relevant sections about the maps. Appendix 11.2: Acronyms in the GIS database summarises the mapped lithologies of the Adelaidean.

4.3 Palaeozoic deformation, magmatism and metasomatism

The large-scale folding that now determines the map pattern and exposure of the Mount Painter and Mount Babbage Inliers in anticline cores is traditionally assigned to the ~500 Ma, thick-skinned Delamerian Orogeny (e.g. Coats and Blissett, 1971; Paul, 1999; McLaren et al., 2006; Armit et al., 2012). It will be discussed below, that the folding must be intimately related to the exhumation of the basement rocks, which took place over a prolonged period of time in the Palaeozoic (Weisheit et al., 2013b). Folding was thus not only restricted to Delamerian times and we will therefore further refer to the folding as "Palaeozoic folding". The total amount of shortening was, however, minor at about 10-20% (Paul et al., 1999). Therefore, only weak structures in outcrop- and thin section scale can be attributed to the Palaeozoic folding. Only the lowermost Adelaidean units, in particular the Woodnamooka Phyllite, developed an axial planar cleavage. Coarse crenulation of BBS (Fig. 14b) may also be attributed to this folding, but other ductile deformation structures are rare or even absent. Large areas of the southern and central MPI were overprinted in the brittle stage by extensive fluid flow. The fluids altered and brecciated basement and cover by potassium metasomatism, iron infiltration and silicification (discussed in Chapter 3 of this PhD thesis). This report introduces new litholological units for the rocks related to this alteration.

4.3.1 Palaeozoic Pegmatites (PEG)

Post-Adelaidean metamorphism reached amphibolite facies in and close to the basement, with growth of biotite, cordierite and andalusite in the lowermost Adelaidean units. Although no

Delamerian granitic intrusion is known in the MPI, a folded pegmatite in the MNG in Arkaroola Creek was dated to ~499 Ma by Elburg et al. (2003) (Fig. 15a). Due to the lack of distinct features of Palaeozoic pegmatites, it is difficult to determine their relative age in the field.

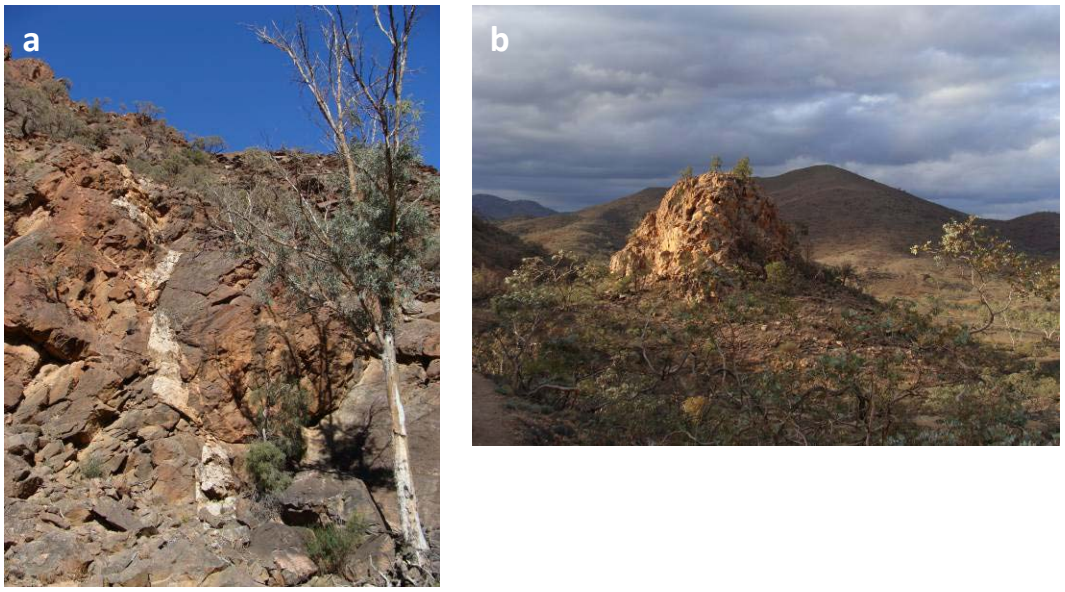

Fig. 15: Field photographs of pegmatites in the MPI. a) Faulted pegmatite in sheared MNG in Arkaroola Creek. K-feldspar and muscovite Rb-Sr geochronology give a Delamerian age (Elburg et al., 2003; 337107E/6649792N). b) The main Pinnacle, outstanding in the soft, coarsely brecciated sedimentary cover at The Pinnacles. The begmatite probably formed also at around 500 Ma and became incorportated in the breccia as a hard clast (337486E/6646848N).

A special occurrence of Cambrian pegmatites can be found in large breccia zones in the Adelaidean cover at the southern MPI (The Needles, Turmaline Hill: section 5.3 Map at Wild Dog Creek and The Needles; The Pinnacles: section 5.2 Map of Sunshine Pound, Arkaroola Creek and The Pinnacles; Sitting Bull, Giant´s Head, Bob´s Knob). The aplitic to pegmatitic leucocratic bodies consist of quartz, albite and K-feldspar with minor biotite and muscovite and locally tourmaline, fluorite and garnet. Graphic intergrowth is rare, but a perthitic exolution texture can be observed at some localities. Unlike the pegmatites in the basement, these bodies do not show any ductile deformation structure and no intrusive relationship to the breccias could be found. They are rather prominent clasts, more resistant to weathering than the soft sedimentary host breccias (see section 4.3.3 Early Palaeozoic metasomatism and brecciation; Weisheit et al., 2013a; Fig. 15). The age of these pegmatites was determined by Elburg et al. (2003) to ~496 Ma (Sm-Nd whole rock, fluorite and garnet) and to ~436 Ma of an errorchron on the Rb-Sr system. Some unpublished Rb-Sr ages of these pegmatites by G. Teale yield ages between 450 and 370 Ma. These ages might be a hint of the resetting of the Rb-Sr system, after their post-tectonic formation in the Palaeozoic.

4.3.2 British Empire Granite (BEG) and related intrusions

The British Empire Granite intruded at ~460-440 Ma close to the centre of the Yankaninna Anticline in metasediments of the RCM (e.g. Elburg et al., 2003; McLaren et al., 2006). The main batholith can be subdivided petrologically and geochemically into an I-type (granodiorite) and a S-type phase (Elburg et al., 2003), both ranging from coarse to fine-grained and being undeformed (Fig. 16a). The peraluminous I-type consists of plagioclase, K-feldspar, quartz, biotite and minor (secondary?) muscovite with apatite, zircon, monazite and titanite. In contrast, the S-type contains more muscovite and K-feldspar and no biotite, but primary magmatic garnet (McLaren et al., 2006). The

RCM at the contact to the pegmatitic and aplitic granite of the BEG show a narrow zone of contact metamorphism (max. 100 m), but no migmatitisation as suggested by McLaren et al. (2006) (Fig. 16b). Migmatites that can be found at "The Tail" of the BEG are the Proterozoic host rock of the intrusion.

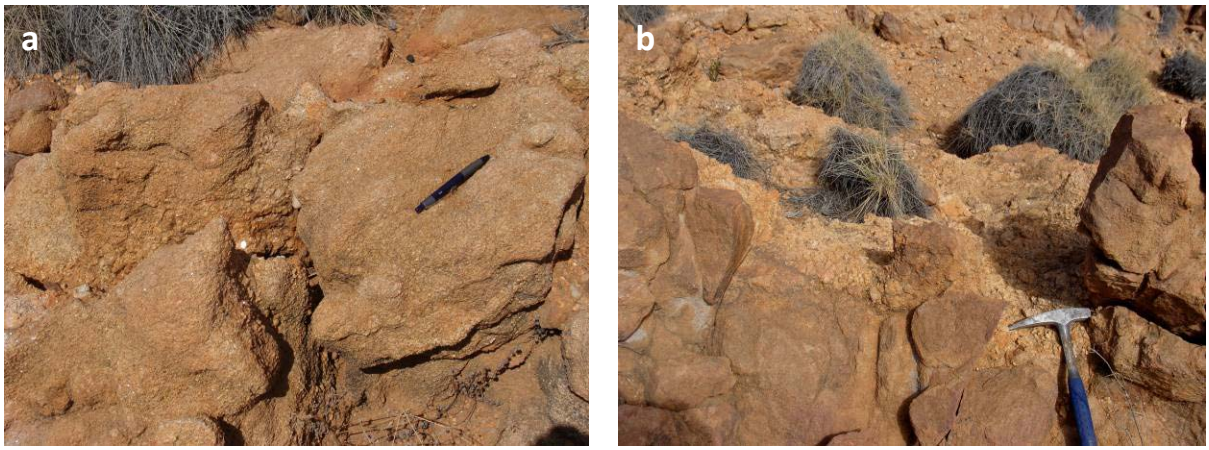

Fig. 16: Field photographs of British Empire Granite (BEG). a) Aplitic and pegmatitic BEG show intermingling structures (355133E/6672172N). The BEG is massive and undeformed. b) Pegmatitic S-Type of the BEG (upper corner of the picture) in contact to massive, biotite-rich RCM (contact metamorphism). Migmatites in contact to the BEG could not be found at this site (355145E/6672155N).

A swarm of undeformed leucocratic biotite and muscovite pegmatites (PEG) occur northwest of Mount Painter in The Armchair area (Coats and Blissett, 1971). A 455±4 Ma U-Pb zircon age of a pegmatite at the Armchair is given by Elburg et al. (2013). They are hence related to the intrusion of the BEG The pegmatite dykes mostly strike EW, roughly parallel to the strike of S_{main} and the axial plane of the Palaeozoic Yankaninna Anticline. These bodies are either defined as Pegmatites (PEG) or Yellow Microgranites (YMG) in the maps. The latter is characterised by fine-grained quartz, K-feldspar, biotite and minor muscovite, without any foliation or annealing structures.

4.3.3 Early Palaeozoic metasomatism and brecciation

Hydrothermal fluid flow that was active during the exhumation of the basement resulted in the formation of impregnation, veins and breccias (partly already described by Coats and Blissett, 1971 and Drexel, 1980). A detailed (geochemical) study of this event(s) is presented in Chapter 3 of this PhD thesis and only a descriptive summary will be given in the following. A model for the formation of these breccias is proposed in Weisheit et al. (2013a).

Pink Pegmatitic "Granite" (PPG)

Extensive K-feldspar alteration affected basement rocks during the Palaeozoic in the southern and eastern central MPI, as well as lower Adelaidean cover sediments at the south of the MPI. A transition from metasedimentary and metagranitic host rocks into pure fine-grained to pegmatitic K-feldspar and quartz rocks can be found in many outcrops (Fig. 17a). Bons and Roessiger (2008) therefore defined these metasomatic rocks as Pink Pegmatitic "Granites" (PPG; called "K-feldspar metasomatite" in Chapter 3 of this PhD thesis). The working term derived from the fact that these rocks were interpreted as (brecciated) granite in drill logs and mapping by exploration companies. Bons and Roessiger (2008) pointed out the metasomatic origin. As the K-feldspar altered rocks form a

distinct lithology for which no suitable term exists in the literature, the historic name was kept. Maps that were produced after 2008 also differentiate between transition stages between host rocks and PPG. These zones are symbolised in MapInfo with transparent layers on top of host rock layers. The transition layer is called "incomplete K-feldspar alteration" in the combined GIS map (called "K-feldspar overprints" in Chapter 3 of this PhD thesis); in single detailed maps terms like "PPG-overprint" or "PPGtisation" may be used. PPG is often, but not always in close proximity to real graphic K-feldspar - quartz ± muscovite pegmatites and K-feldspar - quartz ± magnetite/hematite veins (Fig. 17b).

Important reactions during the K-feldspar metasomatism in thin sections are: the alteration of biotite into microcline, iron-oxide and water (presumably carrying the Mg); the microclinisation of plagioclases and the new-growth of microclines over pre-existing structures (Fig. 17c+d).

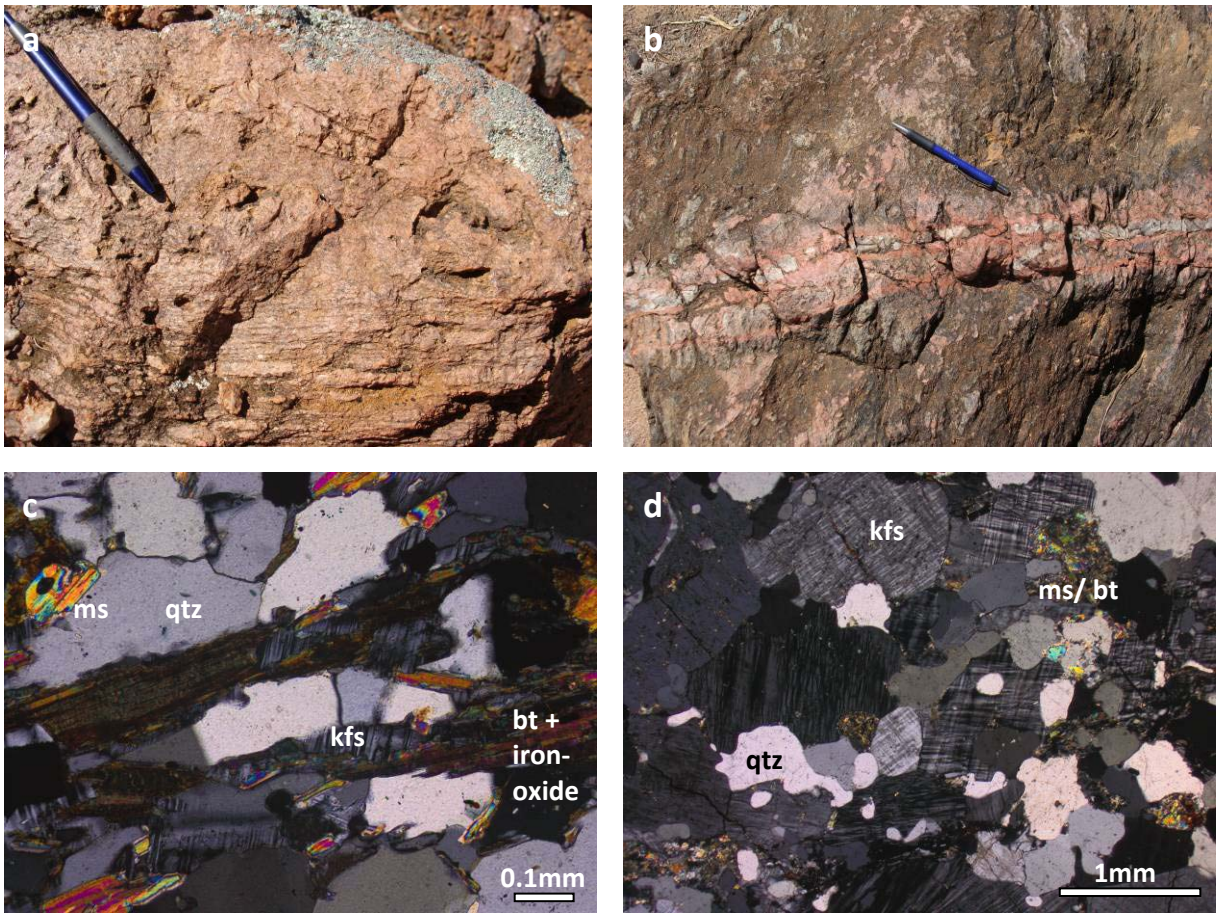

Fig. 17: Field photographs and thin sections of K-feldspar altered rocks. a) Foliated RCM at Radium Creek is gradationally overprinted by K-feldspar and quartz forming the Pink Pegmatitic "Granite" (PPG; 340342E/ 6653066N). Well visible is the breakdown of aligned biotites to the top of the photograph. b) Quartz-feldspar vein crosscutting foliated biotite-rich MNG south of Nooldoonooldona Waterhole (334780E/ 6649090N). The impregnation front at the vein follows the foliation of the host rock. c) Micophotograph of a MNG north of The Pinnacles (337280E/6647968N). Aligned biotites react in situ to microcline and iron oxide under the release of water. d) Advanced K-feldspar alteration of a RCM at East Painter Camp (344334E/6654944N). New-grown microcline (kfs) with equilibrium grain boundaries to other microcline. An irregular reaction texture developed between microcline with quartz (qtz) and ex-biotite (bt). The latter alters into muscovite (ms) and iron oxide.

PPG – Matrix Breccia (PMB)

Pink breccias with a K-feldspar-quartz matrix are classified as PPG-Matrix Breccia (PMB) ("K-feldspar and quartz cemented breccias" in Chapter 3 of this PhD thesis). There is a gradual transition of PPG to PMB, which is used when brecciation is evident in the field. Clasts of this hard, weathering-resistant breccia can be any basement lithology, including the PPG itself (only the Pebble Dyke and Mt. Gee - related units are not represented). They are (sub-)rounded to angular and can be up to metres in size. Fig. 18a shows that K-feldspar alteration is an ongoing process that also affects clasts inside the breccia if not altered yet. PMB covers large areas from Radium Ridge to the east and northwest towards Hidden Valley. The breccia´s formation is interpreted to be a result of fluid-focusing at a structural zone of weakness, defining them as contemporaneous to the PPG (Fig. 18a+b). Clasts of PPG can still be recognised in the quartz - K-feldspar breccia on the thin-section-scale, with rims of feldspar-alteration (Fig. 18c). Later iron-rich fluids used the same pathways (Fig. 18d).

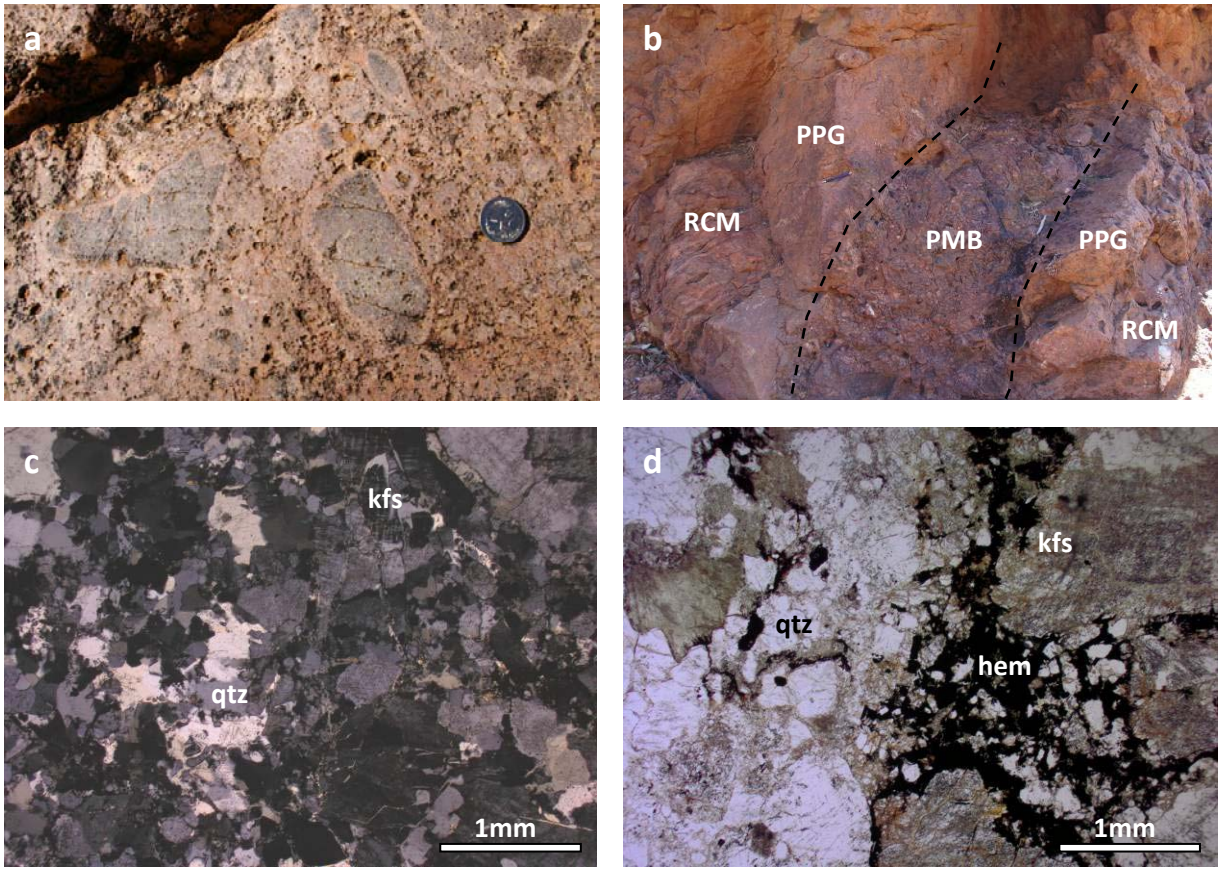

Fig. 18: Field photographs and microphotographs of PPG Matrix Breccia (PMB). a) The breccia at East Painter Gorge consists of quartzitic clasts in a feldspar-quartz matrix. Smaller clasts are completely altered to microcline and quartz; larger clasts show only alteration along the rim and in cracks. b) Outcrop near East Painter Camp (344325E/6654955N). A transition from foliated RCM at the left side of the picture, into a PPG into a PPG Matrix Breccia (PMB) in the centre of the picture is vell developed. A pen for scale is in the left centre of the picture. c) Brecciated PPG in a fine-grained matrix of microcline (kfs) and quartz (qtz) at East Painter Camp (344334E/6654944N). Clasts of zircon and monazite are the last remnants of the RCM host rock. d) PMB is impregnated by fine grained hematite (hem; 344334E/6654944N). This is a first stage of massive Hematite Matrix Breccia (HMB).

PPG and PMB are often crosscut by veins and breccias of quartz – K-feldspar ± hematite (QHF) that can be found all over the mapping areas in basement and cover rocks. Tourmaline is often associated

with the PPG quartz and feldspar veins (TPV). The QHF veins and breccias and the TPV are interpreted to represent late stages of the K-feldspar alteration (Fig. 19).

Fig. 19: Field photograph of a PPG rock that is cut by Quartz – Feldspar ± Hematite veins in Yudnamutana Gorge (346074E/ 6658575N). These veins are also related to the PPG alteration, but they formed in a late stage of mineralisation.

Diopside – Titanite Vein (DTV)

Pegmatitic veins of diopside and titanite (DTV) crop out within basement lithologies along Radium Creek in the centre of the southern MPI (Bakker and Elburg; 2006). Loose pieces of diopside were found to the NW, up to Hidden Valley, but unfortunately no in-situ veins. Bakker and Elburg (2006) studied fluid inclusions of the diverse mineral assemblage of the DTV and demonstrated a transition of highly saline magmatic fluids to colder, almost pure water. A low-temperature hematite-quartz assemblage overprints the DTV, which is now interpreted to be related to the separate Mt. Gee Event (see section 4.3.5 Silicification and the Mt. Gee Event). Field observation suggests that the DTV formed contemporaneous with the early K-feldspar alteration as it crosscut a weakly K-feldspar-altered granite (Fig. 20), includes clasts of PPG and is overprinted by PPG-related quartz-K-felspar veins. The relationship to the Dark- and Hematite Matrix Breccia (see the following) is not known. Elburg et al. (2003) published an U-Pb age on titanite of ~443 Ma.

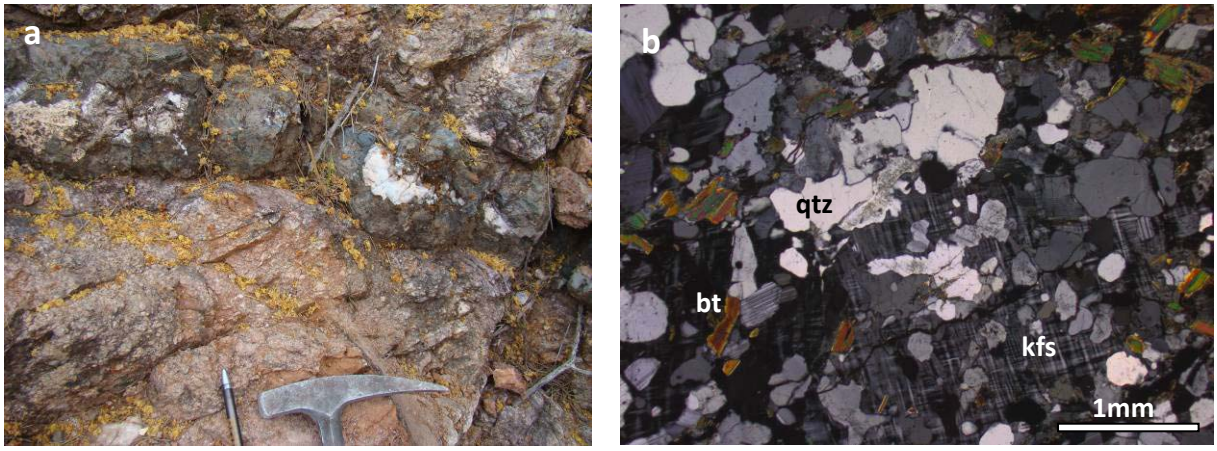

Fig. 20: Field photograph of a diopside-titanite vein (DTV) and thin section of the host rock. a) The small diopside-titanite-calcite vein crosscuts a weakly PPGtised granite northeast of Sunshine Pound (339988E/6651834N). b) The microphotograph of this host granite shows some PPG-related microcline overgrowing the pre-existing recrystallised texture of a weakly foliated quartz-plagioclase-biotite granite.

Dark Matrix Breccia (DMB)

A fine-grained hematitic – chloritic – goethitic dark brownish breccia occurs within the PMB in proximity to the Hematite Matrix Breccia (HMB; described in the following). This fine-grained Dark Matrix Breccia (DMB) can also include any basement lithology, as well as the PMB (Fig. 21a+b). Clasts are heavily altered with a large amount of clays and iron-hydroxides. The transition to the HMB is gradational.

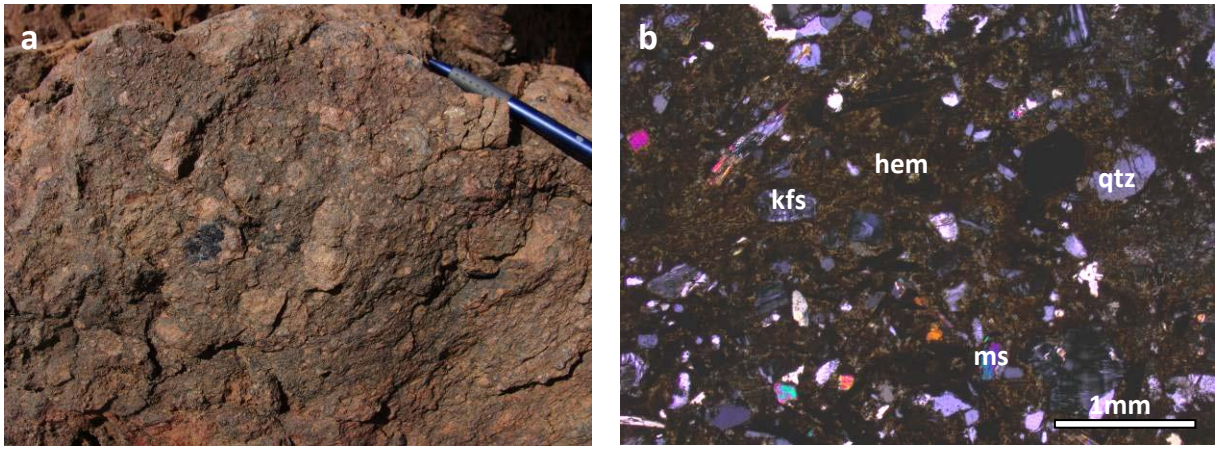

Fig. 21: Field photograph and thin section of a Dark Matrix Breccia (DMB). a) The DMB may include granitic clasts, as well as PPG and PMB clasts in a fine-grained chloritic-hematitic matrix (picture taken in Sunshine Pound; 339892E/6651896N). The tourmaline clast in the centre of the picture indicated that turmalinisation pre-dates the DMB formation. b) Microphotograph of a Dark Matrix Breccia (DMB) at Streitberg (343389E/6657580N). Fine-grained matrix of chlorite, goethite and hematite (hem) with clasts of PPG, PMB and host rocks. The transition into a Hematite Matrix Breccia (HMB) is gradational.

Hematite Matrix Breccia (HMB)

The Hematite Matrix Breccia (Bons and Roessiger, 2008) occurs as irregular, lenticular and sheet-like bodies on the m to 100 m in scale. The matrix consists of fine to medium-grained specular lath-shaped hematite (martite) with minor quartz. Accessory minerals are fluorite, barite, monazite, torbernite, jarosite, rutile/anatase and sulphides. Like in the DMB the round to angular clasts can be any basement rock and PMB, but with a few to a few tens of cm in size they are usually smaller than the clasts in the DMB (Fig. 22a+b). The HMB is the host to the secondary uranium enrichment in the basement. Elburg et al. (2013) dated monazites in the HMB at ~355 Ma.

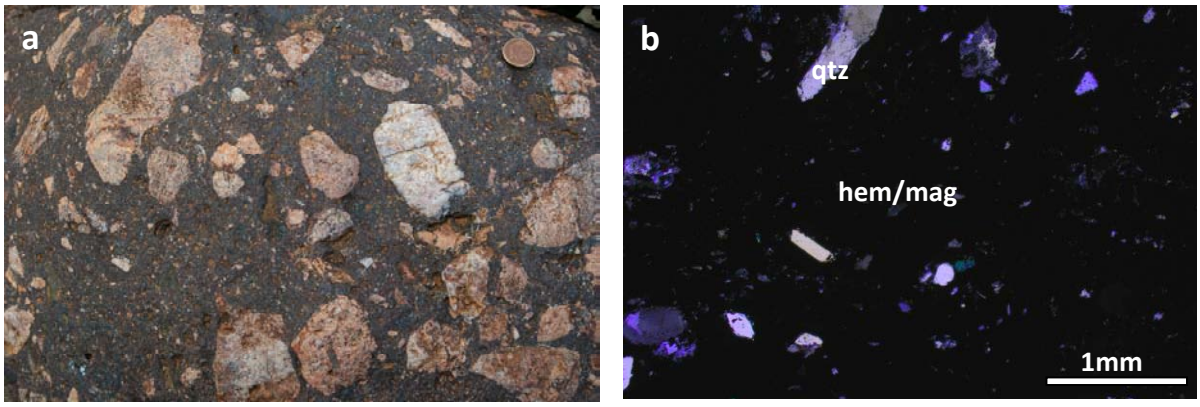

Fig. 22: Field photograph and thin section of a Hematite Matrix Breccia (HMB). a) Sub-rounded to angular clasts of quartzites, granites, PPG and PMB in a fine-grained hematite-quartz matrix at East Painter Camp. The occurrence of torbernite is a macroscopic evidence for the high uranium content in these breccias. b) HMB consists of several generations of martite and hematite with clasts of PPG, PMB and host rocks. The transition from a DMB is gradational (344438E/6654714N).

Quartz – Hematite Breccia (QHB)

This breccia occurs close to the studied copper ore deposits at Yudnamutana, Wheal Turner, Blue Mine, Lady Buxton and British Empire Mine. It composes of a quartz - hematite/magnetite (martite) matrix with pyrite, copper sulfides and titanium-oxides. Often pyrite is pseudomorphically replaced by limonite. A relation of these breccias and veins to the HMB in the centre of the southern MPI is discussed as a possible scenario in the report to the copper ore maps (Lang, 2012). These breccias (and veins) are possibly the host of the primary copper ore.

Magnetite-rich Vein (MGV); Hematite Vein (HEV); Goethite Vein (GOV)

There are a few outcrops of magnetite-rich and hematite-rich veins and alteration zones in basement and cover. They consist of magnetite, hematite (martite), maghemite and sulphides. The latter suggest a relation to the copper ores. Little occurrence of secondary goethite are found in Sunshine Pound.

4.3.4 The Pebble Dyke (PED)

The Pebble Dykes (=Diamictite Dykes; Cowley et al., 2012) play an important role in the interpretation of the hydrothermal events in the southern and central MPI, although their genesis is not totally understood. There are steep dykes in the Mt. Gee – Mt. Painter area with a width from a dm to >10 metres. Contact with the host rock is usually sharp. Their fine-grained matrix is greenish to reddish, and consists mainly of angular to rounded clastic quartz grains. Clasts are well rounded and reach up to boulder size (up to 0.5 m) (Fig. 23). The texture varies from matrix-supported to clast-supported. A 10-20 cm dyke east of Mt. Gee may be traced over a distance of 100 m. A particular feature of these dykes is the variety of clast lithologies, which not only include local basement units like RCM, metagranites and the PPG, but also volcanics of unknown (Gawler, Curnamona; or PEP?) origin. The youngest detrital zircon age is 315±9 Ma and the age spectrum suggests an Antarctic origin of the tillite-like conglomerate (Brugger et al., 2011). The lack of metamorphism or deformation, and the distant origin of clasts and zircons indicate that the Pebble Dyke formed near

the surface in deep cracks. The "clear fluvial origin" (Brugger et al., 2011) is not straightforward, as the dykes are vertical and are clearly infill of vertical structures. We therefore interpret these as (glacial) sediments that filled deep cracks. Considering that no surface sediments are exposed in the area, these cracks must have been several hundreds of metres deep (Bons and Roessiger, 2008).

No matter what the exact origin of the pebble dykes is, they form crucial evidence to separate the K-feldspar alteration and associated breccias that are cut by the pebble dyke, from later, sub-surface Mt-Gee type hydrothermal activity that cuts the pebble dykes.

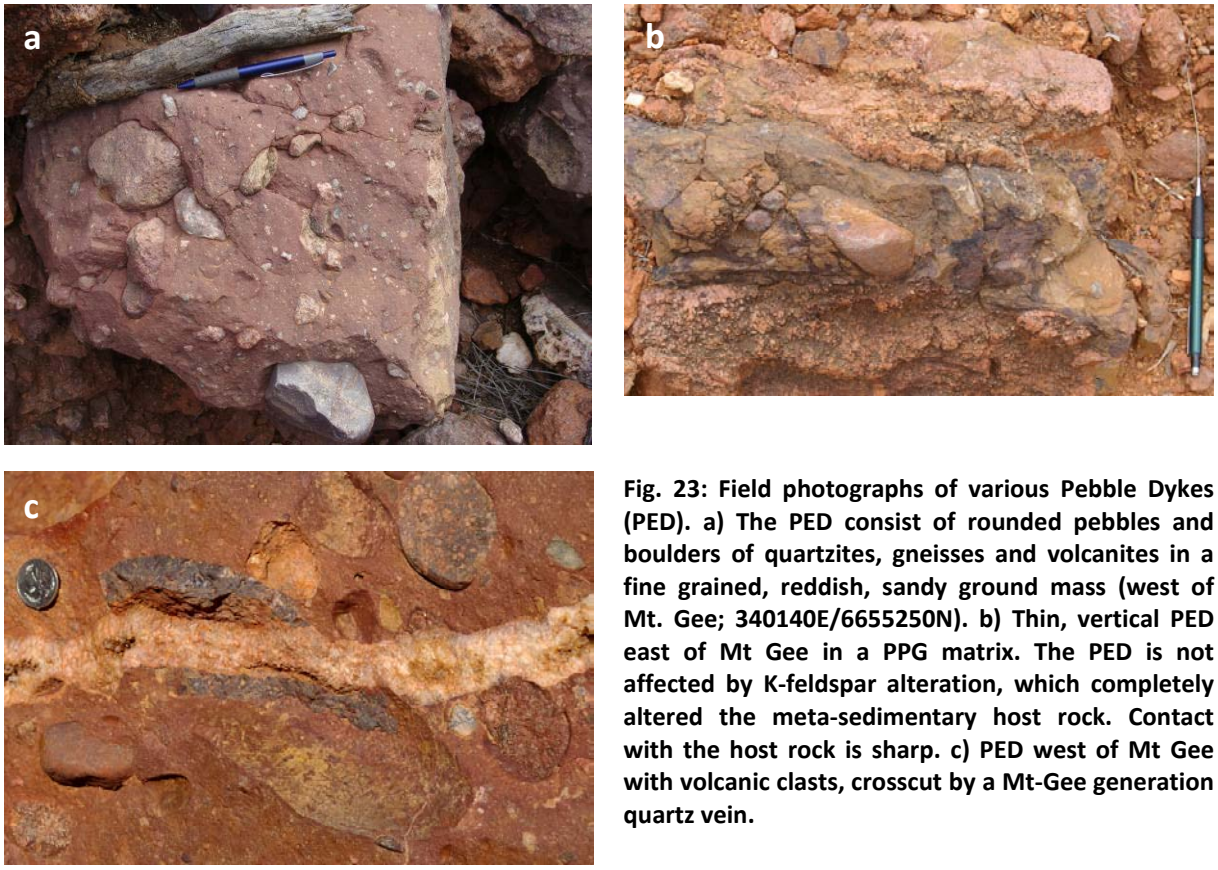

Fig. 23: Field photographs of various Pebble Dykes (PED). a) The PED consist of rounded pebbles and boulders of quartzites, gneisses and volcanites in a fine grained, reddish, sandy ground mass (west of Mt. Gee; 340140E/6655250N). b) Thin, vertical PED east of Mt Gee in a PPG matrix. The PED is not affected by K-feldspar alteration, which completely altered the meta-sedimentary host rock. Contact with the host rock is sharp. c) PED west of Mt Gee with volcanic clasts, crosscut by a Mt-Gee generation quartz vein.

4.3.5 Silicification and the Mt. Gee Event

Some occurrences of silicification in the MPI are interpreted to be a result of a second hydrothermal event. It is distinct from the evolving K-feldspar - iron oxide alteration, which formed the hydrothermal units described above. Extensive silicified rocks and hydrothermal veins can be found in the Mt. Gee-Mt. Painter area and occasionally in the whole southern and east-central MPI. They are concentrated along probably permeable zones, such as hydrothermal breccias and fault zones. The following section interpretes that the formation of all mapped silicified units occurred during the Mt. Gee Event. However, most of them are probably related to the hydrothermal system that caused the K-feldspar alteration (see Chapter 3 of this PhD thesis).

Silicified Matrix Breccia (SMB)

A silica-rich fluid impregnated various host rocks and formed massive breccias with a quartz-rich matrix and sub-rounded to angular clasts. The quartz is fine to medium grained, sometimes

associated with fine-grained hematite, resulting in a shiny, dark-reddish colour of these breccias (jasper-like; Fig. 24). The Silicified Matrix Breccia (SMB) forms weathering-resistant ridges and sheets and may be easily recognised in the field. Silicification is often parallel to zones of preceding intense hydrothermal brecciation (e.g. along PMB) and along the Paralana Fault Zone in the Hot Springs area (section 5.5 Map at Paralana Plateau). SMB is affected by the quartz - hematite Mt. Gee Unit (MGU) at Mount Gee. Therefore these occurrences are interpreted to be an early stage of the Mt. Gee event (see below).

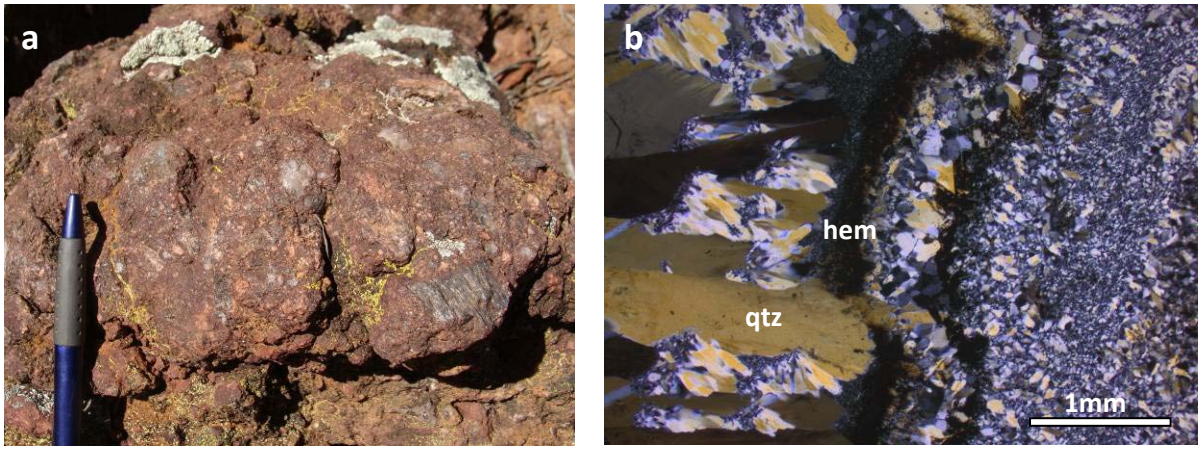

Fig. 24: Field photograph of a Silicified Matrix Breccia (SMB) and a Microphotograph of a Mount Gee type sinter. a) The SMB usually forms hard ridges of reddish quartz breccia with clasts of RCM and PPG (photograph taken south of Mt. Gee; 34329E/6653154N). b) Different generations of needle quartz and hematite grew in open space in the Mount Gee type sinter at Mt. Gee.

Mount Gee Unit (MGU)

Parts of Mount Gee and Mount Painter in the centre of the southern MPI are made of a quartz-hematite sinter of several generations, crosscutting all previous lithologies, including the Pebble Dyke (Fig. 24b, Fig. 25,). The mineralisation formed in open vugs and cracks close to, or at the surface. Mount Gee-type quartz (veins) typically forms rosettes and euhedral milky quartz crystals, often grown on a needle-like mineral (laumontite; Coats and Blissett, 1971), which is usually not present any more ("nail-hole quartz"). The associated breccia is defined as the Mount Gee Unit (MGU) with rounded clast-in-clast breccia of jasper-like quartz-hematite and silicified hematite-feldspar impregnated host rocks (SMB), cemented by Mount Gee-type quartz (Bons and Roessiger, 2008). The MGU forms sheets that dip gently to the northeast. A detailed study of the MGU is summarised in Rehder (2009). MGU veins can be found in the whole southern MPI.

The MGU sinter probably developed during boiling at a hot spring close to and at the surface, as indicated by the textures and complex overprint of quartz/chalcedony and hematite (Drexel and Major, 1987; Brugger et al., 2011). As the MGU cuts the Pebble Dykes, they have to be younger than 315±9 Ma (Brugger et al., 2011). Brugger et al. (2011) dated an U-leaching of a davidite grain at the roots of the MGU to 286±6 Ma. Low temperature thermochronology on MGU-affected rocks indicate that the system was active for more than 100 Myr (Weisheit et al., 2013b).

Fig. 25: Field photograph of a Mt. Gee Unit breccia (340670E/ 6654690N). Several generations of quartz and hematite developed.

Quartz Vein (QZV); Calcite Vein (CAV); Barite Vein (BAV)

Pure hydrothermal quartz veins (QZV) can be found all over the mapping areas. Their time of formation is unclear and may range from late-Delamerian to the Mount Gee event. A few calcite (CAV) and barite veins (BAV) are found in basement and cover, but their age is also unclear.

4.3.6 Soft breccias: The Needles, The Pinnacles and Hidden Valley

A range of extensive breccia zones are developed in the Adelaidean of the upper Callanna Beds, close to or at the unconformity to the basement of the southern MPI (The Needles, Turmaline Hill, The Pinnacles, Sitting Bull, Giant´s Head, Bob´s Knob). These breccias are combined in a single GIS-layer called "breccia", but in the single maps they may be called with their local name (e.g. Needles Breccia, NEB). The largest one is the Needles Breccia (NEB), covering an area of ~2 km² in siltsones, shales, sandstones and dolomites west to Wild Dog Creek (section 5.3 Map at Wild Dog Creek and The Needles). A second studied breccia zone at the southern MPI is located at The Pinnacles (PIB), with an area of only ~0.3 km² at the same stratigraphic level as the NEB (section 5.2 Map of Sunshine Pound, Arkaroola Creek and The Pinnacles). A detailed study on the brecciation is given in Weisheit et al. (2013a).

Clasts within the NEB come from adjacent lithologies of cover sediments, no basement clasts could be found during this study. The size of the angular clasts varies from the >>m down to the cm-scale. The clasts are chaotically distributed in a soft, fine-grained, greenish-white ground mass (Fig. 26). Most of the breccia clasts are altered to actinolite-tremolite-scapolite-bearing calc-silicates, but unaltered sediments can be found as well. Coats and Blissett (1971) associated this medium-temperature-alteration with the intrusion of the prominent leucogratic pegmatites and aplites within the breccias (see section 4.3.1 Palaeozoic Pegmatites (PEG)). But after extensive studies in the field we could not find a direct relationship of the alteration with an intrusion of the pegmatites. The alteration to the actinolite-tremolite-scapolite assemblage is interpreted to be contemporaneous with brecciation. The pegmatite bodies, which range in size from m to 100 m, are interpreted as clasts in the breccia. Quartz-feldspar veins and silicification postdate the breccia formation.

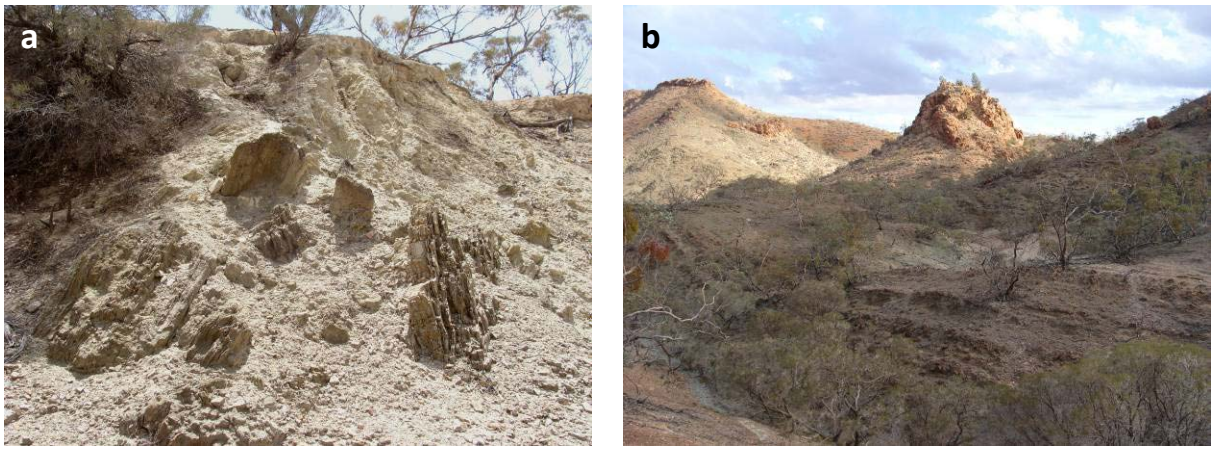

Fig. 26: Field photographs of well weathered breccias in cover sediments. a) The white-greenish breccia at The Needles (NEB) includes m-scale clasts of adjacent Adelaidean dolomites, siltstones and shales (329840E/ 6651470N). Hydrothermal alteration in this area formed actinolite-chlorite assemblages. The soft breccia is prone to kaolinite weathering. b) Well-layered, weakly metamorphosed sediments of the Adelaidean Opaminda Formation (OPF) are brecciated in close proximity to the main Pinnacle pegmatite (339497E/6651882N). Fluids caused actinolite – chlorite alteration of the sediments, but brecciation is less developed than at The Needles.

The PIB at the Pinnacles is less mature than the breccia in the NEB. There are only small zones of soft, phyllosilicatic breccia between large sedimentary clasts, which are barely transported and only tilted relative to their former position in the stratigraphy (Fig. 26b; Fig. 27a). Hydrothermal alteration is restricted to pelitic and calcarious rocks; quartzitic layers within the tens of m size clasts remain mostly unaffected. As in the NEB, the prominent leucogratic pegmatites within the PIB do not show any directly related contact metamorphism with the breccia and also no systematic arrangement of the pegmatites could be observed. At one outcrop, however, a sediment is intruded and metamorphosed by the main Pinnacle pegmatitic body (Fig. 27b). According to the field observation our favored interpretation is that this sediment and the Pinnacle form one large clast in the breccia zone.

The pegmatite intrusions at these breccia zones, which were dated to be late Delamerian (Elburg et al., 2003; Elburg et al., 2012), could be a trigger of the brecciation event, but do not post-date it.

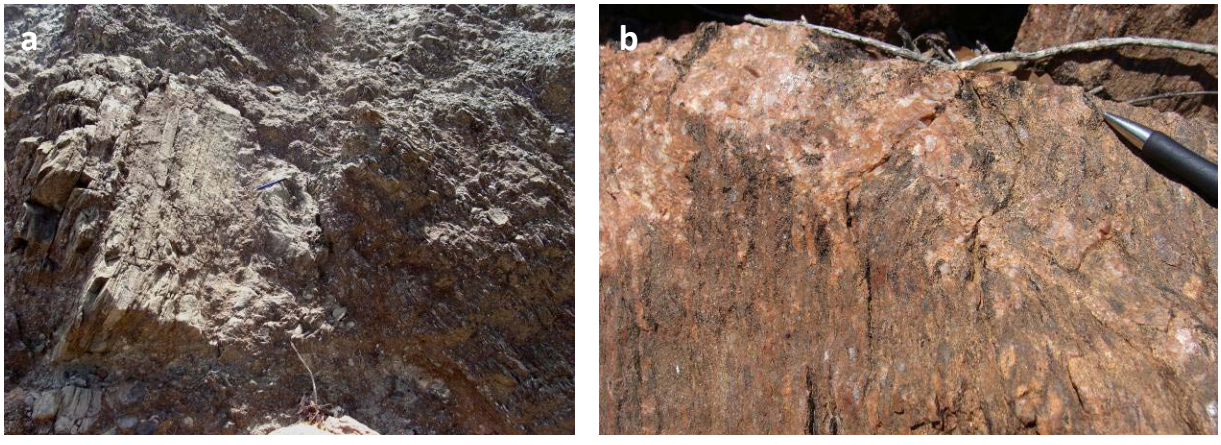

Fig. 27: Field photographs of clasts in the Pinnacles Breccia (PIB). a) The PIB is mainly clast-supported with small breccia zones, which are concentrated in chicken wire-like zones (337498E/ 6647469N). b) Diffuse intrusive contact of a Pinnacle pegmatite with a contact-metamorphic Adelaidean hornfels. This outcrop is interpreted to be part of a large clast within the PIB (337397E/6646842N).

Another prominent occurrence of such a soft breccia is in Hidden Valley, east of the centre of the MPI (section 5.6 Map of Hidden Valley). The brecciated area is ~10 by 1 km, surrounded by metasediments and metagranites of the basement. Clasts of Adelaidean cover units of the Lower Callanna Beds (Coats and Blissett, 1971), as well as high metamorphic grade basement rocks and igneous lithologies of unknown origin range in size from < 1 mm to >100 m (Fig. 28a+b). Leucogratic bodies, as in the breccias of the southern MPI, as well as muscovite-bearing pegmatites can also be found as clasts within the Hidden Valley Breccia (HVB). A detailed list of the lithologies found in Hidden Valley is given in Wülser, 2008. In the GIS database special Hidden Valley lithologies are mapped as HV-... units.

There is no distinct matrix phase in the HVB, as clasts are surrounded by smaller clasts down to the smallest size. Most thin section-scale clasts are corroded and replaced by phyllosilicates (e.g. stilpnomelane; Fig. 28d). The largest 100 m - size clasts display almost no transport, but only tilting from their original position close to the breccias´s margin.

The host rocks of the HVB (essentially locally deformed MNG to the east and quartzitic to metapelitic RCM to the west) are multiply brecciated and altered at the contact to the HVB. Mica-Matrix-Breccia (MMB) and Chloritic Breccia with Feldspars (CFB) that may also be silicified (CSB) can be found in RCM and MNG close to the HVB. These hard breccias are interpreted as an early stage of brecciation. They are incooperated as clasts-in-clasts in PMB that crops out in a >20m wide zone along the whole eastern contact (Fig. 28c). MMB can also be found in the Blue Mine Creek area.

Detailed analysis of the Hidden Valley-type breccias (including the PIB and the NEB) are given in Weisheit et al. (2013a).

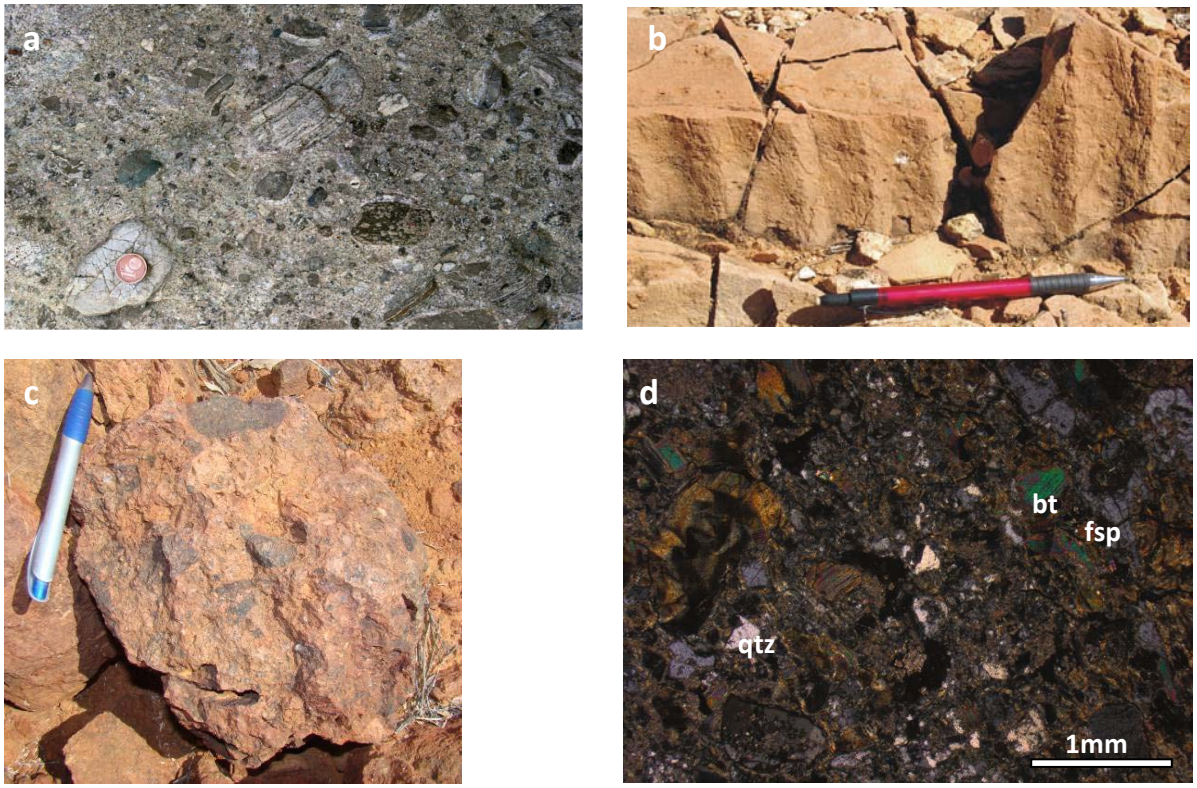

Fig. 28a: Field photographs and thin section of breccias at Hidden Valley. a) Greenish soft Hidden Valley Breccia (HVB) with clasts of altered sediments, mafics, basement metamorphics and breccias. Clasts are often altered along their rims. Fine-grained areas are composed of smaller clasts. b) Wave ripples in a larger

clast of sandstone in the HVB. Sedimentary structures are common in weakly metamorphosed, probably Adelaidean clasts. c) The MNG is multiply brecciated at the contact to Hidden Valley. Black silicified chloritic breccia (CSB) is included in a PPG-Matrix Breccia (PMB) with clasts of MNG (354913E/6667208N). These hard breccias pre-date the formation of the well-weathered Hidden Valley Breccia (HVB). d) Microphotograph of a HVB with clasts of feldspar (fsp) – quartz (qtz) – mica (bt) lithologies surrounded by phyllositlicates (357144E/ 6672720N). The clasts are rounded to angular and show alteration rims due to corrosive wear.

4.3.7 Structures, Interpretation and the Tertiary-Quaternary layer

Traces of faults and fold axial planes are marked in the maps as red and black lines, respectively, with information to direction of movement and plunge in the metadata files. The prominent Paralana Fault Zone follows the hard PMB and SMB at the eastern side of the inlier. Fault striations and slicken sides on these breccias indicate post-brecciation movements along this fault zone with the west side moving upwards and to the south.

Selected strike and dip symbols of the main foliation S_{main} and bedding S_0 in the Adelaidean are incorporated in a single layer.

Areas that were not mapped but interpreted by extrapolation of the mapped geology, or by using geophysical data (radiometrics) or hyperspectral analyses are overlaid with a transparent interpretation layer. The metadata file gives information to the used resource of the extrapolation.

The Tertiary-Quaternary layer (TQY) includes creek gravels, river beds, regolith areas and regions that were not mapped and not extrapolated.

5. Discussion of the geological maps

The focus of the mapping projects in the southern and central MPI lay on the Palaeozoic hydrothermal/metasomatic overprint and brecciation of basement and cover. Other points of interest were to unravel Palaeozoic and pre-Delamerian structures (like cleavages, folds and faults) and the magmatism during the Ordovician.

5.1 Maps of the Mt. Gee – Mt. Painter area: K-feldspar – quartz alteration

The fundamental units of the K-feldspar metasomatism were defined during the mapping project in 2007 in the centre of the southern MPI (Roessiger, 2008). Gradational transitions from foliated, biotite-rich metasediments into massive feldspar-quartz "granites" and their close proximity to breccia zones found in the Mount Gee area resulted in the interpretation of a metasomatic overprint of originally Mesoproterozoic meta-sediments. The same was observed in three adjacent maps of the Radium Ridge area (Kling, 2008), the Streitberg area (Kieslinger, 2010) and the East Painter Camp area (Rehder, 2010). Special focus in these areas lies on the diverse hydrothermal breccias (Fig. 29).

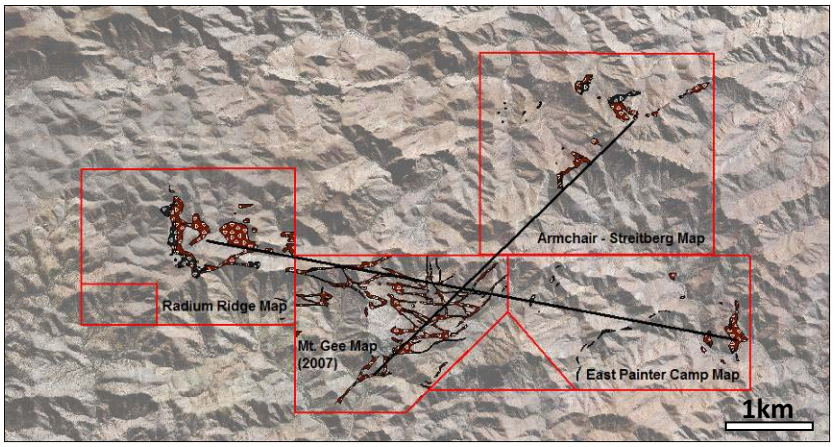

Fig. 29: MapInfo snap-shot showing the location of the Mt. Gee Map (2007) and adjacent mapping areas of the fieldwork in 2008. The trend of the main DMB/HMB-breccia zones are symbolised by the NE-SE and the E-W running arrows. The main hematitic breccias in the three mapping areas are shown with brown (DMB) and black (HMB) polygons. The breccia zones in the Mount Gee Map are PMB.

5.1.1 Mount Gee Map

A metasomatic origin ("granitisation") of the feldspar-quartz rocks in this area was already suggested by Coats and Blissett (1971). The term "granitisation"is misleading because the process of real granite formation and intrusion is not a hydrothermaly driven element-mobilisation. However, the idea that the feldspar-quartz rocks are formed during a secondary alteration is fundamental and confirmed during the mapping in 2007 (Roessiger, 2008).

The gneissic, metapelitic rocks of the RCM in this area are foliated with S_{main} and folded during the Palaeozoic deformation in open, north verging upright folds with fold axes slightly dipping to the WSW (average: 24 →256). These folds can especially be traced with the aid of biotite-rich schists (BBS) and Quartz-Feldspar Gneisses (QFG), which can be followed over distances of several hundred

metres. The core of the Yankaninna Anticline is located to the north of the Mount Gee Map, because the smaller (parasitic) folds mapped in the area are north verging.

All Proterozoic host rocks (RCM, BBS, QFG) are gradationally altered into PPG by the K-feldspar metasomatism, especially in the centre of the map around Mount Gee. The main occurrence of PPG is in the north of the map. Lack of foliations indicates that the PPG formed after any foliation-forming deformation event. It follows pre-existing pathways like foliation and bedding, which is best visible at the contact zones of the PPG with the RCM by the "inter-fingering" of RCM and PPG e.g. in the western part of the map.

Only two types of non-tectonic (hydrothermal) breccias were mapped in the area: the K-feldspar-Quartz Breccia (afterwards defined as PMB) and the Hematite Breccia (HMB). The first one occurs in two sets of small (~10 m), steep zones striking NE-SW and E-W. This suggests a structural control of fluid flow by the main foliation and the Palaeozoic folds. The second one, the Hematite Breccias, mainly occur in extension of these sets and, underneath the Mount Gee sinter, at the intersection of the sets. These iron-rich fluids were mainly guided by the pre-existing PPG-breccia zones and Palaeozoic fold hinges in the area. Other breccia types were defined during subsequent mapping campaigns, the PMB and HMB in this area may thus include these other breccia types.

Occurrences of the Pebble Dykes are restricted to some outcrops in the Frying Pan east of Mount Gee and a big patch and a dyke west of Mount Gee. The dykes strike mainly E-W, sometimes for several tens of metres and they crosscut all previous rock types. The most easterly outcroping Pebble Dyke forms two 90° kinks, resulting in a N-S running section within the main E-W system. This structure is typical for an extensional crack in the crust.

The quartz-hematite sinter of the Mount Gee Unit (MGU) overprints all previous units, including the Pebble Dyke. Its main occurrence is at Mount Gee (and at Mount Painter). Mount Gee type quartz veins can be found in the whole area. The sinter forms large sheets at Mount Gee dipping with about 37° to the northeast.

A detailed study of the Hematite Breccia, the Pebble Dyke and the Mount Gee Unit of this map is given in Roessiger (2008).

5.1.2 Radium Ridge Map

One of the three maps that were produced during the 2008 fieldwork continues the Mount Gee Map to the northwest with the hematitic Radium Ridge in the centre (Kling, 2008). Undifferentiated RCM with layers of BBS and amphibolites, as well as MNG occur in the southern and in the northern part of the map. The strike of the main foliation S_{main} of these units changes from NE-SW in the south to NW-SE in the north, reflecting the folding with the Yankaninna Anticline.

ENE-WSW trending, steep dykes of pegmatites and YMG crosscut the Proterozoic lithologies especially in the northwestern part of the mapping area. The large occurrence of a YMG in the east is part of the Armchair Granite outside of the map.

K-feldspar alteration is recognisable in the whole area, but the rocks were mapped as PPG only in outcrops with extensive new-growth of K-feldspar and with a total overprint of former foliation. The main occurrence of PPG is in the centre of the map, fingering into the host rock parallel to the pre-existing main foliation. Outcrops of PMB are rare and restricted to ridges in the north, probably also guided by pre-existing structures.

DMB and HMB were the focus of this map. They form one of the prominent ore-bodies at Radium Ridge. Both breccia types grade into each other and form several sheets that dip moderately (~30°) between N and E. A steeply E-W striking breccia zone of DMB and HMB seems to connect the sheet-like bodies and may be interpreted as "feeding dykes". The dipping HMB sheets grade from massive and U-rich at the higher end to more layered, lower-grade and DMB-rich at the lower end.

Ridges of steep SMB can be found in the east and the north of the mapping area. They also trend about ENE-WSW and are linked with the MGU and the Mount Gee type quartz veins, which form a ridge in the east.

5.1.3 East Painter Camp Map

The second map of the 2008 fieldwork follows the E-W trending PPG breccia zones to the east of the Mount Gee Map up to the main hematite ore body at East Painter Camp (Rehder, 2010). Special attention of this map lies on the different breccias and their relative time of formation. The diverse breccia zones of the central southern MPI are already studied by Drexel (1980) and Drexel and Major (1987). Their relationship remained unclear, therefore this study renews the definition of the breccias.

Undifferentiated RCM with BBS layers, as well as the QFG, the TPG and the MNG (with patches of BBS) in the south and west of the East Painter Camp Map have a pervasive main foliation S_{main} parallel to the bedding. This foliation is folded in open, north verging folds, with fold axes plunging moderately to the SW or W.

Subsequent overprinting of the Proterozoic rocks into PPG is well developed at the north-eastern part of the map. The pure PPG rocks trend NE-SW in this area and follow the main foliation of the host rocks. The PMB is more prevalent in this area, which takes the whole east and north of the map, also trending NE-SW towards Mount Painter. The transition between PPG and PMB is often sharp, a result of channel-like focusing of the PPG-fluid.

Another transitional pair is the DMB and the HMB, which are found in close proximity to the PMB. These chloritic-goethitic to hematitic breccias used the same fluid pathways as the pre-existing PPG/PMB. The main occurrences of DMB and HMB are north of Mount Painter, at the central breccia zone and in the east of the map at the East Painter breccia. The dip of the different HMB sheets varies from steep to flat-lying.

Silicified ridges of all units occur with a NE-SW trend east of Mount Painter. The silica-rich fluids that impregnated all host rocks in this area are interpreted to be a pre-stage of the Mount Gee Event. Mount Gee type veins and MGU overprint the SPMB and all other host rocks at Mount Painter. Pure MGU is only found at the base of Mount Painter, but Mount Gee type veining occurs along a NE-SW trending zone starting north of Mount Painter.

A detailed thin section analysis of HMB and an oxygen isotope study on PMB, MGU and The Armchair Granite is given in Rehder (2010).

5.1.4 Armchair - Streitberg Map

The Armchair – Streitberg area was the third one to be mapped in 2008 to the northeast of the Mount Gee Map, following the NE-SW trending breccia system. The most prominent units in this mapping area are the PPG and the PMB. Undifferentiated RCM and some MNG outcrops represent

the deformed host rocks in this area, although none are unaffected by the pervasive K-feldspar alteration. Only a few patches of BBS and AMP occur within the RCM and the PPG, also displaying a gradual transition into a K-feldspar-rich rock. Intermingled YMG and PEG intruded approximately parallel to the main foliation S_{main} mainly in the northern part of the mapping area. The main foliation strikes ~E-W. Larger irregular patches of pegmatitic bodies can be found, especially at Mount Ward.

Breccia zones of the PMB are concentrated in the very south of the mapping area, connected to the PMB that trends NE-SW towards Mount Gee and Mount Painter, and in the northern part at Streitberg Ridge and Sillers Lookout. The latter ones strike approximately ENE-WSW along the axial plane of the Yakaninna Anticline. DMB and HMB are also concentrated in this zone in flat lying sheets within the PPG and the PMB. The DMB at The Smiler and at the Streitberg pospect topographically underlies and surrounds sheets of layered HMB, both gently dipping towards the NE. The DMB and HMB at Streitberg Ridge could only be distinguished due to their different scintillator readings. The sheet at Streitberg Ridge dips with ~54° towards the NW. A study on the DMB/HMB sheets in the mapping area is summarised in Kieslinger (2011).

Prominent ridges of steep SMB follow the main fluid pathways in this area with trends to NE-SW and E-W. They overprint all pre-existing units, except of Mount Gee type quartz veins and MGU. The latter ones occur in the south of the mapping area, trending towards Mount Gee and Mount Painter.

5.2 Map of Sunshine Pound, Arkaroola Creek and The Pinnacles: structures

The Sunshine Pound Map connects directly south of the Mount Gee Map including the graben structure of the lower Adelaidean succession at Arkaroola Waterhole and the Pinnacles Breccia (PIB). The point of interest of this map is the question, whether the breccia zones of the Mount Gee – Mount Painter area continue to the south and may somehow be related to the Pinnacles Breccia. The MNG in Sunshine Pound (adopted from Coats and Blissett, 1971) appears to be very diverse in its mineralogical and textural character. Therefore sublayers are introduced to fulfil the observation in the field. Another enhancement of the map is the introduction of transparent alteration layers, such as incomplete-K-feldspar-alteration (or “PPGtisation”) and silicification, representing altered areas where the host rock is still recognisable.

The area was mapped in 2009 and a report with focus on the Palaeozoic structures is provided by Cless (2010).

The map can be subdivided into three geological areas: the basement in Sunshine Pound, the graben system in Arkaroola Creek and the breccia zone of The Pinnacles. Gneissic pelitic and quartzitic RCM that crop out at the northernmost edge of the map could be connected to the southernmost extent of the Mount Gee Map. The gneisses are foliated with S_{main} and folded in several NE-SW trending anticlines and synclines (Fig. 30a), comparable with the Palaeozoic parasitic folds mapped at Mount Gee. The axial planes in the basement could not be traced into the Adelaidean units, which are folded on a larger scale. Axial planar cleavages developed occasionally in mica-rich schists. PPG overprint and feldspar-quartz veins affect the whole area in variable intensity, but PMB forms only a small outcrop along a ridge. Ridges of SMB are quite prominent in this area trending NE-SW and overprinting zones of PPG/PMB (Fig. 30e). They are themselves overprinted by a hematite/goethite ore body at one outcrop west of Radium Creek. The same NE-SW trending pathways were used by several hydrothermal fluids. This structure can be linked further to the SW to a prominent shear zone in the MNG.

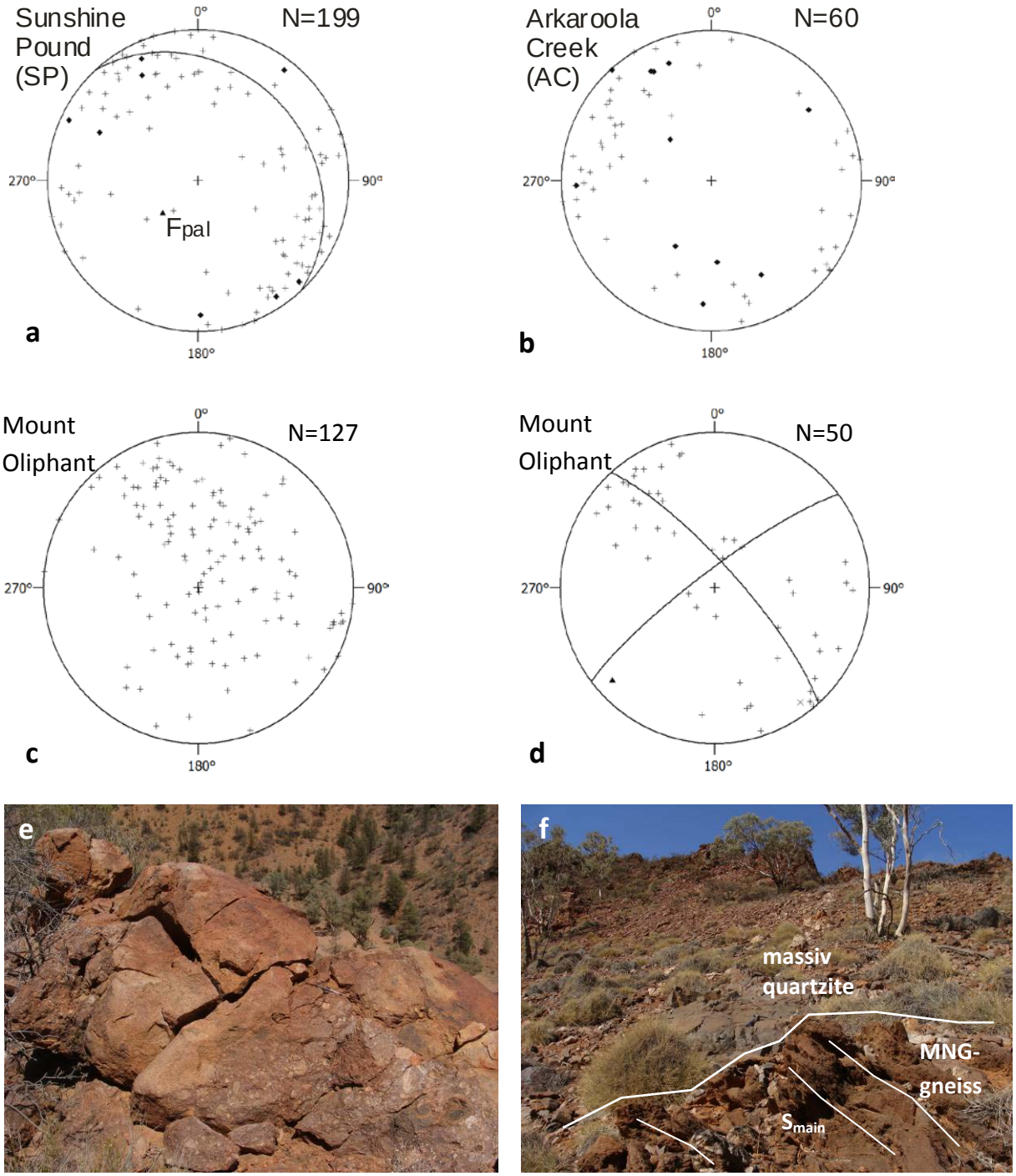

Fig. 30: Stereoplots (equal area procetion, lower hemisphere) of measured foliation and bedding in basement and cover; as well as field photographs. a) Folded main foliation (plus) in RCM and MNG in Sunshine Pound. S_{main} is folded with a mean axis (triangle) that plunges steeply to the SW. Fold plains of measured crenulation cleavage in S_{main} (diamond) strike about NE-SW. Crenulation cleavage and large-scale floding resulted from Palaeozoic, thick-skinned deformation. b) Main foliation in the MNG (plus) and crenulation cleavage (diamond) measured in areas between The Pinnacles and Arkoaroola Creek. The chaotic orientation of S_{main} in the MNG is a result of local refolding and shearing. c) Pole points of the bedding S_0 in the Woodnamoka Phyllite at Mount Oliphant, NE of The Pinnacles. The equal distribution arises from folding and re-folding during the Palaeozoic. d) The first cleavage S_1 (plus) in the Woodnamoka Phyllite developed at an angle to S_0 with a roughly NW-SE strike and was folded during a second compression direction (triangle and corresponding great circle). One measured S_2 plane (cross) strikes steeply NE-SW. e) Prominent ridge of SMB north of Sunshine Pound (340298E/6653142N). Clasts of PPG, RCM, quartzites, MNG and BBS lie in a

fine-grained quartz-hematite (jasper) matrix. The contact to the host rock is sharp and Mount Gee-type quartz veins cut through the SMB. f) Gneissic MNG in contact with Paralana Quartzite (PAQ) of the Adelaidean cover northwest of Arkaroola Waterhole (339132E/6649946N). The unconformity between the main foliation (S_{main}=262/48) in the MNG and the massiv PAQ is angular.

Sunshine Pound consists of a diverse occurrence of metagranites and -granodiorites in different stages of alteration and deformation. The classification of these rocks to be MNG or TPG is based on distinct mineralogical differences in the field and geophysical patterns (radiometrics), but not on geochemical or geochronological studies. The depression of Sunshine Pound itself is an expression of a major structure in this area that provided melt- and fluid pathways for a long time. Zones of highly sheared mica-rich magmatites and migmatites run parallel to each other, forming valleys to the SW of Sunshine Pound with a trend to NE-SW. The host rocks are altered by albitisation, extensive K-feldspar alteration and are locally also brecciated in the extension of the NE-SW running valleys. Large bodies of mafics, quartz veins, DTV, MGU and Mount Gee type quartz are also concentrated in the vicinity of Sunshine Pound. This long-lived extensive deformation, alteration and infiltration in this area lead to well weathered rocks with deep chloritisation/serizitisation/kaolinisation horizons at some outcrops. U-Pb ages of monazites in the shear zones range from 530 Ma to 440 Ma (I. Buick, pers. comm. to M. A. Elburg), but the concentration of amphibolites and the albitised zones parallel to the main foliation point to an even older structure in Sunshine Pound.

The angular unconformity between sheared MNG and massive Paralana Quartzite of the basal Adelaidean to the south of Sunshine Pound indicate that the main foliation S_{main} is older than the Adelaidean sediments (Fig. 30f). Steep ridges of the basal Paralana Quartzite mark the contact to the soft marbles and volcanics of the lower Callanna Group. These sediments are deposited in several 100 m deep graben structures that got folded, faulted and exhumed during the Palaeozoic deformation. The graben fault of the Pinnacles graben and the graben north of Arkaroola are situated at the western side of the systems, trending roughly N-S. The graben fault in the Pinnacles graben is not a reactivation of the NE-SW trending zones in the Sunshine Pound, but a new structure, indicating a significant change of the stress field during extensional tectonic. This graben fault was never reactivated. Clear evidence of an active movement at the margin of the graben is therefore missing. A listric fault could also not be found in the basement. The faults to the east of the Pinnacles graben were instead reactivated during the Palaeozoic deformation, forming sharp borders of the squeezed and tilted, multiply-folded half-grabens. An offsets of lithological boundaries and a NE-SW to E-W trending breccia zone in the Wywyana Formation mark the reactivation of the NE-SW trending structures in the basement during one stage of the Palaeozoic deformation.

The MNG-“triangle” to the west of the Willouran graben at the contact to the Adelaidean sediments displays a large variety of foliation directions and crenulation cleavages. The main foliation in this area is not only the result of the Proterozoic S_{main}-forming deformation. Also Palaeozoic directions developed locally into a main foliation. This is expressed by sudden changes of the directions of the main foliation in the field, to directions parallel to the Palaeozoic crenulation cleavages in adjacent rocks (Fig. 30b). Structural analyses show a weakly developed fold with an axial plane trending ~E-W.

The Woodnamoka Phyllite at Mount Oliphant forms a flat-lying syncline F1, which is folded again during local NW-SE compression F2 (Fig. 30d). S_1 developed in the syncline´s axial plane in roughly NW-SE direction; but it is itself folded with a fold axis F2 dipping gently to the SW. Only one steep S_2 foliation in the F2 axial plane could be measured in the field. The bedding S_0 has a chaotic distribution because of the folding and re-folding (Fig. 30c).

Young pegmatites in the cover are concentrated in the soft Wywyana Formation south and west of Arkaroola Waterhole, associated with PPG-veins and -alteration. Their occurrence lies in the SW-

extension of PPG-alteration in the basement, a fact that is also valid for the breccia zone at The Pinnacles. The age of these pegmatites is Delamerian (Elburg et al, 2003; Elburg et al., 2012), but Rb-Sr ages suggest an overprint during the Ordovician (Elburg et al., 2003) at The Pinnacles (see Fig. 15b).

The PIB itself does not show a clear connection to a major structure in the basement. It is separated from the next outcrop of Wywyana pegmatite by ~1,5 km by a folded, but otherwise unaffected Woodnamoka Phyllite. However, the phyllites form a flat-lying syncline. Therefore the Wywyana Formation is close to the present surface and could connect the PIB with the basement structures below outcrop level. No alteration or brecciation of the MNG close to The Pinnacles could be observed. A small breccia at the contact to the Wywyana Formation at the south-western side of the MNG-"triangle" is the only expression of fault-activity thas is possibly linked to The Pinnacles. The structural pattern in this area indicates that a probably NE-SW deformed and altered MNG intersects with the N-S trending graben fault below The Pinnacles in a depth of a few 10 metres. These structures possibly provided a pathway to concentrate fluids at the contact between basement and Adelaidean. The soft Wywyana Formation that was already intruded by pegmatitic bodies were altered and brecciated easily by the focussed fluids.

5.3 Map at Wild Dog Creek and The Needles: Delamerian folding and brecciation

One of the maps that was constructed during the 2010 fieldwork includes the basement at North Well Creek, the Adelaidean graben at Wild Dog Creek and The Needles Breccia (NEB). The special attention of this map lies on the deformation, alteration and the pegmatites in the basement and the relation to the NEB. A comprehensive report on the map is given by Kocher in Kocher et al. (2011).

The RCM in this area are mostly quartzitic, sometimes enriched in micas, with well-preserved sedimentary structures and a foliation (S_{main}) that is sub-parallel to the bedding. The MNG intruded concordantly into the RCM and is also deformed with the mainly E-W striking foliation S_{main}. The MNG turns into a mica-rich schist with quartz augen at zones of intense shearing. It has in parts been altered into a trondhjemitic rock in the east of the map, which is related to the albitisation at Nooldoonooldoona Waterhole further to the east (Elburg et al., 2001). The basement in this area is intruded by many dyke and sill-like muscovite-bearing pegmatites (Fig. 31a). Boudinage structures of some pegmatites parallel to the E-W striking main foliation indicate a Proterozoic age of at least some of these intrusions. Whether the pegamtites are different in age (e.g. pre-S_{main}-deformation, post-S_{main}-deformation but pre-Proterozoic-deformation and post-Proterozoic-deformation) can hardly be distinguished in the field, because most pegmatites do not show clear deformation structures.

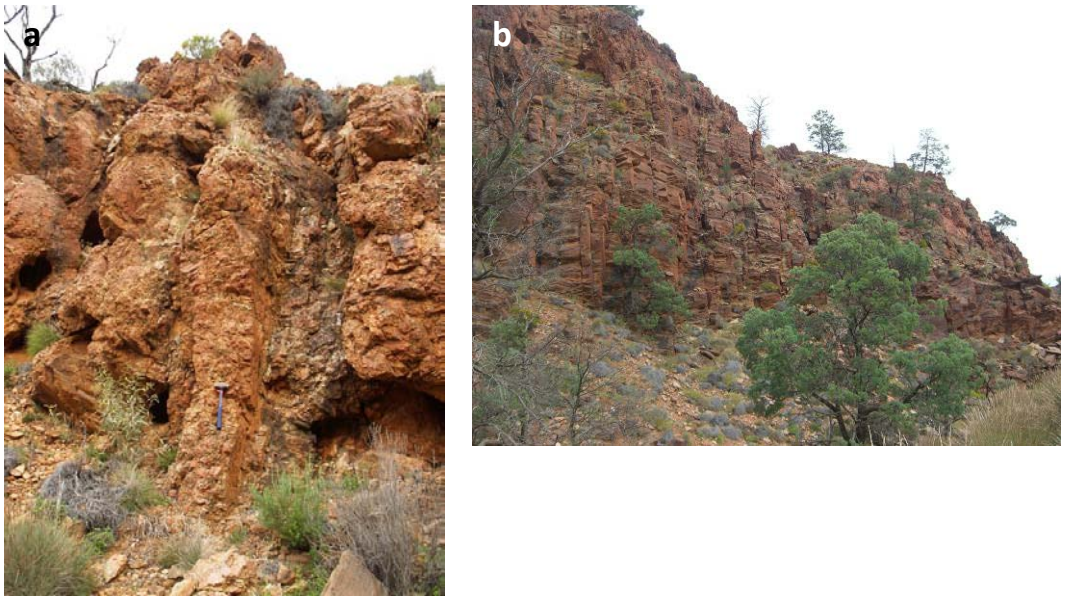

Fig. 31: Field photographs from basement units in the south-western MPI. a) Pegmatitic dyke that crosscut the foliated RCM at North Well Creek (332828E/6650226N). The dyke dips steeply to the east and feeds a sill that intrudes the RCM parallel to the foliation/bedding ($S_{0/main}$=197/42). b) Dominant joints in a quartz-muscovite schist of the RCM are mineralised by the K-feldspar-quartz veins (332979E/6650356N). The N-S trend of these brittle joints developed during N-S compression.

Basement and cover in the mapping area form a Willouran half-graben that is covered by Adelaidean sediments starting with the Opaminda Formation. The contact to the Adelaidean sediments at Hematite Hill in the southeast is marked by a hematite-quartz impregnation of the basal Paralana Quartzite (PAQ). The unconformity was often used by fluids as a pathway, as can be seen for instance at the prominent massive quartz vein at Echo Camp.

Palaeozoic folding is well visible in the mapping area (Fig. 32). The initial orientation of the main foliation S_{main} in the basement and the bedding S_{adl} in the cover was different prior to the Palaeozoic folding. Therfore a southwards dipping recumbent fold formed in the basement, while an open upright fold was formed in the cover. These main folds became refolded during successive deformation in the Palaeozoic, which resulted in folded axial planes in the mapping area. The strike of the major axial plane changes from roughly NW-SE in the east to an E-W direction in the west, with a plunge of the fold axis of ~40° to the west. Smaller parasitic folds and crenulation of mica-rich schists parallel to an inferred major axial plane are related to the Palaeozoic folding in the basement. The Palaeozoic folding resulted in broad structures in the Adelaidean and narrow structures with multiple axial planes in the gneissic related to the distinct rheological differences of basement and cover.

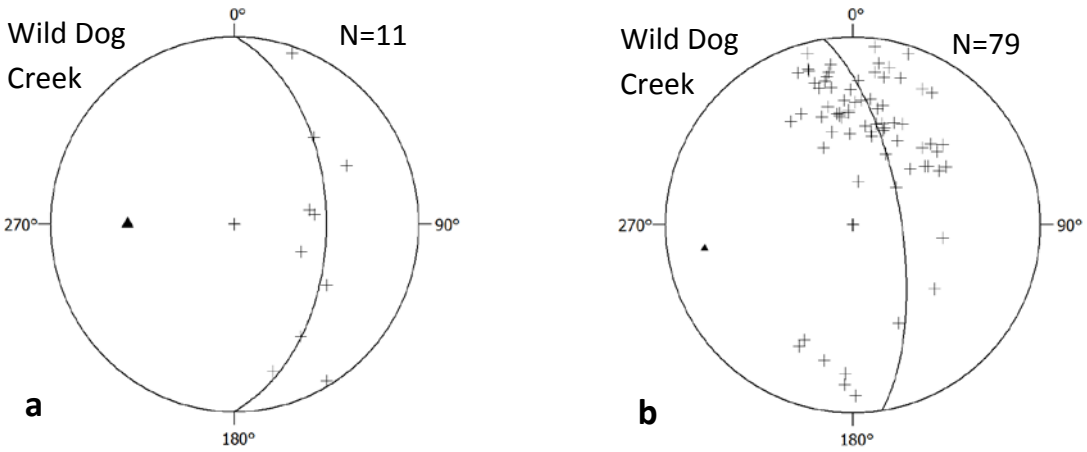

Fig. 32: Stereoplots (equal area projection, lower hemisphere) of bedding and foliation in basement and cover at the graben of Wild Dog Creek. a) Folded Willouran graben sediments form an upright, open fold. The fold axis plunges 41° to the west. b) Weakly developed Palaeozoic fold of the main foliation in the basement. The fold limbs of the recumbent fold dip towards the south. The fold axis pluges with 21° to 261.

The Needles Breccia (NEB) at the west side of the map formed in the hinge of the Yankaninna Anticline at the unconformity in sediments of the Opaminda Formation and the Skillogallee Dolomite. Clasts may reach metres in size and may be intensely altered into actinolite or andalusite bearing rocks. Their origin remains often unclear. The prominent aplites/pegmatites within the NEB are probably hard clasts, similar to the pegmatites in the PIB. They are not deformed, do not show any contact-metamorphic halo and are randomly arranged in the breccia.

The axial plane of the Yankaninna Anticline lies in the south of the mapping area, but it is not acompanied with intense alteration or brecciation in the basement. K-feldspar alteration is only developed in a few small areas with PMB at the contact of MNG and RCM south of the unconformity. K-feldspar alteration probably occurred only in deeper structural levels of the anticline (see Chapters 3 of this PhD thesis and Weisheit et al., 2013b). However, joints and veins mineralised with a quartz-feldspar±hematite paragenesis, which is often accompanied with a halo of PPG alteration. Thes joints display a N-S directed compression in the brittle stage (Fig. 31b). The late, probably PPG-related veins formed mainly in the southern part of the basement, but also in Adelaidean rocks in the Willouran basin and crosscut the NEB. A quartz-hematite assemblage often used the same veins and overprints the earlier quartz-feldspar joints. Silicification and SMB form ridges at the contact between RCM and MNG and along faults in the NEB. The NEB therefore formed between the end stage of the K-feldspar alteration and the silicification. The latter is probably related to the late-stage K-feldspar alteration fluid system, because no Mount Gee type veins or breccias occur in this area.

5.4 Map at Yudnamutana Gorge: extensive K-feldspar – quartz alteration

The map covers an area between the Armchair-Streitberg Map in the west and Paralana Hot Springs in the east. The Paralana Fault Zone bounds the basement to the east, where it is thrust on top of Mesozoic to Cenozoic sediments of the Eromanga Basin. The aim of the map is to follow the K-feldspar alteration from the centre of the southern MPI further to the NE and to clarify the relationship of the different alteration- and breccia zones. A detailed analysis is given by Holzaepfel in Kocher at al. (2011).

RCM outcrops can be found mainly in the northern part of the map as quartzites (RCQ), gneisses (RCG) and undifferentiated mica-rich schists (RCM). Migmatitisation of RCG can be found in the north

of the map. The main foliation S_{main} developed in metasediments, in sills of the MNG and in the concordant TPG (Paralana Hot Springs Gneiss, after Neumann, 2001) in the south of the map. The strike of the schists and gneisses is predominantly NE-SW, turning slightly to NW-SE in the northern corner of the map. This rotation of foliation and lineation is caused by the anticlinal Palaeozoic folding. The axial plane of the Radium Ridge Anticline (after Coats and Blissett, 1971) strikes about NE-SW to E-W in the adjacent map at Paralana Plateau (section 5.5 Map at Paralana Plateau: deformed and undeformed granodiorites). Proterozoic pegmatites intruded in the TPG in Yudnamutana Gorge, whereas PPG-related pegmatitic rocks occur in proximity to the large PMB in the centre of the map.

The contact between the TPG in the SE and the RCM in the NW of the map is overprinted by a wide zone of PMB that includes small areas of un-brecciated PPG (Fig. 33a+b). A transition zone of K-feldspar alteration and vein infiltration developed at the borders of the central breccia. The penetration depth of the K-feldspar alteration is larger into the pelitic metasediments than into the TPG gneiss. NE-SW is the dominating structural direction in the mapping area: A major lithological boundary between RCM and TPG, as well as the main foliation S_{main} and the axial planes of the Proterozoic folds trend about NE-SW. These structural elements provided a major fluid pathway to form the large amounts of K-feldspar-metasomatic breccia. Only a few breccia zones in the east of the map are arranged about N-S, parallel to the trend of the Paralana Fault Zone.

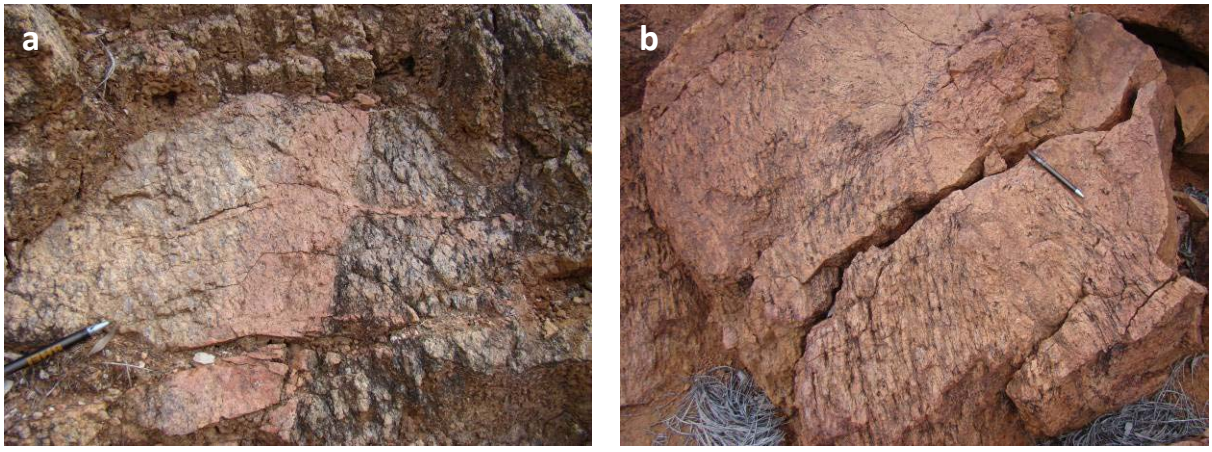

Fig. 33: Field Photographs of PPG and PMB in Yudnamutana Gorge. a) Clearly defined horizon of PPG alteration in a TPG gneiss with aligned biotite, albite and quartz. All host minerals are totally replaced by K-feldspar to the left of the contact zone. The host rock to the right of the alteration zone consists of quartz and feldspar augen and aligned micas. A K-feldspar ± quartz vein crosscuts the structure (348402E/ 6658657N). b) PMB of a K-feldspar-altered TPG gneiss. Clast within the breccia may range from cm to several 10 m in size (348137E/6659001N).

An area of HMB crops out at the northern margin of the PMB zone in close vicinity to the axial plane of the main Palaeozoic fold (Yankaninna Anticline). The HMB is often surrounded by a large zone of DMB. There is a strong alteration of PMB and DMB into kaolinite-rich breccias with calcite- and quartz-veins that can be found all over the Yudnamutana Gorge area.

Steep ridges, as well as flat lying sheets of SMB occur in the north-eastern area of the map along the Paralana Fault Zone (Fig. 34). The most prominent sheet forms a plateau south of Paralana Hot Springs, dipping 5-10 ° to the east. It may have been formed parallel to a Palaeosurface at a certain redox-horizon (ground water table?) and was fed by the steep, fault-related conduits. Mount Gee type veins are not related to the SMB in this area, but they appear occasionally at the northern side of the map in RCM and PMB.

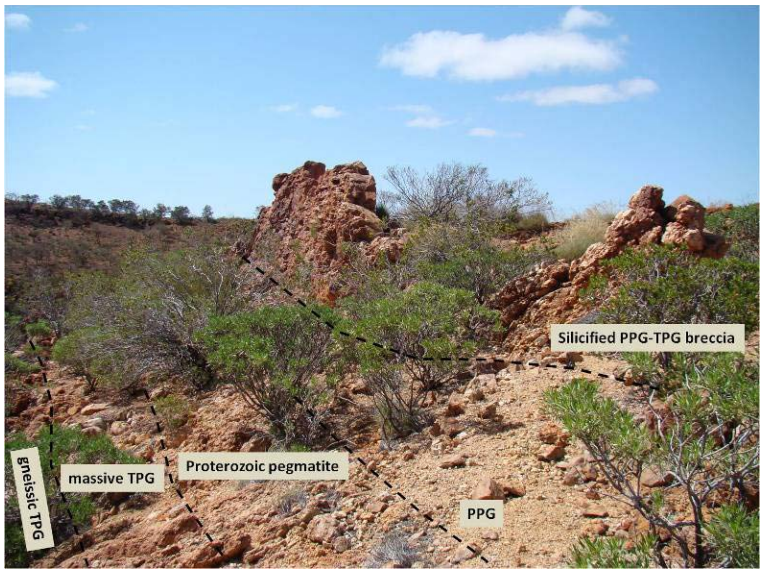

Fig. 34: Outcrop in the north-eastern corner of the mapping area, view to E (349200E/6658648N). Gneissic TPG grades into a massive rapakivi-like granite in contact to a Proterozoic pegmatite. The K-feldspar alteration fluids and later silica-rich fluids used the same pathway in Palaeozoic times.

5.5 Map at Paralana Plateau: deformed and undeformed granodiorites

The Paralana Plateau Map extends the mapping along the Paralana Fault Zone further to the NE up to the southern Hidden Valley Breccia (HVB). The focus of this map is to follow the extension of the PPG alteration and brecciation in the east-central MPI. The K-feldspar alteration narrows at the foot of the Paralana Plateau and concentrates along the Paralana Fault Zone. A possible connection to the HVB, as well as the occurrence of several types of granodiorites is discussed in further detail in the report by Lindhuber in Kocher et al. (2011).

Quartzitic (Freeling Heights Quartzite, after Coats and Blissett, 1971; Yudnamutana Quartzite after Paul, 1998) and gneissic RCM (Paralana Composite Gneiss, after Paul, 1998) are exposed as the major lithological units in this area. The MNG appears as small, sill-like lenses in the RCM, especially close to Hidden Valley. The main foliation S_{main} is developed parallel to the bedding of the RCM and strikes NE-SW in the central part of the map, but rotates towards NW-SE at the south-western most corner. This main anticlinal structure ("Radium Ridge Anticline", after Coats and Blissett, 1971) formed during the Palaeozoic deformation and can be traced further south in the Yudnamutana Gorge Map. The plunge of the fold axis varies between 30 and 45 °, dipping about the SW. Massive quartzites lack in deformation structures, but they preserved their sedimentary bedding. Sedimentary heavy mineral horizons that reflect the younging direction of the quartzite are therefore markers to visualise isoclinal folding. Such isoclinal folding has been found in the north-eastern most part of the map.

A special attention of this map also lies on the different granodiorites that crop out at Paralana Plateau and along NE-SW strike in lenses up to Hidden Valley. These leucocratic rocks appear most time undeformed, but local zones of S_{main} foliation indicate a Proterozoic age. The intrusion age of this igneous rock ("Paralana Granodiorite", Neumann, 1996; or synonymic "Hodgkinson Granodiorite", Fraser and Neumann, 2010) was dated to ~1552 Ma (Fraser and Neumann, 2010). A migmatitisation of this lithology at Paralana Creek occurred at ~1550 Ma (Fraser and Neumann, 2010). A similar gradual migmatitisation can be observed at a deformed body of a granodiorite that

crops out in the very west of the map, at "The Tail" of the BEG (after Coats and Blissett, 1971). The main foliation in this migmatite-granodiorite gneiss runs roughly NE-SW. This migmatite-granodiorite is intruded by pegmatites and aplites of the BEG at the ridge south to the migmatitisation. Neumann (2001) and McLaren et al. (2006) interpreted that this migmatitisation occurred as a result of the formation of the BEG. We conclude, based on our own mappings, that this migmatitisation at The Tail of the BEG is Prozerozoic in age and not related to the Palaeozoic magmatism. The formation of the Radium Ridge Anticline caused the folding of the migmatitc layer, which now crops out at Paralana Creek and at The Tail. The intrusion of the BEG and its related pegmatites and aplites only caused a small aureole of contact-metamorphism in the adjacent RCM.

Elburg et al. (2003) discusses the existence of a leucocratic I-Type part of the British Empire Granite, which was interpreted by McLaren et al. (2006) to be related to the Paralana Granodiorite. An ~442 Ma U-Pb monazite age of the undeformed I-Type is presented in Elburg et al. (2003), and was confirmed with ~441 Ma in Elburg et al. (2012). At least two different (deformed and undeformed) granodiorite intrusions are therefore present in this area. A geochemical study of these rocks is briefly discussed in section 6.1: Geochemical analyses of granodiorites and the Pepegoona Porphyry: preliminary results.

The large feldspatic and silicified breccia zone that is mapped in the Yudnamutana Gorge area continues in the Paralana Plateau map as a ca. 500 m wide zone along the Range Front. The alteration and breccciation follows the NE-SE trending Paralana Fault Zone up to the southern extent of Hidden Valley. It narrows at the eastern and western contact of the Hidden Valley Breccia, but can be mapped further north following the Paralana Fault. Zones of PPG are surrounded by PMB. The K-feldspar alteration is in large areas overprinted by silicified breccias that form a ca. 60 ° north-westwards dipping sheet. Several generations of quartz veins crosscut this breccia zone. Kaolinite weathering of the PMB occurs occasionally along the alteration zone. The feldspatic and silica breccias predate the soft HVB in Hidden Valley and provided an additional fluid pathway.

K-feldspar alteration of basement host rocks can be found in large areas on the Paralana Plateau, as well as in the hinge zone of the Palaeozoic fold and in narrow, S_{main}-parallel zones up to Hidden Valley (Fig. 35). PPG infiltration generally weakens to the north of the mapping area.

Fig. 35: Loose bolder of gneissic RCM northeast of Paralana Hot Springs (349488E/6660908N). A pink K-feldspar alteration is concentrated along the foliation of the gneiss and parallel to the axial plane.

Mount Gee type veining can be found in the southern part of the map, which is so far the furthest occurrence of Mt Gee-type veins away from Mt Gee. The widespread occurrence of MGU lithologies in the southern and central MPI indicates the importance of the sinter event in Permian times.

5.6 Map of Hidden Valley: an extensive, long-lived breccia zone

The breccia in the central and northern part of Hidden Valley was mapped with focus on the lithology, the size and the distribution of the clasts. Although this map does not claim completeness, it gives a brief overview on the breccia´s properties in map scale. Clasts from >500 m down to >10 m in length are drawn in the map. Hydrothermally altered Adelaidean pelites, psammites and carbonates are found in the breccia, as well as metamorphosed basement quartzites, micaschists and metagranites. Clasts of amphibolites, gabbros, felsic undeformed magmatites, migmatites, mylonites and relicts of hard breccias can be found occasionally in the breccia. Pegmatitic bodies usually form hard blocks, from a few metres to tens of metres in size, in the well-weathered breccia (Fig. 37a+b). These pegmatites have, similar to the pegmatites in the NEB and the PIB, no contact-metamorphic aureole to the surrounding breccia. Their size distribution fits with that of all clasts and they are therefore interpreted as clasts. Layering of fine to coarse grained breccia and channels of finer brecciated material in the HVB are hints for a fluidisation processes (Fig. 28a+b; Fig. 36; Weisheit et al., 2013a).

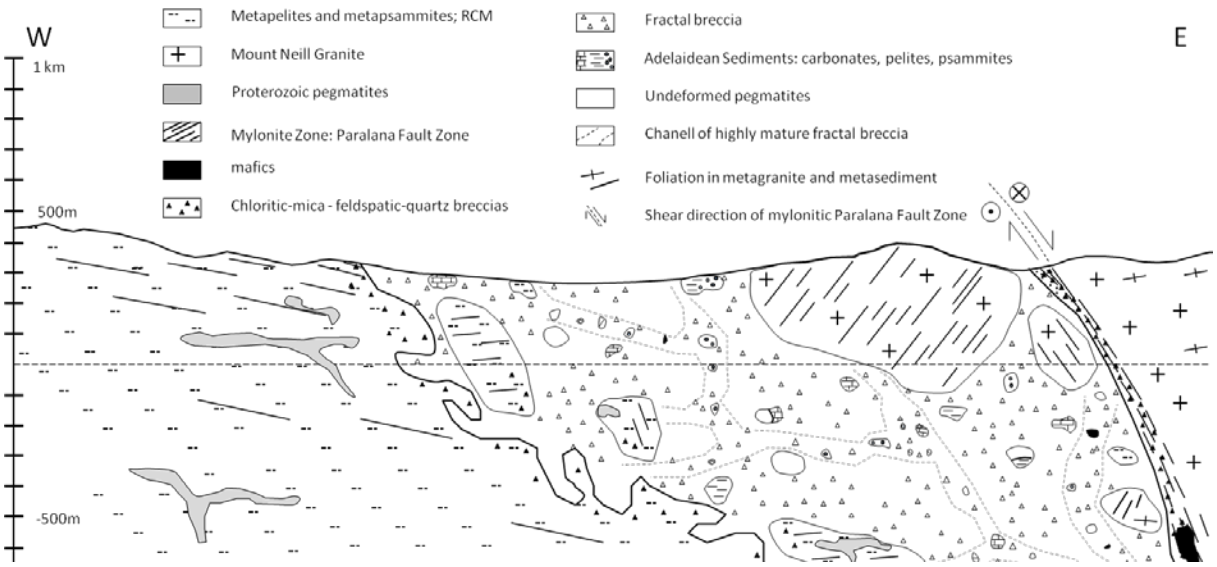

Fig. 36: Schematic profile through the northern Hidden Valley Breccia (HVB), including the 600x400 m clast of mylonitised MNG (see Map of Hidden Valley). The contact of the soft HVB to the Proterozoic basement is marked by hard chloritic breccias, which are overprinted by feldspar and quartz breccias. Sinistral, W-side-up shearing along the Paralana Fault Zone at the lithological contact between MNG and RCM caused the formation of mylonites prior to brecciation. Clasts of basement lithologies, as well as units of the overlying Adelaidean sediments and pegmatites are incorporated in the clast-supported HVB.

The contact of the HVB to the MNG in the east and to the RCM in the west was mapped in detail with GPS (coordinates and elevation) to define its character either as being concordant, faulted, folded or chaotic. In the east, the soft HVB is directly bound by hard, party brecciated mylonite. The contact is steep and straight. On the west side, however, the HVB fingers into RCM. The contact is therefore chaotic, but by trend steep – especially in harder quartzitic metasediments (Fig. 36).

The mylonite (L-tectonite) at the eastern contact of the HVB to MNG developed prior to brecciation during ductile shearing along the Paralana Fault (shear) Zone between the RCM and MNG. The

recorded movement in the mylonite is sinistral with the southeast block moving down. The inlier crossed the brittle-ductile transition during the Palaeozoic exhumation. Hard chloritic-feldspartic ±mica breccia (CFB) breccias formed first at brittle conditions. The mylonite is incorporated as clasts in this breccia. Quartz-feldspar breccia (=PMB) developed after the chloritic breccias. PPG-clasts are in most cases missing in these PMB, but PPG overprint can be found occasionally in the adjacent RCM and MNG (Fig. 37a+b). K-feldspar quartz veins are contemporaneous with the PMB. The youngest mineralisations in this zone are hematite ±quartz matrix breccias and silicification. These different breccias can be found E (MNG) and W (RCM) of the younger HVB. They developed along the whole Paralana Fault Zone at the Paralana Plateau (section 5.5) and at Yudnamutana Gorge (section 5.4). Details on breccia formation are discussed in Weisheit et al. (2013a).

The largest clast in the HVB is a brecciated, mylonitised MNG (600x400 m) in the northern Hidden Valley, which was interpreted by Coats and Blissett (1971) as a Pepegoona Porphyry. 100 m - scale clasts of metapelitic and quartzitic RCM crop out close to their host position at the western side of the HVB. These large clasts were possibly incorporated in the breccia for a short time and only a slight tilt away from their original position occurred during the brecciation process (Weisheit et al., 2013a).

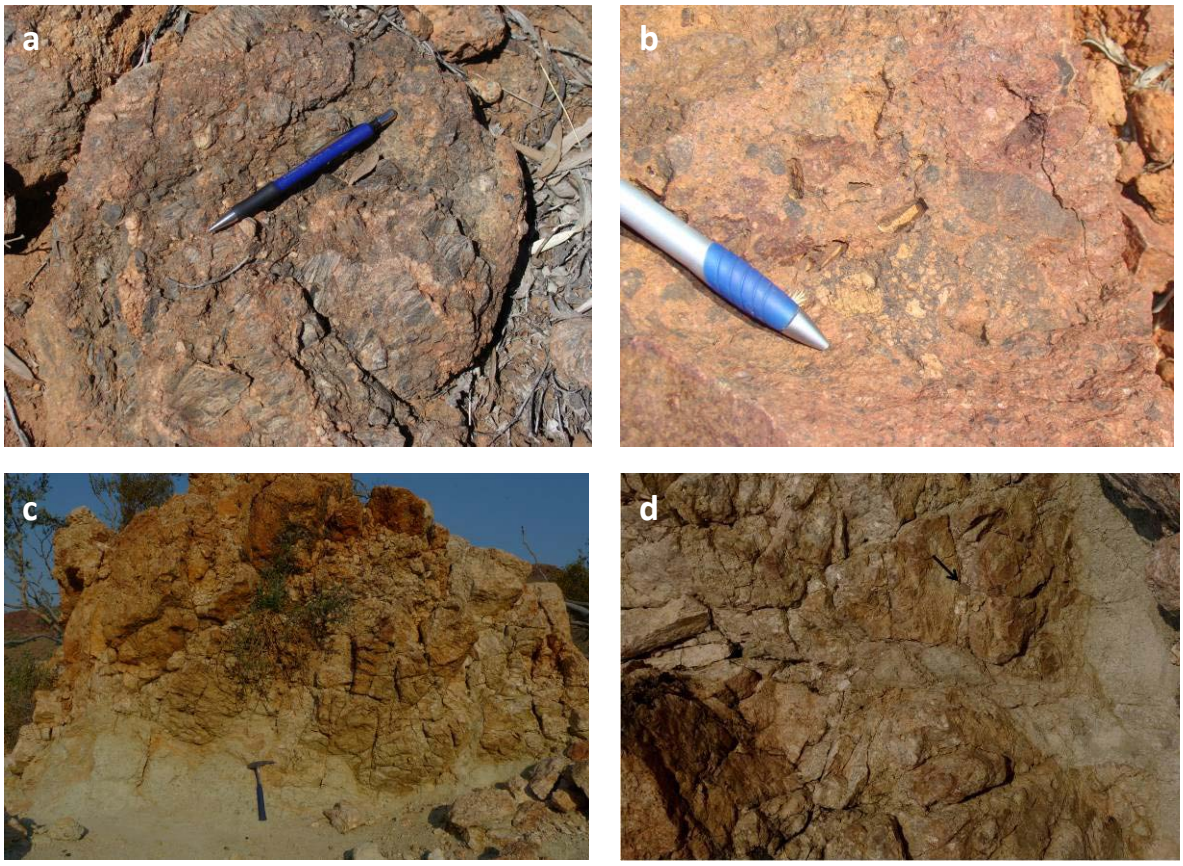

Fig. 37: Field photographs of breccias and pegmatites at Hidden Valley. a) Clast-supported PMB of a mylonite at the eastern contact to the MNG in the northern Hidden Valley (358205E/ 6671645N). Fluids followed the pathways along the Paralana Fault Zone and brecciated the mylonite. b) Matrix-supported PMB at the eastern contact to the MNG in the southern Hidden Valley (354913E/ 6667208N). A chloritic-quartzitic breccia is incorporated as a clast. c) Blob-like, muscovite-rich pegmatite in Hidden Valley. The contact to the Hidden Valley Breccia (HVB) at the geological hammer is sharp (355860E/6669710N). d) Close-up of the contact of the pegmatite in Fig. 37c. The bright-grey HVB "intrudes" the hard, pinkish pegmatite. This chicken-wire structure is typical for fluid-assisted brecciation. Coin for scale.

Mount Adams Quartzite (MAQ), Yagdlin Phyllite (YAP) and MNG are in contact to each other at the south-eastern entrance to Hidden Valley. The granite is party albitised and silicified. A relict foliation strikes NE-SW. Hard, dark-grey, component-supported breccias of massive MNG and RCM (and occasionally mafics) can be found along the extent of the Paralana Fault within the MNG and the YAP. Slickenside on the breccias formed during multiple strike-slip movements along the fault zone. Fabrics in the YAP are a layer-parallel foliation $S_{0/1}$ and an oblique crenulation foliation S_2, which developed during large-scale folding of $S_{0/1}$. The MAQ developed only $S_{0/1}$ as a mineral-shape preferred orientation of accessory micas. The contact between the predominantly massive MNG and the multiply deformed, black-blue YAP is either concordant, with $S_{0/1}$ foliation warping around the MNG, or brecciated. The contact to the MAQ could not be identified. Missing structures in the MNG and the MAQ might be related to their different rheological properties of the more-deformed YAP. A different tectonic evolution of these lithologies (post- or pre-tectonic age) can therefore not be interpreted. Relictic foliation in the MNG and a concordant contact to the metasediments indicate that the MAQ, the YAP and the MNG experienced the same deformation history. Brittle movement in extension to the Paralana Fault Zone and fault fluids overprinted the lithological boundary at a late stage. Therefore, Coats and Blissett (1971) mapped the contact between MNG-YAP-MAQ as faulted.

The quartzitic and metapelitic RCM to the west of Hidden Valley are multiply deformed. A steep main foliation S_{main} strikes NE-SW as cleavages in the axial planes of isoclinal folds (Fig. 50c). S_{main} is folded along a steep, NE-SW running axial plane ("Radium Ridge Anticline", after Coats and Blissett, 1971). This Palaeozoic deformation caused open to closed folds with fold axes dipping moderately to the NE in this area. The fold axis of the Radium Ridge Anticline changes its plunge from NE to SW to the south in the Paralana Plateau and Yudnamutana Gorge areas. The major Palaeozoic anticline in this area is refolded during the formation of smaller E-W striking folds (Fig. 2). This resulted in the chaotic signal of Fig. 38. The axial plane of the Radium Ridge Anticline is cut by the HVB in the north of Hidden Valley and extends further north of the breccia zone. The subsequent convergence and (now eroded) intersection of the main axial plane with the major Paralana Fault Zone is probably the reason of extensive, fluid-driven brecciation in this area.

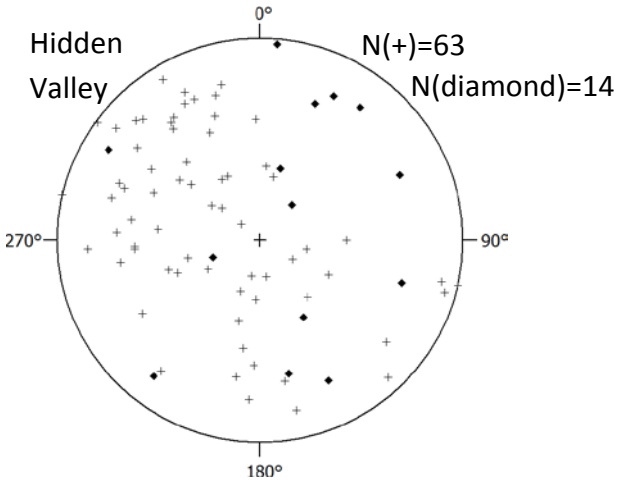

Fig. 38: Pole point stereoplot (equal area projection, lower hemisphere) of measurements of the main foliation (plus) in quartzitic and metapelitic RCM west of Hidden Valley. Axial planes of small Palaeozoic folds are measured in the field (diamond). The chaotic signal is a result of a E-W striking refolding during the Palaeozoic.

5.7 Copper ore deposits in the Lower Adelaidean: relation to the hydrothermal activity in the basement

Four main copper ore deposits in the Lower Adelaidean and their contact to the basement were mapped in detail during the fieldwork in 2010. We investigated the relationship of these deposits to the K-feldspar, iron oxide alteration or silicification and brecciation in the basement. The study areas are Yudnamutana, Blue Mine, Wheal Turner in the west of the southern MPI and, for comparison, Lady Buxton in the east of the inlier. A detailed report about the maps and the copper ore formation is given in Lang (2012).

5.7.1 Lady Buxton Map

The Adelaidean sediments east of the main Paralana Fault Zone are not, or only weakly metamorphosed or deformed. However, extensive hydrothermal fluid flow caused alteration and impregnation of the rocks along the fault zone. The ore deposit of Lady Buxton is located in the vicinity of the Paralana Fault Zone. Wywyana Formation (WYF) carbonates are in a faulted contact with the Wooltana Volcanics (WOV) along a NNE-SSW boundary. The eastwards thrust of the WYF onto the sediments of the Eromanga Basin is to the east of the mine, but not directly exposed. A southwards thrust of Eromanga basin sediments above other basin sediments is exposed in the quarry of Lady Buxton (Fig. 39). The WYF at the deposit is penetrated by Quartz-Hematite Breccia (QHB), which alter the carbonates into a siderite-rich marble and magnetite- and talk-rich scarn. These breccias are host to the primary copper mineral chalcopyrite that is included in martitised magnetite. The QHB forms steep ridges along a NW-SE and a NNE-SSW direction. The main copper mineralisation occurs at the contact of these sets in secondary minerals (mainly malachite) and was mined in small diggings at the beginning of the last century. The QHB displays several generations of brecciation and mineralisation of hematite and jasper-like quartz. Massive magnetite and clear quartz veins are also common in this area. A pure carbonate vein overprints the QHB and overprints faults that strike NNE-SSW and NW-SE. It can be followed into the WOV. The hydrothermal veins probably originate from fluids that derive from the basement, which is only a few ten metres below the present surface.

Fig. 39: Thrust fault at Lady Buxton quarry (348384E/6651023N). Sediments of the Eromanga Basin are thrusted over younger sediments (fault plane: 357/22). The thrust of Adelaidean sediments on top of Eromanga Basin sediments is probably parallel to this local fault, but not exposed at this outcrop.

5.7.2 Wheal Turner and Blue Mine Map

Two main secondary copper ore deposits crop out at the eastern contact of the southern MPI with the Adelaidean sequence. They were mined in the beginning of the 20th century. The secondary copper minerals at Wheal Turner are malachite and chrysocolla. They are mostly concentrated in the Wortupa Quartzite (WOQ), with small occurrences in the Blue Mine Conglomerate (BMC) and in the Opaminda Formation (OPF). At the Blue Mine, the WOQ is host to azurite and malachite concentrations close to an area with hematite impregnation. Basement and cover in this mapping area form a horst and graben structure thas is filled with Adelaidean sediments with the statigraphy up to the Woodnamoka Phyllite (WOP). Horst and graben are covered with the Blue Mine Conglomerate (BMC) and younger units. Fold axes of Palaeozoic folding dip gently to the W and NW.

The Wheal Turner copper mineralisation is bound to roughly N-S striking QHB zones within the massive quartzites of the WOQ. Ridges of PMB that are close to the Wheal Turner Mine follow the same strike. Hovewer, they lack copper-bearing minerals and predate the QHB-bound copper mineralisation. PMB and QHB used the same pathways, which are oblique and parallel to the sedimentary bedding of the Adelaidean succession. Both mineralisations probably formed from fluids that derive from the basement horst some hundred metres below the surface. The basement to the east of the mineralisation consists of metapelitic RCM and massive to sheared MNG, which was folded during the Palaeozoic deformation. The fold axes plunge 44 ° to the SW (Fig. 40). Zones of E-W striking quartz – K-feldspar ± hematite veining, weak PPG-alteration and pegmatite intrusion in the MNG can be found about a km away from the main copper mineralisation (Fig. 41a). QHB as well as pure magnetite veins crosscut the basement in a roughly NW-SE direction – in direct extension to the Wheal Turner Mine (Fig. 41b). Some Mount Gee type quartz veins in the basement close to the unconformity are the farthest occurrence of nail-hole quartz mapped to the west of Mount Gee.

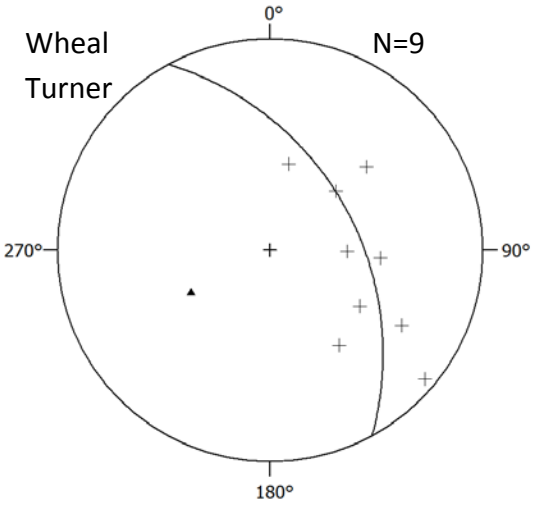

Fig. 40: Stereoplot (equal area projection, lower hemisphere) of a palaeozoic fold in the basement at Wheal Turner. The main foliation is folded with an axis plunging gently to the SW.

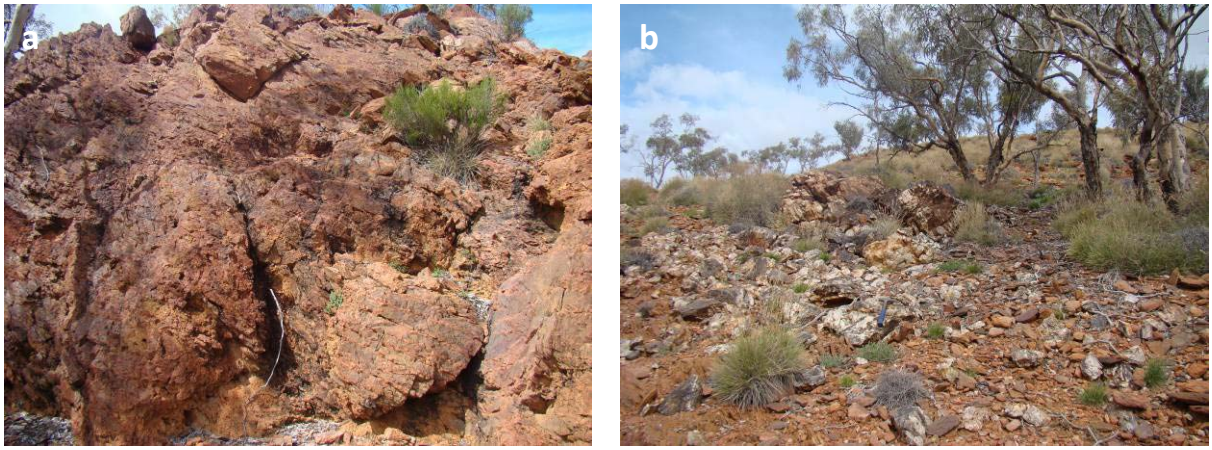

Fig. 41: Field photographs of breccia and vein in basement units at Wheal Turner. a) Brecciated MNG with joints and veins mineralised with K-feldspar and quartz. The strike of these veins is in direct extension to the copper mineralisation that crops out one km to the west (330830E/6656040N). The primary copper probably derived from quartz – hematite veins that used the same fluid pathways. b) Quartz-hematite vein in foliated MNG east of Wheal Turner (331168E/6655386N). The vein cuts the main foliation in the granite and extends in direction of the copper mineralisation in the nearby cover sediments.

The copper mineralisation at Blue Mine is also constrained to a few QHBs that crosscut the layered siltstone-conglomeratic WOQ in NW-SE direction. These breccia zones and veins can be found occasionally in all Lower Adelaidean units down to the basement, where feldspatic-hematitic breccias dominate. PMB, PPG and K-feldspar impregnation of the MNG occur in small areas at the unconformity southeast of Blue Mine and increase towards the east. The whole basement area at the leucocratic pegmatite dyke swarm, west of The Armchair is affected by a K-feldspar alteration. The MNG is partly altered into a biotite-rich gneiss with an E-W trending main foliation S_{main}. Large pure quartz veins, as well as quartz – K-feldspar ± hematite veins and pegmatite dykes cross the basement ~4 km east of the unconformity at Blue Mine (this is about the same distance to the Yudnamutana Mine in the north). However, is is not possible to propose a direct relationship of these breccias to the copper mineralisation at Blue Mine.

Breccia zones with a K-feldspar – quartz (± hematite) and a quartz – hematite matrix are common in basement and cover between Wheal Turner and Blue Mine. They appear as component-supported or matrix-supported breccias and are occasionally kaolinised. Veins of quartz, quartz – hematite, quartz – feldspar, feldspar ± quartz and magnetite ± quartz crop out in the whole area. All mineralising fluids used the same pathways such as bedding, foliation, axial planes and brittle joints. Their relative age and the relation to the copper mineralisation is a matter of further study and discussed in Lang (2012).

5.7.3 Yudnamutana Map

The main copper mineralisation at Yudnamutana is situated in actinolite-marbles of the WYF and at the faulted contact between WYF and WOP. Secondary copper was mined in siltstones and sandstones of the stratigraphically overlying Humanity Seat Formation (HSF). The mineralisations are also associated with QHB. QHB developed in all cover units, mainly in an E-W to NW-SE direction along pre-existing pathways parallel to the bedding/foliation or the fold axial planes. Syn-depositional fault activity caused a disordering of the stratigraphy of the Adelaidean units in the Yudnamutana area. Palaeozoic folding is expressed by a synclinal structure in the west of the map.

The basement south of Yudnamutana consists of massive quartzites and muscovite-andalusite schists of the Freeling Heights Quartzites and an altered variety of the MNG. The latter one is similar to outcrops of Pepegoona Porphyry (PEP) at Pepegoona Gorge in the NE of the MPI. This MNG has distinct quartz and feldspar augen in a fine-grained, reddish-grey matrix and occurs locally as a sheared, gneissic to mylonitic rock (Fig. 42a). It is similar to the PEP mapped elsewhere in the inler (section 4.1.2 Intrusives: meta-igneous rocks and amphibolites). The quartz phenocrysts show irregular embayments and occasionally resorption structures in the thin section-scale. Feldspars and micas are extensively altered and the fine-grained quartz-feldspar-mica matrix is impregnated with iron-oxides (Fig. 42b). Alteration and shearing of the host MNG may have caused the actual texture of this rock, which is mapped as PEP to highlight the similarity to the type locality in the northeast. A detailed study on the Pepegoona "Porphyry" is discussed in section 7.2: Deformed and undeformed granodiorites, migmatites and „porphyries". The localised main foliation in the schists and the gneisses is steep with a strike to E-W.

Veins of different mineral parageneses crosscut basement and cover. They are arranged in brittle sets displaying a main compressional direction to NW-SE (Fig. 43). No certain time-relationship between these quartz±K-feldspar±hematite veins and a few calcite veins could be found in the field. Their distribution indicates a formation during a similar brittle stress field. Therefore a gradual evolution of the fluid during fluid-rock interaction from K-feldspar to more hematite-rich is probable.

The basal unit of the Adelaidean cover at Yudnamutana is the Shanahan Conglomerate (SHC). It consists mainly of well-rounded quartzitic components of the FHQ and a few gneisses (Fig. 42c). The basement components show various deformation structures (foliation, lineation), which proves that the deformation of the basement is pre-Adelaidean (Fig. 42d). An alignment of elongated components indicates that the conglomerate was deformed after its deposition.

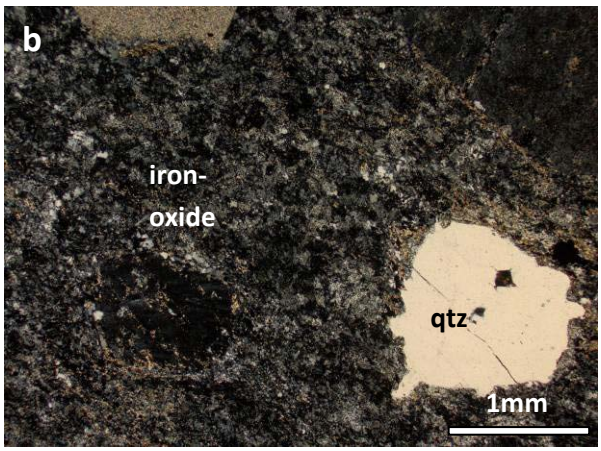

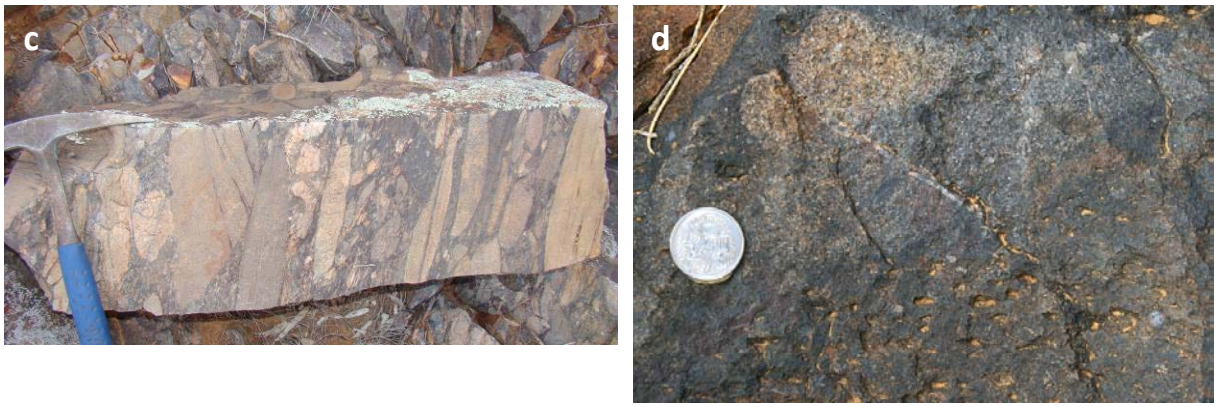

Fig. 42: Field photographs and thin section of outcrops at Yudnamutana. a) Mylonitic gneiss with distinct blueish quartz augen of the MNG. This outcrop southeast of Yudnamutana is similar to outcrops of Pepegoona Porphyry in Pepegoona Gorge (after Coats and Blissett, 1971; 336303E/6659717N). b) Microphotograph of the MNG SE of Yudnamutana with distinct quartz-augen (w.o.v. 4.2 mm; 0336199E/6659906N). The irregular embayments at the quartz phenocryst, the extensive alteration of the feldspars and micas and the massive impregnation of the matrix with iron-oxides indicate several alteration processes that affected this magmatite. c) Shanahan Conglomerate at the contact to the unconformity at Yudnamutana. Components of Freeling Heights Quartzite and foliated granitic gneisses are well rounded, elongated and aligned in a bluish quartzitic groundmass (337156E/6660130N). d) Shanahan Conglomerate at the contact to the unconformity at Yudnamutana, with a clast of foliated MNG at the bottom of the image. The MNG is cleary identified by the distinct blueish quartz augen (bottom right). Image by Paul Bons.

Quartz – hematite and quartz – K-feldspar veins and breccias crosscut the basement rocks adjacent to the unconformity. PPG and PMB overprint the FHQ close to the unconformity in steep zones striking parallel to each other in N-S direction. These breccias are crosscut by quartz-hematite veins that show a typical platy habitus of the hematite ("Petalinka Waterfall type"). A further brecciation and mieralisation of these rocks with a hematite ± quartz (jasper) cement resulted in the formation of component supported HMB, which is surrounded by zones of weathered DMB. Silicification overprints all previous breccias and forms ridges of SMB. An altered and deformed MNG is exposed to the south of the Freeling Heights Quartzite plateau, about 2 km away from the unconformity. Mica-rich varieties of the MNG formed prior to the main foliation, which strikes WNW-ESE in this area. Zones of PPG and PMB, as well as SMB ridges and some quartz – hematite ± K-feldspar veins are exposed in K-feldspar-altered MNG at the leucocratic pegmatite swarm west of The Armchair. There is no direct link between this extensive K-feldspar alteration and the copper ore in Yudnamutana. Nevertheless, silica- and iron rich fluids, which are probably the host of the copper mineralisation, used the pathways provided by PPG and PMB in the basement.

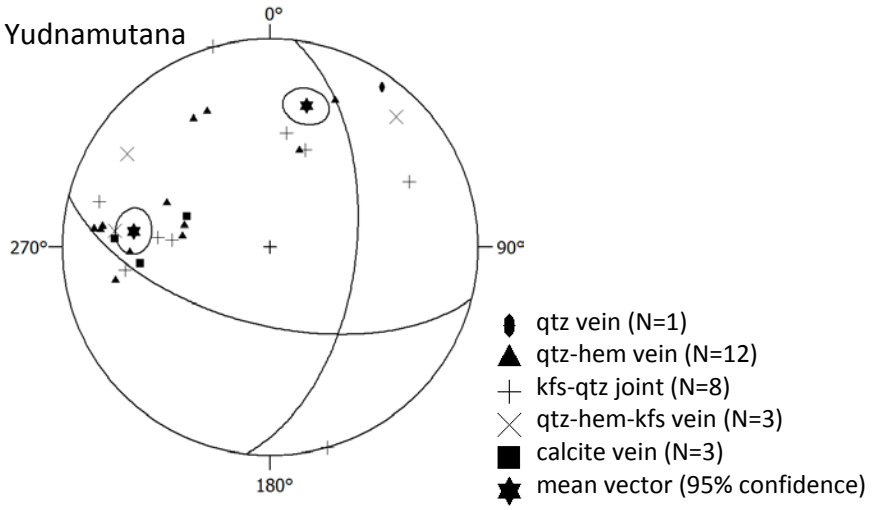

Fig. 43: Stereoplot (equal area projection, lower hemisphere) of different vein types in basement and cover in the Yudnamutana area. A set of brittle joints formed in N-S and in WNW-ESE direction. Single sets formed during NW-SE compression. All measured vein types are formed during NW-SE compression.

5.8 Overview maps in the basement

The areas between the detailed student maps are mapped in less detail to connect the lithologies and structures. Some overview mapping was already discussed in the previous sections when it was related to geological features in the single maps. Special areas are discussed below.

5.8.1 Basement map at Blue Mine Creek

The basement area at Blue Mine Creek was mapped in 2011 with less detail to investigate the distribution of the K-feldspar alteration to the west. PMB (and a little PPG) crop out along the creek, but their occurrence is reduced to small patches and zones striking parallel to the main foliation in the MNG. The MNG in this area occurs as massive, almost undeformed granite with large feldspar phenocrysts and small round quartz. Alteration includes Palaeozoic silicification and Proterozoic muscovitisation. The latter resulted in the formation of a muscovite-schist with bluish quarz-augen. The Freeling Heights Quartzite (FHQ) in the north of this map is massive. Some aligned micas cause a weak foliation that is parallel to S_{main} in the MNG (Fig. 44c). The bedding S_0 in the FHQ and S_{main} are folded during the Palaeozoic deformation with a fold axis plunging steeply to about WSW to W (Fig. 44b). The trace of the axial plane can be extrapolated to the west into the Wheal Turner and Blue Mine Adelaidean sediments. Graphic K-feldspar – plagioclase – quartz – muscovite pegmatites, Mica-Matrix Breccias (MMB), BBS and massive quartz veins formed in the MNG parallel to the foliation. The MMB, muscovite-MNG and the silicified MNG occur as clasts within the PMB (Fig. 44a). Zones of intense clast-supported brecciation formed during massive fluid flow in this area. PMB (but not PPG) dominates in this area. The rocks were brecciated during the localisation of the K-feldspar-alteration fluids. An infiltration and replacement that usually occurs during PPG formation, is missing in this area. There are small occurrences of Mount Gee type quartz. The order of events is: muscovite-alteration of the MNG and Proterozoic deformation producing S_{main}; Palaeozoic folding and pegmatite intrusion; formation of MMB and silicification; K-feldspar alteration (PPG) and brecciation (PMB).

Fig. 44a: PMB within MNG with clasts of Mica-Matrix-Breccia (MMB), MNG and pegmatite (334008E/6656536N). These breccia zones follow the main foliation to ENE-WSW.

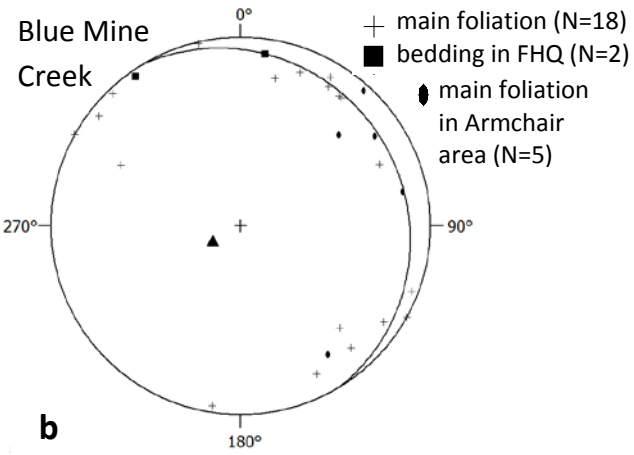

Fig. 44b: Stereoplot of the main foliation in the MNG at Blue Mine Creek. S_{main} is folded during Palaeozoic NNW-SSE compression (fold axes: 78/39 ; triangle). This folding continues to The Armchair area. Bedding in the Freeling Heights Quartzite is parallel to S_{main}.

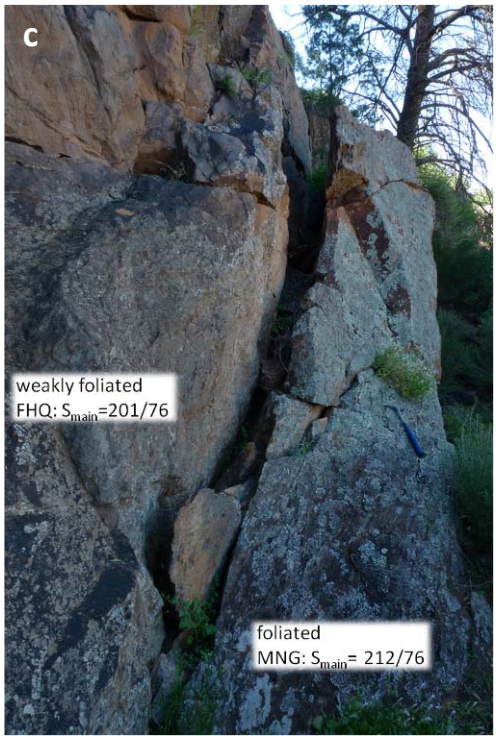

Fig. 44c: Direct contact of sheared MNG with massive FHQ with a few aligned biotites (332271E/6657387N). Both units were deformed during the S_{main}-deformaion.

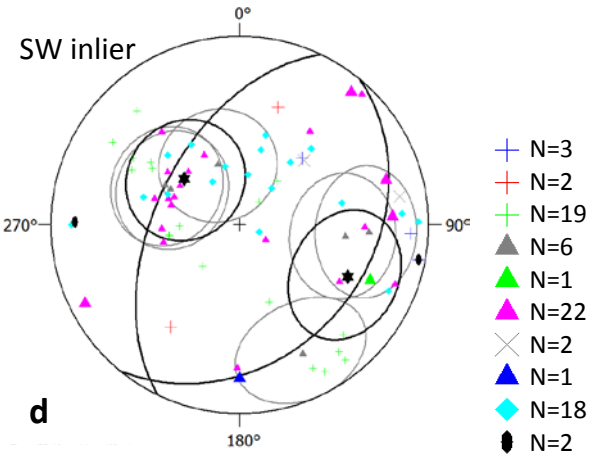

Fig. 44d: Stereoplot of mineralised joints (small) and veins (large symbols) in the Blue Mine Creek area, complemented with measurements from the East Painter Gorge area (azure) and The Armchair (black). Drawn are K-fsp-Hem (azure diamond), Hem-Qz (pink triangle), K-fsp-Hem±Qz (green pluse), Qz-Hem-K-fsp (blue cross), K-fsp-Qz-Hem (red cross), Qz-Tour (grey cross), Qz-veins (blue triangle) and a set of K-fsp-Qz (black ellipse). The mean set of joints (grey triangle and mean black star with 95% confidence interval) and the direction of the veins indicate NE-SW compression.

Mineralised joints and veins were measured in the area of Blue Mine Creek, at The Armchair and at East Painter Gorge to compare their distribution throughout the inlier. Fig. 44d shows a set of joints that developed during NNE-SSW compression, but the statistics is not well defined. A Palaeo-tectonic interpretation of this data is not possible, especially when the measurements are compared with measurements from further south (Fig. 43). The directions of three main vein mineralisations were plotted in Fig. 44d: K-feldspar – hematite (azure diamond), hematite – quartz (pink triangle) and K-

feldspar – hematite ± quartz (green plus). The mineralogy and the mean distribution of thses veins are similar. Therefore they probably formed during the same fluid flow event.

5.8.2 Basement map at The Armchair

The leucocratic Armchair pegmatite is the most prominent one of the pegmatite swarm north and northwest of Mt. Painter. Multiply foliated pelitic RCM, RCM gneiss and MNG in this area are intruded by mica-rich, graphic K-feldspar – quartz pegmatites and aplites. Elburg et al. (2012) conclude that the age of this pegmatite swarm is ~455 Ma. The pegmatites intruded into K-feldspar altered rocks and are altered by K-feldspar metasomatism in this area (Fig. 45a+b). Therefore PPG-related rocks and veins formed prior and after the magmatic intrusions.

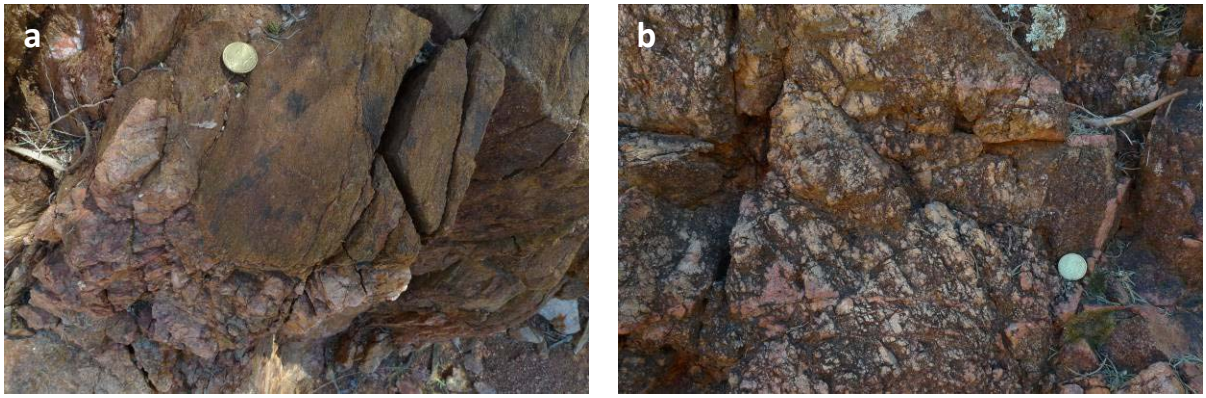

Fig. 45: Field photographs of pegmatite and K-feldspar alteration at the Armchair. a) Foliated pelitic RCM intruded by undeformed, mica-rich pegmatite of the Armchair swarm (341195E/6656630N). b) Close up to the Ordovician pegmatite of Fig. 45a. K-feldspar – quartz veins crosscut the pegmatite and alter its micas.

5.8.3 Basement-cover map at East Painter Gorge

The main focus of this map is the direct comparison of structures in basement and cover east of the Paralana Fault Zone. A folded succession of PAQ, WYF and HSF is at the entrance of East Painter Gorge in contact to almost undeformed, massive MNG. The unconformity is not faulted. A branch of the Paralana Fault Zone formed a NE-SW striking fault breccia in PAQ and MNG in the west of the map. Slickensides and striations on the breccia show sinistral, W-side up movement, but antithetic faults are also common. The shear foliation in the MNG is parallel to the fault breccia. It is a relict of ductile deformation on the Paralana Fault (shear) Zone (Fig. 46a).

A schistosity developed in the Adelaidean sediments prior to the main Palaeozoic folding. S_1 is sub-parallel to the sedimentary bedding of the Adelaidean units, hence defined as $S_{0/1}$. $S_{0/1}$ was folded in NE-SW trending open folds during a NW-SE compression. The fold axes plunge gently to the SW. An axial planar foliation S_2 developed, dipping steeply to the NW. The Proterozoic main foliation in the gneissic MNG to the north of the Adelaidean succession is almost parallel to the Palaeozoic S_2 foliation (Fig. 46b). This is interpreted as a coincidence, and not signifying that the two foliations formed at the same time. The Palaeozoic folding of the Adelaidean succession weakens into the basal PAQ, which is almost not folded and forms a straight layer on top of the basement that dips about 50° to the SW. Palaeozoic structures are therefore not, or onlx weakly developed in the basement. The structures in the Adelaidean PAQ and the basement MNG are truncated at the angular unconformity (Fig. 46c).

A fine-grained quartzite crops out close to the Range Front in the east of the map. It shows heavy mineral sedimentary structures and a faulted contact to the basement MNG. We assigned this coarse-grained quartzite to be part of the Radium Creek Metamorphics. Details on structures in this area will be summarised in Mueller (in prep.).

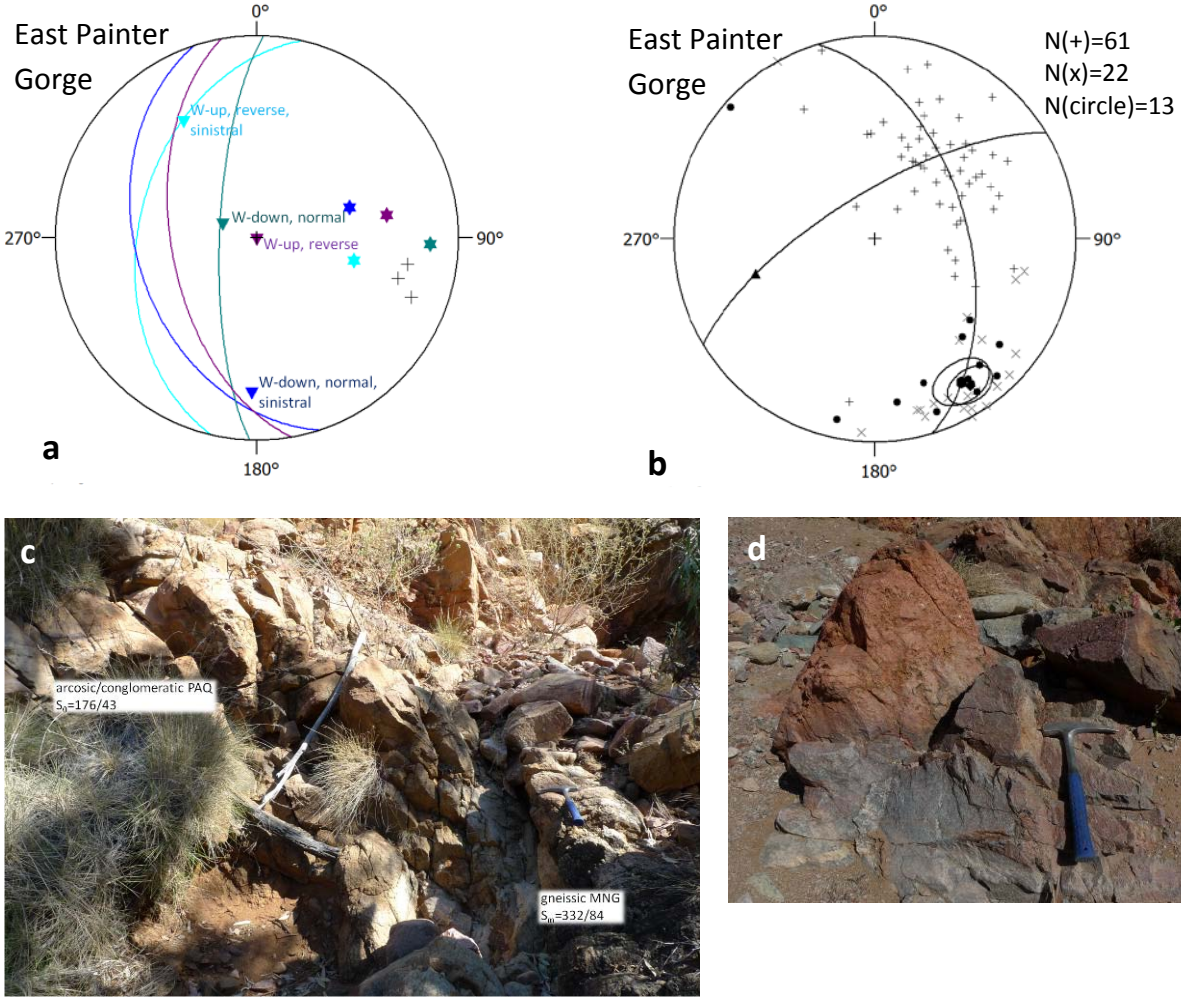

Fig. 46: Stereoplots (equal area projection, lower hemisphere) and field photographs of outcrops in East Painter Gorge area. a) Examples of slickensides (star) and striations (triangle) along the Paralana Fault Zone at East Painter Gorge. Reverse west-side-up movement as well as antithetic faulting occurs in the mapping area. Shear foliation in the adjacent MNG (plus) is parallel to the fault surfaces. That indicates a constant stress field at least during the brittle-ductile transition. b) S_0 and $S_{0/1}$ (plus) in the WYF and the HSF at East Painter Gorge got folded (triangle) during the Palaeozoic deformation. The folds strike ~NE-SW. An axial planar foliation S_2 developed during folding (circle and mean polygon). The Proterozoic main foliation in the basement is parallel to S_2 (cross and mean diamond). c) Direct contact of a gneissic MNG with undeformed arcosic PAQ. Bedding and regional metamorphic foliation are oblique to each other (347801E/6653282N). d) Gradual K-feldspar alteration of a massive MNG north of East Painter Gorge (348238E/6653737N).

Amphibolite dykes and massive quartz dykes are prominent lithologies in the MNG in this area. The amphibolites crosscut the PAQ. They probably form feeding dykes to the Wooltana Volcanics.

K-feldspar alteration and veining (see Fig. 44d) in the MNG is restricted to narrow zones in the valleys. Transitions of MNG into PPG and of amphibolites into PPG are well observable at two outcrops in the east of the map.

6. Sampling

Selected units were sampled during the mapping campaigns for thin section analysis, geochemical and geochronological studies. Several scientific questions are approached:

The sampling of deformed and undeformed Proterozoic rocks (metasediments, metagranites, schists, gneisses, mylonites, migmatites) throughout the southern and central inlier is an important addition to detailed observation and measurements of structural features in the field. Palaeozoic and Proterozoic deformation are a focus of this study. The results are discussed in Weisheit et al. (2013b).

Large samples for major and trace element analyses were taken from a variety of Proterozoic host rocks and younger hydrothermal lithologies. The main focus of the geochemical studies lies on the extensive K-feldspar alteration and its successive stages. A direct transition of host rock into pure PPG and PMB were sampled at one outcrop when possible. K-feldspar altered rocks and unaltered host rocks of the southern and central MPI were sampled to analyse the variability of the alteration. Doubly polished thin sections were produced for microprobe analyses to study the compositional changes in the micrometre-scale. The results are discussed in Chapter 3 of this PhD thesis.

Quartz samples for fluid inclusion measurements were selected from host rocks and alteration products. Pegmatites, quartz –, quartz-feldspar – and quartz-hematite – veins were also collected for fluid inclusion analyses. We aimed to determine the temperature of the wall rock and the temperature of the melt/fluid at the time of the incluision's formation (see Chapter 3 of this PhD thesis).

Samples for zircon, apatite and monazite dating were taken from wall rocks and K-feldspar altered rocks. U/Pb and Hf analyses indicate the provenance of inherited zircons in the altered rocks. Rb/Sr analyses and low-temperature thermochronology may give an age of the overprint during alteration. A low-temperature thermochronology study was also carried out on samples that are affected by the Mount Gee sinter event (Chapter 3 of this PhD thesis and Weisheit et al., 2013b).

Other points of interest are, additional to the main K-feldspar alteration, the metasomatic history of the Pepegoona "Porphyry", the diversity of deformed and undeformed granodioritic rocks, the formation of the Pebble Dyke and the dynamic processes that formed the large breccia zones in the southern MPI and in Hidden Valley. Geochemistry, as well as picture and thin section analysis are used to approach these problems. The analyses of the Pepegoona Porphyry and the granodiorites are discussed below, while the results of Pebble Dyke and Hidden Valley brecciation studies are presented in Weisheit et al. (2013a+b).

6.1 Geochemical analyses of granodiorites and the Pepegoona Porphyry: preliminary results

Fourteen samples of Pepegoona "Porphyry" from Pepegoona Gorge were prepared for ICPOES analyses, carried out at the University of Ghent (details on the measurements are given in Chapter 3 of this PhD thesis). Two separate samples from the Pepegoona Porphyry–like MNG-ocurrence southeast of Yudnamutana were analysed for comparison (Fig. 47).

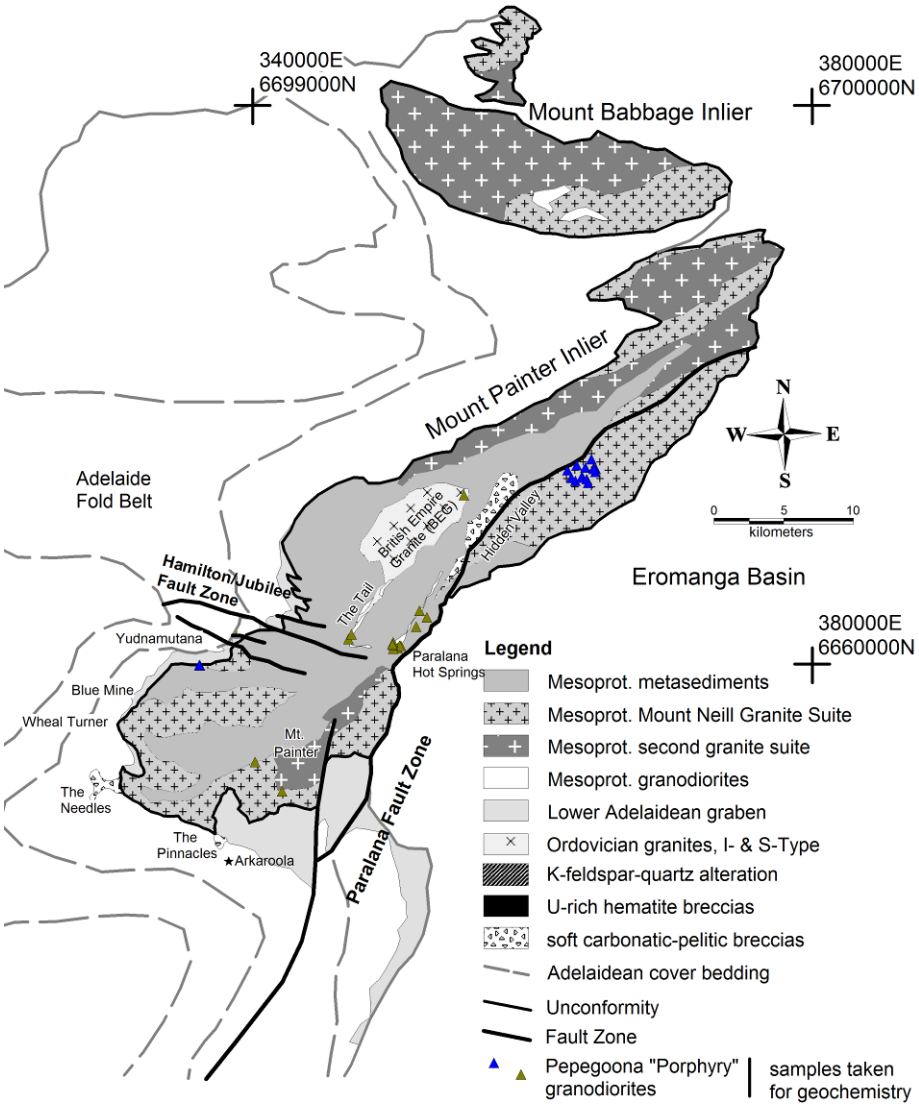

Fig. 47: Sample locations of various deformed and undeformed granodiorites (green triangles) and Pepegoona „Porphyry“ (blue triangles). Undeformed granodiorites intrude deformed samples at The Tail of the British Empire Granite.

The results of the major oxide analyses, as well as results by Armit (2007) and Stewart and Foden (2003) are shown in Fig. 48. Armit (2007) concluded that the Pepegoona “Porphyry” in Pepegoona Gorge is a result of extensive alkali metasomatism of precursor lithologies like the MNG and granodiorites. Our observations in the field and the whole rock analyses (Tab.4 in Chapter 3 of this PhD thesis) confirm this interpretation. The Pepegoona “Porphyry” is depleted in Na_2O and CaO compared to the A-type granitoids (data from Chapter 3 of this PhD thesis) and to the granodiorites in the MPI (presented below). Further geochemical studies have to be carried out to unravel the true nature of the Pepegoona “Porphyry”.

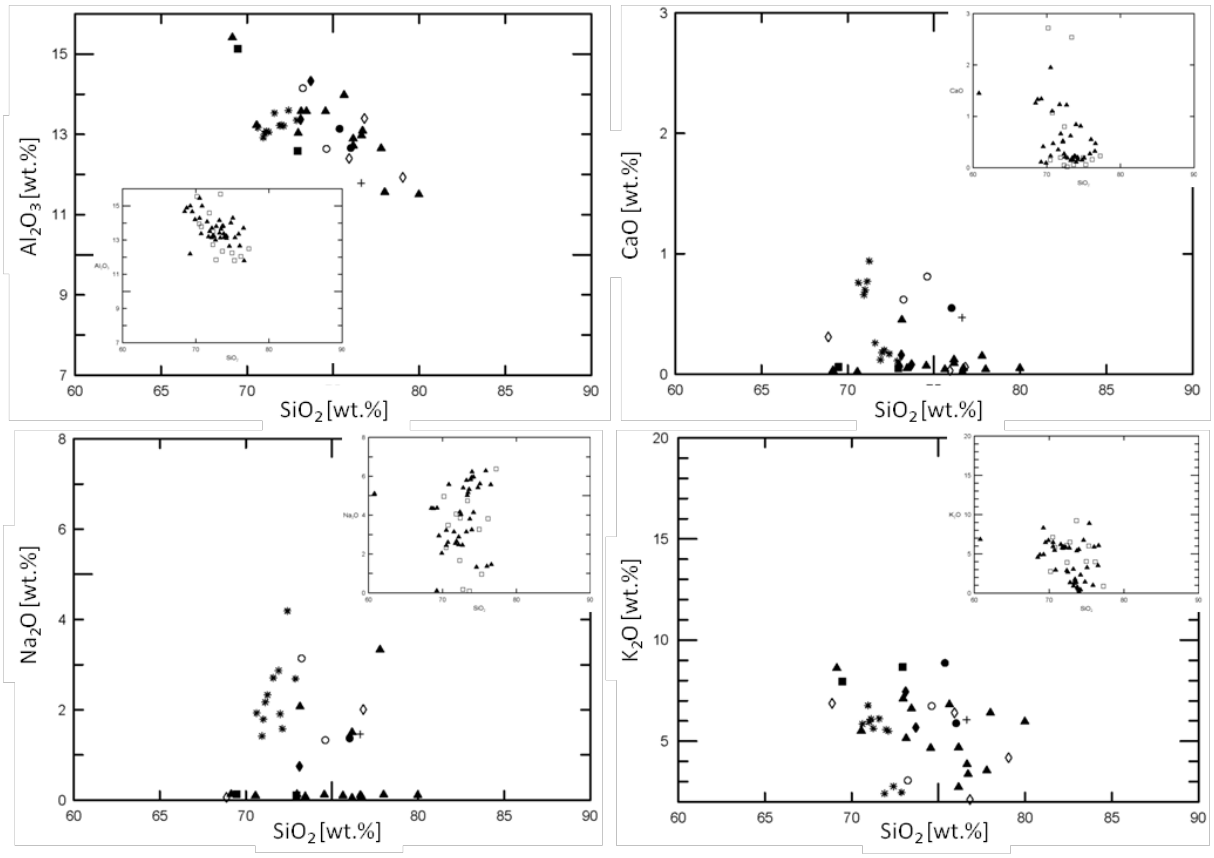

Fig. 48: Harker variation diagrams of the Pepegoona „Prophyry“ (after Coats and Blissett, 1971) in the MPI. This lithology was sampled at Pepegoona Gorge (filled triangle) and southeast of Yudnamutana (filled square). Armit (2007) sampled MNG-porphyry (open diamond), Pepegoona Porphyry (filled diamond), MNG with mega K-feldspar crystals (open circle), MGN gneiss (filled circle) and equigranular MNG (plus) in Pepegoona Gorge. Analyses of Pepegoona Prophyry by Stewart and Foden (2003) are symbolised by stars. Armit (2007) concluded a successive metasomatic overprint of the precursor MNG that resulted in the formation of the Pepegoona „Porphyry“. The Pepegoona Porphyry samples are well depleted in Na_2O and CaO compared to A-type granitiods in the MPI (from Fig.14 in Chapter 3 of this PhD thesis). Our data thus also indicate an alkali metasomatism that resulted in the formation of the “Porphyry”.

Whole rock analyses on the various granodiorites in the MPI are presented in Fig. 49 and in Tab. 4 in the Capter 3 of this thesis. The analysed deformed (~Proterozoic) granodiorites and the undeformed (~Palaeozoic) granodiorites of the BEG define a scattered signal, which is typical for granodioritic compositions (i.e. low K_2O, high Al_2O_3 and CaO content). No siginicant variation between both types of granodiotites is developed in the major elements. A difference in the TiO_2, Zr and Nd content might possibly be significant to differentiate between the various granodiorites geochemically. The undeformed granodiorites have a low TiO_2, Zr and Nd content, compared to the signal of the deformed ones. However, both signals overlap and no significant geochemical variation could be identified during this preliminary study.

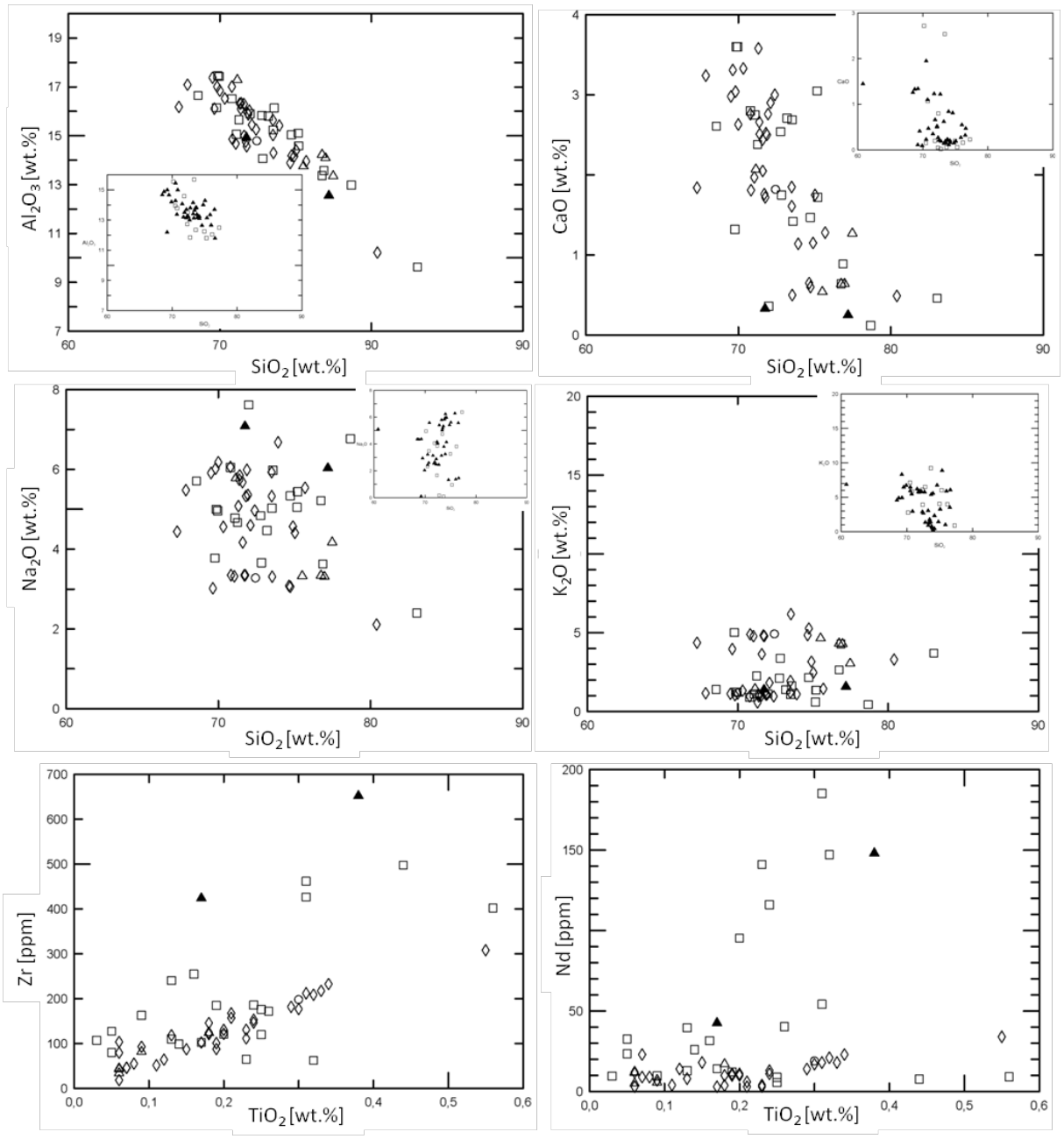

Fig. 49: Harker variation diagrams that show the composition of granodiorites in the MPI. There is no significant variation in the major alkali-oxides between the undeformed I-type BEG (open triangles: this study; open diamond: by Elburg et al., 2003) and various deformed granodiorites (filled triangles: south of Mt. Painter; open squares: Paralana Plateau north of Paralana Hot Springs; filled squares: Paralana Granodiorite samples by Neumann, 2001). The Harker variation diagrams of A-type granitoids of Fig. 14 in Chapter 3 of this PhD thesis are plotted for comparison. A slight variation occurs in the trace elements and the TiO_2 content: the I-type BEG (open triangles) that intrude deformed granodiorite at The Tail of the BEG generally show less TiO_2, Zr and Nd content than the various deformed granodiorites.

7. Implications for the geological evolution of the MPI

The new mapping of selected areas in the southern and central MPI resulted in a new interpretation of the geological history. The most important revision is the definition of new hydrothermal/metasomatic units that differentiate between alteration (transparent GIS-layers), veins, breccias and total replacement of any previous host rock. The development of the alteration pattern can be followed along the different maps from the centre of the southern MPI (at Mount Painter and Mount Gee) to the west, the south and the northeast up to extensive breccia zones and copper mineralisations.

The tectonic evolution of the MPI and of the adjacent Adelaidean units is another focus of the geological mappings. Pre-existing structures guided the alteration fluids during uplift.

7.1 Structures in basement and cover

As outlined in the previous sections, the basement of the MPI consists of a variety of metasediments and meta-igneous rocks. Due to different rheological properties of the diverse Proterozoic units the response to stress during deformation events was variable. Quartzites for instance do not develop a distinct foliation, whereas micas in pelitic units readilly develop a cleavage. Similar effects can be observed in the igneous suites, where rapakivi-like, massive granitoids appear undeformed, while altered, muscovite and biotite-rich zones develop a well-defined schistosity. The expression of deformation is highly variable in different lithologies and locally a strong interference between different events may have developed. Therefore only structures that can be traced regionally are taken into account in the following reconstruction.

A first foliation in basement rocks is today sub-parallel to the bedding S_0 of the sedimentary sequence, which is therefore defined as $S_{0/1}$. $S_{0/1}$ is formed by the orientation of biotites and muscovites in metapelitic rocks that formed during greenschist to amphibolite facies conditions (M1) at a deformation event D1. $S_{0/1}$ occurs generally as a relict, finely crenulated foliation in post-D1 deformed rocks. Elburg et al. (2003) define this foliation as pre-S_{gneiss}, while Armit et al. (2012) describe the relict muscovite foliation, inclusions trails and bedding-parallel dissolution in the RCM units as S_1. Whether the granitoids also intruded already prior to D1 could not be determined, but we found no clear truncation of structures. Other studies record a deformation in the RCM in the northern parts of the MPI that is truncated by the first granitoid suite (Armit et al., 2012).

The second deformation event (D2) produced closed to isoclinal folds F_2 locally with pervasive foliation S_2 parallel to the axial plane (Fig. 50c). Quartzitic rocks usually do not develop an S_2 foliation, but the change in the younging direction of the sedimentary structures such as cross bedding in heavy mineral horizons indicates isoclinal folding during D2. This could be observed in the Mount Adamas Quartzite (MAQ) to the east of southern Hidden Valley and in the Freeling Heights Quartzite (FHQ) south of Yudnamutana. Metapelites deformed well during D2 and developed a biotite, sillimanite and cordierite S_2 foliation, which represent low-pressure, high-temperature metamorphism (M2) (Fig. 50a).

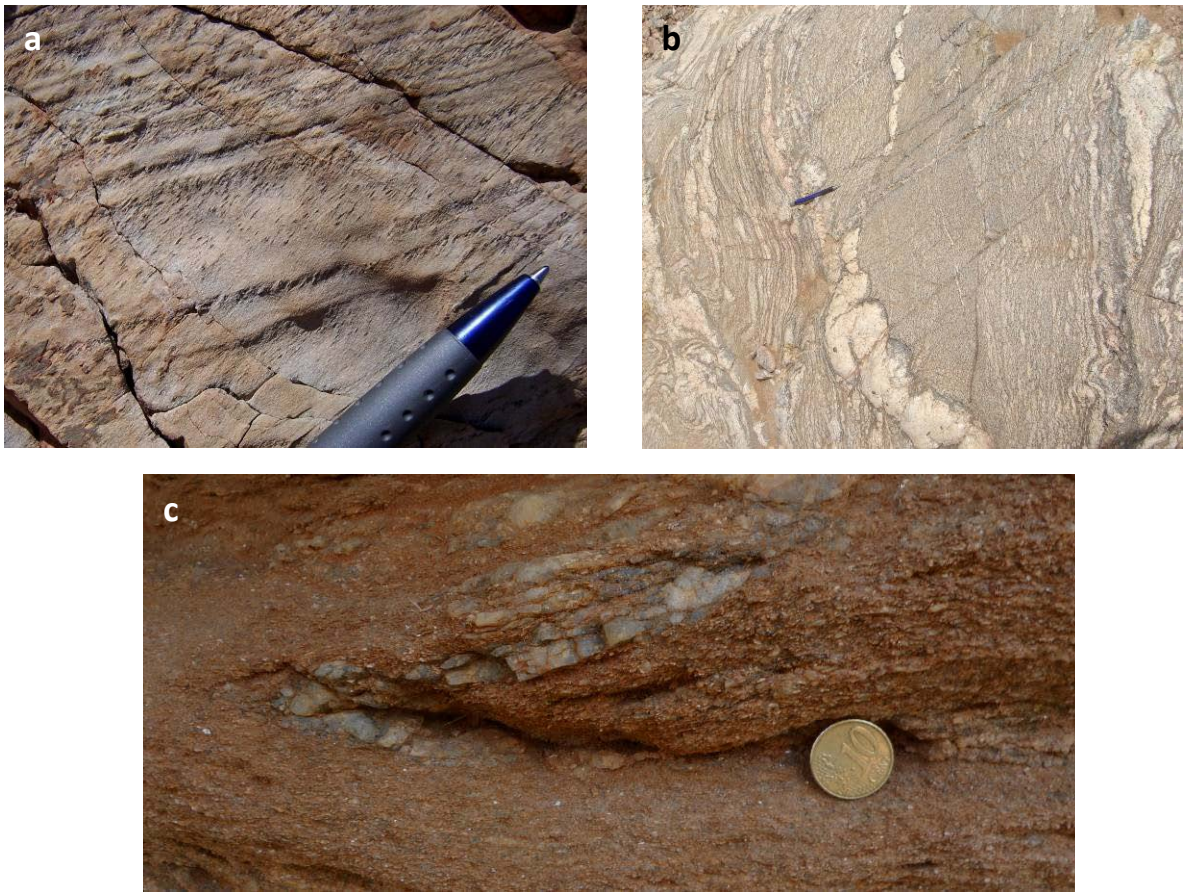

Fig. 50: Field photographs of outcrops in the eastern MPI. a) Yagdlin Phyllite (YAP) south of Hidden Valley with alinged sillimanite parallel to the axial plane of the local closed fold F_2 (note: refraction of the foliation at lithological boundaries). No bedding-parallel foliation developed in this area during D1 (358230E/ 6667670N). b) Migmatite at Paralana Hot Springs (350111E/6661287N). Leucosomes are deformed in buckle folds, which is a result of solid-state folding during the S_{main}-forming deformation. Palaeosomes suggest a magmatic precursor. c) Mica-schist of the RCM-unit west of Hidden Valley (354924E/6670854N). Isoclinal folds and the axial planar foliation formed during D2.

M2 increases in the Paralana Hot Springs area to migmatitic conditions. Leucosomes and melanosomes are folded in the solid state during D2 (Fig. 46b). Peak metamorphism thus occurred prior or during the deformation. S_2 is predominantly an axial planar foliation. It therefore overprints $S_{0/1}$ sub-parallel in the limbs of the folds and forms a crenulation in the isoclinal fold hinges. S_2 and $S_{0/1}$ are therefore in most areas parallel to each other. The intensity of the D2 deformation can be highly variable. Localised shear zones developed in metasediments and metagranites. Their general sense of shear is dextral with a normal movement of the N- / NW-side moving up at the eastern/southeastern limb of the Yankaninna Anticline (east- and south-MPI). The movement directions and orientation of the shear zones differ in the MPI because of the Palaeozoic folding. The S_2 foliation developed as the main foliation S_{main} in most areas of the MPI. Its general strike is from NE-SW in the central inler to E-W in the south. S_2 is described in the literature as a pervasive foliation in gneisses S_{gneiss} (Elburg et al., 2003). Armit et al. (2012) separate the main foliation into two deformation events that produced S_2 and S_3 fabrics.

The Older Granite Suite intrusions are all affected by D2 and show the dominant S_2=S_{main} foliation to variable extents. Strongly boudinaged, stretched pegmatites are found for example at Wild Dog Creek. These intrusions are therefore pre-S2, but it cannot be determined with certainty whether they preceded D1 or not.

The unconformity between the multiply deformed basement rocks and the folded cover is angular. The main foliation $S_{2=main}$ in the basement and the bedding S_{adl} of the Adelaidean sediments are sub-parallel at the unconformity, but may make angles of up to 90° along graben faults.

Basement and cover were folded during the Palaeozoic deformation (mapped as "Delamerian" structures). S_{main} folded into open folds F_{Pal1} with fold axes that plunge towards the NE, SW and W. This change in plunge-direction is caused by refolding during ongoing Palaeozoic compression (Weisheit et al., 2013b). The Palaeozoic deformation locally formed a crenulation cleavage S_{pal1-2} (= S_{main+1}) in basement rocks. This cleavage is pronounced in the pelitic parts of the undifferentiated RCM and in the biotitites that often show at least two Palaeozoic crenulation cleavages (S_{main+1} and S_{main+2}) (Fig. 51a+b). Palaeozoic deformation, however, did not generally produce clearly recognisable structures in the basement. This is in accordance with Paul et al. (1999) who showed that overall strain was relatively weak (≤20% shortening), even thought the large-scale folds are very prominently visible.

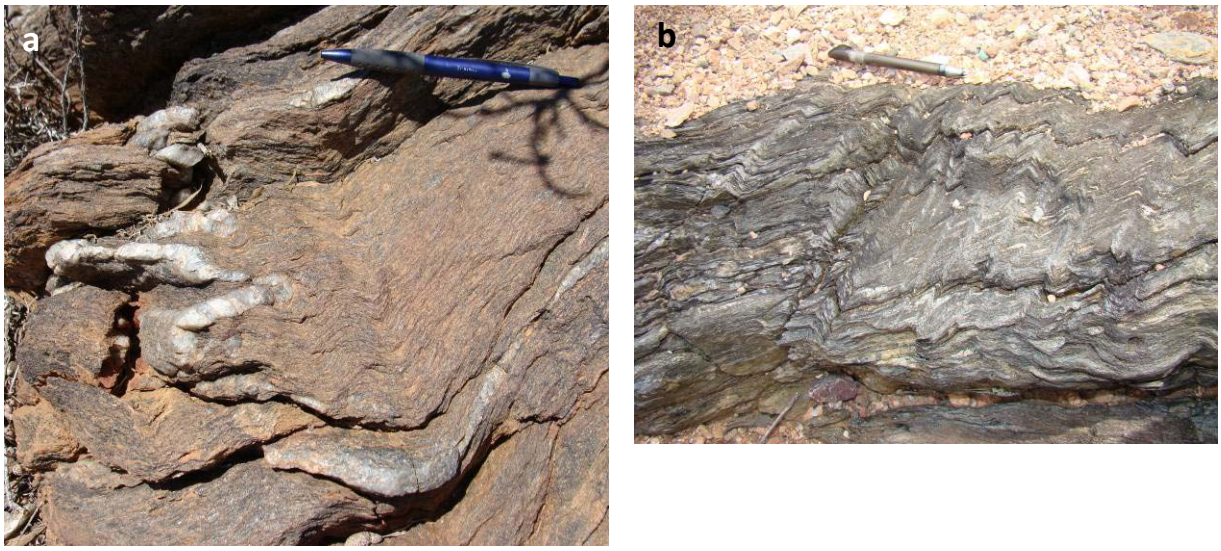

Fig. 51: Field photographs of crenulations cleavage in different basement units. a) Mount Neill Granite (MNG) east of Nooldoonooldoona Waterhole displays isoclinal folding of a quartz vein during the formation of S_2=S_{main} and Palaeozoic kink-folding S_{Pal} (337211E/6648625N). b) Biotite Schist with Palaeozoic kink-folds south of British Empire Mine (342530E/6659210N). Pure biotite schists record different deformation events and show often more than two foliation directions.

An unfolding of Palaeozoic structures in the basement can be calculated to estimate the orientation of S_{main} prior to the Palaeozoic deformation (Weisheit et al., 2013b). This reconstruction results in various orientations of the main foliation within the basement, that trend to flat-lying prior to the Palaeozoic deformation (Weisheit et al., 2013b). The various orientations can be interpreted as an effect of different folding patterns in cover and basement. The gneisses react differently to the Palaeozoic stress than the well-layered, weakly metamorphosed Adelaidean units. That results in different wavelength and amplitude of the Palaeozoic folding in basement and cover. Nevertheless, it is also possible that a folding of the main foliation already occurred in Proterozoic times.

Another reconstruction can be done on the geometry of the early Willouran grabens around the southern MPI (Weisheit et al., 2013b). The graben system ran about NW-SE Prior to the thick skinned Palaeozoic folding. The local NW-SE compression and the formation of the Yankaninna Anticline resulted in the folding of these grabens "above" the southern MPI. Therefore the grabens at The Pinnacles and at Wild Dog Creek are actually outcrops of one folded graben system. The same conclusion can be drawn on the half-grabens to the northeast of Arkaroola and the ones at

Yudnamutana Mine and at the Jubilee Mine area. The soft breccias at The Pinnacles and at The Needles (the NEB and the PIB) had formed at the extension of the graben faults above the horsts.

The overall compression direction in the Northern Flinders Ranges in the Palaeozoic was ~N-S (Weisheit et al., 2013b). The Yankaninna Anticline formed as a first generation fold and became rotated with ongoing N-S compression along the lateral and frontal ramp of the Paralana Fault Zone. After this rotation new E-W trending folds developed as a second fold geration and refolded the Yankaninna Anticline. Therefore the plunge angle and direction of the major fold axis in the MPI changed locally. The exact age of this successive deformation is discussed in the literature as related to the Delamerian Orogeny (E-W trending folds are characteristic in the Northern Flinders Ranges and generally interpreted as being Delamerian-related: e.g. Paul, 1999), or as part of the Alice Springs Orogeny (McLaren et al., 2006; D. Giles, pers. comm.). We show that these structures formed during long-lived deformation in the Palaeozoic, including the Delamerian and Alice Spings Orogenies (Weisheit et al., 2013b).

Some facts help to interpret the progressive Palaeozoic deformation:

- Metamorphic condition at the end of the Adelaidean sedimentation (~11.5 km of sediment west of the Paralana Fault) reached amphibolite facies at the unconformity at a geothermal gradient of 40-50 °C/km (as discussed in section 3.3: The Delamerian Orogeny; Sandiford et al., 1998).
- The amplitude of the Yankaninna Anticline is >10 km. The overall shortening in this area is only modest with 20 % (Paul et al., 1999). The uppermost Adelaidean unit (the Pound Quartzite) is still preserved in the adjacent synclines and therefore did not exhume much. The basement in the core of the anticline instead saw exhumation of >15 km. The Curnamona Craton to the east remained rigid during the thick-skinned folding west of the major Paralana Fault Zone.
- Pegmatitic intrusions are dated between ~500 Ma and 450 Ma (Elburg et al., 2003; Wülser, 2008; Weisheit et al., 2013b). The youngest shearing in the basement was dated to ~475 Ma (Elburg et al., 2003), but it is a mixed age of monazites that range between 530 Ma to 440 Ma (I. Buick, pers. comm. to M. A. Elburg). The 440 Ma diopside-titanite veins (Elburg et al., 2003) and pegmatites that are related to the K-feldspar alteration formed under brittle conditions.
- The intrusion of the British Empire Granite at ~450 Ma occurred at depths between 12 and 14 km (McLaren et al., 2006). The BEG intruded ~2 km below the unconformity.
- McLaren et al. (2002) report a temperature of ca. 400 °C at 430 Ma in lower Adelaidean sediments close to the unconformity. Between 500 Ma and 430 Ma the rocks exhumed ~2-2.5 km (assuming 50 °C/km or 40 °C/km, respectively). A further 50-100 °C (1-2.5 km) cooling occurred at ~400 Ma, followed by a 100 °C (2-2.5km) cooling stage at ~325 Ma (McLaren et al., 2002).
- Detrital zircons in the groundmass of the Pebble Dykes, which we interpret as deep cracks filled with sediment, record a maximum deposition age of 315±9 Ma (Brugger et al., 2011). Therefore the basement was close to the surface at this time.

Taking all these facts into account, the exhumation of the basement accompanies the formation of the Yakaninna Anticline, which is a result of differential vertical movement of at least 10 km that took place over a period of ~200 Ma (that corresponds to an average exhumation rate of only ~50 m/Ma Fig. 52a). Hence, folding cannot be attributed to the Delamerian Orogeny only, but covers both periods of the Delamerian and the Alice Springs Orogenies. The Yankaninna Anticline would have slowly formed by south directed ramping up the Curnamona Craton along the Paralana Fault system (Fig. 52b). Interference with the curved Paralana Fault Zone ramp caused the slight refolding of the main Yankaninna Anticline in ESE-WNW direction.

This issue is in detail discussed in Weisheit et al. (2013b).

A summary of different studies to the deformation and metamorphism in the MPI is given in appendix 11.4.

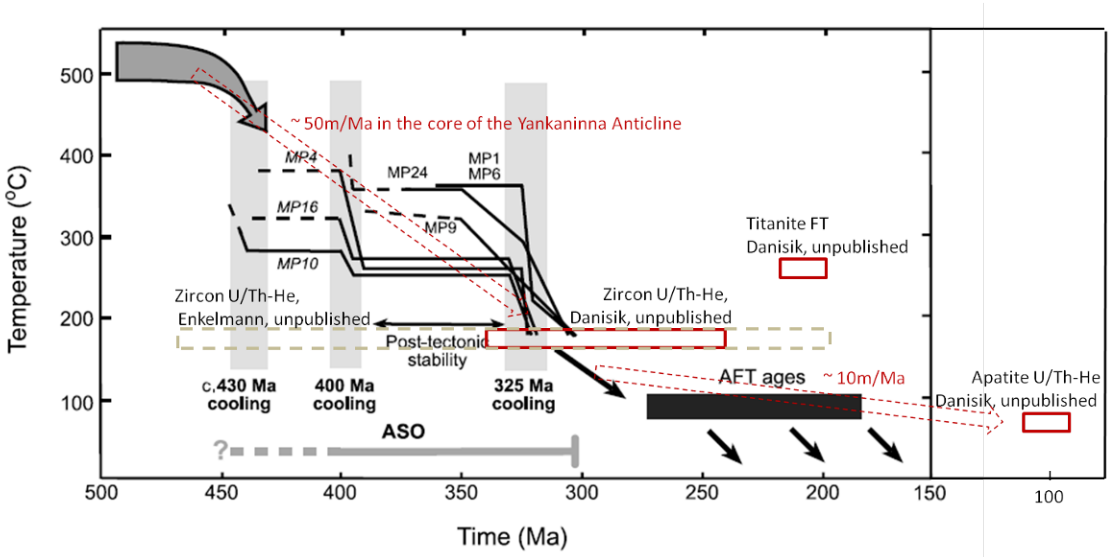

Fig. 52a: Modified figure 6 from McLaren et al. (2002). Unpublished zircon and apatite U/Th-He and titanite FT analyses from rocks in the core of the Yankaninna Anticline (~2 km below the unconformity) are added to the modeled cooling path of K-Ar, Ar-Ar and multiple-diffusion-domain thermal modeling published by McLaren et al. (2002). Approximately 10 km exhumation of basement rocks in the core of the Yankaninna Anticline took place between 500 and 300 Ma (average rate: ~50 m/Ma), decelerating between 300 and 100 Ma to an average exhumation rate of only ~10 m/Ma. Rocks at the southern unconformity only experienced an exhumation of ~3 km between 500 and 325 Ma, resulting in an average exhumation rate of ~20 m/Ma. This differential vertical movement resulted in the present-day folding pattern of gently dipping fold axes to the SW. Today basement crops out in the core of the crustal-scale anticline and the highest stratigraphic level of Adelaidean rocks are preserved in the synclines. Folding is therefore assigned to the most part of the Palaeozoic.

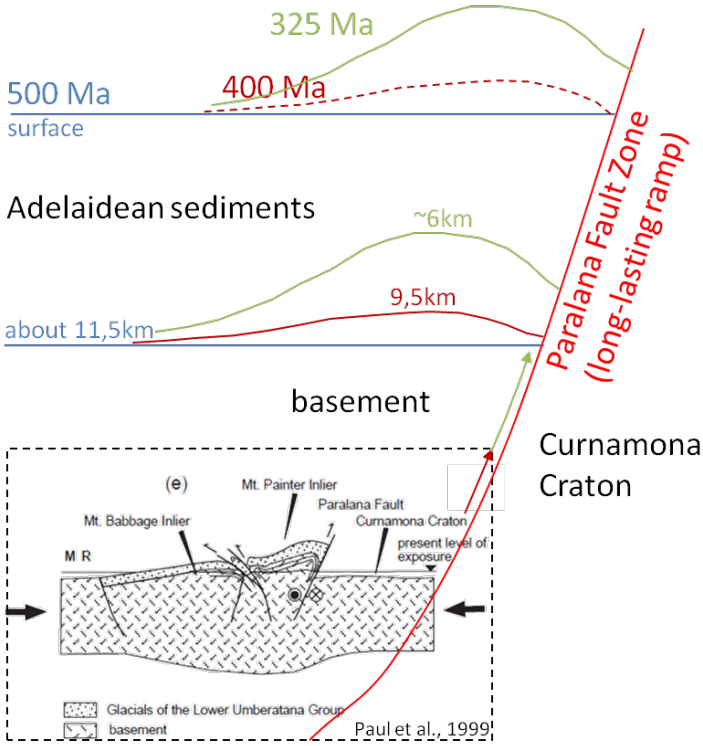

Fig. 52b: Simplified model of the exhumation of the southern unconformity between 500 and 325 Ma, based on the K-Ar and Ar-Ar analyses by McLaren et al. (2002) and a mean geothermal gradient of 40 °C/km. The MPI was exhumed as a transpressive fault-propagation anticline during long-lasting ramping in the Palaeozoic. The same mechanism was proposed by Paul et al. (1999), but they assigned the sinistral, transpressive inversion to be Delamerian in age.

7.2 Deformed and undeformed granodiorites, migmatites and „porphyries“

Granodiorites can be found all over the mapping areas as deformed and undeformed varieties. One focus of the mapping at the Paralana Plateau was on the controversy about a granodioritic type of the Ordovician British Empire Granite (BEG). McLaren et al. (2006) concluded that the BEG only consists of the granitic S-type phase, because the the granodiorite in the vicinity of the BEG appeared deformed. Fraser and Neumann (2010) date this deformed Paralana Granodiorite at The Tail of the BEG as Mesoproterozoic. However, Elburg et al. (2003) date an undeformed granodiorite to ~440 Ma and interpret it as an I-type phase of the BEG. We could find at least two generations of granodiorite during our mapping along the Paralana Plateau and The Tail of the BEG, including one pre- and one post-deformational variety. The most common granodiorites formed prior to S_{main} and can be mapped in the RCM that are folded with the Yankaninna Anticline and crop out at Paralana Gorge and in the vicinity of The Tail. This kind of locally deformed granodiorites can be found to the east of Sunshine Pound and northeast of Hidden Valley. Undeformed granodiorites and aplites are less abundant. The main occurrence of undeformed granodiorites is at The Tail of the BEG, where they intermingle with pegmatitic BEG-granites and intrude deformed Proterozoic granodiorites. Some small occurrences of undeformed granodiorites occur at the Paralana Plateau. These units still have to be mapped in more detail to unravel the relationships of the granodiorites in the MPI. Preliminary geochemical analyses of both varieties could not reveal distinct variations in the major alkali-oxides and only a little variation in the TiO_2, Zr and Nd content. Young, undeformed granodiorites trend towards low concentrations on these elements.

McLaren et al. (2006) discuss the BEG as a product of in-situ melting of the adjacent metasediments, because a <100 m zone of migmatites surrounds the batholith. We could not find any migmatites related to the intrusion of the BEG (Fig. 16b). Migamtitisation of deformed Hodgkinson (Paralana) Granodiorite in proximity to The Tail is realted to the migmatites at Paralana Hot Springs. The Proterozoic migmatitic “layer” is folded during the formation of the Yankaninna Anticline and crops out at Paralana Greek and at The Tail. The migmatites that are interpreted by McLaren et al. (2006) as cogenetic with the BEG are instead much older host rocks.

The nature of the Pepegoona "Porphyry" (PEP) in Pepegoona Gorge northeast of Hidden Valley and of similar outcrops southeast of Yudnamutana and in other localities of the MPI was studied by field observations, petrography and preliminary geochemical analyses. Gradual lithological changes are traceable in the field at Pepegoona Gorge. Massive grey granodiorite, an equigranular granite (MNG) and a porphyritic granite grade into each other at this locality. The geochemical analyses and thin section observations give hints for an alkali-metasomatic overprint of these host rocks. The alteration and the development of a shear texture during the S_{main}-producing deformation (D2) result in a rock with rounded, large "phenocrysts" that show resorption structures and float in a fine-grained, reddish-green matrix. Some of the areas that have been mapped as "Pepeggona Porphyry" by Coats and Blissett (1971) include real porphyritic granites as a host rock, but the predominant part is made of metasomaticaly altered and sheared igneous units. It is difficult to draw lithological boundaries between the different host rocks and the alteration products in the Pepegoona Gorge area. Therefore no map has been created at this area for this report. The interpretation that the PEP mapped by Coats and Blissett (1971) is predominantly an effect of hydrothermal alteration and deformation would solve the problem of the timing of Proterozoic intrusion and deformation. In the case that the MNG is associated with low-level porphyries, it intrude a deformed (?) sedimentary succession (RCM) shallowly, only ~10 Ma after the deposition of the RCM (as quoted in Armit et al., 2012). However, even if the porphyritic MNG is associated with real porphyries, it still may be intruded in depths up to more than 10 km. These intrusion depths have been observed for porphyritic granites in other parts of the world (e.g. Moyen et al., 2003; Seedorff et al., 2008). Metamorphism and ductile deformation are already active in RCM (at a geothermal gradient of 30 °C/km), if they are buried to ~10 km depth at this time. Therefore it is not necessary to invoke an extraordinary dynamic tectonic regime (after Armit et al., 2012) responsible for the structures and textures of the different lithologies.

7.3 The hydrothermal system(s)

The newly defined metasomatic units change the pre-existing maps of the MPI essentially, because some of them cover areas of several square km. Fine grained to pegmatitic quartz-K-feldspar rocks are now interpreted to be a result of an extensive K-feldspar metasomatic overprint that destroyed all previous structures and host mineralogy in an area of ~60 km². The volume of alteration is at least ~30 km³, because a difference in the elevation of K-feldspar altered rocks in the detailed mapped areas at East Painter Gorge and Yudnamutana Gorge is ~600 m. However, the vertical extent of the alteration is more likely much larger. Also K-feldspar altered rocks can be traced a few hundred metres below the surface in drill cores of Marathon Resources Ltd. in the centre of the southern MPI. The K-feldspar impregnation (i.e. the Pink Pegmatitic "Granite": PPG) and –brecciation (PPG-Matrix Breccia: PMB) follows pre-existing structures like the main foliation S_{main} of schists, para- and orthogneisses, as well as the axial plane of the Yankaninna Anticline and fault zones. K-feldspar altered rocks are undeformed and not metamorphosed. Magmatic activity in the Ordovician led to the intrusion of the British Empire Granite (BEG; Elburg et al., 2003) and related dykes of pegmatites and Yellow Microgranite (YMG; Elburg et al., 2012, 2013), contemporaneous with the K-feldspar alteration. Diopside-titanite veins (DTV) yield the same age as the BEG (~440 Ma; Elburg et al., 2003). The minerals in the DTV grew in open voids. PPG-related K-feldspar – quartz mineralisations can also be found on brittle joints in the host rock. Therefore the presently exposed level of the southern MPI was already in the brittle field of the crust (< ~350 °C) during the magmatic-hydrothermal event These observations are at odds with the proposed long-lived thermal event of the 500 Ma Delamerian Orogeny, due to a heating blanket of the Adelaidean sediments (after McLaren et al., 2002). The subsequent folding and re-folding of the km-scale Yankaninna Anticline instead exhumed the basement during the Palaeozoic (see section 7.1: Structures in basement and cover and Weisheit et al., 2013b). An independent heating event, probably with mantle input (Elburg et al., 2003; Elburg et al., 2012) caused the magmatic intrusions related to the BEG and, together with

contemporaneous exhumation, might be a further trigger for extensive fluid flow in the crust. The observation that veins and sets of joints, which are mineralised with K-feldspar, quartz ± hematite formed during varying directions of compression indicates a long-lasting activity of the K-feldspar-alteration fluid during the Palaeozoic exhumation.

The Palaeozoic fluid flow appears to have been focussed along pre-existing zones of weakness with ongoing exhumation and rising of the fluids. Fluid overpressure caused the formation of K-feldspar – quartz matrix breccias (PPG-Matrix Breccia; PMB) at certain levels in the crust and hence created new pathways for further fluid flow. The biotite breakdown in altered rocks released Fe, Mg and H_2O into the fluid. The iron precipitated at certain redox-horizons in sheets of Hematite (martite) Matrix Breccias (HMB) and the residual fluids altered these zones to form chloritic-hematitic Dark Matrix Breccias (DMB). One age obtained for the HMB is ~355 Ma (Elburg et al., 2013), which gives a minimum age of the preceding K-feldspar alteration. Geochemical and mineralogical studies on the development of the fluid and the fluid-rock interaction are discussed in Chapter 3 of this PhD thesis.

Weisheit et al. (2013a) discuss a model that relates the Hidden Valley type breccias (The Pinnacles, The Needles, Hidden Valley) to the Palaeozoic fluid flow system. These breccias resemble each other in their style and structure. The only difference lies in the maturity of the brecciation. Nevertheless, the Hidden Valley Breccia (HVB) within the basement is extraordinary. The most enigmatic aspect of the HVB is the presence of undeformed low-metamorphic grade metasediments (mostly sandstones and marbles), with well-preserved sedimentary structures, such as wave ripples, salt casts and mud cracks. Similar rocks and structures can be found in the Oppaminda Formation (e.g. to the S of Arkaroola Springs) and in the Humanity Seat Formation (e.g. in Arkaroola Creek east of Humanity Seat). The breccia is surrounded by basement rocks and the Adelaidean unconformity is expected to have been a few km above the present outcrop level (see cross sections in Paul et al., 1999; Weisheit et al., 2013b). Wülser (2008) therefore proposed that the basement was thrusted over the Adelaidean sediments, i.e. Hidden Valley would be a tectonic window. The breccia has a sub-vertical boundary to K-feldspar altered and brecciated MNG on its eastern side, with remnants of mylonites. The breccia zones finger into the basement rocks on the west side of the valley, which contradicts the interpretation of a thrust. The Hidden Valley breccia shows no structures (e.g. fault striations) that are typical for tectonic brecciation and indicative of mechanical diminution. Another indication against the thrusting model is that thrust tectonics are incompatible with the large-scale open folding with generally only modest shortening. We therefore favour a hydrothermal origin of the breccia, in which thorough mixing (possibly by fluidisation) of clasts occurred. An indication for the age of this breccia zone is given by Wülser (2008) who dated a muscovite pegmatite in the basement north of Hidden Valley to ~453 Ma. This pegmatite is probably related to the intrusion of the BEG. Pegmatites can also be found as clasts within the HVB, as well as clasts of PMB. The characteristics of fluidisation and collapse structures in the breccia (Weisheit et al., 2013a) indicate that it probably formed at shallow crustal levels.

The formation of the Mount Gee type hematite-quartz sinter postdates the K-feldspar (and iron oxide) metasomatism, and the Pebble Dykes. The sinter probably developed close to the surface with fluid temperatures of ~120 °C (Bakker and Elburg, 2006). Low temperature thermochronology of apatites of the wall rocks could therefore give an age of the hydrothermal overprint, provided that the exhumation already passed the closure temperature of the system (Weisheit et al., 2013b). The same study is done for the Pebble Dyke, which cuts through PPG rocks, but is itself cut by the Mount Gee quartz sinter.

Noticeable is the strong structural control on the movement of all hydrothermal fluids in the MPI. The main alteration directions NE-SW, E-W and N-S resemble the strikes of the main foliation S_{main}, the strike of the axial planes, hinges and limbs of the Palaeozoic folds and the strike of major fault zones. Alteration and brecciation concentrate in intersection zones of these structures.

8. Conclusions

The introduction of new hydrothermal units changes the pre-existing geological maps in a fundamental way. Rocks that are thought to be of a magmatic origin are now related to metasomatic processes, which cover a large area. About 30 % of the southern MPI is altered into massive K-feldspar – quartz rocks and breccias – a process that was guided by numerous fluid pathways in the basement and, to a lesser extent in the cover as well. The evolution of the fluid during fluid-rock interaction and contemporaneous exhumation plays a crucial role in the formation of mineralogical distinct impregnations and breccias. The Palaeozoic fluid flow system, the nature and propagation of the fluids through the crust is discussed in Chapters 3 of this PhD thesis and in Weisheit et al. (2013a).

Structures in the basement and especially in the lower Adelaidean graben systems are complex and depended on local variations in stressfield-patterns, rheological properties of units/sequences and pre-existing zones of weakness. Therefore only structures that occur regionally can be used for a tectonic reconstruction of the multiply deformed basement and the cover sediments. Basement and cover deformed over a long period, covering most of the Palaeozoic.

9. Acknowledgements

The mapping projects in 2007 and 2008 were funded by Marathon Resources Limited. We gratefully acknowledge the support in the field by the staff of Marathon Res.

The German DFG (project BO-1776/8 and BO-1776/8-2 FB 17022615) is thanked for the funding of the fieldwork in 2009 and 2010 and the geochemical analyses.

We like to give our special thanks to Margret and Doug Sprigg and the staff of Arkaroola Sanctuary for their general full support and access to the study area.

A special thank goes to Marlina Elburg (University of KwaZulu-Natal, South Africa). She is one of the applicants for the PhD project and supported the mappings with Marathon Res.. She included her long-standing experience in the MPI´s geology in the supervision and organisation of fieldwork and geochemical analyses of the rock samples.

Eva Enkelmann, Wolfgang Siebel (both University of Tübingen, Germany) and Martin Danisik (Waikato University of Hamilton, New Zealand) are thanked for their geochronological analyses of the samples and the discussion of the data.

We also want to express our gratitude to Steve Hore and Wolfgang Preiss for their support of our fieldwork and help during diverse organisations and, as John Foden, Joel Brugger, Pierre-Alain Wülser and Robin Armit for animated discussions about the MPI´s geology.

The Bachelor and Diplom students Jens Rößiger, Christian Kling, Tobias Rehder, Christian Kieslinger, Burkhard Cless, Simon Kocher, Matthias Lindhuber, Johannes Holzäpfel, Jürgen Lang and Jens Müller are thanked for their work and interest during their mapping projects.

10. References

Armit, R.J., Betts, P.G., Schaefer, B.F., Ailleres, L., 2012. Constraints on long-lived Mesoproterozoic and Palaeozoic deformational events and crustal architecture in the northern Mount Painter Province, Australia. Gondwana Research, 22, 207–226.

Bakker, R. J., Elburg, M. A., 2006, A magmatic-hydrothermal transition in Arkaroola (northern Flinders Ranges, South Australia): from diopside-titanite pegmatites to hematite-quartz growth, Contr. to Min. and Petr. 152(5): 541-569.

Barovich, K.M., Burtt, A. and Hand, M., 2006, Geochemistry and geophysics in the Curnamona Province: can this marriage be saved? In: Korsch, R.J. and Barnes, R.G. (compilers) Broken Hill Exploration Initiative: Abstracts for the September 2006 Conference, Geoscience Australia Record 2006/21, 4-6.

Bierlein, F.P., Arne, D.C., Keay, S.M., and McNaughton, N.J., 2001, Timing relationships between felsic magmatism and mineralisation in the central Victorian gold province, southeast Australia, Australian Journal of Earth Sciences, v. 48, p. 883-899.

Bons, P.D., Roessiger, J., 2008, The Geology of the Mt. Gee area, Mount Painter Inlier, South Australia, Unpublished Industry Report on the mapping project carried out October-November 2007.

Brugger, J., Wülser, P.A., Foden, J., 2011, Genesis and Preservation of a Uranium-Rich Paleozoic Epithermal System with a Surface Expression (Northern Flinders Ranges, South Australia): Radiogenic Heat Driving Regional Hydrothermal Circulation over Geological Timescales, Astrobiology, v. 11, p. 499-508.

Buick, I.S., Storkey, A., Williams, I.S., 2008, Timing relationships between pegmatite emplacement, metamorphism and deformation during the intra-plate Alice Springs Orogeny, central Australia, Journal of Metamorphic Geology, v. 26, p. 915-936.

Campana, B., Coats, R. P., Horwitz, R. & Thatcher, D., 1961a, 1:63'360 Gardiner sheet, Geological Atlas of South Australia.

Campana, B., Coats, R. P., Horwitz, R. & Thatcher, D., 1961b, 1:63'360 Moolawatana sheet, Geological Atlas of South Australia.

Campana, B., Coats, R. P., Horwitz, R. & Thatcher, D., 1961c, 1:63'360 Paralana sheet, Geological Atlas of South Australia.

Campana, B., Coats, R. P., Horwitz, R. & Thatcher, D., 1961d, 1:63'360 Umberatana sheet, Geological Atlas of South Australia.

Celerier, J., Sandiford, M., Hansen, D.L., Quigley, M., 2005, Modes of active intraplate deformation, Flinders Ranges, Australia, Tectonics, Vol. 24.

Chang, Z.S., and Meinert, L.D., 2004, The magmatic-hydrothermal transition - evidence from quartz phenocryst textures and endoskarn abundance in Cu-Zn skarns at the Empire Mine, Idaho, USA: Chemical Geology, v. 210, p. 149-171.

Coats, R.P., Blissett, A.H., 1971, Regional and Economic Geology of the Mount Painter Province, Geological Survey of Sounth Australia, Bulletin 43, 426.

Conor, C.H.H., Preiss, W.V., 2008, Understanding the 1720-1640 Ma Palaeoproterozoic Willyama Supergroup, Curnamona Province, Southeastern Australia: Implications for tectonics, basin evolution and ore genesis, Precambrian Research, v. 166, p. 297-317.

Cowley, W.M., Hore, S.B., Preiss, W.V., Sheard, M.J., Wade C., 2012. A revised stratigraphic scheme for the Mount Painter and Mount Babbage Inliers. SAREIC 2012 Technical forum poster. published in the web http://minerals.dmitre.sa.gov.au/press_and_events/events/sareic_2012_technical_forum.

Daly, S.j., Fanning, C.M., Fairclough, M.C., 1998, Tectonic evolution and exploration potential of the Gawler craton, South Australia, AGSO Journal of Australian Geology and Geophysics, v. 17, p. 145-168.

Direen, N.G., Cadd, A.G., Lyons, P., Teasdale, J.P., 2005, Architecture of Proterozoic shear zones in the Christie Domain, western Gawler Craton, Australia: Geophysical appraisal of a poorly exposed orogenic terrane, Precambrian Research, v. 142, p. 28-44.

Drexel, J.F., 1980, Geology of a portion of the southern Mount Painter Inlier, S. Aust. Dept Mines and Energy Report 80/120, unpublished.

Drexel, J.F. and Major, R.B., 1987, Geology of the uraniferous breccias near Mount Painter, South Australia and revision of rock nomenclature, Quarterly Geological Notes, Geological Survey of South Australia

Elburg, M.A., Andersen, T., Bons, P.D., Weisheit, A., Simonsen, S.L., Smet, I., 2012. Metasomatism and metallogeny of A-type granites of the Mt Painter–Mt Babbage Inliers, South Australia. Lithos, 151, 83–104.

Elburg, M.A., Andersen, T., Bons, P.D., Simonsen, S.L., Weisheit, A., 2013. New constraints on Phanerozoic magmatic and hydrothermal events in the Mt Painter Province, South Australia. Gondwana Research 24, 700-712. doi: 10.1016/j.gr.2012.12.017.

Elburg, M.A., Bons, P.D., Foden, J., Brugger, J., 2003. A newly defined Late Ordovician magmatic-thermal event in the Mt Painter Province, Northern Flinders Ranges, South Australia. Australian Journal of Earth Sciences, 50, 611-631.

Elburg, M.A., Bons, P.D., Dougherty-Page, J., Janka, C.E., Neumann, N., Schaefer, B., 2001, Age and metasomatic alteration of the Mt Neill Granite at Nooldoonooldoona Waterhole, Mt Painter Inlier, South Australia, Australian Journal of Earth Sciences 48, 721-730.

Fanning, C.M., Ashley, P., Cook, N., Teale, G.S., Conor, C., 1998, A geochronological perspective of crustal evolution in the Curnamona Province. In: Gibson, G.M. (Ed.) Broken Hill Exploration Initiative: Abstracts of papers presented at the Fourth Annual Meeting in Broken Hill, Australian Geological Survey Organisation Record 1998/25, 30-35.

Fanning, C.M., Teale, G.S., Robertson, R.S., 2003, Is there a Willyama Supergroup sequence in the Mount Painter Inlier? In: Peljo, M. (compiler) Broken Hill Exploration Initiative: Abstracts from the July 2003 conference, Geoscience Australia Record 2003/13, 38-41.

Flöttmann, T., James, P., Rogers, J., Johnson, T., 1994, Early Paleozoic foreland thrusting and basin reactivation at the Palaeo-Pacific margin of the southeastern Australian Precambrian Craton: a reappraisal of structural evolution of the southern Adelaide Fold-Thrust Belt, Tectonophysics 234, 95–116.

Fraser, G. L., Neumann, N.L., 2010, New SHRIMP U-Pb zircon ages from the Gawler Craton and Curnamona Province, South Australia, 2008 – 2010, Geoscience Australia Record 2010/16, 192-254.

Foden, J., Elburg, M. A., Dougherty-Page, J., Burtt, A., 2006, The timing and duration of the Delamerean Orogeny: correlation with the Ross Orogen and implications for Gondwana assembly, The Journal of Geology, volume 114, p. 189-210.

Hand, M., Reid, A., Jagodzinski, E.A., 2007, Tectonic framework and evolution of the Gawler Craton, Southern Australia, Economic Geology 102, 1377-1395.

Kieslinger, C., 2011, Study of the surroundings of Mount Gee, Arkaroola, Northern Flinders Ranges, South Australia, with special focus on uranium-bearing hematite-matrix breccias, Diplom Thesis, Tübingen University, unpublished.

Kling, C.J.C., 2008, Mapping of Hematite Breccias and their structural occurrence in Radium Ridge Area, Mt. Painter Inlier, South Australia, Bachelor Thesis, Tübingen University, unpublished.

Kocher, S., Holzäpfel, J., Lindhuber, M., 2011, Reports on the 2010 mapping campaign at Mt. Painter Inlier, Northern Flinders Ranges, South Australia, Mapping Reports, Tübingen University, unpublished.

Korsch, R.J., Preiss, W.V., Blewett, R.S., Fabris, A.J., Neumann, N.L., Fricke, C.E., Fraser, G.L., Holzschuh, J., Milligan, P.R., Jones, L.E.A., 2010a, Geological interpretation of deep seismic reflection and magnetotelluric line 08GA-C1: Curnamona Province, South Australia. In: Korsch, R.J. and Kositcin, N. (Eds) South Australian Seismic and MT Workshop, Extended Abstracts, Geoscience Australia Record 2010/10, 42-53.

Kositcin, N., 2010, Geodynamic synthesis of the Gawler Craton and Curnamona Province, Geoscience Australia, Record, 2010/27, 113p.

Lennox, P.G., Trzebski, R., Armstrong, R., Siebel, W., 2005, Structural evolution and granite chronology of the central Molong Zone, Eastern Lachlan fold belt, Australia, Australian Journal of Earth Sciences, v. 52, p. 79-99.

McLaren, S., Sandiford, M., Powell, R., Neumann, N., Woodhead, J., 2006, Paleozoic intraplate crustal anatexis in the Mount Painter Province, South Australia; timing, thermal budgets and the role of crustal heat production, Journal of Petrology 47, 2281-2302.

Mawson, D., 1923, The igneous rocks of the Mount Painter Belt, Transactions of the Royal Society of South Australia, 47: 376-387.

Mildren, S., Sandiford, M., 1995, Heat refraction and low pressure metamorphism in the northern Flinders Ranges, South Australia, Australian Journal of Earth Sciences, 42: 241-247.

Moyen, J.F., Nedelec, A., Martin, H., Jayananda, M., 2003, Syntectonic granite emplacement at different structural levels: the Closepet granite, South India, Journal of Structural Geology, v. 25, p. 611-631.

Myers, J.S., Shaw, R.D., Tyler, I.M., 1996, Tectonic evolution of Proterozoic Australia, Tectonics 15, 1431-1446.

Neumann, N., 2001, Geochemical and isotopic characteristics of South Australian Proterozoic granites: implications for the origin and evolution of high heat-producing terrains, Ph.D. thesis, University of Adelaide, unpublished.

Neumann, N., Hore, S., Fraser, G., 2009a, New SHRIMP geochronology from the Mount Painter Province, South Australia. In: Korsch, R.J. (Ed.) Broken Hill Exploration Initiative: Abstracts for the 2009 conference, Geoscience Australia Record 2009/28.

Nicholl, M.J., and Williams, T., 2006, Comment on "The magmatic-hydrothermal transition - evidence from quartz porphyritic textures and endoskarn abundance in Cu-Zn skarns at the Empire Mine, Idaho, USA" by Z. Chang and L.D. Meinert, Chem. Geol. (2004) 210, 149-171: Chemical Geology, v. 228, p. 286-288.

Page, R.W., Conor, C.H.H., Stevens, B.P.J., Gibson, G.M., Preiss, W.V., Southgate, P.N., 2005b, Correlation of Olary and Broken Hill Domains, Curnamona province: possible relationship to Mt Isa and other North Australian Pb-Zn-Ag-bearing successions, Economic Geology 100, 663-676.

Paul, E., 1998, Geometry and controls on basement-involved deformation in the Adelaide Fold Belt, South Australia, PhD thesis, Adelaide University, unpublished.

Paul, E., Flöttmann, T., Sandiford, M., 1999, Structural geometry and controls on basement-involved deformation in the northern Flinders Ranges, Adelaide Fold Belt, South Australia, Australian Journal of Earth Sciences, 46(3), 343-354.

Pidgeon, R. T., 1980, Report on the U–Pb age of monazite samples 930, 931 and 932 (from the Mount Painter area), South Australian Department of Mines and Energy Open File Envelope.

Preiss, W.V., 1987, The Adelaide Geosyncline: Late Proterozoic stratigraphy, sedimentation, palaeontology and tectonics, Geological Survey of South Australia Bulletin, 53: 34-41.

Preiss, W.V., 2000, The Adelaide Geosyncline of South Australia, and its significance in continental reconstruction, Precambrian Research, 100, 21-63.

Rehder, T., 2010, A complex hydrothermal overprint of the basement rocks in the East Painter area, Arkaroola, Northern Flinders Ranges, South Australia, Diplom mapping report, Tübingen University, unpublished.

Reid, A., Hand, M., Jagodzinski, E.A., Kelsey, D., Pearson, N.J., 2008b, Paleoproterozoic orogenesis within the southeastern Gawler Craton, South Australia, Australian Journal of Earth Sciences 55, 449-471.

Rößiger, J., 2008, Regional study of the Mt. Gee Area, Arkaroola, Northern Flinders Ranges, South Australia, Diplom thesis, Tübingen University, unpublished.

Sandiford, M., Hand, M., McLaren, S., 1998, High geothermal gradient metamorphism during thermal subsidence, Earth and Planetary Science Letters, 163, 149-165.

Sheard, M., Cockshell, C.D., 1992, Seismic interpretation of Mt. Hopeless Line 1, Report book 92/17, Department of Energy and Science SA.

Sheard, M.J., Fanning, C.M., Flint, R.B. 1992, Geochronology and definition of Mesoproterozoic volcanics and granitoids of the Mount Babbage Inlier, northern Flinders Ranges, Quarterly Geological Notes - Geological Survey of South Australia 123, 18-32.

Sprigg, R.C., 1945, Investigation of the uranium deposits at Mount Painter, South Australia, Department of Mines, Report Book 45/1, Department of Mines, South Australia.

Stewart, K., Foden, J., 2003, Mesoproterozoic Granites of South Australia, Department of Primary Industries and Resources, Report Book 2003/15, 142p.

Teale, G.S., 1979, Revision of Nomenclature for Paleozoic Intrusives of the Mount Painter Province, South Australia, Trans. R. Soc. S. Aust. Volume 103(4), pp 95-100.

Teale, G.S., 1980, The occurrence of högbomite and taaffeite in a spinel–phlogopite schist from the Mount Painter Province of South Australia, Mineralogical Magazine 43, 575–577.

Teale, G.S., 1993a, Geology of the Mount Painter and Mount Babbage Inliers. In: Drexel, J.F., Preiss, W.V. and Parker, A.J. (Eds), The geology of South Australia, Volume 1, The Precambrian, South Australia Geological Survey Bulletin 54, 149-156.

Teale, G.S., 1993b, The Nooldoonooldoona Trondhjemite and other newly recognised Mesoproterozoic intrusives in the Mount Painter Province, Geological Survey of South Australia, Quarterly geological notes 125, 20-31.

Teale, G. S., 1995, Highly deformed alkaline granites from the southern Mount Painter Inlier, northern Flinders Ranges, Quarterly Geological Notes Geological Survey of South Australia, 127; Pages: 19-28.

Weisheit, A., 2009, Mount Painter Inlier, South Australia, Deformation history and structural interpretation with the aid of remote sensing and thin section analysis, Diplom thesis, University of Tübingen, unpublished.

Weisheit, A., Bons, P.D., Elburg, M.A., 2013a. Long-lived crustal fluid-flow: the hydrothermal mega-breccia of Hidden Valley, Mt. Painter Inlier, South Australia. International Journal of Earth Sciences, 102, 1219-1236, doi: 10.1007/s00531-013-0875-7.

Weisheit, A., Bons, P.D., Danišík, M., Elburg, M.A., 2013b. Crustal-scale folding: Palaeozoic deformation of the Mt. Painter Inlier, South Australia. Journal of the Geological Society, in press.

Wingate, M.T.D., Campebell, I.H., Compston, W., Gibson, G.M., 1998, Ion-probe U-Pb ages for Neoproterozoic basaltic magmatism in south-central Australia and implications for the break-up of Rodinia, Precambrian Research, 87, 135-159.

Wülser, P.-A., 2010, Uranium metallogeny in the Northern Flinders Ranges region of South Australia, Ph.D. thesis, University of Adelaide, unpublished.

11. Appendix

11.1 Snapshot of the cooperated maps in MapInfo

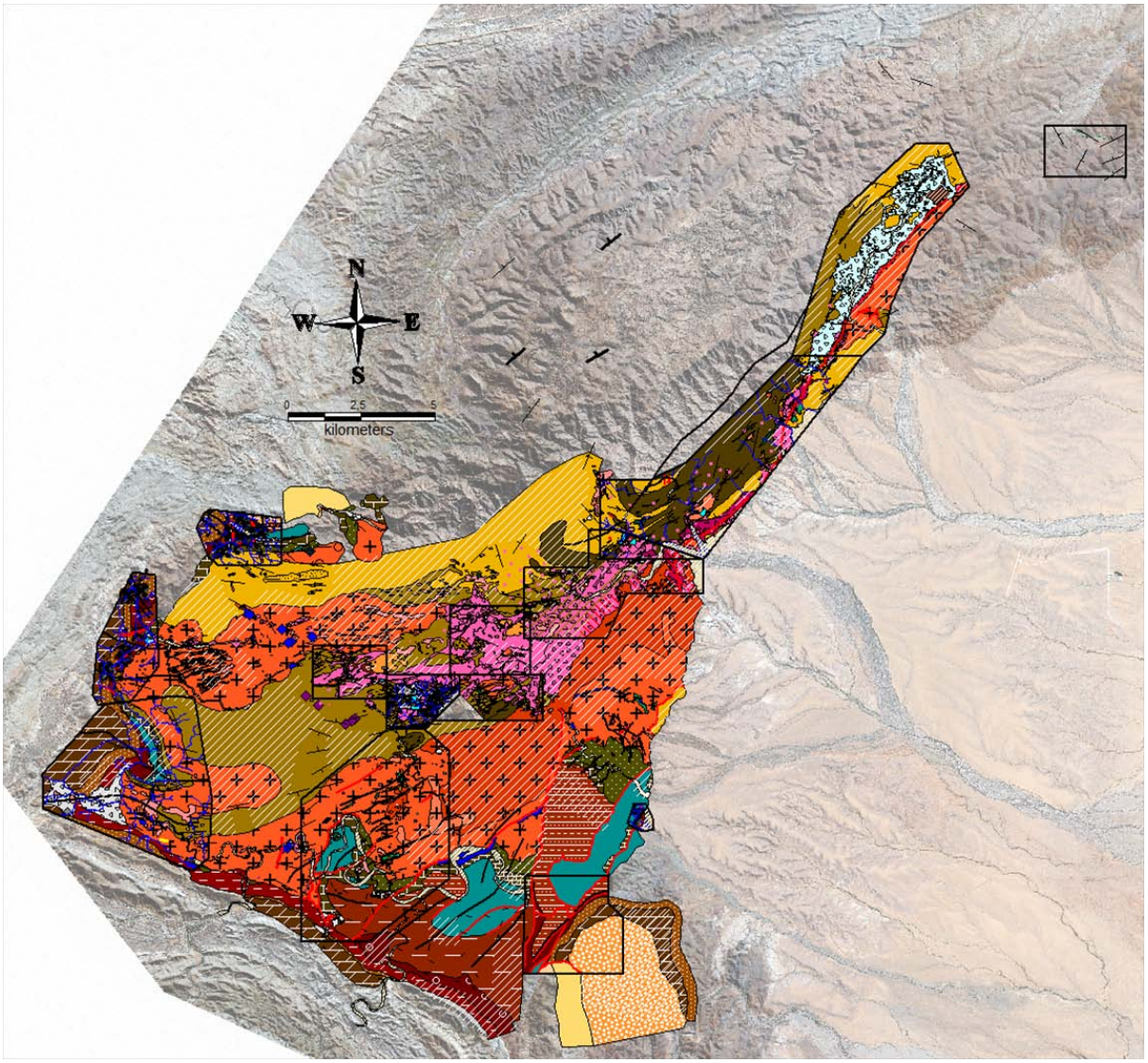

This picture summarises all combined geological layers that were created in MapInfo (Pitney Bowes Software) during the mapping projects. Encircled areas display the detailed maps, which are in detail discussed in separate theses. Transparent layers (e.g. the interpretation) and layers with polylines and points (e.g. faults and veins) are on top of the opaque layers. Details to the layers are given in the report and summarised in the appendix 11.2: Acronyms in the GIS database.

11.2 Acronyms in the GIS database

GIS	Group	Unit/description	acronym
polylines	structures	detailed mapping areas	areas
		folds	folds
		faults	faults
		dip+strike	dip_strike
points and opaque regions	veins	barite vein	BAV
		calcite vein	CAV
		goethite vein	GOV
		diopside-titanite vein	DTV
		hematite vein	HEV
		magnetite vein	MGV
		quartz-hematite-feldspar vein and breccia	QHF
		quartz vein	QZV
		tourmaline-PPG-vein	TPV
	mines	copper mines	Mine
transparent layers	interpretation	interpretation	interpretation
	Tertiary-Quaternary	Tertiary-Quaternary	TQY
	alteration	K-feldspar alteration, host rocks still recogniceable	incomplete_K-fsp_alteration
		albitised MNG	aMNG
		chloritic MNG	cMNG
		mica-rich MNG	mMNG
		biotite-rich RCM	Bt_RCM
		bleached areas	bleached
		Wywyana marble	WYM
	brecciation	dominant clasts in breccia	Breccia_components
	structures	zones of intense foliation	foliation_zones
opaque layers	basement	Radium Creek Metamorphics	RCM
		Radium Creek Metamorphics - Quartzite	RCQ
		Radium Creek Metamorphics - Gneiss	RCG
		andalusite schist	aSCH
		Yagdlin Phyllite	YAP
		Mount Neill Granite	MNG
		Pepegoona Porphyry	PEP
		Terrapinna Granite	TPG
		Granodiorite	GDT
		mafics/amphibolite	MAF
		mylonite	MYL
		migmatite	MIG

		British Empire Granite	BEG
		yellow microgranite	YMG
	alteration	Black Biotite Schist	BBS
	Adelaidean	Balcanoona Formation	BAF
		Tapley Hill Formation	THF
		Bolla Bollana Formation	BBF
		Skillogallee Dolomite	SKD
		Woodnamoka Phyllite	WOQ
		Opaminda Formation	OPF
		Blue Mine Conglomerate	BMC
		Wortupa Quartzite	WOP
		Humanity Seat Formation	HSF
		Wooltana Volcanics	WOV
		Wywyana Formation	WYF
		Shanahan Conglomerate	SHC
		Paralana Quartzite	PAQ
		pelite	pelite
	brecciation	mica-matrix breccia	MMB
		undifferentiated breccia	breccia
		dark matrix breccia	DMB
		hematite matrix breccia	HMB
		Mount Gee unit	MGU
		PPG-matrix breccia	PMB
		pink pegmatitic "granite"	PPG
		quartz-hematite breccia	QHB
		silicified matrix breccia	SMB
	Pebble Dyke	Pebble Dyke	PED
	pegmatite	pegmatite	PEG
	Hidden Valley	HV breccia	HVB
	clasts	HV- chloritic-feldspatic breccia	HV_CFB
	clasts	HV- chloritic-silicified breccia	HV_CSB
	clasts	HV- sedimentary chanell	HV_chanell
	clasts	HV- gabbro	HV_grabbro
	clasts	HV- pebble breccia	HV_pebble
	clasts	HV- phyllite	HV_phyllite
	clasts	HV- plagiogranite	HV_plagiogranite
	clasts	HV- marble	HV_marble
	clasts	HV- pelite	HV_pelite
	clasts	HV- psammite	HV_psammite
	clasts	HV- silt	HV_silt

11.3 Overview to the granitoid studies in the MPI

References are listed in Weisheit (2009).

	geochemical properties	deformation	relationships	age	methode	reference
Older Granite Suite						
Paralana Hot Springs Gneiss	A-type, albitisation: K, Ca, Ba, Rb, U, Pb, Sr, Fe loss, Na, Si, Mg gain, high Th and U (Neumann, 1996 and 2001)	massive granitic to gneissic (Neumann, 2001); strong bt-foliation (Fraser and Neumann, 2010)		1582±6Ma (magmatic cryst.) 1553±4Ma (metamorphic recryst.)	SHRIMP zircon	Fraser and Neumann, 2010
MNG	A-type, albitisation: K, Ca, Ba, Rb, U, Pb, Sr, Fe loss, Na, Si, Mg gain (Neumann, 2001)	most time massive; gneiss-like near Pepegoona Gorge (Armit, 2007) and strongly deformed at Nooldoonooldoona Waterhole (Elburg, 2001) concordant (Coats and Blissett, 1971 and Paul, 1998) recrystallised (Coats and Blissett, 1971)	faulted, intrusive sharp, intrusive gradational contact to Pepegoona Porphyry (Huston, 1995); comagmatic to Pepegoona Porphyry (Neumann, 2001)	1590 ±5Ma	LA-ICPMS zircon	Kromkhun, pers. comm., 2008
				1574 ±3Ma	Pb/Pb zircon	Elburg et al., 2001
				1569 ±14Ma	U/Pb	Fanning, 1995
				1585±3Ma	SHRIMP zircon	Fraser and Neumann, 2010
Pepegoona Porphyry	A-type, albitisation: K, Ca, Ba, Rb, U, Pb, Sr, Fe loss, Na, Si, Mg gain (Neumann, 2001)	most time massive; gneiss-like near Pepegoona Gorge (Armit, 2007) concordant (Coats, 1967 and Paul, 1998) recrystallised (Coats and Blissett, 1971)	near surface intrusion / extrusion (Neumann, 2001)	1645Ma	Rb/Sr	Compston et al., 1966
				1603 ±19Ma	LA-ICPMS zircon	Kromkhun, pers. comm., 2008
				1582 ±3,5Ma	SHRIMP zircon	Jagodzinski and Hore, in prep.
Yerila Granite	A-type, magma mixing, high Th and U (Neumann, 2001); most mafic, enriched in incompatible elements, mantle component (Kromkhun pers. comm.)	most time massive; ESE to EW local shearing (Coats, 1967) and mylonitic to gneissic (Teale, 1993)		1558±4Ma	SHRIMP zircon	Fraser and Neumann, 2010
				1556 ±20Ma	LA-ICPMS zircon	Kromkhun, pers comm., 2008
				1551 ±33Ma	U/Pb zircon	Johnson, 1980
Box Bore Granite	A-type, magma mixing, high Th and U (Neumann, 2001)	strong foliated augen-mylonite (Teale, 1993 and Neumann, 2001) strong gneissic fabric (Fraser and Neumman, 2010)		1592 ±6Ma	LA-ICPMS zircon	Kromkhun, per com., 2008
				1583±2Ma	SHRIMP zircon	Fraser and Neumann, 2010
				1555 ±15Ma	SHRIMP zircon	Teale, 1995
Moolawatana Suite						
Wattleowie	A-type, co-	weak to moderately	gradational into	1566 ±12Ma	LA-ICPMS	Kromkhun,

Granite	magmatic	deformed (Sheard, 1992; Neumann, 2001 and Teale, 1993); gneiss-like and concordant (Coats and Blissett, 1971 and Coats, 1967), strong bt-foliation (Fraser and Neumann, 2010)	Terrapinna Granite (Stewart and Foden, 2003)		zircon	pers. comm., 2008
				1563±3Ma	SHRIMP zircon	Fraser and Neumann, 2010
Terrapinna Granite	A-type, co-magmatic	most time massive rapakivi-like, stressed (Coats and Blisset, 1971), weakly foliated near Prospect Hill (Sheard, 1992), strongly sheared in contact to Wattleowie Granite and SC-fabric near Adelaidean cover (Huston, 1995), NE-SW foliated dip 50-90°W (ENVELOPE 02034, p 1006ff) constists of strong deformed metasediment enclaves (Huston, 1995)	intrudes Yerila Granite; comagmatic with Wattleowie Granite (Coats and Blissett, 1971 and Neumann, 2001)	1567 ±14Ma	LA-ICPMS zircon	Kromkhun, pers. comm., 2008
				1560±3Ma	SHRIMP zircon	Fraser and Neumann, 2010
				1557 ±6Ma	SHRIMP zircon	Fanning, 1995 and Sheard et al., 1992
				1556 ±4Ma	U/Pb zircon	Thornton, 1980
Petermorra Volcanics (MBI)			intruded by Prospect Hill and White Well Granite (Wall, 1995)	1560 ±3Ma		Sheard, 1992
Golden Pole Granite	A-type, co-magmatic	even textured (Teale, 1993), intrudes into Terrapinna Granite (Huston, 1995)	younger than Yerila and Terrapinna Granite (Wall, 1995)			
Con Bore Granite		even textured (Teale, 1993)	emplaced into the Terrapinna Granite (Wall, 1995)			
Younger Granite Suite						
Paralana Granodiorite	I-type, low LREE, U, Th, Rb, Zr, Ti (Neumann, 1996 and 2001)	massive to migmatitic (Neumann, 1996)	Delamerean folding (Neumann, 2001)	1543 - 1538Ma, rim of 1086-1051Ma	Pb/Pb zircon	Neumann, 1996 and Paul, 1998
= Hodgkinson Granodiorite		weak bt-fabric, feldspatic and melt leucosomes (Fraser and Neumann, 2010)		1552±4Ma (magmatic crystallisation) ~520/511Ma and ~467/458Ma (metamorphic recryst.)	SHRIMP zircon	Fraser and Neumann, 2010
=? I-Typ BEG				442Ma	U/Pb monazite	Elburg et al, 2003
Mudnawatana Tonaltite	I-type, similar to Paralana		co-magmatic to Paralana			

	Granodiorite (Neumann, 2001)		Granodiorite (Neumann, 2001)			
British Empire Granite (BEG)	minimum melt, S-type, high U, Rb, K (Neumann, 1996 and 2001); I- (=Parlanana Granodiorite) and S-type (Elburg, 2003)	massive	probably co-genetic to Mudnawatana Tonalite and Paralana Granodiorite (Neumann, 2001)	445Ma (S-type) and 442Ma (I-type)	U/Pb monazite	Elburg et al., 2003

11.4 Summary of deformation and metamorphism studies

References are listed in Weisheit (2009).

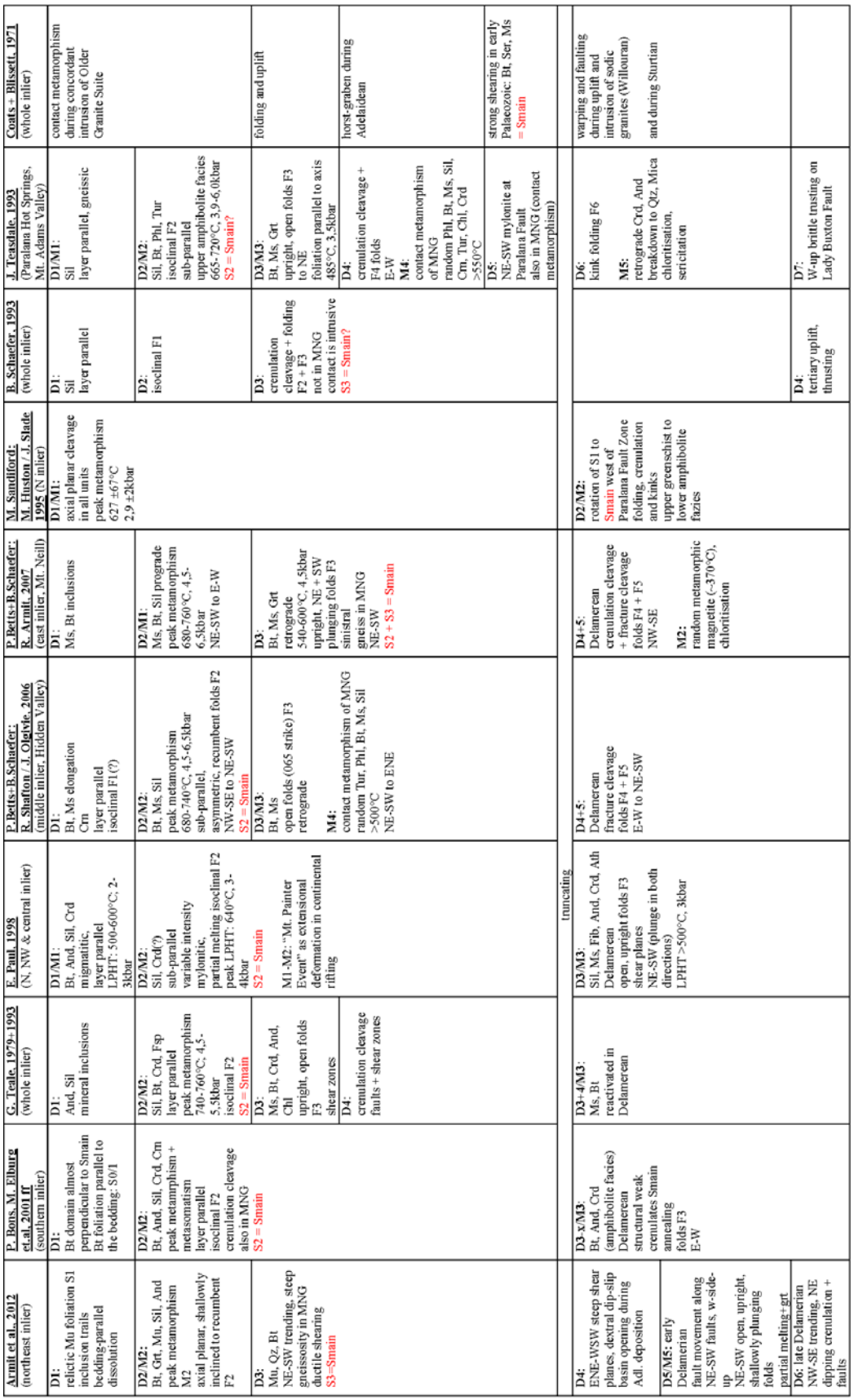

Arnit et al., 2012 (northeast inlier)	P. Bons, M. Elburg et al. 2001 ff (southern inlier)	G. Teale, 1979-1993 (whole inlier)	E. Paul, 1998 (N, NW & central inlier)	P. Betts+B.Schaefer; R. Shaffon / J. Olgivie, 2006 (middle inlier, Hidden Valley)	P. Betts+B.Schaefer; R. Arnit, 2007 (east inlier, Mt. Neill)	M. Sandiford; M. Huston / J. Shade 1995 (N inlier)	B. Schaefer, 1993 (whole inlier)	J. Teasdale, 1993 (Paralana Hot Springs, Mt. Adams Valley)	Coats + Blissett, 1971 (whole inlier)
D1: relictic Mu foliation S1 inclusion trails bedding-parallel dissolution	**D1:** Bt domain almost perpendicular to Smain Bt foliation parallel to the bedding: S0/1	**D1:** And, Sil mineral inclusions	**D1/M1:** Bt, And, Sil, Crd migmatitic, layer parallel LPHT: 500-600°C, 2-3kbar	**D1:** Bt, Ms elongation Crn layer parallel isoclinal F1(?)	**D1:** Ms, Bt inclusions	**D1/M1:** axial planar cleavage in all units peak metamorphism 627 ±67°C 2,9 ±2kbar	**D1:** Sil layer parallel	**D1/M1:** Sil layer parallel, gneissic	contact metamorphism during concordant intrusion of Older Granite Suite
D2/M2: Bt, Grt, Mu, Sil, And peak metamorphism M2 axial planar, shallowly inclined to recumbent F2	**D2/M2:** Bt, And, Sil, Crd, Crn peak metamrphism + metasomatism layer parallel isoclinal F2 crenulation cleavage also in MNG S2 = Smain	**D2/M2:** Sil, Bt, Crd, Fsp layer parallel peak metamorphism 740-760°C; 4,5-5,5kbar isoclinal F2 S2 = Smain	**D2/M2:** Sil, Crd(?) sub-parallel variable intensity mylonitic, partial melting isoclinal F2 peak LPHT: 640°C, 3-4kbar S2 = Smain	**D2/M2:** Bt, Ms, Sil peak metamorphism 680-740°C, 4,5-6,5kbar sub-parallel, asymmetric, recumbent folds F2 NW-SE to NE-SW S2 = Smain	**D2/M1:** Ms, Bt, Sil prograde peak metamorphism 680-760°C, 4,5-6,5kbar NE-SW to E-W		**D2:** isoclinal F1	**D2/M2:** Sil, Bt, Phl, Tur isoclinal F2 sub-parallel upper amphibolite facies 665-720°C, 3,9-6,0kbar S2 = Smain?	folding and uplift
D3: Mu, Qz, Bt NE-SW trending, steep gneissosity in MNG ductile shearing S3=Smain		**D3:** Ms, Bt, Crd, And, Chl upright, open folds F3 shear zones **D4:** crenulation cleavage faults + shear zones	**D3/M3:** Bt, Ms open folds (065 strike) F3 retrograde **M4:** contact metamorphism of MNG random Tur, Phl, Bt, Ms, Sil >500°C NE-SW to ENE M1-M2: "Mt. Painter Event" as extensional deformation in continental rifting	**D3/M3:** Bt, Ms retrograde 540-600°C, 4,5kbar upright, NE + SW plunging folds F3 sinistral gneiss in MNG NE-SW S2 + S3 = Smain		**D3:** crenulation cleavage + folding F2 + F3 not in MNG contact is intrusive S3 = Smain?	**D3/M3:** Bt, Ms, Grt upright, open folds F3 to NE foliation parallel to axis 485°C, 3,5kbar **D4:** crenulation cleavage + F4 folds E-W **M4:** contact metamorphism of MNG random Phl, Bt, Ms, Sil, Crn, Tur, Chl, Crd >550°C **D5:** NE-SW mylonite at Paralana Fault also in MNG (contact metamorphism)	horst-graben during Adelaidean strong shearing in early Palaeozoic: Bt, Ser, Ms = Smain
truncating									
D4: ENE-WSW steep shear planes, dextral dip-slip basin opening during Ad. deposition	**D3-x/M3:** Bt, And, Crd (amphibolite facies) Delamerean structural weak crenulates Smain annealing folds F3 E-W	**D3+4/M3:** Ms, Bt reactivated in Delamerean	**D3/M3:** Sil, Ms, Fib, And, Crd, Alb Delamerean open, upright folds F3 shear planes NE-SW (plunge in both directions) LPHT >500°C, 3kbar	**D4+5:** Delamerean fracture cleavage folds F4 + F5 E-W to NE-SW	**D4+5:** Delamerean crenulation cleavage + fracture cleavage folds F4 + F5 NW-SE **M2:** random metamorphic magnetite (~370°C), chloritisation	**D2/M2:** rotation of S1 to Smain west of Paralana Fault Zone folding, crenulation and kinks upper greenschist to lower amphibolite fazies		**D6:** kink folding F6 **M5:** retrograde Crd, And breakdown to Qtz, Mica chloritisation, sericitation	warping and faulting during uplift and intrusion of sodic granites (Willouran) and during Sturtian
D5/M5: early Delamerian fault movement along NE-SW faults, w-side-up NE-SW open, upright, shallowly plunging folds partial melting+grt							**D4:** tertiary uplift, thrusting	**D7:** W-up brittle trusting on Lady Buxton Fault	
D6: late Delamerian NW-SE trending, NE dipping crenulation + faults									

---------- **CHAPTER 3 (GEOCHEMISTRY)** ----------

Crustal-scale fluid flow and a long-lived Palaeozoic hydrothermal system in the Mount Painter Inlier, South Australia

by

Anett Weisheit[1]

with contributions by

M.A. Elburg[2,3] (second supervisor)

P.D. Bons[1] (first supervisor)

R. Bakker[4] (fluid inclusion study)

A. Soesoo[5] (geostatistical analysis)

W. Siebel[1] (Rb-Sr analysis)

T. Wenzel[1] (EMPA measurements)

H. Taubald[1] (oxygen isotope analysis)

T. Andersen[6] (U-Pb and Lu-Hf analysis)

[1] Faculty of Mathematics and Natural Sciences, Eberhard-Karls University Tübingen

[2] Department of Geology and Soil Science, Ghent University, Belgium

[3] Geology Division, SAEES, University of KwaZulu-Natal, South Africa

[4] Department of Applied Geosciences and Geophysics, Mineralogy and Petrology, University of Leoben, Austria

[5]Institute of Geology, Tallin University of Technology, Estonia

[6] Department of Geosciences, University of Oslo, Norway

Table of Contents

ABSTRACT

Potassium alteration in the Mount Painter Inlier and in the adjacent Adelaidean cover sediments in northern South Australia extends over an area of ~60 km² and locally reaches depths of at least ~500 m. Altered rocks are macroscopically characterised in the new-growth of K-feldspar blasts and the breakdown of mafic minerals. Original textures and deformation structures of orthogneisses, paragneisses, schists and mafic units are gradually obliterated while a new paragenesis of massive K-feldspar, recrystallised quartz and anhedral to euhedral iron-oxide minerals formed. U-Pb and Lu-Hf analyses of zircon grains in totally altered units show that zircon may be the only relict of the precursor rock. The K-feldspar alteration is concentrated along the fold hinge of the crustal-scale Yankaninna Anticline and the Paralana Fault Zone. The Mount Painter Inlier exhumed with the anticlinal folding and the ramping along the Paralana Fault Zone between ~500 and ~300 Ma. Rb-Sr whole rock and muscovite analyses of an altered pegmatite, as well as relative relationships of K-feldspar altered rocks to dated units in the inlier suggest that alteration was active during the Palaeozoic exhumation. Locally it started during or after ~478 Ma (Rb-Sr age of an altered pegmatite) and was active before and after ~443 Ma (published age of a diopside-titanite vein). Field observation and thin section analyses indicate complex overprinting relationships and geochemical analyses result in chaotic signals, suggesting that the alteration system evolved spatially and temporally. Based on the interpretation of a long-lived Palaeozoic exhumation of the inlier and the detailed study of the alteration system we propose a simplified model that integrates exhumation, fluid flow, alteration and brecciation. Trapped, saline connate water got released constantly during decompression at a certain level in the rising anticlinal core in the Palaeozoic. This brine travelled upwards while certain fluid-rock interaction reactions occurred at different levels in the crust, depending on temperature and pressure conditions and the geochemistry of the host rocks. Biotite-breakdown, K-feldspar alteration and -brecciation, iron-oxide formation and silicification occurred during the evolution of the fluid at higher crustal levels and in zones of structural fluid focussing. The basement and partly the cover rocks in the anticlinal core moved through the levels of alteration and brecciation during the long-lived Palaeozoic exhumation, resulting in the observed complex overprinting. Published U-Pb analyses of monazites in iron-oxide ore breccias suggest that the whole alteration system was active at least until ~355 Ma and ceased before ~315 Ma (published zircon U-Pb age of an unaltered unit).

INTRODUCTION

Scope of the work

The Mount Painter Inlier (MPI) in the Northern Flinders Ranges, South Australia, has been a focus of several economic studies in the late 19th and the early 20th century (Fig.1; Coats and Blissett, 1971 and references therein). The exploration targeted uranium-REE-rich magnetite-hematite breccia ores in the centre of the Mesoproterozoic basement (Drexel and Major, 1987, 1990; Elburg et al., 2012, 2013) and minor copper deposits in the Neoproterozoic cover meta-sedimentary rocks close to the unconformity (Coats and Blissett, 1971; Lang, 2012). Copper mineralisations occur only in sub-economic quantities in skarn- and breccia-zones, but exploration of the uranium deposits continued through the 20th century and became banned in recent years (Arkaroola Protection Act 2012). The uranium and copper ores formed during fluid-rock interaction processes (Lang, 2012; Elburg et al., 2013). Various metasomatic rocks, veins and breccia zones in basement and/or cover rocks indicate additionally that fluid flow played an important role in the geological development of the MPI (Coats and Blissett, 1971; Drexel and Major, 1987; Elburg et al., 2001, 2013; Bakker and Elburg, 2006; Weisheit et al., 2013a; Chapter 2 of this PhD thesis). The effect of hydrothermal fluids on middle and upper crustal rocks is a continuing focus of research worldwide (e.g. Simon, 1990; Hemley et al., 1992; Williams, 1994; Moore et al., 2000; Wilkinson, 2001; Derome et al., 2003; Taubald et al, 2004; Baatartsogt et al., 2007; Plümper and Putnis, 2009; Sandström et al., 2010). Hydrothermal alteration processes often lead to economic mineral deposits that occur frequently in zones of structurally focused fluid-flow (e.g. Oreskes and Einaudi, 1992; Evans, 1993; Carrier et al, 2000; Thorkelson et al., 2001; Sandström et al., 2010). The breccia-, alteration- and mineralisation zones in basement and cover of the MPI indicate a complex hydrothermal history with fluid-flow activities in the Mesoproterozoic (Elburg et al., 2001; Elburg et al., 2013), the Palaeozoic (Bakker and Elburg, 2006; Brugger et al., 2011; Elburg et al., 2013; Weisheit et al., 2013b; Chapter 2 of this PhD thesis) and potentially as a continuing event until recent times (Brugger et al., 2005; Weisheit et al., 2013b).

Based on detailed geological mapping of the extensive various alteration zones (Chapter 2 of this PhD thesis), this study addresses the geochemical and structural development of the Palaeozoic alteration and mineralisation activity in the MPI. We will first present the results of petrological and whole rock geochemical analyses of host rock, metasomatite and breccia samples. Selected samples were studied using the electron microprobe, oxygen isotope analyses and fluid inclusion measurements (data-tables and figures are attached at the end of the main text). Following this we will present the results of U-Pb and Lu-Hf measurements in zircons of selected altered rocks that will be compared with signals of the local host rocks (Elburg et al., 2012) to determine the age and nature of the hydrothermal system. Included in the chronological analyses is an undeformed, altered pegmatite that was measured for its Rb-Sr isotope systematics in muscovite and whole rock sample. The results

of the geochronology and of low-temperature thermochronology analyses (Weisheit et al., 2013b) are discussed in a separate section. Finally we will present a model for the regional Palaeozoic fluid flow that includes the geochemical and geochronological results, the structural reconstruction of the basement's exhumation (Weisheit et al., 2013b) and the formation of large breccia zones in basement and cover (Weisheit et al., 2013a).

GEOLOGICAL SETTING

The Mount Painter Inlier (MPI) and the adjacent Mount Babbage Inlier crop out in cores of crustal-scale anticlinal structures in the far north of the Adelaide Fold and Thrust Belt, South Australia (Fig.1). Basement quartzites, phyllites, paragneisses and schists in the MPI represent a succession of metaturbidites that was deposited on the eastern margin of the Archaean Gawler Craton in the early Mesoproterozoic (Fanning et al., 2003; Wülser, 2009; Fraser and Neumann, 2010; Korsch et al., 2010; Armit et al., 2012). This succession, called the Radium Creek Group (RCG; Coats and Blissett, 1971; Cowley et al., 2012) was intruded by two suites of A-type granitoids shortly after their deposition at ~1585-1575 and at ~1565-1555 Ma (Elburg et al., 2001; Stewart and Foden, 2003; McLaren et al, 2006; Elburg et al., 2012). The older Coulthard Suite was affected by pervasive albitisation and local biotitisation, probably related to the intrusion of the younger Moolawatana Suite, prior to a regional deformation event (Elburg et al., 2001, 2012). Mesoproterozoic deformation was contemporaneous with amphibolite-facies metamorphism and post-dates migmatitisation in the area of Paralana Hot Springs (Paul et al., 1999; Weisheit et al., 2013b; Fig.1B). A pervasive gneissic to schistose main foliation developed axial planar to isoclinal folds in all basement rocks (Paul et al., 1999; Elburg et al., 2001; Armit et al., 2012; Weisheit et al., 2013b). The main foliation is a crenulation cleavage that is recorded mainly in pelitic successions of the RCG and in mica-rich metasomatic rocks (Elburg et al., 2001; Elburg et al., 2012; Weisheit et al., 2013b).

Extension in NE-SW direction at ~800 Ma (Wingate et al., 1998) led to the formation of NW-SE running horst and graben faults in the exposed basement (Weisheit et al., 2013b). The major, NE-SW to N-S striking, westwards-dipping Paralana Fault System at the western side of the MPI was active as a normal fault at this time (Fig.1B; Paul et al., 1999; Weisheit et al., 2013b). The early grabens east and west of the Paralana Fault *sensu stricto*, which is the N-S striking section of the system east of Arkaroola village (Fig.1B; Coats and Blissett, 1971), were filled with terrestrial siliciclastics, marine carbonates, dolomites and rift-related, spilitised flood basalts of the Adelaidean Sequence (Coats and Blissett, 1971; Preiss, 1987; Wingate et al., 1998). Regional subsidence until ~530 Ma resulted in the formation of the Adelaidean sedimentary basin that covered the early graben structures on either side of the Paralana Fault *s.s.* (Preiss, 1987; Preiss, 2000; Weisheit et al., 2013b). The unconformity between the basement inlier and the cover sediments was buried ~11.5 to ~13.5 km

west of the Paralana Fault *s.s.* and ~9.5 km east of it (Weisheit et al., 2013b). As a result the metamorphic conditions at the unconformity reached amphibolites facies in the west and greenschist facies in the east (Sandiford et al. 1998; Weisheit et al., 2013b).

Magmatic activity and compression in the southern Adelaidean basin (southern Adelaide Fold Belt; Fig.1A) between ~514 and ~492 Ma define the Delamerian Orogeny in this area (Preiss, 1995; Foden et al., 2006). Crustal-scale folding and the exhumation of the MPI were also interpreted to be a result of this orogeny (e.g. Paul et al., 1999; McLaren et al., 2002; Armit et al., 2012). Weisheit et al. (2013b) recently challenged this model based on the re-interpretation of published K-Ar cooling ages (McLaren et al., 2002) of the MPI and adjacent cover sediments. According to this study Palaeozoic exhumation of the MPI as a crustal-scale anticlinal structure (Yankaninna Anticline) lasted significantly longer (~200 Myr). A small number of deformed pegmatites with ages of ~500 Ma indicate the earliest onset of Palaeozoic deformation in the MPI (Elburg et al., 2003, 2013). Thick-skinned folding and contemporaneous exhumation of basement and cover occurred during N-S directed compression in the Northern Flinders Ranges (Paul et al., 1999; Weisheit et al., 2013b). This also caused reactivation of the Paralana Fault System as a set of sinistral oblique and lateral ramps. Crustal-scale deformation was focused in the hanging wall of the system, while the Curnamona Province to the east remained rigid (Weisheit et al., 2013b).

At ~460-440 Ma met- and peraluminous types of the British Empire Granite (BEG) and related pegmatites and granodiorites intruded into the basement at ~13 km depth (Elburg et al., 2003, 2013; McLaren et al., 2006; Wülser, 2009; Weisheit et al., 2013b). Pegmatitic diopside-titanite veins formed in basement rocks during the same time (Bakker and Elburg, 2006) and local hydrothermal phlogopitisation and monazite-growth are recorded (Elburg et al., 2012). Extensive hydrothermal fluid-flow resulted in the formation of K-feldspar- and quartz-rich rocks and breccias (Bons and Roessiger, 2008), which are interpreted in the early literature as resulting from a “granitisation” process (Coats and Blissett, 1971) and K-feldspar metasomatism (Radium Ridge Breccias; Drexel and Major, 1987). The Palaeozoic hydrothermal activity is focus of this study and will be discussed in the following sections.

Cracks filled with clastic autochtonous and allochtonous sediments formed in the southern MPI during the Carboniferous-Permian Glaciation at ~290 Ma (Brugger et al., 2011). These pebble dykes, or diamictitic dykes (Cowley et al., 2012) can be found in K-feldspar overprinted rocks at least 300 m below the palaeo-surface. They indicate the end of the MPI’s long-lasting exhumation from < ~500 Ma to ~290 Ma and separate the early Palaeozoic hydrothermal activity from a younger sub-surface sinter activity (Weisheit et al., 2013b). Quartz-hematite sinter breccias and -veins formed in the early Permian (Brugger at al., 2011) and overprinted the pebble dykes. The Mt. Gee sinter fluids were active at least until Triassic times, as indicated by zircon (U-Th)/He, titanite and apatite fission

track dating (Weisheit et al., 2013b). As discussed in Weisheit et al. (2013b) apatite (U-Th)/He samples were additionally affected by a modest burial of the province of < ~2 km in Mesozoic times (Krieg et al., 1995). The recent landscape at the MPI is a result of Neogene tectonism (Célérier et al., 2005).

METHODS

Sampling

Samples of host rock and alteration products (metasomatite and breccia) of the Palaeozoic K-feldspar alteration were taken throughout the whole southern and central MPI from basement and cover for thin section analyses (Tab.1). Several samples of about 20x15x10 cm size (7 to 10 kg) were additionally taken at well-exposed transition zones from unaltered to altered rocks. These samples were used for detailed petrological (coverslipped thin sections and doubly polished sections) and geochemical analyses (Tab.1-5).

Quartz samples of unaltered and altered lithologies, as well as pegmatites and hydrothermal quartz veins were prepared for fluid inclusion studies and oxygen isotope measurements (Tab.1; Tab.6+7). A detailed petrography and the analysis of daughter and accidentally trapped minerals with Raman spectroscopy are used for microthermometric analyses to define the trapping conditions of the alteration fluids.

A whole rock powder and muscovite separates were prepared for Rb-Sr isotopic analyses of alteration-related pegmatites (Tab.1; Tab.8). Mineral separation has been done on samples of 5 to 8 kg of unaltered wall rocks and alteration products. Zircon were analysed for U-Pb and Lu-Hf to compare the age and isotopic characteristics of inherited zircons in altered rocks with the host rock signal and to determine an absolute age of the alteration system (Tab.1; Tab.9+10).

Analytical methods

ELECTRON MICROPROBE

Minerals in doubly polished thin sections were analysed with a JEOL 8900 Superprobe at the Department of Geosciences at the University of Tübingen. Feldspar and mica crystals of host rock and alteration products were measured in their original texture. Acceleration voltage was set to 20 kV and the beam current to 20 nA. Feldspar grains were generally measured with a widened beam diameter of 10 µm to avoid alkali loss during analysis. Si, Na, K, Sr, Al, Ca, Ba and Fe were measured in feldspar with the wavelength-dispersive (WDS) technique and recalculated to oxides. As the analysed mica grains absorbed a focused electron beam during the measurements (sample current dropped), a 10 µm

beam was also used for these minerals. The WDS measurements for mica included Si, Na, K, Al, Ca, Ba, Fe, Mg, Ti, Mn, F and Cl. Peak counting times varied between major and minor elements between tens of seconds up to a half a minute. The background was measured half the peak counting time. The average analytical error of the measurements varied between less than 1 % and a few percents for major oxides and up to 20 % for trace elements (Tab.2). As alkalis tend to migrate, they were measured at the beginning of each analysis. Calibration of the microprobe was done with natural as well as synthetic standards which were measured frequently during the analyses. The internal $\phi\rho Z$ correction of JEOL was used to correct the raw data for absorption and fluorescence of the matrix minerals (Armstrong, 1991). The methodology is described in detail in Reed (2005).

WHOLE ROCK ANALYSES

Samples of 7 to 10 kg were analysed for their major oxides (SiO_2, TiO_2, Al_2O_3, Fe_2O_3, MnO, MgO, CaO, Na_2O, K_2O, P_2O_5; in wt.%) and trace elements (Ba, Co, Cr, Ni, Rb, Sr, V, Y, Zn, Zr, Ce, Eu, La, Nb, Nd, Sm, Yb; in ppm). The samples were first crushed with a hammer and a segment was selected as a thin section sample. Two stainless steel jaw crushers were used to reduce the size of the fragments to about 10 mm. Elevated Cr and Ni signals in the samples may derive from the jaw crushers. A quartz mill was used to produce a homogeneous whole rock powder of about 40 μm. The powder was measured with a Bruker AXS S4 Pioneer wavelength dispersive XRF spectrometer (Rh-tube at 4 kW) in the isotope geochemistry laboratory, Department of Geosciences at the University of Tübingen. The dry whole rock sample was fused with lithium tetra-/metaborate in an Oxiflux system from CBR analytical service at 1200 °C. Loss on ignition (LOI) was determined separately at 1000 °C.

Another set of whole rock measurements was done by ICP-OES, carried out at the Department of Analytical Chemistry at the University of Ghent. After determination of LOI at 950 °C, 0.6 g of lithium meta-/tetraborate was added to 0.15 g of sample and heated to 1050 °C for 20 min. The homogeneous melt was dissolved immediately in 2 % nitric acid with a 2 ppm Pt spike. A range of rock standards was dissolved in a similar manner. Measurements were done with a Spectro ARCOS ICP-OES. An argon plasma ionised the sample and standard fluids and specific emission lines of major elements (reported as the oxides SiO_2, TiO_2, Al_2O_3, Fe_2O_3, MnO, MgO, CaO, Na_2O, K_2O, P_2O_5; in wt.%) and trace elements (Be, Sc, V, Cr, Co, Ni, Cu, Zn, Sr, Y, Zr, Ba, La, Ce, Nd, Yb, Hf, Th, Nb; in ppm) were measured.

OXYGEN ISOTOPE RATIOS

Two distinct quartz veins were measured for oxygen isotope ratios at the Department of Geosciences at the University of Tübingen. Quartz, hematite and K-feldspar assemblages of a hydrothermal vein at Petalinka Waterfall (PW) were measured as a function of their distance to the vein's wall. 2 to 4 mg of sample was loaded onto a Pt-sample holder, evacuated to 10^{-6} mbar and

fluorinated overnight with 50 mbars of pure F_2. The samples were heated with a CO_2-laser at a constant temperature of 150 °C. During that process excess F_2 was separate from the extracted O_2 with the aid of KCl under the formation of Cl_2. A molecular sieve collected the extracted O_2 and a Finnigan MAT 252 isotope ratio mass spectrometer measured the oxygen isotope composition. The δ value is expressed relative to the VSMOW standard in permil (‰). The replicate oxygen isotope analyses of the NBS-28 quartz (recommended value $\delta^{18}O$ = 9.64 ‰) and UWG-2 garnet (recommended value $\delta^{18}O$ = 5.8 ‰) standards have and average precision of ± 0.1 ‰ for $\delta^{18}O$. The accuracy of the measurements is commonly better than 0.2 ‰. The same procedure was followed for ten pure quartz samples of a set of >10 m large quartz veins at Echo Camp (EC) to establish potential variations in the oxygen isotope ratios within the veins.

Details on the methodology are given in Hoefs (2009).

FLUID INCLUSIONS

Fluid inclusion analyses in quartz were carried out at the fluid laboratory of the Department of Mineralogy and Petrology at the Montan-University in Leoben (Austria) and at the laboratory of the Department of Geosciences at the University of Tübingen (Germany). Detailed petrographic examinations were done on petrographic microscopes with transmitted and reflected light with magnifications up to 100x. Microthermometry was carried out on a Linkam THMSG 600 stage mounted on an Olympus BX 40 microscope (Leoben) and on the same model Linkam stage mounted on a Leica DMLP microscope (Tübingen). The Olympus BX 40 microscope was equipped with 4x, 10x, 40x and 100x long-working distance objective lenses; the Leica DMLP microscope was equipped with 5x, 10x, 20x and 50x magnification objectives. The arrangements allowed phase transitions to be observed over a temperature range of -193 °C and +600 °C with a measurement accuracy of ±0.2 °C below 100 °C and ± 0.4 °C at higher temperatures. Heating rates may be set individually, but preset rates include 80, 10 and 1 °C/min. H_2O and CO_2 standard measurements were carried out regularly for calibration of the devices and recalculation of the measurements. The methodology for microthermometry is described by Van den Kerkhof and Hain (2001) and Wilkinson (2001).

To study the geochemical composition of the fluid inclusions laser Raman microprobe analyses (Burke, 2001; Bakker, 2004; Baumgartner and Bakker, 2009) were carried out with a Jobin Yvon LABRAM confocal-Raman spectrometer in Leoben. The spectrometer is equipped with a frequency-doubled Nd-YAG laser (100 mW, 532.2 nm) and with a He-Ne laser (633 nm). The diffraction gratings vary between 1200 and 1800 grooves/mm. A Peltier-cooled, slow-scan, CCD matrix-detector analyses the laser signal and an Olympus BX 40 microscope fitted with 10x, 50x and 100x long-working distance objective lenses allows focusing the 532.02 nm laser beam and viewing

the sample. The measurement accuracy of the instrument is ± 3 cm^{-1}. Single measurements were done three times for 20 seconds and a mean value was determined.

GEOCHRONOLOGY

Rb-Sr whole rock and muscovite analyses were carried out with a thermal ionisation mass spectrometer at the Department for Geosciences at the University of Tübingen. For this purpose the whole rock powder and the muscovite grains were spiked with a mixed $^{87}Rb/^{84}Sr$ tracer solution and digested in 48 % HF in capped beakers for 4 days at 140 °C on a hot plate. After dry-down and re-dissolution in 6N HCl and once again in 2.5N HCl the Rb and Sr were isolated by ion exchange chromatography. Sr was loaded on single W filaments with a Ta-HF activator and measured statically with a Finnigan MAT 262 mass spectrometer. Rb was loaded on a Re filament with ultra-pure H_2O and measured in a Re double filament configuration. Normalisation was done to the $^{86}Sr/^{88}Sr$ ratio of 0.1194. Three measurements of the NBS 987 Sr standard yielded an average $^{87}Sr/^{86}Sr$ ratio of 0.710215 ± 0.000011 (certified value: 0.710248). Total procedural blanks were 130 pg for Sr and 556 pg for Rb. Twelve separate loads of USGS granite G2 standard were used to evaluate the reproducibility. The 2σ standard deviation for $^{87}Rb/^{85}Rb$ was 1 % and for $^{87}Sr/^{86}Sr$ was 0.03 %. The isochrons were calculated with the Isoplot 3.0 software (Ludwig, 2001). The methodology is described in Dickin (2009).

U-Pb and Lu-Hf isotope compositions of zircons were analysed by laser-ablation inductively coupled plasma source mass spectrometry using a Nu Plasma HR mass spectrometer and a NewWave LUV213 laser microprobe at the Department of Geosciences, University of Oslo. The analytical protocols, described in detail by Rosa et al. (2009) and Andersen et al. (2009) were used for U-Pb geochronology of zircon, and those of Heinonen et al. (2010) for Lu-Hf. One to three calibration standards were run in duplicate at the beginning and end of each U-Pb analytical session and at regular intervals during sessions. The zircons used for calibration included international zircon standards GJ-01 ($^{207}Pb/^{206}Pb$ age = 609±1 Ma; Belousova et al., 2006), 91500 ($^{207}Pb/^{206}Pb$ age = 1065±1 Ma; Wiedenbeck et al., 1995) and Temora-2 (417±1 Ma, Black et al., 2003; Black et al., 2004) and a multi-grain zircon separate from sample A382, Voinsalmi hypersthene granite, Finland, that has an average age of 1877±2 Ma by ID-TIMS U–Pb (Andersen et al., 2009). 87 LAM-ICPMS ablations on 91500 calibrated against Temora-2 gave an average age of 1059 ± 4 Ma. The long-term (> 2 years) precision is <1 % for $^{206}Pb/^{238}U$ and $^{207}Pb/^{206}Pb$ (2 standard deviations). IsoplotEx 3 (Ludwig, 2003) was used to plot concordia diagrams. The accuracy and the precision of the Lu-Hf measurements were validated with three standards. At the time the analyses were made the $^{176}Hf/^{177}Hf$ isotopic ratio of the measured standards gave 0.282824 ± 0.000080 (2σ) (LV11 $^{176}Hf/^{177}Hf$ solution = 0.282837 ± 0.000028; Heinonen et al., 2010), 0.282679 ± 0.000051 (2σ) (Temora 2 $^{176}Hf/^{177}Hf$ solution = 0.282686 ±

0.00008; Woodhead and Hergt, 2005) and 0.282510 ± 0.000043 (2σ) (Mud Tank $^{176}Hf/^{177}Hf$ solution = 0.282507± 0.00006, Woodhead and Hergt, 2005).

RESULTS

Field observation

OVERVIEW OF THE VARIOUS HYDROTHERMAL ROCKS

The southern and central MPI consists of rocks that are interpreted as products of extensive, post-deformational hydrothermal alteration (Bons and Roessiger, 2008; Chapter 2 of this PhD thesis). Deformed host rocks grade into massive lithologies and breccias (Radium Ridge Breccias; Drexel and Major, 1987) that mainly consist of cm-sized K-feldspar and quartz, while mafic minerals disappear. The K-feldspar alteration affected basement and cover rocks (Coats and Blissett, 1971; Drexel and Major, 1987) over an area of ~60 km² (Fig.2). Alteration is concentrated in the core of the major Yankaninna Anticline and close to the Paralana Fault Zone. The original structures and mineralogical composition have been obliterated in the most altered lithologies; the breakdown of biotite is the most notable result. Metasomatic rocks consist of massive pink K-feldspar and quartz with a texture and mineralogy that macroscopically resemble those of granitoids (Fig.3). They are, however, distinct from real granitoid rocks due to the lack of any mafic mineral and the missing intrusive contacts to the host rocks. Pegmatites of the ~460-440 Ma BEG magmatism and the diopside-titanite veins (Bakker and Elburg, 2006) intrude into K-feldspar metasomatites, but are also affected by the K-feldspar alteration. The contemporaneous BEG, however, has no exposed hydrothermal aureole. Observations at the present erosional level indicate no spatial relationship between alteration effects and Palaeozoic magmatism.

Several types of hydrothermal breccias developed in the southern and central MPI that show overprinting relationships. Chlorite-quartz cemented breccias are included as clasts in the K-feldspar and quartz breccias to the east of Hidden Valley (Fig.4A). Another weathered, dark-brown, chloritic iron-hydroxide breccia is associated with, but pre-dates, massive, black magnetite/hematite ±quartz cemented breccias (Fig.4B). The latter formed as cm-sized veins and as discrete, gently-dipping lenses, of which some are several hundred meters long. These iron oxide, U, REE and Cu ores (~355 Ma; Elburg et al., 2013) include angular to well-rounded clasts of K-feldspar altered rocks and only formed in the central K-feldspar alteration zone north of Mt. Painter (Fig.2). Magnetite/hematite ± quartz veins developed in all basement and lower Adelaidean lithologies and are probably associated with the iron-oxide ores (Lang, 2012; Fig.2). The earliest mineralisation stage in these veins and breccias include chalcopyrite and pyrite grains in martitised magnetites (Lang, 2012). The copper-

sulphide is probably the source for small secondary copper deposits in the lower Adelaidean sediments (Coats and Blissett, 1971).

Steep ridges of quartz-cemented breccia, associated with silicification of the older lithologies, post-date the magnetite/hematite-cemented breccias. They can be found in discrete steep zones in N-S, NE-SW and E-W directions along the Paralana Fault Zone, in the southern MPI and the lower Adelaidean sequence (Fig.2). The quartz-cemented breccias include sub-rounded clasts of all previously formed breccias (Fig.4C), but are cross-cut and overprinted by the distinct Permian to Triassic, sub-surface quartz-hematite Mt. Gee sinter breccia (Fig.4D; Brugger et al., 2011, Weisheit et al., 2013b). Some of the silicified breccias may be contemporaneous with the quartz-hematite sinter and represent "feeding dykes" to the Mt. Gee sinter. The centre of the sinter formation is at Mt. Painter proper, but open veins with characteristic nailhole quartz rosettes (Fig.4E) and platy calcite can be found in the western MPI and at Paralana Hot Springs (Fig.2).

The last generation of breccias are situated dominantly at fault zones and axial fold planes around the inlier. These breccias overprint all previous ones, but a relationship to the quartz-hematite Mt. Gee sinter breccia is missing. The largest breccia of this generation is the 10 km² sized breccia in Hidden Valley at the Paralana Fault Zone in the central MPI. Similar ~100 m² sized breccias occur at The Needles and The Pinnacles in the lower Adelaidean strata in the south of the MPI (Fig.1B). These breccias record thorough mixing of Adelaidean and basement lithologies from the 100 m down to the mm-scale; only little cement of talc, biotite, chlorite and clays formed (Weisheit et al., 2013a). Weisheit et al. (2013a) interpret the Hidden Valley-type breccias to have formed during the formation and exhumation of the anticline and contemporaneous focusing of hydrothermal fluids that arrive from previous alteration and brecciation events. Calculations of the amount of fluid required to form the Hidden Valley breccia result in ~30 km³ (Weisheit et al., 2013a). Possible sources for these fluids are connate water that is released during exhumation, magmatic water of the Ordovician intrusions and mineral-bound water that is released during the breakdown of biotite in K-feldspar altered areas (Weisheit et al., 2013a).

K-FELDSPAR ALTERATION

The K-feldspar alteration in the MPI can be subdivided in three end-member types of occurrences (Fig.2). Zones of host rocks in which the pre-existing textures and structures are still recognisable and which contain undeformed newly grown K-feldspar blasts are said to have undergone *K-feldspar overprinting*. With increasing K-feldspar blastesis and recrystallisation of quartz the pre-existing texture and structure are completely overprinted. These rocks are called *K-feldspar metasomatites*. *K-feldspar and quartz cemented breccias* are the third rock type that are related to the K-feldspar metasomatism (correspond to the Radium Ridge Breccias of Drexel and Major, 1987). These breccias may include components of K-feldspar metasomatites and K-feldspar overprinted

rocks. The three end-member rock types of K-feldspar alteration show a consistent spatial relationship to each other. Usually transitions of less altered lithologies into metasomatites, and then into brecciated rocks occur, while the K-feldspar overprinting generally bounds zones of metasomatites and breccias (Fig.2). Also cm-sized *veins* and *joints* with varying amounts of K-feldspar, quartz, hematite, magnetite and tourmaline are distributed throughout the whole southern and central MPI and in the lower Adelaidean sequence. Restricted zones of K-feldspar alteration occur along these veins; hence they are interpreted to be related to the K-feldspar metasomatism.

K-feldspar metasomatism is most pronounced in the centre of the southern MPI (Fig.2). These areas consist predominantly of metapelitic schists, paragneisses and orthogneisses, which are rich in micas, medium-grained feldspar and quartz. Areas that are predominantly quartzitic e.g. south of Yudnamutana and west of the BEG show little to no K-feldspar blastesis (Fig.2). More restricted zones of K-feldspar alteration can be found along the southern unconformity in basement and cover, close to The Pinnacles, The Needles and the copper occurrences west of the basement.

K-feldspar overprinting is expressed by the growth of cm-sized pink K-feldspar and smaller milky quartz blasts that are usually concentrated along pre-existing foliation planes. The amount of mafic silicate minerals (biotite, amphibole, pyroxene) decreases during the alteration process, while small disseminated hematite or magnetite crystals are abundant in K-feldspar altered rocks (Fig.3A+B). Structures in the host rocks that derive from mineral shape preferred orientations and elongated minerals disappear successively. The overprinting may develop to a stage that no visual indication of the host rock remains in the massive K-feldspar and quartz metasomatites. Usually the alteration can be observed as a gradual change in mineralogy and texture of the host rock (Fig.3A+C), but discrete metasomatic fronts also develop (Fig.3D). The new K-feldspar and quartz blasts in the metasomatites show complex intergrowths without equilibration textures (see Fig.5G+I). These rocks grade sometimes into pegmatitic textures with graphic intergrowths of new K-feldspar and quartz (Fig.3E). Real, undeformed pegmatites (consisting of graphic quartz, feldspar and patchy muscovite clusters) display a gradual change to K-feldspar altered rocks at some outcrops (Fig.3F). These pegmatites are also cross-cut by K-feldspar-quartz veins, which are probably related to the K-feldspar metasomatism (Fig.3G). However, most of the undeformed pegmatites that are located to the north-west of Mt. Painter (Fig.2) are not associated with the K-feldspar alteration. They probably intruded independently prior or during the alteration event, maybe as apophyses of the BEG (Elburg et al., 2013).

K-feldspar- and quartz-cemented breccias (Radium Ridge Breccias) usually occur in narrow zones within K-feldspar metasomatites (Fig.4F), but they affected several square kilometres in the area between Mt. Painter and Paralana Hot Springs (Fig.2). Irregular K-feldspar and quartz crystals build the cement of the breccias with an appreciable amount of euhedral to anhedral magnetite and hematite.

The clasts derive from local rocks and may include K-feldspar metasomatites and overprinted rocks (Fig.4G). Most clasts are completely altered by the K-feldspar metasomatism in the central zones of the K-feldspar brecciation.

Mineralised veins and joints with quartz, ±K-feldspar, ±hematite, ±magnetite and ±tourmaline formed pervasively in the southern and central MPI during the K-feldspar alteration. They occur in all types of basement and cover host rocks. These veins are in quartzitic rocks often the only hint that the quartzites were affected by the K-feldspar metasomatism. Usually they cause a limited impregnation halo of K-feldspar and quartz in their host rocks (Fig.3D; Fig.3G+H). A K-feldspar alteration halo is not observed when the veins cross-cut already altered zones (Fig.3I). The orientation of measured veins is highly variable, ranging from gently to steeply dipping with strike directions from E-W to N-S (Fig.4H). Joints with K-feldspar, quartz and hematite mineralisation in the southern MPI can be grouped in two sets with almost perpendicular slickensides gently dipping to the SE and steeply to the NW. The statistics are, however, poor (Fig.4H). This variation indicates that joint and vein formation occurred during different local tectonic stress directions from ~E-W to ~N-S, probably over a longer period of time. The joints in the eastern MPI at Paralana Hot Springs opened during local NW-SE compression and most veins record N-S compression (Fig.4I).

Petrography of K-feldspar altered rocks

The K-feldspar metasomatites and breccias are in thin section characterised by the following textures. 1) Complete replacement of plagioclase by microcline and the growth of albite rims on pre-existing K-feldspars. 2) Several stages of blastesis of microcline and albite. 3) Breakdown of biotite (and other mafic minerals) to form microcline, muscovite or chlorite together with iron-oxides and 4) replacement of muscovite by K-feldspar and vice versa. The reactions are interpreted to have occurred contemporaneously as well as consecutively.

(1) The replacement of plagioclase by K-feldspar may be recognised in thin sections predominantly by the absence of plagioclase in altered rocks compared to the host rock. Virtually no transition stage can be found in thin section. Albitisation affected the area locally in the Proterozoic prior to the K-feldspar metasomatism (Elburg et al., 2001). Hence albite crystals cannot unambiguously be related to the new, replacement generation, unless they are intergrown with K-feldspars or overgrow them (Fig.5A). Sodium, calcium and aluminium ions may be released into the fluid during the replacement of plagioclase by K-feldspar, while potassium and silica are consumed. The formation of myrmekite textures in altered rocks is a result of the calcium mobility in the fluid (Fig.5B).

(2) The growth of microcline (and to a lesser extent of albite) occurs in various ways. Most often, microcline grows around pre-existing feldspar as rims with irregular grain boundaries (Fig.5A;

Fig.5C+D). The new-grown microcline often contains inclusions of the surrounding minerals or relicts of altered micas. Different growth-rate of blasts, as well as several stages of blastesis may result in complex overgrowths of microcline grains in a single sample (Fig.5E). Other nucleation points for the growth of hydrothermal microcline are grain boundaries between feldspar, quartz and biotite. Feldspar is replaced by microcline during the reaction. The original, often heavily deformed quartz crystals recrystallise at these growth-zones, resulting in locally annealed microstructures and in a highly irregular, lobate contact between the new-grown microcline and the quartz (Fig.5F+G). The biotites are often not affected during this type of growth. The resulting rock is rich in microcline, but still contains its original biotites. Further blastesis of the microcline results in rounded inclusions of quartz. Another common nucleus for the growth of microcline is biotite that is replaced by microcline and iron oxide (see below). Only the breakdown of biotite due to chloritisation is independent from the microclinisation (Fig.5H). Most K-feldspar altered rocks consist of microcline and quartz with relicts of mica (Fig.5I).

(3) The breakdown of biotite occurs in several reactions that are related to the K-feldspar alteration:

a) $KFe_3AlSi_3O_{10}(OH)_2$ (bt) + $0.5O_2 \rightarrow KAlSi_3O_8$ (mc) + Fe_3O_4 (mag) + H_2O (1)

The new-grown microcline may replace the biotite pseudomorphically (Fig.6A+B), but subhedral growth is also common. Blastesis of the microcline results in a total overgrowth and often replacement of biotite with the loss of the sample's foliation (Fig.5I). Iron oxides generally form micro-crystalline aggregates parallel to the cleavage of the biotite (Fig.6A), or occur as subhedral grains of magnetite that overgrow the host biotite (Fig.6B).

Another replacement reaction is the breakdown of biotite to muscovite:

b) 3 $KFe_3AlSi_3O_{10}(OH)_2$ (bt) + 20 $H^+ \rightarrow$

$KAl_2AlSi_3O_{10}(OH)_2$ (ms) + 9 Fe^{2+} + 6 H_4SiO_4 + 2 K^+ (2)

Muscovite often grows pseudomorphically during this reaction (Fig.6C+D) or replaces the biotite as irregular patches that then lose their preferred orientation. Muscovitisation often ends in a total replacement and overgrowth of the original biotite, which is always related to the growth of microcline (Fig.6E).

c) Chloritisation may occur for instance as follows:

3 $K(Fe,Mg)_3AlSi_3O_{10}(OH)_2$ (bt) + 2 $H^+ \rightarrow$

$(Fe,Mg,Al)_6(Si,Al)_4O_{10}(OH)_8$ (chl) + 3 K^+ + Mg^{2+} + Fe_3O_4 (mag) + 7 SiO_2 (qtz) + 3 e^- (3)

The chloritisation of biotite is a late stage hydrothermal alteration. It often occurs in the K-feldspar altered rocks, but is also observed in rocks that have not been affected by K-feldspar alteration. Biotite is generally totally replaced during chloritisation, often associated with the growth of anhedral iron-oxides (Fig.6F). Veins of chlorite can be found in all basement rocks and associated with magnetite/hematite-cemented breccias (U-REE-Cu ores), which are usually enveloped by chlorite-goethite cemented breccias.

A combination of different biotite-breakdown reactions can often be found in the thin sections (Fig.6G), indicating complex temporal and spatial dependencies during the alteration. The reactions are independent of the stage of alteration. Biotite breakdown occurs in K-feldspar overprinted rocks, in K-feldspar metasomatite and in K-feldspar breccia zones.

(4) Iron, magnesium, potassium, silica ions and water are released during the breakdown of biotite. The mobile silica and potassium ions can enhance the replacement of muscovite by K-feldspar (Fig.6E). This reaction occurs the other way around (sericitisation) during low grade metasomatism / weathering, resulting in the formation of microlithic inclusions of muscovite along the cleavages of the weathered K-feldspar (Fig.6H):

$$(K,Na)Al_2AlSi_3O_{10}(OH)_2\,(ms) + 6\ SiO_2\ (qtz) + 2\ K^+ \leftrightarrow$$

$$3\ (K,Na)AlSi_3O_8\ (kfs) + 2\ H^+ \qquad (4)$$

The observed alteration generally start with the growth of euhedral muscovite that replaces biotite along the pre-existing foliation (Fig.6C+D). Patchy aggregates of euhedral, randomly oriented muscovite can overgrow the previous texture (Fig.6E, lower right corner; Fig.6G). The muscovite crystals react with quartz to K-feldspar with ongoing alteration (Fig.6E).

The iron that is released during the breakdown of biotite is typically immobile (see above). It also becomes incorporated into the lattice of new-grown microcline resulting in the distinct pinkish-red colour of the altered metasomatites. Iron may be, however, transported in chlorine-complexes in aqueous fluids:

$$2FeCl_2 + 3H_2O \leftrightarrow Fe_2O_3 + 4\ HCl + 2H^+ + 2e^- \qquad (5a)$$

$$3FeCl_2 + 4H_2O \leftrightarrow Fe_3O_4 + 6\ HCl + 2H^+ + 2e^- \qquad (5b)$$

Magnesium minerals that may have formed from the released magnesium during biotite-breakdown are generally not present in the K-feldspar alteration zones. This element is probably transported with the fluid. Randomly oriented actinolite, scapolite, tremolite and epidote formed in the lower Adelaidean, presumably with the aid of the mobilised magnesium and the released calcium from

the breakdown of plagioclase crystals. However, magnesium and calcium are also present in the Adelaidean units and may derive partly from the original limestones, dolomites and basalts.

Completely K-feldspar altered rocks consist of up to 90 % microcline, some albite and quartz (e.g. Fig.3C+I). Mafic minerals, especially biotites are totally altered and their products overgrow pre-existing textures (Fig.6I). The microcline crystals often show multiple overgrowths, include other minerals and sometimes have a skeleton shape in the most altered rocks (Fig.7A+B). Anatase/rutile often grows in close proximity to altered biotites. The colour of the remaining biotite crystals becomes distinctively green in the case of restricted alteration. This indicates a decrease in titanium, which becomes incorporated in anatase/rutile (Fig.6D). The newly grown muscovite, chlorite and iron-oxide are often concentrated in irregular patches in the rock, resulting in the total loss of pre-existing structures (Fig.6G). Although muscovite is formed during a first stage of alteration, it breaks down to K-feldspar during later stages (Fig.6I; Fig.7C). Only accessory minerals like zircon, apatite and monazite appear unaffected by the K-feldspar alteration reactions and remain in the metasomatites and breccias (Fig.7C-E).

The breccias that formed during the K-feldspar metasomatism are cemented by anhedral K-feldspar, ±quartz and ±iron-oxide. Mosaic breccias form at the first stage of brecciation (Fig.7F) that develop into chaotic breccias with clast-in-clast textures. Clasts derive from the local host rock and are often angular (Fig.7G). The host rocks and the breccias continue to be metasomatised during the brecciation process, provided that they are not yet completely altered. Tourmaline formed during the K-feldspar metasomatism, pre-dates (Fig.7H) and post-dates the K-feldspar brecciation. A similar contemporaneous relationship can be found between the K-feldspar cemented and the hematite-cemented breccia (the U-REE-Cu ore). The latter often overprints the former (Fig.7I), but a reverse overprint is occasionally visible in thin section (Fig.7D+E).

Summary of thin section and field observation

The presented thin section and field observation indicate a general sequence of overprints that is related to the K-feldspar alteration in the MPI. The breakdown of biotite in basement rocks results in the growth of microcline, muscovite, magnetite and chlorite (at a late stage) *in situ* (Fig.6). Alkalis, iron and magnesium become successively enriched in the fluid during these reactions. This evolved fluid probably enhanced the alkali feldspar metasomatism of all feldspars and the growth of large microcline grains that overgrow the pre-existing texture (Fig.5). The growth of microcline along grain boundaries of quartz, K-feldspar and mica did not affect the remaining biotite. Silica was mobile during the growth of microcline, which resulted in a recrystallisation of quartz.

The biotite-breakdown reactions and the alteration of plagioclase resulted in the enrichment of the fluid in silica, calcium, magnesium, iron, titanium and trace elements such as barium, manganese

and copper. These elements are included in mineralised veins and new-grown, randomly oriented minerals of quartz, iron oxide, phlogopite, actinolite, tremolite, scapolite and epidote in basement and cover. Tourmaline probably mineralised from late-stage fluids. Iron/titanium oxide and hydrothermal phlogopite (Elburg et al., 2013) are occasionally overprinted by K-feldspars and form clasts in K-feldspar breccias (Fig.7H), while tourmaline minerals also overprint K-feldspar cemented breccias.

Veins of pegmatitic diopside and titanite that formed in already K-feldspar altered basement from a melt-like fluid (Bakker and Elburg, 2006) contain inclusions of K-feldspar altered rocks and are overgrown by metasomatic microclines. It remains, however, unclear whether there is a relationship between the (magmatic) diopside-titanite veins and the (hydrothermal) K-feldspar alteration.

Chloritisation and veins of chlorite are probably a late stage of the alteration system (Fig.6F; Fig.7A). Chlorite-rich breccias are often included as clasts in sheets of magnetite/hematite breccia ores. The iron-ores contain barite, pyrite and REE-minerals (Elburg et al., 2013) and also include clasts of K-feldspar metasomatites and -breccias. Late K-feldspar brecciation, however, also post-dates the iron-ore breccias (Fig.7D+E). Martitisation, mushketovitisation and the formation of new hematite in the iron-oxide-REE-U ores indicate that the system crossed the magnetite/hematite buffer several times (Rehder, 2010; Elburg et al., 2013).

Electron microprobe analyses (EMPA)

Feldspar (605 measurement points) and mica (187 points) were measured in nine samples of K-feldspar altered rocks and host rocks that derive from the entire alteration zone (Fig.2). Where possible, transition from host rock to altered rock (WD5b; YG17a-d; 10N17b-f; 091e; 10SP33c; ML148a), as well as K-feldspar-alteration veins (SP36b; SP8) and breccias were analysed (10HV1b; 10HV6a; Tab.2).

FELDSPAR

The metasomatic microcline in K-feldspar overprinted rocks is of an almost end-member composition ($An_0Ab_{2-3}Or_{97-98}$). It can often be found at the contact between quartz and original alkali feldspar (Fig.8A). An almost end-member albite ($An_{0.5-2}Ab_{97.5-98.3}Or_{0.6-0.8}$) is often intergrown in patches and veins with this microcline (Fig.8B). The equilibration temperature of this stable coexistence is ~250 °C (McDowell, 1986). New-grown microcline and albite often have a weak porosity with small inclusions of iron-oxide that causes their distinct macroscopic pinkish colour (Fig.8B). Altered original feldspar that is replaced and affected by hydrothermal microcline or albite is on the contrary characterised by a pervasive porosity and irregular grain boundaries (Fig.8C+D). The original alkali feldspar and plagioclase from the unaltered host rock may be found as irregular inclusions within new-grown metasomatic feldspar (Fig.8E).

Albite that replaces and overgrows pre-existing feldspar and pre-dates the growth of microcline (Fig.8C+F) may be a relic of albitisation during the Proterozoic (Elburg et al., 2001).

Intermediate compositions of Na-rich plagioclase ($An_{11-12}Ab_{87-88}Or_1$) and almost end-member K-feldspar ($An_0Ab_{3-8}Or_{91-96}$) occur as pegmatitic new-growth in the centre of K-feldspar metasomatism (YG17d), as well as in K-feldspar overprinted rocks (YG17a+c; 10N17f; ML248a) and breccias (10HV6a). These compositions are distinct from the pure end-members of microcline and albite, but equilibrated during temperature conditions also of ~200-300 °C (Fig.9A; e.g. Stormer, 1975; Whitney and Stormer, 1977).

Fig.9B-D illustrates an example of a microcline-quartz vein that causes the growth of new K-feldspar in the metapelitic host rock (RCG) in sample SP36b. Detailed measurements of the feldspars along a profile through the vein don't result in significant trends and geochemical differences. The K-feldspars in the centre of the vein, at its rim and in the host rock are almost end-member orthoclases (Fig.9C). Only the BaO concentration in centre and rim feldspars is slightly elevated (mean: 0.09 ± 0.009 a%) compared to the feldspars in the RCG (mean: 0.07 ± 0.007 a%; Fig.9D). The differences in the geochemical composition are, however, not significant and vary from sample to sample. Fig.10A for instance shows that the BaO content in pegmatitic microcline (0-0.05 a%) is in general lower than the BaO content of ~0.1 a% in alkali feldspar in the original host rock. The mean BaO content of new-grown microcline and altered feldspar varies from 0-0.13 a%. There is no correlation between BaO and K_2O in the measured samples and a significant metasomatic enrichment or depletion is missing.

The same holds for the FeO content that shows no systematic difference between altered and non-altered feldspar and ranges between 0-0.15 a% (Fig.10B). This indicates that the iron does not substitute for Si or Al in the samples (Nakano et al., 2005), but is included as disseminated iron-oxide in the porous feldspar.

A local trend to more pure end-member composition of albite and microcline is visible only in a few sample profiles through host rock and alteration product (e.g. at location YG17 in Fig.10C+D). The absence of clear alteration trends in all measured oxides indicates disequilibrium conditions and probable multiple overprints.

MICA

The mica in the analysed thin sections can be grouped into *original* (not altered), *original* that are *altered* (Fig.11A) and into *metasomatically* new-grown *biotite* and *muscovite* (Fig.11B). The focus of this study was to define the general composition of the parent and the product mineral during the breakdown reactions of the biotite (see above). Samples that show intermediate stages of alteration were preferably used for EMPA measurements (Fig.11C).

Most of the measured biotite crystals, which are grouped as altered or not-altered, are solid solutions of a phlogopitic composition with a minor annite-component, with respect to their magnesium and iron content (Fig.12A). These "phlogopite" grains have a high Al_2O_3 content that may indicate that these minerals derive from a pseudomorphic alteration of a biotite that lost its iron. The missing trends between "original", "altered" and "new-grown hydrothermal" grains can be explained by such pseudomorphic alteration, which could be observed with an optical microscope at biotites that are pseudomorphically replaced by muscovite (Fig.6C+D). Additionally the analyses may represent a mixed signal from chloritisation of the biotites. Various host rocks and probable multiple overprinting cause also a scatter in the geochemical signal (Fig.12B).

The sampling profile YG17 from original orthogneisses into K-feldspar altered rocks shows only one trend of muscovitisation of "original" phlogopitic biotite with a slight decrease in TiO_2 (Fig.11C; Fig.12C-E). This confirms the results of the thin section analyses that muscovite and green, Ti-poor biotite dominate the altered samples.

Whole rock analyses

A total of 35 samples of original host rocks and alteration products were measured with the XRF method in Tübingen (Germany) and another 8 samples with the ICP-OES method in Ghent (Belgium). Host rocks originate from the entire MPI and include Proterozoic biotite-rich turbiditic gneiss and quartzite of the RCG, A-type granite gneiss and granodiorites (Tab.1; Tab.3+4). These rocks are rich in feldspar, quartz, mica and include accessory minerals like iron-oxide, zircon, monazite and rutile/anatase. Undeformed samples were taken preferably for the analyses. Alteration products were sampled throughout the southern and central MPI and include K-feldspar overprinted rocks, K-feldspar metasomatites and K-feldspar breccias. These rocks consist essentially of the same mineral paragenesis as their protoliths, but the modal percentage of K-feldspar, quartz and iron-oxide increases. Transitions from the original host rock to the K-feldspar altered product were sampled in profiles at seven localities and analysed for their whole rock element concentrations (091a,c-f; 10N17e-g; BC338+BC339, BC341-BC343; 344+348; JH50+51; ML174+175; YG17a-c; Fig.2). After detailed thin section analyses only 11 samples could be grouped as unaltered host rocks, while 28 samples are interpreted as variably K-feldspar altered rocks (Tab.1). Three samples of K-feldspar breccia were measured (091a+c; 10HV1b).

CORRELATION OF ELEMENTS

The correlation of elements was analysed using a correlation matrix of 41 selected samples of alteration products and host rocks (Tab.5). Various Harker variation diagrams of host rocks and different K-feldspar altered rocks show ranges of geochemical compositions that widely overlap (Fig.13). A significant geochemical difference between granitic and meta-turbiditic protolith rocks and

their alteration products is not visible in the data. Outliers in the Harker diagrams are usually the measured K-feldspar breccias, which are overprinted by the iron-oxide cemented breccia.

Only MgO shows obvious depletion in most of the altered samples (Fig.13). Magnesium is incorporated in the mica of the host rock. The mica grains lose their iron at a first stage of alteration; therefore a phlogopitic composition dominates in the samples (see EMPA). Most K-feldspar altered rocks lost all mica and other mafic minerals and are hence depleted in MgO.

The absence of other clear alteration trends in the whole rock analyses could be a result of misinterpretation of original and altered sample. Therefore the measured granitoid host rocks are compared with whole rock composition data taken from the literature (Fig.14; Neumann, 2001; Wülser, 2009; Elburg et al., 2013). The host rocks are already characterised by a wide range of compositions, including K_2O-rich lithologies (Fig.14). However, K-feldspar altered rocks may have been mistaken for original granitoids.

An overlapping range of the whole rock composition of host rocks and alteration products is still pronounced in plots that are more specific to K-feldspar alteration (Fig.15+16). A negative correlation between Na_2O and K_2O is most obvious, which is independent from host rocks or alteration products. This signal may be related to microclinisation and sodium mobility, which was variable in space and time. A positive correlation between K_2O, Ba and Rb indicate that the trace elements are substituted for K in the K-feldspar (Fig.15+16). Also Sr has a positive correlation with Ba and K (Fig.16), while a correlation with CaO is missing. Usually Sr is substituted for Ca in plagioclase, but may, to a lesser extent, also be substituted for K in K-feldspar (Cherniak and Watson, 1992). The Sr-signal is hence related to the modal feldspar content. Fig.16 shows that the Sr vs. Ba signal of host rocks and alteration products overlap, indicating gains and losses during potassium and sodium alteration that interfere with each other.

The components MnO, Ni and Co are close to the detection limit. Additionally Ni and Cr are often artificially enriched in the samples due to the sample preparation with a stainless steel crusher. MnO, Ni, Cr and Co are hence excluded from the interpretation. LREE, Zr and Y show a strong positive correlation, i.e. they behave similar during the alteration process. The major oxides CaO and MgO as well as the metal V have in contrast no to little correlation with any element. This indicates that the REE were immobile while the others were transported, possibly during several alteration processes.

Another positive correlation exists between TiO_2, Fe_2O_3, Zr and Nd. Titanium and iron are incorporated in biotite, iron-titanium-oxide and titanite. Fig.16 shows that host rocks and alteration products form a scatter. This is a result of iron-(titanium)-oxides (and titanite) formation at the expense of biotite. Titanium and zirconium behave similar and are incorporated in titanite, while only

titanium fits in the biotite lattice. A correlation between iron and zirconium suggest that both elements were mobile during the same process and became incorporated in separate phases like iron-(titanium)-oxides and zircon. Neodymium and zirconium show a weak positive correlation and may be concentrated in minerals like feldspar and biotite, which are known to be affected by the alteration process. The correlation between zirconium and titanium results from a substitution for iron in the iron-oxides.

A separate analysis of certain transitions from host rocks into K-feldspar altered rocks on an outcrop scale (10N17; YG17; 091; BC338-343; 344+348) also results in overlapping signals (Fig.17). Either constant values, scatter or opposite trends in the element composition characterise the successive alteration stages. This result reflects the observations in the thin sections that indicate multiple and wide-spread alteration, even in samples which are grouped as “unaltered”.

ISOCON DIAGRAMS

Hydrothermal alteration is generally a process of gains and losses of geochemical components in the metasomatic rock to the host rock. The isocon method is used to calculate the mass-balances of the alteration process (Gresens, 1967; Grant, 1986; Baumgartner and Olsen, 1995; Grant, 2005). Element and oxide concentrations in the product rock C^A are plotted against those in the protolith C^0. The slope of the isocon, which is a straight line through the origin and immobile elements indicates an increase (slope <1) or a loss (slope >1) in the total mass during the metasomatism. An 1:1 isocon line represents an alteration without a mass change (Grant, 1986). Data points that plot above the isocon have been enriched, while elements and oxides below the isocon are depleted during alteration (Gresens, 1967).

Isocon plots of single transition outcrops show various results. Fig.18A shows a plot of the geochemical components of an albitised orthogneiss host rock 10N17g against an average alteration product from 10N17f+e. There is only a slight increase in the Zr and Na_2O concentration, while BaO and REE are depleted. Noticeable is that Al_2O_3, K_2O and SiO_2 plot on the 1:1 isocon. Petrographic analyses clearly show the new-growth of microcline (e.g. Fig. 8B+F) and the breakdown of micas in these samples. The whole rock data hence illustrate either an internal re-distribution of elements or the effect of multiple alteration stages (albitisation, microclinisation, biotite-breakdown, iron-titanium-oxide formation).

The elements MgO, TiO, CaO, Rb and Zr are depleted at the altered paragneiss outcrop 091, while K_2O and Ba are enriched (Fig.18B). Potassium metasomatism at this locality is accompanied with the enrichment of REE, while plagioclase (CaO) and micas (MgO) break down. Na_2O, Al_2O_3 and SiO_2 plot along the 1:1 isocon.

The profile through the altered orthogneiss locality YG17 (Fig.18C) shows a Na_2O and CaO depletion, while MgO, Rb and K_2O are enriched. The high statistical scatter of the other elements around the 1:1 isocon indicates also multiple overprinting episodes at this locality. The same holds for the orthogneiss samples BC338+339 vs. BC341+343 (Fig.18D). The high degree of scatter in all measured elements can be explained by spatial differences of multiple overprinting stages.

The effect of microclinisation (K_2O and Rb) and plagioclase-breakdown (Na_2O and CaO) is well documented in the orthogneiss samples 344 and 348 (Fig.18E). Thin section analyses of these samples show clearly the breakdown of micas and the growth of iron-oxides. An enrichment of Fe_2O_3 is, however, not documented using an 1:1 isocon line, while it is obvious with an isocon line through the zircon signal, assuming that this element is not mobile (see zircon U-Pb and Lu-Hf analyses).

Generally the major elements SiO_2 and Al_2O_3 plot at or close to the 1:1 isocon (Fig.18). Both elements could therefore be considered as almost immobile and only re-distributed within the host rock during all alteration stages.

STATISTICAL ANALYSES

Geostatistical analysis is used for whole rock datasets of protoliths and alteration products that lack in clear geochemical tends (Le Maitre, 1982). Similar samples or similar (alteration) processes, reactions or mineral groups may be better visualised with the aid of correlation matrix and principal component analysis. To exclude variation that arises from the 100 % normalisation of the major oxides, the geostatistical analyses are done on ratios of all oxides with Al_2O_3 or SiO_2 (Tab.5). Al_2O_3 has no correlation with any element and shows only little variability. This characteristic may be a result of a permanent mobilisation during several alteration processes. Because SiO_2 does not show any correlation to elements affected by inferred metasomatic processes, it is also suitable for use as a denominator in oxide ratios. The LOI-value, as well as P_2O_5 show also no correlation with any element and were excluded from further analyses. Apatite crystals (P_2O_5) are according to the thin section analyses unaffected by the alteration process. Also the content of volatile phases and the FeO/Fe_2O_3 ratio (LOI) is independent from the stage of alteration and the elements (Fig.16), suggesting complex overprinting and abundant fluid in the system.

With the aid of the correlation matrix the dataset can be analysed for its principle components, which represent a mathematical abstraction of similar (or different) geochemical behaviour, mineral occurrences, reactions or processes. Usually the first four components (PC_{1-4}) take more than 70 % of the cumulative variability, making them the most important ones for analyses. A plot of all variables (measured elements) in a PC_x vs. PC_y diagram may end in clusters of elements that show specific correlation. Fig.19 compares PCA results of the Al_2O_3 and the SiO_2 normalised dataset. In both cases several elements form inter-correlated clusters of K_2O+Ba+Rb+Sr+V+REE, Fe_2O_3+TiO_2, CaO±Al_2O_3,

Zr+Yb+Y+Nb and separated MgO, SiO_2 and Na_2O in a PC_1 vs. PC_2 plot (Fig.19A). The MgO signal is associated with PC_1 (variability of ~36 %), which may represent chloritisation as an overprinting, late-stage event. Na_2O and the K_2O cluster have a negative correlation in the PC_1-PC_2 space, as well as SiO_2 and $CaO+Al_2O_3$, while the Fe_2O_3 and Zr clusters show a positive correlation to the latter. The separate clusters may be interpreted as represent the process of microclinisation, biotite-breakdown and the formation of iron-titanium-minerals. These reactions and minerals are associated with PC_2 (variability of ~15 %).

The microcline-related cluster and the iron-cluster dominate a plot of PC_2 vs. PC_3 (PC_3 variability = ~13 %; Fig.19B). Microcline (K_2O+Rb+Ba) and plagioclase ($CaO+Na_2O$) have a negative correlation and are distinct from the iron-titanium ores ($Fe_2O_3+TiO_2$+Zr etc.) that correlate with chloritisation(?) (MgO) and the mobility of the REE. The latter clusters may also express the biotite-breakdown reaction, which is accompanied with the iron-mobility. Fig.19C shows that PC_4 (variability of ~10 %) is also dominated by the microcline vs. plagioclase correlation.

The statistical analyses of the whole rock dataset confirm a complex overprinting during the alteration. Single processes that are related to microcline and plagioclase, as well as chloritisation(?), iron-oxide ore / biotite breakdown can be highlighted in the PC-space. The alkali-alteration (microcline vs. plagioclase) can be determined in the first four principal components and is hence the most important process that affects the rocks during several stages of alteration.

Fluid inclusions

Ten samples of K-feldspar-altered and original rocks from various localities in the alteration zones were prepared for fluid inclusion measurements in quartz as thin sections of ~100 µm thickness (Tab.6). Fluid inclusions in the feldspar grains could not be measured, because the feldspars are not transparent in the prepared thin sections. The quartz grains in the samples were grouped for interpretation. *Original quartz* is included in the original texture of the sample and often shows undulatory extinction and deformation structures. *Recrystallised* or *new* quartz (undeformed) probably formed during K-feldspar metasomatism. It is, however, not always possible to distinguish with an optical microscope to which class a given quartz grain belongs. Those are grouped as *unknown.*

The petrographic classification of the observed fluid inclusions in the quartz grains is based on Shepherd et al. (1985) and Wilkinson (2001). All samples contain at room temperature single phase (liquid L or vapour V), two phase (L+V) and multi phase (L+V+ solid S) fluid inclusions. They occur as clusters or networks, trails and single objects, often independent of the type of the measured quartz. Solids that could be identified with microthermometry and Raman analyses in the fluid inclusions are halite, sylvine, hematite, calcite and albite. Some fluid inclusion clusters were interpreted as *primary*, while oriented trails that occur in the whole thin section and cut through several grains are grouped as

secondary. Trails that only developed within a grain are interpreted to be *pseudo-secondary*. Fluid inclusions that could not be classified are grouped as *unknown*.

The diameter of single fluid inclusions in the samples ranges up to ~25 µm. Most of the inclusions, however, have sizes <10 µm making it difficult or impossible to analyse the objects by microthermometry. Shape and the vol.% of the liquid phase were also documented during the petrographic analyses (Tab.6).

Most fluid inclusions that are grouped as primary and pseudo-secondary in original quartz crystals are trails and clusters with a liquid phase and which occasionally include a vapour phase and a salt crystal. Fluid inclusions that additionally include magnetite, hematite, calcite and other, probably trapped minerals, often occur in all quartz crystals as trails and single objects. Therefore they are interpreted as secondary.

One representative example of the analysed thin sections is sample SP2, which includes a K-feldspar-quartz ± tourmaline vein that caused microclinisation in the host biotite-rich meta-sediment, south of Mt. Painter. The muscovite and biotite close to the vein are altered to microcline and new microcline grains grow parallel to the foliation of the host rock. Muscovitisation affects the biotite in the whole thin section.

Fluid inclusions were measured in original quartz-augen in almost unaltered zones, in quartz within the microclinisation-zone and in new quartz within the vein. Secondary and pseudo-secondary trails in the original quartz cross the minerals with three different orientations. They either have rounded to elongated fluid inclusions with a liquid phase, a vapor bubble and a salt crystal, or complex angular inclusions with a liquid and several solid phases (Fig.20A-C). The latter type also occurs as single inclusions. A third type of fluid inclusion occurs in clusters or networks and the inclusions consist of a liquid phase, a vapor bubble and a salt crystal, or only of a liquid and a vapor bubble. The quartz that is surrounded by new-grown microcline in the alteration zone also contains trails, clusters and single fluid inclusions that are similar to the types in the original quartz-augen. Fluid inclusions in quartz that is intergrown with hydrothermal microcline occur as clusters with an irregular shape and contain several solid phases in a liquid (Fig.20D+E), as well as single phase and L+V inclusions (Fig.20F+G). Secondary trails with a single direction cut the quartz crystals and contain elongated L+V fluid inclusions. The young quartz in the vein that is intergrown with tourmaline contains similar L+V trails and clusters of single phase inclusions, inclusions of liquid and vapor phase or a liquid with a hematite crystal (Fig.20H). Single fluid inclusions in this quartz include a liquid with salt crystals and other solid phases (Fig.20I-L). Fluid inclusions with a liquid and a range of probably trapped solid phases occur in all types of quartz. They possibly formed during or after the K-feldspar metasomatism event.

Most liquid phases in the fluid inclusions are highly saline brines that yield a broad peak at ~3440 cm^{-1} in their Raman signal (Burke, 2001; Fig.21A). There are also samples with a H_2O dominated signal that have lower concentrations of dissolved salts in the fluid (Bakker, 2004; Baumgartner and Bakker, 2009). Pure H_2O signals with two broad peaks between 3200-3600 cm^{-1} and peaks at ~2950-2980 cm^{-1} could be measured in fluid inclusions that are comparatively small and only consist of either a single phase or of a liquid phase and a vapor bubble (Fig.21B). These pure H_2O inclusion generations are either primary in young quartz in the vein or secondary in older host rock quartz. They may hence derive from the youngest fluid. No CO_2 or other vapor signal could be identified in this sample.

The first step to quantify the salinity of the fluid inclusion using the Raman signal is to remove the background-signal of the host quartz from the total Raman signal (Baumgartner and Bakker, 2009). To minimise the influence of the orientation of fluid inclusion boundaries and the crystallography orientation of the host quartz on the signal the Raman signal of the host quartz has to be obtained during several measurements while the sample rotates 90° (Baumgartner and Bakker, 2009). This procedure was not conducted during the measurement campaign. However, the solid phases in the fluid inclusions could be identified as calcite (Fig.21C), magnetite (Fig.21D) and hematite (Fig.21E). As all of these phases may co-exist in a single fluid inclusion they are interpreted as trapped crystals that floated in the brine. Some weak Raman signals of solid phases were interpreted as apatite, monazite, rutile and albite. Some fluid inclusions were destroyed during the measurements with the focused laser beam.

Homogenisation temperature (T_h) and melting temperature (T_m) of the solid phases were measured during microthermometric analyses of the sample (Tab.6). The size of the analysed fluid inclusions in most samples ranges from 4 to 14 μm, which is generally too small for accurate measurements. Complex fluid inclusions with a brine signal in the Raman measurements and several solid phases were predominantly meta-stable: the observed vapor bubble disappeared during heating, but did not form again during cooling. Also the melting- and homogenisation temperatures varied significantly. Additionally salt crystals grew or dissolved during the measurements but never return to their original configuration at room temperature, which is another hint for meta-stable conditions (Van den Kerkhof and Hain, 2001).

The few measured melting temperatures for hydrohalite range between -32 and -23 °C, while ice melted between -21.8 and -17.3 °C. Fluid inclusions that record an almost pure H_2O-signal in the Raman spectrum melted at ~ -1 °C. The homogenisation temperatures of the vapor bubble into a liquid range in L+V±halite fluid inclusions between ~80-115 °C, while no homogenisation up to 330 °C could be observed in complex fluid inclusions with more than one solid salt-phase. The fluid inclusions were still intact at this maximum temperature.

A statistically relevant dataset could not be compiled during microthermometric measurements, because of the complex nature, the small sizes and the meta-stable condition of most fluid inclusions. Only some low-saline brines without salt crystals were calculated with the Excel VBA macros by Steele-MacInnis et al. (2010) to 0.6-1.1 wt.% NaCl equivalent and 0.2-3.9 wt.% $CaCl_2$ equivalent. One calculated fluid inclusion resulted in a high $CaCl_2$ equivalent concentration of 11 wt.%. The homogenisation temperature of fluid inclusions with hematite crystals is above 400 °C. Homogenisation of L+V+halite inclusions of all samples range between 84-316 °C, but the relative age of these fluid inclusions is not known.

Estimates of the local pressure during the formation of the fluid inclusions are usually conducted with the aid of the microthermometric data (e.g. Roedder and Bodnar, 1980; Hedenquist et al., 1998; Baker and Lang, 2003). A calculation of the pressure conditions is not possible with the restricted available data set.

Oxygen isotope ratios

Centimetre to tens of decimetre thick veins of milky quartz, K-feldspar and hematite plates cross-cut the quartzitic basement and lower Adelaidean units at Petalinka Waterfall, close to the Yudnamutana mine. The K-feldspar and hematite crystals in the veins are extraordinary large, but evidence for K-feldspar metasomatism at the rims of the veins is missing. Nevertheless due to the distinct paragenesis in these veins they are interpreted as having been formed from fluids of the K-feldspar metasomatism in the basement. Thin section analyses of similar veins in basement and cover showed martitisation and mushketovitisation of the iron-oxide crystals, which probably also affected the Petalinka Waterfall samples.

Single crystals of K-feldspar, quartz and hematite of a ~50 cm large vein were sampled in contact to each other at selected distances from the vein's wall and prepared for oxygen isotope measurements (Tab.7). The isotopic ration of $^{18}O/^{16}O$ is given in the $\delta^{18}O$-notation in permil after Craig (1961), normalised to Vienna standard mean ocean water (VSMOW). The $\delta^{18}O$ values of five quartz samples range between 11.3-11.8 ‰, while two K-feldspars yielded 7.0 and 8.6 ‰. Three hematite samples in contact to the quartz gave $\delta^{18}O$ values of 0.6, 2.6, 2.8 ‰. These low $\delta^{18}O$ values (between zero to 20 ‰) are typical for hydrothermal veins (e.g. Klein and Criss, 1988; Simon, 1990; Bons, 2001; Allan and Yardley, 2007; Baatartsogt et al., 2007).

The fractionation between two mineral phases X and Y can be calculated from experimental mineral-water fractionation curves that depend on the temperature T during crystallisation of the minerals (e.g. O´Neil and Tailor, 1967; O´Neill et al., 1969; Clayton et al, 1975; Matsuhisa et al, 1979; Zheng, 1991; Zheng, 1993):

$$\Delta_{minX-minY} = (\delta_{minX} - \delta_{water}) - (\delta_{minY} - \delta_{water}) \approx 1000 ln\alpha_{minX-water} - 1000 ln\alpha_{minY-water}$$

and

$$1000ln\alpha_{A-B} = \frac{C*10^6}{T^2} + \frac{D*10^3}{T} + E.$$

The fractionation factor α between two phases A and B is given by $\alpha_{A-B} = \frac{1000+\delta_A}{1000+\delta_B}$ (Craig, 1961). The calculated values C, D and E for quartz-water, pure K-feldspar-water and hematite-water curves were used from Zheng (1993). Analysis of the K-feldspar crystals with the EMPA method was not conducted in this sample. However, pure end-member K-feldspar dominates in measured veins of the K-feldspar metasomatism (Fig.9C). The temperature at which the mineral pair quartz-hematite and quartz-K-feldspar crystallised in the vein at Petalinka Waterfall was calculated as a function of the distance to the vein's wall.

Quartz-hematite last equilibrated therefore at 526 ±10°C with a distance of 1 cm from the wall. This temperature increases to 646 ±14 °C at 12 cm from the wall and decreases to 613 ±12°C at a distance of 24 cm from the vein's wall. The quartz-K-feldspar pairs record a much lower equilibration temperature of 299 ±33°C at 17 cm and of 138 ±15°C at 21 cm from the wall (Tab.7; Fig.22A).

This difference and chaotic signal in the equilibration temperatures may result from (1) inappropriate use of a theoretical model of Zheng (1993) for a natural system and/or (2) an open system, which is supported by the observation of martitisation and mushketovitisation as well as by several generations of feldspar in similar veins.

A second oxygen isotope study was done in a wide zone of pure quartz veins north of Arkaroola. These veins formed close to the contact between basement and cover and include zones of sheared Adelaidean sediments and basement granites. The total thickness of the vein area is 250 m and the zone dips steeply to the NW (304/68). Horizontal lineation and dextral shear bands in schistose zones, as well as foliation boudinage indicate a dextral strike slip movement after the formation of the veins, probably developed during the formation of the Yankaninna Anticline. The brecciated veins formed independent from the K-feldspar alteration after the deposition of the Adelaidean cover sediments.

Ten quartz samples were taken along a profile perpendicular to the vein's wall (Tab.7). Their $\delta^{18}O$ values vary between 7.7 and 13.7 ‰, with slight increases and decreases through the profile independent of the distance to the wall (Fig.22B). These low positive values and the irregular variations between the samples point to a hydrothermal origin (Klein and Criss, 1988; Bons, 2001; Allan and Yardley, 2007; Baatartsogt et al., 2007) and possibly multiple stages of alteration.

Rb-Sr analyses

A pegmatite-aplite with large K-feldspar, quartz, muscovite ± garnet crystals in K-feldspar altered basement east of The Needles was used for Rb-Sr analyses. The more fine-grained aplitic part at the rim of the several tens of square metres large pegmatite (WD5c) grades into a K-feldspar altered zone with large K-feldspar grains (WD5b; Fig.23A+B). The whole rock major and trace element analyses show a decrease in potassium and an increase in sodium of the aplitic WD5b relative to the pegmatitic WD5c, although WD5b was collected in an area of K-feldspar blastesis (Tab.3). The missing elevated potassium signal in WD5b could arise from not representative amounts of sample material of the pegmatite.

Restricted alkali-alteration is common around pegmatitic intrusions if post-magmatic fluids become enriched in alkalis during the magmatic-hydrothermal processes (e.g. Bowden, 1985; Webster, 1997). There is no evidence for a correlation between the pegmatite intrusion and the extensive K-feldspar alteration in the case of the MPI hydrothermal system. Pegmatites are not limited to altered zones and the K-feldspar alteration is not restricted to areas of pegmatitic intrusions. The K-feldspar alteration at locality WD5 affected the pegmatite-aplite and the metasedimentary host rock during or after the magmatic intrusion.

Muscovite and whole rock samples of the (K-feldspar altered) aplitic and the pegmatitic part of the intrusion were measured for their $^{87}Rb/^{86}Sr$ and $^{87}Sr/^{86}Sr$ isotope ratios. The calculated Rb-Sr ages of two-point isochrons of 477 ± 5 Ma (WD5b, aplite) and 480 ± 6 Ma (WD5c, pegmatite) overlap within their 2σ errors (Tab.8; Fig.23C+D). The initial $^{87}Sr/^{86}Sr$ ratios are high with 0.8982 ±0.0045 (WD5b) and 0.8740 ±0.0016 (WD5c), pointing towards a contamination with or a derivation from a basement source, whose initial $^{87}Sr/^{86}Sr$ ratio range around 0.78 at 500 Ma (Elburg et al., 2003). However, the initial $^{87}Sr/^{86}Sr$ ratios of WD5c and WD5b change significantly in the second to first decimal place at a small change in the age of 10 Myr. This is a result of the variable distribution of the $^{87}Rb/^{86}Sr$ and $^{87}Sr/^{86}Sr$ isotope ratios in the samples. The variability could be caused by the mixing of the muscovite (cooling age) and the whole rock (crystallisation age) signals. The muscovite samples would result in cooling ages around 500 Ma, if a realistic initial $^{87}Sr/^{86}Sr$ ratio of 0.72 to 0.74 is assumed, while the whole rock samples would be significantly younger (~460 Ma). These differences are an indication that the system is disturbed and that it does not totally reflect the primary crystallisation signal. A belated change in the $^{87}Sr/^{86}Sr$ signal can be caused by the mobilisation of the radiogenic ^{87}Sr into the whole rock sample during alteration processes (e.g. Trumbull, 1993). However, both two-point isochrons result in ages within the 2σ errors. Hence, a slight alteration may have then affected both samples and a weighted mean age of ~478 Ma represents the crystallisation age, which may be slightly disturbed by alteration. According to our observations of the hydrothermal

system in the MPI we prefer the interpretation that the Rb-Sr system stayed open and the samples were affected by alteration.

Zircon U-Pb analyses

217 zircons were separated from five samples that grade into K-feldspar altered rocks at two localities (Tab.9). Thin section analyses and the zirconium signal of the whole rock measurements show that zircon was not mobile during alteration. The U-Pb age signal and the Lu-Hf signature (see next section) of the zircons should hence resemble the signal of the original magmatic host rocks (Elburg et al., 2012).

A mica-rich orthogneiss of the Moolawatana Suite (Terrapinna Granite according to Coats and Blissett, 1971) grades into a K-feldspar altered rock at the locality YG17 west of Paralana Hot Springs. The K-feldspar metasomatite totally lost its original gneissic fabric and is marked by a pegmatitic quartz-K-feldspar mineral assemblage (see Fig.3E). The petrographic and microprobe analyses of several samples along this profile confirm a K-feldspar alteration (e.g. Fig.8A+E; Fig.12C-E). Also the whole rock analyses show a gain of potassium and magnesium, while calcium is lost in the most altered sample (Fig.18D).

Three samples of weakly altered (YG17b), altered orthogneiss (YG17c) and totally altered, pegmatitic K-feldspar metasomatite (YG17d) were selected for zircon separation. The $^{207}Pb/^{206}Pb$ age populations of the magmatic zircons of all three samples show similar distributions with upper intercepts between ~1565 and ~1585 Ma (Fig.24). The maximum frequency of the population lies between 1570 and 1590 Ma (Fig.25A). The fact that the pegmatitic K-feldspar – quartz rock YG17d (Fig.25A) contains a zircon population similar to that of the adjacent samples could indicate that either (1) YG17d is a competent Mesoproterozoic pegmatite associated with A-type magmatism, (2) this sample is a younger pegmatite that picked up zircons from the A-type granites, or (3) YG17d is a highly metasomatised variety of the gneissic host rock. Gradual mineralogical changes between the different samples and missing intrusive contacts that can be observed in a variety of localities independent from the A-Type magmatism point to the interpretation of No. (3).

The same type of relationship has been observed for original orthogneiss and its inferred K-feldspar altered equivalent, north of The Pinnacles at the N17 location. An A-type granite-gneiss of the Coulthard Suite grades into a red, K-feldspar rich rock with remnants of a gneissic foliation with a contact to a pegmatite (see Fig.3F). The whole rock analyses do not show a clear alteration trend at this locality (Fig.17+18B), because the host rock is rich in deformed microcline and plagioclase. New microcline grew post-deformationally in the altered samples (e.g. Fig.8B+E) and biotite broke down to muscovite or microcline and iron-oxide. Both samples have similar zircon populations (Fig.24+25B). The upper intercepts are at ~1580 Ma (Fig.24), while the maximum frequency lies between 1560 and

1580 Ma (Fig.25B). This again is an indication that zircons are not affected by the K-feldspar alteration.

Hf isotope analyses

The analyses of the Lu-Hf isotopic composition were obtained from selected grains that were previously analysed for their U-Pb age (see previous section; Tab.10). Each signal of zircons of altered and original samples in a $^{176}Hf/^{177}Hf$ isotope ratio vs. $^{206}Pb/^{207}Pb$ age diagram falls within the spread of all measured samples (Fig.26). The zircons are hence unaffected during the K-feldspar alteration. The results in the Hf-age analyses of the measured samples are similar to other Mesoproterozoic granitoids in the MPI (Elburg et al., 2012). The large spread in the Hf isotopic composition without a polymodal distribution is typical for the granitoids (Elburg et al., 2012).

DISCUSSION

The presented results of different petrological, geochemical and geochronological analyses of various rock types in basement and cover of the MPI indicate that extensive K-feldspar-quartz-rich rocks and various breccias are a result of pervasive alteration processes. K-feldspar-quartz rocks dominate in the alteration zone, but a range of other breccias and mineralisations are known from detailed mapping and microscopic analyses. In the following we will discuss the presented data and give a possible model for a complex hydrothermal system in the Mount Painter Province.

Microscopic evidences

The K-feldspar-quartz-rich rocks are dominated by near-end member microcline that is intergrown with near-end member albite. These minerals overgrow successively original parageneses and textures from the rim into the centre of an alteration zone, where unoriented, recrystallised quartz and feldspar dominate. Almost pure end-member compositions of feldspar are recognised in several geological environments and interpreted as typical hydrothermally new-grown or replaced feldspars (e.g. Hay et al., 1988; Duffin, 1989; Hardy, 1989; Lee and Parsons, 1997; Harlov et al., 1998; Holness, 2003). K-feldspar that replaces plagioclase is often highly porous and includes sub-microscopic grains of iron-oxides, which is also characteristic for hydrothermal feldspars (Worden et al., 1990; Walker et al., 1995; Putnis et al., 2007; Niedermeier et al., 2009; Sandström et a., 2010). Another typical feature in hydrothermal rocks is epitactic growth during simultaneous dissolution-reprecipitation processes, as well as lobate grain boundaries (Putnis, 2002; Plümper and Putnis, 2009; Sandström et al., 2010), which can be observed in weakly altered rocks in the MPI. However, recrystallisation of quartz and breakdown of mica to K-feldspar under a release of water (section XX) are not described in the literature in association with hydrothermal alteration.

The paragenetic intergrowth of almost end-member microcline with almost end-member albite formed at temperatures of ~250 °C (McDowell, 1986). Coexisting intermediate plagioclase and almost end-member alkali feldspar in the measured samples also formed at temperatures of ~200-300 °C (Stormer, 1975; Whitney and Stormer, 1977). The analysed compositions and their equilibration temperature are typical for hydrothermal feldspar (e.g. Hay et al., 1988; Duffin, 1989; Hardy, 1989). However, fluids get usually trapped at the brittle-ductile transition (~250-300 °C) and the equilibration temperature of the feldspars may not be significant for the temperature of the actual alteration fluid (e.g. Bellot, 2007; Rabinowicz et al., 2010).

Geochemical and geochronological signal

The presented electron microprobe measurements and whole rock analyses of samples that show various stages of alteration result in scattered signals. Clear trends of general enrichment or depletion of elements and oxides in metasediments or granitoids are absent. The measured alteration products trend occasionally towards more end-member compositions in feldspars and towards a muscovitisation and chloritisation of biotite. Totally altered rocks are depleted in MgO as a result of the breakdown of all micas. Some isocon diagrams of altered and original host rocks show indeed enrichments of K_2O and BaO, while CaO, MgO and Na_2O (microclinisation and mica-breakdown) are depleted, but generally the signals of the components plot within the error along the 1:1 isocon. Regardless of the isocon diagrams, the geostatistical analyses of the geochemical components result in distinct clusters that represent the breakdown of plagioclase during microclinisation and the breakdown of biotite / iron-oxide formation / chloritisation. The results of these reactions are observed in the various thin sections of altered rocks.

An increase in K, Ba, Si and a decrease in Ca, Na, Mg and Fe is usually expected in K-feldspar alteration systems (Mehnert and Büsch, 1985; Harlov et al., 1998). The absence of clear general trends of enrichments or depletions of geochemical components in our dataset can be a result of multiple alteration processes of feldspar metasomatism, mica alteration, chloritisation and the formation of iron-titanium oxides. These alteration stages are also spatially variable, suggesting a dependency on the geochemical composition and structural properties of the host rock. Massive quartzites that mainly consist of silica are usually less affected by K-feldspar blastesis than well-foliated, geochemically complex metapelites and orthogneisses. These protoliths already start with a wide geochemical variability, either due to their sedimentary character and/or because of earlier alterations, of which albitisation and biotitisation are recorded in literature (e.g. Elburg et al., 2001, 2013; Neumann, 2001). The quartz-hematite ± fluorite Mt. Gee sinter event had additional effects on the rocks in the southern MPI (Bakker and Elburg, 2006; Brugger et al., 2011). The multiple hydrothermal reactions and the spatial variability of the metasomatism in the southern and central MPI are expressed in the scattered geochemical signal of the measured samples.

Zircon grains may be the only indication of the host rocks in totally altered areas. The U-Pb and Lu-Hf signals of zircons that were separated from K-feldspar metasomatites resemble the signal of the local granitoid host rocks. It might be possible to explain these zircon grains as trace minerals in a magmatic pegmatite, but intrusive contacts are missing and mica grains occur only as relicts in the rock. Our field observations and thin section analyses clearly indicate that the zircon grains are relicts of altered host rocks and stayed unaffected by the hydrothermal overprinting.

A possibility to date the K-feldspar alteration was tested with the Rb-Sr analysis of whole rock and muscovite samples of a pegmatite. One sample was taken from the centre of a magmatic pegmatite with coarse feldspar, quartz and muscovite grains and another from an altered area with K-feldspar blasts and fine-grained feldspar, quartz and relict muscovite. Both samples revealed the same Rb-Sr age within error of ~478 Ma. The variability in the initial Sr-ratios (see section XX) indicates that the samples were slightly affected by hydrothermal alteration, but no total reset occurred. The Rb-Sr age represents hence a magmatic intrusion age.

Fluid sources and fluid-rock interaction

The pervasive alteration in the MPI is either a result of different alteration of several fluids or a complex interaction of alteration processes that are caused by a single evolving fluid. Most observed reactions may be explained by fluid-rock interaction with one evolving fluid. The breakdown of plagioclase and the formation of end-member microcline and some albite, and the breakdown of biotite are the most obvious alteration processes. Both reactions can occur independently in the samples, especially around the margins of the K-feldspar alteration zones, where biotite remains almost unaffected in K-feldspar overprinted rocks. Microclinisation often pre-dates muscovitisation of biotite, while chloritisation of biotite post-dates the muscovitisation in central alteration zones. In the margins of the K-feldspar alteration zone, however, only one biotite breakdown process is usually active. The mobility of metals in the fluid resulted in the formation of iron-titanium oxides, while the formation of silicified breccias indicate that also silica was mobile (Tab.11). The fluid properties must have changed temporally and spatially that these different parageneses of host rocks, metasomatites and breccias could develop.

The occurrence of the major alteration and breccia zone along the hinge zone of the Yankaninna Anticline and along fault structures indicate that fluid flow occurred after or during the Palaeozoic folding of the inlier (Weisheit et al., 2013b). Weisheit et al. (2013a) discuss several possible sources for the Palaeozoic fluid flow. Large-scale fluid convection by the intrusion of the BEG-body and additional magmatic water are probably not the major fluid sources for the K-feldspar alteration, because the magmatic intrusions formed during the alteration. Other fluid sources are the decompressional release of pore water and water that is released during the breakdown of the micas. The breakdown occurred during general Palaeozoic exhumation (Weisheit et al., 2013b) and was not a

metamorphic dehydration. Mica breakdown at low temperatures can only be triggered by a fluid of low water activity (Eugster and Wones, 1962; Wones and Eugster, 1965; Dachs, 1994; Cygan et al., 1996; Nijland et al., 1998; Rajesh et al., 2012) that possibly derived from the decompressed pore water.

The pore water in basement rocks likely derived from trapped surface water (ocean and meteoric) that penetrated several kilometres below the unconformity during the deposition of the Neoproterozoic Adelaidean Sequence (Weisheit et al., 2013a). The salinity of the ocean water probably triggered fluid-rock interaction that lasted for several Myr in the middle crust. It is possible that these reactions resulted in pore water with a high concentration in alkalis and chlorine and a low water activity. This fluid was the starting point of the K-feldspar alteration and the breakdown of the micas.

BIOTITE-BREAKDOWN AND K-FELDSPAR ALTERATION

The breakdown of biotite was probably the first reaction to take place at low levels in the crust after the release of the brine with the low water activity. Microcline and iron-oxides formed, while the mineral-bound water was released into the fluid (reaction (1)). This reaction occurred with fluids that exceeded temperatures >400 °C (Eugster and Wones, 1962; Wones and Eugster, 1965; Dachs, 1994; Cygan et al., 1996). The released water increased the water activity in the brines, which caused a cessation of reaction (1) and probably a start of reaction (2), where biotite altered into muscovite under the release of potassium (Wones and Eugster, 1965). The K-rich fluid travelled upwards and enhanced the alkali alteration in upper crustal levels. It is, however, not possible to form the whole K-feldspar altered area only by the breakdown of the biotite. The amount of the products of reaction (1) and (2) can be calculated with the aid of the molar mass of all involved components and the density of the mineral phases. A rock volume with 25 % biotite would produce ~18 % microcline during the breakdown of the biotite. Totally altered rocks consists of up to 90 % microcline, which hence originated from a separate source.

Orville (1963) described alkali metasomatism as a dynamic process in the crust. The sodium concentration of an alkali-chloride fluid in equilibrium with alkali feldspar rises with a lowering of the fluid temperature, while potassium ions are enriched in high-temperature fluids, provided that the alkalis are available in the fluid and the host rocks (Orville, 1963). These concentration gradients result in an interconnected system in a counter-movement of potassium to low-temperature regions and sodium to high-temperature fluids. Hence K-feldspar metasomatism is more pronounced in cooler areas, while the growth of albite dominates in deeper levels of the crust (Orville, 1963). The feldspars in the protoliths that react with the connected chlorine-rich fluid may be the only reservoir for the dissolved alkalis in the system (Orville, 1963). This process is self-preserving in an uplifting crust with fluid that is decompressionally released, such as in the Palaeozoic Mount Painter Province

(Weisheit et al., 2013b). It results in a broad area of pervasive K-feldspar alteration, which in places overprints albitised rocks. Low temperature parageneses (end-member microcline and end-member albite) dominate at the end of the crustal-scale alteration process, because the hydrothermal fluids also travel upwards and cool. Early rims of albite can be found occasionally in K-feldspar altered rocks in the MPI, but it is not possible to distinguish these textures from the albitisation event that affected basement rocks during the Mesoproterozoic (e.g. Elburg et al., 2001).

The released pore fluid had at least temperatures above 500 °C (at a geothermal gradient of 40 °C/km), because they altered rocks that have been in depth of ~12 km at the time of the BEG's intrusion (Weisheit et al., 2013b). Such hot, chlorine-rich brines are well suitable to transport alkalis, silica and aluminium, which results in pH neutral conditions in the fluid (Orville, 1963; Lagache and Weisbrod, 1977; Williams, 1994; Shibue, 1995; Zeng et al., 1995; Manning et al., 2010; Wohlers et al., 2011). The mobility of silica is obvious in the silicification of breccias. Also the formation of scapolite, tremolite and epidote in marbles of the lower Adelaidean units are a result of Si, Al and Ca mobility. The observed fluid inclusions in altered rocks often contain calcite crystals, and myrmekite textures in altered rocks indicate that Ca was mobile during the alteration.

The fluid inclusions in K-feldspar altered samples in the MPI that contain several salt-phases homogenise at temperatures >330 °C, while fluid inclusions with trapped hematite crystals need temperatures above 400 °C to homogenise. The complexity of the fluid inclusions prevented a detailed analysis of the salinity and other properties of the brines. A comparison with the fluid inclusions study by Bakker and Elburg (2006) in a diopside-titanite vein indicates similarities of the observed complex fluid inclusions in K-feldspar altered rocks with secondary inclusions in diopside and tertiary inclusions in titanite. They are highly saline with ~ 40 equ. mass% NaCl and were trapped at ~350 °C and ~0.8 kbar, using a geothermal gradient of 100 °C/km (Bakker and Elburg, 2006). At a geothermal gradient of 40 °C/km, which is the mean gradient at the MPI according to Mildren and Sandiford (1995) and Sandiford et al. (1998), these inclusions were trapped at a temperature of at least 420 °C in a depth of maximum 10 km. The fluids trapped in the inclusions were probably hotter than their surroundings and hence formed in depths between 3 and 10 km. Some fluid inclusions in the K-feldspar altered rocks homogenise at ~100 °C, indicating that alteration may have occurred during a broad range of temperatures.

This is also indicated by the breakdown of muscovite (that may have been derived from biotite: reaction (2)) into K-feldspar, which occurs at medium temperature conditions (reaction (4); Eugster and Chou, 1979; Hewitt and Wones, 1984; Plümper and Putnis, 2009). The pH of the fluid decreases with this reaction (e.g. Zeng et al., 1995; Evans, 1993). Biotite breaks down to chlorite (reaction (3)) at temperature conditions typically below ~400 °C (Speer, 1984; Spear, 1993;

Komninou and Yardley, 1997), while Fe, Mg, K and silica may be mobile. Silica may precipitate and form silicified breccias at this stage when the pH conditions in the fluid change.

The maximum amount of potassium that can be transported in the fluid decreases with a decrease of the chlorine concentration in the fluid. This effect is enhanced by the decrease in pressure (Lagache and Weisbrod, 1977). Hence the crustal-scale K-feldspar alteration is restricted to a certain level in the crust, depending on the temperature conditions of the fluid and geochemical disequilibrium during fluid-rock interactions. Another possibility of alkali metasomatism is a sudden change in temperature, pressure or a mixing of fluids (Lagache and Weisbrod, 1977; Dipple and Ferry, 1992; Cleverley and Oliver, 2005; Sandström et al., 2010). These processes are not restricted to a certain area in the crust and may occur in more local environments like faults or shear zones.

The presented oxygen isotope study of quartz, K-feldspar and hematite veins resulted in a scattered equilibration temperature signal of the different mineral pairs. Possibly a conversion of magnetite into hematite and multiple fluid flow on the veins affected the oxygen system. An estimation of the equilibration temperature during the vein formation is hence not possible.

IRON-OXIDE ORES AND ADDITIONAL MINERALISATIONS

Iron-oxides are prevalent in K-feldspar altered rocks in the MPI as disseminated euhedral crystals overgrowing pre-existing textures, as anhedral zones in altered biotites or as inclusions in altered feldspars. The most dominant occurrence, however, can be found in magnetite/hematite-quartz lenses that occur as breccias and veins in K-feldspar altered rocks and protoliths. These several hundred meter large ore lenses formed at ~ 355 Ma (Elburg et al., 2013). Iron ions are transported in chlorine-rich brines that may derive from the trapped ocean water or from chlorine in the altered micas (Chou and Eugster, 1977; Eugster and Chou, 1979; Williams, 1994). Most observed fluid inclusions in altered rocks in the MPI include trapped hematite and magnetite crystals that indicate the mobility of iron in the alteration fluid. The solubility of iron oxides decreases with decreasing temperature at constant HCl concentrations (Eugster and Chou, 1979). Hence the dissolved iron precipitates as magnetite or hematite (reaction (5)) with cooling of the fluid and an increase of the oxygen fugacity. The dissolution of iron in a HCl-rich brine can be triggered by the reaction of muscovite to feldspar (reaction (4); Eugster and Chou, 1979).

The sources of the iron in the MPI are probably the biotites that break down into muscovite or K-feldspar and iron oxides (reaction (1) and (2)). A rock volume of 30 km^3 with 25 % biotite would produce ~ 0.7 km^3 magnetite. The massive magnetite/hematite-quartz lenses include only ~ $0.1*10^{-3}$ km^3 of iron-oxide; the rest became disseminated in magnetite and hematite grains in altered rocks.

The iron-oxide ore breccias and veins include pyrite and chalcopyrite (Lang, 2012) and are enriched in U, Cu, REE and Ba (Bons and Roessiger, 2008; Elburg et al., 2013). Also small, post-

deformational Zn and Cu deposits that are associated with iron-oxide veins and breccias formed in lower Adelaidean sediments around the inlier (Coats and Blissett, 1971; Lang, 2012), indicating that metals were mobile during the Palaeozoic hydrothermal alteration. Another Palaeozoic, hydrothermally derived rock type in the MPI are the hyperaluminous phlogopitites that include undeformed spinel and sapphirine (Elburg et al., 2012). They resulted from local desilicification and Mg-enrichment (Elburg et al., 2012), which was probably sourced from the breakdown of the micas.

The Palaeozoic hydrothermal alteration resulted in a large variety of metasomatic rock types that are concentrated along structurally controlled fluid pathways. In the following we will present a model that confederates a long-lived Palaeozoic exhumation and folding of the MPI (Weisheit et al., 2013b) with a complex hydrothermal system that resulted in a spatially diverse distribution of various metasomatites and breccias (Tab.11, Fig.27).

Model of fluid flow and exhumation

Alteration and brecciation in the southern and central MPI occurred in rocks that have been at depths of more than ~12 km after the deposition of the Adelaidean sedimentary basin at ~500 Ma (Weisheit et al., 2013b). K-feldspar metasomatites and breccias, as well as iron-oxide breccias, chloritisation and silicification zones are most concentrated along the hinge zone of the Yankaninna Anticline and major fault structures (Fig.2). K-feldspar alteration occurred at least during or after the intrusion of pegmatites that are related to the BEG-magmatism in the west of the southern MPI (~475 Ma: this study), as well as prior and after the BEG-related pegmatites that intruded in the centre of the southern MPI (~455 Ma: Elburg et al., 2013). The alteration still continued during the formation of the diopside-titanite veins (~443 Ma; Elburg et al., 2003).

Pegmatites in the southern MPI intruded in a depth of ~13 km (Weisheit et al., 2013b). The hyperaluminous rocks that formed at ~455 Ma (Elburg et al., 2012) and the iron-oxide U-REE ores (Elburg et al., 2013), which formed at ~355 Ma in a depth of ~5 km, are likely related to a complex fluid-flow system during that time in the Mount Painter Province. Weisheit et al. (2013b) discuss the crustal-scale folding and exhumation of the Province into the Yankaninna Anticline that occurred almost during the whole Palaeozoic, starting at ~500 Ma or at the latest at 450 Ma and lasting until ~ 315 Ma (age of the pebble dyke; Brugger et al., 2011) or ~286 Ma (age of the Mt. Gee sinter; Brugger et al., 2011). Folding and exhumation occurred either step-wise or with a constant rate, which is different in the anticlinal's core and in the limbs (Weisheit et al., 2013b). Hence, the large-scale alteration in the MPI took place during a prolonged period between ~475 Ma and ~355 Ma, at depths between ~13 km and ~5 km during the formation of the Yankaninna Anticline (Tab.11). The ~460-440 Ma stage of magmatism (Elburg et al., 2003, 2013; McLaren et al., 2006; Wülser, 2009) probably enhanced the fluid system, but there is no field indication that the alteration fluids derived from the

pegmatites or the BEG. As discussed above, pore fluids that were released during decompression during the formation of the anticline are interpreted as the starting source for the alteration.

Field observations and geochemical analyses allow to develop a general model for the MPI's alteration system in the Palaeozoic (Fig.27). Trapped, highly saline connate fluids were released during decompression with the beginning of the exhumation along the Paralana Fault System. The zone of fluid-release was at least at 12 km depth (mean burial of the unconformity), but more likely at ~15 km depth (deepest burial of altered rocks in the inlier) in the middle crust. The hot fluids travelled upwards, focused along foliation zones, faults and the hinge of the young Yankaninna Anticline. As discussed above, the first alteration was the breakdown of biotite into microcline and iron-oxide (reaction (1)), followed by muscovitisation (reaction (2)). The released potassium, water and probably chlorine/fluorine triggered the alkali metasomatism that resulted in weak albitisation at higher temperatures and pervasive microclinisation at lower temperatures and crustal levels. The high concentration of alkalis and probably chlorine in the fluid resulted in a low water activity that forced the final breakdown of the remaining micas (biotite and muscovite into microcline: reactions (2) and (4)). Rising fluids became increasingly focussed and brecciated the rocks. K-feldspar- and quartz-cemented breccia (Radium Ridge Breccias) formed at this stage in unaltered rocks above a zone of massive K-feldspar metasomatism. Alkali metasomatism halted with a lowering of the fluid temperature and pressure and the successive dilution of the fluid with water from the mica-breakdown reaction. This chemically inert fluid travelled further upwards, became focused along major structures and caused, according to Weisheit et al. (2013a), the Hidden Valley-type brecciation (Fig.27A).

The Palaeozoic crustal column in the rising Yankaninna Anticline in the Mount Painter Province can therefore be divided in five major zones (Fig. 27). The pore fluid is released in the deepest zone (1) of the system. Biotite-breakdown into microcline and muscovite (reaction (1) and reaction (2)) occurred in the next higher level (2) in the crust, which is successively followed by the alkali-metasomatism of the feldspars (formation of end-member microcline and some albite) and vein-formation (3). The two uppermost zones are levels of brecciation; first the brecciation that is related to the K-feldspar alteration (4) and the last level (5) includes the Hidden Valley-type brecciation (see Weisheit et al., 2013a). The processes at these higher levels remain active as long as fluid is released in the lowermost level during successive exhumation of the crust through these zones.

The Yankaninna Anticline formed during ~200 Myr in the Palaeozoic. A crustal column of ~15 km exhumed during that time in the core of the major fold. The sum of the released fluids caused the successive stages of overprinting of the inlier. Deeper basement rocks moved through the different crustal levels with ongoing exhumation and rise of the anticline. Areas that have previously been affected by biotite-breakdown were overprinted at a next stage by the K-feldspar alteration, while areas with early K-feldspar metasomatites were overprinted by K-feldspar breccias and so on

(Fig.27A-C). The total area of alteration and brecciation increased with time because of the rise and the expansion of the anticline. The latest fluids of the system that is exposed at the surface were enriched in iron ions that precipitated at certain pressure-temperature-redox or pH horizons as breccia sheets together with chlorite breccias at depths of ~5 km. Silicified breccias formed along fault zones probably from late-stage fluids (Fig.27D+E).

A complex system of fluid flow and fluid-rock interaction is also described in Archaean tonalitic gneisses in eastern Finland (Pajunen and Poutiainen, 1999). Early-stage fluids in the Palaeoproterozoic caused a leaching of Si, Ca, Na and K and the formation of massive kyanite-rich rocks, associated with ductile shearing and brecciation in this area. The late-stage Mg-enrichment resulted in cordierite-sillimanite metasomatism-metamorphism in faults and fractures and the fluid evolved from H_2O-rich to a CO_2 fluid (Pajunen and Poutiainen, 1999). The area of alteration is, however, restricted to narrow zones of a few 100 metres, while about 60 km² of rock are altered at the MPI.

Fluid-induced dehydration of biotite is discussed in the paper by Rajesh et al. (2012) that studied an Archaean gneiss complex in South Africa. In an area of a few metres the local biotite-hornblende gneiss altered into orthopyroxene- and feldspar-bearing patches, probably during the contact with a chlorine-rich brine at low water activity (Rajesh et al., 2012). Savel'eva and Karmanov (2010) record quartz-albite-microcline rocks along a 12 km long fault zone at the Baikal Lake that derive from hydrothermally altered biotite-amphibolite gneisses. However, no similar pervasive K-feldspar alteration and biotite breakdown as observed in the crustal-scale anticline that forms the MPI in South Australia is recorded in the literature.

CONCLUSION AND POSSIBLE FUTURE WORK

The complex, large-scale hydrothermal overprinting at the southern and central MPI is a result of several geological characteristics in this area. Basement rocks were infiltrated with ocean and meteoric water during the formation of horst and graben structures at the beginning of the Adelaidean deposition at ~800 Ma (Preiss, 2000). High heat producing U-rich granites in the basement (Mildren and Sandiford, 1995) caused a rise of the geothermal gradient to ~ 40 °C/km (McLaren et al., 2002) after their burial by ~12 km thick Adelaidean basin sediments (Weisheit et al., 2013b). Compression between ~500 and ~300 Ma resulted in the formation and contemporaneous exhumation of the crustal-scale Yankaninna Anticline at the hanging wall of the Paralana Fault System (Weisheit et al., 2013b). The trapped pore fluids were released during decompression in the core of the anticline and were focused along the hinge zone and fault structures. The elevated temperature and salinity of the fluid

caused several alteration reactions in deeper crustal levels while it caused brecciation at higher zones. Hidden Valley type breccias formed along faults and fold hinges possibly in the uppermost level of brecciation (Weisheit et al., 2013a). Rocks of the Yankaninna Anticline moved through the zones of alteration and brecciation with ongoing exhumation, resulting in complex and large-scale hydrothermal overprinting (Fig.27). The fluid system was possibly enhanced by the magmatic activity between ~500 to ~440 Ma (Elburg et al., 2003, 2013; this study), but fluid-flow continued at least unit ~355 Ma with the formation of the iron-oxide ore deposits (Elburg et al., 2013).

The presented dataset is, due to multiple overprinting, not suitable for mass balance calculations of mobile elements and quantitative analysis of the fluid properties (as has been done by e.g. Simon, 1990; Williams, 1994; Wilkinson, 2001; Derome et al., 2003; Baatartsogt et al., 2007; Plümper and Putnis, 2009; Sandström et al., 2010). Instead samples of protoliths and alteration products have to be used that represent only one alteration stage with single reactions. Such suitable samples are likely located at the rims of the major K-feldspar alteration zone, i.e. south of Mt. Painter, southwest of Paralana Hot Springs and east of Blue Mine.

The general occurrence of the alteration system is known from extensive mapping projects that were carried out in the course of this project. The exact geometry and relation of breccias and metasomatites may be further analysed in the outer zones of the alteration, i.e. southwest of Paralana Hot Springs, southeast and west of Mt. Painter and the Freeling Heights Quartzite and along the Tail of the BEG. A K-feldspar alteration is not known from the northern MPI that probably represents deeper crustal levels. The original crustal base of the alteration may hence be analysed to the east of the Tail and by further mapping of the Paralana Fault Zone to the north.

ACKNOWLEDGEMENTS

We kindly thank the Sprigg family and the staff of Arkaroola station for their ongoing support of our field trips and access to their property. We also thank Steve Hore and Wolfgang Preiss of the geological survey of South Australia DMITRE for suggestive discussions and help during the field work and the shipping of the samples. Joel Brugger, David Giles and Robin Armit are thanked for professional discussions in the field and at the universities. We thank the Diplom and Master students (University of Tübingen) for their initiative in the field and the composition of the detailed geological maps. A special thank goes to Per Jeisecke, Indra Gill-Kopp, Dagmar Kost, Dorothea Mühlbayer-Renner and Elmar Reitter, who did the final thin section preparation, mineral separation and Rb-Sr analyses, respectively, at the University of Tübingen. This project was funded by the DFG grant BO-1776/8-1.

REFERENCES

Allan, M.M., Yardley, B.W.D., 2007. Tracking meteoric infiltration into a magmatic-hydrothermal system: A cathodoluminescence, oxygen isotope and trace element study of quartz from Mt. Leyshon, Australia. Chemical Geology 240, 343-360.

Andersen, T., Andersson, U.B, Graham, S., Åberg, G., Simonsen, S.L., 2009. Granitic magmatism by melting of juvenile continental crust: New constraints on the source of Paleoproterozoic granitoids in Fennoscandia from Hf isotopes in zircon. Journal of the Geological Society London 166, 233-248.

Armit, R.J., Betts, P.G., Schaefer, B.F., Ailleres, L., 2012. Constraints on long-lived Mesoproterozoic and Palaeozoic deformational events and crustal architecture in the northern Mount Painter Province, Australia. Gondwana Research 22, 207–226.

Armstrong, J.T., 1991. Quantitative elemental analysis of individual microparticles with electron beam instruments. NewYork Plenum Electron Probe Quantitation, 261-315.

Baatartsogt, B., Schwinn, G., Wagner, T., Taubald, H., Beitter, T., Markl, G., 2007. Contrasting paleofluid systems in the continental basement: a fluid inclusion and stable isotope study of hydrothermal vein mineralization, Schwarzwald district, Germany. Geofluids 7, 123-147.

Baker, T., Lang, J.R., 2003. Reconciling fluid inclusion types, fluid processes, and fluid sources in skarns: an example from the Bismark Deposit, Mexico. Mineralium Deposita 38, 474-495.

Bakker, R.J., 2004. Raman spectra of fluid and crystal mixtures in the systems H2O, H2O-NaCl and H2O-MgCl2 at low temperatures: Applications to fluid-inclusion research. Canadian Mineralogist 42, 1283-1314.

Bakker, R.J., Elburg, M.A., 2006, A magmatic-hydrothermal transition in Arkaroola (Northern Flinders Ranges, South Australia): from diopside-titanite pegmatites to hematite-quartz growth. Contribution to Mineralogy and Petrology 152, 541–569.

Baumgartner, L.P., Olsen, S.N., 1995. A least-squares approach to mass-transport calculations using the Isocon Method. Economic Geology and the Bulletin of the Society of Economic Geologists 90, 1261-1270.

Baumgartner, M., Bakker, R.J., 2009. Raman spectroscopy of pure H(2)O and NaCl-H(2)O containing synthetic fluid inclusions in quartz-a study of polarization effects. Mineralogy and Petrology 95, 1-15.

Bellot, J.-P., 2007. Extensional deformation assisted by mineralised fluids within the brittle-ductile transition; insights from the southwestern Massif Central, France. Journal of Structural Geology 29, 225-240.

Belousova, E.A., Griffin, W.L., O'Reilly, S.Y., 2006. Zircon crystal morphology, trace element signatures and Hf isotope composition as a tool for petrogenetic modelling: Examples from eastern Australian granitoids. Journal of Petrology 47, 329–353.

Black, L.P., Kano, S.L., Allen, C.M., Aleinikoff, J.N., Davis, D.W., Korsch, R.J., Foudoulis, C., 2003. TEMORA 1: a new zircon standard for Phanerozoic U–Pb geochronology. Chemical Geology 200, 155–170.

Black, L.P., Kamo, S.L., Allen, C.M., Davis, D.W., Aleinikoff, J.N., Valley, J.W., Mundil, R., Campbell, I.H., Korscha, R.J., Williams, I.S., Foudoulis, C., 2004. Improved 206Pb/238U microprobe geochronology by the monitoring of a trace-element-related matrix effect; SHRIMP, ID–TIMS, ELA–ICP–MS and oxygen isotope documentation for a series of zircon standards. Chemical Geology 205, 115–140.

Bons, P.D., 2001. The formation of large quartz veins by rapid ascent of fluids in mobile hydrofractures. Tectonophysics 336, 1-17.

Bons, P.D., Roessiger, J., 2008. The Geology of the Mt. Gee area, Mount Painter Inlier, South Australia. Unpublished industry report on the mapping project carried out October-November 2007.

Bowden, P., 1985. The geochemistry and mineralization of alkaline ring complexes in Africa (a review). Journal of African Earth Sciences 3, 17-39.

Brugger, J., Long, N., McPhail, D.C., Plimer, I., 2005. An active amagmatic hydrothermal system: The Paralana hot springs, Northern Flinders Ranges, South Australia. Chemical Geology 222, 35-64.

Brugger, J., Wülser, P.A., Foden, J., 2011. Genesis and preservation of a uranium-rich paleozoic epithermal system with a surface expression (Northern Flinders Ranges, South Australia): Radiogenic heat driving regional hydrothermal circulation over geological timescales. Astrobiology 11, 499-508.

Burke, E.A.J., 2001. Raman microspectrometry of fluid inclusions. Lithos 55, 139-158.

Carrier, A., Jebrak, M., Angelier, J., Holyland, P., 2000. The silidor deposit, Rouyn-Noranda District, Abitibi Belt: Geology, structural evolution, and paleostress modeling of an Au quartz vein-type deposit in an Archean trondhjemite. Economic Geology and the Bulletin of the Society of Economic Geologists 95, 1049-1065.

Célérier, J., Sandiford, M., Lundbek Hansen, D., Quigley, M., 2005. Modes of active intraplate deformation, Flinders Ranges, Australia. Tectonics 24.

Cherniak, D. J., Watson, E. B., 1992. A study of strontium diffusion in K-feldspar, Na-K feldspar and anorthite using Rutherford Backscattering Spectroscopy. Earth and Planetary Science Letters 113, 411-425.

Chou, I.-M., Eugster, H.P., 1977. Solubility of magnetite in supercritical chloride solutions. American Journal of Sciences 277, 1296-1314.

Clayton, R.N., Goldsmith, J.R., Karel, K.J., Mayeda, T.K., Newton, R.C., 1975. Limits on the effect of pressure on isotopic fractionation. Geochima et Cosmochimica Acta 39, 1197-1201.

Cleverley, J.S., Oliver, N.H.S., 2005. Comparing closed system, flow-through and fluid infiltration geochemical modelling: examples from K-alteration in the Ernest Henry Fe-oxide-Cu-Au system. Geofluids 5, 289-307.

Coats, R.P., Blissett, A.H., 1971. Regional and economic geology of the Mount Painter Province, South Australia. Geological Survey of South Australia, Bulletin 43, 425p.

Cowley, W.M., Hore, S.B., Preiss, W.V., Sheard, M.J., Wade C., 2012. A revised stratigraphic scheme for the Mount Painter and Mount Babbage Inliers. SAREIC 2012 Technical forum poster. published in the web http://minerals.dmitre.sa.gov.au/press_and_events/events/sareic_2012_technical_forum.

Craig, H., 1961. Standard for reporting concentrations of deuterium and oxygen-18 in natural waters. Science 133,1833-1834.

Cygan, G.L., Chou, I.M., Sherman, D.M., 1996. Reinvestigation of the annite equals sanidine plus magnetite plus H-2 reaction using f(H-2)-sensor technique. American Mineralogist 81, 475-484.

Dachs, E., 1994. Annite stability revised 1. Hydrogen-sensor data for the reaction annite=sanidine+magnetite+H-2. Contributions to Mineralogy and Petrology 117, 229-240.

Derome, D., Cuney, M., Cathelineau, M., Fabre, C., Dubessy, J., Bruneton, P., Hubert, A., 2003. A detailed fluid inclusion study in silicified breccias from the Kombolgie sandstones (Northern Territory, Australia): inferences for the genesis of middle-Proterozoic unconformity-type uranium deposits. Journal of Geochemical Exploration 80, 259-275.

Dickin, A., 2009. Radiogenic isotope geology, 2nd ed.. Cambridge University Press, 512 p.

Dipple, G.M., Ferry, J.M., 1992. Metasomatism and fluid-flow in ductile fault zones. Contributions to Mineralogy and Petrology 112, 149-164.

Duffin, M.E., 1989. Nature and origin of authigenic K-feldspar in Precambrian basement rocks of the North-American midcontinent. Geology 17, 765-768.

Drexel, J.F., Major, R.B., 1987. Geology of the uraniferous breccia near Mt Painter, South Australia and revision of rock nomenclature. Geological Survey of South Australia, Quarterly Notes 104, 14-24.

Drexel, J.F., Major, R.B., 1990. Mount Painter uranium—rare earth deposits. in: Hughes, F.E. (ed) Geology of the mineral deposits of Australia and Papua New Guinea. Australian Institute of Mining and Metallurgy, Melbourne, 993-998.

Elburg, M.A., Bons, P.D., Dougherty-Page, J., Janka, C.E., Neumann, N., Schaefer, B., 2001. Age and metasomatic alteration of the Mt Neill Granite at Nooldoonooldoona Waterhole, Mt Painter Inlier, South Australia. Australian Journal of Earth Sciences 48, 721-730.

Elburg, M.A., Bons, P.D., Foden, J., Brugger, J., 2003. A newly defined Late Ordovician magmatic-thermal event in the Mt Painter Province, Northern Flinders Ranges, South Australia. Australian Journal of Earth Sciences 50, 611-631.

Elburg, M.A., Andersen, T., Bons, P.D., Weisheit, A., Simonsen, S.L., Smet, I., 2012. Metasomatism and metallogeny of A-type granites of the Mt Painter–Mt Babbage Inliers, South Australia. Lithos 151, 83–104.

Elburg, M.A., Andersen, T., Bons, P.D., Simonsen, S.L., Weisheit, A., 2013. New constraints on Phanerozoic magmatic and hydrothermal events in the Mt Painter Province, South Australia. Gondwana Research 24, 700-712. doi: 10.1016/j.gr.2012.12.017.

Eugster, A.P., Chou, I.-M., 1979. A model for the deposition of Cornwall-type magnetite deposits. Economic Geology 74, 763-774.

Evans, A.M., 1993. Ore geology and industrial minerals, 3rd ed.. Blackwell Science, Oxford, 390 p.

Eugster, H.P., Wones, D.R., 1962. Stability relations of the ferruginous biotite annite. Journal of Petrology 3, 82-125.

Fanning, C.M., Teale, G.S., Robertson, R.S., 2003. Is there a Willyama Supergroup sequence in the Mount Painter Inlier? In: Peljo, M. (compiler) Broken Hill Exploration Initiative: Abstracts from the July 2003 conference. Geoscience Australia Record 2003/13, 38-41.

Fraser, G.L., Neumann, N.L., 2010. New SHRIMP U-Pb zircon ages from the Gawler Craton and Curnamona Province, South Australia, 2008-2010. Geoscience Australia Record 2010/16, 192-254.

Foden, J., Elburg, M.A., Dougherty-Page, J., Burtt, A., 2006. The timing and duration of the Delamerian Orogeny: Correlation with the Ross Orogen and implications for Gondwana assembly. Journal of Geology 114, 189-210.

Grant, J.A., 1986. The Isocon Diagram - a simple solution to Gresens equation for metasomatic alteration. Economic Geology 81, 1976-1982.

Grant, J. A., 2005. Isocon analysis: A brief review of the method and applications. in: Dini, A., Corteel, C., Deyhle, A. (eds). Element and isotope mobility during water-rock interaction processes. Physics and Chemistry of the Earth 30, 997–1004.

Gresens, R.L., 1967. Composition-volume relationships of metasomatism. Chemical Geology 2, 47-55.

Hardy, L.S., 1989. Hydrothermal potassium-feldspar at the Haile-Gold-Mine, South-Carolina. Economic Geology 84, 2307-2310.

Harlov, D.E., Hansen, E.C., Bigler, C., 1998. Petrologic evidence for K-feldspar metasomatism in granulite facies rocks. Chemical Geology 151, 373-386.

Hay, R.L., Lee, M.C., Kolata, D.R., Matthews, J.C., Morton, J.P., 1988. Episodic potassic diagenesis of Ordovician tuffs in the Mississippi Valley area. Geology 16, 743-747.

Hedenquist, J.W., Arribas, A., Reynolds, T.J., 1998. Evolution of an intrusion centred hydrothermal system: far southeast-Lepanto porphyry and epithermal Cu–Au deposit. Economic Geology 93, 373-404.

Heinonen, A.P., Andersen, T., Rämö, O.T., 2010. Re-evaluation of rapakivi petrogenesis: Source constraints from the Hf isotope composition of zircon in the rapakivi granites and associated mafic rocks of southern Finland. Journal of Petrology 51, 1687-1709.

Hemley, J.J., Cygan, G.L., Fein, J.B., Robinson, G.R., Dangelo, W.M., 1992. Hydrothermal ore-forming processes in the light of studies in rock-buffered systems. 1. Iron-copper-zinc-lead sulfide solubility relations. Economic Geology and the Bulletin of the Society of Economic Geologists 87, 1-22.

Hewitt, D.A., Wones, D.R., 1984. Experimental phase relations of the micas, in: Bailey, S.W. (ed) Reviews in Mineralogy vol. 13 Micas. Mineralogical Society of America, 584 p.

Hoefs, J., 2009. Stable isotope geochemistry, 6 ed.. Springer-Verlag Berlin, Federal Republic of Germany, 285 p.

Holness, M.B., 2003. Growth and albitization of K-feldspar in crystalline rocks in the shallow crust: a tracer for fluid circulation during exhumation?. Geofluids 3, 89-102.

Klein, T.L., Criss, R.E., 1988. An oxygen isotope and geochemical study of meteoric-hydrothermal systems at Pilot Mountain and selected other localities, Carolina Slate Belt. Economic Geology 83, 801-821.

Komninou, A., Yardley, B.W.D., 1997. Fluid-rock interactions in the Rhine Graben: A thermodynamic model of the hydrothermal alteration observed in deep drilling. Geochimica et Cosmochimica Acta 61, 515-531.

Korsch, R.J., Preiss, W.V., Blewett, R.S., Fabris, A.J., Neumann, N.L., Fricke, C.E., Fraser, G.L., Holzschuh, J., Milligan, P.R., Jones, L.E.A., 2010. Geological interpretation of deep seismic reflection and magnetotelluric line 08GA-C1: Curnamona Province, South Australia. In: Korsch, R.J., Kositcin, N. (eds) South Australian Seismic and MT Workshop, Extended Abstracts. Geoscience Australia Record 2010/10, 42-53.

Krieg, G., Alexander, E.M., Rogers, P.A., 1995. Eromanga Basin. In: Drexel J. F., Preiss W. V. (eds) The geology of South Australia, vol. 2, The Phanerozoic. South Australia Geological Survey, Bulletin 54, 347 p.

Lagache, M., Weisbrod, A., 1977. The system: Two alkali feldspars-KCl-NaCl-H2O at moderate to high temperatures and low pressures. Contributions to Mineralogy and Petrology 62, 77-101.

Lang, J., 2012. The copper mineralisations in the Mount Painter Province, Northern Flinders Ranges, South Australia. Unpublished diplom mapping and thesis, University of Tübingen.

Lee, M.R., Parsons, I., 1997. Dislocation formation and albitization in alkali feldspars from the Shap granite. American Mineralogist 82, 557-570.

Le Maitre, R.W., 1982. Numerical petrology; statistical interpretation of geochemical data. Amsterdam Elsevier, 281 p.

Ludwig, K.R., 2001. Users Manual for Isoplot/Ex: A geochronological Toolkit for Microsoft Excel. Berkeley Geochronological Center Special Publication, Berkeley, U.S.A., 1–53.

Ludwig, K.R., 2003. Isoplot/EX version 3.0, A geochronological toolkit for Microsoft Excel. Berkeley Geochronology Center Special Publication, Berkley, U.S.A., 1-70.

Manning, C.E., Antignano, A., Lin, H.A., 2010. Premelting polymerization of crustal and mantle fluids, as indicated by the solubility of albite plus paragonite plus quartz in H2O at 1 GPa and 350-620 degrees C. Earth and Planetary Science Letters 292, 325-336.

Matsuhisa, Y., Goldsmith, J.R., Clayton, R.N., 1979. Oxygen isotopic fractionation in the system quartz-albite-anorthite-water. Geochimica et Cosmochimica Acta 43, 1131- 1140.

McDowell, S.D., 1986. Composition and structural state of coexisting feldspars, Salon Sea geothermal field. Mineralogical Magizine 50, 75-84.

McLaren, S. N., Dunlap, W.J., Sandiford, M., McDougalln, I., 2002. Thermochronology of high heat-producing crust at Mount Painter, South Australia: Implications for tectonic reactivation of continental interiors. Tectonics 21, doi. 10.1029/2000TC001275

McLaren, S., Sandiford, M., Powell, R., Neumann, N., Woodhead, J., 2006. Palaeozoic intraplate crustal anatexis in the Mount Painter Province, South Australia; timing, thermal budgets and the role of crustal heat production. Journal of Petrology 47, 2281-2302.

Mehnert, K.R., Büsch, W., 1985. The formation of K-feldspar megacrysts in granites, migmatites and augengneisses. Neues Jahrbuch für Mineralogie-Abhandlungen 151, 229-259.

Mildren, S., Sandiford, M., 1995. Heat refraction and low-pressure metamorphism in the northern Flinders Ranges, South Australia. Australian Journal of Earth Sciences 42, 241–247.

Moore, J.N., Powell, T.S., Heizler, M.T., Norman, D.I., 2000. Mineralization and hydrothermal history of the Tiwi geothermal system, Philippines. Economic Geology and the Bulletin of the Society of Economic Geologists 95, 1001-1023.

Nakano, S., Akai, J., Shimobayashi, N., 2005. Contrasting Fe-Ca distributions and related microtextures in syenite alkali feldspar from the Patagonian Andes, Chile. Mineralogical Magazine 69, 521-535.

Neumann, N., 2001. Geochemical and isotopic characteristics of South Australian Proterozoic granites: implications for the origin and evolution of high heat-producing terrains. Department of Geology and Geophysics. PhD thesis University of Adelaide.

Niedermeier, D., Putnis, A., Geisler, T., Golla-Schindler, U., Putnis, C., 2009. The mechanism of cation and oxygen isotope exchange in alkali feldspars under hydrothermal conditions. Contributions to Mineralogy and Petrology 157, 65-76.

Nijland, T.G., Touret, J.L.R., Visser, D., 1998. Anomalously low temperature orthopyroxene, spinel, and sapphirine occurrences in metasediments from the Bamble amphibolite-to-granulite facies transition zone (South Norway): possible evidence for localized action of saline fluids. Journal of Geology 106, 575–590.

O'Neil, J.R., Taylor, H.P. jr., 1967. The oxygen isotope and cation exchange chemistry of feldspars. American Mineralogist 52, 1414-1437.

O'Neil, J.R., Clayton, R.N., Mayeda, T.K., 1969. Oxygen isotope fractionation in divalent metal carbonates. Journal of Chemical Physics 51, 5547-5558.

Oreskes, N., Einaudi, M.T., 1992. Origin of hydrothermal fluids at Olympic Dam – preliminary results from fluid inclusions and stable isotopes. Economic Geology and the Bulletin of the Society of Economic Geologists 87, 64-90.

Orville, P.M., 1963. Alkali ion exchange between vapor and feldspar phases. American Journal of Sciences 261, 201-237.

Pajunen, M., Poutiainen, M., 1999. Palaeoproterozoic prograde metasomatic-metamorphic overprint zones in Archaean tonalitic gneisses, eastern Finland. Bulletin of the Geological Society of Finland 71, 73-132.

Paul, E., Flöttmann, T., Sandiford, M., 1999. Structural geometry and controls on basement-involved deformation in the northern Flinders Granges, Adelaide Fold Belt, South Australia. Australian Journal of Earth Sciences 46, 343-354.

Plümper, O., Putnis, A., 2009. The complex hydrothermal history of granitic rocks: multiple feldspar replacement reactions under subsolidus conditions. Journal of Petrology 50, 967-987.

Preiss, W.V., 1987. The Adelaide Geosyncline — Late Proterozoic stratigraphy, sedimentation, paleontology, and tectonics. South Australian Geological Survey Bulletin 53, 438 p.

Preiss, W.V., 1995. Early and middle Paleozoic orogenies, in: Drexel, J.F., Preiss, W.V. (eds) The Geology of South Australia, Vol. 2, The Phanerozoic: South Australia, Geological Survey Bulletin 54, 347 p.

Preiss, W.V., 2000. The Adelaide Geosyncline of South Australia and its significance in Neoproterozoic continental reconstruction. Precambrian Research 100, 21–63.

Putnis, A., 2002. Mineral replacement reactions: from macroscopic observations to microscopic mechanisms. Mineralogical Magazine 66, 689-708.

Putnis, A., Hinrichs, R., Putnis, C.V., Golla-Schindler, U., Collins, L.G., 2007. Hematite in porous red-clouded feldspars: Evidence of large-scale crustal fluid-rock interaction. Lithos 95, 10-18.

Rabinowicz, M., Bystricky, M., Schmocker, M., Toplis, M. J., Rigo, A., Perfettini, H., 2010. Development of fluid veins during deformation of fluid-rich rocks close to the brittle-ductile transition; comparison between experimental and physical models. Journal of Petrology 51, 2047-2066.

Rajesh, H.M., Belyanin, G.A., Safonov, O.G., Kovaleva, E.I., Golunova, M.A., Van Reenen, D.D., 2012. Fluid-induced dehydration of the Paleoarchean Sand River biotite–hornblende gneiss, Central Zone, Limpopo Complex South Africa. Journal of Petrology 54, 41–74, doi. 10.1093/petrology/egs062.

Reed, S.J.B., 2005. Electron microprobe analysis and scanning electron microscopy in geology. Cambridge University Press, 260 p.

Rehder, T., 2010. A complex hydrothermal overprint of the basement rocks in the East Painter area, Arkaroola, Northern Flinders Ranges, South Australia. Diplom thesis, University of Tübingen.

Roedder, E., Bodnar, R.J., 1980. Geological pressure determinations from fluid inclusion studies. Annual Reviews of Earth and Planetary Sciences 8, 263–301.

Rosa, D.R.N., Finch, A.A., Andersen, T., Inverno, C.M.C., 2009. U–Pb geochronology and Hf isotope ratios of magmatic zircons from the Iberian Pyrite Belt. Mineralogy and Petrology 95, 47-69.

Sandiford, M., Hand, M., McLaren, S., 1998. High geothermal gradient metamorphism during thermal subsidence. Earth and Planetary Science Letters 163, 149–165.

Sandström, B., Annersten, H., Tullborg, E.L., 2010. Fracture-related hydrothermal alteration of metagranitic rock and associated changes in mineralogy, geochemistry and degree of oxidation: a case study at Forsmark, central Sweden. International Journal of Earth Sciences 99, 1-25.

Savel'eva, V.B., Karmanov, N.S., 2010. Quartz-albite-microcline metasomatic rocks in the Main Sayan Fault Zone: evolution of metasomatism and composition of accessory minerals. Geology of Ore Deposits 52, 302-321.

Shepherd, T., Rankin, D.H., Alderton, G.M., 1985. A practical guide to fluid inclusions. Blackie Glasgow, 239 p.

Shibue, Y., 1995. An empirical equation of quartz solubility in NaCl solution above 200°C, in: Kahara, Y.K., Chudaev, O.V. (eds) Water-rock interaction: proceedings of the 8th International Symposium on Water-Rock Interaction -- WRI-8, Vladivostok, Russia, 15-19 August 1995, Balkema, Rotterdam.

Simon, K., 1990. Hydrothermal alteration of variscan granites, Southern Schwarzwald, Federal-Republic-of-Germany. Contributions to Mineralogy and Petrology 105, 177-196.

Spear, F.S., 1993. Metamorphic phase equilibria and pressure-temperature-time paths. Mineralogical Society of America Monograph Series 1, 799 p.

Speer, J.A., 1984. Micas in igneous rocks, in: Bailey, S.W., 1984, Reviews in Mineralogy Vol. 13 Micas. Mineralogical Society of America, 584 p.

Steele-MacInnis, M., Bodnar, R.J., Naden, J., 2010. Numerical model to determine the composition of H_2O-NaCl-$CaCl_2$ fluid inclusions based on microthermometric and microanalytical data. Geochimica et Cosmochimica Acta 75, 21-40.

Stewart, K., Foden, J., 2003. Mesoproterozoic granites of South Australia. Department of Primary Industries and Resources Report Book 2003/15, 142 p.

Stormer, J.C., Jr., 1975. A practical two-feldspar geothermometer. American Mineralogist 60, 667-674.

Taubald, H., Morteani, G., Satir, M., 2004. Geochemical and isotopic (Sr, C, O) data from the alkaline complex of Gronnedal-lka (South Greenland): evidence for unmixing and crustal contamination. International Journal of Earth Sciences 93, 348-360.

Thorkelson, D.J., Mortensen, J.K., Davidson, G.J., Creaser, R.A., Perez, W.A., Abbott, J.G., 2001. Early Mesoproterozoic intrusive breccias in Yukon, Canada: the role of hydrothermal systems in reconstructions of North America and Australia. Precambrian Research 111, 31-55.

Tumbull, R.B., 1993. A petrological and Rb-Sr isotopic study of an early Archean fertile granite-pegmatite system; the Sinceni Pluton in Swaziland. Precambrian Research 61, 89-116.

Van den Kerkhof, A.M., Hein, U.F., 2001. Fluid inclusion petrography. Lithos 55, 27-47.

Walker, F.D.L., Lee, M.R., Parsons, I., 1995. Micropores and micropermeable textures in alkali feldspars: geochemical and geophysical implications. Mineralogical Magazine 59, 505-534.

Webster, J.D., 1997. Exsolution of magmatic volatile phases from Cl-enriched mineralizing granitic magmas and implications for ore metal transport. Geochimica et Cosmochimica Acta 61, 1017-1029.

Weisheit, A., Bons, P.D., Elburg, M.A., 2013a. Long-lived crustal fluid-flow: the hydrothermal mega-breccia of Hidden Valley, Mt. Painter Inlier, South Australia. International Journal of Earth Sciences, doi: 10.1007/s00531-013-0875-7.

Weisheit, A., Bons, P.D., Danišík, M., Elburg, M.A., 2013b. Crustal-scale folding: Palaeozoic deformation of the Mt. Painter Inlier, South Australia. Journal of the Geological Society, in press.

Whitney, J.A., Stromer, J.C., Jr., 1977. The distribution of NaAlSi (sub 3) O (sub 8) between coexisting microcline and plagioclase and its effect on geothermometric calculations. American Mineralogist 62, 687-691.

Wiedenbeck, M., Alle, P., Corfu, F., 1995. Three natural zircon standards for U–Th–Pb, Lu–Hf, trace element and REE analyses. Geostandards Newsletter 19, 1–23.

Wilkinson, J.J., 2001. Fluid inclusions in hydrothermal ore deposits. Lithos 55, 229-272.

Williams, P.J., 1994. Iron mobility during synmetamorphic alteration in the Selwyn Range area, NW Queensland - implications for the origin of ironstone-hosted Au-Cu deposits. Mineralium Deposita 29, 250-260.

Wingate, M.T.D., Campbell, I.H., Compston, W., Gibson, G.M., 1998. Ion microprobe U–Pb ages for Neoproterozoic basaltic magmatism in south-central Australia and implications for the breakup of Rodinia. Precambrian Research 87, 135–159.

Wohlers, A., Manning, C.E., Thompson, A.B., 2011. Experimental investigation of the solubility of albite and jadeite in H2O, with paragonite plus quartz at 500 and 600 degrees C, and 1-2.25 GPa. Geochimica et Cosmochimica Acta 75, 2924-2939.

Wones, D.R., Eugster, H.P., 1965. Stability of biotite: Experiment, theory and application. The American Mineralogist 50, 1228-1272.

Woodhead, J.D., Hergt, J.M., 2005. A preliminary appraisal of seven natural zircon reference materials for in situ Hf isotope determination. Geostandards and Geoanalytical Research 29, 183-195.

Worden, R.H., Walker, F.D.L., Parsons, I., Brown, W.L., 1990. Development of microporosity, diffusion channels and deuteric coarsening in perthitic alkali feldspars. Contributions to Mineralogy and Petrology 104, 507-515.

Wülser, P.-A., 2009. Uranium metallogeny in the Northern Flinders Ranges region of South Australia. Ph.D. thesis, University of Adelaide.

Zeng, Y., Ai, R., Ai, Y., 1995. Experimental study on the interaction between feldspar and alkali-chloride solutions at 300°C and 50 MPa under a flow-through condition, in: Kahara, Y.K., Chudaev, O.V. (eds) Water-rock interaction: proceedings of the 8th International Symposium on Water-Rock Interaction -- WRI-8, Vladivostok, Russia, 15-19 August 1995, Balkema, Rotterdam.

Zheng, Y.F., 1991. Calculation of oxygen isotope fractionation in metal-oxides. Geochimica et Cosmochimica Acta 55, 2299-2307.

Zheng, Y.F., 1993. Calculation of oxygen isotope fractionation in anhydrous silicate minerals. Geochimica et Cosmochimica Acta 57, 1079-1091.

FIGURE CAPTIONS

Fig.1: Geological map of South Australia and the Mount Painter Province. A) South Australia consists of three major craton blocks: the Musgrave Province, the Gawler Craton and the Curnamona Province. The Neoproterozoic Adelaide Fold and Thrust Belt developed between the latter two provinces that are partly covered by younger sedimentary basins (Eucla and Murray Basin). B) Multiply deformed Mesoproterozoic rocks of the Mount Painter Inlier (MPI) and the Neoproterozoic Adelaidean cover sediments are folded in 10 km-scale syn- and anticlines. Magmatic rocks intruded into the basement in Palaeozoic times. Potassium alteration, brecciation and vein formation affected ~60 km² of basement and cover rocks in the central and southern Mount Painter Inlier. Sheets of U-rich magnetite/hematite breccias developed within the K-feldspar altered zones. Large, weathered breccia zones crop out at fold hinges and fault zones. They include clasts of cover and basement units down to the µm-scale (Hidden Valley type breccias). The general map of the Mount Painter Inlier is adapted from Coats and Blissett (1971).

Fig.2: Detailed map of the alteration in the southern and central MPI, showing that the K-feldspar alteration fluid concentrated along structural fluid pathways (faults and fold hinges). Pegmatite intrusions are not spatially related to the K-feldspar alteration. Iron-rich breccias, quartz-cemented breccias (Radium Ridge Breccias; Drexel and Major, 1986) and secondary copper deposits in the Lower Adelaidean are

interpreted to be related to late-stage K-feldspar-alteration fluids. Breccias and veins of a quartz-hematite sinter developed at the sub-surface, postdating the K-feldspar alteration. Host rock lithologies adapted after Fig.1.

Fig.3: A) Gradual K-feldspar alteration of an orthogneiss with quartz-augen at the southern unconformity. The K-feldspar blasts overgrow the previous paragenesis. The quartz-augen remain and grow in the K-feldspar altered zone. B) Irregular intergrowth of K-feldspar and quartz impregnation in a quartzite of the lower Adelaidean sequence at The Needles. Potassium alteration is associated with hematite (arrows). C) The host rock loses its structures with increasing K-feldspar alteration. Micas break down and feldspars and quartz grow. This gneissic metapelite south of Mt. Painter gradually alters into a massive, pink K-feldspar and quartz metasomatite. D) Sometimes the K-feldspar alteration front is sharp indicating a barrier for fluid flow. This orthogneiss west of Paralana Hot Springs gradually loses its mafic minerals and the plagioclases. E) YG17: Pegmatitic textures often develop in the centre of the K-feldspar alteration with graphic intergrowth of quartz and feldspars (example of an altered orthogneiss west of Paralana Hot Springs). F) 10N17: An undeformed pegmatite north of The Pinnacles grades into massive K-feldspar-altered orthogneiss, whereas at G) a pegmatite is cut by K-feldspar + quartz veins (arrows). All field observations indicate that pegmatite intruded during the alteration. H+I) Impregnation of the host rock by K-feldspar alteration also occurs along discrete veins of quartz, K-feldspar, ± tourmaline and hematite. These veins often crosscut already K-feldspar-altered rocks.

Fig.4: A) K-feldspar and quartz cemented breccia at the Paralana Fault Zone. Clasts in clasts indicate that these breccias post-date chloritic breccias (arrow; photograph taken at Hidden Valley). B) Magnetite/hematite cemented breccias often incorporate K-feldspar and quartz metasomatites and breccias (photograph taken north of Mt. Painter). C) Quartz-cemented breccia that forms steep ridges. It is associated with silicification of the host rock (photograph taken south of Mt. Painter). D) Typical outcrop of the sinter breccia at Mt. Painter with several generations of quartz and hematite. E) Nailhole quartz rosettes are characteristic for the Mt. Gee Sinter at Mt. Painter. F) Sample 091: A breccia with a K-feldspar, quartz and ±hematite cement cuts through a K-feldspar altered zone in a mica-rich paragneiss south-west of Paralana Hot Springs (pen for scale at arrow). The transition zones are well visible. G) K-feldspar-rich rims around quartzitic clasts in a K-feldspar- and quartz-cemented breccia (Radium Ridge Breccia) indicate that K-feldspar alteration of the clasts is still in progress during the brecciation. Photograph taken north of Mt. Painter. H) Stereoplot of pole-points of mineralised joints and veins in the southern MPI (mineral abbreviations from Kretz (1983)). The mean directions of the joints build a set that is almost perpendicular (pole points with standard deviation circle and mean great circle). The veins have a random distribution between N-S and E-W striking, indicating that joint- and vein formation occurred during several tectonic stress directions. I) Stereoplot of pole points of veins and joints in the eastern MPI at Paralana Hot Springs. The mean direction (pole points with black standard deviation circle and mean great circle) indicates that a set of joints formed during local NW-SE compression, whereas most veins opened during local N-S compression.

Fig.5: Microphotographs of K-feldspar-altered rocks with crossed polarisers. A) Sample BC348: Altered orthogneiss east of Mt. Painter. Original plagioclase crystals are rimmed by quartz and albites and included in large microclines. Albitisation occurred prior to microclinisation. B) Potassium-altered paragneiss west of Paralana Hot Springs. Myrmekite textures develop at contacts to new-grown K-feldspars. C) Original K-feldspar grew during K-feldspar alteration and developed an irregular rim, which is rich in inclusions (sample taken from meta-granite east of Mt. Painter). D) Sample Y52: Altered granite sample south of Yudnamutana. The original feldspars are rimmed by new-grown microcline that contains inclusions of the older minerals. Biotite is altered into iron-oxide-rich masses. E) Sample YG17a: Altered orthogneiss west of Paralana Hot Springs. New-grown K-feldspar has a reaction rim of quartz and inclusions of altered biotites. F) Sample YG17f: Same location as E). New microcline formed at the contact between quartz and original K-feldspar. G) Sample 091g: Growth of K-feldspar at grain boundaries during the recrystallisation of quartz and the breakdown of biotite (sample taken from an altered RCM east of Mt. Painter). H) Meta-sedimentary sample at Mt. Painter. Chloritisation of biotite occurs without K-feldspar alteration. Albite and K-feldspar are only affected by serizitisation. I) Most altered rocks only consist of microcline and quartz and relicts of micas (sample taken south of Mt. Painter). Mineral abbreviations from Kretz (1983).

Fig.6: Microphotographs of K-feldspar-altered rocks with crossed and parallel polarisers. A) Altered metapelite at Mt. Painter. Biotite alters pseudomorphically into microcline and iron oxide. B) K-feldspar altered granite south of Mt. Painter. Biotite alters into microcline and iron-oxide. C) Sample SK080a: Potassium-altered meta-granite east of The Needles. Clearly visible is the breakdown of biotite into muscovite that grew pseudomorphically. D) Sample SP2: Biotite in a meta-sediment south of Mt. Painter alters into muscovite and iron-oxides at the contact to new-grown microcline. E) Sample SP2: Potassium-altered meta-granite south of Mt. Painter. Original biotite totally altered into muscovite, which is altered into microcline with irregular contacts to the surrounding quartz. F) Sample 091b: Metasomatised meta-sediment east of Mt. Painter. Biotite alters into muscovite, chlorite and iron-oxide. New-grown microclines are present in the whole thin section. Microcline and the altered biotite grow around recrystallised quartz. G) Totally altered granite east of Wheal Turner. Biotite reacted to muscovite or chlorite. Whether microcline also grew from biotite is not clear. Subhedral grains of magnetite formed in the sample. H) Feldspars in a meta-granite at Mt. Painter partly weathered into sericite. I) Sample 091d: Totally altered meta-sediment east of Mt. Painter. Microcline overgrows the previous texture with lobate contact to the recrystallised quartz, but with equilibration contact to other microcline grains. The original mica altered into a mass of muscovite and iron-oxides, which grows above the previous texture.

Fig.7: Microphotographs of K-feldspar-altered rocks with crossed polarisers. A) Potassium-altered meta-granite southwest of Mt. Painter. Several mm-sized microcline crystals inter-grow and over-grow the previous texture with a skeleton shape. B) Same image section as in A) but the sample is rotated to 90°. C) Thoroughly altered meta-sediment west of Mt. Painter. Iron-hydroxide and -oxide are disseminated in the sample that consists of hydrothermal microcline and quartz with relicts of micas. Zircon/apatite crystals

seem to be unaffected by the extensive alteration. D+E) Sample 091d: Totally altered meta-sediment east of Mt. Painter. Iron-oxide minerals are brecciated and included as angular clasts in a K-feldspar cemented breccia zone. Zircon and monazite are also brecciated. The sample is cut by a quartz-hematite vein, likely related to the quartz-hematite sinter. F) Sample 091d: Totally altered meta-sediment east of Mt. Painter. Metasomatic microcline brecciated during fluid-focusing and was cemented by new microcline. G) K-feldspar-altered biotite-rich gneiss at Mt. Painter. The metasomatic K-feldspar and quartz texture is brecciated and cemented by K-feldspar. Tourmaline grew prior to the K-feldspar brecciation (H). I) K-feldspar-cemented breccia west of Paralana Hot Springs. Fluids with iron-hydroxides and -oxides used the same pathways and caused further brecciation after the K-feldspar alteration and brecciation.

Fig.8: Back-scattered electron images from K-feldspar altered rocks. A) Sample YG17c: Potassium alteration is generally expressed by the growth of almost pure microcline. In this sample microcline only grows in small rims at the contact between original feldspars and quartz. B) Sample 10N17e: Complex intergrowths between albite and microcline that grew during the K-feldspar alteration. C) Sample ML248a: Plagioclase alters into sodium-rich alkali feldspar at the contact to new-grown microcline. A rim of albite formed around the altered plagioclase. D) Sample YG17d: An unknown mineral totally altered into porous microcline. E) Sample 10N17e: Hydrothermal microcline overgrows previous textures, resulting in inclusion-rich cm-scale blasts. F) Sample YG17c: Almost pure albite grows along grain boundaries of the original texture.

Fig.9: A) The measured feldspars (n=243) in altered rocks can be divided in four groups: (1) Microcline and (2) albite end-members that formed as new-grown blasts and alteration product of former feldspar. Albite is often intergrown with microcline and occurs in rims around older feldspar. (3) K-rich alkali feldspar and (4) Na-rich plagioclase often occur in the centre of veins and broad alteration zones. B-D) Sample SP36b: Profile through a microcline-quartz vein with a rim of microcline within a biotite-rich meta-sediment (back scattered electron image). There is no significant enrichment or depletion of oxides through the profile. All measured microclines are of an almost end-member composition. Only the BaO content slightly increases in rim and centre feldspar.

Fig.10: Variation diagrams of original (diamond), altered (triangle), new metasomatic (plus), new pegmatitic (circle) and breccia cement (star) microcline. A) The BaO content in microcline of altered and non-altered samples is independent from the K content, indicating disequilibrium and multiple overprinting. B) There is no distinct geochemical trend in the measured elements of all microclines. For example a plot of SiO_2+Al_2O_3 vs. FeO gives only a scattered signal. C+D) Sample YG17 (K-feldspar-altered orthogneiss) shows a trend to an end-member composition from original to new-grown albite.

Fig.11: Microphotographs with crossed polarisers and back scattered electron images of K-feldspar altered samples. A+A‘) Sample ML248a: Potassium altered gneiss with remnants of original mica. The altered mica is now rich in magnesium, iron and aluminium and has inclusions of quartz and hydrothermal microcline. B+B‘) Sample 091e: Biotite in contact to new-grown microcline alters into muscovite with

magnesium and iron. C+C‘) Sample YG17a: Sampling profile through an altered orthogneiss with transition from original into altered mica. The mica is altered into a phlogopite-like composition and developed a complex intergrowth between hydrothermal plagioclase.

Fig.12: Variation diagrams of original (diamond), altered (triangle) and new metasomatic (plus) mica. A) The composition of all measured mica range between phlogopitic, more Fe-rich biotite and muscovite. These compositions are independent from the grouping into original, altered or new-grown metasomatic mica. The enrichment of MgO and Al_2O_3 in the phlogopite signals suggests that these minerals are already alteration products. B) Original and altered mica of the meta-igneous rocks overlap with the mica-signals in the meta-sediment samples. No general enrichment or depletion of elements is traceable. C-E) Only a profile through a K-feldspar alteration zone of sample YG17 shows a decrease of K_2O/Al_2O_3 (alteration index), MgO and FeO with increasing alteration of the mica. The TiO_2 content in these samples decreases slightly.

Fig.13: Harker variation diagrams that show the relation of unaltered host rocks and their alteration products (filled symbols: metasediments; open symbols: granitoids). Triangle: host rock; square: K-feldspar overprinted rocks; diamond: K-feldspar metasomatites; plus: K-feldspar cemented breccias; star: pegmatitic K-feldspar centres; open cross: K-feldspar altered clasts or pegmatites in Hidden Valley breccia. The composition of the rocks overlaps in all measured components and differences in the composition of altered metasediments or granites is not distinct. Only the MgO-content in K-feldspar altered rocks trend to low values.

Fig.14: Harker variation diagrams of the measured A-type granitoid host rocks (open squares) and samples of A-type granitoids in the MPI that are published in literature (filled triangles). The range in their compositions is similar. Published samples from Elburg et al. (2013), Neumann (2001) and Wülser (2009).

Fig.15: Plots of various geochemical components against K_2O. There is no significant variation between the geochemical composition of host rocks and K-feldspar altered rocks. A negative trend between Na_2O and K_2O and a positive between BaO and K_2O indicate that microclinisation and albitisation affected the rocks. Symbols as in Fig.13.

Fig.16: Plots of various geochemical components of host rocks and alteration products. The correlation between Sr-Ba is related to the modal abundance of K-feldspar while the correlation of TiO_2-Fe_2O_3 reflects the abundance of iron-titanium-oxides, biotite and/or titanite. There are no differences between altered and original rocks. Symbols as in Fig.13.

Fig.17: Plots of various geochemical components against K_2O of samples from profiles through alteration transitions at 5 outcrops. Grey arrows point from host rock to the most altered sample. The MgO-content slightly decreases at the transition from an albitised A-type granite at locality 10N17 (open triangle), while no other clear trends at this locality are visible. Na_2O, Fe_2O_3 and Zr slightly increase during alteration of an A-type granite at locality BC338-343, while MgO decreases (filled triangle). An alteration

of orthogneisses at outcrop YG17 resulted in a decrease of Na_2O and an increase in MgO (open square). A transition from a meta-sediment into K-feldspar cemented breccias at outcrop 091 shows no variation in the composition (filled square). The high Fe_2O_3 content in the breccia b derives from abundant iron-oxides in the sample. The samples BC344+348 (open diamond) record a slight decrease in Na_2O during the alteration of the A-type granite.

Fig.18: Isocon diagram of altered rock plotted against the protolith. Data points that include negative values are removed from the diagram. A) Isocon diagram of the mean of two altered samples against the albitised host rock at 10N17. Ba and REE are depleted, while Zr and Na_2O slightly increased. B) Plot of the mean signal of four alteration products against that of three protoliths at locality 091. Gains and losses of various components are well visible. C) One alteration product is plotted against two protolith samples of location YG17. The high scatter suggests multiple overprinting. D) A plot of samples 341 and 343 against samples 339 and 338 results in a large scatter. E) Plot of sample 348 against 344. K_2O and Rb are enriched, while most other components decrease. An increase in iron and the microclinisation of the altered sample is best expressed with an isocon line through the immobile zircon.

Fig.19: Plots of various principle components that derive from correlation matrix of host rock and alteration product. Normalisation was done to SiO_2 or Al_2O_3. A) Plot of PC_1-PC_2 with clusters of components related to microcline, biotite and iron-titanium minerals and possible chlorite. B) Plot of PC_2-PC_3. Microcline and plagioclase have a negative correlation possibly related to microclinisation and plagioclase-breakdown. Iron and REE mobility may be related to biotite-breakdown and iron-titanium ores. C) A plot of PC_3-PC_4 also highlights the negative correlation between microcline and plagioclase.

Fig.20: Microphotographs of fluid inclusions in quartzes of the RCG-sample SP2 that is cut by a K-feldspar-quartz and tourmaline vein with a rim of microclinisation. The sample was collected south of Mt. Painter. A) Large, angular fluid inclusions with a single phase or a liquid (L) and vapor (V) phase in an original quartz-auge. B) A single, irregular fluid inclusion with L+V and a halite crystal (solid S) in RCG quartz. C) Trail of rounded inclusions with L+V and a trapped hematite crystal (S) in original quartz. D) Single fluid inclusions with L+V and 2-3 solid phases in a quartz in the microcline zone. E) L+V and two solid phases (halite and hematite) in an elongated single fluid inclusion in the microcline zone. F) Single, rounded L+V inclusion in microcline zone. G) A cluster of rounded, single-phase inclusions, occasionally with a vapor phase in the microcline zone. H) Complex cluster with single phase fluid inclusions that often include trapped hematite in a quartz surrounded by tourmaline. I) Complex fluid inclusion with several solid phases, V and L in the same quartz as in H). J) Halite crystal in a L+V+S fluid inclusion in a quartz within a tourmaline. K) Several cubic crystals in a L+V+S fluid inclusion in a quartz that is inter-grown with tourmaline. L) Single fluid inclusions occur in the same quartz as K) with 4-5 solid phases with L+V.

Fig.21: Raman-signals of liquids and solids in different fluid inclusions in sample SP2. A) A discrete peak at ~3440 cm^{-1} derives from a concentrated brine, while in B) no salts are dissolved in the liquid phase and the distinct H_2O-signal developed. Calcite (C), magnetite (D) and hematite (E) could be

analysed during measurements of the solid phases. Peaks at ~204, 354 and at 464 cm^{-1} correspond to the background signal of quartz.

Fig. 22: Results of oxygen isotope measurements in a quartz, K-feldspar and hematite vein at Petalinka Waterfall in cover quartzites at Yudnamutana mine (A) and in a zone of deformed pure quartz veins close to the contact of basement and cover north of Arkaroola (B). A) The temperature range of quartz-hematite and quartz-K-feldspar pairs in the vein at Petalinka Waterfall varies between ~ 650 to 140 °C, independent from the distance to the wall. B) The $\delta^{18}O$ values of multiple ENE-WSW trending quartz veins that pre-date the Palaeozoic deformation vary between 7.7 and 10 ‰ with one exception of 13.7 ‰. The samples were taken perpendicular to the strike of the veins.

Fig. 23: Sample location and Rb-Sr results of outcrop WD5b and WD5c. A) WD5c is an undeformed pegmatite with quartz, K-feldspar, muscovite ±garnet that intruded at brittle conditions (open voids) in metasediments east of The Needles. B) The pegmatite grades into a feldspar-rich, more fine-grained zone (WD5b), probably altered during the K-feldspar metasomatism. C+D) The two-point Rb-Sr analysis of muscovite and whole rock of WD5c gives an age of 480.4 ±6.2 Ma. The age of WD5b is with 477.4 ±5.1 within the error of the age of WD5c. The initial $^{87}Sr/^{86}Sr$ ratios are high, suggesting derivation from or contamination with basement material.

Fig.24: Concordia diagrams of K-feldspar altered and original orthogneisses of two localities in the MPI. The zircon $^{206}Pb/^{207}Pb$ age distribution is similar in all samples of each locality.

Fig. 25: Zircon $^{207}Pb/^{206}Pb$ age of original and K-feldspar altered metagranites. A) The frequency distribution of zircon ages in little and elevated K-feldspar-altered orthogneiss (YG17b+c) resembles the distribution in pegmatitic K-feldspar metasomatites (YG17d). The samples were taken west of Paralana Hot Springs (see Fig.3E). B) The zircon population in original orthogneiss north of The Pinnacles (N17g) also resembles the population of the K-feldspar-altered variety (N17e: see Fig.3F bottom).

Fig.26: The initial $^{176}Hf/^{177}Hf$ isotopic compositions of original and K-feldspar-altered orthogneisses range within the spread of all analysed samples; without an evidence for a polymodal distribution.

Fig.27: A-C) Simplified model of the Palaeozoic exhumation of the Yankaninna Anticline along the Paralana Fault Zone and contemporaneous crustal-scale alteration. The alteration system can be divided into several levels in the crust that were crossed during exhumation. A) Trapped pore water released in the anticlinal core. A narrow zone of biotite-breakdown, alkali-metasomatism and brecciation developed. The breakdown of micas added additional available fluid. B) The zone of alteration increased with the rise of the anticline. Previously altered areas got overprinted by breccias (triangles). C) The amount of available fluid increased with the rise of the fold. A complex overprinting relation developed temporally and spatially in the alteration system. D+E) Summary of the fluid-rock interaction during the Palaeozoic

alteration in the MPI. The mineral reactions depend on temperature and pressure of the host rocks and fluids, as well as on structures and lithological characteristics.

TABLE CAPTIONS

Tab.1: Details on all samples taken for geochronology, geochemistry, oxygen isotope and fluid inclusion analyses.

Tab.2a: Electron microprope analyses of feldspar in various samples. Measurements were conducted at the University of Tübingen under the supervision of T. Wenzel.

Tab.2b: Electron microprope analyses of feldspar in various samples. Measurements were conducted at the University of Tübingen under the supervision of T. Wenzel.

Tab.2c: Electron microprope analyses of mica in various samples. Measurements were conducted at the University of Tübingen under the supervision of T. Wenzel.

Tab.2d: Electron microprope analyses of mica in various samples. Measurements were conducted at the University of Tübingen under the supervision of T. Wenzel.

Tab.3: Whole rock X-ray fluorescence analyses of various samples. Measurements were conducted at the University of Tübingen by H. Taubald.

Tab.4: Whole rock ICPOES analyses of various samples. Measurements were conducted at the University of Ghent under the supervision of M. Elburg.

Tab.5: Correlation matrix analyses of selected whole rock data. The statistical analyses were done under the supervision of A. Soessoo.

Tab.6: Fluid inclusion and microthermotetric analyses of various samples. Measurements were conducted at the University of Tübingen and Leoben under the supervision of R. Bakker.

Tab.7: Oxygen isotope analyses of various samples. Measurements were conducted at the University of Tübingen by H. Taubald.

Tab.8: Rb-Sr analyses of a pegmatitic and an altered aplitic sample. Measurements were conducted at the University of Tübingen by W. Siebel.

Tab.9: U-Pb analyses of various samples. Measurements were conducted at the University of Oslo by M. Elburg and T. Andersen.

Tab.10: Lu-Hf analyses of the samples taken for U-Pb studies. Measurements were conducted at the University of Oslo by M. Elburg and T. Andersen.

Tab.11: Summary of alteration reactions and their correlation to local geological events.

Fig.1:

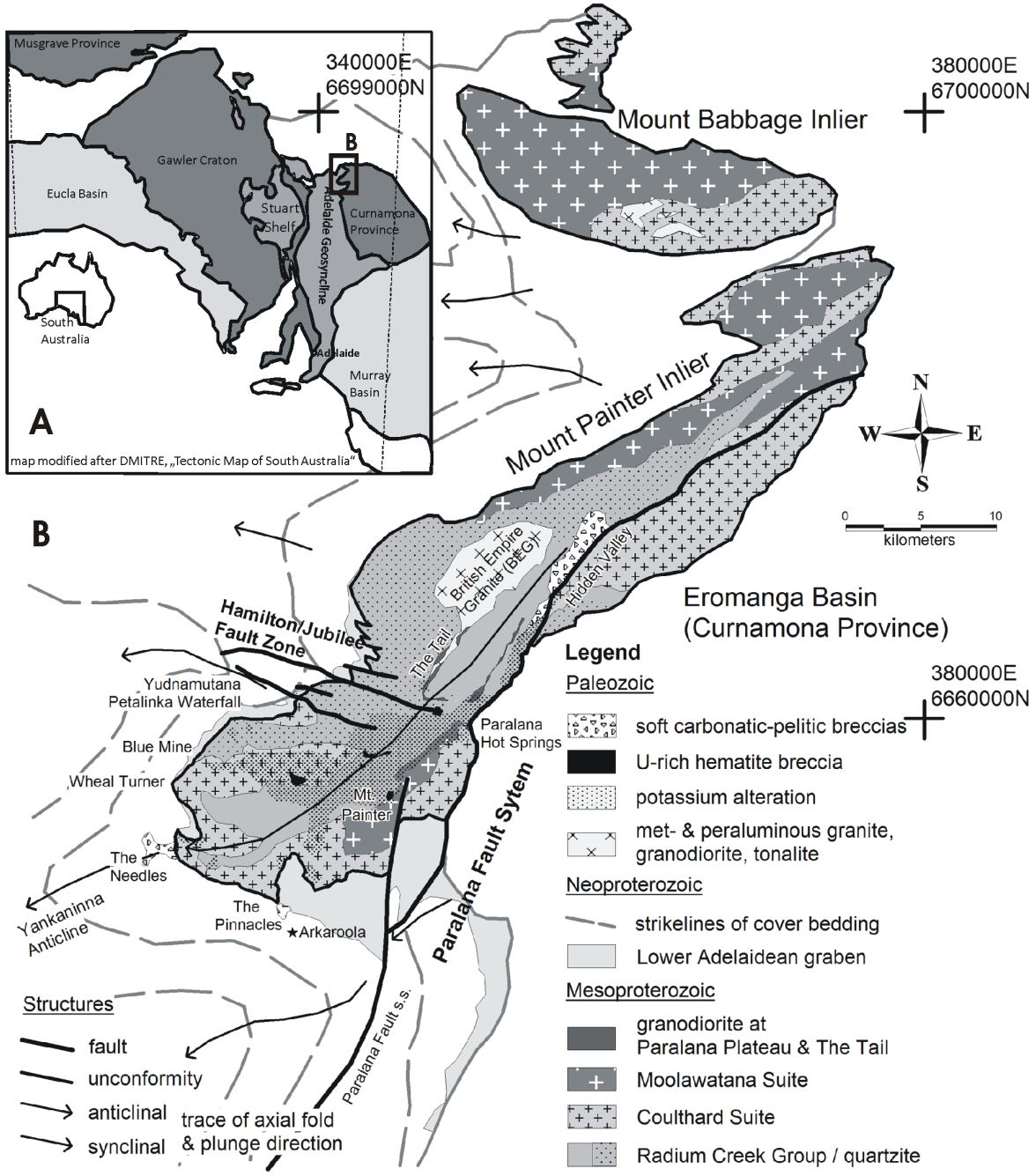

Fig.1: Geological map of South Australia and the Mount Painter Province. A) South Australia consists of three major craton blocks: the Musgrave Province, the Gawler Craton and the Curnamona Province. The Neoproterozoic Adelaide Fold and Thrust Belt developed between the latter two provinces that are partly covered by younger sedimentary basins (Eucla and Murray Basin). B) Multiply deformed Mesoproterozoic rocks of the Mount Painter Inlier (MPI) and the Neoproterozoic Adelaidean cover sediments are folded in 10 km-scale syn- and anticlines. Magmatic rocks intruded into the basement in Palaeozoic times. Potassium alteration, brecciation and vein formation affected ~60 km² of basement and cover rocks in the central and southern Mount Painter Inlier. Sheets of U-rich magnetite/hematite breccias developed within the K-feldspar altered zones. Large, weathered breccia zones crop out at fold hinges and fault zones. They include clasts of cover and basement units down to the µm-scale (Hidden Valley type breccias). The general map of the Mount Painter Inlier is adapted from Coats and Blissett (1971).

Fig.2:

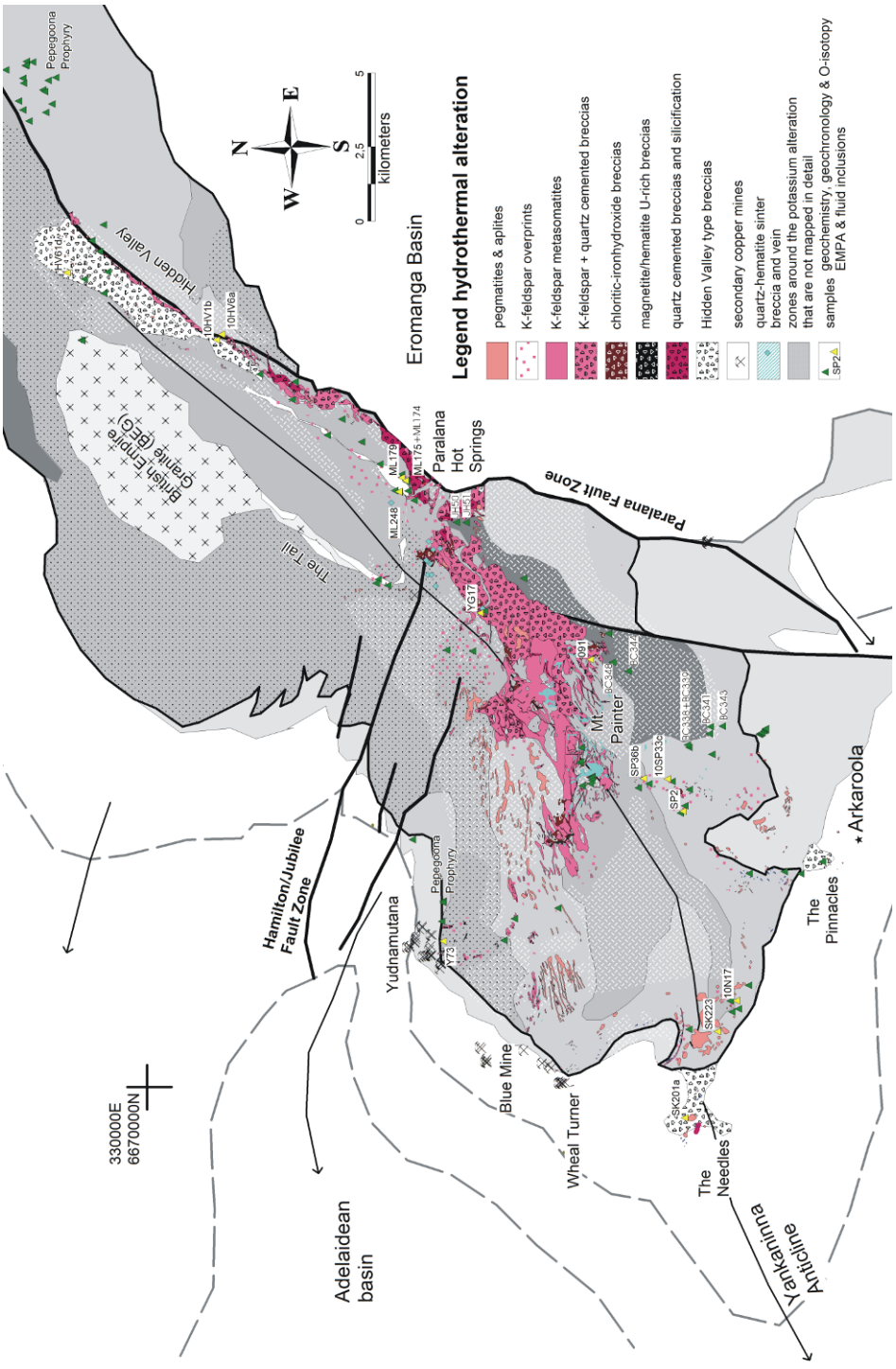

Fig.2: Detailed map of the alteration in the southern and central MPI, showing that the K-feldspar alteration fluid concentrated along structural fluid pathways (faults and fold hinges). Pegmatite intrusions are not spatially related to the K-feldspar alteration. Iron-rich breccias, quartz-cemented breccias (Radium Ridge Breccias; Drexel and Major, 1986) and secondary copper deposits in the Lower Adelaidean are interpreted to be related to late-stage K-feldspar-alteration fluids. Breccias and veins of a quartz-hematite sinter developed at the sub-surface, postdating the K-feldspar alteration. Host rock lithologies adapted after Fig.1.

Fig.3:

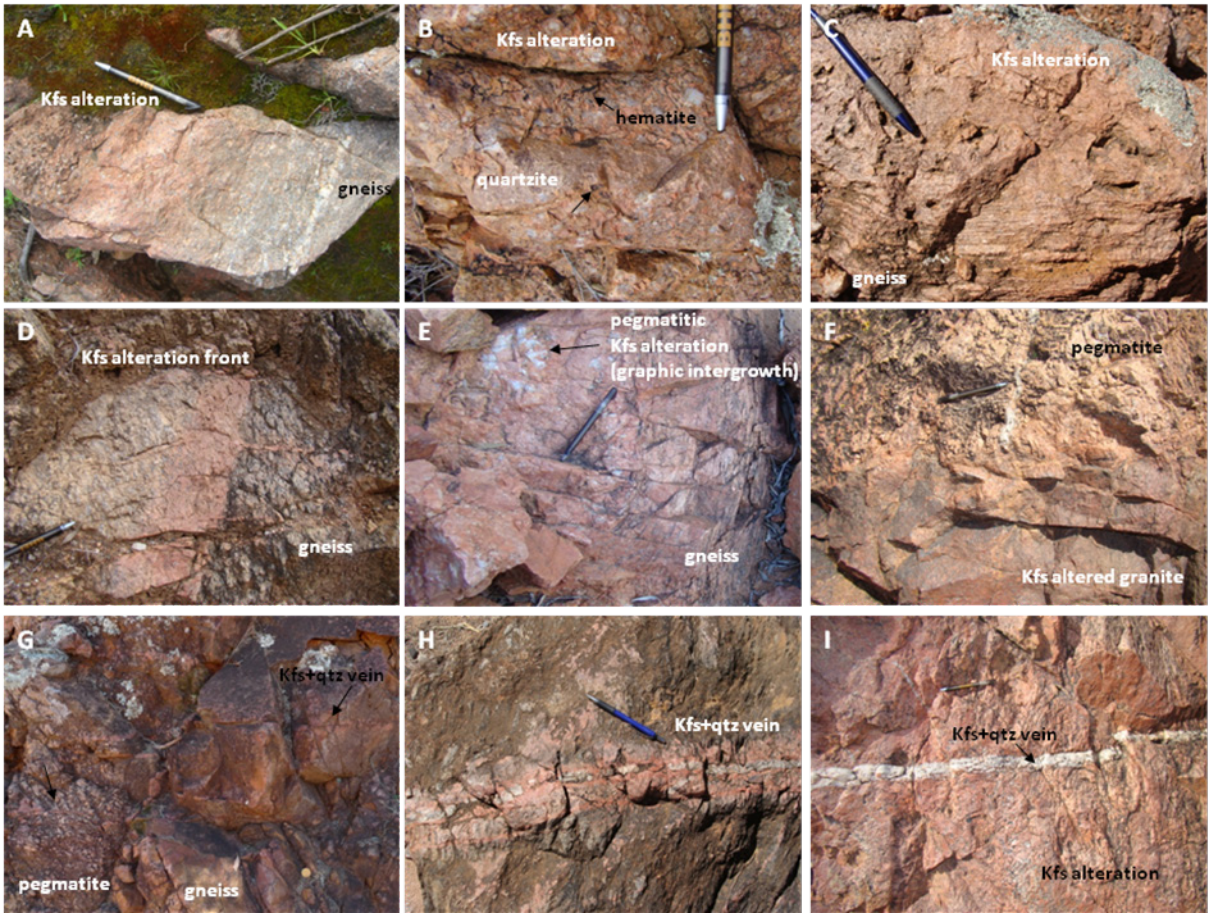

Fig.3: A) Gradual K-feldspar alteration of an orthogneiss with quartz-augen at the southern unconformity. The K-feldspar blasts overgrow the previous paragenesis. The quartz-augen remain and grow in the K-feldspar altered zone. B) Irregular intergrowth of K-feldspar and quartz impregnation in a quartzite of the lower Adelaidean sequence at The Needles. Potassium alteration is associated with hematite (arrows). C) The host rock loses its structures with increasing K-feldspar alteration. Micas break down and feldspars and quartz grow. This gneissic metapelite south of Mt. Painter gradually alters into a massive, pink K-feldspar and quartz metasomatite. D) Sometimes the K-feldspar alteration front is sharp indicating a barrier for fluid flow. This orthogneiss west of Paralana Hot Springs gradually loses its mafic minerals and the plagioclases. E) YG17: Pegmatitic textures often develop in the centre of the K-feldspar alteration with graphic intergrowth of quartz and feldspars (example of an altered orthogneiss west of Paralana Hot Springs). F) 10N17: An undeformed pegmatite north of The Pinnacles grades into massive K-feldspar-altered orthogneiss, whereas at G) a pegmatite is cut by K-feldspar + quartz veins (arrows). All field observations indicate that pegmatite intruded during the alteration. H+I) Impregnation of the host rock by K-feldspar alteration also occurs along discrete veins of quartz, K-feldspar, ± tourmaline and hematite. These veins often crosscut already K-feldspar-altered rocks.

Fig.4:

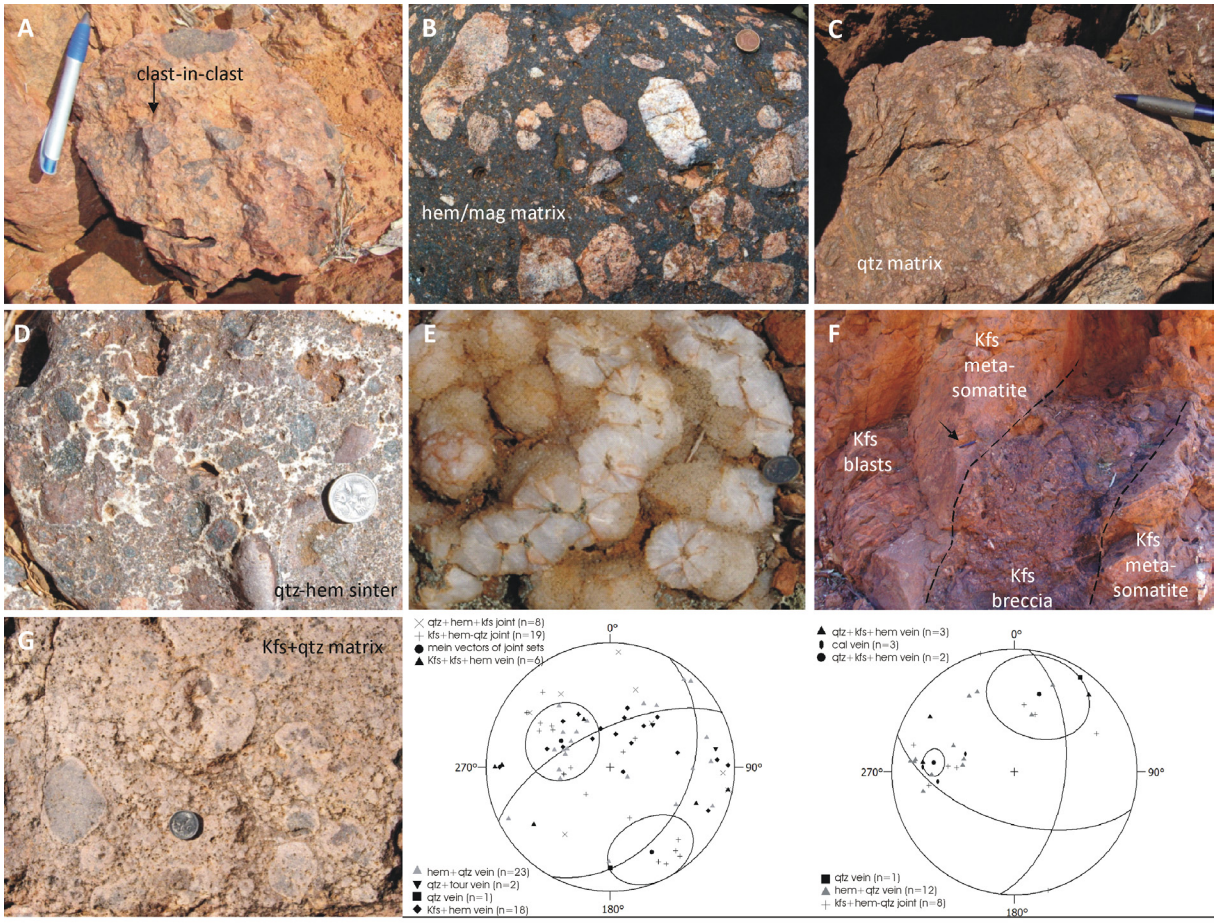

Fig.4: A) K-feldspar and quartz cemented breccia at the Paralana Fault Zone. Clasts in clasts indicate that these breccias post-date chloritic breccias (arrow; photograph taken at Hidden Valley). B) Magnetite/hematite cemented breccias often incorporate K-feldspar and quartz metasomatites and breccias (photograph taken north of Mt. Painter). C) Quartz-cemented breccia that forms steep ridges. It is associated with silicification of the host rock (photograph taken south of Mt. Painter). D) Typical outcrop of the sinter breccia at Mt. Painter with several generations of quartz and hematite. E) Nailhole quartz rosettes are characteristic for the Mt. Gee Sinter at Mt. Painter. F) Sample 091: A breccia with a K-feldspar, quartz and ±hematite cement cuts through a K-feldspar altered zone in a mica-rich paragneiss south-west of Paralana Hot Springs (pen for scale at arrow). The transition zones are well visible. G) K-feldspar-rich rims around quartzitic clasts in a K-feldspar- and quartz-cemented breccia (Radium Ridge Breccia) indicate that K-feldspar alteration of the clasts is still in progress during the brecciation. Photograph taken north of Mt. Painter. H) Stereoplot of pole-points of mineralised joints and veins in the southern MPI (mineral abbreviations from Kretz (1983)). The mean directions of the joints build a set that is almost perpendicular (pole points with standard deviation circle and mean great circle). The veins have a random distribution between N-S and E-W striking, indicating that joint- and vein formation occurred during several tectonic stress directions. I) Stereoplot of pole points of veins and joints in the eastern MPI at Paralana Hot Springs. The mean direction (pole points with black standard deviation circle and mean great circle) indicates that a set of joints formed during local NW-SE compression, whereas most veins opened during local N-S compression.

Fig.5:

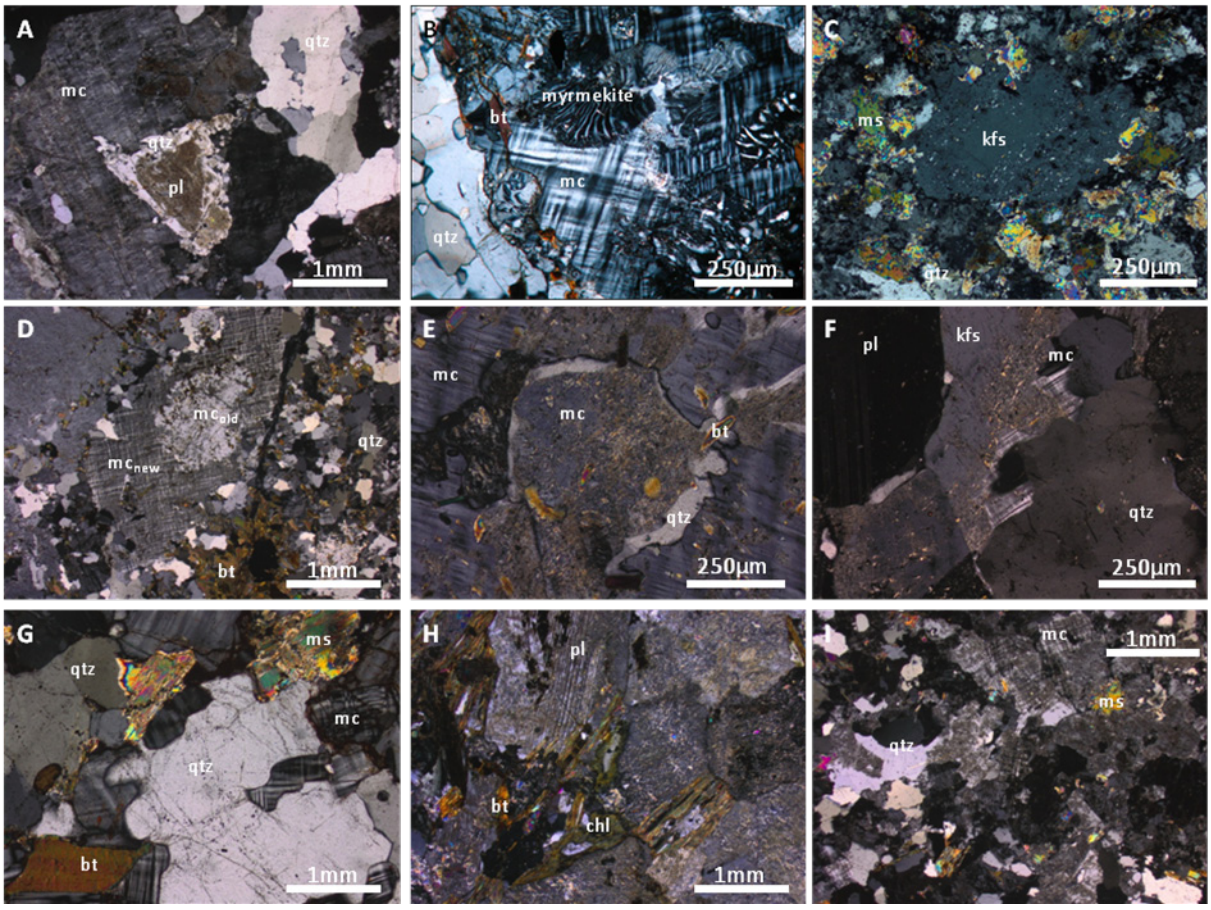

Fig.5: Microphotographs of K-feldspar-altered rocks with crossed polarisers. A) Sample BC348: Altered orthogneiss east of Mt. Painter. Original plagioclase crystals are rimmed by quartz and albites and included in large microclines. Albitisation occurred prior to microclinisation. B) Potassium-altered paragneiss west of Paralana Hot Springs. Myrmekite textures develop at contacts to new-grown K-feldspars. C) Original K-feldspar grew during K-feldspar alteration and developed an irregular rim, which is rich in inclusions (sample taken from meta-granite east of Mt. Painter). D) Sample Y52: Altered granite sample south of Yudnamutana. The original feldspars are rimmed by new-grown microcline that contains inclusions of the older minerals. Biotite is altered into iron-oxide-rich masses. E) Sample YG17a: Altered orthogneiss west of Paralana Hot Springs. New-grown K-feldspar has a reaction rim of quartz and inclusions of altered biotites. F) Sample YG17f: Same location as E). New microcline formed at the contact between quartz and original K-feldspar. G) Sample 091g: Growth of K-feldspar at grain boundaries during the recrystallisation of quartz and the breakdown of biotite (sample taken from an altered RCM east of Mt. Painter). H) Meta-sedimentary sample at Mt. Painter. Chloritisation of biotite occurs without K-feldspar alteration. Albite and K-feldspar are only affected by serizitisation. I) Most altered rocks only consist of microcline and quartz and relicts of micas (sample taken south of Mt. Painter). Mineral abbreviations from Kretz (1983).

Fig.6:

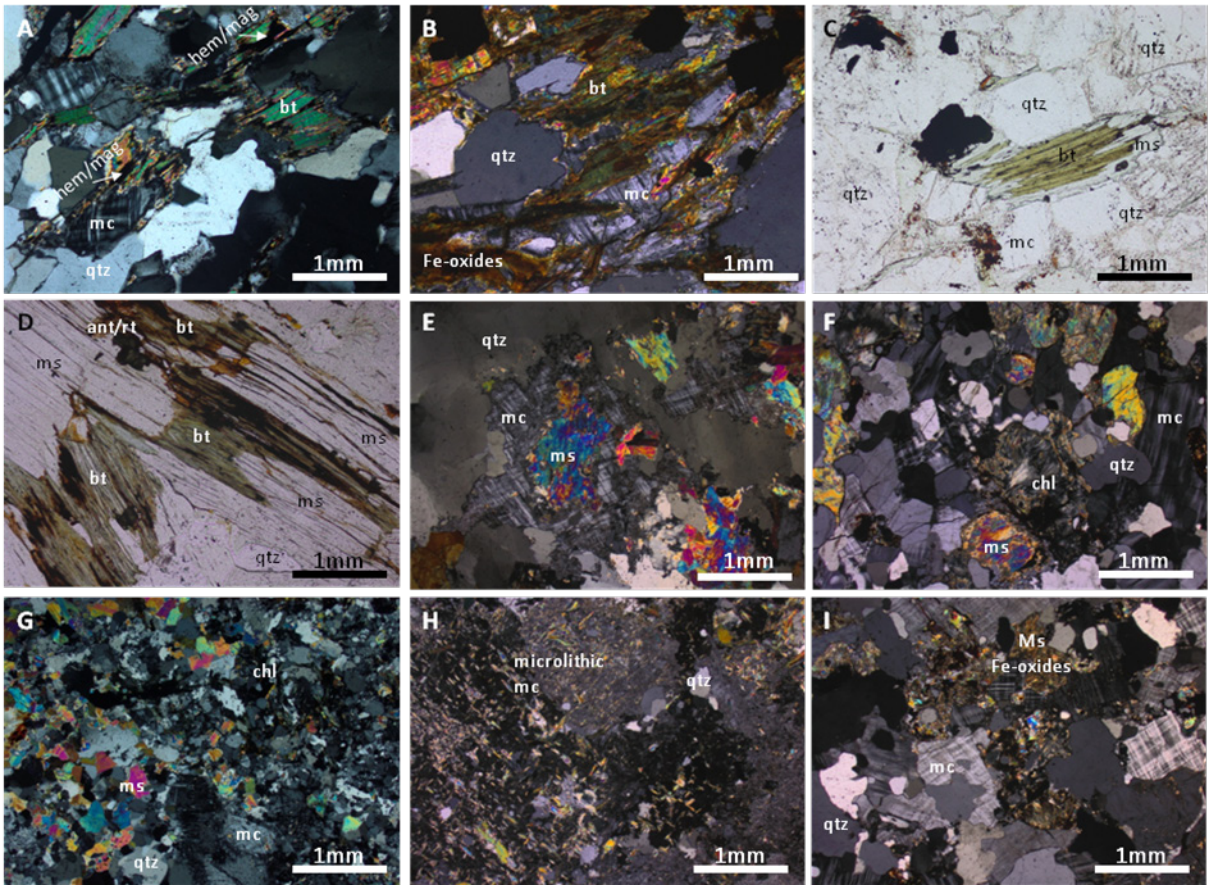

Fig.6: Microphotographs of K-feldspar-altered rocks with crossed and parallel polarisers. A) Altered metapelite at Mt. Painter. Biotite alters pseudomorphically into microcline and iron oxide. B) K-feldspar altered granite south of Mt. Painter. Biotite alters into microcline and iron-oxide. C) Sample SK080a: Potassium-altered meta-granite east of The Needles. Clearly visible is the breakdown of biotite into muscovite that grew pseudomorphically. D) Sample SP2: Biotite in a meta-sediment south of Mt. Painter alters into muscovite and iron-oxides at the contact to new-grown microcline. E) Sample SP2: Potassium-altered meta-granite south of Mt. Painter. Original biotite totally altered into muscovite, which is altered into microcline with irregular contacts to the surrounding quartz. F) Sample 091b: Metasomatised meta-sediment east of Mt. Painter. Biotite alters into muscovite, chlorite and iron-oxide. New-grown microclines are present in the whole thin section. Microcline and the altered biotite grow around recrystallised quartz. G) Totally altered granite east of Wheal Turner. Biotite reacted to muscovite or chlorite. Whether microcline also grew from biotite is not clear. Subhedral grains of magnetite formed in the sample. H) Feldspars in a meta-granite at Mt. Painter partly weathered into sericite. I) Sample 091d: Totally altered meta-sediment east of Mt. Painter. Microcline overgrows the previous texture with lobate contact to the recrystallised quartz, but with equilibration contact to other microcline grains. The original mica altered into a mass of muscovite and iron-oxides, which grows above the previous texture.

Fig.7:

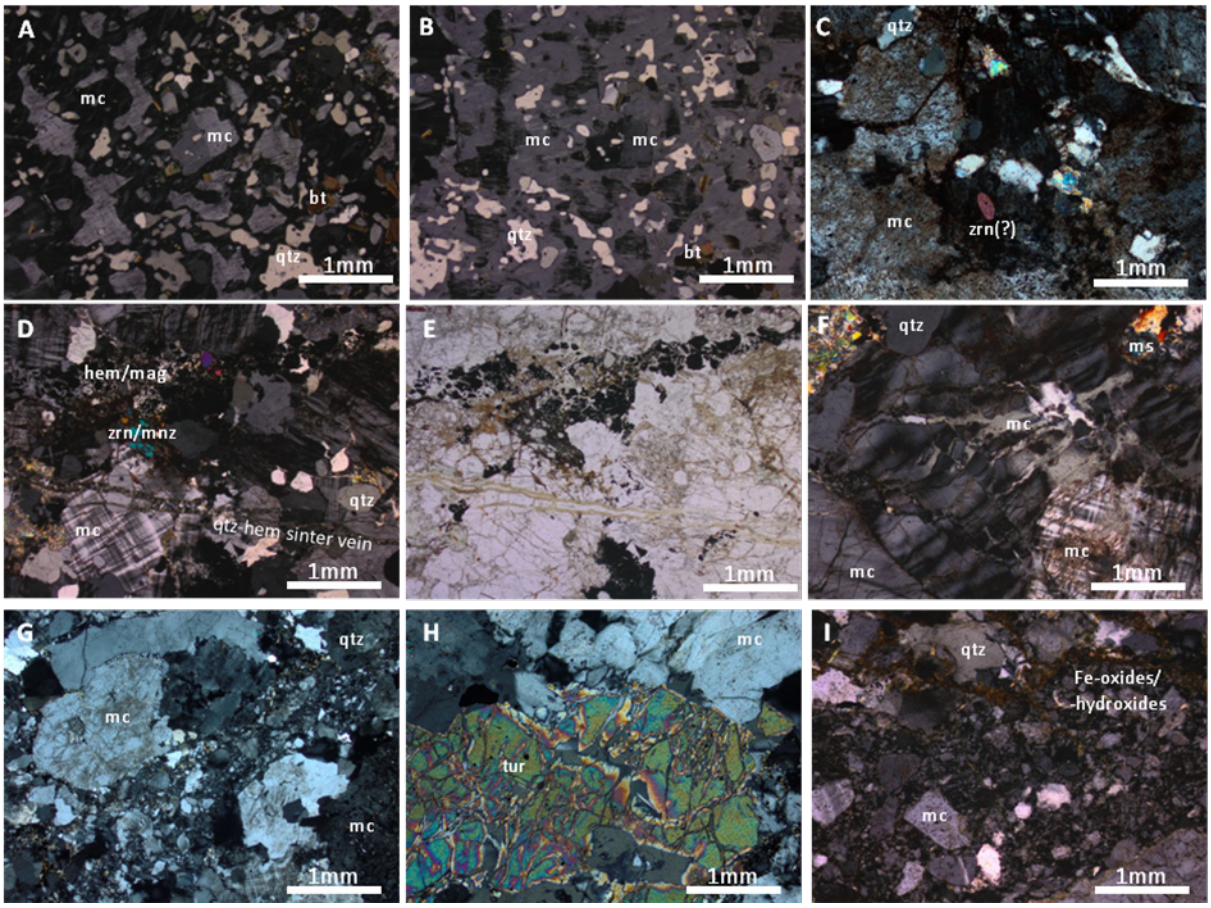

Fig.7: Microphotographs of K-feldspar-altered rocks with crossed polarisers. A) Potassium-altered meta-granite southwest of Mt. Painter. Several mm-sized microcline crystals inter-grow and over-grow the previous texture with a skeleton shape. B) Same image section as in A) but the sample is rotated to 90°. C) Thoroughly altered meta-sediment west of Mt. Painter. Iron-hydroxide and -oxide are disseminated in the sample that consists of hydrothermal microcline and quartz with relicts of micas. Zircon/apatite crystals seem to be unaffected by the extensive alteration. D+E) Sample 091d: Totally altered meta-sediment east of Mt. Painter. Iron-oxide minerals are brecciated and included as angular clasts in a K-feldspar cemented breccia zone. Zircon and monazite are also brecciated. The sample is cut by a quartz-hematite vein, likely related to the quartz-hematite sinter. F) Sample 091d: Totally altered meta-sediment east of Mt. Painter. Metasomatic microcline brecciated during fluid-focusing and was cemented by new microcline. G) K-feldspar-altered biotite-rich gneiss at Mt. Painter. The metasomatic K-feldspar and quartz texture is brecciated and cemented by K-feldspar. Tourmaline grew prior to the K-feldspar brecciation (H). I) K-feldspar-cemented breccia west of Paralana Hot Springs. Fluids with iron-hydroxides and -oxides used the same pathways and caused further brecciation after the K-feldspar alteration and brecciation.

Fig.8:

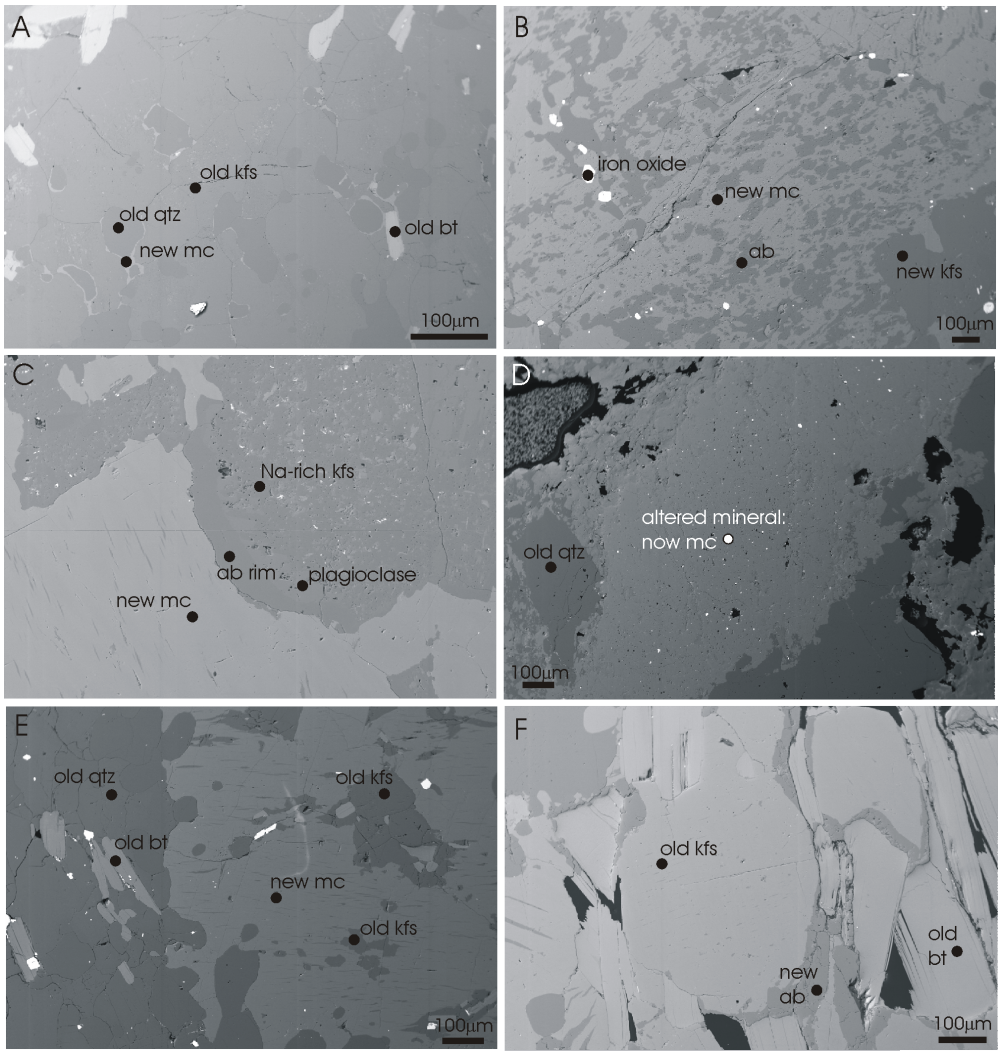

Fig.8: Back-scattered electron images from K-feldspar altered rocks. A) Sample YG17c: Potassium alteration is generally expressed by the growth of almost pure microcline. In this sample microcline only grows in small rims at the contact between original feldspars and quartz. B) Sample 10N17e: Complex intergrowths between albite and microcline that grew during the K-feldspar alteration. C) Sample ML248a: Plagioclase alters into sodium-rich alkali feldspar at the contact to new-grown microcline. A rim of albite formed around the altered plagioclase. D) Sample YG17d: An unknown mineral totally altered into porous microcline. E) Sample 10N17e: Hydrothermal microcline overgrows previous textures, resulting in inclusion-rich cm-scale blasts. F) Sample YG17c: Almost pure albite grows along grain boundaries of the original texture.

Fig.9:

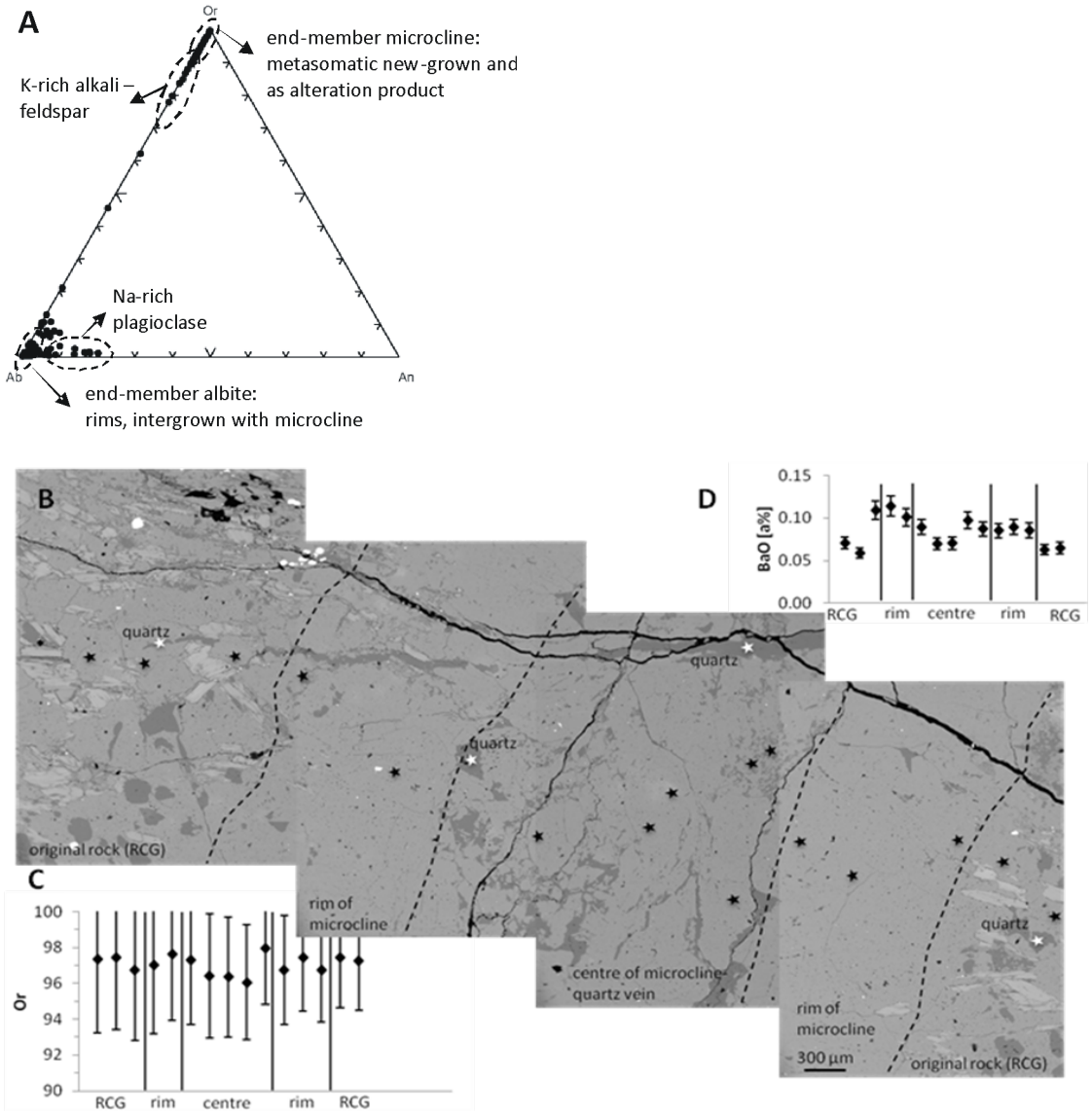

Fig.9: A) The measured feldspars (n=243) in altered rocks can be divided in four groups: (1) Microcline and (2) albite end-members that formed as new-grown blasts and alteration product of former feldspar. Albite is often intergrown with microcline and occurs in rims around older feldspar. (3) K-rich alkali feldspar and (4) Na-rich plagioclase often occur in the centre of veins and broad alteration zones. B-D) Sample SP36b: Profile through a microcline-quartz vein with a rim of microcline within a biotite-rich meta-sediment (back scattered electron image). There is no significant enrichment or depletion of oxides through the profile. All measured microclines are of an almost end-member composition. Only the BaO content slightly increases in rim and centre feldspar.

Fig.10:

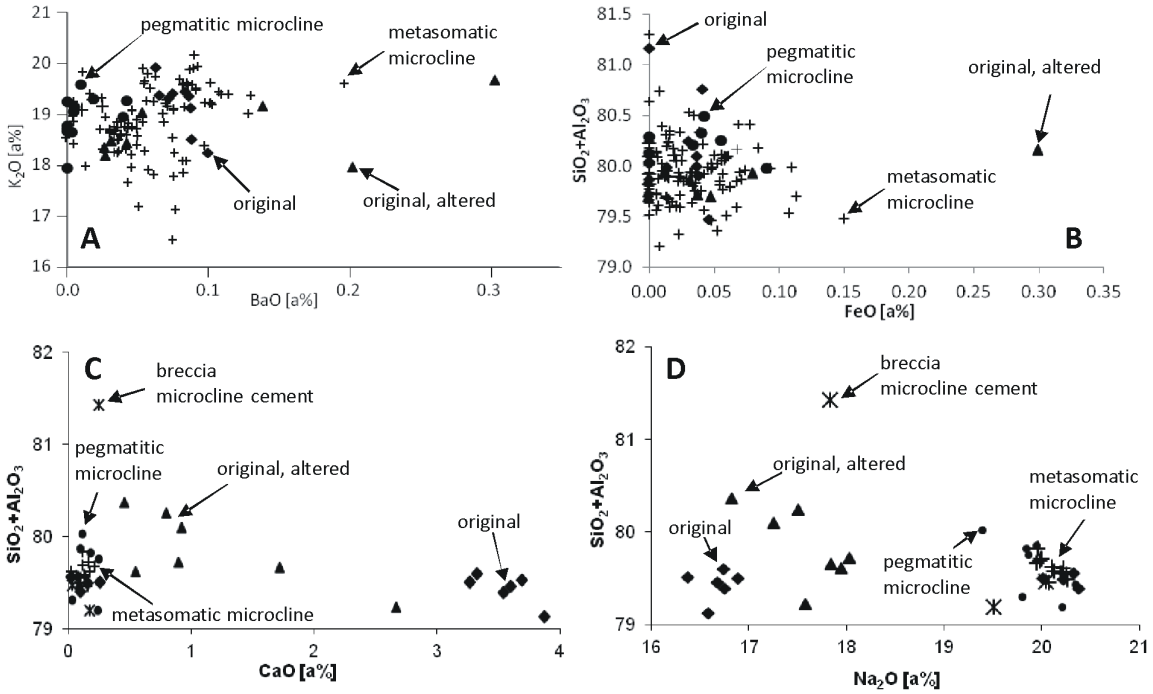

Fig.10: Variation diagrams of original (diamond), altered (triangle), new metasomatic (plus), new pegmatitic (circle) and breccia cement (star) microcline. A) The BaO content in microcline of altered and non-altered samples is independent from the K content, indicating disequilibrium and multiple overprinting. B) There is no distinct geochemical trend in the measured elements of all microclines. For example a plot of SiO_2+Al_2O_3 vs. FeO gives only a scattered signal. C+D) Sample YG17 (K-feldspar-altered orthogneiss) shows a trend to an end-member composition from original to new-grown albite.

Fig.11:

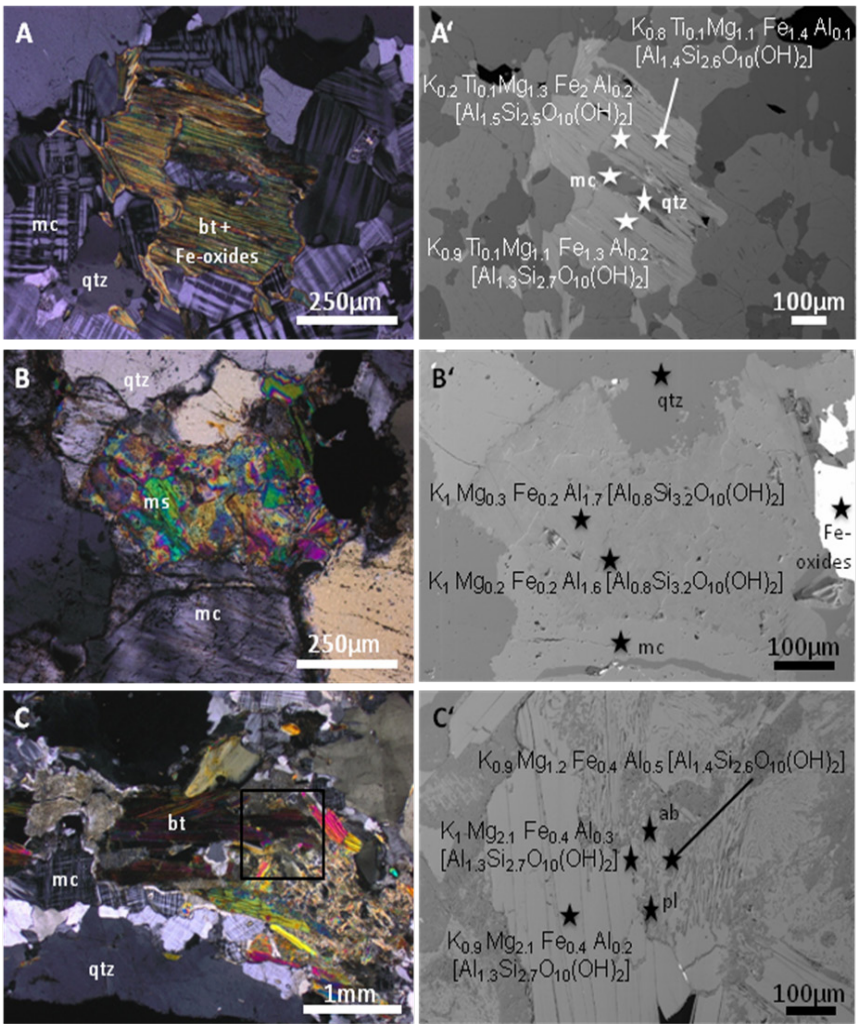

Fig.11: Microphotographs with crossed polarisers and back scattered electron images of K-feldspar altered samples. A+A') Sample ML248a: Potassium altered gneiss with remnants of original mica. The altered mica is now rich in magnesium, iron and aluminium and has inclusions of quartz and hydrothermal microcline. B+B') Sample 091e: Biotite in contact to new-grown microcline alters into muscovite with magnesium and iron. C+C') Sample YG17a: Sampling profile through an altered orthogneiss with transition from original into altered mica. The mica is altered into a phlogopite-like composition and developed a complex intergrowth between hydrothermal plagioclase.

Fig.12:

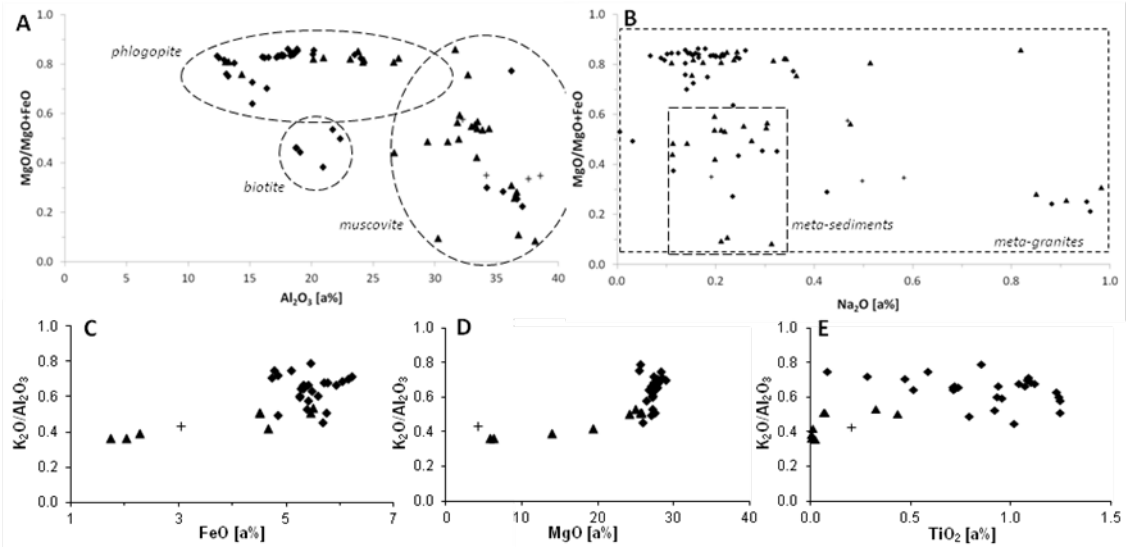

Fig.12: Variation diagrams of original (diamond), altered (triangle) and new metasomatic (plus) mica. A) The composition of all measured mica range between phlogopitic, more Fe-rich biotite and muscovite. These compositions are independent from the grouping into original, altered or new-grown metasomatic mica. The enrichment of MgO and Al_2O_3 in the phlogopite signals suggests that these minerals are already alteration products. B) Original and altered mica of the meta-igneous rocks overlap with the mica-signals in the meta-sediment samples. No general enrichment or depletion of elements is traceable. C-E) Only a profile through a K-feldspar alteration zone of sample YG17 shows a decrease of K_2O/Al_2O_3 (alteration index), MgO and FeO with increasing alteration of the mica. The TiO_2 content in these samples decreases slightly.

Fig.13:

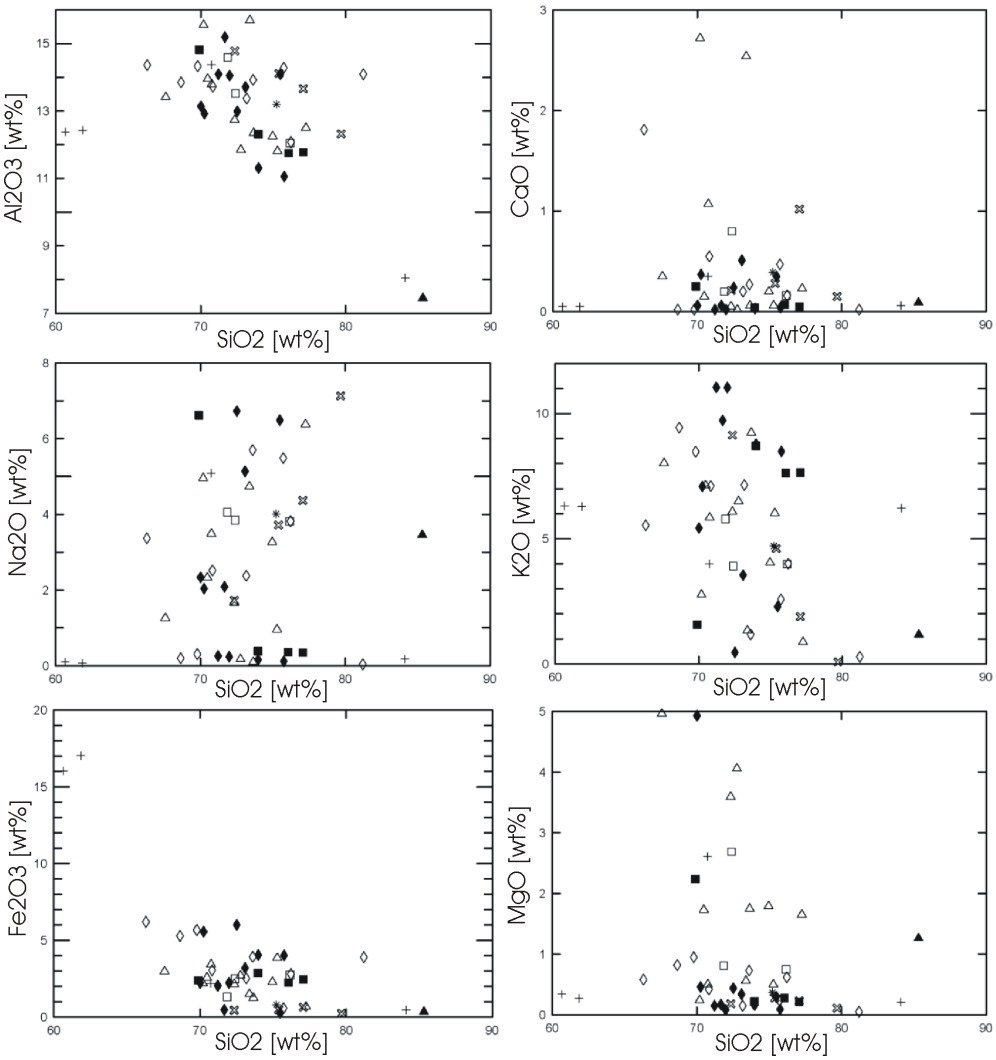

Fig.13: Harker variation diagrams that show the relation of unaltered host rocks and their alteration products (filled symbols: metasediments; open symbols: granitoids). Triangle: host rock; square: K-feldspar overprinted rocks; diamond: K-feldspar metasomatites; plus: K-feldspar cemented breccias; star: pegmatitic K-feldspar centres; open cross: K-feldspar altered clasts or pegmatites in Hidden Valley breccia. The composition of the rocks overlaps in all measured components and differences in the composition of altered metasediments or granites is not distinct. Only the MgO-content in K-feldspar altered rocks trend to low values.

Fig.14:

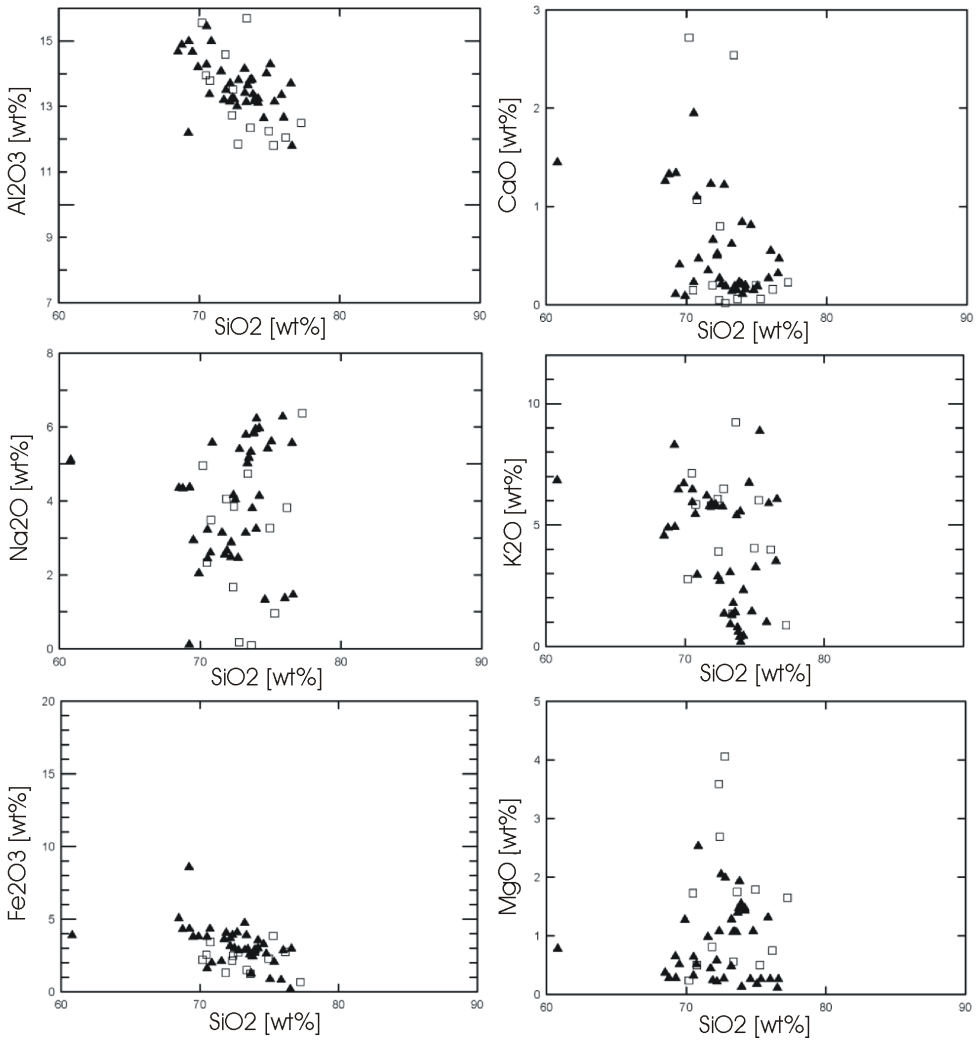

Fig.14: Harker variation diagrams of the measured A-type granitoid host rocks (open squares) and samples of A-type granitoids in the MPI that are published in literature (filled triangles). The range in their compositions is similar. Published samples from Elburg et al. (2013), Neumann (2001) and Wülser (2009).

Fig.15:

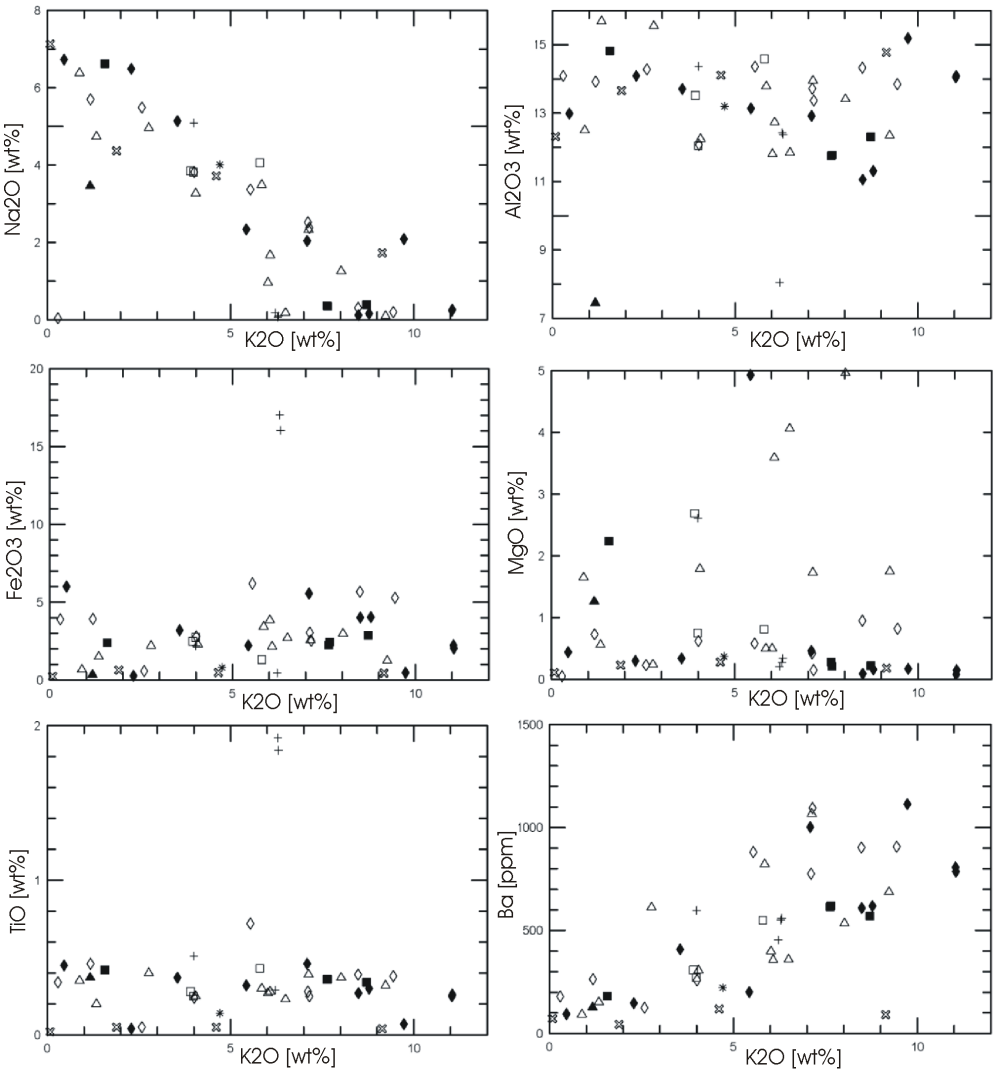

Fig.15: Plots of various geochemical components against K_2O. There is no significant variation between the geochemical composition of host rocks and K-feldspar altered rocks. A negative trend between Na_2O and K_2O and a positive between BaO and K_2O indicate that microclinisation and albitisation affected the rocks. Symbols as in Fig.13.

Fig.16:

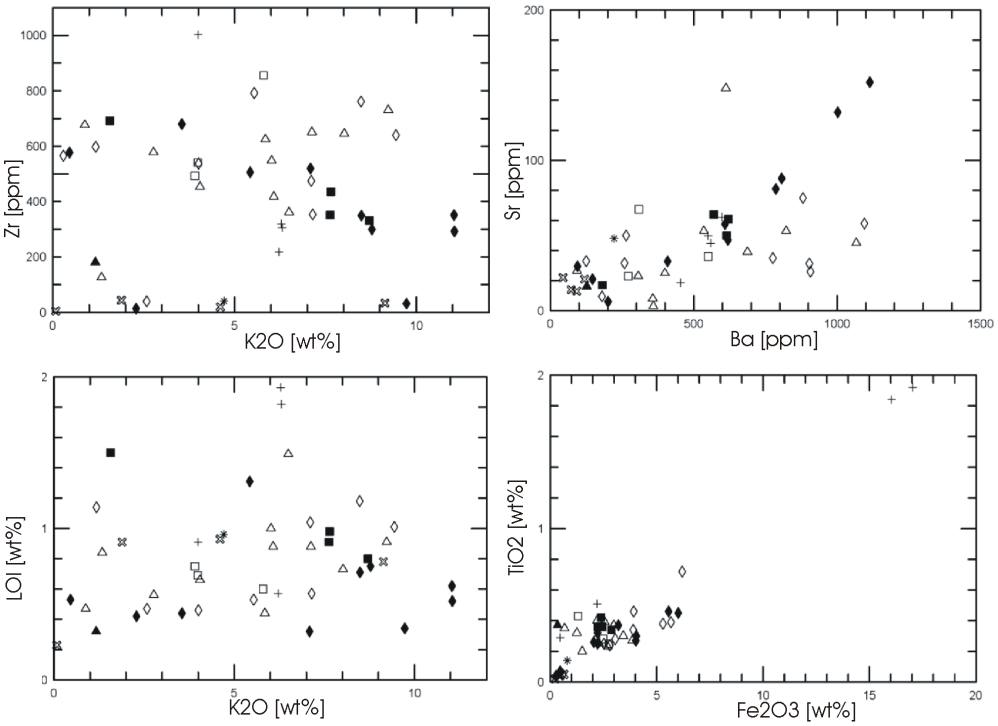

Fig.16: Plots of various geochemical components of host rocks and alteration products. The correlation between Sr-Ba is related to the modal abundance of K-feldspar while the correlation of TiO_2-Fe_2O_3 reflects the abundance of iron-titanium-oxides, biotite and/or titanite. There are no differences between altered and original rocks. Symbols as in Fig.13.

Fig.17:

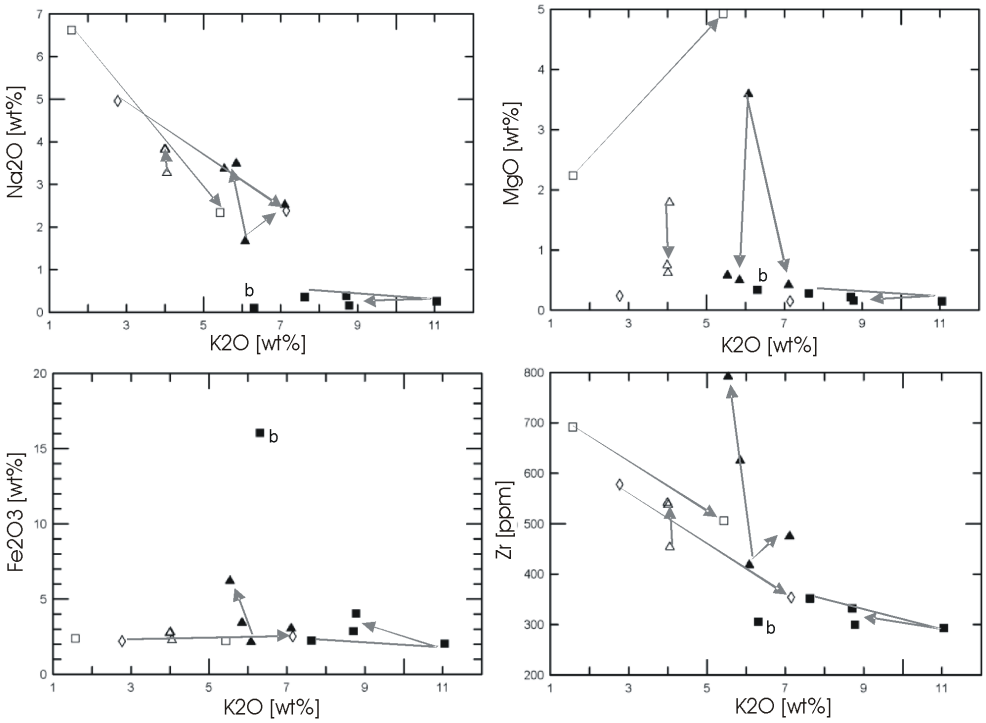

Fig.17: Plots of various geochemical components against K_2O of samples from profiles through alteration transitions at 5 outcrops. Grey arrows point from host rock to the most altered sample. The MgO-content slightly decreases at the transition from an albitised A-type granite at locality 10N17 (open triangle), while no other clear trends at this locality are visible. Na_2O, Fe_2O_3 and Zr slightly increase during alteration of an A-type granite at locality BC338-343, while MgO decreases (filled triangle). An alteration of orthogneisses at outcrop YG17 resulted in a decrease of Na_2O and an increase in MgO (open square). A transition from a meta-sediment into K-feldspar cemented breccias at outcrop 091 shows no variation in the composition (filled square). The high Fe_2O_3 content in the breccia b derives from abundant iron-oxides in the sample. The samples BC344+348 (open diamond) record a slight decrease in Na_2O during the alteration of the A-type granite.

Fig.18:

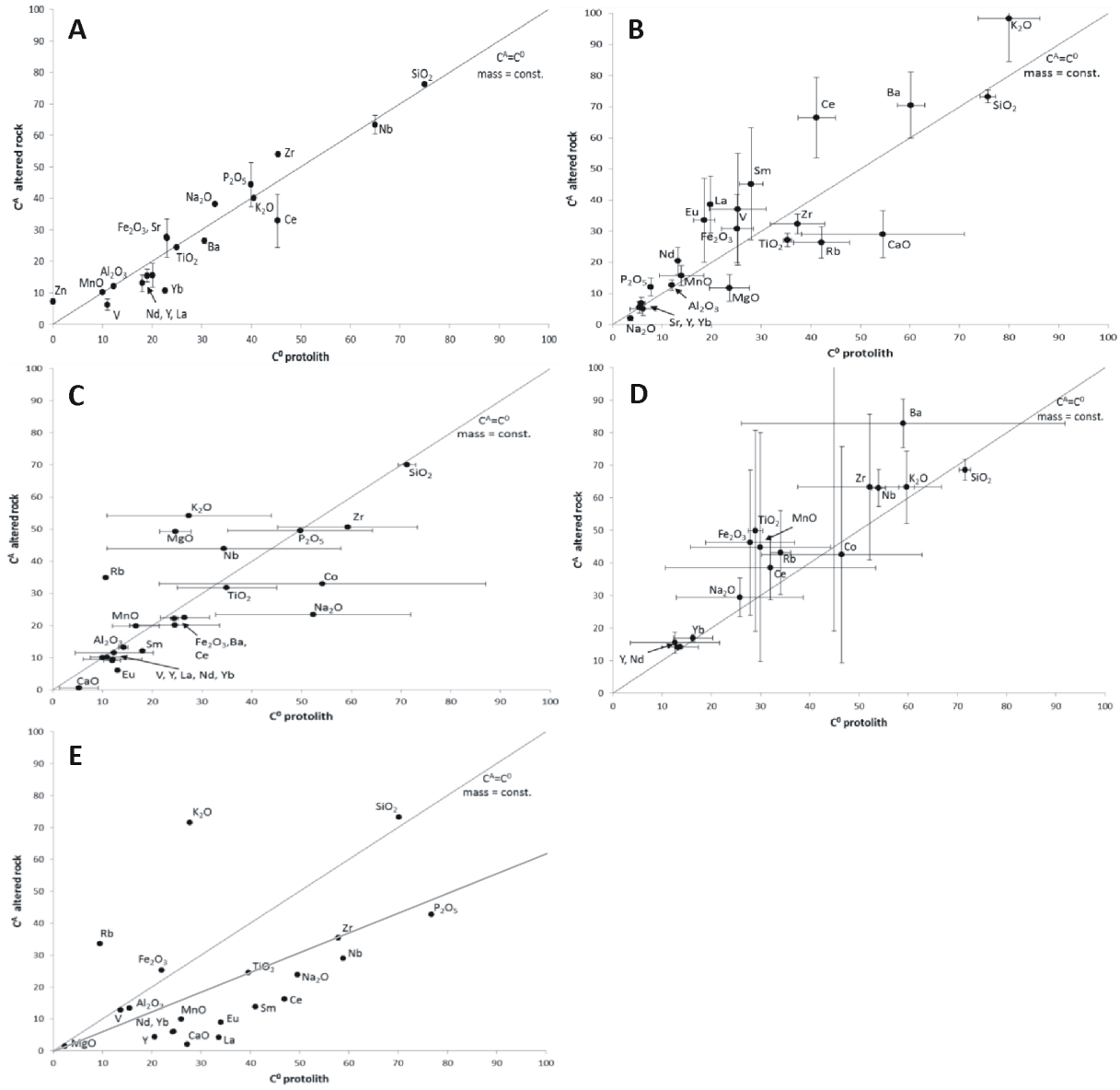

Fig.18: Isocon diagram of altered rock plotted against the protolith. Data points that include negative values are removed from the diagram. A) Isocon diagram of the mean of two altered samples against the albitised host rock at 10N17. Ba and REE are depleted, while Zr and Na_2O slightly increased. B) Plot of the mean signal of four alteration products against that of three protoliths at locality 091. Gains and losses of various components are well visible. C) One alteration product is plotted against two protolith samples of location YG17. The high scatter suggests multiple overprinting. D) A plot of samples 341 and 343 against samples 339 and 338 results in a large scatter. E) Plot of sample 348 against 344. K_2O and Rb are enriched, while most other components decrease. An increase in iron and the microclinisation of the altered sample is best expressed with an isocon line through the immobile zircon.

Fig.19:

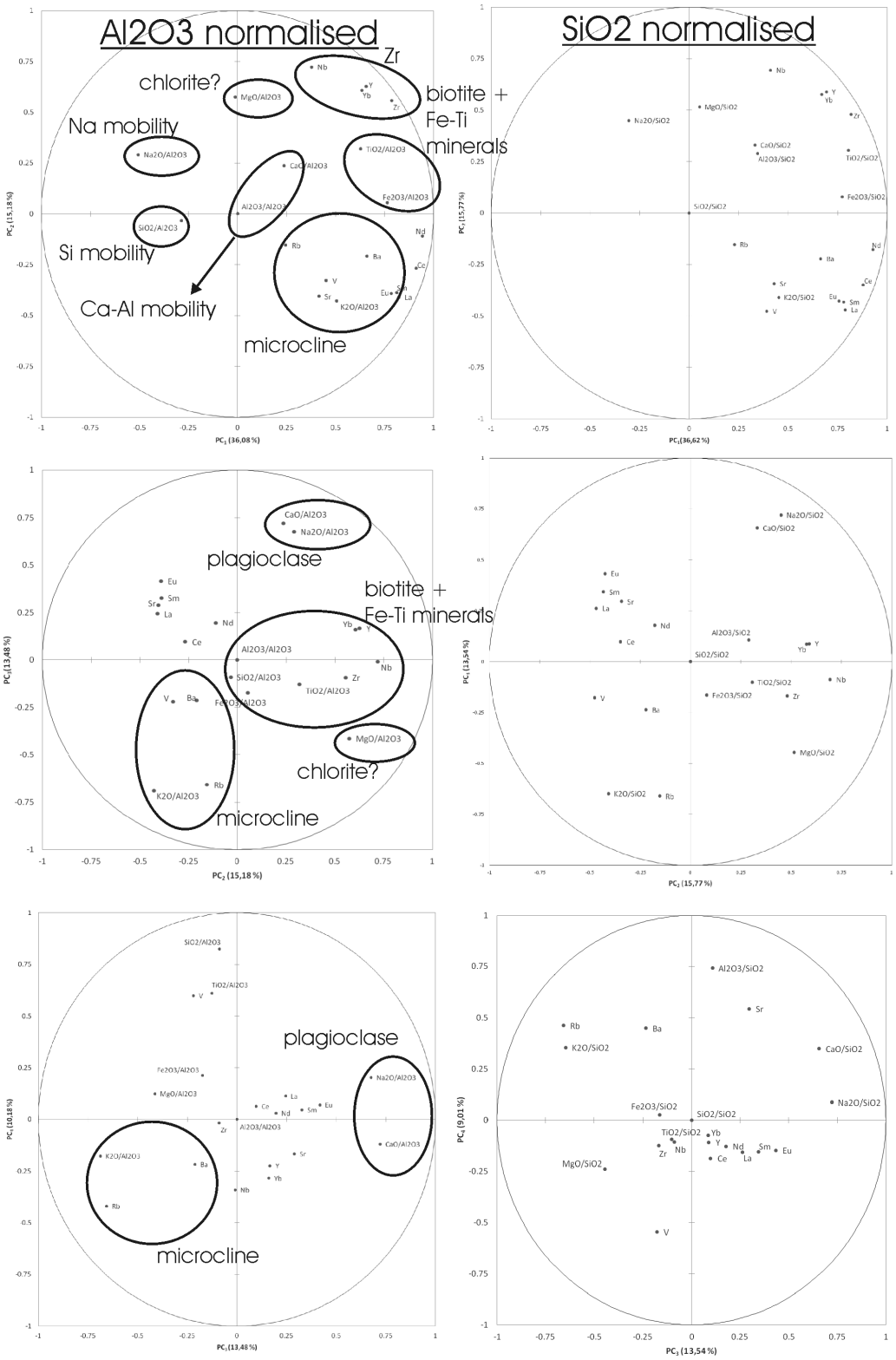

Fig.19: Plots of various principle components that derive from correlation matrix of host rock and alteration product. Normalisation was done to SiO_2 or Al_2O_3. A) Plot of PC_1-PC_2 with clusters of components related to microcline, biotite and iron-titanium minerals and possible chlorite. B) Plot of PC_2-PC_3. Microcline and plagioclase have a negative correlation possibly related to microclinisation and plagioclase-breakdown. Iron and REE mobility may be related to biotite-breakdown and iron-titanium ores. C) A plot of PC_3-PC_4 also highlights the negative correlation between microcline and plagioclase.

Fig.20:

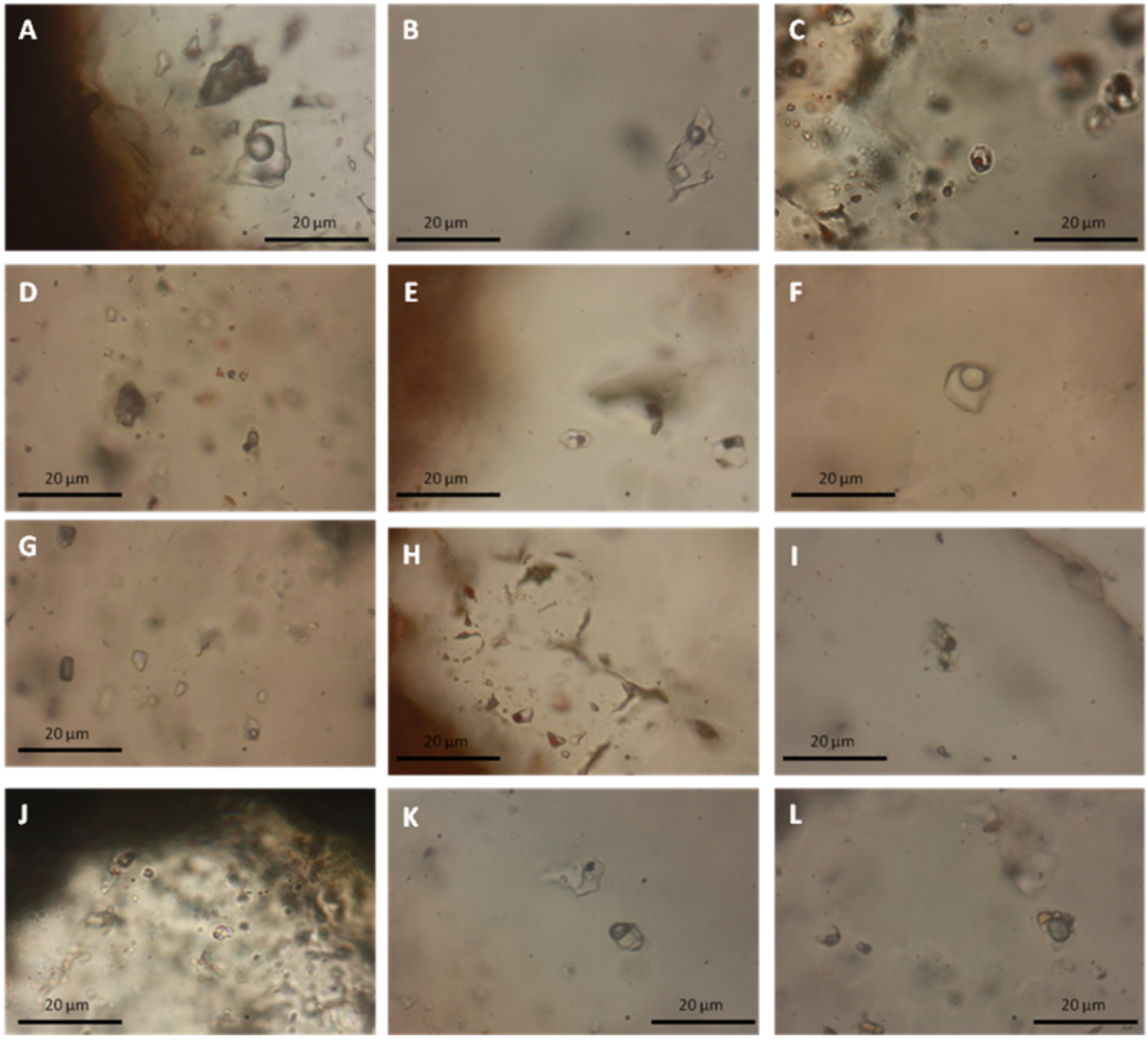

Fig.20: Microphotographs of fluid inclusions in quartzes of the RCG-sample SP2 that is cut by a K-feldspar-quartz and tourmaline vein with a rim of microclinisation. The sample was collected south of Mt. Painter. A) Large, angular fluid inclusions with a single phase or a liquid (L) and vapor (V) phase in an original quartz-auge. B) A single, irregular fluid inclusion with L+V and a halite crystal (solid S) in RCG quartz. C) Trail of rounded inclusions with L+V and a trapped hematite crystal (S) in original quartz. D) Single fluid inclusions with L+V and 2-3 solid phases in a quartz in the microcline zone. E) L+V and two solid phases (halite and hematite) in an elongated single fluid inclusion in the microcline zone. F) Single, rounded L+V inclusion in microcline zone. G) A cluster of rounded, single-phase inclusions, occasionally with a vapor phase in the microcline zone. H) Complex cluster with single phase fluid inclusions that often include trapped hematite in a quartz surrounded by tourmaline. I) Complex fluid inclusion with several solid phases, V and L in the same quartz as in H). J) Halite crystal in a L+V+S fluid inclusion in a quartz within a tourmaline. K) Several cubic crystals in a L+V+S fluid inclusion in a quartz that is inter-grown with tourmaline. L) Single fluid inclusions occur in the same quartz as K) with 4-5 solid phases with L+V.

Fig.21:

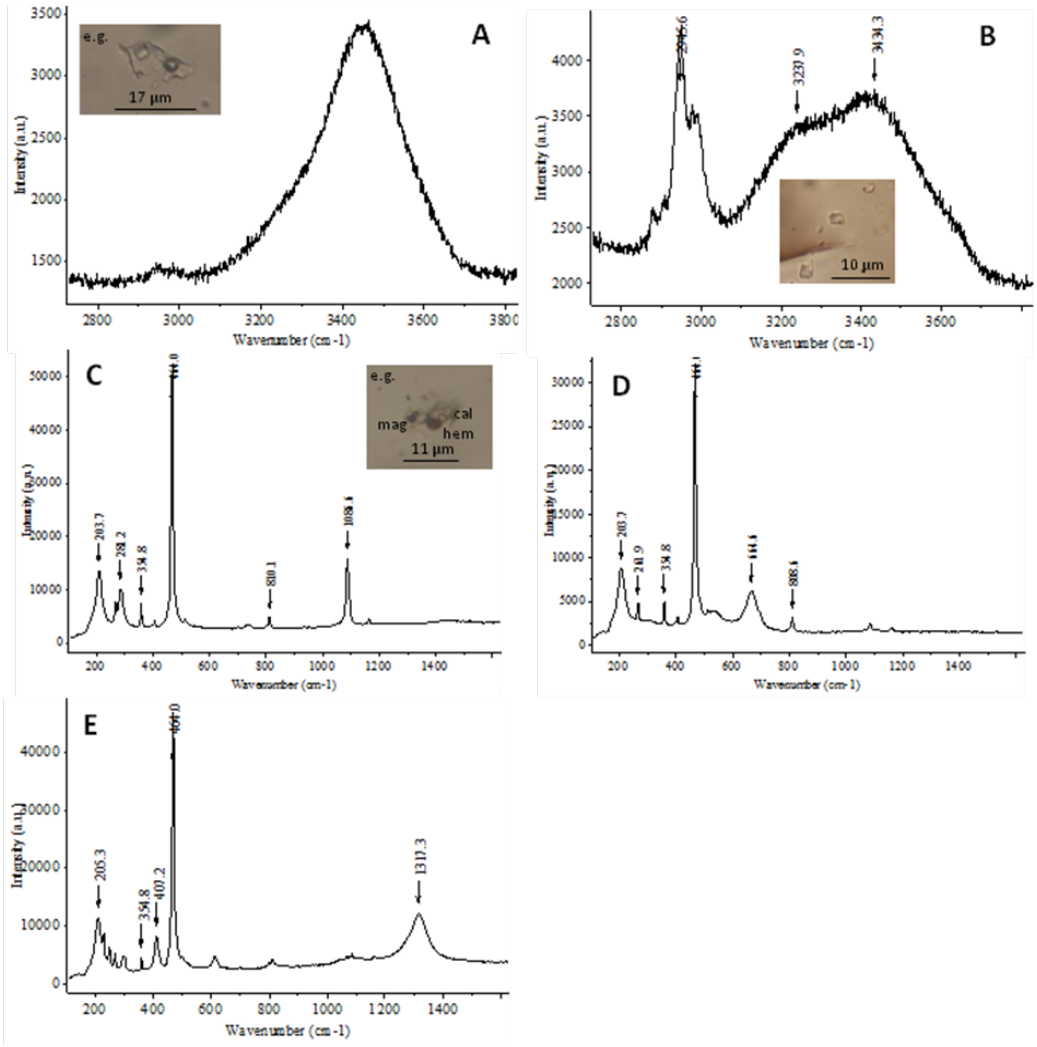

Fig.21: Raman-signals of liquids and solids in different fluid inclusions in sample SP2. A) A discrete peak at ~3440 cm^{-1} derives from a concentrated brine, while in B) no salts are dissolved in the liquid phase and the distinct H_2O-signal developed. Calcite (C), magnetite (D) and hematite (E) could be analysed during measurements of the solid phases. Peaks at ~204, 354 and at 464 cm^{-1} correspond to the background signal of quartz.

Fig.22:

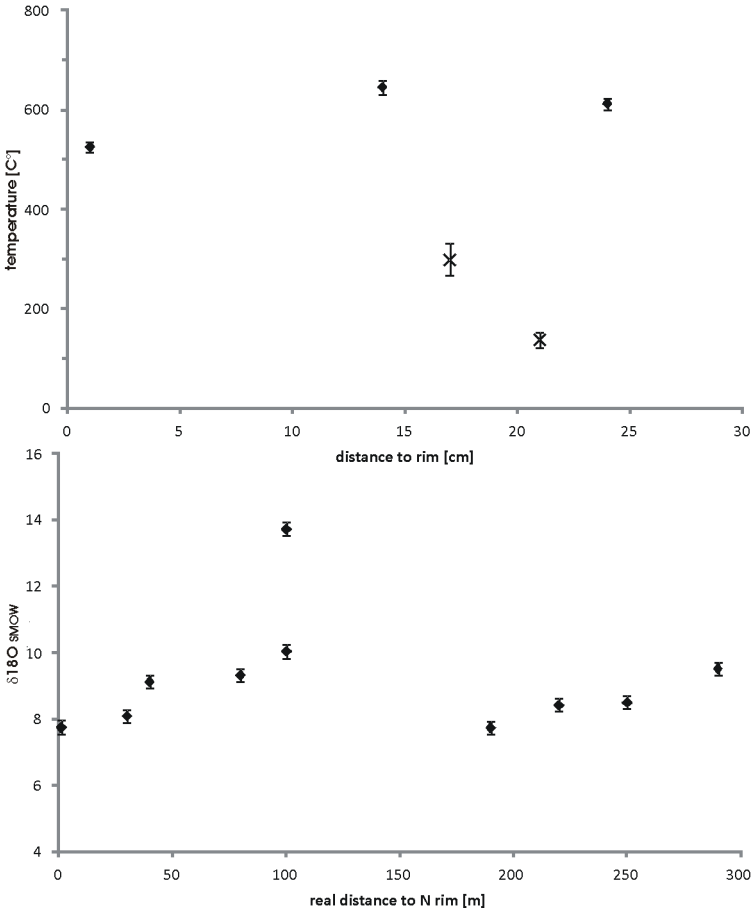

Fig. 22: Results of oxygen isotope measurements in a quartz, K-feldspar and hematite vein at Petalinka Waterfall in cover quartzites at Yudnamutana mine (A) and in a zone of deformed pure quartz veins close to the contact of basement and cover north of Arkaroola (B). A) The temperature range of quartz-hematite and quartz-K-feldspar pairs in the vein at Petalinka Waterfall varies between ~ 650 to 140 °C, independent from the distance to the wall. B) The $\delta^{18}O$ values of multiple ENE-WSW trending quartz veins that pre-date the Palaeozoic deformation vary between 7.7 and 10 ‰ with one exception of 13.7 ‰. The samples were taken perpendicular to the strike of the veins.

Fig.23:

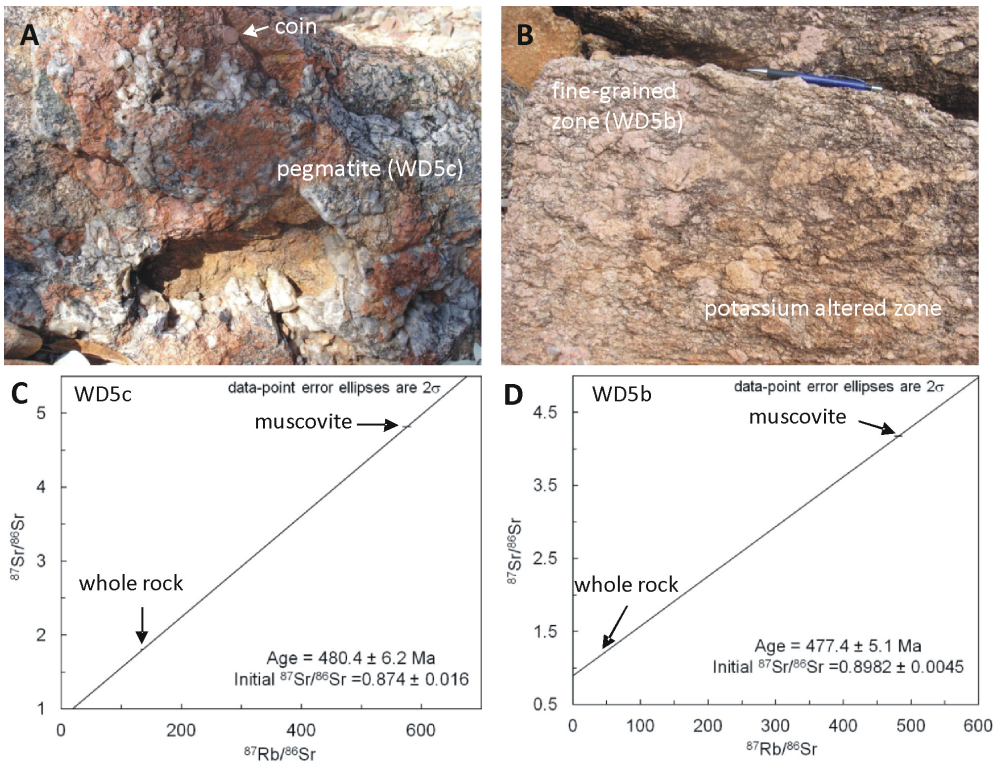

Fig. 23: Sample location and Rb-Sr results of outcrop WD5b and WD5c. A) WD5c is an undeformed pegmatite with quartz, K-feldspar, muscovite ±garnet that intruded at brittle conditions (open voids) in metasediments east of The Needles. B) The pegmatite grades into a feldspar-rich, more fine-grained zone (WD5b), probably altered during the K-feldspar metasomatism. C+D) The two-point Rb-Sr analysis of muscovite and whole rock of WD5c gives an age of 480.4 ±6.2 Ma. The age of WD5b is with 477.4 ±5.1 within the error of the age of WD5c. The initial $^{87}Sr/^{86}Sr$ ratios are high, suggesting derivation from or contamination with basement material.

Fig.24:

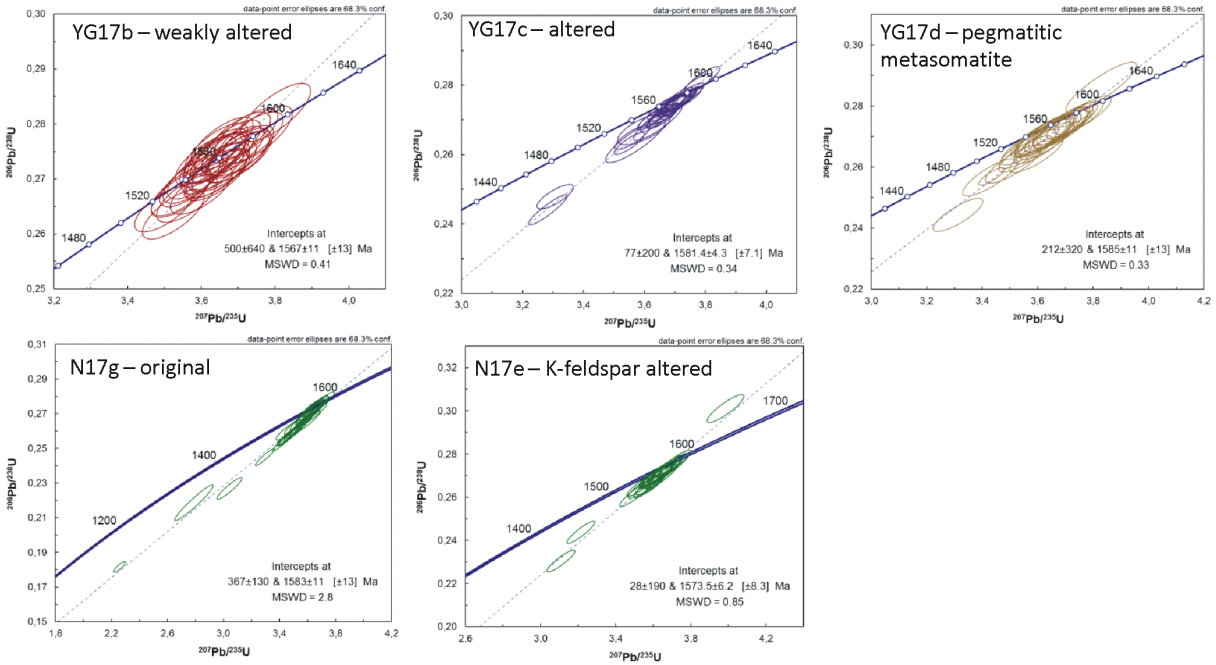

Fig.24: Concordia diagrams of K-feldspar altered and original orthogneisses of two localities in the MPI. The zircon $^{206}Pb/^{207}Pb$ age distribution is similar in all samples of each locality.

Fig.25:

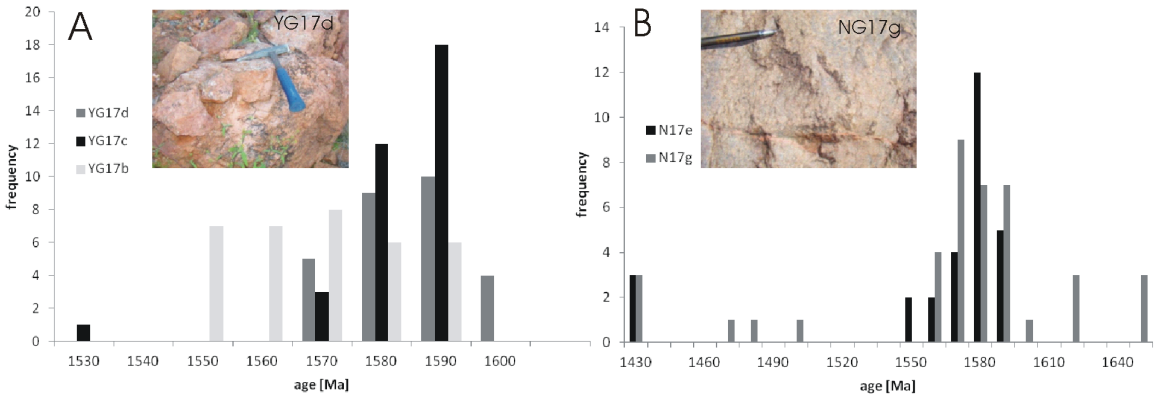

Fig. 25: Zircon $^{207}Pb/^{206}Pb$ age of original and K-feldspar altered metagranites. A) The frequency distribution of zircon ages in little and elevated K-feldspar-altered orthogneiss (YG17b+c) resembles the distribution in pegmatitic K-feldspar metasomatites (YG17d). The samples were taken west of Paralana Hot Springs (see Fig.3E). B) The zircon population in original orthogneiss north of The Pinnacles (N17g) also resembles the population of the K-feldspar-altered variety (N17e: see Fig.3F bottom).

Fig.26:

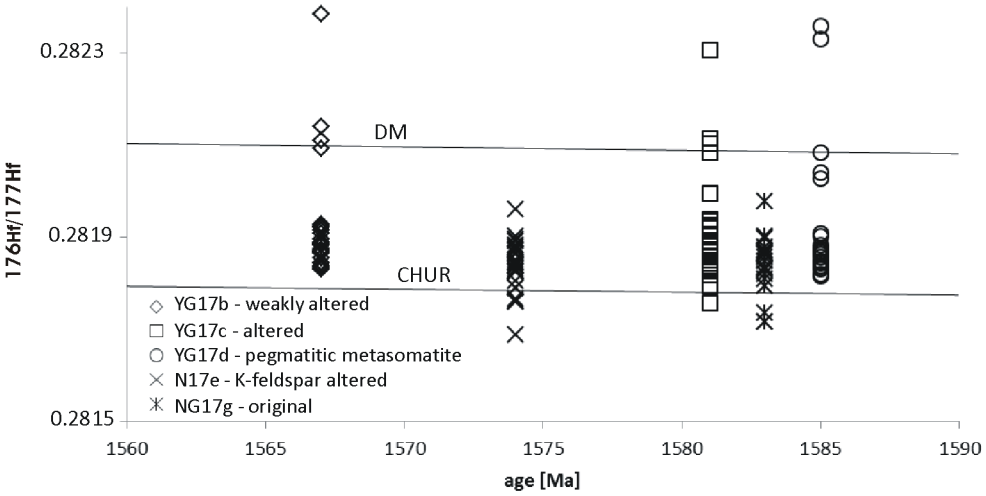

Fig.26: The initial $^{176}Hf/^{177}Hf$ isotopic compositions of original and K-feldspar-altered orthogneisses range within the spread of all analysed samples; without an evidence for a polymodal distribution.

Fig.27:

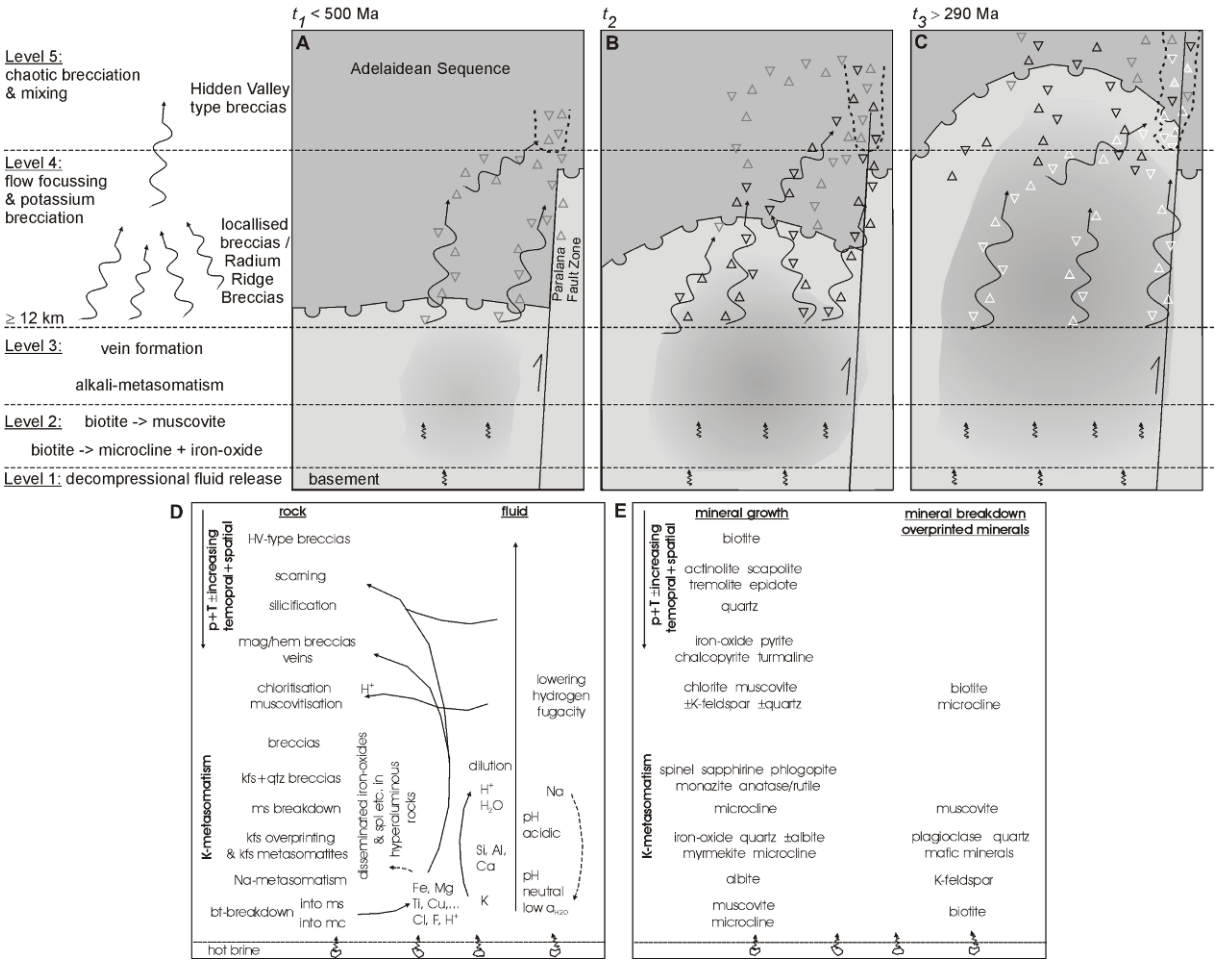

Fig.27: A-C) Simplified model of the Palaeozoic exhumation of the Yankaninna Anticline along the Paralana Fault Zone and contemporaneous crustal-scale alteration. The alteration system can be divided into several levels in the crust that were crossed during exhumation. A) Trapped pore water released in the anticlinal core. A narrow zone of biotite-breakdown, alkali-metasomatism and brecciation developed. The breakdown of micas added additional available fluid. B) The zone of alteration increased with the rise of the anticline. Previously altered areas got overprinted by breccias (triangles). C) The amount of available fluid increased with the rise of the fold. A complex overprinting relation developed temporally and spatially in the alteration system. D+E) Summary of the fluid-rock interaction during the Palaeozoic alteration in the MPI. The mineral reactions depend on temperature and pressure of the host rocks and fluids, as well as on structures and lithological characteristics.

Tab.1: Details on all samples taken for geochronology, geochemistry, oxygen isotope and fluid inclusion analyses.

sample	easting (GDA94)	northing (GDA94)	comment	separates	thin section	EMPA	whole rock	$\delta^{18}O$	fluid inclusion	raman	Rb-Sr	(U-Th)/He
218	0358986	6671372	original orthogneiss	zrn; ap; qtz								
218	0358986	6671372	granitic kfs-ms+bt-qtz	nein			x					
228	0358463	6671770	chloritised orthogneiss	zrn; ap								
256	0355102	6672127	BEG	zrn; ap								x
265	0340083	6655225	kfs breccia, wall rock of Pebble Dyke	zrn; ap								
266	0340853	6655295	kfs breccia, wall rock of Pebble Dyke	zrn; ap								x
269	0341368	6655245	volcanic pebble	zrn; ap								
276	0339415	6651757	qtz vein south of Mt. Painter	pure qtz								
344	0341141	6650844	original orthogneiss	zrn; ap; ms; qtz			x					
348	0344249	6654199	kfs overprited orthogneiss	zrn; ap; ms; qtz			x					
091a	0344334	6654944	kfs + qtz cemented breccia		EMPA		x					
091c	0344334	6654944	kfs metasomatite into breccia		EMPA		x					
091d	0344334	6654944	kfs metasomatite		EMPA		x					
091e	0344334	6654944	kfs overprinted paragneiss		EMPA	x	x					
091f	0344334	6654944	kfs overprinted paragneiss		EMPA		x					
10HV1b	0355110	6667559	chloritic-qtzitic-feldspatic breccia		normal/EMPA/FLINC	x	x					
10HV6a	0355297	6667392	breccia with kfs-qtz+-hem?-veins		normal/EMPA/FLINC	x						
10N17a	0332837	6650015	pegmatite		EMPA/FLINC							
10N17b	0332837	6650015	pegmatite		EMPA	x						
10N17c	0332837	6650015	pegmatite		EMPA	x						
10N17d	0332837	6650015	pegmatite		EMPA/FLINC	x						
10N17e	0332837	6650015	kfs overprint	zrn; ap; mnz	EMPA	x	x					
10N17f	0332837	6650015	weak kfs overprint	zrn; ap; mnz	EMPA	x	x					
10N17g	0332837	6650015	original orthogneiss	zrn; ap; mnz	EMPA	x	x					
10SP33c	0340314	6652338	kfsp overprint - clast in di-ttn vein		EMPA/FLINC	x						
267a	0340895	6655268	granitic pebble in Pebble Dyke	zrn; ap								x
AC34b	0337125	6649583	open void qtz in breccia	pure qtz								
AN=SP37	0340017	6653328	ghoetite	ghoetite								x
BC230	0362488	6673884	original granodiorite				x					
BC235	0362773	6673321	granodiorite				x					
BC237	0363059	6673113	kfs overprinted orthogneiss				x					
BC240	0363533	6673416	orthogneiss				x					

BC241	0363482	6673353	orthogneiss				x					
BC243	0363858	6673240	porphyry				x					
BC244	0363952	6672982	foliated porphyry				x					
BC248	0364473	6673764	orthogneiss				x					
BC249	0364494	6673974	orthogneiss				x					
BC251	0364206	6674666	orthogneiss				x					
BC254b	0355085	6672101	fine grained orthogneiss				x					
BC275	0339165	6651906	kfs-qtz-hem vein in orthogneiss with kfs overprinting rim						x	x		
BC338	0341383	6651624	orthogneiss				x					
BC339	0341460	6651666	orthogneiss				x					
BC341	0341840	6650926	kfs overprinted orthogneiss				x					
BC342	0342076	6650892	granodiorite	zrn; ap; mnz			x					
BC343	0342089	6650487	kfs overprinted orthogneiss				x					
BM25	0335959	6656042	kfs overprinted bt-rich orthogneiss		normal		x					
EC14	0341821	6649246	Echo Camp qtz	pure qtz				x				
EC15	0341840	6649217	Echo Camp qtz	pure qtz				x				
EC16	0341848	6649211	Echo Camp qtz	pure qtz				x				
EC17	0341867	6649174	Echo Camp qtz	pure qtz				x				
EC18a	0341876	6649154	Echo Camp qtz	qtz+kfs				x				
EC18b	0341876	6649154	Echo Camp qtz	red qtz				x				
EC21	0341940	6649077	Echo Camp qtz	pure qtz				x				
EC22	0341963	6649044	Echo Camp qtz	pure qtz				x				
EC23	0341996	6649033	Echo Camp qtz	pure qtz				x				
EC24	0342009	6649027	Echo Camp qtz	pure qtz				x				
EP7	0345212	6654335	orthogneiss				x					
H11	0358099	6671498	qtz-hem sinter in orthogneiss	qtz								
H9a	0338272	6660942	big qtz-vein	pure qtz								
H9b	0338272	6660942	massive qtz+hem	qtz+platy hem								
HEG1	0340397	6654887	mica-schist	zrn; ap								
HEG2	0340396	6654888	kfs overprint	zrn; ap								
HEG3	0340393	6654886	kfs overprinted paragneiss	zrn; ap								
HEG4	0340392	6654885	kfs overprinted paragneiss	zrn; ap								
HEG5	0340388	6654887	kfs overprinted paragneiss	zrn; ap								
HEG6	0340343	6654906	paragneiss	zrn; ap								
HEG7	0340265	6654900	mica-schist	zrn; ap								x
HEG8	0340161	6654942	mica-schist	zrn; ap								
HV4b	0357406	6671234	microgranite	zrn; ap								
HV53b	0356678	6671355	granitic pl-kfs-qtz-ms+bt				x					
HV56	0357152	6672009	aplitic pl-qtz				x					

HV61d	0357379	6672603	Hidden Valley breccia		normal/EMPA	x						
JH179	0344619	6658917	microgranite				x					
JH191	0347071	6657200	original orthogneiss		normal		x					
JH195a	0345968	6658505	microgranite		normal		x					
JH50	0348965	6659458	orthogneiss		normal		x					
JH51	0348956	6659129	altered orthogneiss		normal		x					
ML005a	0349986	6661397	migmatite		normal		x					
ML005b	0349986	6661397	migmatite		normal		x					
ML005c	0349986	6661397	migmatite				x					
ML005e1	0349986	6661397	kfs overprint		normal		x					
ML005e2	0349986	6661397	migmatite: leucosome		normal		x					
ML005e3	0349986	6661397	migmatite: melanosome				x					
ML174	0350335	6661149	fine grained orthogneiss				x					
ML175	0350367	6661186	kfs overprinted orthogneiss		EMPA/FLINC				x	x		
ML179	0350473	6661309	orthogneiss	zrn; ap; mnz	EMPA		x					
ML180b1	0350576	6661309	orthogneiss				x					
ML180b2	0350576	6661309	granodiorite	zrn; ap; mnz			x					
ML192	0349706	6660894	kfs overprint in quartzite				x					
ML197a1	0350474	6661317	granodiorite				x					
ML197a2	0350474	6661317	granodiorite				x					
ML197b	0350474	6661317	fine grained orthogneiss				x					
ML205	0351671	6662662	paragneiss	zrn; ap; mnz			x					
ML229	0350929	6662054	kfs overprinted paragneiss				x					
ML237	0352442	6663330	paragneiss				x					
ML240	0351903	6663820	migmatite	zrn; ap; mnz			x					
ML248a1	0349995	6661415	kfs overprinted orthogneiss				x					
ML248a2	0349995	6661415	kfs overprinted orthogneiss		EMPA/FLINC	x	x					
ML258	0353096	6665004	quartzite				x					
ML286a1	0353957	6666106	gabbro clast in Hidden Valley breccia		normal		x					
ML286b	0353957	6666106	gabbro clast in Hidden Valley breccia				x					
ML292	0353697	6664908	mafite		normal		x					
Olm3	0350024	6661102	granodiorite		normal		x					
Olm7	0350027	6661552	granodiorite	zrn; ap; mnz			x					
Olm8	0349998	6661380	migmatite				x					
P30	0337124	6647849	pegmatite in pelites	qtz; kfs								
P32	0337532	6647113	aplitic Pinnacle	qtz; kfs								
P43	0337191	6648400	qtz-vein	pure qtz								
PG11	0363928	6674097	orthogneiss		normal		x					
PG14a	0363156	6674237	orthogneiss		normal		x					

PG5b	0362858	6674098	orthogneiss		normal		x					
PG7b	0363758	6674066	mylonite		normal		x					
PG8	0364358	6674013	mylonite		normal		x					
PG9	0364363	6673980	orthogneiss		normal		x					
PW_1	0335511	6659958	Petalinka Waterfall qtz+platy hem	qtz-kfs				x				
PW_2	0335511	6659958	Petalinka Waterfall qtz+platy hem	qtz-hem				x				
PW_3	0335511	6659958	Petalinka Waterfall qtz+platy hem	qtz-hem				x				
PW_5	0335511	6659958	Petalinka Waterfall qtz+platy hem	qtz-hem				x				
PW-4	0335511	6659958	Petalinka Waterfall qtz+platy hem	qtz-kfs				x				
SK040	0332828	6650226	pegmatite									
SK054a	0333362	6649604	kfs metasomatite		normal		x					
SK080	0331871	6651623	kfs metasomatite				x					
SK201a	0328895	6651772	quartzite		EMPA/FLINC							
SK201b	0328895	6651772	quartzite				x					
SK201c	0328895	6651772	quartzite				x					
SK223	0331803	6650652	kfs metasomatite	zrn; ap	EMPA		x					
SP2	0339225	6651825	kfs-qtz-tur vein in paragneiss with kfs overprinting rim							x		
SP32a	0340233	6652191	di-ttn vein	qtz+di								
SP36b	0340329	6653154	kfs overprinted paragneiss		normal/EMPA/FLINC	x				x		
SP38	0030723	6653621	pegmatite qtz in paragneiss	pure qtz								
SP52a	0340151	6652972	granodiorite				x					
SP8	0339959	6651605	pegmatitic kfs metasomatite			x						
WD5b	0332466	6650170	kfs overprinted pegmatite ms+bt-kfs-	zrn; ap; ms; qtz		x	x				x	
WD5c	0332466	6650170	pegmatite ms+bt-kfs-qtz	zrn; ap; ms; qtz	normal		x				x	
WD6	0332570	6649956	pegmatite kfs-qtz				x					
Y52	0334879	6657865	orthogneiss		normal		x					
Y54	0335609	6657507	bt-rich orthogneiss		normal		x					
Y6	0336199	6659906	orthogneiss		normal		x					
Y73	0334852	6659920	silicified kfs breccia		EMPA							
Y7b	0336149	6659920	orthogneiss		normal		x					
YG17a	0345905	6658668	weakly kfs overprinted orthogneiss	zrn; ap; mnz	EMPA	x	x					
YG17b	0345905	6658668	kfs overprinted orthogneiss	zrn; ap; mnz	EMPA	x	x					
YG17c	0345905	6658668	kfs metasomatite	zrn; ap	EMPA/FLINC	x	x					
YG17d	0345905	6658668	pegmatitic kfs metasomatite	zrn; ap	EMPA	x						
YG24	0346835	6661774	granodiorite	zrn; ap; mnz	normal		x					
YG25	0347040	6662109	pegmatite with pl-kfs-qtz+-bt		normal		x					
YG28	0346914	6662178	pegmatitic qtz-kfs-mica	zrn; ap; mnz	normal		x					
YG7b	0344653	6659794	kfs metasomatite		normal		x					

Tab.2a: Electron microprope analyses of feldspar in various samples. Measurements were conducted at the University of Tübingen under the supervision of T. Wenzel.

Point	position	Na2O [wt%]	K2O [wt%]	SrO [wt%]	Al2O3 [wt%]	CaO [wt%]	BaO [wt%]	SiO2 [wt%]	FeO [wt%]	Total [wt%]	Mineral
Standards											
A_Albit		11.71	0.14	0.00	19.64	0.02	0.02	68.72	0.00	100.24	ab
A_Baryt		0.21	0.01	0.01	0.08	0.01	68.12	0.08	0.00	68.52	brt
A_Coelestin		0.01	0.00	57.82	0.00	0.00	0.00	0.00	0.02	57.85	celestine
A_Diopsid		0.02	0.00	0.03	0.06	25.55	0.04	51.89	0.08	77.67	di
A_Hematit		0.00	0.00	0.00	0.03	0.00	0.03	0.07	92.08	92.21	hem
A_Sanidin		2.97	12.17	0.05	18.72	0.00	1.13	65.17	0.15	100.37	sa
Samples											
SP36b_1	RCG	0.33	16.57	0.00	18.40	0.01	0.20	65.73	0.05	101.29	kfs
SP36b_2	RCG	0.37	16.58	0.00	18.35	0.00	0.26	65.39	0.02	100.96	kfs
SP36b_3	RCG	0.32	15.33	0.00	18.41	0.02	0.27	65.34	0.05	99.73	kfs
SP36b_4	RCG	0.26	16.50	0.00	18.41	0.01	0.24	65.38	0.00	100.81	kfs
SP36b_5	RCG	0.28	16.57	0.00	18.38	0.00	0.23	65.21	0.02	100.69	kfs
SP36b_6	RCG	0.35	15.55	0.00	18.26	0.00	0.24	64.98	0.05	99.44	kfs
SP36b_7	RCG	0.38	16.18	0.00	18.20	0.00	0.24	64.94	0.05	99.99	kfs
SP36b_9	kfs rim	0.41	15.44	0.00	18.13	0.02	0.20	64.24	0.00	98.45	kfs
SP36b_10	kfs rim	0.42	14.75	0.00	18.27	0.03	0.22	64.06	0.00	97.74	kfs
SP36b_11	kfs rim	0.35	16.38	0.00	18.21	0.00	0.25	63.99	0.07	99.25	kfs
SP36b_12	central kfs vein	0.53	16.34	0.00	18.60	0.00	0.21	65.15	0.04	100.87	kfs
SP36b_14	central kfs vein	0.35	15.98	0.00	18.52	0.02	0.19	65.10	0.09	100.25	kfs
SP36b_13	central kfs vein	0.69	15.48	0.00	18.52	0.06	0.27	64.29	0.00	99.31	kfs
SP36b_15	central kfs vein	0.29	15.88	0.00	18.42	0.01	0.35	63.81	0.03	98.78	kfs
SP36b_16	kfs rim	0.35	15.90	0.00	18.33	0.01	0.18	63.92	0.00	98.69	kfs
SP36b_17	kfs rim	0.82	15.32	0.00	18.68	0.03	0.23	64.73	0.05	99.86	kfs
SP36b_19	RCG	0.28	15.28	0.00	18.45	0.02	0.27	64.90	0.00	99.20	kfs
SP36b_20	RCG	0.29	16.48	0.00	18.45	0.00	0.21	64.88	0.00	100.31	kfs
SP36b_21	kfs rim	0.26	16.66	0.00	18.49	0.00	0.25	65.17	0.05	100.88	kfs
SP36b_22	kfs rim	0.33	16.46	0.00	18.45	0.01	0.28	63.46	0.02	99.00	kfs
SP8_23	central kfs vein	11.48	0.12	0.00	19.65	0.29	0.00	67.84	0.12	99.50	ab
SP8_24	central kfs vein	11.46	0.15	0.00	19.69	0.25	0.00	68.61	0.05	100.20	ab
SP8_25	central kfs vein	11.43	0.12	0.00	19.74	0.33	0.03	69.02	0.08	100.74	ab
SP8_26	central kfs vein	0.01	0.01	0.00	0.00	0.00	0.00	101.23	0.02	101.28	qtz
SP8_27	central kfs vein	0.27	16.11	0.00	18.35	0.01	0.11	65.55	0.05	100.46	kfs
SP8_8	kfs metasomatite	11.54	0.15	0.00	19.70	0.29	0.06	68.12	0.09	99.95	ab
SP8_7	kfs metasomatite	0.33	16.35	0.00	18.37	0.00	0.05	64.76	0.07	99.94	kfs
WD5b_1	kfs metasomatite	0.98	15.88	0.00	18.35	0.00	0.00	64.65	0.05	99.92	kfs
WD5b_2	kfs metasomatite	11.51	0.11	0.00	19.74	0.26	0.00	67.53	0.00	99.15	ab
WD5b_3	kfs metasomatite	0.01	0.00	0.00	0.00	0.01	0.04	100.13	0.01	100.20	qtz

WD5b_4	kfs metasomatite	10.21	0.13	0.00	21.84	2.60	0.04	64.86	0.06	99.74	ab
WD5b_5	kfs metasomatite	0.38	16.57	0.00	18.67	0.01	0.03	63.99	0.01	99.66	kfs
WD5b_6	kfs metasomatite	10.07	0.12	0.00	21.89	2.62	0.04	64.79	0.01	99.53	ab
WD5b_7	kfs metasomatite	0.79	15.94	0.00	18.74	0.02	0.00	64.30	0.04	99.83	kfs
WD5b_8	kfs metasomatite	10.18	0.17	0.00	21.87	2.57	0.00	65.69	0.08	100.56	ab
WD5b_9	kfs metasomatite	0.69	15.73	0.00	18.52	0.01	0.01	64.34	0.00	99.29	kfs
WD5b_10	kfs metasomatite	0.01	0.02	0.00	0.00	0.01	0.00	99.34	0.04	99.42	qtz
WD5b_11	kfs metasomatite	10.13	0.25	0.00	21.66	2.34	0.02	64.98	0.01	99.38	ab
WD5b_12	kfs metasomatite	0.49	16.29	0.00	18.64	0.02	0.01	64.73	0.01	100.20	kfs
WD5b_13	kfs metasomatite	0.62	16.50	0.00	18.72	0.01	0.00	64.97	0.04	100.86	kfs
WD5b_14	kfs metasomatite	0.01	0.01	0.00	0.00	0.00	0.00	101.17	0.00	101.19	qtz
WD5b_15	kfs metasomatite	0.00	0.00	0.02	0.00	0.00	0.00	100.04	0.00	100.06	qtz
WD5b_16	kfs metasomatite	10.42	0.12	0.00	21.83	2.57	0.00	65.46	0.00	100.40	ab
WD5b_17	kfs metasomatite	0.84	15.20	0.00	18.69	0.01	0.00	64.86	0.04	99.64	kfs
WD5b_18	kfs metasomatite	0.63	15.98	0.00	18.97	0.01	0.00	64.79	0.07	100.45	kfs
WD5b_19	kfs metasomatite	11.46	0.10	0.00	19.84	0.43	0.00	67.79	0.01	99.63	ab
WD5b_20	kfs metasomatite	10.42	0.11	0.00	21.60	2.30	0.00	65.42	0.04	99.90	ab
WD5b_21	kfs metasomatite	0.66	16.23	0.00	18.69	0.01	0.01	64.59	0.00	100.20	kfs
SP8_9	kfs metasomatite	11.30	0.11	0.00	19.77	0.34	0.03	68.48	0.01	100.04	ab
SP8_10	kfs metasomatite	0.07	2.37	0.00	16.24	1.26	0.01	65.92	0.35	86.22	clay?
SP8_11	kfs metasomatite	0.25	16.83	0.00	18.36	0.00	0.16	64.77	0.03	100.39	kfs
SP8_12	kfs metasomatite	11.57	0.13	0.00	19.75	0.33	0.00	68.73	0.03	100.55	ab
SP8_13	kfs metasomatite	3.81	1.30	0.00	14.15	5.36	0.01	54.60	0.39	79.62	mess
SP8_14	kfs metasomatite	0.01	0.00	0.00	0.00	0.00	0.03	99.69	0.01	99.74	qtz
SP8_15	kfs metasomatite	0.05	8.06	0.00	21.59	0.00	0.02	63.44	3.25	96.41	clay?
SP8_16	kfs metasomatite	0.00	0.00	0.00	0.01	0.00	0.00	100.18	0.02	100.21	qtz
SP8_17	kfs metasomatite	11.56	0.14	0.00	19.59	0.19	0.04	68.29	0.07	99.88	ab
SP8_18	kfs metasomatite	0.25	16.34	0.00	18.31	0.00	0.12	65.21	0.00	100.23	kfs
SP36b_28	RCG	0.28	15.98	0.00	18.14	0.01	0.19	64.28	0.04	98.92	kfs
SP36b_29	RCG	0.28	16.43	0.00	18.33	0.00	0.16	64.14	0.05	99.39	kfs
SP36b_30	RCG	0.03	0.06	0.00	0.38	0.04	0.02	97.93	0.04	98.50	qtz
SP36b_31	RCG	0.36	16.35	0.00	18.22	0.01	0.30	64.33	0.00	99.57	kfs
SP36b_32	kfs rim	0.33	16.22	0.00	18.33	0.01	0.31	63.54	0.02	98.75	kfs
SP36b_33	kfs rim	0.25	16.31	0.00	18.42	0.02	0.28	65.01	0.00	100.29	kfs
SP36b_34	central kfs vein	0.02	0.03	0.01	0.69	0.10	0.00	99.67	0.03	100.56	qtz
SP36b_35	central kfs vein	0.30	16.85	0.00	18.36	0.02	0.24	62.74	0.01	98.52	kfs
SP36b_36	central kfs vein	0.40	16.18	0.00	18.33	0.00	0.19	64.24	0.00	99.34	kfs
SP36b_37	central kfs vein	0.34	16.27	0.00	18.42	0.13	0.19	64.20	0.00	99.55	kfs
SP36b_38	central kfs vein	0.43	16.28	0.00	18.65	0.02	0.27	64.25	0.03	99.93	kfs
SP36b_39	central kfs vein	0.02	0.08	0.00	0.58	0.07	0.04	100.05	0.03	100.87	qtz
SP36b_40	central kfs vein	0.23	16.99	0.00	18.61	0.00	0.24	64.81	0.00	100.89	kfs

SP36b_41	central kfs vein	0.00	0.00	0.00	0.63	0.01	0.01	100.14	0.00	100.79	qtz
SP36b_42	kfs rim	0.36	16.64	0.00	18.55	0.01	0.24	64.27	0.02	100.09	kfs
SP36b_43	kfs rim	0.30	16.96	0.00	18.55	0.00	0.25	64.53	0.00	100.58	kfs
SP36b_44	kfs rim	0.00	0.02	0.00	0.41	0.03	0.01	98.62	0.01	99.10	qtz
SP36b_45	kfs rim	0.37	16.70	0.00	18.47	0.01	0.24	64.96	0.02	100.76	kfs
SP36b_46	RCG	0.28	16.97	0.00	18.75	0.02	0.17	64.16	0.06	100.41	kfs
SP36b_47	RCG	0.02	0.02	0.00	0.00	0.01	0.02	101.10	0.02	101.17	qtz
SP36b_48	RCG	0.30	16.42	0.00	18.41	0.02	0.18	64.79	0.00	100.12	kfs
SP36b_49	RCG	0.01	0.02	0.00	0.00	0.02	0.00	100.74	0.02	100.81	qtz
avg. analytical error (1σ)		4.26	7.95	8.62	7.95	2.81	10.12	20.89	9.76		

Tab.2b: Electron microprope analyses of feldspar in various samples. Measurements were conducted at the University of Tübingen under the supervision of T. Wenzel.

Point	position	SiO2 [wt%]	Na2O [wt%]	K2O [wt%]	SrO [wt%]	Al2O3 [wt%]	CaO [wt%]	BaO [wt%]	FeO [wt%]	Total [wt%]	Mineral
Standards											
A_ab_1		69.55	11.79	0.15	0.00	19.67	0.07	0.03	0.00	101.26	ab
A_Sanidin_1		64.90	2.99	12.04	0.03	18.63	0.01	1.13	0.12	99.85	sa
A_Celestine_1		0.00	0.01	0.00	57.72	0.01	0.00	0.04	0.00	57.78	celestine
A_Diopsid_1		53.07	0.01	0.01	0.00	0.05	26.70	0.01	0.04	79.89	di
A_Diopsid_2		51.92	0.01	0.01	0.00	0.04	26.28	0.01	0.05	78.33	di
A_Haematit		0.20	0.00	0.01	0.00	0.00	0.00	0.00	89.91	90.13	hem
A_Baryt		0.10	0.11	0.01	0.07	0.05	0.00	67.75	0.01	68.09	brt
A_ab2		69.28	11.71	0.10	0.00	19.51	0.01	0.01	0.00	100.62	ab
Samples											
YG17a-1_1a	Kfs metasomatite	65.660	1.048	15.560	0.000	18.730	0.022	0.093	0.008	101.121	90% or 9% ab
YG17a-1_2a	Kfs metasomatite	65.720	1.390	15.100	0.000	18.670	0.000	0.094	0.008	100.982	88% or 12%ab
YG17a-1_3a	Kfs metasomatite	65.460	0.965	15.640	0.000	18.600	0.008	0.092	0.000	100.765	91% or 9% ab
YG17a-2_1a	original, altered	64.740	0.066	16.580	0.000	18.670	0.013	0.834	0.042	100.945	99% or
YG17a-2_2a	original, altered	66.45	10.52	0.60	0.00	21.72	1.83	0.04	0.12	101.28	88% ab
YG17a-2_3a	original, altered	65.500	0.977	15.730	0.000	18.670	0.012	0.084	0.000	100.973	91% or 9% ab
YG17a-3_1a	Kfs metasomatite	65.230	0.793	16.090	0.000	18.730	0.028	0.091	0.028	100.990	92% or 7% ab
YG17a-3_2a	Kfs metasomatite	65.270	0.822	15.870	0.000	18.630	0.025	0.111	0.023	100.750	92% or 7% ab
YG17a-3_3a	Kfs metasomatite	69.57	11.88	0.08	0.00	19.64	0.17	0.05	0.02	101.42	98% ab
YG17a-3_4a	Kfs metasomatite	69.26	11.93	0.08	0.00	19.71	0.19	0.01	0.01	101.18	98% ab
YG17a-4_1	Kfs metasomatite	64.210	1.141	15.440	0.000	18.510	0.021	0.121	0.000	99.443	90% or 10% ab
YG17a-4_2	Kfs metasomatite	64.450	0.788	15.820	0.000	18.590	0.018	0.110	0.014	99.791	93% or 7% ab
YG17a-4_3	Kfs metasomatite	64.650	0.970	15.450	0.000	18.540	0.021	0.136	0.007	99.774	91% or 9% ab
YG17a-5_1	original, altered	65.63	10.45	1.42	0.00	21.43	0.57	0.01	0.39	99.90	89% ab
YG17a-5_2	original, altered	65.36	10.36	0.46	0.00	22.21	2.84	0.00	0.02	101.25	85% ab
YG17a-5_3	original, altered	65.050	0.526	16.210	0.000	18.520	0.015	0.382	0.062	100.765	95% or 5% ab
YG17a-5_4	original, altered	65.340	1.002	15.200	0.000	18.530	0.037	0.559	0.104	100.771	90% or 9% ab
YG17a-10_1	Kfs metasomatite	65.470	0.893	15.630	0.000	18.650	0.027	0.103	0.039	100.811	92% or 8% ab
YG17a-10_2	Kfs metasomatite	65.680	0.969	15.630	0.000	18.610	0.016	0.133	0.015	101.054	91% or 9% ab
YG17a-10_3	Kfs metasomatite	69.38	11.99	0.10	0.00	19.60	0.15	0.00	0.00	101.22	99% ab
YG17a-10_4	Kfs metasomatite	69.50	11.86	0.16	0.00	19.61	0.12	0.05	0.03	101.33	99% ab
YG17a-10_5	Kfs metasomatite	37.540	0.099	10.730	0.000	14.680	0.000	0.000	7.950	70.999	mica
YG17a-11_1	Kfs metasomatite	65.110	0.913	15.780	0.000	18.700	0.016	0.108	0.000	100.627	92% or 8% ab
YG17a-11_2	Kfs metasomatite	65.110	0.866	15.670	0.000	18.730	0.027	0.121	0.000	100.524	92% or 8% ab
YG17a-11_3	Kfs metasomatite	69.04	11.90	0.20	0.00	19.65	0.17	0.04	0.11	101.10	98% ab
YG17a-12_1	original, altered	65.73	9.77	1.84	0.00	21.87	0.48	0.02	0.36	100.07	87% ab
YG17a-12_2	original	69.04	11.91	0.21	0.00	20.05	0.28	0.00	0.00	101.49	98% ab
YG17a-12_3	original	69.90	12.15	0.08	0.01	19.70	0.03	0.00	0.00	101.87	99% ab
YG17a-12_5	original	69.89	12.20	0.11	0.00	19.65	0.11	0.00	0.01	101.97	99% ab
YG17a-12_6	original	69.28	12.04	0.10	0.00	19.85	0.17	0.02	0.03	101.49	99% ab
YG17a-12_7	Kfs metasomatite	65.130	0.919	15.850	0.000	18.660	0.023	0.131	0.000	100.712	92% or 8% ab
YG17a-12_8	Kfs metasomatite	69.34	11.86	0.10	0.00	19.72	0.18	0.03	0.00	101.23	99% ab
YG17a-17_1	original (?)	65.120	1.077	15.550	0.000	18.600	0.000	0.070	0.000	100.417	90% or 10% ab
YG17a-17_2	original (?)	64.830	0.978	15.610	0.000	18.690	0.000	0.084	0.049	100.242	91% or 9% ab

YG17a-17_3	inclusion	101.99	0.00	0.00	0.00	0.00	0.00	0.01	0.00	102.00	qtz
YG17a-16_1	original (?)	65.230	0.909	15.650	0.000	18.810	0.047	0.116	0.000	100.761	92% or 8% ab
YG17a-16_2	original (?)	64.870	1.003	15.330	0.000	18.650	0.037	0.072	0.016	99.979	91% or 9% ab
YG17a-16_3	rim	101.32	0.00	0.01	0.01	0.01	0.02	0.00	0.03	101.39	qtz
YG17a-15_1	original (?)	65.100	1.041	15.450	0.000	18.550	0.029	0.097	0.000	100.267	91% or 9% ab
YG17a-15_2	original (?)	64.900	1.092	15.200	0.000	18.580	0.027	0.068	0.000	99.868	90% or 10% ab
YG17a-15_3	original (?)	68.71	11.98	0.09	0.00	19.56	0.16	0.00	0.00	100.50	99% ab
YG17a-15_4	original (?)	68.78	11.95	0.13	0.00	19.64	0.16	0.00	0.00	100.66	99% ab
YG17a-14_1	Kfs metasomatite (?)	64.910	0.912	15.490	0.000	18.670	0.043	0.086	0.014	100.124	92% or 8% ab
YG17a-14_2	Kfs metasomatite (?)	65.170	1.070	15.470	0.000	18.530	0.049	0.112	0.013	100.414	90% or 9% ab
YG17a-14_3	rim	69.13	11.80	0.11	0.00	19.63	0.23	0.00	0.07	100.96	98% ab
YG17b-2_7	Kfs metasomatite	65.550	2.530	13.560	0.000	18.640	0.021	0.113	0.024	100.438	78% or 22% ab
YG17b-2_8	Kfs metasomatite	65.170	1.252	15.310	0.000	18.620	0.000	0.052	0.000	100.405	89% or 11% ab
YG17b-2_9	Kfs metasomatite	69.36	12.01	0.08	0.00	19.52	0.10	0.03	0.01	101.11	99% ab
YG17b-2_10	Kfs metasomatite	102.09	0.02	0.00	0.00	0.02	0.00	0.01	0.01	102.14	qtz
YG17b-3_1	Kfs metasomatite	65.400	0.909	15.630	0.000	18.840	0.000	0.106	0.000	100.885	92% or 8% ab
YG17b-3_2	Kfs metasomatite	65.710	0.949	15.600	0.000	18.660	0.007	0.054	0.017	100.997	92% or 8% ab
YG17b-3_3	Kfs metasomatite	69.38	12.01	0.12	0.00	19.65	0.09	0.01	0.01	101.27	99% ab
YG17b-4_1	original (?)	65.650	0.920	15.710	0.000	18.720	0.010	0.049	0.000	101.059	92% or 8% ab
YG17b-4_2	original (?)	65.650	1.060	15.590	0.000	18.790	0.024	0.081	0.037	101.232	91% or 9% ab
YG17b-4_3	original (?)	69.38	11.95	0.09	0.02	19.78	0.07	0.03	0.02	101.34	99% ab
YG17b-5_1	Kfs metasomatite (?)	65.250	0.718	16.120	0.000	18.690	0.010	0.133	0.014	100.935	94% or 6% ab
YG17b-5_2	Kfs metasomatite (?)	65.380	0.812	16.040	0.000	18.570	0.010	0.098	0.000	100.911	93% or 7% ab
YG17b-5_3	Kfs metasomatite (?)	69.23	12.00	0.08	0.00	19.69	0.07	0.00	0.07	101.14	99% ab
YG17b-5_4	Kfs metasomatite (?)	69.92	12.06	0.11	0.01	19.56	0.02	0.01	0.02	101.71	99% ab
YG17b-7_1	Kfs metasomatite	65.200	0.908	15.810	0.000	18.730	0.010	0.089	0.000	100.747	92% or 8% ab
YG17b-7_2	Kfs metasomatite	65.110	0.996	15.740	0.000	18.740	0.018	0.073	0.024	100.702	91% or 9% ab
YG17b-7_3	Kfs metasomatite	69.31	11.98	0.10	0.00	19.88	0.14	0.05	0.05	101.51	99% ab
YG17b-8_1	Kfs metasomatite (?)	65.320	0.786	15.810	0.000	18.650	0.014	0.101	0.000	100.681	93% or 7% ab
YG17b-8_2	Kfs metasomatite (?)	65.390	1.123	15.690	0.000	18.640	0.021	0.131	0.000	100.996	90% or 10% ab
YG17b-8_3	Kfs metasomatite (?)	69.54	12.10	0.11	0.00	19.85	0.11	0.03	0.02	101.76	99% ab
YG17b-8_4	Kfs metasomatite (?)	69.25	11.82	0.09	0.00	19.78	0.12	0.00	0.00	101.06	99% ab
YG17b-9_1	Kfs metasomatite	65.420	0.990	15.700	0.000	18.580	0.010	0.044	0.000	100.744	91% or 9% ab
YG17b-9_2	Kfs metasomatite	65.410	1.052	15.400	0.000	18.860	0.027	0.118	0.007	100.875	90% or 9% ab
YG17b-9_3	Kfs metasomatite	69.10	12.08	0.07	0.00	19.72	0.10	0.03	0.04	101.14	99% ab
YG17b-9_4	Kfs metasomatite	68.78	11.73	0.08	0.00	19.65	0.10	0.00	0.00	100.35	99% ab
YG17b-10_1	original, altered	50.60	0.24	7.42	0.00	30.63	0.59	0.05	2.60	92.13	K-Al-Fe-Si-OH
YG17b-10_2	original, altered	47.69	0.25	9.75	0.00	29.63	0.15	0.04	2.62	90.13	K-Al-Fe-Si-OH
YG17b-10_3	original, altered	51.23	0.24	7.34	0.00	30.81	0.60	0.08	2.59	92.89	K-Al-Fe-Si-OH
YG17c-1_1	Kfs metasomatite	65.720	0.551	16.170	0.000	18.280	0.010	0.031	0.092	100.853	95% or 5% ab
YG17c-1_2	Kfs metasomatite	65.200	0.581	16.160	0.000	18.300	0.000	0.071	0.045	100.358	95% or 5% ab
YG17c-2_1	original	101.67	0.02	0.01	0.00	0.00	0.00	0.00	0.00	101.70	qtz
YG17c-2_2	original	65.35	9.83	0.22	0.00	22.32	3.53	0.00	0.13	101.38	82% ab 16% an
YG17c-2_3	original, altered	67.44	10.57	1.11	0.00	20.47	0.95	0.05	0.14	100.72	89% ab
YG17c-3_1	original	65.07	9.86	0.29	0.00	22.56	3.77	0.00	0.01	101.56	81% ab 17% an
YG17c-3_2	original	64.76	9.61	0.33	0.00	22.71	3.92	0.06	0.03	101.42	80% ab 18% an
YG17c-3_3	original	64.77	9.80	0.31	0.00	22.87	4.14	0.00	0.10	101.99	80% ab 18% an

YG17c-3_4	Kfs metasomatite	65.060	0.496	16.110	0.000	18.650	0.011	0.073	0.000	100.400	95% or 5% ab
YG17c-4_1	original	65.20	9.81	0.21	0.00	22.45	3.83	0.01	0.03	101.55	81% ab 17% an
YG17c-4_2	original, altered	66.34	10.29	1.19	0.00	22.15	0.85	0.02	0.14	100.98	89% ab
YG17c-4_3	Kfs metasomatite	65.320	0.518	15.990	0.000	18.620	0.000	0.077	0.101	100.627	95% or 5% ab
YG17c-6_1	original	65.48	9.94	0.25	0.00	22.28	3.48	0.00	0.08	101.51	83% ab 16% an
YG17c-6_2	original, altered	66.13	10.14	1.40	0.00	22.18	0.98	0.00	0.22	101.05	87% ab
YG17c-6_3	Kfs metasomatite	65.360	0.530	16.090	0.000	18.370	0.000	0.000	0.097	100.447	95% or 5% ab
YG17d-1_1	pegmatitic Kfs	65.590	1.680	14.660	0.000	18.840	0.069	0.143	0.000	100.982	85% or 15% ab
YG17d-1_2	pegmatitic Kfs	65.080	0.874	15.880	0.000	18.550	0.063	0.115	0.020	100.582	92% or 8% ab
YG17d-1_3	pegmatitic Kfs	69.62	11.78	0.10	0.00	19.63	0.19	0.02	0.04	101.39	98% ab
YG17d-1_4	pegmatitic Kfs	101.83	0.01	0.03	0.00	0.08	0.06	0.00	0.08	102.09	qtz
YG17d-2_1	pegmatitic Kfs	64.870	0.683	16.430	0.000	18.460	0.034	0.047	0.030	100.553	94% or 6% ab
YG17d-2_2	pegmatitic Kfs	65.300	0.480	16.630	0.000	18.360	0.000	0.152	0.062	100.984	96% or 4% ab
YG17d-2_3	pegmatitic Kfs	69.05	11.41	0.13	0.00	19.61	0.13	0.00	0.42	100.75	99% ab
YG17d-2_4	pegmatitic Kfs	69.23	11.91	0.11	0.00	19.78	0.27	0.02	0.11	101.43	98% ab
YG17d-3_1	pegmatitic Kfs	65.540	0.931	15.920	0.000	18.570	0.008	0.067	0.027	101.063	92% or 8% ab
YG17d-3_2	pegmatitic Kfs	65.130	0.706	16.380	0.000	18.380	0.010	0.069	0.068	100.743	94% or 6% ab
YG17d-3_3	pegmatitic Kfs	68.98	11.72	0.06	0.00	19.66	0.26	0.02	0.09	100.79	98% ab
YG17d-3_4	pegmatitic Kfs	68.23	11.60	0.09	0.00	19.28	0.03	0.00	1.04	100.27	99% ab
YG17d-4_1	pegmatitic Kfs	65.670	0.648	16.010	0.000	18.560	0.000	0.108	0.074	101.069	94% or 6% ab
YG17d-4_2	pegmatitic Kfs	64.930	0.643	16.300	0.000	18.450	0.000	0.049	0.077	100.449	94% or 6% ab
YG17d-4_3	pegmatitic Kfs	67.64	11.83	0.13	0.00	19.64	0.25	0.03	0.28	99.80	98% ab
YG17d-4_4	qtz	101.99	0.02	0.05	0.00	0.17	0.03	0.00	0.04	102.29	qtz
YG17d-4_5	pegmatitic Kfs	35.35	0.19	3.26	0.00	19.44	1.95	0.07	21.33	81.58	mess
YG17d-4_6	pegmatitic Kfs	32.87	0.16	3.60	0.00	17.44	1.05	0.03	24.52	79.67	mess
YG17d-5_1	pegmatitic Kfs clast	65.580	0.731	16.140	0.000	18.600	0.027	0.014	0.007	101.099	93% or 7% ab
YG17d-5_2	pegmatitic Kfs clast	65.390	0.853	16.040	0.000	18.610	0.030	0.016	0.031	100.970	92% or 7% ab
YG17d-5_3	Kfsp cement (?)	68.65	11.53	0.56	0.00	19.49	0.19	0.00	0.68	101.09	96% ab
YG17d-5_4	Kfsp cement (?)	68.80	11.80	0.23	0.00	19.33	0.03	0.02	0.27	100.48	99% ab
YG17d-6_1	pegmatitic Kfs clast	65.900	1.176	15.350	0.000	18.670	0.037	0.039	0.071	101.243	89% or 10% ab
YG17d-6_2	pegmatitic Kfs clast	66.060	0.919	15.720	0.000	18.540	0.057	0.016	0.016	101.329	92% or 8% ab
YG17d-6_3	Kfsp cement (?)	72.54	10.43	0.17	0.00	17.47	0.26	0.01	0.40	101.28	98% ab
YG17d-6_4	cement (?)	91.59	1.46	0.43	0.00	3.75	0.05	0.03	2.74	100.05	qtz
YG17d-8_1	pegmatitic Kfs clast	65.300	0.910	15.700	0.000	18.660	0.060	0.104	0.052	100.787	92% or 8% ab
YG17d-8_2	pegmatitic Kfs clast	65.370	0.821	15.770	0.000	18.700	0.057	0.107	0.034	100.859	92% or 7% ab
YG17d-8_3	qtz	101.83	0.01	0.00	0.00	0.06	0.01	0.00	0.00	101.91	qtz
YG17d-8_4	qtz	101.33	0.00	0.00	0.00	0.40	0.00	0.02	0.00	101.74	qtz
YG17d-8_5	pegmatitic Kfs clast	35.02	0.14	1.66	0.00	17.01	0.47	0.00	22.34	76.64	mess
YG17d-10_1	pegmatitic Kfs clast	64.860	0.180	16.810	0.000	18.320	0.045	0.258	0.193	100.666	98% or
YG17d-10_2	pegmatitic Kfs clast	64.880	0.381	16.540	0.000	18.380	0.008	0.230	0.139	100.558	97% or
10N17b-1_1	pegmatitic Kfs	69.35	12.06	0.09	0.00	19.82	0.12	0.00	0.06	101.49	99% ab
10N17b-1_2	pegmatitic Kfs	69.83	11.91	0.15	0.00	19.72	0.13	0.03	0.06	101.83	99% ab
10N17b-2_1	pegmatitic Kfs	69.64	12.04	0.11	0.00	19.62	0.13	0.00	0.12	101.66	99% ab
10N17b-2_2	pegmatitic Kfs	69.55	12.08	0.11	0.00	19.46	0.15	0.00	0.03	101.37	99% ab
10N17b-2_3	pegmatitic Kfs	65.230	0.079	16.470	0.000	18.290	0.020	0.542	0.027	100.658	99% or
10N17b-3_1	original (?)	69.21	11.74	0.17	0.00	19.90	0.38	0.04	0.00	101.44	97% ab
10N17b-3_2	original (?)	69.48	11.69	0.15	0.00	19.66	0.19	0.00	0.05	101.22	98% ab

10N17b-3_3	original (?)	65.330	0.027	16.850	0.000	18.170	0.000	0.164	0.000	100.541	100% or
10N17b-5_1	Kfsp cement (?)	69.85	12.23	0.05	0.00	19.76	0.02	0.01	0.00	101.92	100% ab
10N17b-5_2	Kfsp cement (?)	69.84	12.02	0.05	0.00	19.71	0.02	0.02	0.00	101.66	100% ab
10N17b-5_3	Kfsp cement (?)	65.700	0.069	16.530	0.000	18.220	0.025	0.100	0.000	100.644	99% or
10N17b-6_1	Kfsp cement (?)	70.03	12.08	0.07	0.02	19.50	0.03	0.00	0.00	101.73	99% ab
10N17b-6_2	Kfsp cement (?)	69.87	12.03	0.10	0.00	19.81	0.14	0.00	0.05	102.00	99% ab
10N17c-1_1	pegmatitic Kfs	102.35	0.00	0.00	0.00	0.01	0.00	0.00	0.00	102.36	qtz
10N17c-1_2	pegmatitic Kfs	68.80	11.86	0.11	0.00	19.94	0.43	0.02	0.05	101.21	97% ab
10N17c-1_3	pegmatitic Kfs	65.220	0.077	16.720	0.000	18.150	0.013	0.150	0.000	100.330	99% or
10N17c-2_1	pegmatitic Kfs	69.40	11.62	0.11	0.00	20.04	0.44	0.03	0.04	101.68	97% ab
10N17c-2_2	pegmatitic Kfs	68.65	11.81	0.16	0.00	19.69	0.40	0.00	0.00	100.71	97% ab
10N17c-3_1	pegmatitic Kfs	69.18	11.77	0.14	0.00	19.89	0.42	0.02	0.03	101.44	97% ab
10N17c-3_2	pegmatitic Kfs	69.37	11.89	0.09	0.01	19.99	0.42	0.03	0.02	101.82	98% ab
10N17c-3_3	pegmatitic Kfs	66.020	0.043	16.790	0.000	18.200	0.021	0.032	0.000	101.105	100% or
10N17c-3_4	pegmatitic Kfs	49.990	0.055	10.580	0.000	27.960	0.061	0.016	3.730	92.392	mica
10N17c-4_1	pegmatitic Kfs (?)	69.73	11.89	0.12	0.00	19.77	0.19	0.00	0.05	101.75	98% ab
10N17c-4_2	pegmatitic Kfs (?)	69.20	12.04	0.10	0.00	19.75	0.24	0.03	0.04	101.39	98% ab
10N17d-1_1	pegmatitic Kfs	68.32	11.47	0.58	0.00	19.66	0.47	0.02	0.11	100.63	95% ab
10N17d-1_2	pegmatitic Kfs	68.47	11.77	0.12	0.00	19.76	0.47	0.01	0.02	100.61	97% ab
10N17d-1_3	pegmatitic Kfs	65.580	0.475	16.290	0.000	18.360	0.022	0.015	0.032	100.774	96% or 4% ab
10N17d-2_1	pegmatite	68.79	11.88	0.08	0.00	20.02	0.51	0.01	0.00	101.28	97% ab
10N17d-2_2	pegmatite	68.69	11.65	0.21	0.00	19.84	0.50	0.01	0.08	100.98	97% ab
10N17d-2_3	pegmatite	65.330	0.280	16.580	0.000	18.510	0.000	0.248	0.081	101.029	97% or
10N17d-3_1	clast (?)	69.11	11.81	0.15	0.00	19.72	0.26	0.02	0.00	101.06	98% ab
10N17d-3_2	clast (?)	69.00	11.81	0.13	0.00	19.87	0.38	0.00	0.02	101.22	98% ab
10N17d-3_3	matrix (?)	65.330	0.355	16.250	0.000	18.570	0.024	0.218	0.000	100.747	97% or
10N17d-3_4	matrix (?)	65.500	0.456	16.120	0.000	18.480	0.000	0.183	0.000	100.739	96% or 4% ab
10N17d-4_1	matrix (?)	65.110	0.533	16.190	0.000	18.440	0.000	0.222	0.042	100.537	95% or 5% ab
10N17d-4_2	matrix (?)	65.160	0.439	16.520	0.000	18.620	0.009	0.204	0.000	100.952	96% or 4% ab
10N17d-4_3	clast (?)	68.97	11.69	0.19	0.00	20.09	0.41	0.00	0.09	101.44	97% ab
10N17d-4_4	clast (?)	68.76	11.73	0.10	0.00	19.80	0.46	0.00	0.00	100.84	97% ab
10N17d-5_1	pegmatite	68.89	11.60	0.13	0.00	19.70	0.35	0.00	0.13	100.80	98% ab
10N17d-5_2	pegmatite	69.04	11.58	0.09	0.00	19.56	0.40	0.01	0.04	100.72	98% ab
10N17d-5_3	pegmatite	65.210	0.601	16.310	0.000	18.410	0.000	0.157	0.009	100.697	95% or 5% ab
10N17d-5_4	pegmatite	65.360	0.552	16.140	0.000	18.490	0.000	0.210	0.009	100.761	95% or 5% ab
10N17d-6_1	Kfs metasomatite	65.440	0.416	16.270	0.000	18.580	0.010	0.282	0.043	101.041	96% or 4% ab
10N17d-6_2	Kfs metasomatite	65.020	0.252	16.600	0.000	18.410	0.000	0.223	0.146	100.651	98% or
10N17d-7_1	Kfs metasomatite	64.950	0.438	16.370	0.000	18.320	0.000	0.297	0.019	100.393	96% or 4% ab
10N17d-7_2	Kfs metasomatite	65.480	0.432	16.240	0.000	18.470	0.000	0.286	0.030	100.938	96% or 4% ab
10N17d-8_1	Kfs metasomatite	65.370	0.409	16.280	0.000	18.530	0.010	0.172	0.019	100.790	96% or 4% ab
10N17d-8_2	Kfs metasomatite	65.020	0.363	16.580	0.000	18.350	0.012	0.154	0.087	100.567	97% or 3% ab
10N17d-8_3	Kfs metasomatite (?)	69.81	11.92	0.13	0.01	19.67	0.15	0.00	0.05	101.74	99% ab
10N17d-8_4	inclusion	102.08	0.00	0.01	0.00	0.00	0.00	0.00	0.00	102.09	qtz
10N17d-8_5	inclusion	101.74	0.00	0.01	0.00	0.00	0.01	0.02	0.01	101.79	qtz
10N17d-9_1	Kfs metasomatite (?)	65.030	0.443	16.320	0.000	18.230	0.000	0.071	0.066	100.160	96% or 4% ab
10N17d-9_2	Kfs metasomatite (?)	65.380	0.496	16.160	0.000	18.610	0.019	0.096	0.047	100.809	95% or 5% ab
10N17d-9_3	Kfs metasomatite (?)	69.04	11.78	0.14	0.00	19.74	0.27	0.00	0.01	100.98	98% ab

10N17d-9_4	Kfs metasomatite (?)	69.36	11.90	0.11	0.00	19.78	0.35	0.00	0.00	101.49	98% ab
10N17d-10_1	original (?)	64.940	0.435	15.980	0.000	18.350	0.000	0.128	0.066	99.899	96% or 4% ab
10N17d-10_2	original (?)	65.250	0.408	16.140	0.000	18.620	0.000	0.118	0.030	100.565	96% or 4% ab
10N17d-10_3	original (?)	68.79	11.96	0.08	0.00	20.16	0.48	0.04	0.02	101.52	97% ab
10N17d-10_4	original (?)	69.11	11.87	0.06	0.00	20.03	0.38	0.04	0.00	101.50	98% ab
10N17d-11_1	original (?)	69.15	11.84	0.23	0.02	19.60	0.31	0.02	0.03	101.20	97% ab
10N17d-11_2	original (?)	69.71	11.96	0.07	0.00	19.55	0.02	0.02	0.06	101.38	100% ab
10N17d-15_1	original (?)	69.08	11.74	0.10	0.00	19.78	0.43	0.00	0.00	101.13	97% ab
10N17d-15_2	original (?)	69.33	11.80	0.12	0.00	19.86	0.41	0.00	0.08	101.60	97% ab
10N17d-15_3	original (?)	65.590	0.034	16.390	0.000	18.220	0.000	0.080	0.000	100.314	100% or
10N17d-16_1	original (?)	47.000	0.172	11.000	0.000	29.770	0.015	0.051	4.260	92.269	mica
10N17d-16_2	original (?)	47.010	0.099	10.970	0.000	29.790	0.000	0.063	4.140	92.072	mica
10N17d-16_3	original (?)	68.19	11.76	0.10	0.00	19.50	0.48	0.00	0.05	100.08	97% ab
10N17d-16_4	original (?)	101.67	0.00	0.02	0.00	0.24	0.01	0.00	0.03	101.97	qtz
10N17d-17_1	original	47.880	0.076	10.880	0.000	27.410	0.016	0.049	3.730	90.041	mica
10N17d-17_2	original (?)	65.100	0.979	15.320	0.000	18.380	0.024	0.216	0.170	100.188	91% or 9% ab
10N17d-17_3	original (?)	68.69	11.64	0.11	0.00	19.79	0.45	0.00	0.06	100.74	97% ab
10N17d-17_4	original (?)	68.71	11.73	0.12	0.00	19.82	0.53	0.00	0.03	100.94	97% ab
10N17e-1_1	original, altered (?)	67.65	11.31	0.22	0.00	20.52	1.37	0.01	0.05	101.12	93% ab 6% an
10N17e-1_2	original, altered (?)	67.50	11.23	0.16	0.00	20.85	1.64	0.00	0.00	101.38	92% ab 7% an
10N17e-6_1	original, altered (?)	67.88	11.26	0.16	0.00	20.63	1.46	0.00	0.04	101.43	92% ab 7% an
10N17e-6_2	original, altered (?)	67.37	11.18	0.19	0.00	20.78	1.57	0.00	0.03	101.12	92% ab 7% an
10N17e-6_3	original, altered (?)	64.720	0.959	15.580	0.000	18.390	0.000	0.107	0.000	99.756	91% or 9% ab
10N17e-2_1	Kfs metasomatite	65.660	0.590	15.920	0.000	18.450	0.000	0.067	0.043	100.730	95% or 5% ab
10N17e-2_2	Kfs metasomatite	65.800	0.609	15.870	0.000	18.610	0.009	0.096	0.016	101.010	94% or 6% ab
10N17e-5_1	Kfs metasomatite	65.640	0.929	15.660	0.000	18.560	0.020	0.077	0.018	100.903	92% or 8% ab
10N17e-5_2	Kfs metasomatite	65.510	0.986	15.630	0.000	18.630	0.000	0.092	0.000	100.848	91% or 9% ab
10N17e-5_3	Kfs metasomatite	67.54	11.19	0.09	0.00	20.79	1.49	0.00	0.03	101.13	93% ab 7% an
10N17e-5_4	Kfs metasomatite	67.71	10.53	1.37	0.00	20.57	1.41	0.03	0.06	101.68	86% ab
10N17e-7_1	Kfs metasomatite	65.320	0.784	15.970	0.000	18.450	0.014	0.103	0.011	100.651	93% or 7% ab
10N17e-7_2	Kfs metasomatite	65.290	0.682	15.910	0.000	18.640	0.020	0.128	0.000	100.670	94% or 6% ab
10N17e-7_3	original (?)	67.70	11.11	0.11	0.00	20.84	1.43	0.01	0.01	101.20	93% ab 7% an
10N17e-10_1	Kfs metasomatite (?)	65.350	0.777	15.740	0.000	18.590	0.016	0.108	0.035	100.616	93% or 7% ab
10N17e-10_2	Kfs metasomatite (?)	65.360	0.710	15.810	0.000	18.610	0.027	0.103	0.041	100.660	93% or 6% ab
10N17e-10_3	Kfs metasomatite (?)	69.13	11.82	0.08	0.00	19.79	0.42	0.00	0.06	101.30	98% ab
10N17e-10_4	Kfs metasomatite (?)	68.78	11.74	0.10	0.00	20.08	0.64	0.00	0.02	101.35	99% ab
10N17e-9_1	Kfs metasomatite (?)	65.600	0.900	15.510	0.000	18.570	0.029	0.098	0.000	100.707	92% or 8% ab
10N17e-9_2	Kfs metasomatite (?)	65.290	0.804	15.460	0.000	18.460	0.039	0.113	0.063	100.228	92% or 7% ab
10N17e-8_1	original, altered (?)	65.730	0.860	15.550	0.000	18.540	0.000	0.130	0.026	100.836	92% or 8% ab
10N17e-8_2	original, altered (?)	65.190	0.611	16.020	0.000	18.500	0.000	0.069	0.079	100.469	95% or 5% ab
10N17e-8_3	original, altered (?)	68.00	11.34	0.16	0.00	20.35	1.02	0.02	0.04	100.92	94% ab 4% an
10N17e-8_4	original, altered (?)	68.25	11.75	0.10	0.00	19.99	0.71	0.00	0.03	100.84	96% ab 3% an
10N17e-12_1	original, altered (?)	65.040	0.310	16.340	0.000	18.320	0.014	0.144	0.122	100.289	97% or 3% ab
10N17e-12_2	original, altered (?)	64.830	0.558	16.100	0.000	18.320	0.012	0.021	0.272	100.114	95% or 5% ab
10N17e-12_3	original, altered (?)	68.64	11.65	0.11	0.00	19.91	0.53	0.00	0.19	101.03	97% ab 3% an
10N17e-12_4	original, altered (?)	68.46	11.47	0.37	0.00	20.15	0.79	0.00	0.09	101.32	94% ab 4% an
10N17e-11_1	Kfs metasomatite (?)	65.420	0.615	15.910	0.000	18.650	0.000	0.083	0.020	100.697	94% or 6% ab

10N17e-11_2	Kfs metasomatite (?)	65.250	0.429	16.240	0.000	18.370	0.000	0.098	0.051	100.438	96% or 4% ab
10N17e-11_3	Kfs metasomatite (?)	68.14	11.40	0.23	0.00	20.35	0.81	0.04	0.04	101.02	95% ab 4% an
10N17e-11_4	Kfs metasomatite (?)	68.69	11.34	0.36	0.00	20.17	0.90	0.01	0.07	101.54	94% ab 4% an
10N17f-1_3	original	102.18	0.00	0.01	0.00	0.00	0.01	0.01	0.02	102.24	qtz
10N17f-1_4	original	102.13	0.00	0.02	0.00	0.00	0.00	0.02	0.00	102.17	qtz
10N17f-2_1	original (?)	65.240	0.542	16.250	0.000	18.380	0.000	0.131	0.064	100.607	95% or 5% ab
10N17f-2_2	original (?)	65.620	0.590	16.200	0.000	18.620	0.000	0.127	0.026	101.184	95% or 5% ab
10N17f-2_3	original	102.39	0.00	0.04	0.00	0.02	0.00	0.00	0.05	102.50	qtz
10N17f-2_4	original	102.44	0.02	0.01	0.00	0.00	0.00	0.00	0.08	102.54	qtz
10N17f-3_1	original (?)	67.85	11.22	0.19	0.00	20.73	1.38	0.00	0.05	101.42	93% ab 6% an
10N17f-3_2	original (?)	67.78	11.25	0.17	0.00	20.52	1.26	0.02	0.15	101.14	93% ab 6% an
10N17f-6_1	Kfs metasomatite (?)	65.160	1.028	15.490	0.000	18.520	0.019	0.058	0.043	100.317	91% or 9% ab
10N17f-6_2	Kfs metasomatite (?)	64.840	0.840	15.580	0.000	18.560	0.020	0.076	0.061	99.977	92% or 8% ab
10N17f-6_3	Kfs metasomatite (?)	69.13	11.79	0.06	0.00	20.09	0.39	0.00	0.07	101.53	98% ab
10N17f-6_4	Kfs metasomatite (?)	68.68	11.67	0.08	0.00	20.10	0.63	0.00	0.00	101.16	97% ab
10N17f-9_1	Kfs metasomatite	65.620	1.171	15.240	0.000	18.540	0.012	0.129	0.017	100.729	90% or 10% ab
10N17f-9_2	Kfs metasomatite	65.480	0.791	15.840	0.000	18.660	0.011	0.086	0.019	100.887	93% or 7% ab
10N17f-9_3	Kfs metasomatite	67.97	11.35	0.11	0.00	20.41	1.25	0.00	0.00	101.09	94% ab 6% an
10N17f-9_4	Kfs metasomatite	67.97	11.22	0.09	0.00	20.70	1.49	0.00	0.03	101.50	93% ab 7% an
10N17f-5_1	original (?)	65.760	1.124	15.290	0.000	18.690	0.022	0.107	0.000	100.993	90% or 10% ab
10N17f-5_2	original (?)	65.680	1.191	15.320	0.000	18.690	0.022	0.118	0.019	101.039	90% or 10% ab
10N17f-5_3	original (?)	68.11	11.31	0.07	0.00	20.87	1.56	0.01	0.01	101.95	93% ab 7% an
10N17f-5_4	original (?)	68.52	11.31	0.07	0.00	20.94	1.26	0.00	0.05	102.14	94% ab 6% an
10N17f-10_1	Kfs metasomatite	64.150	1.152	15.210	0.000	18.440	0.023	0.126	0.000	99.101	90% or 10% ab
10N17f-10_2	Kfs metasomatite	64.390	0.954	15.680	0.000	18.380	0.000	0.085	0.007	99.497	92% or 8% ab
10N17f-10_3	Kfs metasomatite	68.41	11.65	0.07	0.00	19.87	0.51	0.00	0.00	100.51	97% ab
10N17f-10_4	Kfs metasomatite	68.45	11.73	0.06	0.00	19.98	0.53	0.00	0.03	100.77	97% ab
10N17f-8_1	Kfs metasomatite	65.590	0.857	16.060	0.000	18.620	0.010	0.101	0.027	101.265	92% or 7% ab
10N17f-8_2	Kfs metasomatite	65.850	0.869	15.550	0.000	18.620	0.021	0.071	0.000	100.980	92% or 8% ab
10N17f-8_3	Kfs metasomatite	66.10	10.79	0.11	0.00	20.72	1.88	0.02	0.05	99.67	91% ab 9% an
10N17f-7_1	original (?)	68.01	11.17	0.47	0.00	20.57	1.41	0.00	0.07	101.70	91% ab 6% an
10N17f-7_2	original (?)	69.60	11.86	0.13	0.00	19.88	0.48	0.00	0.06	102.01	97% ab 2% an
10N17f-7_3	Kfs metasomatite (?)	65.520	0.425	16.400	0.000	18.630	0.014	0.056	0.071	101.116	96% or 4% ab
091e-3_1	Kfs metasomatite	65.610	0.706	15.790	0.000	18.530	0.026	0.085	0.062	100.809	94% or 6% ab
091e-3_2	Kfs metasomatite	65.280	0.680	15.810	0.000	18.540	0.010	0.138	0.095	100.554	94% or 6% ab
091e-4_1	Kfs metasomatite	65.540	0.851	15.790	0.000	18.650	0.000	0.140	0.029	101.000	92% or 8% ab
091e-4_2	Kfs metasomatite	65.270	0.638	15.830	0.000	18.540	0.031	0.094	0.120	100.523	94% or 6% ab
091e-4_3	Kfs metasomatite	102.29	0.00	0.04	0.00	0.02	0.00	0.00	0.03	102.37	qtz
091e-7_1	Kfs metasomatite	65.410	0.705	15.740	0.000	18.550	0.023	0.108	0.142	100.678	94% or 6% ab
091e-7_2	Kfs metasomatite	65.370	0.690	15.850	0.000	18.680	0.000	0.121	0.063	100.774	94% or 6% ab
091e-7_3	Kfs metasomatite	98.66	0.02	0.52	0.00	1.89	0.08	0.00	0.14	101.30	qtz
091e-6_1	Kfs metasomatite	65.110	0.619	16.020	0.000	18.630	0.020	0.077	0.087	100.563	94% or 6% ab
091e-6_2	Kfs metasomatite	65.230	0.613	15.790	0.000	18.540	0.025	0.101	0.076	100.375	94% or 6% ab
091e-6_3	Kfs metasomatite	101.68	0.00	0.03	0.00	0.05	0.01	0.00	0.04	101.81	qtz
091e-9_1	Kfs metasomatite	65.350	0.610	15.690	0.000	18.620	0.031	0.106	0.054	100.461	94% or 6% ab
091e-9_2	Kfs metasomatite	64.930	0.696	15.710	0.000	18.500	0.015	0.097	0.058	100.005	94% or 6% ab
091e-10_1	Kfs metasomatite	65.280	0.833	15.740	0.000	18.540	0.022	0.119	0.046	100.580	93% or 7% ab

091e-10_2	Kfs metasomatite	65.530	0.665	16.010	0.000	18.420	0.033	0.139	0.071	100.867	94% or 6% ab
091e-10_3	Kfs metasomatite	101.83	0.01	0.02	0.00	0.03	0.00	0.00	0.00	101.89	qtz
091e-10_4	Kfs metasomatite	101.55	0.00	0.02	0.00	0.01	0.00	0.02	0.00	101.60	qtz
091e-11_1	Kfs metasomatite	65.590	0.576	15.860	0.000	18.490	0.031	0.130	0.065	100.742	95% or 5% ab
091e-11_2	Kfs metasomatite	65.600	0.747	15.690	0.000	18.730	0.011	0.101	0.079	100.958	93% or 7% ab
091e-8_1	Kfs metasomatite	65.290	0.757	15.510	0.000	18.590	0.034	0.137	0.024	100.342	93% or 7% ab
091e-8_2	Kfs metasomatite	65.320	1.130	14.890	0.000	18.620	0.039	0.120	0.019	100.137	89% or 10% ab
091e-14_1	Kfs metasomatite	65.130	0.768	15.340	0.000	18.510	0.000	0.103	0.017	99.868	93% or 7% ab
091e-14_2	Kfs metasomatite	65.170	0.753	15.330	0.000	18.590	0.010	0.100	0.050	100.004	93% or 7% ab
091e-14_3	Kfs metasomatite	102.17	0.01	0.06	0.00	0.00	0.01	0.04	0.00	102.28	qtz
091e-12_1	Kfs metasomatite	65.590	0.786	15.490	0.000	18.570	0.000	0.117	0.109	100.662	93% or 7% ab
091e-12_2	Kfs metasomatite	65.450	0.779	15.360	0.000	18.410	0.011	0.094	0.020	100.124	93% or 7% ab
091e-13_1	Kfs metasomatite	65.260	0.612	15.930	0.000	18.640	0.014	0.151	0.062	100.669	94% or 6% ab
091e-13_2	Kfs metasomatite	65.240	0.477	16.120	0.000	18.590	0.010	0.130	0.000	100.567	96% or 4% ab
091e-16_1	Kfs metasomatite	65.080	0.602	16.100	0.000	18.510	0.000	0.129	0.000	100.421	95% or 5% ab
091e-16_2	Kfs metasomatite	65.510	0.568	15.920	0.000	18.570	0.014	0.122	0.025	100.728	95% or 5% ab
091e-17_1	Kfs metasomatite	65.540	0.551	15.610	0.000	18.480	0.010	0.000	0.100	100.291	95% or 5% ab
091e-17_2	Kfs metasomatite	65.420	0.601	15.690	0.000	18.550	0.008	0.094	0.000	100.364	94% or 6% ab
091e-15_1	Kfs metasomatite (?)	65.550	0.158	16.390	0.000	18.600	0.000	0.361	0.087	101.146	99% or
091e-15_2	Kfs metasomatite (?)	64.820	0.126	16.390	0.000	18.360	0.000	0.226	0.074	99.997	99% or
091e-15_3	Kfs metasomatite (?)	47.770	0.111	11.570	0.000	32.220	0.000	0.000	3.400	95.071	mica
10SP33c-2_1	Kfs metasomatite	69.17	11.92	0.16	0.00	19.50	0.03	0.03	0.23	101.04	99% ab
10SP33c-2_2	Kfs metasomatite	69.06	11.54	0.64	0.00	19.56	0.02	0.00	0.41	101.23	97% ab 3% or
10SP33c-2_3	Kfs metasomatite	69.39	12.05	0.03	0.00	19.70	0.00	0.00	0.00	101.17	100% ab
10SP33c-2_4	Kfs metasomatite	65.360	0.040	16.570	0.000	18.160	0.000	0.174	0.000	100.304	100% or
10SP33c-2_5	Kfs metasomatite	65.550	0.024	15.990	0.000	18.170	0.010	0.229	0.010	99.983	100% or
ML248a-1_1	Kfs metasomatite	65.500	1.085	15.170	0.000	18.700	0.024	0.162	0.008	100.649	90% or 10% ab
ML248a-1_2	Kfs metasomatite	65.930	1.810	14.070	0.000	18.720	0.008	0.210	0.034	100.782	84% or 16% ab
ML248a-1_3	Kfs metasomatite	68.94	10.58	1.91	0.00	19.64	0.12	0.05	0.04	101.28	89% ab 10% or
ML248a-1_4	Kfs metasomatite	69.51	11.80	0.23	0.00	19.58	0.10	0.05	0.01	101.28	98% ab
ML248a-2_1	Kfs metasomatite	64.830	0.977	14.940	0.000	18.710	0.011	0.170	0.020	99.658	91% or 9% ab
ML248a-2_2	Kfs metasomatite	65.440	0.873	15.420	0.000	18.640	0.000	0.212	0.000	100.585	92% or 8% ab
ML248a-2_3	Kfs metasomatite	68.91	10.64	1.77	0.00	19.41	0.07	0.01	0.03	100.84	90% ab 10% or
ML248a-3_1	Kfs metasomatite	65.400	0.865	15.440	0.000	18.630	0.014	0.154	0.000	100.503	92% or 8% ab
ML248a-3_2	Kfs metasomatite	65.530	1.460	14.530	0.000	18.800	0.010	0.214	0.000	100.544	87% or 13% ab
ML248a-3_3	original, altered	72.54	8.84	0.96	0.00	18.10	0.43	0.00	0.05	100.92	mess
ML248a-3_4	original, altered	79.73	8.40	0.06	0.01	13.82	0.18	0.03	0.00	102.22	mess
ML248a-3_5	original, altered	69.28	11.86	0.17	0.00	19.86	0.16	0.01	0.12	101.46	98% ab
ML248a-3_6	original, altered	68.68	11.52	0.34	0.00	20.19	0.19	0.00	0.04	100.96	98% ab
ML248a-3_7	original, altered	65.470	0.883	14.990	0.000	18.700	0.033	0.209	0.044	100.329	92% or 8% ab
ML248a-3_8	original, altered	102.42	0.01	0.00	0.00	0.00	0.00	0.00	0.02	102.45	qtz
ML248a-3_9	original, altered	64.38	9.70	0.21	0.05	22.96	4.37	0.00	0.02	101.69	79% ab 20% an
ML248a-4_1	Kfs metasomatite	65.570	0.921	15.320	0.000	18.750	0.000	0.229	0.018	100.808	92% or 8% ab
ML248a-4_2	rim	69.14	11.75	0.17	0.00	20.05	0.32	0.00	0.01	101.44	98% ab
ML248a-4_3	original, altered	68.75	11.64	0.31	0.02	20.07	0.41	0.01	0.04	101.25	96% ab
ML248a-4_4	original, altered	65.70	10.43	0.13	0.01	22.24	2.99	0.00	0.01	101.52	86% ab 14% an
ML248a-5_1	Kfs metasomatite (?)	65.340	0.898	15.430	0.000	18.590	0.031	0.187	0.000	100.476	92% or 8% ab

ML248a-5_2	Kfs metasomatite (?)	65.670	0.697	15.420	0.000	18.500	0.017	0.150	0.000	100.454	93% or 7% ab
ML248a-6_1	Kfs metasomatite	69.24	11.79	0.09	0.00	19.47	0.02	0.00	0.04	100.65	99% ab
ML248a-6_2	Kfs metasomatite	69.25	11.76	0.05	0.00	19.45	0.03	0.00	0.05	100.58	100% ab
10HV6a-1_1	Kfs metasomatite (?)	69.00	12.08	0.08	0.00	19.89	0.34	0.00	0.03	101.42	98% ab
10HV6a-1_2	Kfs metasomatite (?)	69.33	11.96	0.12	0.00	19.73	0.09	0.03	0.02	101.27	99% ab
10HV6a-2_1	Kfs metasomatite (?)	68.90	11.89	0.41	0.00	19.78	0.27	0.01	0.01	101.27	97% ab
10HV6a-2_2	Kfs metasomatite (?)	69.08	11.92	0.13	0.00	19.88	0.28	0.00	0.01	101.30	98% ab
10HV6a-4_1	Kfs metasomatite (?)	68.72	11.72	0.29	0.00	19.59	0.19	0.04	0.02	100.56	98% ab
10HV6a-4_2	Kfs metasomatite (?)	69.08	11.97	0.07	0.00	19.82	0.32	0.03	0.04	101.33	98% ab
10HV6a-3_1	Kfs metasomatite (?)	69.37	11.84	0.05	0.00	19.73	0.32	0.01	0.00	101.32	98% ab
10HV6a-3_2	Kfs metasomatite (?)	69.10	11.86	0.18	0.00	19.71	0.27	0.00	0.08	101.20	98% ab
10HV6a-3_3	Kfs metasomatite (?)	37.55	0.07	9.99	0.00	13.75	0.03	0.00	13.00	74.39	mica
10HV6a-7_1	original, altered	68.48	11.29	0.73	0.00	19.35	0.22	0.02	0.22	100.32	95% ab 4% or
10HV6a-7_2	original, altered	65.000	0.245	15.930	0.000	18.190	0.010	0.143	0.384	99.901	98% or
10HV6a-5_1	original, altered	68.47	11.39	0.68	0.00	19.47	0.02	0.04	0.26	100.33	96% ab 4% or
10HV6a-5_2	original, altered	68.63	11.63	0.79	0.00	19.48	0.10	0.03	0.13	100.78	95% ab 4% or
10HV6a-6_1	original, altered	68.08	11.65	0.18	0.00	19.30	0.17	0.02	0.12	99.51	98% ab
10HV6a-6_2	original, altered	68.98	11.31	0.77	0.00	19.23	0.03	0.02	0.22	100.57	96% ab 4% or
10HV6a-6_3	original, altered	37.110	0.103	10.150	0.000	13.530	0.010	0.000	12.800	73.703	mica
10HV6a-8_1	Kfs metasomatite (?)	68.41	10.32	2.32	0.00	19.24	0.04	0.04	0.30	100.66	87% ab 13% or
10HV6a-8_2	Kfs metasomatite (?)	68.46	10.64	1.89	0.00	19.29	0.02	0.13	0.18	100.62	89% ab 10% or
10HV6a-8_3	Kfs metasomatite (?)	64.080	0.803	14.130	0.000	18.430	0.075	0.130	0.526	98.173	92% or 8% ab
10HV6a-8_4	Kfs metasomatite (?)	65.590	2.180	13.100	0.000	18.310	0.011	0.112	0.366	99.669	80% or 20% ab
10HV6a-9_1	Kfs metasomatite (?)	68.30	11.60	0.64	0.00	19.48	0.01	0.03	0.13	100.19	96% ab 3% or
10HV6a-9_2	Kfs metasomatite (?)	69.59	11.83	0.25	0.00	19.62	0.01	0.00	0.07	101.37	99% ab
10HV6a-9_3	Kfs metasomatite (?)	65.700	1.275	14.130	0.000	18.480	0.007	0.127	0.116	99.835	mess
10HV6a-10_1	Kfs metasomatite (?)	68.72	10.93	1.31	0.00	19.63	0.25	0.03	0.07	100.94	92% ab 7% or
10HV6a-10_2	Kfs metasomatite (?)	68.80	11.16	1.29	0.00	19.51	0.05	0.04	0.28	101.12	93% ab 7% or
10HV6a-10_3	Kfs metasomatite (?)	68.94	11.37	0.77	0.00	19.49	0.09	0.04	0.25	100.95	96% ab 4% or
avg. analytical error (1σ) Pl		12.50	5.38	7.62	3.05	5.66	4.63	3.57	5.28		
avg. analytical error (1σ) Kfs		4.212	0.470	1.195	0.000	1.949	0.017	0.097	1.313		

Tab.2c: Electron microprope analyses of mica in various samples. Measurements were conducted at the University of Tübingen under the supervision of T. Wenzel.

Point	position	Na2O [wt%]	MgO [wt%]	K2O [wt%]	BaO [wt%]	SiO2 [wt%]	Al2O3 [wt%]	CaO [wt%]	TiO2 [wt%]	MnO [wt%]	FeO [wt%]	Total [wt%]	Mineral
Standards													
A_Albit_1		11.550	0.000	0.155	0.000	68.860	19.890	0.095	0.000	0.000	0.000	100.551	ab
A_Diopsid_1		0.010	18.610	0.000	0.000	51.970	0.051	25.590	0.069	0.040	0.000	96.340	di
A_Sanid_1		2.970	0.000	12.030	1.150	64.310	19.350	0.023	0.033	0.000	0.132	99.998	sa
A_Baryt_1		0.133	0.000	0.000	67.670	0.126	0.034	0.000	1.644	0.000	0.000	69.607	brt
A_SrTiO3_1		0.000	0.014	0.000	0.000	0.000	0.000	0.000	47.050	0.000	0.068	47.133	Sr titanate
A_Rhodonit_1		0.000	0.870	0.000	0.000	45.610	0.010	6.350	0.000	37.790	1.710	92.340	rdn
A_Hematite_1		0.000	0.000	0.000	0.000	0.066	0.000	0.000	0.009	0.000	90.010	90.085	hem
A_Rhodonit_2		0.000	0.920	0.000	0.000	46.480	0.010	6.720	0.000	38.440	1.530	94.100	rdn
A_Baryt_2		0.123	0.000	0.015	64.600	0.070	0.019	0.014	1.690	0.000	0.038	66.570	brt
Samples													
YG17A-6_1	original	0.092	20.870	10.630	0.000	40.020	18.270	0.000	1.050	0.087	7.440	98.458	phl
YG17A-6_2	original	0.080	20.930	10.570	0.000	39.890	18.390	0.000	1.097	0.102	7.520	98.578	phl
YG17A-6_3	original	0.106	20.810	10.520	0.000	39.850	18.460	0.010	1.094	0.083	7.420	98.353	phl
YG17A-6_4	original	0.103	20.590	10.770	0.010	39.760	18.470	0.014	1.072	0.077	7.020	97.887	phl
YG17A-6_5	original	0.100	20.750	10.510	0.000	39.760	18.470	0.014	1.077	0.132	7.420	98.233	phl
YG17A-6_6	original	0.089	20.660	10.680	0.000	39.760	18.440	0.000	1.080	0.117	7.360	98.186	phl
YG17A-6_7	original	0.091	20.880	10.720	0.000	39.420	18.280	0.011	1.097	0.124	7.150	97.774	phl
YG17A-6_8	original	0.087	20.330	10.370	0.000	39.320	18.200	0.011	1.060	0.110	6.930	96.418	phl
YG17A-6_9	original	0.079	20.330	10.710	0.000	38.870	18.270	0.008	1.039	0.101	7.030	96.437	phl
YG17A-6_10	original	0.071	20.480	10.520	0.000	38.950	18.140	0.015	1.046	0.086	7.000	96.308	phl
YG17A-7_1	original	0.097	19.870	10.470	0.000	38.580	17.900	0.000	1.346	0.127	6.840	95.230	phl
YG17A-7_2	original	0.100	19.660	10.620	0.000	38.200	17.830	0.013	1.345	0.112	7.000	94.880	phl
YG17A-7_3	original	0.093	20.130	10.480	0.000	39.060	18.250	0.018	1.343	0.092	7.110	96.575	phl
YG17A-7_4	original	0.092	20.160	10.590	0.000	39.010	18.180	0.012	1.396	0.102	6.930	96.471	phl
YG17A-8_1	original	0.067	19.910	10.730	0.000	38.820	19.900	0.013	0.754	0.064	7.010	97.268	phl
YG17A-8_2	original, altered	0.180	17.820	10.600	0.000	36.380	23.580	0.039	0.636	0.027	7.160	96.421	phl
YG17A-8_3	original, altered	0.088	18.440	10.720	0.000	36.870	22.540	0.000	0.473	0.075	7.250	96.456	phl
YG17A-8_4	original, altered	11.360	0.010	0.110	0.037	67.890	20.560	0.447	0.000	0.000	0.071	100.486	ab
YG17A-8_5	original, altered	9.930	0.000	0.130	0.000	64.900	22.830	2.980	0.018	0.000	0.065	100.852	pl
YG17A-8_6	original, altered	0.578	2.210	1.188	0.000	43.980	17.870	3.280	0.010	0.009	2.230	71.355	unknown
YG17A-9_1	qtz	0.000	0.010	0.000	0.000	100.770	0.010	0.010	0.000	0.007	0.026	100.833	qtz
YG17A-9_2	original	0.110	21.070	10.620	0.000	39.650	17.890	0.025	0.858	0.125	6.330	96.679	phl
YG17A-9_3	original	0.130	19.110	10.990	0.022	36.800	23.290	0.000	0.116	0.167	6.820	97.445	phl
YG17A-9_4	original	0.088	20.600	10.720	0.000	39.030	20.090	0.000	0.418	0.130	6.480	97.556	phl
YG17A-9_5	original	0.100	20.960	10.780	0.000	39.960	18.830	0.010	0.700	0.126	6.340	97.807	phl
YG17A-9_6	original	11.490	0.000	0.076	0.017	69.440	20.730	0.447	0.022	0.011	0.064	102.296	ab
YG17A-13_1	original, altered	0.062	14.210	9.570	0.054	41.110	25.660	0.084	0.010	0.061	6.060	96.881	phl
YG17A-13_2	original, altered	11.280	0.058	0.132	0.000	69.500	20.740	0.390	0.000	0.000	0.144	102.244	ab
YG17A-13_3	original, altered	0.140	19.250	10.640	0.041	37.310	23.430	0.033	0.099	0.103	6.000	97.046	phl
YG17A-13_4	original, altered	0.129	19.350	10.720	0.000	37.600	23.570	0.012	0.090	0.109	6.050	97.630	phl
YG17A-18_1	original	0.122	21.540	10.540	0.000	39.000	15.820	0.017	1.591	0.085	8.160	96.875	phl
YG17A-18_2	original	0.102	21.120	10.690	0.000	39.020	15.980	0.010	1.595	0.066	8.220	96.803	phl

YG17A-18_3	original	0.126	20.650	10.370	0.000	39.450	16.200	0.057	1.610	0.072	7.950	96.486	phl
YG17A-19_1	original	0.130	20.190	10.700	0.000	39.350	17.030	0.000	1.638	0.065	7.500	96.602	phl
YG17A-19_2	original	0.121	20.470	10.590	0.000	39.210	16.940	0.000	1.515	0.062	7.580	96.487	phl
YG17A-19_3	original	0.145	20.420	10.700	0.000	39.130	16.870	0.007	1.568	0.065	7.820	96.725	phl
YG17b-11_1	original	0.130	20.220	10.590	0.000	39.590	17.290	0.008	1.800	0.024	7.230	96.883	phl
YG17b-11_2	original	0.119	20.270	10.670	0.000	39.490	17.560	0.000	1.830	0.025	7.400	97.364	phl
YG17b-11_3	original	0.116	20.570	10.570	0.000	39.320	17.450	0.000	1.840	0.071	7.650	97.587	phl
YG17b-2_1	original	0.095	19.420	10.590	0.000	39.650	17.870	0.000	1.820	0.049	7.110	96.604	phl
YG17b-2_2	original	0.156	20.200	10.430	0.000	39.980	18.650	0.010	1.166	0.083	6.440	97.115	phl
YG17b-2_6	original, altered	0.467	10.300	10.730	0.000	43.070	30.910	0.008	0.000	0.042	3.010	98.536	phl
YG17b-6_1	original	0.136	19.310	10.670	0.000	38.660	19.780	0.000	1.495	0.051	7.530	97.632	phl
YG17b-6_2	qtz	0.000	0.000	0.010	0.030	102.190	0.010	0.000	0.023	0.013	0.084	102.361	qtz
YG17b-6_3	original	0.150	18.590	10.810	0.000	36.580	23.780	0.000	0.496	0.043	7.330	97.779	phl
YG17b-6_4	original, altered	0.204	4.140	11.120	0.045	46.220	34.440	0.013	0.029	0.017	2.220	98.447	ms
YG17b-10_1	original	0.194	19.010	10.570	0.000	38.300	20.500	0.010	1.253	0.036	7.220	97.092	phl
YG17b-10_2	original	0.295	17.910	10.470	0.000	36.930	23.760	0.000	0.553	0.045	7.570	97.533	phl
YG17b-10_3	original	0.195	14.990	10.620	0.000	39.190	26.340	0.038	0.017	0.034	5.750	97.173	phl
YG17b-10_4	original, altered	0.198	4.470	9.870	0.053	49.050	30.420	0.119	0.000	0.000	2.560	96.739	ms
YG17c-5_1	original	0.123	15.760	10.280	0.000	38.240	14.400	0.015	3.200	0.155	15.380	97.553	phl
YG17c-5_2	original	0.138	15.690	10.210	0.000	38.100	14.500	0.016	3.170	0.140	15.820	97.784	phl
YG17d-7_1	metasomatic	0.250	2.840	11.180	0.096	46.870	29.040	0.018	0.276	0.000	3.720	94.291	ms
YG17d-7_2	metasomatic	0.308	2.760	11.240	0.098	47.890	29.580	0.023	0.272	0.020	3.810	96.002	ms
YG17d-7_3	metasomatic	0.252	3.630	11.290	0.177	46.430	29.200	0.020	0.380	0.027	4.330	95.736	ms
10N17b-4_1	metasomatic	0.265	0.832	11.100	0.006	45.080	33.770	0.043	0.397	0.000	2.850	94.342	ms
10N17b-4_2	metasomatic	0.315	0.807	11.410	0.026	45.720	35.650	0.033	0.401	0.000	2.620	96.982	ms
10N17b-4_3	metasomatic	0.108	1.476	11.520	0.086	46.680	31.090	0.000	0.193	0.010	4.740	95.904	ms
10N17d-12_1	original, altered	0.106	1.910	11.460	0.077	47.000	30.520	0.027	0.322	0.040	4.670	96.133	ms
10N17d-12_2	original, altered	0.118	0.317	11.310	0.074	45.520	33.300	0.000	0.342	0.010	4.600	95.591	ms
10N17d-12_3	original, altered	0.105	3.190	11.320	0.046	47.140	29.130	0.009	0.275	0.000	3.900	95.116	ms
10N17d-13_1	original, altered	0.092	16.160	1.520	0.000	36.760	21.300	0.415	0.016	0.132	11.310	87.705	mess
10N17d-13_2	original	0.131	0.957	11.410	0.100	46.520	32.230	0.021	0.260	0.023	4.140	95.791	ms
10N17d-13_3	original, altered	0.084	15.830	2.930	0.020	41.220	17.290	0.576	0.016	0.114	11.990	90.070	mess
10N17d-13_4	original	0.221	1.126	10.600	0.090	45.190	29.840	0.315	0.216	0.018	4.520	92.135	ms
10N17d-13_5	original, altered	0.083	16.870	2.090	0.000	37.660	18.140	0.398	0.000	0.131	12.580	87.952	mess
10N17d-13_6	original, altered	0.294	13.360	1.330	0.000	46.250	14.600	1.660	0.018	0.134	11.280	88.927	mess
10N17d-13_7	original, altered	0.215	11.530	0.888	0.014	3.040	25.180	0.708	0.012	0.069	8.800	50.457	mess
Standards													
A_Albit_2		11.500	0.000	0.134	0.000	69.160	20.010	0.040	0.010	0.000	0.013	100.867	
A_Diopsid_2		0.009	18.840	0.009	0.014	55.820	0.071	25.820	0.056	0.050	0.056	100.744	
A_Hematite_2		0.000	0.000	0.011	0.035	0.104	0.035	0.000	0.017	0.000	90.150	90.352	
A_Sanid_2		2.830	0.000	12.010	1.160	64.910	18.980	0.027	0.019	0.000	0.156	100.092	
A_Hematite_3		0.010	0.000	0.000	0.000	0.062	0.029	0.011	0.000	0.016	90.460	90.588	
Samples													
10N17e-3_1	original	0.092	20.540	10.470	0.000	40.060	14.410	0.000	1.181	0.527	9.310	96.590	mess
10N17e-3_2	original	0.105	20.380	10.460	0.000	39.770	14.410	0.000	1.277	0.556	9.280	96.239	mess
10N17e-4_1	original	0.097	19.630	10.210	0.000	39.790	14.950	0.016	1.487	0.599	9.600	96.379	mess

10N17e-4_2	original	0.079	19.480	10.350	0.000	39.560	15.090	0.031	1.454	0.597	9.840	96.481	mess
10N17f-4_1	original	0.109	17.150	10.520	0.000	37.730	16.430	0.000	1.700	0.128	11.450	95.217	mess
10N17f-4_2	original	0.116	17.400	10.240	0.000	37.390	16.440	0.000	1.670	0.160	11.200	94.616	mess
10SP33c-1_1	original	0.516	0.734	10.990	0.109	45.730	34.220	0.000	0.588	0.029	4.300	97.215	ms
10SP33c-1_4	original	0.512	0.850	11.060	0.096	46.160	33.700	0.023	0.593	0.015	4.070	97.081	ms
10SP33c-1_5	original	0.474	0.807	10.980	0.091	46.200	33.750	0.000	0.619	0.012	4.040	96.973	ms
10SP33c-3_2	original, altered	0.488	0.809	10.920	0.119	45.940	33.420	0.000	0.595	0.015	4.170	96.477	ms
10SP33c-3_3	original, altered	0.454	0.878	10.850	0.103	45.770	33.510	0.019	0.556	0.000	4.000	96.140	ms
10SP33c-3_4	original, altered	0.254	3.080	11.040	0.000	47.750	29.260	0.022	0.576	0.000	4.250	96.232	ms
10SP33c-3_5	original, altered	0.527	0.955	10.990	0.118	46.280	33.270	0.016	0.516	0.000	3.800	96.472	ms
ML248-7_1	original, altered	0.177	10.030	9.690	0.000	36.010	17.140	0.042	2.500	0.337	20.630	96.556	bt
ML248-7_2	original, altered	0.163	10.170	9.910	0.000	36.220	17.230	0.018	2.580	0.301	20.890	97.482	bt
ML248-7_3	original, altered	0.132	10.160	8.060	0.000	34.630	17.030	0.056	2.260	0.318	22.390	95.036	bt
ML248-7_4	original, altered	0.062	10.260	2.190	0.000	30.220	17.310	0.117	0.919	0.295	28.800	90.173	bt
ML248-7_5	inclusion	0.850	0.000	15.940	0.228	64.930	19.150	0.014	0.030	0.000	0.192	101.334	or
ML248-7_6	inclusion	0.000	0.000	0.096	0.000	100.650	0.135	0.029	0.012	0.000	0.118	101.040	qtz
ML248-8_1	original	0.451	1.523	10.840	0.000	45.470	32.510	0.012	1.196	0.026	3.560	95.588	mess
ML248-8_2	original	0.405	1.113	10.980	0.007	46.150	32.980	0.021	0.944	0.017	3.820	96.436	mess
ML248-8_3	original	0.023	14.930	0.057	0.035	27.770	18.530	0.049	0.044	0.404	26.410	88.252	bt
ML248-8_4	original	0.011	16.350	0.065	0.000	28.320	18.310	0.042	0.045	0.598	25.000	88.740	mess
ML248-8_5	original	0.000	0.000	0.010	0.000	100.520	0.010	0.000	0.000	0.011	0.054	100.605	qtz
ML248-9_1	original, altered	0.034	14.570	0.050	0.026	27.210	19.460	0.061	0.031	0.373	28.060	89.875	bt
ML248-9_2	original, altered	0.000	18.150	0.055	0.013	28.760	18.260	0.066	0.042	0.650	23.120	89.116	mess
ML248-9_3	original, altered	0.052	0.073	0.039	0.000	30.820	6.570	28.300	29.780	0.019	2.050	97.704	Ca-Ti-Si
ML248-9_4	original, altered	0.037	0.048	0.029	0.000	30.490	7.380	28.690	27.750	0.010	1.880	96.314	Ca-Ti-Si
ML248-9_5	original, altered	0.400	1.016	10.900	0.029	46.190	33.060	0.000	1.043	0.012	3.830	96.481	mess
ML248-9_6	original, altered	0.384	1.185	10.820	0.000	45.270	33.170	0.022	1.073	0.014	4.170	96.108	mess
10HV1b-8_1	original	0.107	18.950	10.120	0.000	39.560	12.520	0.019	1.213	0.048	11.410	93.948	phl
10HV1b-8_2	original	0.084	19.680	10.150	0.000	39.500	12.500	0.016	1.332	0.000	11.300	94.562	phl
10HV1b-8_4	original, altered	0.064	22.450	9.190	0.000	44.890	11.480	0.196	0.198	0.062	7.360	95.890	mess
10HV1b-8_5	original, altered	0.073	20.460	10.090	0.000	41.020	12.460	0.034	1.309	0.038	10.710	96.195	mess
10HV1b-9_1	metasomatic (?)	0.075	16.620	10.620	0.024	38.290	18.010	0.035	0.468	0.045	12.930	97.116	mess
10HV1b-9_2	metasomatic (?)	0.101	16.370	10.390	0.025	38.290	18.810	0.016	0.466	0.025	12.650	97.143	mess
10HV6a-11_1	original	0.047	21.920	10.320	0.000	42.430	12.180	0.008	1.213	0.010	8.120	96.248	phl
10HV6a-11_2	original	0.059	21.550	10.220	0.000	42.700	12.330	0.010	1.285	0.039	8.410	96.603	phl
10HV6a-11_3	original	0.088	16.990	10.470	0.000	38.080	15.680	0.013	2.440	0.012	12.980	96.754	phl
10HV6a-11_4	original	0.094	18.110	10.410	0.000	39.070	14.670	0.011	2.140	0.031	12.340	96.877	phl
10HV6a-11_5	original	0.085	20.370	10.460	0.000	40.810	13.330	0.008	1.349	0.000	9.070	95.482	phl
10HV6a-11_6	original	0.063	21.160	10.560	0.000	41.720	12.690	0.000	1.254	0.000	8.740	96.187	phl
10HV6a-12_1	original, altered	0.083	19.000	10.270	0.000	38.930	13.430	0.000	1.730	0.015	10.770	94.228	mess
10HV6a-12_2	original, altered	0.098	17.550	10.260	0.000	37.180	14.900	0.000	2.270	0.040	12.940	95.238	mess
10HV6a-12_3	original, altered	0.118	21.840	10.120	0.000	39.630	12.730	0.012	1.285	0.026	9.170	94.932	mess
10HV6a-12_4	original, altered	0.097	21.390	10.170	0.000	40.510	12.430	0.021	1.185	0.020	9.010	94.833	mess
091e-1_1	original, altered	0.113	2.660	11.560	0.000	46.490	30.610	0.007	0.210	0.024	4.050	95.725	ms
091e-1_2	original, altered	0.116	2.170	11.350	0.048	47.340	30.850	0.000	0.087	0.000	3.380	95.341	ms
091e-1_3	original, altered	0.161	2.390	11.390	0.014	47.610	30.050	0.084	0.183	0.000	3.520	95.402	ms
091e-1_4	original, altered	0.162	2.650	11.140	0.024	46.980	30.480	0.038	0.126	0.017	3.600	95.218	ms

091e-2_1	original, altered	0.138	2.670	11.370	0.062	47.530	30.630	0.014	0.188	0.000	3.810	96.412	ms
091e-2_2	original, altered	0.146	2.290	10.880	0.017	49.450	29.250	0.000	0.013	0.027	4.140	96.214	ms
091e-2_3	original, altered	0.108	1.960	11.370	0.021	48.270	31.740	0.012	0.153	0.015	2.980	96.629	ms
091e-2_4	original, altered	0.167	0.342	10.630	0.416	43.770	34.740	0.046	0.048	0.000	6.660	96.819	ms
091e-5_1	original, altered	0.078	1.890	12.180	0.038	52.020	27.090	0.033	0.060	0.015	3.560	96.964	ms
091e-5_2	original, altered	0.062	1.102	14.100	0.075	55.180	24.690	0.025	0.050	0.013	2.480	97.776	ms
091e-5_3	original, altered	0.112	0.108	13.050	0.000	54.450	27.990	0.000	0.013	0.009	1.850	97.581	ms
091e-5_4	original, altered	0.064	1.511	12.450	0.061	51.120	28.570	0.035	0.055	0.017	2.860	96.743	ms
avg. analytical error (1σ)		2.252	8.874	4.467	7.793	15.777	9.330	4.540	5.120	4.484	13.246		

Tab.2d: Electron microprope analyses of mica in various samples. Measurements were conducted at the University of Tübingen under the supervision of T. Wenzel.

point	position	SiO2	TiO2	Al2O3	FeO	MnO	MgO	CaO	Na2O	K2O	F	Cl	total	mineral
HV61d_1-1	metasomatic	60.18	0.00	0.13	4.79	0.03	28.10	0.05	0.09	0.02	0.00	0.03	93.41	tlc
HV61d_1-2	metasomatic	59.42	0.00	0.17	4.71	0.03	28.06	0.05	0.08	0.02	0.00	0.02	92.56	tlc
HV61d_1-3	metasomatic	60.99	0.03	0.15	5.00	0.02	29.03	0.07	0.09	0.00	0.00	0.02	95.40	tlc
HV61d_1-4	metasomatic	62.15	0.00	0.11	5.22	0.03	29.41	0.04	0.08	0.01	0.00	0.02	97.06	tlc
HV61d_1-5	metasomatic	59.74	0.00	0.66	5.15	0.01	28.29	0.04	0.18	0.01	0.00	0.02	94.10	tlc
HV61d_1-6	metasomatic	59.94	0.00	0.31	5.01	0.01	28.88	0.10	0.16	0.03	0.00	0.04	94.48	tlc
HV61d_3-1	metasomatic	58.14	0.01	0.87	4.34	0.00	27.66	0.06	0.23	0.04	0.00	0.06	91.41	tlc
HV61d_3-2	metasomatic	58.27	0.01	1.87	4.73	0.01	28.95	0.15	0.54	0.11	0.00	0.11	94.75	tlc
HV61d_3-3	metasomatic	58.86	0.00	1.12	4.46	0.00	28.53	0.04	0.23	0.08	0.00	0.05	93.37	tlc
HV61d_3-4	metasomatic	59.88	0.01	1.12	4.14	0.02	29.40	0.05	0.27	0.06	0.00	0.03	94.97	tlc
HV61d_3-5	metasomatic	57.55	0.02	1.55	4.20	0.01	28.24	0.07	0.33	0.09	0.00	0.06	92.12	tlc
HV61d_3-6	metasomatic	57.99	0.01	1.07	4.21	0.01	27.98	0.06	0.28	0.06	0.00	0.08	91.74	tlc
HV61d_2-1	original (?)	41.54	1.76	13.99	3.74	0.03	25.12	0.07	0.09	10.05	0.21	0.49	97.08	phl
HV61d_2-2	original (?)	40.54	1.77	14.63	4.11	0.01	24.63	0.02	0.06	10.17	0.14	0.50	96.57	phl
HV61d_2-3	original (?)	42.36	1.67	13.55	3.74	0.02	25.29	0.05	0.10	9.88	0.27	0.51	97.45	phl
HV61d_4-1	original (?)	41.77	1.65	14.14	3.45	0.00	25.65	0.01	0.03	10.22	0.17	0.52	97.62	phl
HV61d_4-2	original (?)	40.31	1.78	14.60	3.41	0.01	24.74	0.01	0.04	10.39	0.08	0.52	95.90	phl
HV61d_5-1	original (?)	40.35	1.72	14.97	3.85	0.00	24.60	0.03	0.08	10.30	0.13	0.46	96.48	phl
HV61d_5-2	original (?)	41.10	1.69	14.19	3.69	0.02	25.15	0.01	0.07	10.17	0.15	0.50	96.73	phl
HV61d_6-1	original (?)	40.95	1.63	14.42	4.49	0.02	24.80	0.05	0.09	10.08	0.14	0.54	97.20	phl
HV61d_6-2	original (?)	41.32	1.62	13.89	3.98	0.02	24.67	0.10	0.08	9.87	0.33	0.53	96.42	phl
HV61d_7-1	original (?)	41.81	1.61	13.56	3.60	0.02	25.32	0.04	0.07	9.77	0.23	0.49	96.51	phl
HV61d_7-2	original (?)	41.61	1.61	14.15	3.68	0.00	25.24	0.05	0.08	9.85	0.17	0.47	96.91	phl
HV61d_8-1	original (?)	39.88	1.85	15.26	4.12	0.00	24.28	0.02	0.03	10.31	0.15	0.47	96.36	phl
HV61d_8-2	original (?)	39.19	1.92	15.66	3.92	0.02	24.22	0.00	0.07	10.45	0.10	0.46	96.01	phl
HV61d_8-3	original (?)	40.99	1.84	14.31	3.91	0.02	25.06	0.02	0.06	10.25	0.11	0.50	97.05	phl
HV61d_8-4	original (?)	42.04	1.82	13.95	3.91	0.03	25.56	0.02	0.07	10.04	0.17	0.49	98.10	phl
HV61d_9-1	original	40.55	1.74	14.41	3.93	0.00	24.69	0.06	0.08	10.00	0.17	0.51	96.14	phl
HV61d_9-2	original	40.73	1.73	14.56	3.57	0.00	24.92	0.02	0.04	10.29	0.18	0.49	96.53	phl
HV61d_10-1	original	40.47	1.61	14.76	4.00	0.01	24.69	0.00	0.03	10.35	0.15	0.50	96.58	phl
HV61d_10-2	original	40.60	1.55	14.62	3.70	0.00	24.89	0.03	0.04	10.13	0.14	0.52	96.22	phl
HV61d_13-1	original	42.14	1.58	13.90	3.72	0.01	25.50	0.01	0.05	9.93	0.23	0.53	97.60	phl
HV61d_13-2	original	41.44	1.21	13.80	3.53	0.00	25.51	0.02	0.05	9.87	0.24	0.56	96.23	phl
HV61d_11-1	original	40.58	1.75	14.19	3.23	0.02	25.08	0.01	0.04	10.26	0.16	0.49	95.81	phl
HV61d_11-2	original	41.21	1.76	13.82	3.71	0.01	25.21	0.02	0.03	10.02	0.18	0.50	96.47	phl
HV61d_12-1	metasomatic (?)	40.76	1.83	13.62	4.04	0.00	24.69	0.71	0.11	9.74	0.38	0.49	96.37	phl
HV61d_12-2	metasomatic (?)	40.96	1.78	13.87	3.97	0.01	24.75	0.03	0.08	10.05	0.27	0.51	96.29	phl
HV61d_14-1	metasomatic (?)	41.70	1.74	13.82	3.41	0.00	25.37	0.06	0.10	9.95	0.25	0.50	96.91	phl
HV61d_14-2	metasomatic (?)	41.62	1.77	13.55	3.63	0.02	25.02	0.08	0.13	9.68	0.32	0.50	96.32	phl
10HV1b_1-1	metasomatic	38.49	1.99	14.43	13.42	0.02	17.94	0.04	0.10	10.02	3.63	0.24	100.31	phl
10HV1b_1-2	metasomatic	38.57	2.12	14.82	13.33	0.00	18.06	0.01	0.09	10.18	3.52	0.24	100.94	phl
10HV1b_1-3	metasomatic	38.08	2.43	14.30	13.65	0.02	17.47	0.01	0.11	10.35	3.45	0.24	100.11	phl
10HV1b_1-4	metasomatic	37.72	0.03	11.71	9.21	0.29	18.93	0.95	0.10	2.64	0.73	0.13	82.44	mess
10HV1b_1-5	metasomatic	39.22	1.76	13.80	11.93	0.02	18.71	0.03	0.11	9.94	4.05	0.24	99.81	mess

10HV1b_1-6	metasomatic	39.82	0.02	12.23	9.70	0.07	21.14	1.41	0.06	1.57	0.64	0.07	86.74	mess
10HV1b_2-1	metasomatic	37.92	2.12	14.93	14.34	0.03	16.51	0.01	0.09	10.05	2.94	0.25	99.18	phl
10HV1b_2-2	metasomatic	38.72	2.05	15.40	14.55	0.05	17.14	0.04	0.11	10.12	2.90	0.26	101.33	phl
10HV1b_2-3	metasomatic	38.57	1.73	14.91	13.38	0.06	16.99	0.03	0.07	10.19	3.25	0.35	99.53	phl
10HV1b_2-4	metasomatic	37.74	2.21	15.14	14.51	0.02	16.46	0.02	0.09	10.09	3.13	0.22	99.63	phl
10HV1b_3-1	metasomatic	38.86	1.87	14.90	13.77	0.04	17.31	0.01	0.09	9.81	3.02	0.25	99.92	phl
10HV1b_3-2	metasomatic	38.52	2.03	14.74	13.68	0.03	17.06	0.00	0.10	10.15	2.93	0.26	99.50	phl
10HV1b_3-3	metasomatic	39.25	1.89	14.33	13.01	0.03	18.26	0.01	0.08	10.29	3.55	0.20	100.90	phl
10HV1b_3-4	metasomatic	39.14	1.99	14.80	14.04	0.04	17.65	0.02	0.09	9.93	3.25	0.32	101.26	phl
10HV1b_3-5	metasomatic	38.72	1.83	14.70	14.03	0.06	17.18	0.03	0.07	10.09	3.12	0.41	100.24	phl
avg. analytical error (1σ)		8.18	0.81	5.71	4.20	0.04	4.07	0.24	0.09	4.33	1.37	0.19	3.38	

Tab.3: Whole rock X-ray fluorescence analyses of various samples. Measurements were conducted at the University of Tübingen by H. Taubald.

Sample	SiO_2 (wt.%)	TiO_2 (wt.%)	Al_2O_3 (wt.%)	Fe_2O_3 (wt.%)	MnO (wt.%)	MgO (wt.%)	CaO (wt.%)	Na_2O (wt.%)	K_2O (wt.%)	P_2O_5 (wt.%)	LOI (wt.%)	Ba (ppm)	Co (ppm)	Cr (ppm)	Ni (ppm)	Rb (ppm)	Sr (ppm)	V (ppm)
218	72.45	0.43	14.71	1.32	0.01	0.82	0.20	4.09	5.85	0.07	0.60	550	60	b.d.	185	197	36	22
344	70.35	0.40	15.58	2.20	0.03	0.24	2.73	4.97	2.78	0.08	0.56	612	216	b.d.	125	95	148	14
348	73.58	0.25	13.45	2.54	0.01	0.15	0.20	2.40	7.19	0.04	0.57	1095	129	b.d.	121	336	58	13
Y52	70.74	0.39	14.00	2.57	0.03	1.74	0.15	2.34	7.16	0.07	0.88	1067	17	8	101	274	45	7
Y54	73.42	0.23	11.96	2.72	0.01	4.10	0.02	0.18	6.56	0.04	1.49	359	101	14	86	328	3	10
YG17a	69.89	0.42	14.82	2.39	0.02	2.24	0.25	6.62	1.57	0.06	1.50	181	31	19	97	106	17	10
YG17b	70.58	0.32	13.25	2.24	0.02	4.97	0.06	2.36	5.47	0.05	1.31	201	33	3	99	349	6	10
091a	60.66	1.84	12.38	16.04	0.01	0.34	0.05	0.10	6.31	0.10	1.82	559	55	22	173	204	45	246
091c	73.51	0.30	11.24	4.01	0.02	0.16	0.03	0.16	8.72	0.15	0.75	619	149	b.d.	76	228	47	52
091C	72.02	0.30	11.01	4.09	0.02	0.15	0.04	0.16	8.74	0.15	0.77	638	72	b.d.	77	210	53	59
091D	71.18	0.26	14.08	2.04	0.02	0.15	0.02	0.26	11.05	0.10	0.52	786	b.d.	b.d.	98	300	81	23
091E	74.16	0.35	12.34	2.88	0.01	0.22	0.05	0.39	8.73	0.07	0.80	570	32	b.d.	127	382	64	28
091F	76.53	0.36	11.82	2.26	0.02	0.28	0.07	0.36	7.68	0.08	0.91	615	b.d.	b.d.	126	461	50	29
10N17g	74.97	0.25	12.25	2.29	0.01	1.79	0.20	3.27	4.05	0.04	0.66	306	106	b.d.	29	185	23	11
BC338	72.61	0.28	12.78	2.16	0.02	3.60	0.05	1.68	6.10	0.04	0.88	357	35	13	71	326	8	12
BC339	70.73	0.30	13.78	3.43	0.04	0.50	1.07	3.49	5.85	0.05	0.44	822	58	7	102	355	53	1
BC341	70.92	0.28	13.74	3.05	0.02	0.42	0.55	2.52	7.12	0.05	1.04	776	19	b.d.	11	523	35	b.d.
BC343	66.58	0.72	14.42	6.22	0.07	0.58	1.82	3.38	5.56	0.20	0.53	881	66	27	143	341	75	17
EP7	73.94	0.32	12.40	1.25	0.02	1.76	0.06	0.11	9.27	0.04	0.91	687	b.d.	b.d.	175	379	39	21
HV53B	75.16	0.05	14.07	0.48	0.01	0.28	0.28	3.71	4.60	0.06	0.93	119	87	3	35	226	21	3
HV56	79.38	0.02	12.27	0.23	0.00	0.11	0.15	7.10	0.08	0.02	0.23	72	88	b.d.	10	5	14	4
JH195a	75.93	0.14	13.32	0.81	0.01	0.37	0.39	4.05	4.75	0.07	0.96	222	48	b.d.	14	206	48	13
ML052	70.90	0.14	16.54	1.47	0.02	0.54	2.80	6.06	0.90	0.04	0.50	190	66	15	28	57	422	11
ML192	72.30	0.07	15.33	0.47	0.00	0.17	0.06	2.11	9.82	0.06	0.34	1114	17	4	26	377	152	8
ML248a	70.32	0.46	12.93	5.57	0.03	0.46	0.37	2.04	7.10	0.13	0.32	1002	83	14	139	295	132	12
SK054a	67.10	0.37	13.31	2.96	0.03	4.92	0.35	1.25	7.96	0.07	0.73	535	19	17	104	371	53	12
SK080a	68.94	0.38	13.91	5.31	0.01	0.82	0.02	0.20	9.48	0.07	1.01	907	24	20	140	392	26	31
SK201a	75.68	0.04	14.13	0.27	0.02	0.30	0.35	6.51	2.30	0.27	0.32	147	27	11	28	292	21	6
SK201b	84.71	0.37	7.40	0.34	0.01	1.25	0.09	3.44	1.16	0.05	0.42	127	105	34	37	76	16	31
SK223	75.77	0.27	11.89	3.87	0.01	0.50	0.06	0.97	6.06	0.04	1.00	399	70	32	110	260	25	16
SP52a	71.67	0.38	14.91	0.95	0.01	2.02	0.33	7.08	1.39	0.06	0.74	85	89	b.d.	128	73	38	12
WD5B	76.65	0.05	13.59	0.64	0.02	0.23	1.02	4.35	1.88	0.07	0.91	44	251	b.d.	27	164	22	3
WD5c	71.02	0.04	14.51	0.44	0.01	0.18	0.21	1.70	8.97	0.20	0.78	92	166	10	8	607	13	2
WD5C	70.84	0.04	14.52	0.46	0.01	0.18	0.22	1.68	8.84	0.19	0.86	88	29	b.d.	32	550	23	6
WD6	75.50	0.05	14.24	0.58	0.01	0.23	0.47	5.47	2.57	0.06	0.47	125	63	b.d.	31	156	33	4

Sample	Y (ppm)	Zn (ppm)	Zr (ppm)	Ce (ppm)	Eu (ppm)	La (ppm)	Nb (ppm)	Nd (ppm)	Sm (ppm)	Yb (ppm)	Sum (wt.%)
218	188	b.d.	856	372	1.6	114	82	135	22.4	21.8	100.82
344	206	b.d.	578	469	3.4	337	59	242	41.1	24.5	100.23
348	43	b.d.	354	163	0.9	42	29	60	13.8	6.1	100.56
Y52	148	b.d.	651	338	1.4	134	67	153	20	16.9	100.37
Y54	105	b.d.	362	125	0.1	31	63	44	5	13.1	100.89
YG17a	162	b.d.	692	300	1.3	131	51	133	18	17.9	99.98
YG17b	95	b.d.	506	225	0.6	91	44	101	12	11.5	100.82
091a	209	b.d.	306	545	2.8	249	54	167	33.9	25.2	99.99
091c	66	b.d.	300	810	4.3	486	25	261	58	8.0	99.35
091C	66	b.d.	284	806	4.0	494	25	217	51.9	8.4	97.75
091D	35	b.d.	293	564	2.4	304	0	165	32.4	4.8	99.95
091E	57	b.d.	332	443	2.0	201	0	134	29.6	8.0	100.23
091F	49	b.d.	352	423	1.7	193	0	130	26.3	7.4	100.62
10N17g	190	b.d.	454	453	2.1	201	65	180	29	22.6	100.02
BC338	111	b.d.	418	169	0.1	30	53	62	4	13.5	100.38
BC339	163	b.d.	625	471	2.1	204	55	190	31	19.1	99.96
BC341	137	b.d.	475	454	1.8	215	67	177	28	17.7	100.13
BC343	145	52	792	315	1.3	102	59	132	18	16.1	100.40
EP7	144	b.d.	731	548	2.2	188	97	177	32.7	17.6	100.39
HV53B	7	b.d.	20	b.d.	0.8	4	18	2	12.5	2.6	99.69
HV56	b.d	b.d.	5	b.d.	0.7	b.d.	b.d.	b.d.	8.7	0.4	99.61
JH195a	76	b.d.	41	231	0.7	106	38	69	11	10.2	100.93
ML052	7	b.d.	99	56	1.0	37	b.d.	26	b.d.	1.2	100.15
ML192	24	b.d.	32	b.d.	0.0	11	b.d.	17	b.d.	4.5	100.90
ML248a	53	b.d.	520	751	3.5	406	b.d.	265	47	5.9	100.10
SK054a	111	b.d.	645	281	0.9	109	54	122	15	13.0	99.29
SK080a	123	b.d.	640	344	1.3	148	54	149	21	14.2	100.44
SK201a	b.d	b.d.	14	b.d.	0.0	b.d.	74	13	b.d.	0.6	100.25
SK201b	4	b.d.	181	b.d.	0.0	8	b.d.	22	b.d.	1.1	99.29
SK223	138	b.d.	548	250	0.9	90	71	97	14	16.0	100.64
SP52a	99	b.d.	652	446	2.1	189	69	148	26.5	11.2	99.89
WD5B	23	b.d.	44	46	1.0	12	31	12	13.7	4.3	99.46
WD5c	2	b.d.	34	b.d.	0.0	b.d.	26	16	4	3.4	98.16
WD5C	5	b.d.	33	83	0.3	0	23	12	10.8	3.7	97.93
WD6	16	b.d.	40	66	0.8	25	33	20	10.8	3.1	99.71

Tab.4: Whole rock ICPOES analyses of various samples. Measurements were conducted at the University of Ghent under the supervision of M. Elburg.

sample	SiO2 (wt.%)	TiO2 (wt.%)	Al2O3 (wt.%)	Fe2O3 (wt.%)	MnO (wt.%)	MgO (wt.%)	CaO (wt.%)	Na2O (wt.%)	K2O (wt.%)	P2O5 (wt.%)	total	Be (ppm)	Sc (ppm)	V (ppm)	Cr (ppm)	Co (ppm)	Ni (ppm)
091A	61.27	1.90	12.32	16.87	0.01	0.27	0.05	0.07	6.23	0.10	99.07	3.64	19.77	223.80	33.24	98.89	2.27
091c average	75.42	0.27	11.01	4.00	0.01	0.09	0.04	0.12	8.45	0.14	99.55	3.06	4.34	53.28	12.65	111.52	4.03
091D	71.81	0.25	14.01	2.22	0.01	0.08	0.02	0.24	11.01	0.09	99.75	2.43	4.29	20.20	7.72	87.23	b.d.
091F	76.27	0.36	11.66	2.41	0.01	0.20	0.04	0.34	7.57	0.08	98.94	3.71	6.23	18.65	3.93	133.56	b.d.
10HV1B	70.82	0.51	14.39	2.20	0.01	2.62	0.35	5.09	4.01	0.14	100.13	12.87	8.67	16.67	4.46	39.85	b.d.
10HV9sec	82.68	0.29	7.91	0.45	0.00	0.21	0.06	0.17	6.11	0.42	**98.31**	2.97	4.55	11.11	22.66	30.36	b.d.
10N17E	75.60	0.24	11.98	2.78	0.01	0.62	0.16	3.79	3.98	0.04	99.19	9.61	4.28	4.87	1.65	192.74	b.d.
10N17F	75.58	0.24	11.95	2.73	0.01	0.75	0.16	3.79	3.96	0.05	99.23	7.35	3.75	7.47	38.77	145.86	14.29
BC230sec2	78.31	0.20	12.74	1.33	0.00	1.00	0.15	3.35	3.57	0.01	100.67	7.56	4.39	2.50	b.d.	11.13	b.d.
BC235	69.71	0.21	13.07	3.89	0.01	6.32	0.02	0.09	5.44	0.02	98.78	3.04	6.82	4.96	5.56	61.46	2.27
BC237sec	78.62	0.19	11.65	3.14	0.00	0.56	0.05	0.12	6.45	0.03	100.80	2.95	9.25	6.71	4.11	17.73	b.d.
BC240 average	75.89	0.26	12.95	2.41	0.01	3.90	0.05	0.08	3.34	0.05	98.92	3.04	9.01	17.98	4.74	26.51	b.d.
BC241 average	76.03	0.23	12.86	5.84	0.00	0.24	0.02	0.11	3.83	0.04	99.20	3.06	9.99	11.83	8.68	11.02	b.d.
BC243sec	73.03	0.37	13.50	5.29	0.02	0.45	0.05	0.08	6.57	0.07	99.43	2.67	11.90	27.01	6.89	26.36	b.d.
BC244 average	68.70	0.42	15.31	5.41	0.03	0.72	0.03	0.13	8.56	0.07	99.36	4.32	8.50	22.31	9.32	12.98	b.d.
BC248 average	72.77	0.37	13.51	4.65	0.02	0.50	0.45	2.06	5.11	0.06	99.49	5.97	11.12	21.92	5.31	30.06	b.d.
BC249	73.84	0.37	13.44	4.80	0.02	1.69	0.07	0.12	4.62	0.07	99.03	5.94	11.75	21.04	5.58	18.24	b.d.
BC251	75.85	0.34	12.84	3.76	0.02	0.43	0.12	1.49	4.67	0.06	99.58	4.13	8.59	19.03	6.08	50.67	b.d.
BC254B_1	76.09	0.06	14.11	0.49	0.01	0.12	0.63	3.31	4.28	0.04	99.13	1.83	8.23	4.43	5.69	49.85	b.d.
BC254B-2 average	76.64	0.06	14.03	0.48	0.01	0.12	0.63	3.30	4.27	0.04	99.58	1.80	8.02	4.32	2.50	49.18	b.d.
BC342 average	76.65	0.17	12.46	0.78	0.01	1.39	0.25	5.98	1.57	0.02	99.29	5.44	3.73	2.79	6.41	153.76	b.d.
BM25	68.89	0.38	14.15	5.59	0.01	0.94	0.01	0.30	8.38	0.06	98.71	1.76	6.02	12.25	5.57	10.54	b.d.
JH179	73.32	0.21	15.57	1.24	0.01	0.49	1.45	5.33	1.78	0.04	99.42	2.99	3.68	15.91	6.02	150.99	b.d.
JH50	80.62	0.33	13.99	3.87	0.00	0.05	0.02	0.04	0.29	0.06	99.27	4.05	6.51	13.03	2.12	17.04	b.d.
JH51	76.25	0.35	12.34	0.67	0.01	1.63	0.23	6.30	0.87	0.06	98.70	1.20	5.21	10.59	5.19	33.95	b.d.
ML005A	72.41	0.32	13.99	2.76	0.02	1.08	1.74	3.64	3.36	0.11	99.42	1.80	7.98	16.55	3.83	24.69	b.d.
ML005Bsec	67.82	0.23	16.48	3.89	0.02	0.79	2.58	5.65	1.38	0.09	98.92	2.64	5.81	28.60	3.75	35.20	b.d.
ML005C	40.42	0.44	19.13	9.40	0.05	18.73	0.02	0.22	10.02	0.01	**98.43**	1.25	6.42	28.99	2.42	8.75	5.13
ML005E1 average	69.50	0.24	16.08	2.81	0.02	0.80	1.31	3.76	5.00	0.10	99.61	2.42	4.98	18.71	6.92	20.25	b.d.
ML005E2 average	74.50	0.05	14.97	0.73	0.01	0.18	3.02	5.01	0.60	0.04	99.12	3.05	2.19	5.97	4.18	213.02	b.d.
ML005E3sec	70.64	0.31	14.97	4.07	0.02	0.67	2.73	4.75	1.11	0.09	99.36	3.07	5.04	25.23	9.50	21.79	b.d.
ML174 average	78.11	0.16	12.88	0.75	0.00	0.07	0.12	6.72	0.44	0.03	99.28	2.43	2.49	3.12	4.44	53.88	b.d.
ML179	72.05	0.56	15.91	2.05	0.00	0.28	0.36	7.63	1.13	0.11	100.08	2.46	5.05	29.01	14.01	72.33	b.d.
ML180B1average	82.38	0.13	9.56	0.51	0.01	0.06	0.46	2.38	3.67	0.05	99.21	1.81	1.86	6.20	8.57	138.22	b.d.
ML180B2 average	74.62	0.05	15.02	1.03	0.01	0.13	1.47	5.34	2.16	0.03	99.86	4.87	1.87	12.14	6.40	133.06	b.d.
ML197A1	72.31	0.19	14.99	1.69	0.01	0.50	2.64	4.95	1.05	0.03	**98.35**	5.59	2.72	17.19	3.83	38.19	b.d.
ML197A2 average	72.32	0.13	15.73	1.25	0.01	0.44	2.52	4.81	2.10	0.06	99.37	4.62	2.53	12.62	6.77	173.57	b.d.
ML197B average	76.37	0.03	13.49	0.56	0.00	0.11	0.89	3.61	4.27	0.03	99.36	3.01	1.85	5.23	3.03	156.52	b.d.
ML205	75.06	0.17	14.56	0.97	0.01	0.51	1.72	5.43	1.36	0.02	99.80	4.45	3.13	11.43	3.16	15.93	b.d.
ML229	72.74	0.37	13.65	3.18	0.01	0.34	0.51	5.12	3.54	0.07	99.52	4.17	7.79	30.27	5.87	19.31	b.d.

ML237	76.72	0.31	13.36	0.40	0.02	0.61	0.64	5.21	2.64	0.04	99.95	4.02	2.56	7.72	4.80	21.50	b.d.
ML240	72.38	0.25	15.63	1.55	0.01	0.55	2.68	4.42	1.38	0.03	98.88	2.92	4.85	14.53	5.83	61.53	b.d.
ML248A1	72.67	0.45	13.02	6.03	0.01	0.44	0.24	6.75	0.47	0.13	100.21	1.80	5.52	12.94	8.41	109.94	b.d.
ML258	73.36	0.20	15.69	1.50	0.01	0.56	2.54	4.74	1.34	0.02	99.96	2.93	4.18	14.41	10.37	128.47	b.d.
ML286Asec3	47.61	0.20	20.09	6.07	0.02	8.41	12.24	3.52	1.38	0.01	99.55	0.44	28.03	86.62	454.06	17.43	80.73
ML286Bsec	47.26	0.20	19.59	5.88	0.02	8.20	12.25	3.73	1.24	0.02	**98.37**	0.42	26.92	86.09	416.54	14.17	84.64
ML292 average	48.20	2.35	15.39	14.36	0.25	6.05	8.79	3.04	0.47	0.44	99.34	3.08	45.88	331.00	70.20	47.01	7.05
OLM3	73.69	0.09	16.16	0.65	0.01	0.45	1.43	5.99	1.65	0.03	100.14	4.84	2.45	8.02	7.83	89.31	b.d.
OLM7_1	70.50	0.25	17.56	1.68	0.02	0.80	3.63	5.00	1.24	0.09	100.77	1.77	3.58	23.51	9.29	125.99	b.d.
OLM7-2 average	70.03	0.25	17.51	1.68	0.02	0.81	3.61	5.01	1.25	0.08	100.25	1.68	3.57	23.77	6.98	129.24	b.d.
OLM8 average	70.79	0.20	15.56	2.92	0.02	0.52	2.36	4.64	2.25	0.09	99.34	3.02	4.93	14.41	3.74	144.54	b.d.
PG14A	78.91	0.16	11.35	1.28	0.01	0.86	0.05	0.10	5.89	0.04	98.65	2.45	8.02	5.62	4.52	20.51	b.d.
PG7b average	76.45	0.28	12.77	1.85	0.01	6.05	0.09	0.05	2.74	0.08	100.37	2.34	8.66	32.26	3.40	12.97	b.d.
PG8	75.08	0.37	13.88	2.75	0.02	0.20	0.04	0.10	6.76	0.06	99.27	3.62	10.35	22.81	10.60	15.28	b.d.
PG9	72.35	0.34	12.92	5.71	0.07	0.45	0.08	0.13	7.04	0.06	99.16	3.04	9.17	18.58	4.48	19.07	0.00
Y6 average	70.51	0.42	12.17	4.48	0.00	0.48	0.05	0.11	8.38	0.05	**96.66**	1.76	6.06	13.90	38.80	46.04	15.00
Y7b average	69.56	0.46	15.14	5.59	0.02	1.15	0.06	0.13	7.96	0.05	100.13	2.41	8.25	19.13	2.56	35.89	b.d.
YG17C	72.28	0.28	13.50	2.49	0.01	2.68	0.80	3.84	3.90	0.04	99.83	6.13	6.21	9.93	6.72	77.39	b.d.
YG24sec	70.39	0.18	17.11	1.38	0.03	0.62	2.05	5.72	1.42	0.05	98.94	4.45	4.51	16.46	5.46	59.18	b.d.
YG25	77.49	0.09	13.35	0.49	0.00	0.06	1.27	4.17	3.05	0.03	100.02	2.05	1.84	8.70	1.65	86.79	b.d.
YG7b average	73.80	0.47	13.95	3.93	0.03	0.73	0.27	5.71	1.18	0.18	100.25	3.14	6.51	19.85	3.00	64.59	b.d.

sample	Cu (ppm)	Zn (ppm)	Sr (ppm)	Y (ppm)	Zr (ppm)	Ba (ppm)	La (ppm)	Ce (ppm)	Nd (ppm)	Yb (ppm)	Hf (ppm)	Th (ppm)	Nb (ppm)
091A	30.36	21.25	49.79	227.68	319.53	550.55	265.33	480.87	177.29	12.14	1.82	36.43	52.82
091c average	55.14	10.11	57.55	75.36	349.98	609.16	441.13	738.58	220.26	4.29	13.17	129.58	27.88
091D	45.54	3.04	88.03	45.54	351.87	806.67	312.74	547.13	174.28	3.04	15.18	167.60	21.86
091F	40.78	17.92	60.87	57.46	435.81	620.84	199.57	369.47	132.22	3.09	16.68	176.09	21.62
10HV1B	4.90	23.28	62.31	217.52	1002.49	597.72	292.89	565.56	200.98	11.64	31.86	89.46	73.53
10HV9sec	5.19	b.d.	18.59	609.89	218.53	454.05	1747.62	2888.46	857.71	33.39	10.39	127.62	4.75
10N17E	4.20	7.80	31.63	139.89	537.53	258.54	182.51	387.84	148.89	10.21	19.81	124.88	65.44
10N17F	6.74	6.74	23.00	167.92	541.73	271.67	128.70	269.04	111.54	11.03	20.22	121.96	61.29
BC230sec2	7.06	5.22	25.38	123.97	467.98	246.16	229.22	418.19	146.71	14.30	23.76	181.68	na
BC235	7.30	3.04	9.25	101.01	679.56	405.17	27.38	82.15	21.91	9.74	27.38	206.89	102.84
BC237sec	48.10	8.13	22.32	113.80	236.61	273.77	20.11	49.62	12.68	10.20	11.76	117.44	na
BC240 average	3.04	2.13	9.58	104.07	289.17	70.97	129.33	287.26	126.89	6.69	11.56	83.99	22.82
BC241 average	45.28	0.92	15.21	36.10	300.28	294.64	90.55	197.62	81.37	3.67	11.01	121.45	31.51
BC243sec	212.41	8.05	29.03	88.98	449.32	564.29	128.36	276.25	117.46	6.60	15.57	66.22	na
BC244 average	36.40	28.69	32.54	58.00	526.68	1025.20	124.94	261.61	104.58	4.32	17.89	60.47	32.08
BC248 average	22.99	18.51	40.39	115.86	527.64	489.66	120.04	252.92	101.83	7.17	15.83	65.99	32.55
BC249	11.88	7.13	14.64	115.25	485.48	327.88	118.81	252.48	102.77	7.72	14.85	62.38	28.51
BC251	10.02	8.26	30.91	106.73	360.23	462.71	136.80	264.76	110.27	6.49	12.97	76.66	24.18
BC254B_1	3.05	b.d.	62.04	30.50	34.17	162.43	11.59	23.18	11.59	2.44	4.27	10.37	15.86
BC254B-2 average	3.90	b.d.	61.67	29.97	44.81	161.70	11.99	25.77	11.99	2.40	4.79	8.09	16.78
BC342 average	13.00	b.d.	25.66	131.17	424.19	117.47	36.57	89.46	42.61	10.88	20.55	151.72	87.65
BM25	18.20	7.83	31.32	137.18	761.35	903.08	122.90	271.43	106.65	9.39	21.72	73.19	41.88
JH179	10.78	4.79	303.04	10.78	123.17	234.87	25.15	47.31	17.37	1.20	5.99	8.38	14.37
JH50	25.48	12.16	9.50	104.83	566.00	179.79	147.69	302.90	120.47	6.95	16.22	66.02	37.07
JH51	7.51	b.d.	26.58	139.53	676.66	92.89	124.36	268.85	108.14	9.01	21.33	50.32	39.50
ML005A	4.19	21.54	190.58	324.31	62.66	585.07	201.05	366.79	147.20	22.14	4.19	136.43	13.76
ML005Bsec	10.88	30.52	230.92	155.63	65.19	152.24	181.81	322.81	140.98	12.31	3.09	123.31	na
ML005C	7.05	36.52	8.32	13.17	497.41	198.61	7.99	32.92	7.68	1.88	12.54	251.11	129.16
ML005E1 average	37.88	20.31	292.79	148.79	186.19	949.75	167.27	302.42	116.06	9.70	9.70	131.21	10.30
ML005E2 average	10.06	3.05	302.50	27.15	79.94	67.45	53.99	93.03	32.64	1.83	4.27	31.72	b.d.
ML005E3sec	13.49	24.53	287.78	61.94	461.83	108.91	301.73	536.60	185.21	2.45	14.72	258.80	14.11
ML174 average	16.40	b.d.	34.15	109.03	254.88	430.79	41.31	98.40	31.59	8.50	13.97	170.38	112.38
ML179	8.60	0.00	133.61	12.90	402.04	182.19	10.44	32.56	9.21	1.23	14.13	8.60	12.90
ML180B1average	3.93	b.d.	142.87	47.45	240.76	737.21	38.38	83.11	39.59	3.63	13.90	60.44	12.69
ML180B2 average	3.34	2.74	221.08	38.03	127.66	406.39	27.38	54.46	23.42	3.04	6.69	17.95	b.d.
ML197A1	5.28	12.27	277.99	11.34	184.85	120.91	16.00	34.02	12.12	1.24	8.23	2.95	1.71
ML197A2 average	3.70	9.25	342.75	8.32	109.93	380.12	13.87	31.14	12.95	0.62	6.17	9.25	b.d.
ML197B average	4.21	9.03	236.44	40.62	107.21	787.08	18.95	31.59	9.63	3.01	7.82	10.53	b.d.
ML205	4.56	5.56	295.04	24.27	102.51	297.35	21.88	29.08	14.21	1.75	6.49	10.44	na
ML229	4.20	4.13	32.89	96.56	679.80	408.71	168.99	362.07	101.36	8.36	21.15	52.12	na

ML237	5.96	1.29	77.09	92.35	426.51	165.31	70.50	154.52	54.28	8.57	19.33	223.32	na
ML240	4.48	12.15	302.33	100.03	171.89	248.47	63.46	114.95	40.27	7.77	8.05	39.57	na
ML248A1	25.26	13.23	29.57	80.00	577.39	94.32	441.52	765.75	252.04	3.61	20.45	376.56	13.84
ML258	8.80	6.46	290.18	27.58	126.83	152.23	36.97	63.96	22.89	1.76	5.87	10.56	b.d.
ML286Asec3	11.94	2.49	158.81	8.23	15.72	41.25	5.99	12.59	1.96	0.84	b.d.	b.d.	na
ML286Bsec	9.03	3.24	146.94	7.68	82.01	41.99	5.52	16.14	b.d.	0.83	1.13	b.d.	na
ML292 average	6.74	75.26	143.24	65.92	267.46	80.36	38.08	76.19	41.46	6.48	0.63	7.63	46.97
OLM3	6.04	0.60	217.73	34.46	163.11	285.12	15.11	38.69	9.67	3.63	7.86	7.25	3.02
OLM7_1	2.95	21.83	645.04	7.67	176.23	358.69	10.03	27.14	8.85	0.59	7.67	0.00	b.d.
OLM7-2 average	2.49	19.93	643.86	7.39	119.85	361.18	10.85	23.41	5.65	0.48	5.98	b.d.	b.d.
OLM8 average	18.84	19.88	228.20	171.23	120.65	439.48	129.27	232.66	95.33	14.54	6.60	99.90	1.83
PG14A	6.13	11.04	18.87	150.30	232.80	328.67	63.19	134.96	57.67	12.88	12.88	112.26	28.22
PG7b average	2.49	2.06	8.75	53.19	319.12	156.76	238.55	349.99	79.14	4.24	12.98	85.49	20.11
PG8	248.74	3.62	29.69	124.98	460.49	522.22	109.88	221.58	92.98	9.06	16.90	62.79	17.51
PG9	6.07	41.90	32.36	85.62	425.40	555.79	94.72	210.09	79.54	7.29	14.57	66.79	22.47
Y6 average	14.85	1.46	33.15	85.02	848.39	863.02	54.88	181.24	64.24	8.94	26.82	66.23	42.63
Y7b average	6.37	5.89	31.05	84.29	908.20	866.03	84.20	216.98	71.36	8.56	29.43	78.42	45.38
YG17C	32.51	0.00	67.46	78.51	493.21	308.52	107.33	230.00	85.25	6.75	16.56	53.97	17.79
YG24sec	13.91	8.08	467.70	24.69	124.11	534.43	22.63	50.06	16.99	2.26	6.98	7.58	na
YG25	1.72	4.18	172.52	9.09	81.97	353.60	6.59	13.38	5.62	0.70	6.57	0.25	na
YG7b average	17.59	3.61	50.01	221.32	597.89	263.80	483.95	856.99	291.74	16.89	24.22	466.23	39.27

Tab.5: Correlation matrix analyses of selected whole rock data. The statistical analyses were done under the supervision of A. Soessoo.

Correlation matrix of original whole rock analyses

Variablen	SiO2	TiO2	Al2O3	Fe2O3	MnO	MgO	CaO	Na2O	K2O	P2O5	LOI	V	Cr	Co	Ni	Sr	Y	Zr	Ba	La	Ce	Nd	Yb	Nb	Eu	Rb	Sm
SiO2	**1.00**	-0.48	-0.70	-0.61	-0.56	-0.27	-0.28	0.22	-0.48	-0.34	-0.24	0.13	-0.02	0.28	-0.47	-0.34	-0.53	-0.62	-0.54	-0.31	-0.39	-0.48	-0.52	-0.41	-0.25	-0.46	-0.28
TiO2	-0.48	**1.00**	-0.07	0.73	0.71	0.21	0.29	-0.19	0.14	0.28	0.04	0.41	0.44	-0.26	0.74	0.23	0.60	0.84	0.47	0.44	0.56	0.64	0.55	0.32	0.40	0.08	0.41
Al2O3	-0.70	-0.07	**1.00**	0.03	0.18	-0.14	0.41	0.26	0.16	0.22	0.05	-0.48	-0.34	0.00	0.08	0.37	0.25	0.14	0.24	0.00	-0.02	0.07	0.27	0.22	0.06	0.19	0.05
Fe2O3	-0.61	0.73	0.03	**1.00**	0.63	0.07	0.19	-0.38	0.34	0.36	0.09	0.31	0.40	-0.16	0.56	0.23	0.44	0.64	0.57	0.54	0.62	0.65	0.39	0.22	0.47	0.28	0.51
MnO	-0.56	0.71	0.18	0.63	**1.00**	0.13	0.58	0.00	0.04	0.49	-0.07	-0.02	0.30	-0.05	0.40	0.23	0.42	0.58	0.35	0.30	0.38	0.46	0.39	0.29	0.32	0.15	0.32
MgO	-0.27	0.21	-0.14	0.07	0.13	**1.00**	-0.22	-0.18	0.00	-0.28	0.50	-0.10	0.25	-0.27	0.14	-0.37	0.30	0.35	-0.19	-0.19	-0.09	-0.04	0.28	0.38	-0.31	0.09	-0.27
CaO	-0.28	0.29	0.41	0.19	0.58	-0.22	**1.00**	0.41	-0.34	0.27	-0.23	-0.22	-0.01	0.48	0.11	0.46	0.37	0.21	0.09	0.19	0.10	0.26	0.37	0.21	0.30	-0.20	0.24
Na2O	0.22	-0.19	0.26	-0.38	0.00	-0.18	0.41	**1.00**	-0.86	-0.18	-0.22	-0.50	-0.09	0.31	-0.36	-0.06	0.01	-0.18	-0.43	-0.31	-0.39	-0.28	0.00	-0.03	-0.15	-0.68	-0.23
K2O	-0.48	0.14	0.16	0.34	0.04	0.00	-0.34	-0.86	**1.00**	0.32	0.06	0.33	-0.11	-0.42	0.35	0.28	0.00	0.19	0.63	0.34	0.42	0.33	0.03	0.01	0.21	0.78	0.28
P2O5	-0.34	0.28	0.22	0.36	0.49	-0.28	0.27	-0.18	0.32	**1.00**	-0.17	0.22	0.15	0.24	0.08	0.26	-0.14	0.02	0.15	0.30	0.24	0.23	-0.14	-0.18	0.27	0.34	0.27
LOI	-0.24	0.04	0.05	0.09	-0.07	0.50	-0.23	-0.22	0.06	-0.17	**1.00**	-0.03	0.08	-0.15	0.07	-0.51	0.29	0.21	-0.26	-0.11	-0.03	-0.03	0.31	0.43	-0.18	0.23	-0.12
V	0.13	0.41	-0.48	0.31	-0.02	-0.10	-0.22	-0.50	0.33	0.22	-0.03	**1.00**	0.12	-0.09	0.43	0.07	0.01	0.19	0.20	0.51	0.50	0.40	-0.02	-0.15	0.44	-0.04	0.45
Cr	-0.02	0.44	-0.34	0.40	0.30	0.25	-0.01	-0.09	-0.11	0.15	0.08	0.12	**1.00**	-0.08	0.15	-0.15	0.11	0.29	-0.02	-0.21	-0.18	-0.09	0.06	0.11	-0.31	-0.03	-0.31
Co	0.28	-0.26	0.00	-0.16	-0.05	-0.27	0.48	0.31	-0.42	0.24	-0.15	-0.09	-0.08	**1.00**	-0.27	0.02	-0.14	-0.32	-0.34	-0.01	-0.18	-0.11	-0.12	-0.08	0.12	-0.33	0.06
Ni	-0.47	0.74	0.08	0.56	0.40	0.14	0.11	-0.36	0.35	0.08	0.07	0.43	0.15	-0.27	**1.00**	0.25	0.50	0.80	0.52	0.39	0.54	0.55	0.47	0.35	0.41	0.14	0.44
Sr	-0.34	0.23	0.37	0.23	0.23	-0.37	0.46	-0.06	0.28	0.26	-0.51	0.07	-0.15	0.02	0.25	**1.00**	0.06	0.08	0.64	0.47	0.36	0.42	0.05	-0.26	0.46	0.04	0.40
Y	-0.53	0.60	0.25	0.44	0.42	0.30	0.37	0.01	0.00	-0.14	0.29	0.01	0.11	-0.14	0.50	0.06	**1.00**	0.84	0.27	0.33	0.46	0.60	0.99	0.83	0.34	-0.02	0.35
Zr	-0.62	0.84	0.14	0.64	0.58	0.35	0.21	-0.18	0.19	0.02	0.21	0.19	0.29	-0.32	0.80	0.08	0.84	**1.00**	0.46	0.37	0.55	0.65	0.81	0.68	0.36	0.14	0.39
Ba	-0.54	0.47	0.24	0.57	0.35	-0.19	0.09	-0.43	0.63	0.15	-0.26	0.20	-0.02	-0.34	0.52	0.64	0.27	0.46	**1.00**	0.44	0.50	0.53	0.26	0.07	0.39	0.40	0.40
La	-0.31	0.44	0.00	0.54	0.30	-0.19	0.19	-0.31	0.34	0.30	-0.11	0.51	-0.21	-0.01	0.39	0.47	0.33	0.37	0.44	**1.00**	0.95	0.93	0.31	0.00	0.95	0.04	0.96
Ce	-0.39	0.56	-0.02	0.62	0.38	-0.09	0.10	-0.39	0.42	0.24	-0.03	0.50	-0.18	-0.18	0.54	0.36	0.46	0.55	0.50	0.95	**1.00**	0.96	0.44	0.17	0.91	0.14	0.94
Nd	-0.48	0.64	0.07	0.65	0.46	-0.04	0.26	-0.28	0.33	0.23	-0.03	0.40	-0.09	-0.11	0.55	0.42	0.60	0.65	0.53	0.93	0.96	**1.00**	0.59	0.28	0.90	0.10	0.91
Yb	-0.52	0.55	0.27	0.39	0.39	0.28	0.37	0.00	0.03	-0.14	0.31	-0.02	0.06	-0.12	0.47	0.05	0.99	0.81	0.26	0.31	0.44	0.59	**1.00**	0.84	0.32	0.04	0.34
Nb	-0.41	0.32	0.22	0.22	0.29	0.38	0.21	-0.03	0.01	-0.18	0.43	-0.15	0.11	-0.08	0.35	-0.26	0.83	0.68	0.07	0.00	0.17	0.28	0.84	**1.00**	0.04	0.08	0.07
Eu	-0.25	0.40	0.06	0.47	0.32	-0.31	0.30	-0.15	0.21	0.27	-0.18	0.44	-0.31	0.12	0.41	0.46	0.34	0.36	0.39	0.95	0.91	0.90	0.32	0.04	**1.00**	-0.09	0.99
Rb	-0.46	0.08	0.19	0.28	0.15	0.09	-0.20	-0.68	0.78	0.34	0.23	-0.04	-0.03	-0.33	0.14	0.04	-0.02	0.14	0.40	0.04	0.14	0.10	0.04	0.08	-0.09	**1.00**	0.01
Sm	-0.28	0.41	0.05	0.51	0.32	-0.27	0.24	-0.23	0.28	0.27	-0.12	0.45	-0.31	0.06	0.44	0.40	0.35	0.39	0.40	0.96	0.94	0.91	0.34	0.07	0.99	0.01	**1.00**

Correlation matrix of Al2O3-normalised whole rock analyses

Variablen	SiO2/ Al2O 3	TiO2/ Al2O 3	Fe2O 3/Al2 O3	MnO/ Al2O 3	MgO/ Al2O 3	CaO/ Al2O 3	Na2O /Al2O 3	K2O/ Al2O 3	V	Cr	Co	Ni	Sr	Y	Zr	Ba	La	Ce	Nd	Yb	Nb	Eu	Rb	Sm
SiO2/Al2O3	**1.00**	0.33	-0.15	-0.12	0.13	-0.28	0.22	-0.18	0.40	0.35	0.11	-0.21	-0.31	-0.34	-0.27	-0.33	-0.13	-0.17	-0.22	-0.36	-0.31	-0.17	-0.32	-0.18
TiO2/Al2O3	0.33	**1.00**	0.61	0.65	0.25	0.15	-0.14	0.15	0.54	0.55	-0.23	0.62	0.13	0.42	0.69	0.35	0.38	0.47	0.52	0.37	0.18	0.30	0.01	0.31
Fe2O3/Al2O3	-0.15	0.61	**1.00**	0.59	0.06	0.12	-0.47	0.42	0.38	0.40	-0.15	0.54	0.19	0.40	0.59	0.53	0.57	0.64	0.66	0.35	0.19	0.49	0.27	0.53
MnO/Al2O3	-0.12	0.65	0.59	**1.00**	0.14	0.54	-0.08	0.05	0.07	0.35	-0.06	0.40	0.19	0.38	0.56	0.34	0.33	0.40	0.47	0.34	0.25	0.32	0.14	0.33
MgO/Al2O3	0.13	0.25	0.06	0.14	**1.00**	-0.24	-0.14	0.01	-0.06	0.30	-0.24	0.11	-0.39	0.25	0.30	-0.22	-0.21	-0.13	-0.07	0.24	0.34	-0.34	0.06	-0.30
CaO/Al2O3	-0.28	0.15	0.12	0.54	-0.24	**1.00**	0.32	-0.41	-0.23	0.00	0.48	0.09	0.44	0.35	0.20	0.08	0.18	0.09	0.25	0.36	0.20	0.29	-0.20	0.23
Na2O/Al2O3	0.22	-0.14	-0.47	-0.08	-0.14	0.32	**1.00**	-0.95	-0.41	0.03	0.30	-0.42	-0.13	-0.09	-0.25	-0.49	-0.35	-0.44	-0.35	-0.11	-0.12	-0.22	-0.73	-0.31
K2O/Al2O3	-0.18	0.15	0.42	0.05	0.01	-0.41	-0.95	**1.00**	0.45	-0.09	-0.41	0.38	0.21	0.00	0.20	0.58	0.40	0.48	0.37	0.02	0.00	0.26	0.75	0.34
V	0.40	0.54	0.38	0.07	-0.06	-0.23	-0.41	0.45	**1.00**	0.12	-0.09	0.43	0.07	0.01	0.19	0.20	0.51	0.50	0.40	-0.02	-0.15	0.44	-0.04	0.45
Cr	0.35	0.55	0.40	0.35	0.30	0.00	0.03	-0.09	0.12	**1.00**	-0.08	0.15	-0.15	0.11	0.29	-0.02	-0.21	-0.18	-0.09	0.06	0.11	-0.31	-0.03	-0.31
Co	0.11	-0.23	-0.15	-0.06	-0.24	0.48	0.30	-0.41	-0.09	-0.08	**1.00**	-0.27	0.02	-0.14	-0.32	-0.34	-0.01	-0.18	-0.11	-0.12	-0.08	0.12	-0.33	0.06
Ni	-0.21	0.62	0.54	0.40	0.11	0.09	-0.42	0.38	0.43	0.15	-0.27	**1.00**	0.25	0.50	0.80	0.52	0.39	0.54	0.55	0.47	0.35	0.41	0.14	0.44
Sr	-0.31	0.13	0.19	0.19	-0.39	0.44	-0.13	0.21	0.07	-0.15	0.02	0.25	**1.00**	0.06	0.08	0.64	0.47	0.36	0.42	0.05	-0.26	0.46	0.04	0.40
Y	-0.34	0.42	0.40	0.38	0.25	0.35	-0.09	0.00	0.01	0.11	-0.14	0.50	0.06	**1.00**	0.84	0.27	0.33	0.46	0.60	0.99	0.83	0.34	-0.02	0.35
Zr	-0.27	0.69	0.59	0.56	0.30	0.20	-0.25	0.20	0.19	0.29	-0.32	0.80	0.08	0.84	**1.00**	0.46	0.37	0.55	0.65	0.81	0.68	0.36	0.14	0.39
Ba	-0.33	0.35	0.53	0.34	-0.22	0.08	-0.49	0.58	0.20	-0.02	-0.34	0.52	0.64	0.27	0.46	**1.00**	0.44	0.50	0.53	0.26	0.07	0.39	0.40	0.40

La	-0.13	0.38		0.57	0.33	-0.21	0.18	-0.35	0.40		0.51	-0.21	-0.01	0.39	0.47	0.33	0.37	0.44	**1.00**	0.95	0.93	0.31	0.00	0.95	0.04	0.96
Ce	-0.17	0.47		0.64	0.40	-0.13	0.09	-0.44	0.48		0.50	-0.18	-0.18	0.54	0.36	0.46	0.55	0.50	0.95	**1.00**	0.96	0.44	0.17	0.91	0.14	0.94
Nd	-0.22	0.52		0.66	0.47	-0.07	0.25	-0.35	0.37		0.40	-0.09	-0.11	0.55	0.42	0.60	0.65	0.53	0.93	0.96	**1.00**	0.59	0.28	0.90	0.10	0.91
Yb	-0.36	0.37		0.35	0.34	0.24	0.36	-0.11	0.02		-0.02	0.06	-0.12	0.47	0.05	0.99	0.81	0.26	0.31	0.44	0.59	**1.00**	0.84	0.32	0.04	0.34
Nb	-0.31	0.18		0.19	0.25	0.34	0.20	-0.12	0.00		-0.15	0.11	-0.08	0.35	-0.26	0.83	0.68	0.07	0.00	0.17	0.28	0.84	**1.00**	0.04	0.08	0.07
Eu	-0.17	0.30		0.49	0.32	-0.34	0.29	-0.22	0.26		0.44	-0.31	0.12	0.41	0.46	0.34	0.36	0.39	0.95	0.91	0.90	0.32	0.04	**1.00**	-0.09	0.99
Rb	-0.32	0.01		0.27	0.14	0.06	-0.20	-0.73	0.75		-0.04	-0.03	-0.33	0.14	0.04	-0.02	0.14	0.40	0.04	0.14	0.10	0.04	0.08	-0.09	**1.00**	0.01
Sm	-0.18	0.31		0.53	0.33	-0.30	0.23	-0.31	0.34		0.45	-0.31	0.06	0.44	0.40	0.35	0.39	0.40	0.96	0.94	0.91	0.34	0.07	0.99	0.01	**1.00**

Correlation matrix of SiO2-normalised whole rock analyses

Variablen	TiO2/SiO2	Al2O3/SiO2	Fe2O3/SiO2	MnO/SiO2	MgO/SiO2	CaO/SiO2	Na2O/SiO2	K2O/SiO2	V	Cr	Co	Ni	Sr	Y	Zr	Ba	La	Ce	Nd	Yb	Nb	Eu	Rb	Sm
TiO2/SiO2	**1.00**	0.22	0.77	0.76	0.22	0.36	-0.12	0.19	0.37	0.42	-0.26	0.74	0.25	0.61	0.85	0.49	0.43	0.55	0.63	0.56	0.34	0.39	0.10	0.40
Al2O3/SiO2	0.22	**1.00**	0.25	0.37	0.01	0.44	0.22	0.30	-0.40	-0.20	-0.09	0.21	0.40	0.36	0.32	0.36	0.08	0.10	0.20	0.37	0.29	0.11	0.27	0.11
Fe2O3/SiO2	0.77	0.25	**1.00**	0.67	0.09	0.25	-0.31	0.37	0.29	0.41	-0.16	0.55	0.24	0.44	0.64	0.57	0.52	0.59	0.64	0.39	0.23	0.45	0.28	0.49
MnO/SiO2	0.76	0.37	0.67	**1.00**	0.15	0.61	0.06	0.09	-0.03	0.30	-0.06	0.40	0.23	0.42	0.58	0.36	0.29	0.37	0.45	0.39	0.29	0.30	0.16	0.31
MgO/SiO2	0.22	0.01	0.09	0.15	**1.00**	-0.20	-0.16	0.04	-0.11	0.24	-0.27	0.15	-0.35	0.30	0.36	-0.17	-0.18	-0.09	-0.03	0.28	0.38	-0.30	0.10	-0.26
CaO/SiO2	0.36	0.44	0.25	0.61	-0.20	**1.00**	0.43	-0.29	-0.21	0.01	0.46	0.13	0.46	0.38	0.23	0.11	0.20	0.11	0.27	0.38	0.21	0.30	-0.18	0.24
Na2O/SiO2	-0.12	0.22	-0.31	0.06	-0.16	0.43	**1.00**	-0.81	-0.51	-0.08	0.29	-0.32	-0.02	0.08	-0.12	-0.39	-0.27	-0.35	-0.23	0.06	0.01	-0.13	-0.65	-0.21
K2O/SiO2	0.19	0.30	0.37	0.09	0.04	-0.29	-0.81	**1.00**	0.31	-0.08	-0.43	0.36	0.30	0.02	0.23	0.65	0.34	0.42	0.34	0.05	0.02	0.20	0.78	0.27
V	0.37	-0.40	0.29	-0.03	-0.11	-0.21	-0.51	0.31	**1.00**	0.12	-0.09	0.43	0.07	0.01	0.19	0.20	0.51	0.50	0.40	-0.02	-0.15	0.44	-0.04	0.45
Cr	0.42	-0.20	0.41	0.30	0.24	0.01	-0.08	-0.08	0.12	**1.00**	-0.08	0.15	-0.15	0.11	0.29	-0.02	-0.21	-0.18	-0.09	0.06	0.11	-0.31	-0.03	-0.31
Co	-0.26	-0.09	-0.16	-0.06	-0.27	0.46	0.29	-0.43	-0.09	-0.08	**1.00**	-0.27	0.02	-0.14	-0.32	-0.34	-0.01	-0.18	-0.11	-0.12	-0.08	0.12	-0.33	0.06
Ni	0.74	0.21	0.55	0.40	0.15	0.13	-0.32	0.36	0.43	0.15	-0.27	**1.00**	0.25	0.50	0.80	0.52	0.39	0.54	0.55	0.47	0.35	0.41	0.14	0.44
Sr	0.25	0.40	0.24	0.23	-0.35	0.46	-0.02	0.30	0.07	-0.15	0.02	0.25	**1.00**	0.06	0.08	0.64	0.47	0.36	0.42	0.05	-0.26	0.46	0.04	0.40
Y	0.61	0.36	0.44	0.42	0.30	0.38	0.08	0.02	0.01	0.11	-0.14	0.50	0.06	**1.00**	0.84	0.27	0.33	0.46	0.60	0.99	0.83	0.34	-0.02	0.35
Zr	0.85	0.32	0.64	0.58	0.36	0.23	-0.12	0.23	0.19	0.29	-0.32	0.80	0.08	0.84	**1.00**	0.46	0.37	0.55	0.65	0.81	0.68	0.36	0.14	0.39
Ba	0.49	0.36	0.57	0.36	-0.17	0.11	-0.39	0.65	0.20	-0.02	-0.34	0.52	0.64	0.27	0.46	**1.00**	0.44	0.50	0.53	0.26	0.07	0.39	0.40	0.40
La	0.43	0.08	0.52	0.29	-0.18	0.20	-0.27	0.34	0.51	-0.21	-0.01	0.39	0.47	0.33	0.37	0.44	**1.00**	0.95	0.93	0.31	0.00	0.95	0.04	0.96
Ce	0.55	0.10	0.59	0.37	-0.09	0.11	-0.35	0.42	0.50	-0.18	-0.18	0.54	0.36	0.46	0.55	0.50	0.95	**1.00**	0.96	0.44	0.17	0.91	0.14	0.94
Nd	0.63	0.20	0.64	0.45	-0.03	0.27	-0.23	0.34	0.40	-0.09	-0.11	0.55	0.42	0.60	0.65	0.53	0.93	0.96	**1.00**	0.59	0.28	0.90	0.10	0.91
Yb	0.56	0.37	0.39	0.39	0.28	0.38	0.06	0.05	-0.02	0.06	-0.12	0.47	0.05	0.99	0.81	0.26	0.31	0.44	0.59	**1.00**	0.84	0.32	0.04	0.34
Nb	0.34	0.29	0.23	0.29	0.38	0.21	0.01	0.02	-0.15	0.11	-0.08	0.35	-0.26	0.83	0.68	0.07	0.00	0.17	0.28	0.84	**1.00**	0.04	0.08	0.07
Eu	0.39	0.11	0.45	0.30	-0.30	0.30	-0.13	0.20	0.44	-0.31	0.12	0.41	0.46	0.34	0.36	0.39	0.95	0.91	0.90	0.32	0.04	**1.00**	-0.09	0.99
Rb	0.10	0.27	0.28	0.16	0.10	-0.18	-0.65	0.78	-0.04	-0.03	-0.33	0.14	0.04	-0.02	0.14	0.40	0.04	0.14	0.10	0.04	0.08	-0.09	**1.00**	0.01
Sm	0.40	0.11	0.49	0.31	-0.26	0.24	-0.21	0.27	0.45	-0.31	0.06	0.44	0.40	0.35	0.39	0.40	0.96	0.94	0.91	0.34	0.07	0.99	0.01	**1.00**

Tab.6: Fluid inclusion and microthermotetric analyses of various samples. Measurements were conducted at the University of Tübingen and Leoben under the supervision of R. Bakker.

		fluid inclusions					microthermometry			
sample	**host rock**	**generation**	**shape**	**phases**	**raman liquid**	**raman solid**	**eutecticum (°C)**	**melting T (°C) hydrosalt**	**melting T (°C) ice**	**homogenisation T (°C)**
SP2	qtz vein with tur	single	elongate	L+S+salt	brine	mag				
		single	round	L+salt	brine					
		single	round	L+V	brine					
		single	complex	L+V+S	brine	cal, mag, hem, ab				
	RCM	single	round	L+V	brine					
		trail	round	L+V+S	brine+H2O	hem, cal, mag				
		cluster	round	L+V+salt	brine					
		cluster	round	L+V+S+salt	brine	mag				
		single	round	L+V+S	brine	hem				
		trail	round	L+V+salt	brine					
		cluster	round	L+V	brine					
		trail	round	L+V+S	brine	cal, hem, mag				
	kfs overprint	cluster	round	L+V	brine+H2O					
		single	round	L+V+S	brine	cal, mag, hem		not visible	not visible	not visible
		single	round	L+V+S+salt	brine	hem, cal		not visible	not visible	not visible
		trail	elongate	L+V	brine+H2O			metastable	metastable	metastable
		cluster	complex	L+V+S	brine	hem, cal, mag		not visible	not visible	not visible
	qtz in tur	trail	elongate	L+V	brine				-1.0	
		single	round	L+V+salt	brine			metastable	metastable	metastable
		cluster	angular	L+V	brine			(-29,6)-(-29,5)		metastable
		single	round	L+V+S	brine	mag, cal				
		cluster	round	L+V+S	brine+H2O	hem, cal				
	qtz vein	single	round	L+V+S	brine	hem, cal, ap?, mnz?				
		trail	angular	L+V	brine					
		cluster	angular	L+V	brine					
ML175	kfs metasomatite	trail	complex	L+V+salt		hem				
		trail	angular	L+V	brine+H2O					
		cluster	round	L+V+salt	brine		(-20,2) - (-24,1)		(-0,6) - (-0,7)	
		trail	round	L+V	H2O					
BC275	orthogneiss	trail	elongate	L+V	brine+H2O					
		trail	round	L+V+S+salt	brine	hem, rt	~ (-70)		~ (-50)	
		single	round	L	brine		(-29,9) - (-51,6)	(-37,7) - (-38,7)	(-2,3) - (-4,2)	
		cluster	round	L+V+salt	brine		(-40,8) - (-44,0)			155 - 316
		cluster	round	L+V+S+salt	brine	cal, hem, mag				
		cluster	round	L	brine+H2O		(-46,8) - (-61,5)		(-7,6) - (-12,7)	
	kfs overprint	trail	round	L	brine+H2O					

		trail	round	L+V	brine					
		single	round	L+V+S	brine	hem				
		single	elongate	L+V+S+salt	brine	hem, cal, mag				
	qtz in tur	trail	complex	L	brine+H2O					
		cluster	complex	L+V+S+salt	brine	hem, cal, mag				
		single	round	L	brine, CO2					
SP36b	RCM	trail	round	L	brine+H2O					
		single	round	L	brine+H2O					
		trail	angular	L+V+S+salt	brine	hem, cal				
	sinter qtz	trail	round	L	brine+H2O					
		cluster	round	L	brine+H2O					

Tab.7: Oxygen isotope analyses of various samples. Measurements were conducted at the University of Tübingen by H. Taubald.

sample	mineral	$d^{18}O_{SMOW}$	mineral pair	αa-b	1000lnα	T (°C)	error (°C)	distance from vein rim (cm)
PW2	hematite	**2.8**	PW2 qtz-hem	1.008860041	8.821021407	646	14	14
PW3	hematite	**2.5**	PW3 qtz-hem	1.009331904	9.288630333	613	12	24
PW5	hematite	**0.6**	PW5 qtz-hem	1.01087605	10.81733134	526	10	1
PW1	k-feldspar	**7.0**	PW1 qtz-kfs	1.00431397	4.304691956	138	15	21
PW4	k-feldspar	**8.6**	PW4 qtz-kfs	1.002823632	2.819653095	299	33	17
PW1	quartz	**11.3**						
PW2	quartz	**11.7**						
PW3	quartz	**11.8**						
PW4	quartz	**11.5**						
PW5	quartz	**11.5**						

sample	mineral	$d^{18}O_{SMOW}$	distance from vein rim (m)
EC14	quartz	**7.8**	1
EC15	quartz	**8.1**	30
EC16	quartz	**9.1**	40
EC17	quartz	**9.3**	80
EC18a	quartz	**10.0**	100
EC18b	quartz	**13.7**	100
EC21	quartz	**7.7**	190
EC22	quartz	**8.4**	220
EC23	quartz	**8.5**	250
EC24	quartz	**9.5**	290

overall analytical presicion ± 0,2
T korrigiert

Tab.8: Rb-Sr analyses of a pegmatitic and an altered aplitic sample. Measurements were conducted at the University of Tübingen by W. Siebel.

Sample	Rb (ppm)	Sr (ppm)	87Rb/86Sr	87Sr/86Sr	dSr(2σ)	Initial 87Sr/86Sr	Age (Ma)
WD5b whole rock	162.5	11.08	44.4730	1.200774	16		
WD5b muscovite	1281	10.31	481.353	4.172743	56	0.8982±45	477.4±5.1
WD5c muscovite	1168	8.228	575.90	4.815656	67		
WD5c whole rock	683.2	16.25	134.625	1.795139	23	0.874±16	480.4±6.2

The Sr ratios are not corrected!

Sr-Standard: NBS 987 0.710204 ± 10 (certified value: 0.710248)
NBS 987 0.710228 ± 10 (certified value: 0.710248)
NBS 987 0.710214 ± 13 (certified value: 0.710248)

Error for age calculation: dx = 1%
dy = 0.03%

Tab.9: U-Pb analyses of various samples. Measurements were conducted at the University of Oslo by M. Elburg and T. Andersen.

sample	$^{206}Pb_c$(%)	U (ppm)	$^{207}Pb/^{206}Pb$	1SE	$^{206}Pb/^{238}U^*$	1SE	207Pb/206Pb age (Ma)	1σ (Ma)	207Pb/235Pb age (Ma)	1σ (Ma)	206Pb/238Pb age (Ma)	1σ (Ma)
N17g28	0.00	203	0.0986	0.0004	0.2658	0.0038	1598	8	1553	12	1519	19
N17g30	0.00	35	0.0975	0.0005	0.2572	0.0036	1578	9	1518	12	1475	18
N17g29c_front	0.00	661	0.0994	0.0006	0.2463	0.0051	1614	11	1499	17	1419	26
N17g29c_end	0.00	601	0.0994	0.0008	0.2315	0.0035	1613	14	1451	13	1342	18
N17g29c_all	0.00	630	0.0995	0.0004	0.2404	0.0038	1614	7	1480	13	1389	20
N17g29r	0.00	236	0.0976	0.0004	0.2618	0.0041	1579	7	1533	13	1499	21
N17g31	0.00	152	0.0975	0.0004	0.2564	0.0034	1578	8	1516	11	1471	17
N17g26	0.00	281	0.0980	0.0004	0.2630	0.0037	1586	8	1539	12	1505	19
N17g26c	0.00	616	0.1023	0.0004	0.1915	0.0027	1666	8	1328	11	1129	15
N17g26c_cor	1.10	616	0.0934	0.0004	0.1893	0.0027	1496	7	1254	11	1118	15
N17g25c	0.00	1415	0.0814	0.0004	0.0952	0.0013	1232	9	738	8	586	8
N17g25c_corr	0.52	1415	0.0773	0.0004	0.0947	0.0013	1128	10	708	8	583	8
N17g25r	0.00	347	0.0979	0.0004	0.2625	0.0035	1585	8	1537	11	1503	18
N17g24	0.00	379	0.0979	0.0004	0.2536	0.0034	1584	8	1509	11	1457	17
N17g22	0.00	281	0.0981	0.0004	0.2590	0.0035	1588	8	1528	11	1485	18
N17g23	0.00	59	0.0980	0.0005	0.2571	0.0037	1586	9	1521	12	1475	19
N17g20r	0.00	346	0.0976	0.0004	0.2700	0.0036	1579	8	1557	11	1541	18
N17g20c	0.00	1316	0.0925	0.0009	0.2186	0.0069	1478	18	1353	25	1275	36
N17g20c2	0.00	934	0.1357	0.0008	0.0160	0.0002	2174	10	266	3	102	1
N17g21	0.00	343	0.0975	0.0004	0.2666	0.0036	1577	8	1546	11	1524	18
N17g09c	0.00	681	0.0918	0.0004	0.1772	0.0026	1463	8	1194	11	1052	14
N17g09r	0.00	389	0.0981	0.0004	0.2703	0.0037	1589	8	1562	11	1542	19
N17g10c	0.00	1091	0.1020	0.0005	0.0204	0.0004	1662	9	256	4	130	2
N17g10r	0.00	774	0.0976	0.0004	0.2450	0.0033	1579	8	1480	11	1413	17
N17g12	0.00	807	0.0979	0.0004	0.1636	0.0024	1585	8	1184	11	977	13
N17g15	0.00	96	0.0967	0.0007	0.2721	0.0038	1562	12	1556	12	1552	19
N17g16	0.00	70	0.0965	0.0006	0.2722	0.0038	1558	12	1554	12	1552	20
N17g07	0.00	348	0.0971	0.0006	0.2726	0.0035	1569	12	1560	11	1554	18
N17g05	0.00	445	0.0972	0.0006	0.2768	0.0038	1570	12	1573	12	1575	19
N17g04	0.00	574	0.0970	0.0006	0.2734	0.0034	1567	12	1562	11	1558	17
N17g03	0.00	497	0.0967	0.0006	0.2752	0.0034	1562	12	1565	11	1567	17
N17g11c	0.00	1501	0.0901	0.0006	0.1817	0.0020	1428	11	1199	9	1076	11
N17g11r	0.00	460	0.0964	0.0006	0.2734	0.0034	1556	11	1557	11	1558	17
N17g56	0.00	534	0.0970	0.0006	0.2746	0.0036	1566	11	1565	12	1564	18
N17g54	0.00	230	0.0963	0.0006	0.2599	0.0033	1553	12	1516	11	1489	17
N17g53	0.00	54	0.0966	0.0007	0.2708	0.0037	1560	12	1551	12	1545	19

N17g52	0.00	460	0.0973	0.0007	0.2269	0.0041	1572	13	1418	15	1318	22
N17g50	0.00	84	0.0969	0.0006	0.2684	0.0051	1566	12	1546	16	1532	26
N17g51	0.00	460	0.0971	0.0006	0.2687	0.0036	1569	12	1549	12	1534	18
N17g55	0.00	284	0.0968	0.0006	0.2644	0.0044	1563	12	1534	14	1512	22
N17e35	0.00	724	0.0976	0.0006	0.2764	0.0036	1579	12	1576	12	1573	18
N17e34	0.00	561	0.0976	0.0006	0.2722	0.0038	1579	12	1564	12	1552	19
N17e33	0.00	330	0.0977	0.0006	0.2661	0.0033	1580	12	1546	11	1521	17
N17e32c	0.00	233	0.0976	0.0007	0.2693	0.0035	1579	12	1555	12	1537	18
N17e32r	0.00	424	0.0980	0.0007	0.2695	0.0037	1587	12	1559	12	1538	19
N17e30	0.00	760	0.0974	0.0006	0.2716	0.0034	1576	12	1560	11	1549	17
N17e28	0.00	343	0.0976	0.0006	0.2726	0.0035	1578	12	1564	11	1554	18
N17e22b	0.00	113	0.0972	0.0007	0.2696	0.0035	1571	12	1553	12	1539	18
N17e22	0.00	198	0.0695	0.0005	0.0959	0.0011	914	14	662	7	590	7
N17e22_corr	0.17	198	0.0681	0.0005	0.0957	0.0011	871	15	651	7	589	7
N17e23r	0.00	242	0.0972	0.0006	0.2615	0.0038	1572	12	1528	13	1497	19
N17e23c_cor	0.04	148	0.0960	0.0008	0.3010	0.0043	1547	14	1631	13	1696	21
N17e24	0.00	227	0.0977	0.0006	0.2716	0.0036	1580	11	1562	12	1549	18
N17e17	0.00	241	0.0978	0.0006	0.2748	0.0036	1583	12	1573	12	1565	18
N17e16	0.00	53	0.0978	0.0007	0.2653	0.0037	1583	13	1545	12	1517	19
N17e15c	0.00	480	0.0978	0.0007	0.2304	0.0033	1583	12	1435	12	1337	18
N17e15r	0.00	420	0.0956	0.0006	0.2438	0.0034	1541	11	1461	12	1406	18
N17e14r	0.00	269	0.0966	0.0006	0.2653	0.0033	1559	11	1535	11	1517	17
N17e25	0.00	64	0.0968	0.0006	0.2699	0.0034	1564	12	1550	11	1540	17
N17e26	0.00	114	0.0972	0.0007	0.2706	0.0042	1571	13	1555	13	1544	21
N17e27	0.00	603	0.0974	0.0006	0.2744	0.0035	1575	12	1568	11	1563	17
N17e31c2	0.00	448	0.0971	0.0006	0.2708	0.0035	1569	12	1555	11	1545	18
N17e31c1_corr	10.00	1322	0.0683	0.0005	0.0651	0.0009	878	14	485	6	407	5
N17e31r	0.00	646	0.0978	0.0006	0.2652	0.0034	1583	12	1544	11	1516	17
N17e31r_corr	0.19	646	0.0963	0.0006	0.2647	0.0034	1553	12	1530	11	1514	17
N17e36	0.00	422	0.0970	0.0006	0.2704	0.0043	1567	12	1553	14	1543	22
N17e21c	0.00	39	0.0972	0.0007	0.2649	0.0036	1571	13	1538	12	1515	18
N17e21r	0.00	246	0.0972	0.0007	0.2706	0.0040	1570	12	1555	13	1544	20
Y60b2	0.00	448	0.0977	0.0006	0.2719	0.0035	1581	11	1564	11	1551	18
Y60b1	0.00	313	0.1610	0.0013	0.4472	0.0074	2467	13	2428	17	2383	33
Y60b3r	0.00	455	0.1587	0.0013	0.4392	0.0072	2441	13	2398	17	2347	32
Y60b3c	0.00	136	0.2380	0.0029	0.5461	0.0121	3106	18	2985	24	2809	51
Y60b4	0.00	170	0.1033	0.0006	0.2966	0.0040	1685	11	1679	12	1674	20
Y60b5	0.00	171	0.2064	0.0020	0.5258	0.0105	2877	15	2813	21	2724	44
Y60b6	0.00	134	0.0978	0.0006	0.2741	0.0034	1582	11	1570	11	1562	17
Y60b7	0.00	53	0.1023	0.0006	0.2895	0.0035	1665	11	1651	11	1639	17
Y60b8	0.00	80	0.1080	0.0007	0.3115	0.0042	1767	11	1757	12	1748	21

Y60b9	0.00	59	0.0975	0.0007	0.2715	0.0035	1577	13	1560	11	1549	18
Y60b10	0.00	322	0.1135	0.0007	0.3267	0.0043	1856	12	1838	13	1822	21
Y60b11	0.00	100	0.0974	0.0006	0.2723	0.0032	1575	12	1562	11	1553	16
Y60b12	0.00	264	0.1596	0.0013	0.4353	0.0070	2452	14	2395	17	2329	32
Y60b13	0.00	115	0.0955	0.0006	0.1834	0.0055	1539	11	1247	22	1086	30
Y60b14	0.00	207	0.0981	0.0006	0.2745	0.0032	1587	10	1574	11	1563	16
Y60b15c	0.00	105	0.1030	0.0007	0.2898	0.0038	1680	11	1658	12	1641	19
Y60b16	0.00	87	0.1041	0.0007	0.2923	0.0043	1699	11	1673	13	1653	21
Y60b17	0.00	138	0.1035	0.0006	0.2875	0.0034	1688	11	1655	11	1629	17
Y60b20	0.00	182	0.0981	0.0006	0.2779	0.0040	1589	10	1584	12	1581	20
Y60b18	0.00	151	0.1080	0.0007	0.3044	0.0039	1765	11	1737	12	1713	19
Y60b19	0.00	92	0.1043	0.0007	0.2937	0.0037	1702	11	1678	12	1660	19
Y60b21	0.00	221	0.0990	0.0006	0.2765	0.0033	1605	10	1587	11	1574	17
Y60b22c_front	0.00	102	0.0991	0.0007	0.2324	0.0031	1608	13	1451	12	1347	16
Y60b22c_corr	0.74	105	0.0960	0.0007	0.2289	0.0025	1548	14	1415	10	1329	13
Y60b22r	0.00	217	0.1020	0.0006	0.2864	0.0037	1661	10	1640	12	1624	18
Y60b23	0.00	105	0.1009	0.0006	0.2794	0.0033	1640	10	1611	11	1588	17
Y60b24	0.00	174	0.1060	0.0006	0.2960	0.0035	1732	11	1699	11	1671	17
Y60b25	0.00	109	0.1060	0.0007	0.2978	0.0035	1731	11	1703	11	1681	18
Y60b26r	0.00	104	0.0988	0.0006	0.2728	0.0032	1602	11	1575	11	1555	16
Y60b26c	0.00	356	0.0987	0.0006	0.2733	0.0034	1599	11	1575	11	1557	17
Y60b27	0.00	123	0.1059	0.0007	0.2966	0.0044	1730	11	1699	13	1675	22
Y60b28	0.00	103	0.1055	0.0007	0.2969	0.0039	1723	11	1697	12	1676	20
Y60b29	0.00	345	0.1006	0.0006	0.2817	0.0033	1635	10	1615	11	1600	17
Y60b30	0.00	238	0.1045	0.0006	0.2923	0.0034	1706	10	1676	11	1653	17
Y60b31	0.00	93	0.0968	0.0006	0.2440	0.0029	1563	10	1471	10	1407	15
Y60b32	0.00	132	0.0984	0.0006	0.2691	0.0031	1593	11	1560	10	1536	16
Y60b33	0.00	129	0.1035	0.0007	0.2930	0.0036	1688	12	1671	11	1657	18
Y60b34	0.00	181	0.0991	0.0006	0.2724	0.0032	1608	11	1576	11	1553	16
Y60b35	0.00	127	0.1140	0.0008	0.3233	0.0043	1864	11	1833	13	1806	21
Y60b36c	0.00	117	0.1000	0.0006	0.2741	0.0032	1625	11	1589	11	1562	16
Y60b37c	0.00	941	0.0895	0.0005	0.1978	0.0022	1414	11	1254	9	1164	12
Y60b37r	0.00	495	0.0973	0.0006	0.2435	0.0032	1574	11	1474	11	1405	16
Y60b38	0.00	99	0.1037	0.0007	0.2931	0.0037	1692	12	1672	12	1657	18
Y60b39	0.00	189	0.1028	0.0007	0.2927	0.0036	1676	11	1664	11	1655	18
Y60b40	0.00	304	0.1081	0.0007	0.3085	0.0041	1767	11	1749	12	1733	20
Y60b41	0.00	260	0.0978	0.0006	0.2657	0.0031	1583	11	1546	10	1519	16
Y60b42	0.00	203	0.1015	0.0006	0.2847	0.0039	1653	11	1631	12	1615	19
Y60b43	0.00	352	0.1051	0.0007	0.2960	0.0039	1716	12	1691	12	1672	19
Y60b44	0.00	538	0.1141	0.0007	0.3275	0.0043	1866	12	1845	12	1826	21
Y60b45c	0.00	228	0.1705	0.0013	0.4638	0.0074	2563	13	2515	16	2456	32

Y60b45r	0.00	251	0.1537	0.0011	0.3609	0.0053	2388	12	2191	15	1987	25
Y60b46	0.00	147	0.0975	0.0006	0.2715	0.0032	1576	11	1560	10	1549	16
Y60b47	0.00	97	0.1015	0.0006	0.2829	0.0036	1651	11	1625	11	1606	18
YG17b3	0.00	861	0.0975	0.0010	0.2709	0.0028	1577	20	1559	12	1546	14
YG17b4	0.00	1118	0.0970	0.0010	0.2783	0.0030	1567	20	1576	12	1583	15
YG17b5	0.00	823	0.0965	0.0010	0.2739	0.0031	1558	20	1559	12	1560	16
YG17b6	0.00	871	0.0961	0.0010	0.2708	0.0029	1551	20	1547	12	1545	15
YG17b7	0.00	354	0.0961	0.0010	0.2699	0.0029	1550	19	1545	12	1540	15
YG17b8	0.00	781	0.0961	0.0010	0.2693	0.0029	1549	19	1542	12	1537	15
YG17b9	0.00	962	0.0958	0.0010	0.2734	0.0029	1544	19	1552	12	1558	15
YG17b10	0.00	770	0.0959	0.0010	0.2766	0.0031	1545	19	1562	12	1574	15
YG17b2c	0.00	829	0.0959	0.0010	0.2754	0.0031	1545	19	1558	12	1568	16
YG17b11	0.00	1172	0.0966	0.0010	0.2757	0.0033	1559	20	1565	13	1570	17
YG17b12	0.00	983	0.0962	0.0010	0.2739	0.0035	1552	20	1557	13	1561	18
YG17b13	0.00	830	0.0963	0.0010	0.2739	0.0030	1553	20	1557	12	1560	15
YG17b14	0.00	620	0.0961	0.0010	0.2677	0.0029	1549	19	1537	12	1529	15
YG17b15	0.00	100	0.0959	0.0011	0.2645	0.0027	1546	20	1527	12	1513	14
YG17b16	0.00	1217	0.0962	0.0010	0.2673	0.0028	1551	19	1537	12	1527	14
YG17b17	0.00	997	0.0964	0.0010	0.2737	0.0030	1555	19	1558	12	1559	15
YG17b20	0.00	866	0.0967	0.0010	0.2776	0.0030	1562	19	1572	12	1579	15
YG17b19c	0.00	1074	0.0967	0.0011	0.2740	0.0031	1562	19	1562	12	1561	15
YG17b21	0.00	540	0.0969	0.0011	0.2719	0.0030	1565	20	1557	12	1551	15
YG17b22r	0.00	664	0.0969	0.0011	0.2664	0.0028	1566	20	1541	12	1523	14
YG17b23	0.00	1048	0.0971	0.0011	0.2752	0.0029	1570	20	1568	12	1567	15
YG17b24	0.00	467	0.0972	0.0011	0.2722	0.0029	1570	19	1560	12	1552	15
YG17b25	0.00	209	0.0970	0.0011	0.2636	0.0030	1567	19	1533	12	1508	15
YG17b26c	0.00	678	0.0977	0.0011	0.2821	0.0035	1581	19	1593	13	1602	18
YG17b27	0.00	790	0.0976	0.0011	0.2774	0.0032	1578	19	1578	13	1578	16
YG17b29	0.00	266	0.0974	0.0011	0.2710	0.0030	1574	19	1558	12	1546	15
YG17b30	0.00	804	0.0978	0.0011	0.2751	0.0030	1582	20	1573	12	1567	15
YG17b31	0.00	909	0.0977	0.0011	0.2747	0.0030	1581	20	1572	12	1565	15
YG17b32	0.00	413	0.0974	0.0011	0.2680	0.0029	1576	20	1550	12	1530	15
YG17b33	0.00	1299	0.0975	0.0011	0.2723	0.0031	1577	21	1563	13	1553	15
YG17b34r	0.00	636	0.0976	0.0011	0.2708	0.0031	1579	21	1559	13	1545	16
YG17b34c	0.00	1323	0.0979	0.0011	0.2781	0.0034	1584	21	1583	13	1582	17
YG17b5bis	0.00	995	0.0979	0.0011	0.2739	0.0031	1584	21	1571	13	1561	15
YG17b5tris	0.00	886	0.0980	0.0011	0.2741	0.0031	1586	21	1572	13	1561	16
YG17C5	0.00	886	0.0976	0.0011	0.2673	0.0030	1579	21	1549	13	1527	15
YG17C6	0.00	743	0.0979	0.0005	0.2707	0.0019	1584	9	1561	7	1544	10
YG17C7	0.00	690	0.0981	0.0005	0.2703	0.0019	1588	9	1562	7	1542	10

YG17C1	0.00	674	0.0976	0.0005	0.2800	0.0022	1580	9	1586	7	1591	11
YG17C2	0.00	349	0.0975	0.0005	0.2743	0.0020	1577	9	1569	7	1562	10
YG17C3r	0.00	328	0.0972	0.0005	0.2421	0.0020	1570	9	1467	8	1397	10
YG17C3c	0.00	547	0.0948	0.0005	0.2313	0.0020	1524	9	1414	8	1342	10
YG17C4r	0.00	811	0.0978	0.0005	0.2718	0.0020	1583	9	1564	7	1550	10
YG17C8	0.00	519	0.0976	0.0005	0.2815	0.0025	1579	9	1590	8	1599	13
YG17C9r	0.00	704	0.0976	0.0005	0.2441	0.0029	1578	9	1477	10	1408	15
YG17C9c	0.00	991	0.0982	0.0007	0.2692	0.0034	1589	12	1559	12	1537	17
YG17C10r	0.00	101	0.0973	0.0005	0.2745	0.0021	1574	9	1568	7	1564	10
YG17C11	0.00	637	0.0975	0.0006	0.2649	0.0022	1576	11	1541	8	1515	11
YG17C12	0.00	554	0.0979	0.0005	0.2716	0.0019	1584	10	1564	7	1549	10
YG17C13	0.00	1095	0.0977	0.0004	0.2753	0.0021	1580	8	1573	7	1567	10
YG17C14	0.00	1093	0.0975	0.0004	0.2764	0.0020	1576	8	1574	7	1573	10
YG17C15	0.00	795	0.0971	0.0004	0.2735	0.0022	1568	8	1563	7	1559	11
YG17C16	0.00	174	0.0973	0.0005	0.2701	0.0020	1573	9	1555	7	1542	10
YG17C17	0.00	1142	0.0973	0.0004	0.2706	0.0020	1572	8	1556	7	1544	10
YG17C18	0.00	1153	0.0975	0.0004	0.2750	0.0020	1576	8	1570	7	1566	10
YG17C19r	0.00	416	0.0968	0.0007	0.2478	0.0023	1563	13	1483	9	1427	12
YG17C20	0.00	1013	0.0981	0.0009	0.2639	0.0042	1589	16	1543	14	1510	21
YG17C21	0.00	292	0.0979	0.0005	0.2744	0.0023	1584	8	1572	8	1563	12
YG17C22	0.00	680	0.0978	0.0005	0.2697	0.0020	1583	8	1557	7	1539	10
YG17C23	0.00	1041	0.0979	0.0005	0.2755	0.0021	1585	8	1576	7	1569	11
YG17C24	0.00	940	0.0979	0.0005	0.2754	0.0021	1585	8	1575	7	1568	11
YG17C25r	0.00	572	0.0979	0.0005	0.2632	0.0021	1584	8	1539	7	1506	11
YG17C26	0.00	955	0.0981	0.0005	0.2764	0.0021	1588	8	1580	7	1573	11
YG17C28	0.00	321	0.0978	0.0005	0.2741	0.0021	1582	8	1570	7	1562	11
YG17C29	0.00	1095	0.0978	0.0005	0.2757	0.0021	1583	9	1575	7	1570	11
YG17C31	0.00	798	0.0979	0.0005	0.2741	0.0023	1584	9	1571	8	1562	12
YG17C32	0.00	829	0.0979	0.0005	0.2740	0.0021	1585	8	1571	7	1561	11
YG17C33	0.00	1224	0.0979	0.0005	0.2773	0.0022	1585	8	1581	7	1578	11
YG17C34	0.00	845	0.0978	0.0005	0.2755	0.0022	1582	9	1574	7	1569	11
YG17d6	0.00	387	0.0969	0.0005	0.2569	0.0019	1566	9	1512	7	1474	10
YG17d5	0.00	1027	0.0982	0.0005	0.2769	0.0021	1590	9	1582	7	1576	11
YG17d4	0.00	797	0.0987	0.0010	0.2641	0.0039	1600	19	1548	14	1511	20
YG17d3	0.00	1025	0.0985	0.0010	0.2770	0.0042	1596	19	1585	15	1576	21
YG17d2	0.00	808	0.0984	0.0010	0.2754	0.0041	1593	19	1579	14	1568	21
YG17d1c	0.00	101	0.0981	0.0010	0.2686	0.0040	1588	19	1557	14	1534	20
YG17d1r	0.00	670	0.0976	0.0010	0.2644	0.0039	1578	19	1540	14	1512	20
YG17d7	0.00	367	0.0980	0.0010	0.2725	0.0041	1587	18	1568	14	1553	21
YG17d8	0.00	280	0.0981	0.0010	0.2736	0.0041	1587	18	1571	15	1559	21
YG17d9	0.00	297	0.0980	0.0010	0.2672	0.0040	1587	18	1552	14	1527	20

YG17d10r	0.00	394	0.0983	0.0010	0.2443	0.0036	1593	19	1484	14	1409	19
YG17d11	0.00	845	0.0982	0.0010	0.2723	0.0041	1590	19	1568	15	1552	21
YG17d12	0.00	973	0.0977	0.0010	0.2712	0.0042	1581	19	1561	15	1547	21
YG17d13	0.00	623	0.0978	0.0010	0.2734	0.0042	1582	19	1568	15	1558	21
YG17d14	0.00	849	0.0980	0.0010	0.2747	0.0042	1586	18	1574	15	1565	21
YG17d15	0.00	191	0.0974	0.0010	0.2694	0.0041	1575	19	1553	15	1538	21
YG17d16	0.00	869	0.0977	0.0010	0.2714	0.0042	1580	18	1562	15	1548	21
YG17d26	0.00	801	0.0979	0.0010	0.2721	0.0043	1585	19	1565	15	1551	22
YG17d17c	0.00	97	0.0972	0.0010	0.2660	0.0042	1571	20	1542	15	1520	22
YG17d17r	0.00	253	0.0971	0.0010	0.2860	0.0055	1569	20	1599	18	1622	28
YG17d18	0.00	701	0.0976	0.0011	0.2610	0.0041	1579	20	1530	15	1495	21
YG17d19c	0.00	517	0.0975	0.0011	0.2698	0.0043	1576	20	1555	15	1540	22
YG17d19r	0.00	799	0.0969	0.0010	0.2567	0.0040	1565	20	1511	15	1473	21
YG17d20	0.00	861	0.0974	0.0011	0.2708	0.0044	1574	19	1557	15	1545	22
YG17d21	0.00	648	0.0970	0.0011	0.2672	0.0043	1566	20	1543	15	1527	22
YG17d22	0.00	619	0.0972	0.0011	0.2707	0.0044	1571	20	1556	16	1544	22
YG17d23	0.00	905	0.0970	0.0011	0.2699	0.0044	1568	20	1552	16	1540	22
YG17d24	0.00	713	0.0972	0.0011	0.2703	0.0044	1571	20	1554	16	1543	22

Tab.10: Lu-Hf analyses of the samples taken for U-Pb studies. Measurements were conducted at the University of Oslo by M. Elburg and T. Andersen.

Sample	$^{176}Hf/^{177}Hf$	1s	$^{176}Lu/^{177}Hf$	1s	$^{176}Yb/^{177}Hf$	1s
YG17b1c	0.281857	0.000012	0.0015	0.0001	0.0825	0.0013
YG17b1r	0.281971	0.000016	0.0019	0.0001	0.0642	0.0024
YG17b2c	0.281912	0.000009	0.0014	0.0000	0.0905	0.0010
YG17b2r	0.281927	0.000010	0.0010	0.0000	0.0397	0.0016
YG17b3	0.281935	0.000014	0.0009	0.0000	0.0539	0.0015
YG17b4	0.281871	0.000012	0.0009	0.0000	0.0532	0.0018
YG17b5	0.281927	0.000016	0.0014	0.0000	0.0834	0.0019
YG17b6	0.281873	0.000016	0.0014	0.0001	0.0681	0.0019
YG17b7	0.281953	0.000013	0.0010	0.0000	0.0581	0.0010
YG17b8	0.281913	0.000011	0.0010	0.0000	0.0557	0.0015
YG17b9	0.281859	0.000008	0.0007	0.0000	0.0431	0.0007
YG17b10	0.281964	0.000011	0.0014	0.0000	0.0770	0.0019
YG17b11	0.281865	0.000009	0.0010	0.0000	0.0569	0.0002
YG17b12	0.281922	0.000009	0.0011	0.0000	0.0663	0.0016
YG17b13	0.281928	0.000010	0.0014	0.0000	0.0827	0.0015
YG17b14	0.281863	0.000008	0.0006	0.0000	0.0351	0.0006
YG17b15	0.281909	0.000011	0.0008	0.0000	0.0462	0.0016
YG17b16	0.281867	0.000008	0.0008	0.0000	0.0479	0.0016
YG17b17	0.281910	0.000009	0.0007	0.0000	0.0379	0.0007
YG17b19	0.281909	0.000007	0.0012	0.0000	0.0697	0.0026
YG17b20	0.281878	0.000009	0.0008	0.0000	0.0435	0.0009
YG17b21	0.281886	0.000009	0.0006	0.0000	0.0355	0.0003
YG17b22r	0.282108	0.000012	0.0005	0.0000	0.0303	0.0008
YG17b22c	0.281894	0.000009	0.0021	0.0001	0.1177	0.0043
YG17b22r2	0.281900	0.000007	0.0006	0.0000	0.0351	0.0008
YG17b25	0.281943	0.000010	0.0007	0.0000	0.0357	0.0005
YG17b26c	0.281900	0.000007	0.0011	0.0000	0.0656	0.0006
YG17b26r	0.282212	0.000015	0.0024	0.0001	0.0816	0.0015
YG17b28c	0.281996	0.000010	0.0025	0.0001	0.1512	0.0061
YG17b28rStart	0.282408	0.000010	0.0008	0.0000	0.0346	0.0005
YG17b28rEnd	0.282138	0.000013	0.0009	0.0000	0.0382	0.0006
YG17b34c	0.281995	0.000018	0.0022	0.0001	0.1361	0.0110
YG17b34r	0.281890	0.000010	0.0007	0.0000	0.0433	0.0001
YG17b33	0.281889	0.000008	0.0006	0.0000	0.0370	0.0004
YG17c14	0.281879	0.000009	0.0006	0.0000	0.0384	0.0004
YG17c25r	0.281944	0.000037	0.0062	0.0006	0.2331	0.0220
YG17c25c	0.282086	0.000023	0.0030	0.0001	0.1846	0.0051
YG17c24	0.282009	0.000020	0.0029	0.0001	0.1106	0.0035

YG17c26	0.281921	0.000009	0.0013	0.0001	0.0820	0.0062
YG17c28	0.281888	0.000009	0.0010	0.0000	0.0621	0.0037
YG17c29	0.281883	0.000011	0.0009	0.0000	0.0552	0.0031
YG17c21	0.281896	0.000009	0.0010	0.0000	0.0613	0.0030
YG17c22	0.281847	0.000013	0.0006	0.0000	0.0398	0.0007
YG17c23	0.281982	0.000013	0.0015	0.0000	0.0894	0.0025
YG17c17	0.282150	0.000017	0.0015	0.0001	0.0939	0.0034
YG17c19r	0.281954	0.000014	0.0006	0.0000	0.0372	0.0004
YG17c19c	0.282195	0.000017	0.0037	0.0000	0.2019	0.0024
YG17c11	0.281892	0.000010	0.0006	0.0000	0.0348	0.0004
YG17c16	0.281952	0.000010	0.0010	0.0000	0.0605	0.0028
YG17c12	0.281906	0.000009	0.0008	0.0000	0.0500	0.0022
YG17c13	0.281950	0.000012	0.0015	0.0000	0.0936	0.0020
YG17c10r	0.281947	0.000022	0.0007	0.0000	0.0405	0.0021
YG17c10c	0.282104	0.000014	0.0055	0.0001	0.3291	0.0100
YG17c09r	0.281962	0.000030	0.0039	0.0001	0.1435	0.0052
YG17c09c	0.281860	0.000019	0.0022	0.0001	0.1342	0.0053
YG17c08	0.281858	0.000008	0.0007	0.0000	0.0433	0.0011
YG17c07	0.282323	0.000009	0.0006	0.0001	0.0226	0.0011
YG17c07-2	0.282139	0.000010	0.0008	0.0001	0.0341	0.0011
YG17c03c	0.282053	0.000025	0.0078	0.0002	0.4641	0.0110
YG17c03r	0.281861	0.000011	0.0009	0.0000	0.0558	0.0015
Y60B47	0.281943	0.000014	0.0014	0.0000	0.0809	0.0042
Y60B46	0.281762	0.000020	0.0023	0.0001	0.0856	0.0034
Y60B45	0.281148	0.000008	0.0005	0.0000	0.0333	0.0012
Y60B44	0.281431	0.000021	0.0008	0.0000	0.0627	0.0004
Y60B43	0.281767	0.000017	0.0014	0.0000	0.1013	0.0033
Y60B42	0.281863	0.000013	0.0012	0.0000	0.0806	0.0006
Y60B41	0.281844	0.000012	0.0012	0.0000	0.0748	0.0012
Y60B40	0.281728	0.000011	0.0008	0.0000	0.0525	0.0001
Y60B39	0.281802	0.000009	0.0008	0.0000	0.0500	0.0007
Y60BB38	0.281781	0.000013	0.0007	0.0000	0.0463	0.0006
Y60B37c	0.281781	0.000020	0.0031	0.0001	0.1906	0.0061
Y60B36	0.281941	0.000012	0.0009	0.0000	0.0572	0.0012
Y60B35	0.281635	0.000012	0.0010	0.0001	0.0769	0.0065
Y60B32	0.281999	0.000009	0.0010	0.0000	0.0672	0.0023
Y60B33	0.281909	0.000008	0.0014	0.0000	0.0918	0.0020
Y60B34	0.281776	0.000011	0.0007	0.0000	0.0478	0.0011
Y60B31	0.281900	0.000012	0.0009	0.0000	0.0580	0.0009
Y60B30	0.281857	0.000017	0.0022	0.0002	0.0744	0.0016
Y60B29	0.282005	0.000012	0.0017	0.0000	0.1085	0.0027

Y60B28	0.281575	0.000013	0.0006	0.0000	0.0416	0.0005
Y60B27	0.281567	0.000011	0.0008	0.0000	0.0532	0.0002
Y60B26c	0.281718	0.000012	0.0014	0.0000	0.1003	0.0009
Y60B26r	0.281714	0.000009	0.0009	0.0000	0.0462	0.0013
Y60B25	0.281520	0.000017	0.0007	0.0000	0.0496	0.0006
Y60B24	0.281584	0.000010	0.0006	0.0000	0.0422	0.0001
Y60B23	0.281945	0.000013	0.0014	0.0000	0.0943	0.0024
Y60B22c	0.281998	0.000013	0.0025	0.0001	0.1671	0.0025
Y60B21	0.281890	0.000011	0.0010	0.0000	0.0544	0.0012
Y60B17	0.281772	0.000014	0.0006	0.0000	0.0391	0.0001
Y60B13	0.281704	0.000015	0.0009	0.0001	0.0572	0.0012
Y60B19	0.281851	0.000012	0.0007	0.0000	0.0360	0.0003
Y60B18	0.281692	0.000010	0.0009	0.0000	0.0555	0.0017
Y60B20	0.281855	0.000011	0.0008	0.0000	0.0554	0.0014
Y60B12	0.281292	0.000011	0.0008	0.0000	0.0497	0.0009
Y60B11	0.281693	0.000015	0.0008	0.0000	0.0490	0.0006
Y60B10	0.281452	0.000010	0.0008	0.0000	0.0616	0.0016
Y60B02	0.281969	0.000013	0.0022	0.0000	0.1364	0.0026
Y60B01	0.281227	0.000010	0.0010	0.0000	0.0601	0.0012
Y60B03c	0.281026	0.000011	0.0006	0.0000	0.0366	0.0013
Y60B03r	0.281230	0.000011	0.0008	0.0000	0.0414	0.0013
Y60B04	0.281825	0.000010	0.0009	0.0000	0.0554	0.0004
Y60B04bis	0.281874	0.000010	0.0011	0.0000	0.0657	0.0008
Y60B05	0.281080	0.000010	0.0012	0.0000	0.0803	0.0017
Y60B08	0.281675	0.000008	0.0012	0.0000	0.0747	0.0008
Y60B09	0.281701	0.000013	0.0009	0.0000	0.0533	0.0004
Y60B14	0.281945	0.000015	0.0021	0.0002	0.0865	0.0018
Y60B16	0.281878	0.000009	0.0008	0.0000	0.0432	0.0006
Y60B15	0.281756	0.000010	0.0009	0.0000	0.0567	0.0013
Y60B07	0.281838	0.000013	0.0010	0.0000	0.0643	0.0005
Y60B06	0.281695	0.000005	0.0007	0.0000	0.0406	0.0007
Y60B06	0.281705	0.000009	0.0006	0.0000	0.0401	0.0006
N17E35	0.281905	0.000010	0.0010	0.0000	0.0642	0.0008
N17E34	0.281902	0.000017	0.0008	0.0000	0.0459	0.0008
N17E33r	0.281865	0.000014	0.0006	0.0000	0.0366	0.0004
N17E33c	0.281969	0.000030	0.0094	0.0015	0.6255	0.1100
N17E32r	0.281890	0.000022	0.0013	0.0000	0.0489	0.0009
N17E32c	0.281786	0.000011	0.0009	0.0000	0.0507	0.0016
N17E30	0.281893	0.000015	0.0010	0.0001	0.0529	0.0019
N17E28	0.281813	0.000015	0.0008	0.0000	0.0437	0.0004
N17E28bis	0.281899	0.000012	0.0009	0.0000	0.0343	0.0009

N17E36	0.281958	0.000017	0.0018	0.0001	0.0655	0.0036
N17E31r	0.281834	0.000012	0.0023	0.0002	0.1585	0.0180
N17E31c2	0.281852	0.000011	0.0009	0.0000	0.0596	0.0016
N17E31c1	0.281962	0.000027	0.0067	0.0008	0.4782	0.0610
N17E26	0.281872	0.000015	0.0009	0.0000	0.0582	0.0005
N17E25	0.281900	0.000012	0.0006	0.0000	0.0336	0.0007
N17E24	0.281849	0.000012	0.0006	0.0000	0.0326	0.0003
N17E23r	0.281860	0.000008	0.0008	0.0000	0.0442	0.0007
N17E23c	0.281923	0.000016	0.0032	0.0001	0.1730	0.0036
N17E22	0.282428	0.000016	0.0005	0.0000	0.0222	0.0002
N17E22b	0.281981	0.000014	0.0006	0.0000	0.0348	0.0008
N17E21r	0.281852	0.000014	0.0008	0.0000	0.0430	0.0006
N17E21c	0.281862	0.000021	0.0008	0.0000	0.0413	0.0009
N17E17	0.281916	0.000010	0.0008	0.0000	0.0400	0.0012
N17E16	0.281864	0.000016	0.0009	0.0000	0.0523	0.0002
N17E15r	0.281932	0.000009	0.0012	0.0001	0.0556	0.0026
N17E15c	0.281872	0.000017	0.0028	0.0002	0.1346	0.0055
N17E14r	0.281893	0.000016	0.0009	0.0000	0.0568	0.0023
N17E14c	0.282160	0.000043	0.0227	0.0012	1.2945	0.0720
N17E09c	0.282006	0.000020	0.0067	0.0002	0.4324	0.0140
N17G30	0.281845	0.000013	0.0004	0.0000	0.0274	0.0003
N17G31	0.281838	0.000010	0.0009	0.0001	0.0394	0.0004
N17G29r	0.281999	0.000014	0.0033	0.0001	0.1195	0.0019
N17G29c	0.281988	0.000025	0.0053	0.0004	0.3846	0.0380
N17G28	0.281882	0.000013	0.0015	0.0000	0.1187	0.0039
N17G26r	0.281884	0.000014	0.0012	0.0001	0.0643	0.0028
N17G26c	0.281905	0.000028	0.0063	0.0005	0.3660	0.0260
N17G24	0.281908	0.000015	0.0017	0.0002	0.0795	0.0060
N17G22	0.281915	0.000017	0.0028	0.0002	0.1076	0.0035
N17G23	0.281758	0.000017	0.0007	0.0000	0.0444	0.0013
N17G21	0.281861	0.000020	0.0022	0.0002	0.0851	0.0061
N17G20r	0.281913	0.000010	0.0015	0.0001	0.0662	0.0015
N17G20c	0.282047	0.000016	0.0050	0.0005	0.3126	0.0260
N17G11r	0.282052	0.000013	0.0024	0.0002	0.1010	0.0063
N17G11c	0.281921	0.000030	0.0068	0.0005	0.3199	0.0130
N17G09r	0.281878	0.000013	0.0028	0.0001	0.1010	0.0055
N17G09c	0.282158	0.000021	0.0085	0.0002	0.6174	0.0200
N17G03	0.281886	0.000009	0.0006	0.0000	0.0387	0.0005
N17G04	0.281910	0.000012	0.0010	0.0000	0.0504	0.0007
N17G05	0.281899	0.000010	0.0012	0.0001	0.0617	0.0027
N17G07	0.281838	0.000010	0.0006	0.0000	0.0411	0.0002

N17G15	0.281908	0.000011	0.0012	0.0000	0.0672	0.0008
N17G16	0.281886	0.000008	0.0008	0.0000	0.0513	0.0009
YG17d01r	0.282381	0.000030	0.0017	0.0001	0.0565	0.0030
YG17d01c	0.281878	0.000014	0.0005	0.0000	0.0310	0.0002
YG17d02	0.281870	0.000011	0.0008	0.0000	0.0565	0.0012
YG17d03	0.281862	0.000014	0.0014	0.0000	0.0948	0.0004
YG17d04 start	0.281857	0.000015	0.0008	0.0000	0.0602	0.0005
YG17d04 total	0.281933	0.000024	0.0010	0.0000	0.0664	0.0014
YG17d05	0.281876	0.000012	0.0010	0.0000	0.0665	0.0006
YG17d06	0.281874	0.000010	0.0009	0.0000	0.0612	0.0007
YG17d15	0.282043	0.000013	0.0005	0.0000	0.0343	0.0002
YG17d16	0.281901	0.000014	0.0008	0.0000	0.0513	0.0006
YG17d14	0.281878	0.000011	0.0010	0.0000	0.0682	0.0003
YG17d07	0.281883	0.000010	0.0005	0.0000	0.0340	0.0007
YG17d08	0.281890	0.000014	0.0009	0.0000	0.0600	0.0014
YG17d09	0.282077	0.000020	0.0012	0.0001	0.0536	0.0018
YG17d13	0.281882	0.000012	0.0008	0.0000	0.0560	0.0027
YG17d11	0.281846	0.000010	0.0009	0.0000	0.0643	0.0010
YG17d18	0.281939	0.000013	0.0041	0.0005	0.1852	0.0099
YG17d19r start	0.282415	0.000022	0.0019	0.0001	0.0634	0.0013
YG17d19c	0.281913	0.000012	0.0010	0.0000	0.0638	0.0017
YG17d20	0.281896	0.000011	0.0007	0.0000	0.0463	0.0004
YG17d21	0.281934	0.000015	0.0008	0.0000	0.0563	0.0007
YG17d17r	0.282163	0.000020	0.0026	0.0001	0.0923	0.0048
YG17d17c	0.281889	0.000023	0.0006	0.0000	0.0426	0.0008
YG17d22	0.281857	0.000015	0.0008	0.0000	0.0475	0.0005
YG17d23	0.281878	0.000011	0.0014	0.0000	0.0885	0.0022

Tab.11: Summary of alteration reactions and their correlation to local geological events.

regional event	alteration	number	reaction	consumed components	released components	temperature	age
Mt. Gee quartz sinter event (end of anticline folding and exhumation)						surface	~286 Ma (U leaching from Davidite: Brugger et al., 2011)
formation of the pebble dykes (end of anticline folding and exhumation)						≥ 300 m depth	~315 Ma (zircon U/Pb: Brugger, 2011)
anticlinal folding and exhumation (Weisheit et al., 2013b)	scarning in Adelaidean			Mg^{2+}, Ca^{2+}, Al^{3+}, Si^{4+}		hydrothermal	
	silicification			Si^{4+}		brittle	
	chloritisation			K^+, Fe^{2+}, Mg^{2+}, Al^{3+}, Si^{4+}		brittle	
	$FeCl_2$ → hem (iron oxide ores)	(5b)	$3\ FeCl_2 + 4\ H_2O \rightarrow Fe_3O_4 + 6\ HCl + 2\ H^+ + 2\ e^-$	Fe^{2+}	H^+	> ~300 °C	~355 Ma (monazite U/Pb: Elburg et al., 2013)
	$FeCl_2$ → mgt (iron oxide ores)	(5a)	$2\ FeCl_2 + 3\ H_2O \rightarrow Fe_2O_3 + 4\ HCl + 2\ H^+ + 2\ e^-$	Fe^{2+}	H^+		
	kfs → ms (muscovitisation)	reverse (4)	$3\ (K,Na)AlSi_3O_8 + 2\ H^+ \rightarrow (K,Na)Al_2AlSi_3O_{10}(OH)_2 + 6\ SiO_2 + 2\ K^+$	H^+	K^+		
	bt → chl (chloritisation)	(3)	$3\ K(Fe,Mg)_3AlSi_3O_{10}(OH)_2 + 2\ H^+ \rightarrow (Fe,Mg,Al)_6(Si,Al)_4O_{10}(OH)_8 + 3\ K^+ + Mg^{2+} + Fe_3O_4 + 7\ SiO_2 + 3\ e^-$	H^+	Fe^{2+}, Mg^{2+}, K^+, Si^{4+}	< ~400 °C	
	phlogopitisation (hyperaluminous rocks)		$KFe_3AlSi_3O_{10}(OH)_2 + Mg^{2+} \rightarrow KMg_3AlSi_3O_{10}(OH)_2 + Fe^{2+}$	Mg^{2+}	Fe^{2+}		~455 Ma (zircon U/Pb: Elburg et al., 2012)
	ms → kfs (microclinisation)	(4)	$(K,Na)Al_2AlSi_3O_{10}(OH)_2 + 6\ SiO_2 + 2\ K^+ \rightarrow 3\ (K,Na)AlSi_3O_8 + 2\ H^+$	K^+, Si^{4+}	H^+ or **H_2O**	~400 °C	

	ab → kfs (potassium alteration)		$(Na,Ca)Al_{1-2}Si_{2-3}O_8 + K^+ \rightarrow KAlSi_3O_8 + Na^+ + Ca^{2+}$	K^+	Na^+, Ca^{2+}, Al^{3+}	last equilibration: ~200-300 °C	
	kfs → ab (sodium alteration)		$KAlSi_3O_8 + Na^+ \rightarrow NaAlSi_3O_8 + K^+$	Na^+	K^+	last equilibration: ~200-300 °C	
	bt → ms (muscovitisation)	(2)	$3\ KFe_3AlSi_3O_{10}(OH)_2 + 20\ H^+ \rightarrow KAl_2AlSi_3O_{10}(OH)_2 + 9\ Fe^{2+} + 6\ H_4SiO_4 + 2\ K^+$	H^+	Fe^{2+}, Mg^{2+}, K^+, Si^{4+}		
	bt → mc (microclinisation)	(1)	$KFe_3AlSi_3O_{10}(OH)_2 + 0.5\ O_2 \rightarrow KAlSi_3O_8 + Fe_3O_4 + H_2O$	O_2	**H_2O**, Fe^{2+}, Mg^{2+}	> ~400 °C	≤ ~478 Ma (Rb/Sr: this study) > < ~455 Ma (zircon U/Pb: Elburg et al., 2013) > < ~443 Ma (titanite U/Pb: Elburg et al., 2003)
cessation of deposition in the Adelaidean basin						MPI basement covered by ~12 km sediments	~500 Ma (Preiss, 2000)

---------- **APPENDIX 1 (WEISHEIT ET AL. 2013B)** ----------

Crustal-scale folding: Palaeozoic deformation of the Mt. Painter Inlier, South Australia

A. Weisheit[1], P.D. Bons[1*], M. Danišík[2], M.A. Elburg[3]

[1]Department of Geosciences, Eberhard-Karls University Tübingen, Wilhelmstraße 56, 72074 Tübingen, Germany

[2] Department of Earth and Ocean Sciences, The University of Waikato, Private Bag 3105, Hamilton 3240, New Zealand

[3]Geology Division, SAEES, University of KwaZulu-Natal, Private Bag X54001, Durban 4000, South Africa

[*]corresponding author; E-Mail: paul.bons@uni-tuebingen.de; Phone: +49 7071 2976469

Number of words of text: 7865

Number of words in references: 2861

Number of tables: 4

Number of figures: 9

Abbreviated title: Crustal-scale folding

Abstract: The Mt. Painter Inlier (Northern Flinders Ranges, South Australia) exhumed in the Yankaninna Anticline, in the hanging wall of the major NE-SW running Paralana Fault System. Regional north-south compression resulted in SE-directed oblique and lateral ramping onto the rigid Curnamona Province. Formation of the crustal-scale anticline caused ≤15 km exhumation of basement rocks in the core of the anticline. Currently exposed rocks reached the surface in Permian times. Folding and thrusting commenced between *c.* 500 and *c.* 450 Ma and lasted until the Permian Period. Contrary to previous studies, only a minor part of the deformation can be attributed to the *c.* 500 Ma Delamerian Orogeny, with most of the tectonic activity being contemporaneous with the Alice Springs and Lachlan Orogenies. New Permo-Triassic zircon and apatite (U-Th)/He ages, as well as a titanite fission track age point to a long-lived near-surface hydrothermal event that overprinted the basement and cover rocks. Hydrothermal reheating and burial below at the very most 2 km Mesozoic Eromanga Basin sediments resulted in partial or full rejuvenation of the apatite (U-Th)/He system.

Keywords: Northern Flinders Ranges; Mt. Painter Inlier; exhumation; crustal-scale folding; (U-Th)/He dating; fission track dating

Crustal-scale folding and faulting is known from many orogenic belts, such as the Alpine Orogens (Fügenschuh *et al.* 1997; Schellart 2002; Ziv *et al.* 2010), the Himalayan Orogens (Burg *et al*. 1997; Maheo *et al.* 2004; Mukhopadhyay & Sharma 2010), the Variscan or the Panafrican belts (Konopasek *et al.* 2001; Passchier *et al.* 2002; Llana-Funez & Marcos, 2007). Crustal deformation and thickening in these areas usually occurred during a restricted period of time, usually contemporaneous with, or followed by exhumation. Continent-continent collision deformation and exhumation in the Phanerozoic usually lasted for several tens of Myr (e.g. Suppe *et al*. 1992; Fügenschuh *et al.* 1997, Chen *et al.* 2002), while Proterozoic collisions usually affect the crust for > 100 Myr (e.g. Gower t al. 2008; Hildebrand et al. 2012). Deformation in Archaean to Proterozoic inter-cratonic settings, however, may be long-lived, although probably intermittent, and can remain similar for > Gyr (e.g. Holdsworth & Pinheiro 2000; Spaggiari 2007).

In the case of the Proterozoic Mt. Painter region in the Northern Adelaide Fold Belt, South Australia (Fig. 1), crustal-scale folding and faulting have been interpreted as a result of intra-crustal Delamerian (Pan-African) deformation, spanning *c.* 20 Myr at *c.* 500 Ma (Preiss 1987, 2000; Teale 1993; Paul *et al.* 1999; Elburg *et al.* 2001; McLaren *et al.* 2006; Armit *et al.* 2012). It is generally assumed that the gross structure of the Mt. Painter Inlier (MPI) had formed >400 Ma and was exhumed during Palaeozoic times (McLaren *et al.* 2002). This was recently challenged by Elburg *et al.* (2012) and Weisheit *et al.* (2013), who suggested that folding was not restricted to the Delamerian Orogeny, but lasted throughout almost the entire Palaeozoic Era.

Here we present new structural and thermochronological data from the Mt. Painter region that confirms long-lived crustal-scale deformation in the Northern Flinders Ranges by far exceeded the duration of the Delamerian Orogeny as recorded in the southern Adelaide Fold Belt. In the following we first provide an overview of the geological setting and present our new mapping results and structural analyses. Our presentation of the new model of the inlier's tectonothermal evolution will be then be described from higher to lower temperatures. We start with the reinterpretation of published (higher-temperature) Ar-Ar data, and then work the way down to lower-temperature history based on

published apatite fission track data and new data from titanite fission track, zircon, apatite and goethite (U-Th)/He analyses. Finally, we demonstrate that igneous and hydrothermal activity, 10 km-scale crustal folding and exhumation of the MPI occurred contemporaneously during *c.* 200 Myr, spanning the Delamerian and Alice Springs Orogenies in central and southern Australia.

Geological Setting

The Northern Flinders Ranges in South Australia are characterised by 10 km-scale folds that affect crystalline basement and the overlying Neoproterozoic (Adelaidean) cover succession (Fig. 1b; Preiss 1987, 2000; Paul *et al.* 1999). This area of crustal-scale folds is separated from the rigid Gawler Craton by the Norwest Fault System to the west and from the Curnamona Province by the Paralana Fault System to the east (Fig. 1b). The strike-slip components of these oblique-slip faults are dextral and sinistral, respectively. It formed during moderate north-south shortening of *c.*10-20 % between both cratons (Paul *et al.* 1999). So far, most authors attributed the crustal-scale deformation to the Delamerian Orogeny at *c.* 500 Ma (Coats & Blissett 1971; Paul *et al.* 1999; Foden *et al.* 2006), while exhumation and refolding of the existing folds occurred during Palaeozoic times, possibly as an effect of the Alice Springs Orogeny (e.g. Teale 1993; Paul *et al.* 1999; McLaren *et al.* 2002, 2006; Armit *et al.* 2012). The Delamerian Orogeny is defined by low pressure - high temperature metamorphism and the intrusion of syn- to post-tectonic granitoids in the southern Adelaide Fold and Thrust Belt (Preiss 1987; Foden *et al.* 2006). Style and intensity of deformation in this area (Flöttmann *et al.* 1994; Flöttmann & James 1997) differ from the structures in the northern Adelaide Fold and Thrust Belt (=Northern Flinders Ranges; Paul *et al.* 1999). The major east-west-striking folds in the centre of the Northern Flinders Ranges fold-and-thrust belt turn to a NE-SW strike in sinistral transpression along the eastern Paralana Fault System. Here, Mesoproterozoic basement, the Mt. Painter Inlier (MPI), is exposed in one of the major anticlines (Yankaninna Anticline) in the hanging-wall of the Paralana Fault System (Fig. 1b; Coats & Blissett 1971; Paul *et al.* 1999; Fraser & Neumann 2010).

Proterozoic Aeon

The oldest lithology in the MPI is a deltaic or shoal-water environment succession (Radium Creek Group; Coats & Blissett 1971; Cowley *et al.* 2012) with a maximum depositional age of *c.* 1590-1580 Ma (Fig. 1c and 2; U-Pb detrital zircon analyses; Fanning 2003; Wülser 2009; Fraser & Neumann 2010). At *c.* 1585-1575 Ma, a first suite of granitoids (Coulthard Suite dated by Pb-Pb and U-Pb of zircon; Neumann 2001; Elburg *et al.* 2001, 2012; Stewart & Foden 2003) intruded the (meta-) sediments, followed by the U-rich, high heat-producing Moolawatana Suite at *c.* 1565-1555 Ma (U-Pb zircon, Pb-Pb K-feldspar and whole rock data; Sheard & Cockshell 1992; McLaren *et al.* 2006; Fraser & Neumann 2010; Elburg *et al.* 2012). The latter appears to be associated with albitisation of the older lithologies (Neumann 2001; Elburg *et al.* 2001; 2012). Metasomatism, metamorphism and deformation of the basement occurred prior to the deposition of the Adelaidean sedimentary cover (e.g. Teale 1993; Paul *et al*. 1999; Dipple *et al.* 2005; Elburg *et al.* 2001, 2012).

Intra-cratonic rifting during NE-SW extension resulted in the formation of NW-SE striking horst and graben systems in the southern MPI during Neoproterozoic times (Preiss 1987; Paul *et al.* 1999). The early graben structures were filled with sediments and flood basalts that extruded at *c.* 830 Ma, based on correlation with dolerite dykes dated by U-Pb on baddeleyite (Wingate *et al.* 1998). Ongoing extension and subsidence resulted in the formation of the large Adelaidean sedimentary cover basin along the full extent of the Adelaide Rift Complex that now forms the Adelaide Fold and Thrust Belt (Fig. 1a; Preiss 1987). Sedimentation of marine and terrestrial sediments continued until the onset of the Delamerian Orogeny at *c.* 500 Ma (Preiss 1987; Foden *et al.* 2006). The Adelaidean succession reaches a thickness of 10-12 km at the MPI (Coats & Blissett, 1971; Paul *et al.* 1999). The geothermal gradient at that time is estimated to be high at 40-50 °C/km, which was caused by the high concentration of heat producing elements in the basement granitoids (U, Th, K; Mildren & Sandiford 1995; Sandiford *et al.* 1998; McLaren *et al.* 2002, 2006). Therefore the temperature at the base of the Adelaidean basin reached c. 500 °C at the cessation of sedimentation at c. 500 Ma.

Palaeozoic magmatism and hydrothermal alteration

At *c.* 460-440 Ma, granites (metaluminous and peraluminous British Empire Granite), granodiorites and leucocratic pegmatites intruded the basement and adjacent cover sediments of the MPI (U-Pb ages of monazite and zircon; Elburg *et al.* 2003, 2013; McLaren *et al.* 2006; Wülser 2009). The inferred intrusion depth of the British Empire Granite (Fig. 1c) is about 13 km (McLaren *et al.* 2006). Pegmatitic diopside-titanite veins intruded the southern MPI at about the same time (Fig. 1c and 3a; U-Pb age of titanite; Elburg *et al.* 2003). Based on fluid inclusions, Bakker & Elburg (2006) obtained conditions of 510 ± 20 °C at 130 ± 10 MPa (*c.* 5 km depth) for the formation of these veins, assuming a 100 °C/km geothermal gradient. A greater depth of 12-13 km results if the 40-50 °C/km gradient is applied instead. Considering that the vein-forming fluids were probably hotter than their host rock, the veins formed between *c.* 5 and 13 km depth.

The pegmatites and the diopside-titanite veins intrude and are overprinted by hydrothermal K-feldspar alteration and breccia zones (Coats & Blissett 1971; Drexel & Major 1987; Brugger *et al.* 2005). About 60 km^2 of K-feldspar altered basement and cover rocks are now exposed (Weisheit *et al.* 2013). Palaeozoic fluid flow is also expressed by mineralisations of Fe-oxide-U-Cu-REE ores (*c.* 355 Ma, U-Pb monazite; Elburg *et al.* 2013).

Steep, decimetre to >metre-wide dykes, filled with rounded clasts of allochthonous and local (K-feldspar-altered) lithologies in a non-metamorphic fine-grained sandy matrix cut basement rocks near Mt. Painter and Mt. Gee. These diamictite dykes (Cowley *et al.* 2012), previously also referred to as "pebble dykes" (Coats & Blissett 1971; Brugger *et al.* 2011), are interpreted as deep cracks filled with allochthonous and autochthonous (glacial) sediments. The youngest detrital zircons in the matrix of the dykes are of Permian age (315 ± 8 Ma: U-Pb zircon; Brugger *et al.* 2011). The age of the dykes is also assumed Permian, based on the glacial nature of the dyke material and their likely Antarctic provenance, which indicates transport during the Late Carboniferous to Early Permian Glaciation (320-290 Ma; Eyles *et al.* 2002; Jones & Fielding 2004; Veevers 2006). The centre of the MPI thus exhumed from its deepest burial at *c.* 500 Ma to near-surface levels at *c.* 300 Ma.

According to McLaren *et al*. (2002), the MPI cooled below *c.* 500 °C (Ar-Ar hornblende) after the 460-440 Ma intrusion of the British Empire Granite. Based on modelled K-Ar and Ar-Ar hornblende, mica and K-feldspar ages, McLaren *et al*. (2002) proposed three steps of fast cooling of the whole inlier at *c.* 430 Ma, *c.* 400 Ma and finally down to the closure temperature of K-feldspar between 300 and 150 °C at *c.* 325 Ma. These authors interpreted this cooling signal as a stepwise exhumation of the Delamerian Yankaninna Anticline.

Outcrops of a near-surface quartz-hematite-calcite-fluorite sinter breccia and veins (Mt. Gee Sinter; Fig. 3b; Coats & Blissett 1971; Brugger *et al.* 2011) can be found scattered throughout the centre of the MPI (Fig. 1c). These breccias and veins overprint the (K-feldspar-altered) basement rocks, as well as the diamictite dykes (Fig. 3c). They formed during near-surface boiling of an almost pure H_2O-fluid of 140-100 °C (Bakker & Elburg 2006) at *c.* 290 Ma (U-Pb age of a davidite; Brugger *et al.* 2011). This age is consistent with a formation of the diamictite dyke during the 320-290 Ma Carboniferous-Permian Glaciation (e.g. Jones & Fielding 2004). It should be noted that Bakker & Elburg (2006) and Brugger *et al.* (2005, 2011) regarded the various hydrothermal rocks (K-feldspar-altered breccias, Fe-oxide breccias, Mt. Gee Sinter) as products of a single, but long lasting-event that may even be linked to the present-day hot springs (Paralana Hot Springs, Brugger *et al.* 2005). However, the cross-cutting relationships with the diamictite dykes allow a separation of middle- to upper-crustal pre-Permian, and near-surface post-Permian hydrothermal activity (Elburg *et al.* 2013; Weisheit *et al.* 2013). That the presently exposed rocks were near the surface at *c.* 290 Ma seems contradictory to apatite fission track ages that indicate cooling below *c.* 110 °C between 260 and 175 Ma (Mitchell *et al.* 2002). As discussed below, these cooling ages can be interpreted as the waning stages of hydrothermal activity, rather than being related to exhumation as proposed by Mitchell *et al.* (2002).

Extension in Jurassic to mid-Cretaceous times (*c.* 200-90 Ma) led to the renewed formation of horst and graben structures to the east of the MPI. Up to *c.* 2.5 km of sediments were deposited in the centre of the newly formed Eromanga Basin, which thins to a few 100 metres at its margins where the MPI lies (Fig. 1c; Krieg *et al.* 1995). Some Mesozoic sediments on top of the northern MPI (Coats &

Blissett 1971) indicate burial of the inlier during that time as well. The final and recent exhumation of the inlier started in the Neogene along the Paralana Fault System (Célérier *et al.* 2005).

Methods

Detailed geological mapping and structural analyses were carried out in and around the southern and central Mt. Painter Inlier. Samples from basement and Adelaidean cover rocks were taken for microstructural analyses. The software move^{TM}2010 was used for 3D modelling of the Yankaninna Anticline.

A set of apatite, zircon, titanite and goethite samples was prepared for (U-Th)/He measurements and fission track (FT) dating to reconstruct the cooling and exhumation history of the MPI. The closure temperatures of the used mineral systems are *c.* 310-265 °C (titanite FT; Coyle & Wagner 1998), *c.* 180 ± 20 °C (zircon (U-Th)/He; Reiners *et al.* 2004), *c.* 110 ± 10 °C (apatite FT; Green *et al*. 1986) and *c.* 75-55 °C (apatite (U-Th)/He; Schuster et al. 2006). (U-Th)/He method applied to supergene goethite records the age of goethite formation at the surface (Shuster *et al.* 2005). Details on the methods are given in Zeitler *et al.* (1987), Farley *et al.* (1996), Farley (2002), Meesters & Dunai (2002a,b), Reiners *et al.* (2004), Reiners (2005) and Schuster *et al*. (2006) for (U-Th)/He and in Gleadow & Lovering (1974), Wagner & Van den haute (1992); Galbraith & Laslett (1993), Reiners & Farley (1999) and Siebel *et al.* (2009) for the FT method.

Apatite and zircon (U-Th)/He dating was performed on clear, inclusion-free, euhedral grains, which were hand-picked under a binocular and a petrographic microscope. Single grains with a minimum diameter of 80 μm, were packed into platinum (apatite) and niobium tubes (zircon) and measured for He by isotope dilutions on the Patterson Ltd.-designed helium-extraction lines with a quadrupole mass-spectrometer at the Department for Geosciences of the University of Tübingen (Germany), and at the John de Laeter Centre of Isotope Research in Perth (Australia). Apatites and

zircons were degassed at *c.* 960 °C and *c.* 1250 °C, respectively, under ultrahigh vacuum using a 960 nm diode (Tübingen) and Nd-YAG (Perth) lasers. To verify complete degassing in the first step, each grain was heated and measured again. The re-extractions generally revealed <1 % of He of the first heating. Samples analysed for He in Tübingen were sent for U-Th measurements to the University of Arizona at Tucson, where they were spiked, dissolved and analysed by isotope dilution using inductively coupled plasma mass spectrometry (ID-ICP-MS). Samples degassed in Perth were analysed in-house for U-Th using the same procedure (Evans *et al.* 2005). Uncertainty of the mean (U-Th)/He ages was calculated as standard deviation of at least three replicates per sample.

A centimetre-sized, fresh, homogeneous, high-quality black goethite was used for (U-Th)/He dating. The sample was crushed in a steel mortar; shards were then handpicked under a binocular microscope, ultrasonically cleaned in ethanol and left to dry. Single shards were loaded into Nb tubes. He and U-Th were measured using isotope-dilution mass spectrometry (quadrupole gas mass-spectrometer and ICP-MS, respectively) at the John de Laeter Centre of Isotope Research (Perth). Helium was extracted at *c.* 500 °C under ultra-high vacuum. Following the He measurements, Nb tubes containing the samples were retrieved from the laser cell, spiked, dissolved in 200 µl of 50 % HCl in Teflon vials loaded in Parr bombs and heated to 210 °C for 60 hours. Beside sample solutions, each Parr bomb also contained one blank and two spiked standard solutions for blank correction and calibration purposes. All solutions were analysed for U-Th by ID-ICP-MS. The total analytical uncertainty (TAU) was calculated as the square root of the sum of squares of uncertainty on He and weighted uncertainties on U and Th measurements. Given the large size and polycrystalline character of the dated sample, (U-Th)/He ages were not corrected for alpha ejection (Farley *et al.* 1996). The ages were also not corrected for diffusive loss (Shuster *et al.* 2005).

For FT analysis, titanite crystals were embedded in epoxy and polished to 4π geometry. Spontaneous tracks were revealed by etching with a solution of 1 HF : 2 HNO_3 : 3 HCl : 6 H_2O at 23 °C for six minutes (Gleadow & Lovering 1974). FT dating was carried out using the external detector method (Gleadow 1981) with low-uranium muscovite sheets (Goodfellow mica™). The IUGS-recommended zeta calibration approach was taken for age determination (Hurford & Green 1983).

Zeta values (Hurford 1998) of 283.5 ± 6.2 (titanite) for dosimeter glass CN-5 have been derived from six titanite age standards from the Fish Canyon Tuff. FT ages were calculated with TrackKey 4.1 (Dunkl 2002).

In the following we discuss the geological history of the MPI in chronological order. We first present and interpret the results of our detailed mapping and structural analysis, followed by the discussion of the timing of Palaeozoic folding and exhumation. We used robust Ar-Ar plateau ages (defined by McLaren *et al.* (2002) as "that part of an age spectrum where the gases of consecutive steps are within 2σ error of one another and together comprise at least 50 % of the gas release". A plateau-like signal was observed "if one or two steps in such a sequence are discordant") of samples from basement and cover units published by McLaren *et al.* (2002). Results of low-temperature thermochronology are presented last.

Results

Deformation history and structural reconstruction

The Mesoproterozoic Era

A pervasive to localised NE-SW to east-west-striking main foliation S_m, mainly defined by biotite and sillimanite, is found throughout almost the whole MPI (S_{gneiss} in Elburg *et al.* 2003 and S_{2+3} in Armit *et al.* 2012; Fig. 4). The Adelaidean unconformity truncates this foliation at a low angle of about ten degrees (Fig. 3d). Biotite, sillimanite and cordierite parageneses in meta-pelites indicates low-pressure, high-temperature metamorphism during the S_m-forming deformation event (Paul 1998; Armit *et al.* 2012). S_m formed axial planar to closed and isoclinal folds and is a crenulation cleavage of an earlier foliation S_{m-1} (Fig. 3e,f). Hence, at least one deformation event pre-dates the main foliation. The metamorphic grade in the basement increases to migmatitic conditions in the Paralana Hot Springs area. Isoclinal buckle folds of leucosomes with S_m as the axial-planar foliation indicate that the leucosomes solidified before folding. Partial melting therefore occurred pre- to syn-S_m (Fig. 3g).

Adelaidean cover sediments and the main basement foliation S_m were folded during the formation of the Yankaninna Anticline. The original orientation of S_m can be found by rotating the cover layers back to horizontal and passively rotating S_m along with these (Fig. 4; Tab. 1). Figure 4 shows that the main foliation S_m was shallowly dipping with a mean orientation of *c.* 10° towards 283° prior to the deposition of the Neoproterozoic Adelaidean cover. The large spread in orientations may be due to (1) variations in S_m prior to deposition of the Adelaidean succession, (2) tilting of basement during Neoproterozoic horst-graben formation and (3) ductile deformation within the basement during formation of the Yankaninna Anticline (see below).

The Neoproterozoic Era

Extensional tectonics in early Neoproterozoic times led to the formation of horst and graben structures in the exhumed and deformed Mesoproterozoic basement (Preiss 1987, 2000). The lowermost Adelaidean strata were deposited in NW-SE running grabens (Fig. 5). These grabens deepened from the NW (≤1 km) to the SE where >2 km thick graben sediments are found. They were passively folded during formation of the Yankaninna Anticline and now crop out on the western margin of the basement (graben at the Needles and at Yudnamutana) and in the southeast (graben north of Arkaroola; Fig. 1c and Fig. 5a). Whereas graben faults strike east-west on the NW limb of the anticline (e.g. the Hamilton and Jubilee Faults, Fig. 1c), they run about north-south on the SE limb. This can be explained by the passive folding of an originally *c.* 310° striking graben by the Yankaninna Anticline with a SW-plunging fold axis (Fig. 5; Tab. 1). The graben structures on either side of the basement are thus in fact outcrops of one and the same graben structure, which we informally name the Mt. Oliphant Graben System, after Mt. Oliphant in one of the deepest parts of the graben north of Arkaroola Village (Fig. 5b). Graben faults, such as the Hamilton and Jubilee Faults cannot be traced all the way across the basement, probably because of heavy overprinting by hydrothermal activity.

Localised deposition in the lower Adelaidean grabens was followed by widespread sedimentation in the first of a number of rift and sag cycles (Preiss 1987, 2000). While some of the early graben

faults (e.g. at the Pinnacles) were deactivated before deposition of mid-Adelaidean succession, others remained active longer. The Hamilton and Jubilee Faults still cause an offset of about 2 km in the mid-Adelaidean strata.

There is a distinct difference in metamorphic grade east and west of the Paralana Fault *sensu stricto* (Coats & Blissett 1971). The Paralana Fault *s.s.*, located east of Arkaroola Village, is the branch of the Paralana Fault System that gave it its name (Fig. 1c). Whereas the unconformity was buried up to *c.* 13.5 km just west of the Paralana Fault *s.s.* (Paul *et al.* 1999), it was only buried to *c.* 9.5 km east of it (Fig. 5c). This is confirmed by fluid inclusions in veins in shales east of the Paralana Fault *s.s.* that indicate a burial of 3-6 km of a horizon that is *c.* 4 km above the unconformity (Bons *et al.* 2007). The total thickness of the Adelaidean succession decreases to the east of the Paralana Fault System, where seismic surveys reveal a maximum thickness of *c.* 6 km (Korsch *et al.* 2010). The north-south-striking Paralana Fault *s.s.* thus became active during deposition of the Adelaidean succession and was one of several step faults with a west-down movement (and unknown horizontal offset) bounding a basin that deepened westwards.

The significant differences in the thickness of the sedimentary pile on either side of the Paralana Fault *s.s.* directly affected the metamorphic grade of the rocks at the unconformity. At an elevated geothermal gradient of 40-50 °C/km (Mildren & Sandiford 1995; Sandiford *et al.* 1998; McLaren *et al.* 2002, 2006) the lower Adelaidean sediments west of the fault experienced amphibolite facies conditions close to 500 °C, while the same stratigraphic level east of the fault only reached depths of greenschist facies conditions. The various metamorphic minerals, including cleavage-forming biotite, are aligned sub-parallel to the sedimentary bedding and the mineral-in isograds are parallel to the unconformity (Coats & Blissett 1971; Mildren & Sandiford 1995). This suggests that the metamorphic grade of the Adelaidean units is a result of static burial of the unconformity and independent from the Delamerian Orogeny.

The Palaeozoic Era

The Adelaidean strata and crystalline basement of the MPI were folded into the 10 km-scale Yankaninna Anticline (Fig. 5a,b; Coats & Blissett 1971; Preiss 1987; Paul *et al.* 1999). The steep axial plane strikes NE-SW in the northeastern part of the inlier and turns towards east-west in the SW (Fig. 1). The crest of the anticline is located east of the British Empire Granite and north of Paralana Hot Springs. Here the fold strikes NE-SW with a gently NE plunging fold axis in the northeastern part of the inlier. Towards the SW, the fold hinge plunges between 20 and 50° towards the SW to W (Fig. 4).

Apart from the large-scale folding and smaller, 100 m-scale parasitic folds of the main foliation S_m in the basement, few deformation structures developed during Palaeozoic folding. Within the basement, only centimetre-scale crenulation cleavages (S_{pal}) and kink folds in almost pure biotite schists can be attributed to this folding (Fig. 3h). Palaeozoic folding caused the formation of a steep, axial-planer crenulation cleavage (S_{pal}) in suitable lower-Adelaidean units, in particular in phyllites north of Arkaroola Village (Fig. 1b in Elburg *et al.* 2003). Minor crenulations locally overprint this dominant Palaeozoic foliation. Crenulations in the phyllites post-date the growth of porphyroblasts (Fig. 3i).

The Yankaninna Anticline developed during progressive north-south compression (Fig. 1b; Paul *et al.* 1999). Structural profiles trough the fault system show that the late-Neoproterozoic Paralana Fault System became reactivated with a sinistral, NW-up movement. Maximum vertical displacement (>10 km) occurred in the NE-SW striking section of the fault system NE of Paralana Hot Springs, where these faults formed oblique ramps. Vertical movement decreases to the south, where these faults turn to north-south striking and become lateral ramps. Sinistral offset is in the order of a few kilometres. The deepest sections of these faults are now exposed in the Hidden Valley area, where mylonites are found with sinistral strike-slip and oblique-slip movement.

Basement and cover rocks within the Yankaninna Anticline were thrust up during formation of the anticline. Meanwhile, rocks in the cores of adjacent synclines maintained their approximate burial depth. Assuming that no high-elevation mountain range formed during this intra-continental deformation, the formation of the anticline resulted in exhumation of rocks in its core. Here we use the

term "exhumation" for a reduction in the absolute distance between a volume of rock and the surface (England & Molnar 1990). This opens up the possibility to determine the rate of formation of the Yankaninna Anticline by measuring the rate of exhumation. In the following section we evaluate published and new thermochronology data and show that the Yankaninna Anticline grew over a period of approximately 200 Myr.

Timing of folding and exhumation

To reconstruct the timing of the crustal scale folding, exhumation and fluid flow in the MPI we use published Ar-Ar plateau cooling ages (McLaren *et al.* 2002) and several low-temperature thermochronology methods (Fig. 6; Mitchell *et al.* 2002; this study). The geothermal gradient down to the Adelaidean unconformity was estimated at 40-50°C/km (Mildren & Sandiford 1995; Sandiford *et al.* 1998; McLaren *et al.* 2002, 2006). The present day heat flow in the region is about double the crustal average (McLaren *et al.* 2006), which indicates that the geothermal gradient is still high. For the interpretation of cooling ages, we assumed a constant gradient of 40 °C/km since 500 Ma. Deviations from this value may have occurred, but would not change the results significantly. Errors in maximum burial depth at the end of Adeaidean deposition are estimated to be *c.* 1 km. The surface temperature is assumed to be 20 °C.

Exhumation to near-surface levels

McLaren *et al.* (2002) interpret their modelled K-Ar and Ar-Ar cooling ages of hornblende, muscovite, biotite and K-feldspar in basement and cover samples as reflecting cooling and exhumation over a prolonged period during Palaeozoic times, with several stages of mid-Palaeozoic, fast cooling (*c.* 430 Ma, *c.* 400 Ma and *c.* 325 Ma). Fault activity and a possible re-heating during magmatism and metamorphism (Elburg *et al*. 2003; 2013) were not taken into account. This interpretation is based on the assumption that the Yankaninna Anticline exhumed after its formation. With this assumption, samples retain their relative depth difference during exhumation. However, it is not feasible to first have a >10 km amplitude fold which then passively exhumed. Instead, as the fold grew, rocks in the

core of the anticline exhumed faster than those in the limbs and their relative depth difference decreased. The data of McLaren *et al*. (2002) show that rocks in the MPI were exhumed over a prolonged time and samples from greatest depth reached their closure temperatures later than those from shallower depth in the hinge of the anticline (Fig. 7).

The maximum burial depth of the Adelaidean unconformity at the onset of the Delamerian Orogeny (Fig. 6) and the current level and shape of this unconformity in the Yankaninna Anticline as shown in Fig. 5a and 5b are based on our own mapping and that of Coats & Blissett (1971). This structure achieved its present shape by *c.* 290 Ma at the latest, based on the near-surface, <315 Ma diamictite dyke and the *c.* 290 Ma Mt. Gee hydrothermal system. Using the Ar-Ar hornblende, muscovite and biotite plateau ages of McLaren *et al.* (2002) we constrain the shape, and hence the average growth rate of the anticline over time (Fig. 7, 8, 9). K-feldspar Ar-Ar cooling ages are not taken into account because of the strong dependence of the closure temperature on the (poorly known) size of diffusion domains (300-150 °C, Lovera *et al.* 1989). With the limited data available, we need to make the assumption that the anticline maintained its shape, but increased its amplitude over time.

McLaren *et al*. (2002) report two hornblende plateau ages (closure temperature *c.* 500 ± 50 °C; Harrison 1981): 446 ± 1 Ma for sample MP31 of a flood basalt at the base of the Mt. Oliphant Graben System with a maximum burial depth of *c.* 12.4 km and 432 ± 1 Ma for sample MP28 of an amphibolite dyke intruding basement quartzites near the British Empire Granite with a maximum burial depth of *c.* 15 km. An exhumation rate of 0.19 ± 0.11 km/Myr (1.4-3.6 km / 12-16 Myr) is obtained when identical exhumation rates for the two samples are assumed (Fig. 7a). Slightly different rates result, if the different exhumation rates as a function of burial depth are taken into account. However, as the samples were still close to their maximum burial depth, the difference is not significant. If constant rates are assumed for the initial exhumation, both samples would still have been at their original burial depth at *c.* 450 Ma (Fig. 7b). Earlier, Delamerian initiation of exhumation would have resulted in a larger difference in cooling ages between the two samples.

By the time of the intrusion of the British Empire Granite (460-440 Ma), the core of the anticline had risen by *c.* 1.7 km ± 1.0 km, according to the structural reconstructions (Fig. 9). The British Empire Granite thus intruded at *c.* 13.3 km ± 1.5 km, which is in accordance with earlier, petrologic and thermal estimates (McLaren *et al*. 2006).

Muscovites from a quartzite sample in the vicinity of the British Empire Granite (*c.* 3 km below the unconformity) closed their Ar-Ar system at *c.* 375 Ma (*c.* 350 ± 50 °C; Hames & Bowring 1994), while basement gneisses, pegmatite, biotite schist and Neoproterozoic phyllite samples at the unconformity in the southern MPI went through the closure temperature of biotites (*c.* 300 ± 50 °C; Harrison *et al.* 1985) at about this time. At 375 Ma the unconformity above the central MPI reached a depth of *c.* 6 km, while it rose more slowly in the southern limb of the anticline (Fig. 9). The mean exhumation rate in the centre of the inlier between 440 and 375 Ma was *c.* 0.08 ± 0.04 km/Myr (at a depth of 13.3 ± 1.5 km at 440 Ma).

The inlier reached the surface at the latest at *c.* 290 Ma with the formation of the Mt. Gee Sinter (Fig. 8; Brugger *et al*. 2011). This implies an average exhumation at the hinge of the anticline of 0.08-0.11 km/Myr since 375 Ma. About half of the total exhumation, and hence folding, thus occurred after 375 Ma. Only a very minor part of the exhumation can potentially be attributed to the Delamerian Orogeny and even this is doubtful as the hornblende ages indicate commencement of exhumation at *c.* 450 Ma.

Final exhumation and hydrothermal overprint: results of low-temperature thermochronology

A total of 12 samples, collected from the southern and central MPI, were used for thermochronology analyses. BEM4 is a sample of an undeformed metaluminous variety of the British Empire Granite, taken at the eastern side near the base of the Palaeozoic granite intrusion (Fig. 6; Tab. 2). BEM5 was collected close to BEM4 and represents the peraluminous variety of the granite. Both samples are from an intrusion in metasediments that were at a maximum depth of *c.* 15 km after the deposition of the Adelaidean sediments, as inferred from the structural reconstructions. The monazite U-Pb ages of these samples form a cluster at *c.* 440 Ma (Elburg *et al.* 2003). Single zircon (U-Th)/He

ages of BEM4 (n=3) and BEM5 (n=4) are scattered between 245 ± 16 and 11 ± 0.7 Ma (Tab. 3). The scatter is likely related to the radiation damage and zoning of parent nuclides, since all zircons have high-U cores of Mesoproterozoic age (Elburg *et al.* 2012, 2013). Therefore, their average age was not calculated and they are not included in the interpretation. Apatite (U-Th)/He ages of BEM4 (n=3), in contrast, reproduce very well (all replicates overlap within one-sigma error) and give an average age of 110 ± 3 Ma.

Sample GT2 is from a shear zone in the basement south of Mt. Painter, which had a maximum burial depth of *c.* 14 km. Monazite U-Pb analyses revealed mixed ages between 530 and 440 Ma (Elburg *et al.* 2003; Buick, pers. comm.). Zircon (U-Th)/He ages (n=2) of GT2 reproduce within one-sigma error and give an average age of 313 ± 3 Ma.

A goethite sample collected on the surface of a gneiss (SP47) revealed an average (U-Th)/He age of 20.0 ± 6 Ma (n=8). This age gives the time of ferruginisation, oxidation, or gossan formation when the basement must have been at the surface.

TIL1c and BC267a are volcanic and granitic pebbles in a sedimentary diamictite dyke; BC265 and BC266 were collected from the wall rock of these dykes to test whether the pebbles and the wall rock experienced different exhumation. Zircon (U-Th)/He ages of TIL1c (n=4) gave an average age of 323 ± 19 Ma. Two similar ages of *c.* 344 and *c.* 307 Ma, and one much older age of *c.* 491 Ma were obtained from three zircons in sample BC267a (Tab. 3). Zircons of BC265 gave an average age of 239 ± 45 Ma (n=3). The scatter in ages is even greater for the single apatite measurements of BC265 and BC266, which show a wide spread between *c.* 179 and *c.* 23 Ma. The (U-Th)/He zircon age of the host rock is clearly younger than the (U-Th)/He zircon age of the pebble boulders, which rather resemble the results of the shear zone GT2 with ages around 320 Ma. The younger zircon age of the wall rock of 238 ± 45 Ma could be a result of an overprint by the quartz-hematite Mt. Gee Sinter.

ARK533 (n=7) is a meta-granite clast within the Permian quartz-hematite Mt. Gee Sinter. The mean zircon (U-Th)/He age of 264 ± 21 Ma overlaps within the error with that of BC265 (239 ± 45

Ma). Apatite (U-Th)/He ages of ARK533 give an average age of 91 ± 3 Ma (n=4), which is close to the apatite age of BEM4 (110 ± 3 Ma).

At the base of the Mt. Gee Sinter, wall-rock samples of meta-granites were sampled from different distances to the sinter. HEG1, closest to the sinter, gave a scattered zircon (U-Th)/He signal with an average age of 337 ± 57 Ma (n=3), which is similar to 345 ± 6 Ma (n=2) for sample HEG7, 50 m away from the sinter. The (U-Th)/He ages of the two samples do not appear to have been reset by the Mt. Gee Sinter event. Instead, they, and sample GT2, probably record cooling during exhumation.

Finally, TTN1 is a titanite sample from a diopside-titanite vein (*c.* 440 Ma, U-Pb titanite; Elburg *et al.* 2003), whose FT age of 209 ± 10 Ma is appreciably younger than the rest of the samples (Tab. 4).

Final exhumation and hydrothermal overprint: interpretation of low-temperature thermochronology

The presented zircon (U-Th)/He ages that show good reproducibility (closure temperature *c.* 180 ± 20 °C at *c.* 3-6 km depth) cluster around 350-300 Ma and fit well into the general integrated exhumation trend of *c.* 0.1 km/Myr derived from the Ar-Ar data of McLaren *et al.* 2002 (Fig. 8). An exhumation rate of these samples can, however, not be calculated from their age-elevation relationship, as the difference in the recent elevation is low (*c.* 250 m; Tab. 2) and the isotherms need not have been horizontal.

The MPI reached the surface in the early Permian Period (Brugger *et al.* 2011), which is consistent with the integrated exhumation rate of *c.* 0.1 km/Myr. However, two zircon (U-Th)/He samples record a highly scattered signal and plot well outside of the Palaeozoic exhumation trend (ARK533 and BC265). Also the apatite FT data (closure temperature *c.* 110 °C = 2-3 km depth) report by Mitchell *et al.* (2002) show a wide range of Mesozoic ages (Fig. 8). The titanite FT age (closure temperature *c.* 265-310 °C = 6-7 km) and the apatite (U-Th)/He ages (closure temperature *c.* 75-55 °C or *c.* 1 km) are also younger than the regional exhumation trend. An unpublished apatite FT age of the diopside-titanite vein is with 127 ± 7 Ma well outside of the regional trend (M. Elburg & S. Glorie, unpublished data).

The low-temperature thermochronology data were potentially affected by the burial of the MPI during the formation of the Mesozoic Eromanga Basin. This burial was certainly less than the maximum of 2.5 km that is recorded in the centre of the basin (Krieg *et al.* 1995). However, even with an unlikely stable geothermal gradient of 40 °C/km and a regionally constant burial of 2.5 km, the MPI would be heated only to 120 ° *C*. This burial alone does not explain the zircon (U-Th)/He, apatite and titanite FT ages that indicate higher temperatures in late Palaeozoic and Mesozoic times. Only the apatite (U-Th)/He ages may have been affected, even if the MPI was buried by at least 1 km.

There are another two processes that can influence FT and (U-Th)/He ages of the zircons and apatites in the MPI: 1) lowering of the closure temperatures of the minerals due to radiation damage (Flowers *et al.* 2009) and 2) change of the geothermal gradient due to equilibration and reheating during burial and regional/local hydrothermal fluid flow (Timar-Geng *et al.* 2004; Filip *et al.* 2007). Especially the second processes could have resulted in the scattered ages that are recorded in our data (Fig. 8). We believe that the partial reheating of the MPI is caused by the Mesozoic burial, as well as by local/regional hydrothermal activity during the quartz-hematite Mt. Gee Sinter event.

Sinter-formation in the southern MPI started in the early Permian Period (Brugger *et al.* 2011). According to our titanite FT age of the overprinted diopside-titanite veins (Fig. 3a) this sinter event was active at least until the late Triassic Period. With Mesozoic burial of the MPI the sinter-activity may have ceased, but this long-lasting hydrothermal event probably resulted in a locally elevated geothermal gradient that equilibrated with time (Fig. 8). This could explain the scattered and relatively young apatite FT and apatite (U-Th)/He ages.

After the Mesozoic burial the MPI must have again reached the surface at the latest at *c.* 20 Ma, when the goethite sample formed (Fig. 8). This interpretation is supported by the style of sedimentation in the Eromanga Basin that changed from low-energy, paralic conditions to alluvial fans in the Miocene during the initial uplift of the Northern Flinders Ranges (Célérier *et al.* 2005, and references therein). The exhumation path of the MPI since 200 Ma cannot be constrained from

geological observations. A slow mean exhumation rate of *c.* 0.01 km/Myr in Tertiary times could be possible, as it is indicated from apatite FT ages all over Australia (Kohn *et al.* 2002).

Discussion

The Yankaninna Anticline is a large fold in which all structural elements present at the onset of the Palaeozoic Era were passively folded (Fig. 5b). The fold pattern of S_m in the basement closely mimics, but does not exactly match that of the bedding in the overlying Adeaidean succession, because of the small angle between S_m and bedding before folding (Fig. 3d). From the current map pattern, it is not immediately obvious that the east-west-striking faults, such as the Hamilton and Jubilee Faults, active in the Neoproterozoic, belong to the same set as those in the south-eastern limb of the anticline (Fig. 5a). Considering that these faults were formed well before the folding, it becomes clear that they originally formed a single *c.* 310°-striking Mt. Oliphant Graben System (Fig. 5c).

The north-south to NE-SW-striking Paralana Fault System developed after the Mt. Oliphant Graben System, but still during deposition of the Adelaidean succession. During Palaeozoic times, this fault system was reactivated as a set of lateral and oblique ramps against which the MPI was pushed up and towards the south (Fig. 5a). Older faults on the NW-limb of the developing anticline were passively rotated to an east-west-strike, but not reactivated. Graben faults on the SW-limb, however, rotated towards a north-south-strike, which is closer to that of the Paralana Fault System. This allowed these faults to be reactivated, as can be observed NE of Mt. Oliphant. Here the old graben faults have thick quartz veins with slickensides and striations that indicate sinistral, transpressive movement. The formation of the Yankaninna Anticline, and, by inference, folds throughout the Northern Flinders Ranges (Fig. 1b), is here explained by a single, but prolonged event. However, the above shows that structural elements progressively changed their position and orientation within the growing anticline and could have become de- or reactivated at various points in time. The overall single folding event may therefore locally appear as a series of distinct events. This observation applies especially to the

phyllites north of Arkaroola Village that were affected by a complex interference of local small-scale faulting and folding.

The data of McLaren *et al*. (2002) show that exhumation took place over a *c.* 200 Myr period in Palaeozoic times. We have argued that this exhumation is not the result of passively exhuming a Delamerian fold, but represents the actual growth of the Yankaninna Anticline. It was suggested by Elburg *et al.* (2013) that the data of McLaren *et al*. (2002) may have been affected by igneous and hydrothermal heat pulses. Although potentially of local importance, we regard heat pulses of minor overall importance, based on the following argument. A conservative estimate for the heat production of rocks in the MPI is $5 \pm 1 \cdot 10^{-6}$ W/m^3 (Mildren & Sandiford 1995). With an area of 500 km² and a crustal section of 10 km the basement units would have produced a total of $1.5 \cdot 10^{23}$ J within 200 Myr. One intrusion such as the British Empire Granite at an estimated volume of 20 km³ would have contributed *c.* 0.01 % to the total heat budget if it cooled 500 °C after intrusion. Hydrothermal fluids could also have caused thermal pulses. However, cooling 30 km³ of hot fluids (Weisheit *et al*. 2013) by 300 °C would have contributed <0.05 % to the total heat budget. Furthermore, the data from various locations in the central and southern MPI show a strong consistency between the various mineral systems and their structural position in the Yankaninna Anticline (Fig. 7). We therefore infer that the data mostly record cooling by exhumation with only minor local effects of thermal pulses.

McLaren *et al.* (2002) proposed step-wise cooling and exhumation of the MPI at *c.* 430 Ma, *c.* 400 Ma and *c.* 325 Ma. In their model (their Fig. 7), folding was assumed to have taken place during the Delamerian Orogeny, after which all rocks experienced the same Palaeozoic cooling history as the fold was passively exhumed. This model is in contrast to our model, where we interpret the same data as reflecting different exhumation rates as a function of the structural position of the samples within the developing anticline. This allows us to constrain the development of the anticline at different points in time and average exhumation rates during the intervening periods (Fig. 9). Rates most probably varied, as proposed by McLaren *et al.* (2002). This is not contradictory to our model. The only difference is that we interpret their exhumation rates as reflecting growth of the Yankaninna fold itself, rather than its passive exhumation.

Low temperature thermochronology data (Mitchell *et al.* 2002; this study) cannot be explained by cooling resulting from exhumation as these postdate the time that the presently outcropping rocks reached the near-surface. Evidence for this are the diamictite dykes and the near-surface Mt. Gee Sinter deposit that was active from at least *c.* 290 Ma (Brugger *et al.* 2011). Burial under Mesozoic Eromanga Basin sediments cannot explain the various Permian to Jurassic apatite, zircon and titanite FT ages. Only the *c.* 100 Ma apatite (U-Th)/He ages could be the result of burial under at least 1 km of Eromanga Basin sediments and their subsequent exhumation in Cretaceous-Tertiary times (Fig. 8).

Other low-temperature thermochronology data can only be explained with resetting by hydrothermal fluids of the Mt. Gee system. The low closure temperatures are easily reset by hydrothermal and ore-forming fluids (Bojar *et al*. 1998; Arnaud & Eide 2000; Balogh & Dunkl 2005; Dempster & Persano 2006, Kelley *et al.* 2006; Marton *et al.* 2010). A *c.* 210 Ma titanite fission track age indicates that these hydrothermal fluids must have reached temperatures above *c.* 265 °*C.* The sample comes from a 440 Ma diopside-titanite vein in the centre of the MPI (Bakker & Elburg 2006), which was overprinted by Mt. Gee Sinter deposits (Fig. 3a). Our low-temperature thermochronology data of hydrothermally overprinted samples are all older than *c.* 190 Ma (except apatite (U-Th)/He), indicating that hydrothermal activity decreased after this time (Fig. 8). However, the active Paralana Hot Springs indicate that hydrothermal activity may have lasted from the Permian Period until today (Brugger *et al*. 2005).

Most of the exhumation of the MPI occurred during mid-Palaeozoic times at a time of major metamorphic, magmatic and deformation activities in the Harts Ranges in central Australia (450-300 Ma Alice Springs Orogeny; Buick *et al.* 2008) and subduction and terrane amalgamation in the Lachlan Fold Belt in SE-Australia (450-370 Ma; Chappell *et al*. 1988; Turner *et al*. 1996; Soesoo *et al.* 1997; Gray & Foster 2004; Fig. 2). The *c.* 500 Ma Delamerian Orogeny that is recorded in the south of the Adelaide Fold Belt in the Mount Lofty and southern Flinders Ranges (Foden *et al.* 2006) only played a minor role in the crustal-scale deformation in the MPI, contrary to previous interpretations that interpreted only the refolding of the mainly Delamerian structure as a far-field effect of the Alice Springs Orogeny (e.g. Paul *et al.* 1999; McLaren *et al.* 2002; Armit *et al.* 2012). Instead, the

Yankaninna Anticline grew over a long period of time by south-directed ramping onto the Curnamona Province. The Yankaninna Anticline is, however, not an isolated structure, but is only one of many similar folds in the Northern Flinders Ranges. This implies that the whole region experienced a long period of north-south shortening of the previous Adelaidean Basin between the rigid Gawler and Curnamona Provinces. It remains to be investigated what the implications of this newly recognised regional intra-continental Palaeozoic deformation are for the tectonic evolution of central and southern Australia and how the folding and concomitant erosion relate to Palaeozoic sedimentary basins (e.g. Gravestock 1995).

Conclusions

The Mt. Painter Inlier forms the core of the Yankaninna Anticline, which is part of the Northern Adelaide Fold and Thrust Belt. Our mapping and structural analysis allowed construction of the present-day fold shape and reconstruction of the system before folding. The Mesoproterozoic basement is truncated by the *c.* 800 Ma Adelaidean unconformity. The angle between the unconformity and the main foliation in the basement was found to be about ten degrees. Initial Adelaidean succession deposition occurred in *c.* 310°-striking grabens, followed by widespread deposition. The NE-SW to north-south trending Paralana Fault System became active during Adelaidean succession deposition. At the end of deposition, by *c.* 500 Ma, the Adelaidean unconformity was buried *c.* 11.5 km west of the Parallana Fault *s.s.*, and 1-2 km deeper in the early Adelaidean grabens.

Folding commenced with the *c.* 500 Ma Delamerian Orogeny at the earliest, but possibly as late as *c.* 450 Ma. In the study area, south-directed ramping up the Curnamona Province along the Paralana Fault System resulted in the formation of the Yankaninna Anticline in which the core rose by *c.* 15 km. This folding passively rotated all previous structural elements, including the early Adelaidean grabens, which are now found exposed at nearly right angles to each other on the NW and SE limb of the fold.

Folding in the Northern Flinders Ranges has traditionally been interpreted as Delamerian in age, with subsequent Palaeozoic exhumation of the folds. We show that very limited folding occurred during the Delamerian Orogeny. Instead, the Yankaninna Anticline grew over a prolonged period of *c.* 200 Myr up to the Permian Period. Younger low-temperature thermochronological data indicate a major near-surface hydrothermal event (Mt. Gee event) that lasted at least until *c.* 180 Ma.

We kindly thank the Sprigg family for access to their land and continuing support during the field trips. Steve Hore and Wolfgang Preiss are thanked for their inspiring discussions and cooperation during our projects. Johannes Holzäpfel, Christian Kieslinger, Christian Kling, Simon Kocher, Jürgen Lang, Matthias Lindhuber, Jens Müller, Tobias Rehder and Jens Roessiger contributed to the fieldwork. Klaus Warber is thanked for the 3D modelling. This project was funded by Marathon Ltd. and the German Science Foundation (DFG, grant BO-1776/8-1). We are grateful to Eva Enkelmann, who carried out the low-temperature analyses and interpretations in Tübingen. We thank Wolfgang Preiss and an anonymous reviewer for their helpful comments.

References cited

Armit, R. J., Betts, P. G., Schaefer, B. F. & Ailleres, L. 2012. Constraints on long-lived Mesoproterozoic and Palaeozoic deformational events and crustal architecture in the northern Mt. Painter Province, Australia. *Gondwana Research*, **22**, 207-226.

Arnaud, N. O. & Eide, E. 2000. Brecciation-related argon redistribution in alkali feldspars; an in naturo crushing study. *Geochimica et Cosmochimica Acta*, **64**, 3201-3215.

Bakker, R. J. & Elburg, M. A. 2006. A magmatic-hydrothermal transition in Arkaroola (Northern Flinders Ranges, South Australia): from diopside-titanite pegmatites to hematite-quartz growth. *Contributions to Mineralogy and Petrology,* **152**, 541-569.

Balogh, K. & Dunkl, I. 2005. Argon and fission track dating of Alpine metamorphism and basement exhumation in the Sopron Mts. (Eastern Alps, Hungary); thermochronology or mineral growth? *Mineralogy and Petrology*. **83**, 191-218.

Bojar, A.-V., Neubauer, F. & Fritz, H. 1998. Cretaceous to Cenozoic thermal evolution of the southwestern South Carpathians; evidence from fission-track thermochronology. *Tectonophysics*, **297**, 229-249.

Bons, P. D., Montenari, M., Bakker, R. J. & Elburg, M. 2007. Potential evidence of fossilised Neoproterozoic deep life: SEM observations on calcite veins from Oppaminda Creek, Arkaroola, South Australia. *International Journal of Earth Sciences*, **98**, 327-343.

Buick, I. S., Storkey, A. & Williams, I. S. 2008. Timing relationships between pegmatite emplacement, metamorphism and deformation during the intra-plate Alice Springs Orogeny, central Australia. *Journal of Metamorphic Geology*, **26**, 915-936.

Burg, J.-P., Davy, P., Nievergelt, P., Oberli, F., Seward, D., Diao Z. & Meier, M. 1997. Exhumation during crustal folding in the Namche-Barwa syntaxis. *Terra Nova*, **9**, 53-56.

Brugger, J., Long, N., McPhail, D. C. & Plimer, I. 2005. An active amagmatic hydrothermal system: The Paralana hot springs, Northern Flinders Ranges, South Australia. *Chemical Geology*, **222**, 35-64.

Brugger, J., Wülser, P. A. & Foden, J. 2011. Genesis and preservation of a uranium-rich Paleozoic epithermal system with a surface expression (Northern Flinders Ranges, South Australia): Radiogenic heat driving regional hydrothermal circulation over geological timescales. *Astrobiology*, **11**, 499-508.

Célérier, J., Sandiford, M., Lundbek Hansen, D. & Quigley, M. 2005. Modes of active intraplate deformation, Flinders Ranges, Australia. *Tectonics,* **24**.

Chappell, B. W., White, A. J. R. & Hine, R. 1988. Granite provinces and basement terranes in the Lachlan Fold Belt, southeastern Australia. *Australian Journal of Earth Sciences*, **35**, 505-521.

Chen, J., Burbank, D. W., Scharer, K. M., Sobel, E., Yin, J., Rubin, C. & Zhao, R., 2002. Magnetochronology of the Upper Cenozoic strata in the Southwestern Chinese Tian Shan: rates of Pleistocene folding and thrusting. *Earth and Planetary Science Letters*, **195**, 113-130.

Coats, R. P. & Blisset, A. H. 1971. Regional and economic geology of the Mount Painter Province. Geological Survey of South Australia, *Bulletin,* **43**, pp. 425.

Cowley, W. M., Hore, S. B., Preiss, W. V., Sheard, M. J. & Wade C. 2012. A revised stratigraphic scheme for the Mount Painter and Mount Babbage Inliers. *SAREIC 2012 Technical forum poster*. World Wide Web Address: http://minerals.dmitre.sa.gov.au/press_and_events/events/sareic_2012_technical_forum

Coyle, D. A. & Wagner, G. A. 1998. Positioning the titanite fission-track partial annealing zone. *Chemical Geology*, **149**, 117–125.

Dempster, T. J. & Persano, C. 2006. Low-temperature thermochronology; resolving geotherm shapes or denudation histories? *Geology*, **34**, 73-76.

Dipple, G., Bons, P. D. & Oliver, N. H. S. 2005. A vector of high-temperature paleo-fluid flow deduced from mass transfer across permeability barriers (quartz veins). *Geofluids*, **5**, 67–82.

Drexel, J. F. & Major, R. B. 1987. Geology of the uraniferous breccia near Mt Painter, South Australia and revision of rock nomenclature. Geological Survey of South Australia. *Quarterly Notes*, **104**, 14-24.

Dunkl, I. 2002. TRACKKEY: a Windows program for calculation and graphical presentation of fission track data. *Computer Geosciences*, **28**, 3–12.

Elburg, M. A., Bons, P. D., Dougherty-Page, J., Janka, C. E., Neumann, N. & Schaefer, B. 2001. Age and metasomatic alteration of the Mt Neill Granite at Nooldoonooldoona Waterhole, Mt Painter Inlier, South Australia. *Australian Journal of Earth Sciences*, **48**, 721-730.

Elburg, M. A., Bons, P. D., Foden, J. & Brugger, J. 2003. A newly defined Late Ordovician magmatic-thermal event in the Mt Painter Province, Northern Flinders Ranges, South Australia. *Australian Journal of Earth Sciences*, **50**, 611-631.

Elburg, M. A., Andersen, T., Bons, P. D., Weisheit, A., Simonsen, S. L. & Smet, I., 2012. Metasomatism and metallogeny of A-type granites of the Mt Painter - Mt Babbage Inliers, South Australia. *Lithos*, **151**, 83-104.

Elburg, M. A., Andersen, T., Bons, P. D., Simonsen, S. L. & Weisheit, A. 2013. New constraints on Phanerozoic magmatic and hydrothermal events in the Mt Painter Province, South Australia. *Gondwana Research*, doi: 10.1016/j.gr.2012.12.017.

England, P. & Molnar, P. 1990. Surface uplift, uplift of rocks, and exhumation of rocks. *Geology*, **18**, 1173–1177.

Evans, N. J., Byrne, J. P., Keegan J. T. & Dotter L. E. 2005. Determination of uranium and thorium in zircon, apatite, and fluorite: Application to laser (U-Th)/He thermochronology. *Journal of Analytical Chemistry*, **60**, 1159–1165.

Eyles, N., Mory, A. J. & Backhouse, J. 2002. Carboniferous-Permian palynostratigraphy of West Australian marine rift basins; resolving tectonic and eustatic controls during Gondwanan glaciations. *Palaeogeography Palaeoclimatology Palaeoecology*, **184**, 305-319.

Fanning, C. M., Teale, G. S. & Robertson, R. S. 2003. Is there a Willyama Supergroup sequence in the Mount Painter Inlier? *In*: Peljo, M. (compiler) *Broken Hill Exploration Initiative: Abstracts from the July 2003 conference*. Geoscience Australia Record **2003/13**, 38-41.

Farley, K. A., Wolf, R. A. & Silver, L. T., 1996. The effects of long alpha-stopping distances on (U-Th)/He dates. *Geochimica et Cosmochimica Acta*, **60**, 4223-4230.

Farley, K. A. 2002. (U-Th)/He dating: Techniques, calibrations, and applications. *Reviews in Mineralogy and Geochemistry,* **47**, 819-843.

Filip, J., Ulrych, J., Asamovic, J. & Balogh, K. 2007. Apatite fission track implications for timing of hydrothermal fluid flow in Tertiary volcanics of the Bohemian Massif. *Journal of Geosciences*, **52**, 211-220.

Flöttmann, T., James, P., Rogers, J. & Johnson, T. 1994. Early Paleozoic foreland thrusting and basin reactivation at the palaeo-Pacific margin of the Southeastern Australian Precambrian Craton - a reappraisal of the structural evolution of the Southern Adelaide Fold-Thrust Belt. *Tectonophysics*, **234**, 95-116.

Flöttmann, T. & James, P., 1997. Influence of basin architecture on the style of inversion and fold-thrust belt tectonics - the southern Adelaide Fold-Thrust Belt, South Australia. *Journal of Structural Geology*, **19**, 1093-1110.

Flowers, R. M., Ketcham, R. A., Shuster, D. L. & Farley, K. A. 2009. Apatite (U-Th)/He thermochronometry using a radiation damage accumulation and annealing model. *Geochimica et Cosmochimica Acta*, **73**, 2347-2365.

Foden, J., Elburg, M. A., Dougherty-Page, J. & Burtt, A. 2006. The timing and duration of the Delamerian Orogeny: Correlation with the Ross Orogen and implications for Gondwana assembly. *Journal of Geology*, **114**, 189-210.

Fraser, G. L. & Neumann, N. L. 2010. New SHRIMP U-Pb zircon ages from the Gawler Craton and Curnamona Province, South Australia, 2008-2010. *Geoscience Australia Record*, **2010/16**.

Fügenschuh, B., Seward, D. & Mancktelow, N. 1997. Exhumation in a convergent orogen; the western Tauern Window. *Terra Nova*, **9**, 213-217.

Galbraith, R. F. & Laslett, G. M. 1993. Statistical-Models for Mixed Fission-Track Ages. *Nuclear Tracks and Radiation Measurements*, **21**, 459-470.

Gleadow, A. J. W. & Lovering, J. F. 1974. The effect of weathering on FT dating. *Earth and Planetary Sciences Letters*, **22**, 163–168.

Gleadow, A. J. W. 1981. Fission track dating methods: what are the real alternatives? *Nuclear Tracks and Radiation Measurements*, **5**, 3–14.

Gower, C. F., Kamo, S. L., Kwok, K. & Krogh, T. E. 2008, Proterozoic southward accretion and Grenvillian orogenesis in the interior Grenville Province in eastern Labrador; evidence from U/Pb geochronological investigations. *Precambrian Research*, **165**, 61-95.

Gravestock, D. I. 1995. Western Warburton basin. In: Drexel J. F. & Preiss W. V. (eds) *The geology of South Australia, Vol. 2, The Phanerozoic.* South Australia Geological Survey, Bulletin **54,** 41-43.

Gray, D. R. & Foster, D. A. 2004. Tectonic evolution of the Lachlan Orogen, southeast Australia: historical review, data synthesis and modern perspectives. *Australian Journal of Earth Sciences*, **51**, 773-817.

Green, P. F., Duddy, I. R., Gleadow, A. J. W., Tingate, P. T. & Laslett, G. M. 1986. Thermal annealing of fission tracks in apatite: 1. A qualitative description. *Chemical Geology: Isotopic Geoscience section*, **59**, 237–253, doi: 10.1016/0168-9622(86)90074-6.

Hames, W. E. & Bowring, S. A. 1994. An empirical evaluation of the argon diffusion geometry in muscovite. *Earth and Planetary Science Letters*, **124**, 161-169.

Harrison, T. M. 1981. Diffusion of 40Ar in hornblende. *Contributions to Mineralogy and Petrology*, **78**, 324-331.

Harrison, T. M., Duncan, I. & McDougall, I. 1985. Diffusion of 40Ar in biotite: Temperature, pressure and compositional effects. *Geochimica et Cosmochimica Acta*, **49**, 2461-2468.

Hildebrand, R. S., Hoffman, P. F., &Bowring, S.A. 2010. The Calderian Orogeny in Wopmay Orogen (1.9 Ga), northwestern Canadian Shield. *Geological Society of America Bulletin*, **122**, 794-814.

Holdsworth, R. E. & Pinheiro, R. V. L. 2002. The anatomy of shallow-crustal transpressional structures; insights from the Archaean Carajas fault zone, Amazon, Brazil. *Journal of Structural Geology*, **22**, 1105-1123.

Hurford, A. J. & Green, P. F. 1983. The zeta age calibration of fission-track dating. *Chemical Geology*, **41**, 285–312.

Hurford, A. J. 1998. ZETA: the ultimate solution to fission-track analysis calibration or just an interim measure. *In*: Van den Haute, P & de Corte, F. (eds) *Advances in fission-track geochronology*. Kluwer Academic, Dordrecht, 19–32.

Jones, A. T. & Fielding, C. R. 2004. Sedimentological record of the late Paleozoic glaciation in Queensland, Australia. *Geology*, **32**, 153-156.

Kelley, D. L., Kelley, K. D., Coker, W. B., Caughlin, B. & Doherty, M. E. 2006. Beyond the obvious limits of ore deposits; the use of mineralogical, geochemical, and biological features for the remote detection of mineralization. *Economic Geology and the Bulletin of the Society of Economic Geologists*, **101**, 729-752.

Kohn, B. P., Gleadow, A. J. W., Brown, R. W., Gallagher, K., O'Sullivan, P. B. & Foster, D. A. 2002. Shaping the Australian crust over the last 300 million years: insights from fission track thermotectonic imaging and denudation studies of key terranes. *Australian Journal of Earth Sciences*, **49**, 697-717.

Konopasek, J., Schulmann, K. & Lexa, O. 2001. Structural evolution of the central part of the Krusne hory (Erzgebirge) Mountains in the Czech Republic; evidence for changing stress regime during Variscan compression. *Journal of Structural Geology*, **23**, 1373-1392.

Korsch, R. J., Preiss, W. V., Blewett, R. S., Fabris, A. J., Neumann, N. L., Fricke, C. E., Fraser, G. L., Holzschuh, J., Milligan, P. R. & Jones, L. E. A. 2010. Geological interpretation of deep seismic reflection and magnetotelluric line 08GA-C1: Curnamona Province, South Australia. *In*: Korsch, R. J. & Kositcin, N. (eds) *South Australian Seismic and MT Workshop, Extended Abstracts*. Geoscience Australia Record, **2010/10**, 42-53.

Krieg, G., Alexander, E. M., Rogers, P. A. 1995. Eromanga Basin, *In*: Drexel J. F. & Preiss W. V. (eds) *The geology of South Australia, vol. 2, The Phanerozoic. South Australia.* Geological Survey, Bulletin **54**, 101-105.

Llana-Funez, S. & Marcos, A. 2007. Convergence in a thermally softened thick crust; Variscan intracontinental tectonics in Iberian Plate rocks. *Terra Nova* **19**, 393-400.

Lovera, O. M., Richter, F. M., Harrison, T. M. 1989. The 40Ar/39Ar thermochronometry for slowly cooled samples having a distribution of diffusion domain sizes. *Journal of Geophysical Research*, **94**, 17, 917-17,935.

Maheo, G., Pecher, A., Guillot, S., Rolland, Y. & Delacourt, C. 2004. Exhumation of Neogene gneiss domes between oblique crustal boundaries in south Karakorum, northwest Himalaya, Pakistan. *Geological Society of America Special Paper*, **380**, 141-154.

Marton, I., Moritz, R. & Spikings, R. 2010. Application of low temperature thermochronology to hydrothermal ore deposits; formation, preservation and exhumation of epithermal gold systems from the eastern Rhodopes, Bulgaria. *Tectonophysics*, **483**, 240-254.

McLaren, S. N., Dunlap, W. J., Sandiford, M. & McDougalln, I. 2002. Thermochronology of high heat-producing crust at Mount Painter, South Australia: Implications for tectonic reactivation of continental interiors. *Tectonics*, **21**, doi: 10.1029/2000TC001275.

McLaren, S., Sandiford, M., Powell, R., Neumann, N. & Woodhead, J. 2006. Palaeozoic intraplate crustal anatexis in the Mount Painter Province, South Australia; timing, thermal budgets and the role of crustal heat production. *Journal of Petrology*, **47**, 2281-2302.

Meesters, A. G. C. A. & Dunai, T. J. 2002a. Solving the production-diffusion equation for finite diffusion domains of various shapes - Part II. Application to cases with alpha-ejection and nonhomogeneous distribution of the source. *Chemical Geology*, **186**, 57-73.

Meesters, A. G. C. A. & Dunai, T. J. 2002b. Solving the production-diffusion equation for finite diffusion domains of various shapes - Part 1. Implications for low-temperature (U-Th)/He thermochronology. *Chemical Geology*, **186**, 333-344.

Mildren, S. D. & Sandiford, M. 1995. Heat refraction and low-pressure metamorphism in the Northern Flinders Ranges, South Australia. *Australian Journal of Earth Sciences*, **42**, 241-247.

Mitchell, M. M., Kohn, B. P., O'Sullivan, P. B., Hartley, M. J. & Foster, D. A. 2002. Low-temperature thermochronology of the Mt Painter Province, South Australia. *Australian Journal of Earth Sciences*, **49**, 551-563.

Mukhopadhyay, S. & Sharma, J. 2010. Crustal scale detachment in the Himalayas; a reappraisal. *Geophysical Journal International*, **183**, 850-860.

Neumann, N. 2001. *Geochemical and isotopic characteristics of South Australian Proterozoic granites: implications for the origin and evolution of high heat-producing terrains*. PhD thesis. Department of Geology and Geophysics. University of Adelaide., Adelaide.

Passchier, C. W., Trouw, R. A. J., Ribeiro, A. & Paciullo, F. V. P. 2002. Tectonic evolution of the southern Kaoko Belt, Namibia. *Journal of African Earth Sciences*, **35**, 61-75.

Paul, E. 1998. *Geometry and controls on basement-involved deformation in the Adelaide Fold Belt, South Australia*. PhD thesis. Department of Geology and Geophysics. University of Adelaide, Adelaide.

Paul, E., Flöttmann, T. & Sandiford, M., 1999. Structural geometry and controls on basement-involved deformation in the northern Flinders Ranges, Adelaide Fold Belt, South Australia. *Australian Journal of Earth Sciences*, **46**, 343-354.

Preiss, W. V. 1987. The Adelaide Geosyncline — Late Proterozoic stratigraphy, sedimentation, paleontology, and tectonics. *South Australian Geological Survey Bulletin* **53**, pp. 438.

Preiss, W.V. 2000. The Adelaide Geosyncline of South Australia and its significance in Neoproterozoic continental reconstruction. *Precambrian Research*, **100**, 21-63.

Reiners, P. W. & Farley, K. A. 1999. Helium diffusion and (U-Th)/He thermochronometry of titanite. *Geochimica et Cosmochimica Acta*, **63**, 3845–3859.

Reiners, P. W., Spell T. L., Nicolescu S. & Zanetti K. A. 2004. Zircon (U-Th)/He thermochronometry: He diffusion and comparisons with 40Ar/39Ar dating. *Geochimica et Cosmochimica Acta*, **68**, 1857–1887.

Reiners, P. W. 2005. Zircon (U-Th)/He thermochronometry. *Reviews in Mineralogy and Geochemistry*, **58**, 151–176.

Rutherford, L., Hand, M. & Barovich, K. 2007. Timing of Proterozoic metamorphism in the southern Curnamona Province: implications for tectonic models and continental reconstructions. *Australian Journal of Earth Sciences*, **54**, 65-81.

Sandiford, M., Hand, M. & McLaren, S. 1998. High geothermal gradient metamorphism during thermal subsidence. *Earth and Planetary Science Letters*, **163**, 149-165.

Schellart, W. P. 2002. Alpine deformation at the western termination of the Axial Zone, southern Pyrenees. *Journal of the Virtual Explorer*, **8**, 35-55.

Schuster, D. L., Flowers, R. M. & Farley, K. A. 2006. The influence of natural radiation damage on helium diffusion kinetics in apatite. *Earth and Planetary Science Letters*, **249**, 148–161, doi:10.1016/j.epsl.2006.07.028.

Sheard, M. & Cockshell, C. D. 1992. Seismic interpretation of Mt. Hopeless Line 1. Department of Energy and Science SA Report book **92/17**, pp. 176.

Shuster, D. L., Vasconcelos, P. M., Heim, J. A. & Farley, K. A. 2005. Weathering geochronology by (U-Th)/He dating of goethite. *Geochimica et Cosmochimica Acta*, **69**, 659-673.

Siebel, W., Danišík, M. & Chen, F. 2009. From emplacement to unroofing: thermal history of the Jiazishan gabbro, Sulu UHP terrane, China. *Mineralogy and Petrology*, **96**, 163-175.

Soesoo, A., Bons, P. D., Gray, D. R. & Foster, D. A. 1997. Divergent double subduction: tectonic and petrologic consequences. *Geology,* **25**, 55-758.

Spaggiari, C. V. 2007. The Jack Hills greenstone belt, Western Australia; Part 1, Structural and tectonic evolution over >1.5 Ga. *Precambrian Research*, **155**, 204-228.

Stewart, K. & Foden, J. 2003. Mesoproterozoic granites of South Australia. Department of Primary Industries and Resources, Report Book **2003/15**, pp. 142.

Suppe J., Chou, G. T. & Hook, S. C. 1992. Rates of folding and faulting determined from growth strata. Thrust tectonics. *Chapman & Hall London, United Kingdom*, 105-121.

Teale G. S. 1993. Mount Painter and Mount Babbage Inliers. *In*: Drexel J. F., Preiss W. V. & Parker A. J. (eds) *The Geology of South Australia, Vol. 1 The Precambrian*. Geological Survey of South Australia Bulletin **54**, 93–100.

Timar-Geng, Z., Fügenschuh, B., Schaltegger, U. & Wetzel, A. 2004. The impact of the Jurassic hydrothermal activity on zircon fission track data from the southern Upper Rhine Graben area. *Schweizerische Mineralogische und Petrographische Mitteilungen*, **84**, 257-269.

Turner, S. P., Kelley, S. P., VandenBerg, A. H. M., Foden, J. D., Sandiford, M. & Flöttmann, T. 1996. Source of the Lachlan Fold Belt flysch linked to convective removal of the lithospheric mantle and rapid exhumation of the Delamerian-Ross Fold Belt. *Geology*, **24**, 941-944.

Veevers, J. J. 2006. Updated Gondwana (Permian-Cretaceous) Earth history of Australia. *Gondwana Research*, **9**, 231-260.

Wagner, G. A. & Van den haute, P. 1992. Fission-track dating. Enke Verlag, Stuttgart, pp. 285.

Weisheit, A., Bons, P. D. & Elburg, M. A. 2013. Long-lived crustal fluid-flow: the hydrothermal mega-breccia of Hidden Valley, Mt. Painter Inlier, South Australia. *International Journal of Earth Sciences*, doi: 10.1007/s00531-013-0875-7.

Wingate, M. T. D., Campbell, I. H., Compston, W. & Gibson, G. M. 1998. Ion microprobe U–Pb ages for Neoproterozoic basaltic magmatism in south-central Australia and implications for the breakup of Rodinia. *Precambrian Research*, **87**, 135–159.

Wülser, P. A. 2009. *Uranium metallogeny in North Flinders Ranges region of South Australia*. PhD thesis. Adelaide, Adelaide University.

Zeitler, P. K., Herczeg, A. L., Mcdougall, I. & Honda, M. 1987. U-Th-He Dating of Apatite - a Potential Thermochronometer. *Geochimica et Cosmochimica Acta*, **51**, 2865-2868.

Ziv, A., Katzir, Y., Avigad, D. & Garfunkel, Z. 2010. Strain development and kinematic significance of the Alpine folding on Andros (western Cyclades, Greece). *Tectonophysics*, **488**, 248-255.

Figure captions

Fig.1: Location and geological map of the Northern Flinders Ranges and the Mt. Painter Inlier (MPI; after Coats & Blissett, 1971 and Paul *et al.* 1999). (a) The Neoproterozoic Adelaide Rift Complex that is later deformed into the Adelaide Fold and Thrust Belt formed between the Archean Gawler Craton and the Palaeoproterozoic Curnamona Province. (b) The Northern Flinders Ranges are characterised by an arcuate pattern of 10 km-scale folds that formed between the dextral Norwest Fault and the sinistral Paralana Fault System. The MPI is exposed in the core of the NE-SW trending Yankaninna Anticline. (c) Most of the MPI is formed by multiply deformed Mesoproterozoic basement, intruded by Palaeozoic magmatic intrusions (British Empire Granite) and overprinted by breccia zones. Locations of hydrothermal diopside-titanite veins and younger, Permian Mt. Gee quartz sinter occurrences are shown.

Fig. 2: Summary of the geological and structural evolution of the Mt. Painter Province, based on published geochronological studies and low-temperature thermochronology of this study (bold circles). Differential exhumation of the basement between 500-300 Ma resulted in the formation of a crustal-scale anticline. The regional exhumation signal of the cooling ages is overprinted by local hydrothermal alteration. Australian regional events are shown for comparison. See text for description of the structural elements. Mineral abbreviations after Kretz 1983. MPI: Mount Painter Inlier; BEG: British Empire Granite. 1. Fanning *et al*. (2003); 2. Wülser (2009); 3. Fraser & Neumann (2010); 4. Neumann (2001); 5. Elburg *et al.* (2001); 6. Steward & Foden (2003); 7. Elburg *et al.* (2012); 8. Sheard & Cockshell (1992); 9. McLaren *et al.* (2006); 10. Rutherford *et al.* (2007); 11. Paul *et al.* (1999); 12. Armit *et al.* (2012); 13. Wingate *et al.* (1998); 14. Preiss (2000); 15. Elburg *et al.* (2003); 16. Elburg *et al.* (2013); 17. Weisheit *et al.* (2013); 18. Wülser *et al.* (2011); 19. Foden *et al*. (2006); 20. McLaren *et al.* (2002); 21. this study; 22. Brugger *et al.* (2011); 23. Mitchell *et al.* (2002); 24. Gray & Forster (2004); 25. Buick *et al.* (2008).

Fig. 3: (a) Pegmatitic diopside (Di) and titanite (Ttn) veins (south of Mt. Painter) are overprinted by hydrothermal quartz-hematite Mt. Gee Sinter and platy calcite that grew in open voids. (b) Typical hematite-quartz crusts of Mt. Gee Sinter that can be found in veins and breccia zones throughout the southern MPI. (c) A diamictite dyke is cut by a Mt. Gee Sinter vein, indicating that the Mt. Gee event postdated the diamictite dyke. (d) The contact between the sheared basement gneisses and the Adelaidean cover sediments has a low angle at the unconformity. (e) Microphotograph of a biotite schist NW of the Pinnacles. Biotite (Bt) and quartz (Qtz) form the main foliation S_m which is a crenulation cleavage that post-dates an older foliation S_{m-1}. (f) The main Mesoroterozoic deformation formed tight to isoclinal folds with the main foliation (S_m) parallel to the axial plane. The kink-folding of S_m formed during the Palaeozoic deformation. (g) Leucosomes and melanosomes of a migmatite at Paralana Hot Springs are sheared and folded in the solid stage during the formation of S_m. (h) Typical Palaeozoic kink-folds that developed mainly in mica-rich basement units. (i) Microphotograph of a phyllite in the Mt. Oliphant Graben System east of the Pinnacles. The main Palaeozoic biotite-quartz (Bt, Qtz) foliation in the phyllite developed parallel to bedding. Crenulation of the main foliation occured after the growth of intertectonic ? andalusite (ex-And) porphyroblasts that are now completely altered, while feldspar (Kfs) porphyroblasts grew post-tectonically.

Fig. 4: (a) Stereoplots of poles (plus) to the main foliation S_m in selected areas (see map Fig.4 (b)) in the southern and central MPI and (c) poles to bedding (cross) in the overlying Adelaidean succession. The fold axis of the Palaeozoic Yankaninna Anticline (triangle) in the Adelaidean succession plunges gently to the WSW. S_m in the basement is folded with fold axes (triangle) that change in plunge direction from west at North Well Creek to SW in the northwestern Paralana area. Poles of crenulation cleavage planes are plotted with diamonds. (d) Unfolding of the basement's S_m (dot) shows that it made a small angle with the Adelaidean beds with a mean dip direction and dip (square) of 283/10 prior to the Palaeozoic folding.

Fig. 5: Structural block-diagram of the present-day MPI and 3D reconstruction of the unconformity surface with contour line of the unconformity´s current outcrop. (a) The MPI forms the core of the

thick-skinned Yankanina Anticline at the hanging wall of the steep Paralana Fault System. It exhumed from depths >15 km, while the cores of the adjacent synclines exhumed only about 2 km. (b) Three-dimenional model of the current Adelaidean unconformity surface, constructed with move™2010. The surface in the centre of the anticlinal core reaches a maximum height of *c.* 3 km above the present land surface. Well visible is the folded Mt. Oliphant Graben System between the Needles and the Pinnacles. (c) Schematic block-diagram of the Mt. Oliphant Graben System prior to Palaeozoic folding.

Fig. 6: Sample location of published analyses (McLaren *et al.* 2002; Mitchell *et al.* 2002) and of this study. The simplified map of the MPI shows the contour lines of maximum burial depth after deposition of the Adelaidean succession, as well as the location of the profile of Fig. 8.

Fig. 7: (a) Ar-Ar plateau ages from McLaren *et al*. (2002) as a function of maximum burial depth, showing that more deeply buried samples exhumed later than shallower ones. Exhumation rate during passage through the hornblende closing temperature is *c.* 0.2 km/Myr. (b) Same ages plotted at the depth at their closure temperature (at 40 °C/km and a surface temperature of 20 °C). Initial exhumation at 0.2 km/Myr appears to have commenced later than the 500 Ma Delamerian Orogeny. Dashed arrow shows the mean exhumation rate with full exhumation at *c.* 300 Ma. Periods of fast exhumation according to McLaren *et al*. (2002) are shown as grey bands in both graphs.

Fig. 8: Temperature (depth) vs. age diagram of published Ar-Ar data (McLaren *et al.*, 2002), apatite FT samples (Mitchell *et al.*, 2002) and new low-temperature thermochronology analyses. The depth is calculated assuming a geothermal gradient of 40 °C/km and 20 °C at the surface. The mean exhumation rate of the central and southern MPI is 0.1 km/Myr between <500 Ma and *c.* 300 Ma when the currently outcropping rocks reached the surface. Here they remained until the end of the Triassic Period (*c.* 200 Ma). Zircon, apatite and titanite (U-Th)/He ages are overprinted by the hydrothermal Mt. Gee Sinter event. A Mesozoic burial of 2 km may have affected the low -

temperature thermochronology samples. A goethite sample formed at the surface in early Miocene times.

Fig. 9: Profile along the hinge of the Yankaninna Anticline (line A-A'-A" in Fig. 6), showing the exhumation of the Adelaidean unconformity and Mt. Oliphant Graben System at different points in time: deepest burial at *c.* 500 Ma (purple), *c.* 440 Ma when the BEG intruded (red), *c.* 375 Ma and at *c.* 300 Ma, when the current outcropping surface had reached the surface. Profiles are based on plateau Ar-Ar ages of McLaren *et al.* (2002) on hornblende (red arrows), muscovite (green arrows) and biotite (blue arrows), assuming a geothermal gradient of 40 °C/km and a surface temperature of 20 °C. Sample numbers from McLaren *et al.* (2002).

Fig.1:

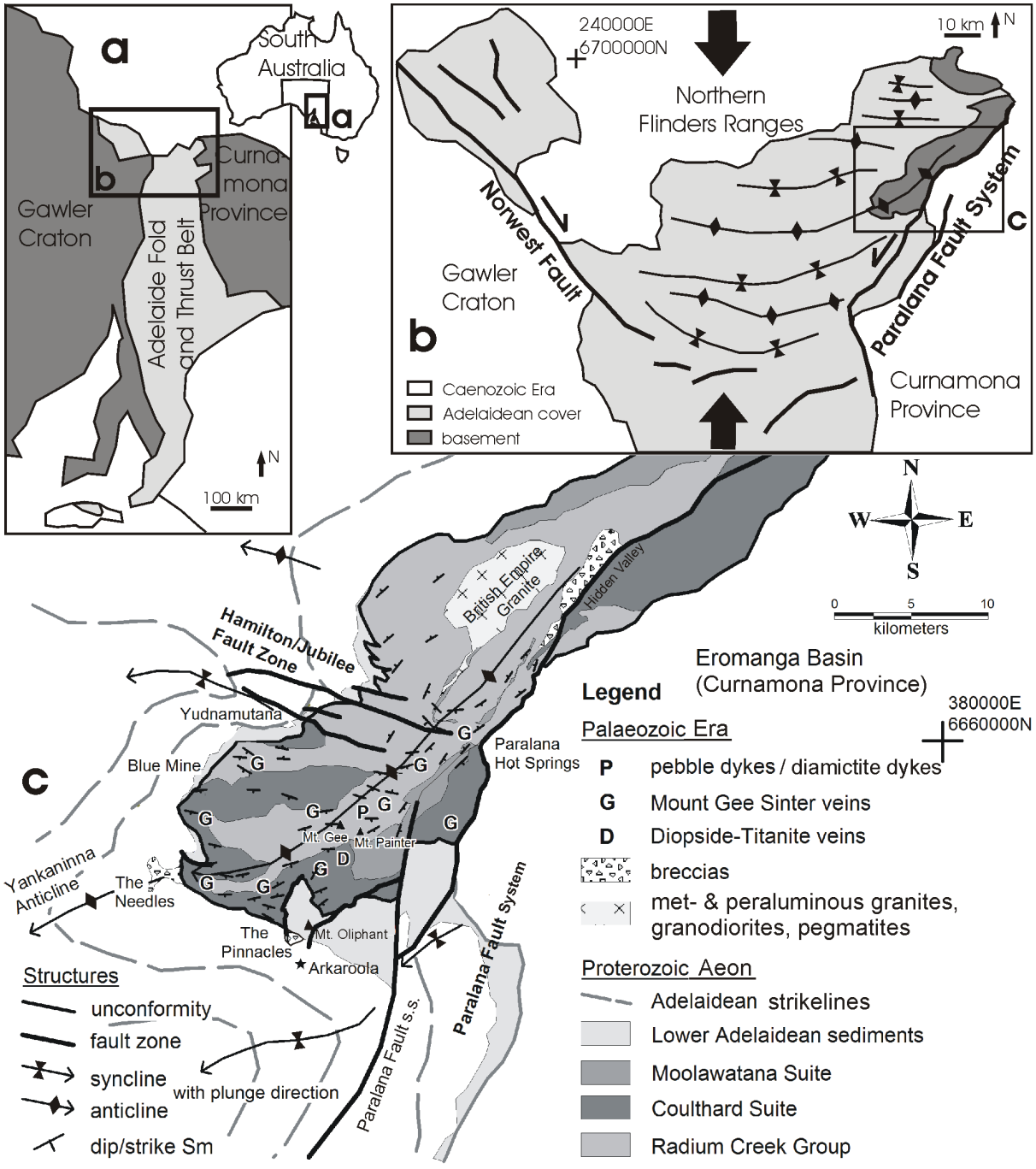

Fig.1: Location and geological map of the Northern Flinders Ranges and the Mt. Painter Inlier (MPI; after Coats & Blissett, 1971 and Paul *et al.* 1999). (a) The Neoproterozoic Adelaide Rift Complex that is later deformed into the Adelaide Fold and Thrust Belt formed between the Archean Gawler Craton and the Palaeoproterozoic Curnamona Province. (b) The Northern Flinders Ranges are characterised by an arcuate pattern of 10 km-scale folds that formed between the dextral Norwest Fault and the sinistral Paralana Fault System. The MPI is exposed in the core of the NE-SW trending Yankaninna Anticline. (c) Most of the MPI is formed by multiply deformed Mesoproterozoic basement, intruded by Palaeozoic magmatic intrusions (British Empire Granite) and overprinted by breccia zones. Locations of hydrothermal diopside-titanite veins and younger, Permian Mt. Gee quartz sinter occurrences are shown.

Fig.2:

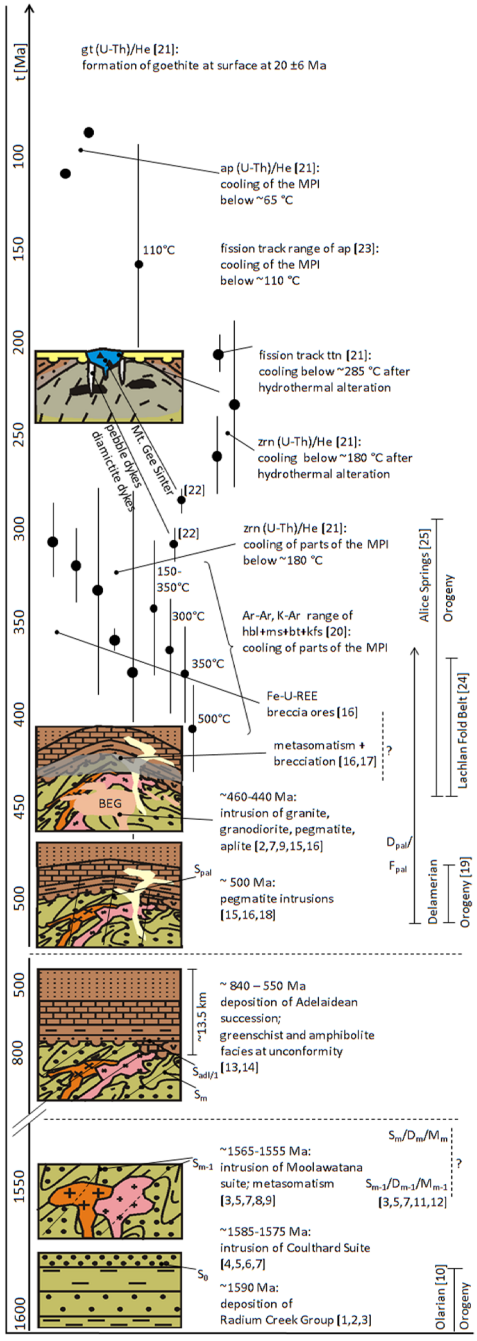

Fig. 2: Summary of the geological and structural evolution of the Mt. Painter Province, based on published geochronological studies and low-temperature thermochronology of this study (bold circles). Differential exhumation of the basement between 500-300 Ma resulted in the formation of a crustal-scale anticline. The regional exhumation signal of the cooling ages is overprinted by local hydrothermal alteration. Australian regional events are shown for comparison. See text for description of the structural elements. Mineral abbreviations after Kretz 1983. MPI: Mount Painter Inlier; BEG: British Empire Granite. 1. Fanning *et al.* (2003); 2. Wülser (2009); 3. Fraser & Neumann (2010); 4. Neumann (2001); 5. Elburg *et al.* (2001); 6. Steward & Foden (2003); 7. Elburg *et al.* (2012); 8. Sheard & Cockshell (1992); 9. McLaren *et al.* (2006); 10. Rutherford *et al.* (2007); 11. Paul *et al.* (1999); 12. Armit *et al.* (2012); 13. Wingate *et al.* (1998); 14. Preiss (2000); 15. Elburg *et al.* (2003); 16. Elburg *et al.* (2013); 17. Weisheit *et al.* (2013); 18. Wülser *et al.* (2011); 19. Foden *et al.* (2006); 20. McLaren *et al.* (2002); 21. this study; 22. Brugger *et al.* (2011); 23. Mitchell *et al.* (2002); 24. Gray & Forster (2004); 25. Buick *et al.* (2008).

Fig.3:

Fig. 3: (a) Pegmatitic diopside (Di) and titanite (Ttn) veins (south of Mt. Painter) are overprinted by hydrothermal quartz-hematite Mt. Gee Sinter and platy calcite that grew in open voids. (b) Typical hematite-quartz crusts of Mt. Gee Sinter that can be found in veins and breccia zones throughout the southern MPI. (c) A diamictite dyke is cut by a Mt. Gee Sinter vein, indicating that the Mt. Gee event postdated the diamictite dyke. (d) The contact between the sheared basement gneisses and the Adelaidean cover sediments has a low angle at the unconformity. (e) Microphotograph of a biotite schist NW of the Pinnacles. Biotite (Bt) and quartz (Qtz) form the main foliation S_m which is a crenulation cleavage that post-dates an older foliation S_{m-1}. (f) The main Mesoroterozoic deformation formed tight to isoclinal folds with the main foliation (S_m) parallel to the axial plane. The kink-folding of S_m formed during the Palaeozoic deformation. (g) Leucosomes and melanosomes of a migmatite at Paralana Hot Springs are sheared and folded in the solid stage during the formation of S_m. (h) Typical Palaeozoic kink-folds that developed mainly in mica-rich basement units. (i) Microphotograph of a phyllite in the Mt. Oliphant Graben System east of the Pinnacles. The main Palaeozoic biotite-quartz (Bt, Qtz) foliation in the phyllite developed parallel to bedding. Crenulation of the main foliation occured after the growth of intertectonic ? andalusite (ex-And) porphyroblasts that are now completely altered, while feldspar (Kfs) porphyroblasts grew post-tectonically.

Fig.4:

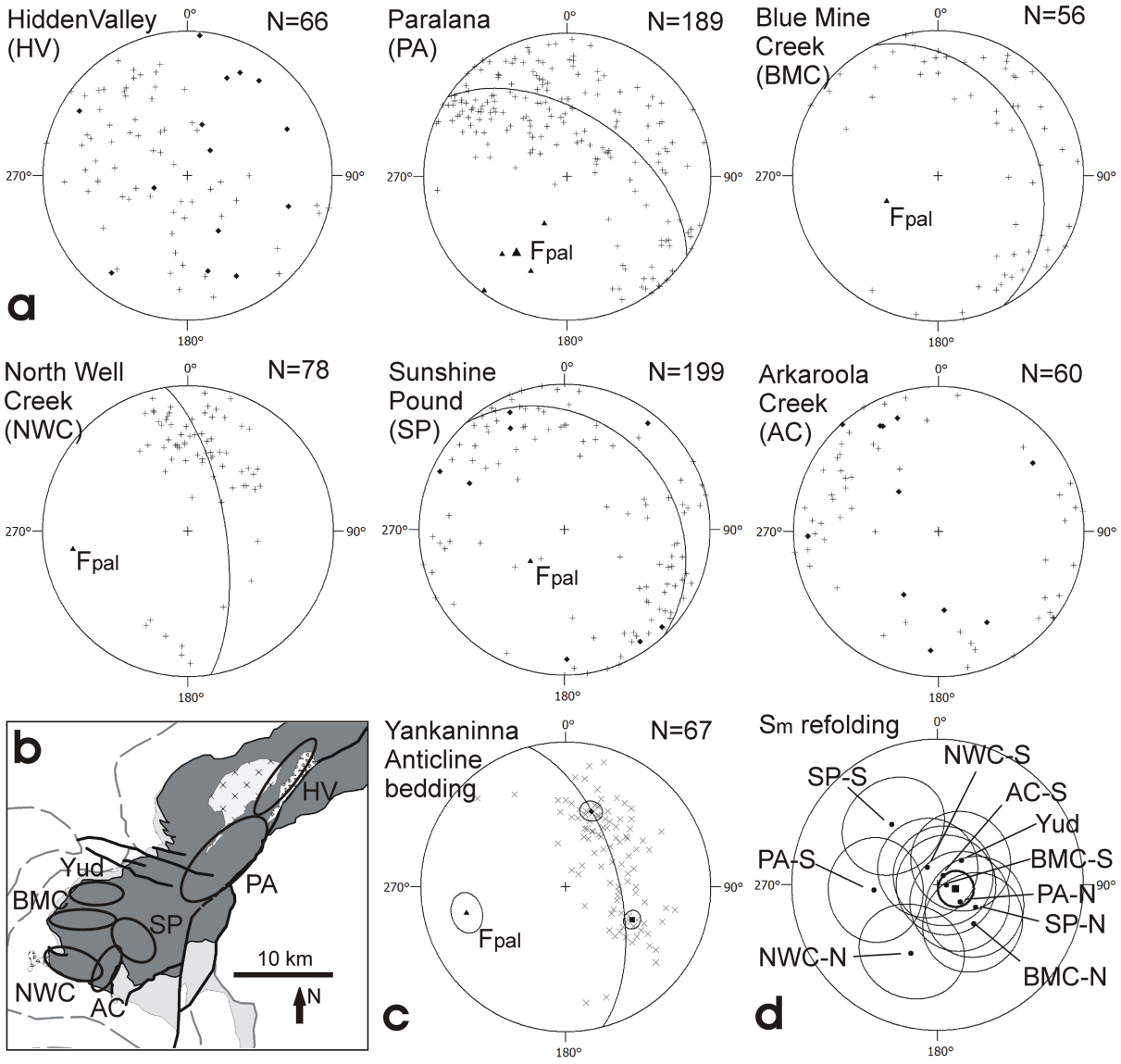

Fig. 4: (a) Stereoplots of poles (plus) to the main foliation S_m in selected areas (see map Fig.4 (b)) in the southern and central MPI and (c) poles to bedding (cross) in the overlying Adelaidean succession. The fold axis of the Palaeozoic Yankaninna Anticline (triangle) in the Adelaidean succession plunges gently to the WSW. S_m in the basement is folded with fold axes (triangle) that change in plunge direction from west at North Well Creek to SW in the northwestern Paralana area. Poles of crenulation cleavage planes are plotted with diamonds. (d) Unfolding of the basement's S_m (dot) shows that it made a small angle with the Adelaidean beds with a mean dip direction and dip (square) of 283/10 prior to the Palaeozoic folding.

Fig.5:

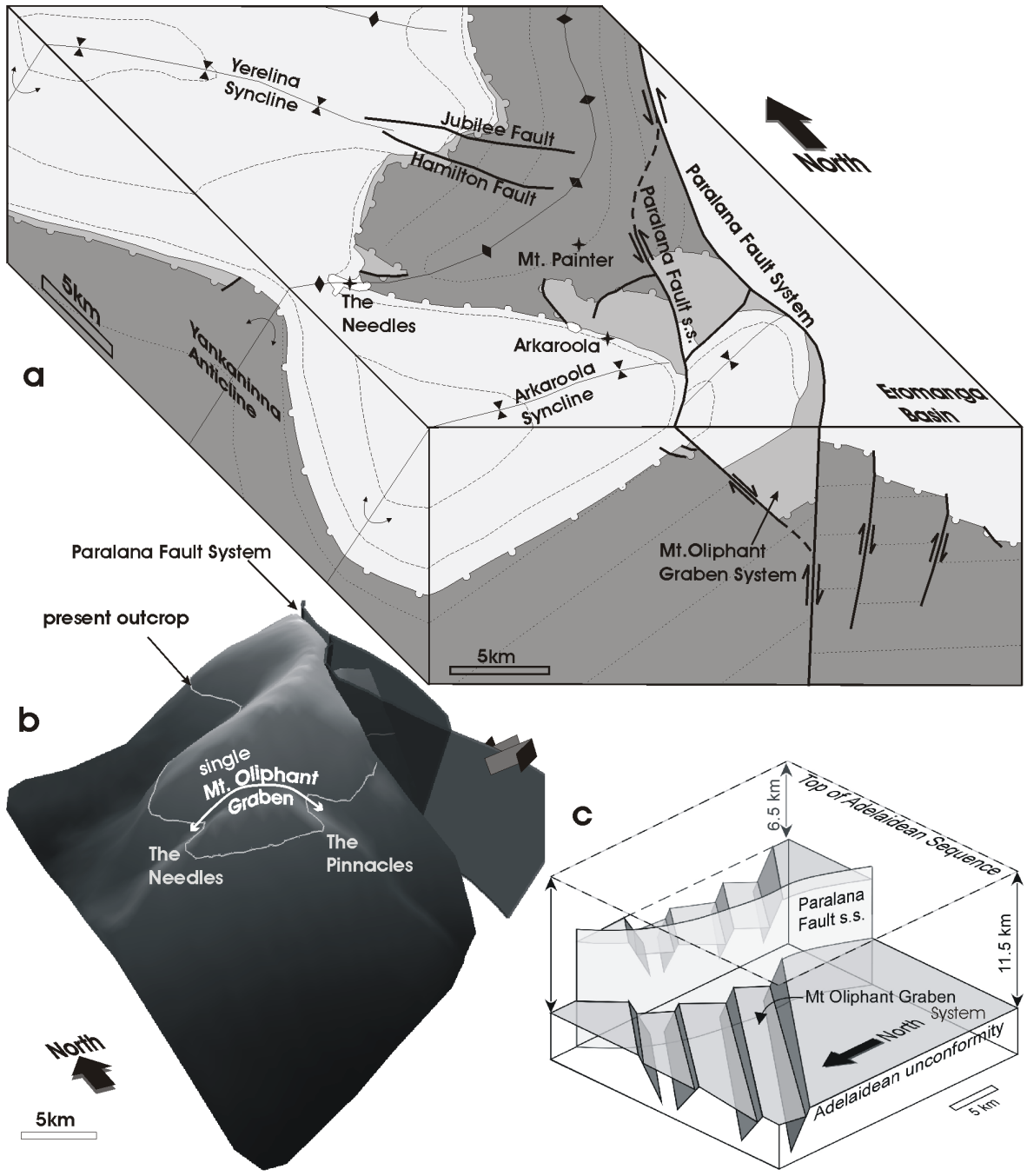

Fig. 5: Structural block-diagram of the present-day MPI and 3D reconstruction of the unconformity surface with contour line of the unconformity´s current outcrop. (a) The MPI forms the core of the thick-skinned Yankanina Anticline at the hanging wall of the steep Paralana Fault System. It exhumed from depths >15 km, while the cores of the adjacent synclines exhumed only about 2 km. (b) Three-dimenional model of the current Adelaidean unconformity surface, constructed with move^{TM}2010. The surface in the centre of the anticlinal core reaches a maximum height of *c.* 3 km above the present land surface. Well visible is the folded Mt. Oliphant Graben System between the Needles and the Pinnacles. (c) Schematic block-diagram of the Mt. Oliphant Graben System prior to Palaeozoic folding.

Fig.6:

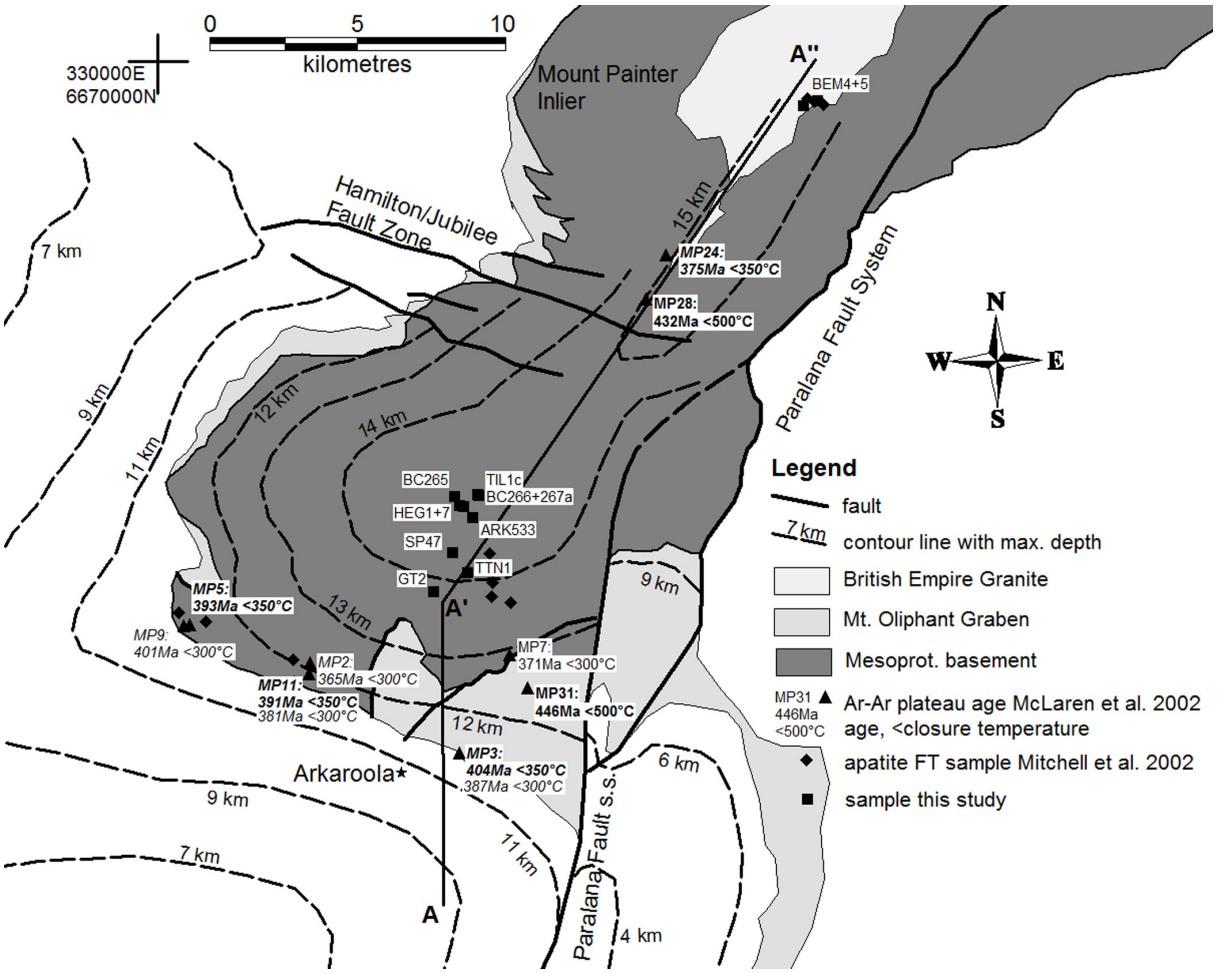

Fig. 6: Sample location of published analyses (McLaren *et al.* 2002; Mitchell *et al.* 2002) and of this study. The simplified map of the MPI shows the contour lines of maximum burial depth after deposition of the Adelaidean succession, as well as the location of the profile of Fig. 8.

Fig.7:

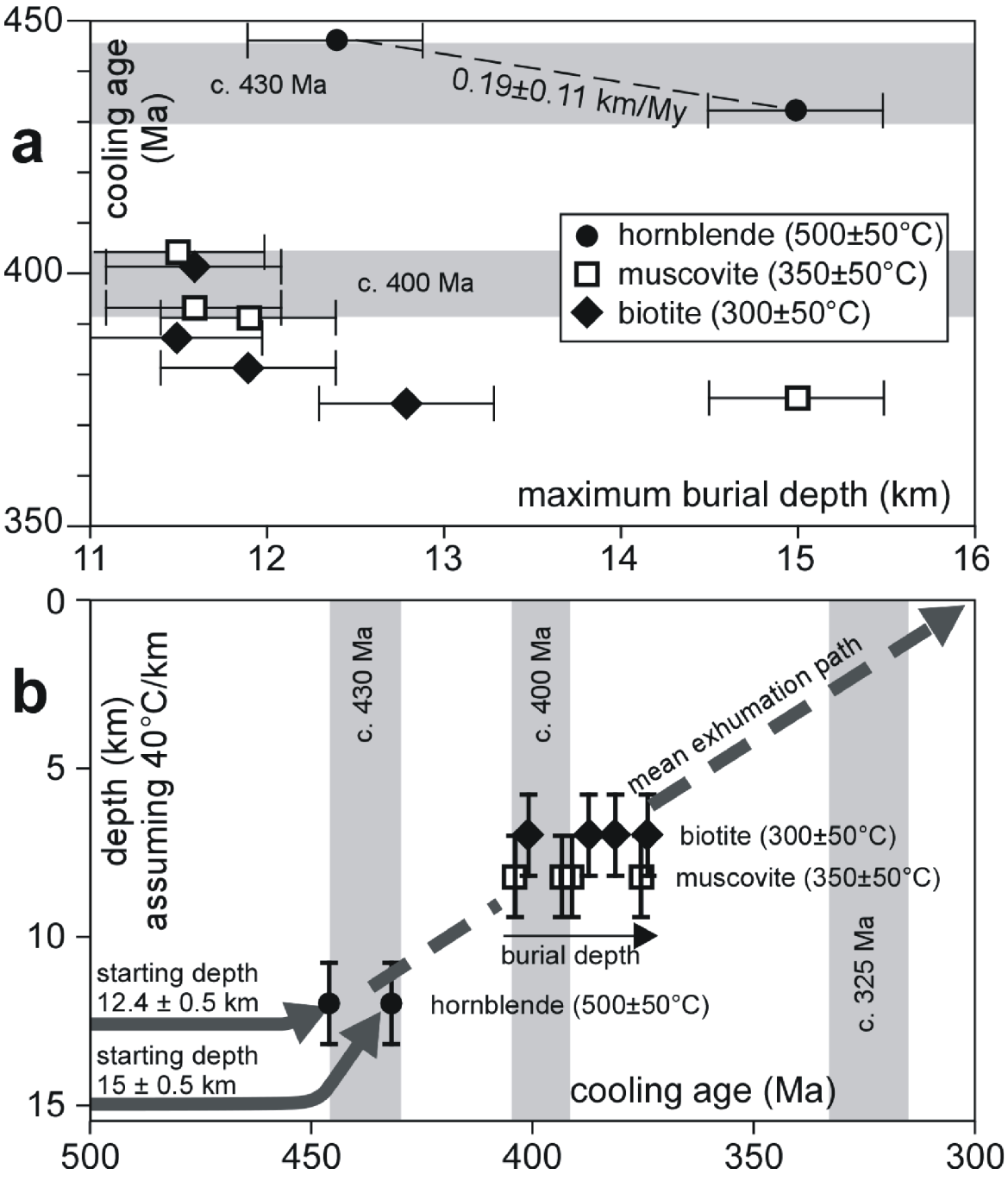

Fig. 7: (a) Ar-Ar plateau ages from McLaren *et al*. (2002) as a function of maximum burial depth, showing that more deeply buried samples exhumed later than shallower ones. Exhumation rate during passage through the hornblende closing temperature is *c.* 0.2 km/Myr. (b) Same ages plotted at the depth at their closure temperature (at 40 °C/km and a surface temperature of 20 °C). Initial exhumation at 0.2 km/Myr appears to have commenced later than the 500 Ma Delamerian Orogeny. Dashed arrow shows the mean exhumation rate with full exhumation at *c.* 300 Ma. Periods of fast exhumation according to McLaren *et al*. (2002) are shown as grey bands in both graphs.

Fig.8:

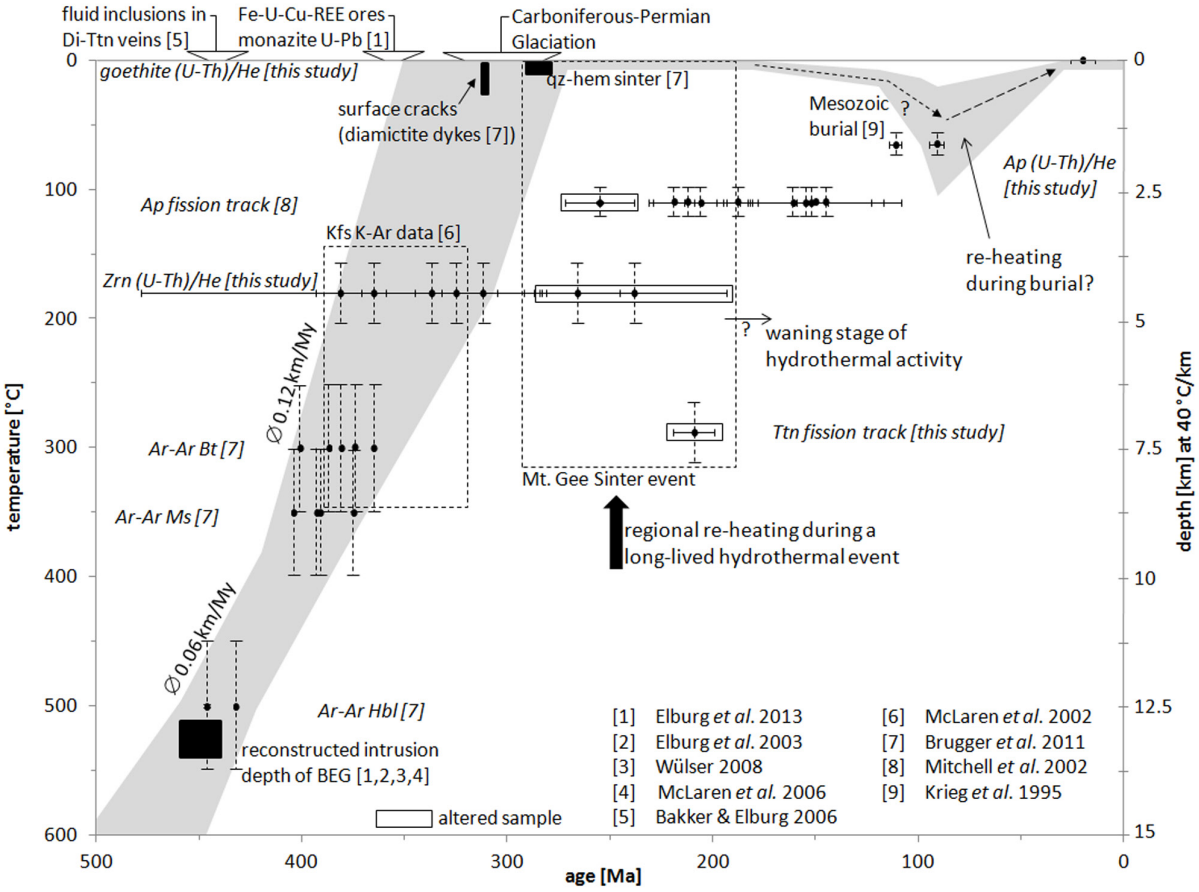

Fig. 8: Temperature (depth) vs. age diagram of published Ar-Ar data (McLaren *et al.*, 2002), apatite FT samples (Mitchell *et al.*, 2002) and new low-temperature thermochronology analyses. The depth is calculated assuming a geothermal gradient of 40 °C/km and 20 °C at the surface. The mean exhumation rate of the central and southern MPI is ≤0.1 km/Myr between <500 Ma and *c.* 300 Ma when the currently outcropping rocks reached the surface. Here they remained until the end of the Triassic Period (*c.* 200 Ma). Zircon, apatite and titanite (U-Th)/He ages are overprinted by the hydrothermal Mt. Gee Sinter event. A Mesozoic burial of ≤2.5 km may have affected the low-temperature thermochronology samples. A goethite sample formed at the surface in early Miocene times.

Fig.9:

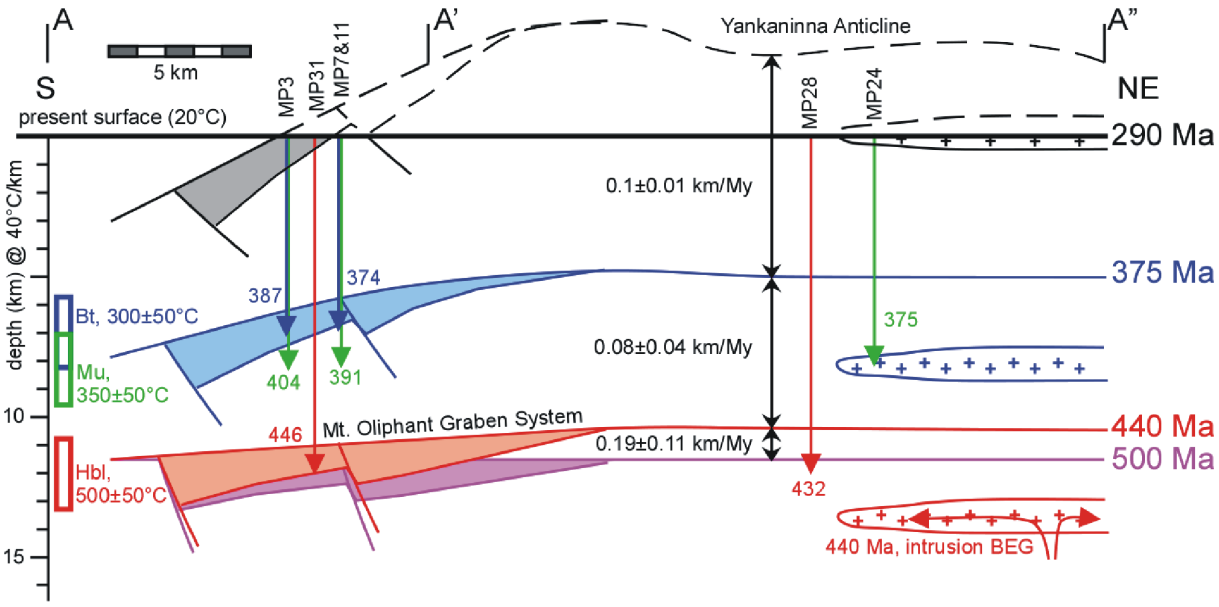

Fig. 9: Profile along the hinge of the Yankaninna Anticline (line A-A'-A" in Fig. 6), showing the exhumation of the Adelaidean unconformity and Mt. Oliphant Graben System at different points in time: deepest burial at *c.* 500 Ma (purple), *c.* 440 Ma when the BEG intruded (red), *c.* 375 Ma and at *c.* 300 Ma, when the current outcropping surface had reached the surface. Profiles are based on plateau Ar-Ar ages of McLaren *et al.* (2002) on hornblende (red arrows), muscovite (green arrows) and biotite (blue arrows), assuming a geothermal gradient of 40 °C/km and a surface temperature of 20 °C. Sample numbers from McLaren *et al.* (2002).

---------- **APPENDIX 2 (WEISHEIT ET AL., 2013A)** ----------

Long-lived crustal-scale fluid-flow: The hydrothermal mega-breccia of Hidden Valley, Mt. Painter Inlier, South Australia

Anett Weisheit[1], Paul D. Bons[1*], Marlina A. Elburg[2]

[*]corresponding author; E-Mail: paul.bons@uni-tuebingen.de;

Phone: +49 7071 2976469; fax: +49 7071 293060

[1]Department of Geosciences, Eberhard-Karls University Tübingen, Wilhelmstraße 56, 72074 Tübingen, Germany

[2]Geology Division, SAEES, University of KwaZulu-Natal, Private Bag X54001, Durban 4000, South Africa

Abstract

The Palaeozoic Hidden Valley breccia in the Northern Flinders Ranges of South Australia is exceptional for (1) its size of about 10 km^2, (2) the large continuous range in clast sizes from tens of microns to hundreds of meters and (3) thorough mixing of lithologies of different provenance, some originally kilometres apart stratigraphically. The size distribution follows a single fractal dimension of about unity over at least 6 orders of magnitude, implying that a single process was responsible for diminution from the 100 m scale, down to <mm. The breccia formed during >12 km exhumation which lasted about 200 Myrs, starting during the ~500 Ma Delamerian Orogeny and continuing during the Alice Springs Orogeny. Fluids released during exhumation were structurally focussed towards Hidden Valley, where an estimated 20 (5-30) km^3 total fluid volume caused the extensive brecciation. Brecciation initiated in Neoproterozoic cover meta-sedimentary rocks, at a level that is now fully exhumed. As hydrothermal fluid ascent continued with ongoing exhumation, the level of brecciation shifted down into the underlying Mesoproterozoic basement rocks, taking with it clasts of cover rocks. In this model, rocks pass through the zone of brecciation, which can thus incorporate a variety of lithologies that were originally kilometres apart.

Keywords: hydraulic brecciation, hydrothermal alteration, fluid flow, Flinders Ranges, Mount Painter Inlier

Abbreviations:

MPI = Mount Painter Inlier

BEG = British Empire Granite

HV = Hidden Valley

1. Introduction

Breccias are rocks composed of fragments or clasts of broken rock in a matrix of finer clasts and/or a cement of newly precipitated minerals (e.g. Sibson, 1986; Lazincka, 1989; Reimold et al., 1994; Lorilleux et al., 2002; Mort and Woodcock, 2008). Understanding the formation of breccias is of direct economic importance as many ore deposits, such as the world-class Olympic Dam deposit, are breccia-hosted (Lazincka, 1989; Oreskes and Einaudi, 1990; Jébrak, 1997; McPhie et al., 2011). Apart from sedimentary and impact breccias, breccias can form by a variety of processes, such as tectonic comminution, fluid-assisted or hydraulic brecciation, and wear abrasion (Jébrak, 1997). One way to determine the genesis of breccias is the analysis of the clast-size distribution and clast morphology. The fractal dimensions of clast shape and size distribution, in particular, have been used to classify breccia types and origins, as these dimensions are related to the process of fragmentation (Blenkinsop, 1991; Hyslip and Vallejo, 1997; Jébrak, 1997; Perfect, 1997; Lorilleux et al., 2002; Storti et al., 2003; Barnett, 2004; Clark et al., 2006a; Keulen et al., 2007). However, Mort and Woodcock (2008) argue that the clast-size distribution only may not be significant to characterise different breccias and instead use clast concentration and rotation.

In some cases, breccias contain a mixture of clasts that must have been carried over long distances. For example, Oliver et al. (2006a) report on breccia pipes, which they interpret as having formed by fluidisation. With clasts of over 10 m in size, the inferred flow rates must have been in excess of 5 m/s to carry these clasts up several kilometres.

Here we report on an unusually large, ca. 10 km^2, Palaeozoic breccia from Hidden Valley in a basement inlier in the Northern Flinders Ranges, South Australia (Fig.1). Remarkable features of this breccia are the huge range in clast sizes (from tens of microns to hundreds of metres) and the thorough mixing of lithologies, some of which were originally kilometres apart. Fractal analysis over the entire size range indicates that a single process was responsible for the formation of the breccia. We will show that pervasive alteration and brecciation of basement rocks and the formation of the Hidden Valley breccia occurred during >12 km of exhumation over an approximately 200 Myrs period of time. Similar to brecciation in the Cloncurry District (Oliver et al., 2006a), brecciation at Hidden

Valley breccia probably involved fluidisation, but with (some) clasts transported downwards relative to their present-day position.

2. Regional Setting

2.1 Proterozoic geology

The Mt. Painter Inlier (MPI, Fig.1a) in South Australia is an approximately 10x60 km tectonic window that exposes a basement of Mesoproterozoic metasediments (Radium Creek Group; Fig.2a) and two suites (±1575 Coulthard suite and ±1555 Ma Moolawatana suite) of mostly A-type granitoids (Coats and Blissett, 1971; Elburg et al., 2001; Fanning et al., 2003; Fraser and Neumann, 2010; Cowley et al., 2012; Elburg et al., 2012), surrounded by Neoproterozoic (800-500 Ma) meta-sedimentary rocks and basalts of the Adelaidean Sequence that unconformably overlie the basement (Preiss, 1987, 2000). The east side of the system is separated by the Paralana Fault System from Mesozoic and younger sediments of the Eromanga Basin on the Curnamona Craton (Wülser et al., 2011). Mesoproterozoic metamorphism reached local anatexis, and deformation produced a penetrative gneissic foliation that affected all Mesoproterozoic basement rocks (Elburg et al., 2001; Dipple et al., 2005; Armit et al., 2012). This main foliation was preceded by at least one earlier deformation phase (Teale, 1993; Elburg et al., 2001; Fig.2a+b).

By approximately 800 Ma, the basement was exposed, with the main foliation making a small angle to the erosion surface. Deposition of the Adelaidean Sequence commenced in a horst-and-graben setting, with the lowermost graben sediments and basalts variable in thickness (Preiss, 1987). The Paralana Fault system was active during this period as it bounds the Lower Adelaidean Sequence grabens. Whereas the Paralana Fault system was reactivated in the Palaeozoic, most other Neoproterozoic faults were not reactivated later on.

The lower Adelaidean Sequence is thickest in the southeast, and disappears further northwest. Sedimentation continued until the Cambrian, at which stage the Adelaidean unconformity at the MPI was buried to a depth of ~12 km (Sandiford et al., 1998; McLaren et al., 2002). Mineral assemblages with cordierite, andalusite and biotite in the lowermost Adelaidean rocks indicate amphibolite-facies metamorphism, with temperatures of ~500 °C (Coats and Blissett, 1971; Mildren and Sandiford, 1995;

Sandiford et al., 1998; McLaren et al., 2002). The metamorphic grade is consistent with a geothermal gradient of ~40-50 °C/km, which is attributed to the high heat production of the Mesoproterozoic granites according to Mildren and Sandiford (1995) and Sandiford et al. (1998).

2.2 Palaeozoic exhumation

Basement and cover are folded into large, 10 km scale open folds that now determine the map pattern (Paul et al., 1999; Fig.1a+b). The MPI forms the core of the NE-SW to EW trending Yankaninna Anticline (Coats and Blissett, 1971). Folding is traditionally attributed to the ~515-490 Ma Delamerian Orogeny that formed the Adelaide Fold Belt in South Australia (Drexel and Preiss, 1995; Paul et al., 1999; Foden et al., 2006). Shortening in the Northern Flinders Ranges, west of the Paralana Fault System is estimated at a modest 10-20 % by Paul et al. (1999), whereas the Curnamona Craton east of the fault zone remained rigid and did not fold (Fig.1b). Delamerian ages in the MPI are only recorded in pegmatites that intruded both basement and lowermost Adelaidean units (Elburg et al., 2003; Wülser et al., 2011). Radiogenic isotope ratios of Delamerian leucogranites are best explained by the involvement of a mantle-derived component (Elburg et al., 2013).

At 460-440 Ma, the British Empire Granite (BEG), as well as aplite and pegmatite dykes, and diopside-titanite veins intruded the basement (Elburg et al., 2003; Bakker and Elburg, 2006; McLaren et al., 2006; Wülser, 2009). McLaren et al. (2002) report a fast cooling to ~400 °C at ~430 Ma in lower Adelaidean meta-sedimentary rocks close to the unconformity. The 100 °C cooling at the level of the unconformity indicates that the first few km of exhumation took place before ~430 Ma. A further 50-100 °C cooling occurred at ~400 Ma, followed by a 100-200 °C cooling stage at ~325 Ma (Figure 6 in McLaren et al., 2002). The rocks thus cooled 250-400 °C down to 100-250 °C, corresponding to exhumation to a depth of ~2.5-6 km by 325 Ma.

Unusual rocks, the "pebble dykes" (“diamictite dykes”, Skirrow, 2011; Cowley et al., 2012) crop out in the centre of the MPI. Here, diamictite-like conglomerates, are found as vertical E-W striking dykes of 10 cm to >10 m width (Fig.2c). The rounded clasts in a fine sandy matrix in the pebble dykes are of various lithologies, some not found in the MPI and near surroundings. The pebble dykes are not metamorphosed and interpreted as sediments transported from possibly as far as

Antarctica (Brugger et al., 2011). The maximum age of the pebble dykes is constrained by the youngest detrital zircon age of 315±9 Ma (Brugger et al., 2011). Because of the glacio-fluvial character of the pebble-dyke sediment and the zircon provenance, the dykes are assumed to have formed during the 280 Ma Permian glaciation (Brugger et al., 2011). As the sediment is found in steep and narrow structures, we interpret these dykes to represent deep cracks that were filled with sediment (similar dykes are found for instance in Finland and Sweden: Bergman et al., 1982; Friese et al., 2010). The importance of the pebble dykes here is that they provide evidence that the basement rocks in the core of the Yankaninna Anticline reached the surface after ~315 Ma, probably by the Permian (Brugger et al., 2011).

Structural reconstructions show that the basement in the core of the Yankaninna Anticline exhumed ~15 km, while uppermost Adelaidean Sequence rocks are still exposed in the cores of the adjacent synclines (Paul et al., 1999). Therefore, significant exhumation only occurred in the hinge of the anticline (Fig.1b). There is a difference in vertical movement between the anticline and the synclines of well over 10 km, which occurred over a period of ~200 Myrs, between the Cambrian (~500 Ma) and Permian (~300 Ma). It is this differential vertical movement that resulted in uplift and exhumation, as well as the current fold pattern. Therefore, folding cannot be attributed to the Delamerian Orogeny only, but took place over most of the Palaeozoic, covering both the Delamerian and Alice Springs Orogenies. During that time the Curnamona Craton further to the east remained rigid and did not exhume. The Yankaninna Anticline formed by south directed ramping up the Curnamona Craton along the Paralana Fault system. The eastern-most branches of the Paralana Fault zone along the range front record Neogene activity (Célérier et al., 2005), while no active movement is visible along the branches within the mountain range.

2.3 Palaeozoic hydrothermal/metasomatic activity

The centre of the MPI saw extensive Palaeozoic hydrothermal/metasomatic activity (Elburg et al., 2003; Bakker and Elburg, 2006; Elburg et al., 2012). The original meta-sedimentary Radium Creek Group and the metagranites are altered into an orange-pink feldspar-quartz rock with a granite-like appearance and remnants of the original gneissic foliation (Fig.2d). The alteration involved

dehydration of biotite and growth of microcline. Biotite remnants can be found as small patches in the altered rock (Fig.2e) and as inclusions in porphyroblastic microcline (Fig.2b). Biotite is partly or completely removed over an area of ~60 km^2. This dehydration reaction would have released H_2O, as well as Mg and Fe. Iron oxides, mostly magnetite that is martitised into hematite, are abundant as a disseminated phase in the K-feldspar-altered rocks and occur as 10-100 m-scale U-bearing breccia bodies (Fig.1a, Fig.2f) that are associated with heavily altered and chloritised metasediments and K-feldspar altered rocks (Elburg et al., 2012). Pervasively altered rocks grade into K-feldspar±quartz-cement breccia zones (Fig.2g) that cover many square kilometres (Radium Ridge Breccias, Drexel and Major, 1987, 1990). Field relationships indicate that these breccias are contemporaneous with aplites and pegmatites and overprint them, suggesting that fluid activity occurred from at least ~440 Ma. Clasts are from local origin, either more or less altered Radium Creek Group and gneisses or K-feldspar-altered rocks. Quartz-K-feldspar-hematite±tourmaline veins extend to the Adelaidean cover and are associated with extensive actinolite-tremolite skarning, dolomitisation and minor Cu deposits (Coats and Blissett, 1971).

Pegmatitic diopside-titanite veins intruded in the core of the Yankaninna Anticline at ~440 Ma (Bakker and Elburg, 2006). They contain secondary hematite-bearing fluid inclusions in the titanite, which are assumed to be related to the K-feldspar alteration and iron-mobilisation. The trapping temperature is estimated at ~350 °C and ~0.8 kbar using a geothermal gradient of 100 °C/km (Bakker and Elburg, 2006). Using a more plausible 40 °C/km geothermal gradient (Sandiford et al., 1998) and lithostatic pressure of the fluids gives a temperature of ~420 °C at a depth of ~10 km. At a higher geothermal gradient the temperature and the maximum depth decrease. The actually depth of entrapment could thus be less, if the fluids were hotter than their surroundings. The fluid inclusions are secondary, so the rocks that now outcrop in the core of the Yankaninna Anticline must have been at a depth >10 km at 440 Ma. With a maximum depth of these rocks of ~15 km, the secondary hematite-bearing fluids were trapped <440 Ma and after ≥5 km of exhumation. This is compares well with an estimated exhumation of 2-3 km at this time according to McLaren et al. (2002). It follows that K-feldspar alteration occurred during the exhumation of the inlier.

Biotite dehydration on such a scale is common at higher temperatures in amphibolite and granulite facies terranes, where it can lead to partial melting (e.g. Graphchikov et al., 1999; Janak et al., 1999; Gardien et al., 2000; Scrimgeour et al., 2001; Rajesh et al., 2012). However, cases of biotite dehydration at lower temperatures in the upper crust and at the scale observed in the MPI are not reported in the literature. Low-grade growth of microcline at the cost of biotite is described by Holness (2003), who proposed the H_2O-consuming reaction biotite + H_2O $\rightarrow$ chlorite + K-feldspar. It is, however, of interest to note, that in their study the reaction products are not found adjacent to each other, and the reported case could potentially be similar to the K-feldspar producing biotite dehydration observed at Mt. Painter. Biotite dehydration requires a reduced H_2O activity (Nijland et al., 1998; Rajesh et al., 2012), which may have been facilitated by the very high salinities, up to 40 % NaCl equivalent, observed in fluid inclusions by Bakker and Elburg (2006). This could explain the unexpected scarcity of chlorite, with chlorite only abundant near iron-oxide breccias.

2.4 Near-surface hydrothermal activity

Quartz-hematite sinters with large open voids (Fig.2h) at Mt. Gee and Mt. Painter in the centre of the MPI are the remnants of a near-surface hydrothermal system that was dated at ~290 Ma by Brugger at al. (2011). This age is consistent with the fact that the deposits cross-cut the pebble dykes. Quartz of this Mt. Gee Sinter (Drexel and Mayor, 1987) has a distinct morphology (Fig.2i), which allows to distinguish the sinter deposits from earlier Palaeozoic hydrothermal breccias and veins. Although a previous study (Bakker and Elburg, 2006) treated all hydrothermal activity as a single, but evolving event, we consider the pre-pebble dyke K-feldspar alteration event as distinct from the post-pebble dyke, near-surface Mt. Gee Sinter event (Elburg et al., 2013). A complicating factor is that earlier breccias can be overprinted (in the form of silicification) by the Mt. Gee Sinter event or even more recent fluid flow, which is still ongoing in parts of the inlier (Brugger et al., 2005).

3. The Hidden Valley breccia

Hidden Valley is a ca. 1x10 km valley formed by a friable and easily weathering breccia, surrounded by hills of basement granitoids in the east and metamorphic rocks in the west (Fig.1c,

Fig.3a). The relatively sharp, straight and steep eastern margin lies in the extension of the Paralana Fault system along hard K-feldspar-altered granitoids and breccias. Mylonites, overprinted by brittle deformation structures, indicate both west side up and sinistral strike-slip movement. The western margin is more irregular with breccia zones fingering into the unaltered host rocks (Fig.1c). The breccia is typically pale grey-green and mostly unconsolidated (Fig.3b). We will refer to this breccia as Hidden Valley-type breccia (HV-type breccia). Most clasts are heavily altered with new growth of biotite, chlorite, talc and clays (Fig.4a). Clasts are mostly well rounded and range in size from <mm to >100 m. Large clasts stand out as isolated blocks in the landscape, as do 1 to >10 m-sized pegmatite blocks (Fig.1c, Fig.3a).

Clasts are highly variable in lithology, including all types of quartzites, schists and granitoid gneisses from the surrounding basement, mylonitised basement rocks, gabbro, pegmatite, feldspar-altered rocks and breccias, as well as marbles, carbonates and clastic sedimentary rocks of lower metamorphic grade, with sedimentary structures, such as wave ripples, mudcracks and salt casts (Wülser, 2009; Fig.3c). Despite the intense alteration, these metasediments are recognisable as lowermost Adelaidean (Coats and Blissett, 1971). As the Adelaidean unconformity was a few kilometres above the current level of exposed rocks at Hidden Valley (Fig.1b), the clasts must have moved down this distance relative to the basement wall rock of the breccia. Clasts of Adelaidean sedimentary rocks range up to tens of metres in size and are usually strongly altered, whereas some clasts of the surrounding gneisses and pegmatites are relatively unaltered. The breccia is thus characterised by a thorough mixing of basement and cover clasts, which were originally several km in vertical distance apart. However, the largest clasts, in the order of 100 m, were only slightly tilted and did not move far from their original position at the margin of the valley. Channel-like zones of relatively fine-grained soft breccia can be found cutting through areas with coarser clasts. These zones may exhibit graded bedding and grain-size sorting, indicative of clast transport by fluid flow (McCallum, 1985; Jébrak, 1997). A brannerite pegmatite clast within the Hidden Valley breccia was dated by LA-ICPMS at 367±13 Ma (Wülser, 2009).

Similar, but smaller occurrences of HV-type breccia can be found in the southwest of the MPI at fault structures and in anticlinal fold hinges, for example at the Pinnacles and the Needles (Elburg et

al., 2003; Fig.1a, Fig.3d). HV-type breccias contain K-feldspar altered rocks and pegmatites, which indicates that the formation of the HV-type breccias is either contemporaneous with the K-feldspar alteration or post-dates it. Clasts of Mt. Gee Sinter-type breccias and veins are absent in HV-type breccias and the Mt. Gee event is therefore assumed to post-date the HV-type brecciation.

In the literature the Hidden Valley breccia was interpreted as formed by diapirism (Coats and Blissett, 1971). Diapirism of evaporitic Lower Adelaidean Sequence beds is also proposed for breccia zones found throughout the Flinders Ranges (Preiss, 1987; Preiss et al., 1993; Backe et al., 2010). A problem with Hidden Valley is that the breccia is found stratigraphically below these beds, which would be inconsistent with a rising salt diapir. Large-scale, east-directed thrusting of basement rocks over the Adelaidean Sequence was therefore proposed by Campana et al. (1961) and Wülser (2009) to explain the occurrence of Adelaidean Sequence clasts within the breccia. However, there is no evidence in the field for such thrusting. As mentioned before, the breccia zone is bound to the east by a steep fault structure and in the west, the breccia fingers into the host rock. Below we first present a detailed analysis of the breccia properties (shape and size distribution), which indicate that the whole HV-breccia is a fluidisation and/or collapse breccia (McCallum, 1985; Jébrak, 1997; Lorilleux et al., 2002; Oliver et al., 2006a). Following this we discuss the required amount and origin of brecciating fluids to explain the formation of the Hidden Valley breccia and similar breccias in the MPI and possibly throughout the Flinders Ranges.

4. Breccia statistics

4.1 Methods

Clast shape and size distributions were analysed using micrographs, field images, and the map of northern Hidden Valley (Tab.1; Fig.4). Additional size measurements were made in the field. Outlines of clasts were drawn by hand to perform a particle analysis with the freeware program ImageJ. Area, circumference, and ellipticity were measured for each clast. Instead of area, the mean diameter was measured in the field. The clast areas were then calculated from the diameters, assuming a circular shape.

For a fractal clast-area distribution, a straight line results when the number of clasts larger than a certain area ($N_{\geq A}$) is plotted against that area (A) in a log-log plot (Epstein, 1947; Marone and Scholz, 1989; Perfect, 1997). In that case:

$$N_{\geq A} = k \cdot A^{-D_{2D}} \quad (1)$$

D_{2D} is the 2-dimensional (area) fractal dimension. In the literature, the fractal dimension D_S is usually quoted for the one-dimensional (diameter) size distribution with $D_S = D_{2D}+1$. Here we use D_{2D}, since we mostly measured areas. k is related to the number of clasts in the area under consideration. Hydrothermal and corrosive wear breccias tend to have lower D_{2D} values (~1) than those formed by wear abrasion and shear (~2-3), according to Jébrak (1997) and Barnett (2004).

The shape of clasts is defined by various parameters. Ellipticity (E) is the axial ratio of the best-fit ellipse of a clast, and therefore a measure of its elongation. The ellipticity ranges from one for a circle to infinity for a line. The roughness or irregularity of the clast surface is expressed by the circularity (C), being the ratio of clast-area to perimeter, normalised to unity of a circle. A smooth elliptical surface will give a C value close to 1, while an irregular surface or very non-circular shape results in values <1. Another measure of the roughness of the clast surface is the boundary fractal dimension D_R, which can be measured in various ways (Bérubé and Jébrak, 1999). Here we used the Euclidean distance method, where the boundary of the clast is traced by ribbons of increasing width. If a straight line, with slope R, is obtained in a log-log plot of ribbon area against ribbon width, the boundary fractal dimension (D_R) is defined as $D_R = 2-R$ (Jébrak, 1997). Only few measurements of D_R have been made, as these are more cumbersome than for the other shape parameters and only relevant when the resolution of the clast surface is sufficiently high. A high D_R, in combination with a low D_{2D} would indicate corrosive wear in the classification scheme of Jébrak (1997).

4.2 Area distribution

The clasts in Hidden Valley are highly variable in size. To characterise the size distribution of the breccia, we measured the clast area distributions from microphotographs of two thin sections (HVTS1-2), from several field photographs with different scales (HVPH1-9 and HVFD1+2; Fig.4a-c)

and from the geological map of northern Hidden Valley (HVMAP; Fig.1c; Tab.1). All samples have straight sections in $N_{>A}$ versus A log-log plots, indicating fractal distributions (Fig.5a) with D_{2D} values ~1 (Tab.1). At the low end of the range, the curves flatten off, which is a result of under-sampling of the smallest clasts towards the resolution limit. Curves tend to steepen at the high end of the range. This is interpreted as an artefact related to poor statistics and bias related to avoiding images mostly covered by one or a few very large clasts. Similar clast-size distributions, with $D_{2D}\approx1$, were obtained from three photographs of the HV-type breccia at the Pinnacles and at the Needles each (NE1-3, PI1-3 and PIMAP; Fig.5b; Tab.1), as well as from the K-feldspar cemented Radium Ridge Breccias (KFS1-3; Fig.5c).

If in a certain sample area the number of clasts larger than a certain area is X, then that number will be nX in a sample area that is n times larger. The frequency of small clasts visible in a thin section or field photograph can thus be scaled to that for the map area by multiplying $N_{>A}$ by the ratio of the map area and the sample area. This way, the area frequencies of all samples were recalculated for the whole 3.2 km^2 area of the northern Hidden Valley map (Fig.1c). A best fit through the HV-breccia samples gives a single fractal distribution, with $D_{2D} = 1.03$, from 10^{-8} m^2 to 10^4 m^2, or from the 0.1 mm to 100 m scale (Fig.5d). Only the largest clasts on the map fall outside this range. The fact that the medium size ranges of individual samples line up with a slope of 1.03 indicates that this range indeed gives the true fractal dimension and that the steepening of the slope at the large end of the range in individual samples is an artefact. Fig.5d also includes the analysed photographs of the Needles and the Pinnacles breccias and a map from large clasts at the Pinnacles, which plot on the straight section defined by the Hidden Valley measurements. Considering that the field observations and breccia characteristics are similar within these breccias, it is likely that the breccias at the Needles, the Pinnacles and in Hidden Valley formed during a similar brecciation event (i.e. D_{2D} is similar). The fact that the Radium Ridge Breccias also plot on the straight section indicates that the process of brecciation is comparable in the whole inlier.

The total area covered by clasts can be calculated by integrating the product of the frequency of a clast area (the negative derivative of Eq.1) and that area, from the smallest clast area (~10^{-9} m^2) to the largest clast, for which $N_{\geq A}=1$. In the case of Hidden Valley this gives a total clast area of 3.5 km^2,

which is close to the 3.2 km^2 map area. This means that the breccia is essentially composed of clasts only, without voids or cement of newly precipitated minerals. At one scale, clasts appear to be embedded in a fine-grained matrix, but because of the fractality, this matrix is actually the same breccia with finer clasts at a smaller scale below the measurement limit. The overall single fractal dimension indicates the operation of a single brecciation process from the tens of μm to the 100 m scale (Fig.5d). The presence of very large, >100 m clasts outside of the fractal range could reflect the initial stages of brecciation, which did not yet achieve the characteristic fractal distribution (Fig.5d).

4.3 Shape of clasts

The morphology of clasts is another indicator of the brecciation process (Jébrak, 1997; Bérubé and Jébrak, 1999; Lorilleux et al., 2002). The boundary fractal dimension D_R of the clasts in Hidden Valley range between 1.03 and 1.06 for clasts in the size range between 1 and 100 cm^2 (field photographs) and 1.07 and 1.23 in thin section (between 0.1 and 1 mm^2) (Fig.6a+b). This increase of D_R values with decrease of the clast size is probably related to corrosive wear at the small scale, which is observed at the thin section scale. In a plot of D_R vs. D_{2D} the measured Hidden Valley clasts plot in the field of hydraulic brecciation of Jébrak (1997), although low D_{2D} values are found in breccias that formed during tectonic brittle fracturing (Keulen et al., 2007; Mort and Woodcock, 2008).

To characterise the shape of the clasts of the measured breccias the circularity is plotted against the ellipticity in Fig.6c. All clasts have a high circularity (~0.8) and low ellipticity (~1.5) and are therefore well rounded and close to circular in shape. No preferred orientation of elongate clasts was observed. Well-rounded clasts are generally an expression of mature breccias (Lorilleux et al., 2002). Circularity (Fig.6d) and ellipticity are only weakly dependent on clast size. A slight decrease in circularity and increase in ellipticity for the thin-section scale clasts reflect their more irregular shape, in accordance with their slightly increased D_R value.

4.4 Summary

In summary, the Hidden Valley breccia and other HV-type breccia occurrences are characterised by a single area distribution with D_{2D} close to unity, spanning a size range from <mm to

~100 m. Integration of clast areas shows that clasts fill the whole sample area, implying there is little or no matrix of newly precipitated cement or voids. Clasts are close to circular and mostly well rounded, with a weak tendency for the very smallest clasts (<<mm) to have a more irregular shape and rougher surface. K-feldspar and quartz-cemented Radium Ridge Breccias share these characteristics, but differ from HV-type breccias in their clast composition. While HV-type breccias have a diverse mix of clast lithologies of various origins, the Radium Ridge Breccias only contain clasts of local origin.

5. Discussion

5.1 Process of brecciation

Three main mechanisms for the formation of the HV-type breccias can be considered: (1) chemical abrasion or corrosive wear, (2) tectonic wear abrasion and shearing, and (3) hydraulic fracturing and collapse (Jébrak, 1997; Lorilleux et al., 2002). Although the extensive alteration is indicative for reactive fluids, chemical abrasion is discarded as the main mechanism. First, chemical abrasion cannot explain the transport and thorough mixing of lithologies. Second, the rounded and smooth clast morphology is not typical for chemical abrasion, where higher D_R values are to be expected than measured (Jébrak, 1997; Barnett, 2004).

If the breccia would have formed by tectonically induced mechanical diminution and abrasion (e.g. during thrusting), indicators of strong shearing and faulting, such as striations on clasts, shape preferred orientations, shear bands, or higher D_{2D} values and crackle or mosaic breccias, would be expected (Jébrak, 1997; Keulen et al., 2007; Mort and Woodcock, 2008; Wright et al., 2009). All these structures are absent in the breccias under consideration. Faults that could potentially have caused tectonic brecciation would be (a) the branch of the Paralana Fault Zone that bounds Hidden Valley to the east, or (b) the inferred flat-lying thrust of basement over cover rocks, as suggested for the southern Hidden Valley by Wülser (2009), following the interpretation by Campana et al. (1961). Brecciation caused by the Paralana Fault Zone is deemed unlikely, as HV-type breccias are only found along a ~10 km section of the >70 km exposure of the fault branch. Apart from the lack of field evidence for an east-directed, flat-lying thrust, such thrusting is inconsistent with the general style of

deformation in the area with steep faults and upright folds (Paul et al., 1999; Fig. 1b). A further argument against a tectonic origin of the breccias is that similar breccias are found at other localities, such as The Needles and The Pinnacles, where faults are absent or only active before brecciation, respectively (Fig.1b in Elburg et al., 2003).

A range of observations indicates that the extraordinarily large Hidden Valley breccia was formed by hydraulic or fluid-assisted brecciation. In a hydraulic breccia, fracturing is caused by fluid pressure, not by applied tectonic stresses. Hydraulic breccias are characterised by low D_R and low D_{2D} values, according to Barnett (2004) and Jébrak (1997). The Hidden Valley breccia falls well within their fields for hydraulic brecciation (Fig.6a). Corrosive wear would cause higher D_R values, which are only found for the smallest clasts (<<1 mm^2), where this process may have come into play.

However, the fractal dimensions alone are not sufficient to determine the brecciation process (Keulen et al., 2007; Mort and Woodcock, 2008). Another indication for a hydraulic origin of the breccia is the strong alteration, suggesting the passage of large fluid volumes. Rounding of the clasts, the wide size distribution, thorough mixing of lithologies, and flow structures are indicative of long-distance transport by turbulent fluidisation (McCallum, 1985; Oliver et al., 2006a) and/or of collapse (Jébrak, 1997). In case of fluidisation, fluid flow velocities must be high enough, in the order of metres per second, to be able to lift and transport rock fragments. In case of the fluidised breccia pipes and dykes in the Cloncurry District, Australia, fluidisation brought clasts up several kilometres (Oliver et al., 2006a). In case of Hidden Valley, Adelaidean metasediment clasts were brought down by at least a few kilometres (Fig.1b). Whether clasts were brought up as well is difficult to ascertain, as there are no known lithologies that would have only occurred in situ below the present exposure level. However, as the Adelaidean clasts from above are mixed in with basement clasts, clasts must have had significant differential vertical movement to juxtapose lithologies that were originally kilometres apart vertically.

5.2 Quantifying the amount of fluids

It is unlikely that the whole of the Hidden Valley breccia was formed in a single pass of fluid flow. This would have required all fluids to accumulate and be released in a single event. Release of

fluid batches over a prolonged period of time is more likely (Bons and van Milligen, 2001). Passage of a single batch of fluid would first lead to dilation and lifting of clasts, followed by collapse, as is schematically shown in Fig.7. During collapse, clasts are mixed, which implies that some clasts experience a net downward movement. The downward movement distance (Δz) cannot be more than the vertical extent (Δh) of the fluid batch. Δz would be related to the amount of dilation ($\phi \leq 1$). A dilation factor of one would mean that a batch of pure fluid would completely lift its roof, which would be the maximum possible dilation. A rough estimate of Δz would be $\Delta z \leq \phi \Delta h$ (2), which is the amount of fluid in a single batch per unit area. The total vertical movement (ΔZ) after passage of all batches is the sum of individual movements:

$$\Delta Z = \sum \Delta z \leq \sum \phi \Delta h \tag{3}$$

The total volume of fluid (V_f) passing through a breccia zone of cross-sectional area B is then:

$$V_f = B \sum \phi \Delta h \geq B \Delta Z \tag{4}$$

Even without knowing Δh and Δz, we can use Eq.(4) to calculate the total volume of fluid passing through the system. A probable value for ΔZ is ~2 km, with a minimum of 0.5 km and a maximum of 3 km (Fig.1b). This is the estimated height of the Adelaidean unconformity above the present exposure, based on structural profiles through the MPI (after Paul et al., 1999; Fig.1b). Adelaidean clasts inside the breccia must have moved down, relative to the present land surface, by at least that distance. The estimated fluid volume for the B = 10 km^2 Hidden Valley breccia is thus at least V_f = 20 km^3 (5 - 30 km^3). The integrated fluid flux is thus 2000 (500-3000) m^3 per square metre of breccia. If the fluid that caused the brecciation was a vapour formed by boiling, the original volume of liquid fluid would be significantly less. However, no unambiguous indicators for boiling were observed, and this possibility is left for further investigation.

5.3 Fluid sources

Hydraulic brecciation by fluids implies fluid pressures that exceed the minimum compressive stress and are thus far above hydrostatic pressure. Such fluids flow upwards. Fluid sources for the brecciation must thus be sought lower in the system. However, the distribution of ~60 km² of Radium

Ridge Breccias in the core of the folded inlier and the location of Hidden Valley at the convergence of the Yankaninna Anticline hinge and the Paralana Fault system suggest strong focusing of fluids (Fig.1a+b). This way a large region of the crust could have been tapped to form the Hidden Valley breccia. There are four possible fluid sources: (1) large-scale fluid convection, (2) biotite dehydration, (3) decompressional release of pore water (Staude et al., 2009) trapped below the Adelaidean unconformity, and (4) fluids released by igneous intrusions.

(1) Large-scale convective fluid circulation is often invoked to explain the formation of ore bodies, breccias and other expressions of fluid-rock interaction (e.g. McCaig, 1988; Oliver et al., 2006b; Boiron et al., 2010). One problem with this model is that the intense brecciation requires fluid pressures that exceed the lithostatic pressure, which drives fluid up and away from their source. Rather than drawing in more fluids, as a circulation model requires, the hydraulic-potential gradients would drive fluids away (Bons et al., 2012; Bons and Gomez-Rivas, in press). A second problem is that circulation requires a driving force, such as heat released by igneous intrusions. Although some intrusions (e.g. the British Empire Granite and aplites/pegmatites) are known from the area and period of brecciation, it is questionable whether their extent suffices to uphold a long-lived fluid circulation system on the scale to produce the extensive brecciation.

(2) Dehydrating 1 m^3 of biotite produces ~0.1 m^3 of H_2O at atmospheric pressure. Mapping showed that biotite in ~60 ±10 km^2 of basement schists and gneisses is partly or wholly dehydrated into K-feldspar and quartz bearing rocks (Fig.1a). If we assume that the vertical extent of dehydration roughly equals the exhumation (≥12 km) and the original rock contained 30 % biotite (25-50 %) of which on average 50 % dehydrated, the total volume of released fluid would be 720 km^3 x 0.3 x 0.5 x 0.1 = 10.8 km^3 (7.5-21 km^3). The volume of fluid produced by biotite dehydration in a 60 km^2 area is at the lower end of the estimated fluid volume that is required to produce the Hidden Valley breccia. However, biotite dehydration may extend further to the south and east, where basement rocks are now covered below Tertiary sediments. Drilling to the east of the Paralana Fault system in the Eromanga Basin did show altered basement below the basin sediments (Sheard and Cockshell, 1992), but no systematic analysis has been done yet. An additional, but unknown amount of fluid could thus be tapped from the east of the Paralana Fault System.

(3) Surface fluids can penetrate deeply into exhumed crust, as is known from, for example, the KTB deep drilling project in Bavaria, Germany (Emmermann and Lauterjung, 1997). Here a fluid-filled porosity is found down to the bottom of the well at 9 km in crystalline rocks. Fluids at depth are highly saline, due to hydration reactions that extract H_2O from the fluid (Moeller et al., 1997; Yardley et al., 2010). Desiccation draws down fluid from the surface (Stober and Bucher, 2004) and continues until the high salinity buffers the hydration reactions. The Mesoproterozoic basement was therefore probably infiltrated by surface fluids down to a depth of ≥ 9 km at the time of the deposition of the Adelaidean Sequence (Bons and Gomez-Rivas, in press). Prior to the onset of exhumation and decompression in the Mount Painter Province the unconformity was buried by ~12 km and the connate water equilibrated to lithostatic pressure. Buried pore fluids have been invoked as a source for fluids in hydrated, Delamerian-age shear zones in the southern Curnamona Province (Clark et al., 2006b) and in Alice Springs Orogeny-age shear zones in the Reynolds-Anmatjira Ranges in Central Australia (Raimondo et al., 2011). In the case of the MPI we assume a moderate area of 20 x 30 km that provided its fluids for localisation at Hidden Valley and a porosity of 0.5-1 % down to 10 km, giving a pore-fluid volume of 24-48 km^3. This takes into account that the unconformity is presently ~2 km above Hidden Valley, and that therefore only 8 km of the infiltrated zone would be below the current outcrop. The ~12 km exhumation corresponds to ~4 kbar decompression. Using the rough estimate that 1 kbar decompression releases ~5 % of available fluid (Staude et al., 2009), we obtain ~5-10 km^3 of fluid available for brecciation. The available fluid budget again appears insufficient to produce the Hidden Valley breccia. However, pore fluids may have played a more complex role in combination with the previous mentioned mechanism (biotite dehydration) through their very high salinity (Bakker and Elburg, 2006), and hence very low water activity to facilitate the biotite-dehydration reaction.

(4) Igneous intrusions in the form of aplites, pegmatites and the British Empire Granite occurred in the Palaeozoic (Elburg et al., 2003; McLaren et al., 2006; Wülser, 2009) and could potentially have released fluids upon crystallisation. The only known large intrusion, the British Empire Granite, is ~30 km^2 in area, and, if 2 km thick, ~60 km^3 in volume (Fig.1a). At 4 wt.% water content, such an intrusion could have produced 6.5 km^3 fluid. Several equivalent intrusions would need to be invoked below current exposure level to produce the Hidden Valley breccia. This is

possible, but not favoured as a scenario, as the surroundings of the British Empire Granite do not show signs of heavy alteration. However, Staude et al. (2009) also discusses a release of a significant amount of fluid due to additional heat, e.g. during an intrusion event. A 100 °C temperature increase can lead to a release of 24 % of the available pore fluid (Staude et al., 2009). Applying this to the 24-48 km^3 available pore fluid gives ~6-12 km^3, if intrusions would have heated the whole area by ~100 °C.

The size of the Hidden Valley breccia is evidence that a large volume of fluid passed through the system. The aforementioned single fluid sources appear only sufficient for each to provide the lower end of the estimated 5-30 km^3 range of the required fluid volume. Combinations of the fluid sources do, however, seem to provide enough fluid. It could further be considered that the formation of the Hidden Valley breccia involved boiling and gas/vapour phases (e.g. Hulen and Nielson, 1988; Craw and McKeag, 1995; Xiao et al., 2002), in which much less liquid fluid would be required. However, indications for boiling were not observed in the field.

5.4 Brecciation

Above we have argued that the 10 km^2 Hidden Valley breccia would have required ~5-30 km^3 of fluid. Evidence for fluid flow is found throughout the MPI in the form of K-feldspar alteration, veins and breccias. Fluid flow occurred contemporaneously with ≥12 km exhumation during the ~200 Myrs in the Palaeozoic, starting at the ~500 Ma Delamerian Orogeny and lasting up to 290 Ma at the latest. Large areas in the centre of the MPI have lost biotite, which dehydrated to form K-feldspar, a process that would have released large quantities of fluid. Considering the potential fluid sources for brecciation (see above), we regard that this biotite dehydration is at least a significant fluid source.

There are two arguments for a main fluid source below at least 12 km depth. First, secondary, hematite-bearing fluid inclusions reported by Bakker and Elburg (2006) were trapped at ~420 °C at an assumed 40 °C/km geothermal gradient, and hence at a depth of ~10 km. We can thus infer that these fluids came from below 10 km. Second, K-feldspar alteration is strongest in the centre of the inlier and decreases towards the Adelaidean unconformity, which was buried to a maximum depth of ~12 km. That only rocks buried to such depths were affected by biotite breakdown and extensive K-feldspar

alteration indicates that the fluid activity took place at these depths. This would be the case if the fluids were sourced from biotite dehydration, but also if the alteration was the product of hydrothermal fluids, for example fluid released by felsic intrusions and fluid released by decompression and heating by these intrusions.

Based on the central hypothesis that fluids were released during exhumation at a depth below ~12 km, we propose the following model for the formation of the various breccias at the MPI where, at any one moment in time, the system can be divided in roughly three levels, which are from bottom to top (Fig.8):

1) Lower fluid-release level: Lithologies in this zone, estimated to be below ~12 km, are altered into a mostly K-feldspar and quartz (±disseminated Fe-oxides) bearing rock. This alteration involves the breakdown of biotite and the additional release of H_2O. Alteration is pervasive over large areas in the inlier. Fluids escape upwards from this level.

2) Intermediate flow focussing and brecciation level: Fluids released below ascend with their flow being focussed by pre-existing structures, such as the Paralana Fault zone and the developing Yankaninna Anticline. Flow focussing and the concomitant increase in fluid-rock ratios leads to the formation of breccia zones. The K-feldspar and quartz Radium Ridge Breccias and the Fe-oxide breccias formed at this level.

3) Upper chaotic brecciation and mixing level: Ongoing flow focussing further increases the fluid-rock ratio. Together with the low overburden pressure at this shallow level, this allows fluidisation of the breccias and fluid batches to cause significant dilation and mixing of clasts upon collapse of the dilatant zones (Fig.7). The Hidden Valley, Pinnacles and Needles breccias were formed at this level.

Fluid release, ascent, and brecciation occurred during, and were most likely caused by exhumation. This means that rocks ascended through the three levels as they were exhumed (Fig.8). Rocks in the centre of the inlier were buried ~15 km (~3 km below the Adelaidean unconformity) by ~500 Ma. During exhumation, these rocks were first pervasively altered to pink feldspar-quartz assemblages in level 1. Released fluids of the alteration zone were expelled and focussed upwards, producing breccia zones in the overlying rocks (level 2) and, higher up (level 3), further brecciation

and mixing, which would initially have been inside the Adelaidean cover. By the time secondary fluid inclusions (see above) formed in the diopside and titanite veins (Bakker and Elburg, 2006), the rocks in the centre of the inlier had exhumed to level 2 at a depth of <10 km. Rocks below that level now entered level 1 of alteration and released further fluid, which caused brecciation in the previously dehydrated rocks above them. Since brecciation is localised, we now find large areas of pervasively altered rocks, cut by Radium Ridge Breccia zones. As exhumation continued, fewer and fewer rocks that are now exposed in the centre of the inlier were affected by ascending fluids, as fluid flow was more and more localised towards the surface.

Chaotic brecciation and mixing (level 3) commenced within the Adelaidean cover, as the Adelaidean unconformity was initially buried ~12 km. With ongoing exhumation, the base of the chaotic breccia zone penetrated ever further down into the rock column (Fig.8). Rocks entering level 3 brecciated and their clasts mixed with those from the overlying breccia. While rocks in general ascended, some clasts could remain at depth, or even descend, to mix with clasts from below (Fig.7). This explains how the Hidden Valley breccia can contain Adelaidean Sequence clasts, even though the unconformity is now ~2 km above the current exposure level. Fluid-flow and brecciation in Hidden Valley continued at least until ~367 Ma, after the intrusion of a pegmatitic brannerite vein dated by Wülser (2009).

One advantage of the above model is that the same fluids are responsible for the variety of altered and brecciated rocks that form at different levels as the fluids ascend and focus their flow. This limits the amount of fluid needed. However, a significant amount of fluid is still needed, as the Hidden Valley breccia itself required ~5-30 km^3 of fluid. In the proposed model, these fluids are released over a period of up to 200 Myrs over a broad area. They were focussed towards the 10 km^2 Hidden Valley breccia. Integrated fluid fluxes here are estimated at 2000 (500-3000) m^3/m^2. To lift clasts and produce fluidisation structures, flow velocities in the order of m/s are needed (Oliver et al., 2006a). Such a high flow velocity cannot be maintained over a ~200 Myrs period and must thus have occurred in short periods or bursts. Such fluid release was proposed for the formation of large quartz veins by Bons (2001) and modelled by Bons and van Milligen (2001). In their model, fluid pressure builds up as long as fractures are closed. Failure leads to rapid rise of fluid batches in mobile hydrofractures (Bons,

2001) and may trigger avalanches of fluid release. Ascent rates of such hydrofractures can theoretically be in the order of m/s (Dahm, 2000) and minimum fluid ascent rates of 0.1 m/s has been determined for mineral veins (Okamoto and Tsuchiya, 2009).

5.5. Other occurrences of similar breccias

Considering the extent of the fluid flow and alteration, it seems unlikely that it constituted a unique event that only occurred in the MPI. We suggest that the same process may have occurred throughout the Central Flinders Ranges. Here many breccia zones in the Adelaidean cover, which are interpreted as relicts of salt diapirs, formed along hinges of thick-skinned anticlinal structures and basement-penetrating faults (Preiss, 1987; Preiss et al., 1993; Backé et al., 2010 and references therein). These 100s metres to kilometre-scale breccias consist of basement and Adelaidean clasts from mm to km-scale and arise from depths of ~2-6 km (Backé et al., 2010). These "diapirs" carry iron-oxide-quartz and barite veins and show hydrothermal alteration (Preiss, 1987; Preiss et al., 1993). They are generally assumed to have formed by the diapiric rise of lower Adelaidean evaporites (e.g. Dyson, 1998; Dyson 1999; Backé et al., 2010). Breccias from the Oraparinna Diapir (Fig. 3e), however, show a strong similarity with HV-type breccias, including alteration, lithological mixing, rounding, and wide size distribution. Mineralised veins (Fig. 3f) associated with these breccias are indicative of hydrothermal activity. We thus suggest to consider the possibility that at least some of the "diapirs" are in fact not diapirs, but HV-style breccias that resulted from exhumation in anticlinal structures, as was the case at the MPI. However, more research is needed to investigate this novel hypothesis.

The period of exhumation and brecciation in the MPI coincided with the Alice Springs Orogeny at ~450-300 Ma (Buick et al., 2008). The effects of this orogenic phase are most clearly recognised in the Central Australian Harts and Reynolds Ranges, and include magmatism, high-grade metamorphism and retrograde shear zones (Buick et al., 2008; Raimondo et al., 2011). It is possible that the HV breccia is a shallow-level expression of the same kind of processes that gave rise to the Central Australian retrograde shear zones.

6. Conclusions

The Hidden Valley breccia is unique in its size and thorough mixing of clasts that were originally km's apart. Fractal analysis shows that clast-size distribution follows a single power law, with exponent D_{2D}~1 from <mm to about the 100 m scale. This indicates that a single process caused the brecciation at all scales. Alteration, low D_{2D}, round clast shape and absence of tectonic structures indicates that the breccia is of hydrothermal origin.

Its formation during Palaeozoic exhumation can only be understood in the context of the extensive K-feldspar alteration and brecciation in the surrounding MPI. We propose a model where fluids at depth cause extensive pervasive alteration before ascending to form localised K-feldspar and quartz cemented breccia zones. Structures, such as folds and old Neoproterozoic faults focus the ascending fluids in ever-narrower zones. The whole process takes place during, and is probably caused by the differential exhumation of a crustal-scale anticlinal structure. As a result, ascending rocks pass through the different levels of fluid flow, alteration and brecciation. The deepest rocks that are now exposed were initially pervasively altered and subsequently cut by breccia zones produced by fluids that were released below. At the uppermost, focused level of the fluid flow system dilatant brecciation and subsequent collapse causes thorough mixing of clasts in the Hidden Valley type breccias.

Exhumation is essential to explain the mixing of clasts inside the Hidden Valley breccia. Chaotic brecciation and mixing commenced within the Adelaidean Sequence cover localised along fault zones and fold hinges. As the MPI exhumed, rocks below entered the chaotic brecciation level and mixed with clasts from above. Eventually the basement entered this level and basement clasts mixed with Adelaidean Sequence clasts, even though the unconformity is now estimated ~2 km above the present land surface.

Exhumation took place throughout most of the Palaeozoic, coinciding with the Alice Springs Orogeny. In Central Australia Alice Springs orogenic activity is known to be associated with hydrated shear zones (Raimondo et al., 2011), but long-standing fluid flow and tectonic activity in the Mt. Painter during this period has so far been proposed by only very few authors (Brugger et al., 2005; Elburg et al. 2012, 2013). Our work not only provides a model for the formation of the very large

Hidden Valley breccia, but also indicates that Alice Springs activity may be far more important in the South Australian Flinders Ranges than hitherto assumed and may also explain the wide-spread breccia "diapirs" found throughout this area.

Acknowledgements

This project was funded by the German Science Foundation (DFG) grant BO-1776/8-1 and by Marathon Resources Ltd. We thank Johannes Holzäpfel, Christian Kieslinger, Christian Kling, Simon Kocher, Jürgen Lang, Matthias Lindhuber, Tobias Rehder, Jens Roessiger, and Ingrid Smet for their contributions to mapping and sampling. This work would not have been possible without the hospitality and support of Arkaroola Wilderness Sanctuary, and in particular Marg and Doug Sprigg.

Figure and table captions

Fig 1 a) Location and simplified geological map of the Mt. Painter Inlier (MPI) and adjacent Adelaidean Sequence cover (adopted from Coats and Blissett, 1971). The zone of K-feldspar alteration and brecciation (Radium Ridge Breccias) is added to the map. b) Cross section X-Y through the central MPI illustrating the post-Delamerian differential exhumation and the location of the Hidden Valley breccia (based on profiles by Paul et al., 1999). c) Geological map of northern Hidden Valley. The largest clasts reach a diameter of ~300 m

Fig 2 a) Field photograph of Radium Creek Group gneiss, showing strong schistosity (S_m). b) Micrograph of deformed Mesoproterozoic biotite schist with a main Proterozoic crenulation cleavage (S_m) that is overgrown by post-deformational feldspar neoblasts. c) Thin vertical pebble dyke cutting heavily K-feldspar altered Radium Creek Group. d) Radium Creek Group gneiss that is gradually overprinted by K-feldspar alteration and loses its foliation. e) Strongly K-feldspar-altered Radium Creek Group gneiss. Only very small patches of biotite (arrow) from the biotite-schist precursor remain, still aligned along the Mesotproterozoic main foliation. f) Iron ore breccia with rounded clasts of basement rocks and altered K-feldspar lithologies. g) K-feldspar and quartz cemented breccia of K-

feldspar altered rocks (Radium Ridge Breccia). h) Near-surface Mt. Gee-type quartz-hematite sinter from Mt. Gee. i) Nailhole quartz rosettes typical for Mt. Gee Sinter

Fig 3 a) Overview of northern Hidden Valley, looking east. The two hills in the back (arrows) are large clasts in the breccia. Bright patches in the foreground are pegmatite blocks. b) Hidden Valley breccia with rounded to angular clasts of sedimentary and metamorphic rocks. 23 mm coin for scale. c) Wave ripples in a clast of Adelaidean sandstone in the Hidden Valley breccia. d) Overview of the Pinnacles breccia, looking SE. Two large pegmatite clasts (arrows) crop out in the weathered breccia. (e) Breccia from the Oraparinna Diapir in the Flinders Ranges, so far interpreted as formed by salt diapirism, but possibly of hydrothermal origin instead. (f) Hydrothermal dolomite-hematite-barite veins from the same locality as (e) in the Oraparinna Diapir.

Fig 4 Selected photographs of analysed breccia samples and the hand-drawings of the clasts. a) Thin section HVTS2 of a soft Hidden Valley breccia, showing 1/8 of the analyzed area. Well visible are the angular to rounded clasts of rock fragments and minerals, as well as a microcrystalline mass of talc, biotite, chlorite and clays in which clasts are difficult to recognize. b-c) Outcrop photographs of typical Hidden Valley-type breccias (HVPH8 and HVPH4, respectively) with a variety of heavily altered rounded clasts. d) Radium Ridge Breccia with rounded clasts of K-feldspar altered host rock (KFSP3). e) Brecciated metasediments at the Needles (NE2). f) Breccia at the Pinnacles with rounded and altered metasedimentary clasts (PI1)

Fig 5 Results of size analyses on the various breccias, where the number of clasts ($N_{>A}$) larger than a certain area (A) is plotted against that area. The slope of straight sections in these double logarithmic plots is the fractal dimension D_{2D}. a) Hidden Valley. b) The Needles and the Pinnacles and c) Radium Ridge Breccias. d) All analyses plotted together in a single graph, recalculated for an area of 3.2 km^2, which is the area of the map of northern Hidden Valley (Fig.1c). All analyses combined give a fractal dimension of D_{2D}=1.03

Fig 6 Results of shape analyses on the various breccias. a) Graph of D_R against D_{2D} with the fields for different brecciation processes of Jébrak (1997). All data, except one for the smallest clasts, plot well in the field for hydraulic brecciation. b) Graph of boundary fractal dimension (D_R) against area. Only the smallest clasts have elevated D_R values indicative of corrosive wear. c) The shape of a clast can be defined with its circularity and its ellipticity. A value for circularity ~1 means well rounded. The mean values of KFSP and HV photographs plot at high circularity, whereas data from the thin sections HVTS1+2 trend towards more irregular shapes, potentially due to corrosive wear. d) Graph of circularity as a function of clast area shows that there is no significant change in circularity with area. Variability in circularity is, however, larger for smaller clasts

Fig. 7 Schematic sketch of the HV-type brecciation shown at three stages t_1 to t_3. Fluid batches with a height of Δh move upwards if the fluid-rock ratio is high enough. After passage of the fluid batch (t_3), clasts have move down or up a distance Δz. See text for further explanation

Fig. 8 Simplified model of hydrothermal alteration and brecciation levels. During differential exhumation between ~500-300 Ma the MPI moved through these levels. a) Situation after the deposition of the Adelaidean Sequence and at the beginning of the differential exhumation. Fluid focusing results in early Hidden Valley-type brecciation in Adelaidean rocks. b) Basement rocks move through the zone of alteration and brecciation. Hidden Valley-type brecciation continues at zones of maximum fluid-focusing. c) Continuing fluid-release results in multiple overprinting and brecciation. With ongoing exhumation basement rocks move through the zone of Hidden Valley-type brecciation and start to mix with Adelaidean sedimentary rocks (see Fig. 7)

Table 1 Results of the breccia analysis of all measured samples. Mean D_{2D} values are the mean of the slopes of all straight sections in a log$N$>A vs. log$A$ plot. N total: number of all measured clasts; N selection: number of clasts in a straight section. See text for further description

References cited

Armit RJ, Betts PG, Schaefer BF, Ailleres L (2012) Constraints on long-lived Mesoproterozoic and Palaeozoic deformational events and crustal architecture in the northern Mount Painter Province, Australia. Gondwana Res 22: 207-226

Backé G, Baines G, Giles D, Preiss W, Alesci A (2010) Basin geometry and salt diapirs in the Flinders Ranges, South Australia: Insights gained from geologically-constrained modelling of potential field data. Mar Petrol Geol 27: 650-665

Bakker RJ, Elburg MA (2006) A magmatic-hydrothermal transition in Arkaroola (Northern Flinders Ranges, South Australia): from diopside-titanite pegmatites to hematite-quartz growth. Contrib Mineral Petr 152: 541-569

Barnett W (2004) Subsidence breccias in kimberlite pipes - an application of fractal analysis. Lithos 76: 299-316

Bergman L, Tynni R, Winterhalter B (1982) Paleozoic sediments in the rapakivi area of the Aland Islands. Geological Survey of Finland. Bulletin 317

Bérubé D, Jébrak M (1999) High precision boundary fractal analysis for shape characterization. Comput Geosci-UK 25: 1059-1071

Blenkinsop TG (1991) Cataclasis and Processes of Particle-Size Reduction. Pure Appl Geophys 136: 59-86

Boiron M-C, Cathelineau M, Richard A (2010) Fluid flows and metal deposition near basement/cover unconformity: lessons and analogies from Pb-Zn-F-Ba systems for the understanding of Proterozoic U deposits. Geofluids 10: 270-292

Bons PD (2001) The formation of large quartz veins by rapid ascent of fluids in mobile hydrofractures. Tectonophysics 336: 1-17

Bons, P.D., Gomez-Rivas, E. *(in press*) Gravitational fractionation of isotopes and dissolved components as a first-order process in hydrothermal crustal fluids. Economic Geology.

Bons PD, van Milligen BP (2001) A new experiment to model self-organized critical transport and accumulation of melt and hydrocarbons from their source rocks. Geology 29: 919-922

Bons PD, Elburg MA, Gomez-Rivas E (2012) A review of the formation of tectonic veins and their microstructures. J Struct Geol. doi:10.1016/j.jsg.2012.07.005

Brugger J, Long N, McPhail DC, Plimer I (2005) An active amagmatic hydrothermal system: The Paralana hot springs, Northern Flinders Ranges, South Australia. Chemical Geology 222: 35-64

Brugger J, Wülser PA, Foden J (2011) Genesis and preservation of a uranium-rich paleozoic epithermal system with a surface expression (Northern Flinders Ranges, South Australia): Radiogenic heat driving regional hydrothermal circulation over geological timescales. Astrobiology 11: 499-508

Buick IS, Storkey A, Williams IS (2008) Timing relationships between pegmatite emplacement, metamorphism and deformation during the intra-plate Alice Springs Orogeny, central Australia. J Metamorph Geol 26: 915-936

Campana B., Coats RP., Horwitz R., Thatcher D (1961) Paralana sheet, Geological Atlas of South Australia, 1: 63,360 Series. Geological Survey South Australia

Célérier J, Sandiford M, Lundbek HD, Quigley M (2005) Modes of active intraplate deformation, Flinders Ranges, Australia. Tectonics 24, TC6006, doi: 10.1029/2004TC001679

Clark C, Mumm AS, Collins AS (2006a) A coupled micro- and macrostructural approach to the analysis of fluid induced brecciation, Curnamona Province, South Australia. J Struct Geol 28: 745-761

Clark C, Hand M, Faure K, Schmidt M (2006b) Up-temperature flow of surface-derived fluids in the mid-crust: the role of pre-orogenic burial of hydrated fault rocks. J Metamorph Geol 24: 367-387

Coats RP, Blissett AH (1971) Regional and economic geology of the Mount Painter Province. Geological Survey of South Australia. Bulletin 43

Cowley WM, Hore SB, Preiss WV, Sheard MJ, Wade C (2012) A revised stratigraphic scheme for the Mount Painter and Mount Babbage Inliers. SAREIC 2012 Technical forum poster. IOP Publishing minerals.dmitre:

http://minerals.dmitre.sa.gov.au/press_and_events/events/sareic_2012_technical_forum

Craw D, McKeag SA (1995) Structural Control of Tertiary Au-Ag-Bearing Breccias in an Extensional Environment, Nelson Area, Southern Nevada, USA. Miner Deposita 30: 1-10

Dahm T (2000) On the shape and velocity of fluid-filled fractures in the earth. Geophys J Int 142: 181-192

Dipple GM, Bons P, Oliver NHS (2005) A vector of high-temperature paleo-fluid flow deduced from mass transfer across permeability barriers (quartz veins). Geofluids 5: 67-82

Drexel JF, Major RB (1987) Geology of the uraniferous breccia near Mt Painter, South Australia and revision of rock nomenclature. Geological Survey of South Australia. Quarterly Notes 104: 14-24

Drexel JF, Major RB (1990) Mount Painter uranium – rare earth deposits. In: Hughes FE (ed) Geology of the Mineral Deposits of Australia and Papua New Guinea. Australian Institute of Mining and Metallurgy, Melbourne, pp 993-998

Drexel JF, Preiss WV (1995) The geology of South Australia. Volume 2: The Phanerozoic. Geological Survey of South Australia. Bulletin 54

Dyson IA (1998) The "Christmas tree diapir" and salt glacier at Pinda Springs, central Flinders Ranges. Primary Industries and Resources SA. MESA Journal 10: 40-43

Dyson IA (1999) The Beltana Diapir – a salt withdrawal minibasin in the northern Flinders Ranges. Primary Industries and Resources SA. MESA Journal 15: 40-46

Elburg MA, Bons PD, Dougherty-Page J, Janka CE, Neumann N, Schaefer B (2001) Age and metasomatic alteration of the Mt Neill Granite at Nooldoonooldoona Waterhole, Mt Painter Inlier, South Australia. Aust J Earth Sci 48: 721-730

Elburg MA, Bons PD, Foden J, Brugger J (2003) A newly defined Late Ordovician magmatic-thermal event in the Mt Painter Province, Northern Flinders Ranges, South Australia. Aust J Earth Sci 50: 611-631

Elburg MA, Andersen T, Bons PD, Weisheit A, Simonsen SL, Smet I (2012) Metasomatism and metallogeny of A-type granites of the Mt Painter - Mt Babbage Inliers, South Australia. Lithos 151: 83-104

Elburg MA, Andersen T, Bons PD, Simonsen SL, Weisheit A (2013). New constraints on Phanerozoic magmatic and hydrothermal events in the Mt Painter Province, South Australia. Gondwana Research. doi: 10.1016/j.gr.2012.12.017

Emmermann R, Lauterjung J (1997) The German Continental Deep Drilling Program KTB: Overview and major results. J Geophys Res 102: 18179-18201

Epstein B (1947) The mathematical description of certain breakage mechanism leading to the logarithmic-normal distribution. J. Franklin Institute 244: 471-477

Fanning CM, Teale GS, Robertson RSI (2003) Is there a Willyama Supergroup sequence in the Mount Painter Inlier?. In: Peljo M (ed) Broken Hill Exploration Initiative. Geoscience Australia Record 13: 38-41

Foden J, Elburg MA, Dougherty-Page J, Burtt A (2006) The timing and duration of the Delamerian Orogeny: Correlation with the Ross Orogen and implications for Gondwana assembly. J Geol 114: 189-210

Fraser GL, Neumann NL (2010) New SHRIMP U-Pb zircon ages from the Gawler Craton and Curnamona Province, South Australia, 2008-2010. Geoscience Australia Record 2010/16.

Friese N, Vollbrecht A, Leiss B, Jacke O (2010) Cambrian sedimentary dykes in the Proterozoic basement of the Västervik area (southeast Sweden): episodic formation inferred from macro- and microfabrics. Int J Earth Sci. doi: 10.1007/s00531-009-0508-3

Gardien V, Thompson AB, Ulmer P (2000) Melting of biotite plus plagioclase plus quartz gneisses: the role of H2O in the stability of amphibole. J Petrol 41: 651-666

Graphchikov AA, Konilov AN, Clemens JD (1999) Biotite dehydration, partial melting, and fluid composition: Experiments in the system KAlO2-FeO-MgO-SiO2-H2O-CO2. Am Mineral 84: 15-26

Holness MB (2003) Growth and albitization of K-feldspar in crystalline rocks in the shallow crust: a tracer for fluid circulation during exhumation?. Geofluids 3: 89-102

Hulen JB, Nielson DL (1988) Hydrothermal Brecciation in the Jemez Fault Zone, Valles Caldera, New-Mexico - Results from Continental Scientific Drilling Program Core Hole Vc-1. J Geophys Res 93 (B6): 6077-6089

Hyslip JP, Vallejo LE (1997) Fractal analysis of the roughness and size distribution of granular materials. Eng Geol 48: 231-244

Janak M, Hurai V, Ludhova L, O'Brien PJ, Horn EE (1999) Dehydration melting and devolatilization during exhumation of high-grade metapelites: the Tatra Mountains, Western Carpathians. J Metamorph Geol 17: 379-395

Jébrak M (1997) Hydrothermal breccias in vein-type ore deposits: A review of mechanisms, morphology and size distribution. Ore Geol Rev 12: 111-134

Keulen N, Heilbronner R, Stünitz H, Boullier A-M, Ito H (2007) Grain size distribution of fault rocks: A comparison between experimentally and naturally deformed granitoids. J Struct Geol 29: 1282-1300

Lazincka P (1989) Breccias and ores. Part 1: History, organization and petrography of breccias. Ore Geol Rev 4: 315-344

Lorilleux G, Jébrak M, Cuney M, Baudemont D (2002) Polyphase hydrothermal breccias associated with unconformity-related uranium mineralization (Canada): from fractal analysis to structural significance. J Struct Geol 24: 323-338

Marone C, Scholz CH (1989) Particle-Size Distribution and microstructures within simulated fault gouge. J Struct Geol 11: 799-814

McCaig AM (1988) Deep fluid circulation in fault zones. Geology 16: 867-870

McCallum ME (1985) Experimental evidence for fluidization processes in breccia pipe formation. Econ Geol 80: 1523-1543

McLaren S, Dunlap WJ, Sandiford M, McDougall I (2002) Thermochronology of high heat-producing crust at Mount Painter, South Australia: Implications for tectonic reactivation of continental interiors. Tectonics 21: 1-18

McLaren S, Sandiford M, Powell R, Neumann N, Woodhead J (2006) Palaeozoic intraplate crustal anatexis in the Mount Painter Province, South Australia: Timing, thermal budgets and the role of crustal heat production. J Petrol 47: 2281-2302

McPhie J, Kamenetsky VS, Chambefort I, Ehrig K, Green N (2011) Origin of the supergiant Olympic Dam Cu-U-Au-Ag deposit, South Australia: Was a sedimentary basin involved?. Geology 39: 795-798

Mildren SD, Sandiford M (1995) Heat refraction and low-pressure metamorphism in the Northern Flinders Ranges, South Australia. Aust J Earth Sci 42: 241-247

Mort K, Woodcock NH (2008) Quantifying fault breccia geometry: Dent Fault, NW England. J Struct Geol 30: 701-709

Moeller P, Weise SM, Althaus E, Bach W, Behr HJ, Borchardt R, Braeuer K, Drescher J, Erzinger J, Faber E, Hansen BT, Horn EE, Huenges E, Kaempf H, Kessels W, Kirsten T, Landwehr D, Lodemann M, Machon L, Pekdeger A, Pielow HU, Reutel C, Simon K, Walther J, Weinlich FH, Zimmer M (1997) Paleofluids and recent fluids in the upper continental crust; results from the German Continental Deep-Drilling Program (KTB). J Geophys Res 102 (B8)

Nijland TG, Touret JLR, Visser D (1998) Anomalously low temperature orthopyroxene, spinel, and sapphirine occurrences in metasediments from the Bamble amphibolite-to-granulite facies transition zone (South Norway): Possible evidence for localized action of saline fluids. J Geol 106: 575-590

Okamoto A, Tsuchiya N (2009) Velocity of vertical fluid ascent within vein-forming fractures. Geology 37: 563-566

Oliver NHS, Rubenach MJ, Fu B, Baker T, Blenkinsop TG, Cleverley JS, Marshall LJ, Ridd PJ, (2006a) Granite-related overpressure and volatile release in the mid crust: fluidized breccias from the Cloncurry District, Australia. Geofluids 6: 346-358

Oliver NHS, McLellan JG, Hobbs BE, Cleverley JS, Ord A, Feltrin L (2006b) Numerical Models of Extensional Deformation, Heat Transfer, and Fluid Flow across Basement-Cover Interfaces during Basin-Related Mineralization. Econ Geol 101: 1-31

Oreskes N, Einaudi MT (1990) Origin of rare-earth element-enriched hematite breccias at the Olympic-Dam Cu-U-Au-Ag deposit, Roxby Downs, South Australia. Econ Geol 85: 1-28

Paul E, Flöttmann T, Sandiford M (1999) Structural geometry and controls on basement-involved deformation in the northern Flinders Ranges, Adelaide Fold Belt, South Australia. Aust J Earth Sci 46: 343-354

Perfect E (1997) Fractal models for the fragmentation of rocks and soils: a review. Eng Geol 48: 185-198

Preiss WV, Belperio AP, Cowley WM, Rankin LR (1993) Neoproterozoic. In: Drexel JF, Preiss WV, Parker AJ (eds) The Geology of South Australia: The Precambrian. South Australian Geological Survey. Bulletin 1, 170–203

Preiss WV (1987) The Adelaide Geosyncline: Late Proterozoic stratigraphy, sedimentation, palaeontology and tectonics. Geological Survey of South Australia. Bulletin 53

Preiss WV (2000) The Adelaide Geosyncline of South Australia and its significance in Neoproterozoic continental reconstruction. Precambrian Res 100: 21-63

Rajesh HM, Belyanin GA, Safonov OG, Kovaleva EI, Golunova MA, Van Reenen DD (2012) Fluid-induced Dehydration of the Paleoarchean Sand River Biotite–Hornblende Gneiss, Central Zone, Limpopo Complex, South Africa. J Petrol. doi: 10.1093/petrology/egs062

Raimondo T, Clark C, Hand M, Faure K (2011) Assessing the geochemical and tectonic impacts of fluid-rock interaction in mid-crustal shear zones: a case study from the intracontinental Alice Springs Orogen, central Australia. J Metamorph Geol 29: 821-850

Reimold WU, Koeberl C, Bishop J (1994) Roter Kamm Impact Crater, Namibia - Geochemistry of Basement Rocks and Breccias. Geochim Cosmochim Ac 58: 2689-2710

Sandiford M, Hand M, McLaren S (1998) High geothermal gradient metamorphism during thermal subsidence. Earth Planet Sc Lett 163: 149-165

Scrimgeour I, Smith JB, Raith JG (2001) Palaeoproterozoic high-T, low-P metamorphism and dehydration melting in metapelites from the Mopunga Range, Arunta Inlier, central Australia. J Metamorph Geol 19: 739-757

Sheard M, Cockshell CD (1992) Seismic interpretation of Mt. Hopeless Line 1. Department of Energy and Science SA. Report book 92/17

Sibson RH (1986) Brecciation Processes in Fault Zones - Inferences from Earthquake Rupturing. Pure Appl Geophys 124: 159-175

Skirrow RG (ed) (2011) Uranium mineralization events in Australia: geochronology of the Nolans Bore, Oasis, Kintyre, Mt Gee-Armchair, and Maureen uranium deposits. Geoscience Australia Record 2011/12

Staude S, Bons PD, Markl G (2009) Hydrothermal vein formation by extension-driven dewatering of the middle crust: An example from SW Germany. Earth Planet Sc Lett 286: 387-395

Storti F, Billi A, Salvini F (2003) Particle size distributions in natural carbonate fault rocks: insights from non-self-similar cataclasis. Earth Planet Sc Lett 206: 173-186

Stober I, Bucher K (2004) Fluid sinks within the earth's crust. Geofluids 4: 143-151

Teale GS (1993) Mount Painter and Mount Babbage Inliers. In: Drexel JF, Preiss WV, Parker AJ (eds) The Geology of South Australia, Geological Survey of South Australia Bulletin 54(1), pp 93–100

Wright V, Woodcock NH, Dickson JAD (2009) Fissure fills along faults: Variscan examples from Gower, South Wales. Geol Mag 146: 890-902

Wülser PA (2009) Uranium metallogeny in North Flinders Ranges region of South Australia. Dissertation, Adelaide University, Adelaide.

Wülser PA, Brugger J, Foden J, Pfeifer HR (2011) The sandstone-hosted Beverley Uranium deposit, Lake Frome Basin, South Australia: Mineralogy, geochemistry, and a time-constrained model for its genesis. Econ Geol 106: 835-867

Xiao XJ, Gu LX, Ni P (2002) Multi-episode fluid boiling in the Shizishan copper-gold deposit at Tongling, Anhui Province: its bearing on ore formation. Sci China Ser D 45: 34-44

Yardley BWD, Harlov DE, Heinrich W (2010) Rates of retrograde metamorphism and their implications for crustal rheology. Geofluids 10: 234-240 Brugger, J., Long, N., McPhail, D.C. and Plimer, I., 2005. An active amagmatic hydrothermal system: The Paralana hot springs, Northern Flinders Ranges, South Australia. Chemical Geology, 222: 35-64.

Fig.1:

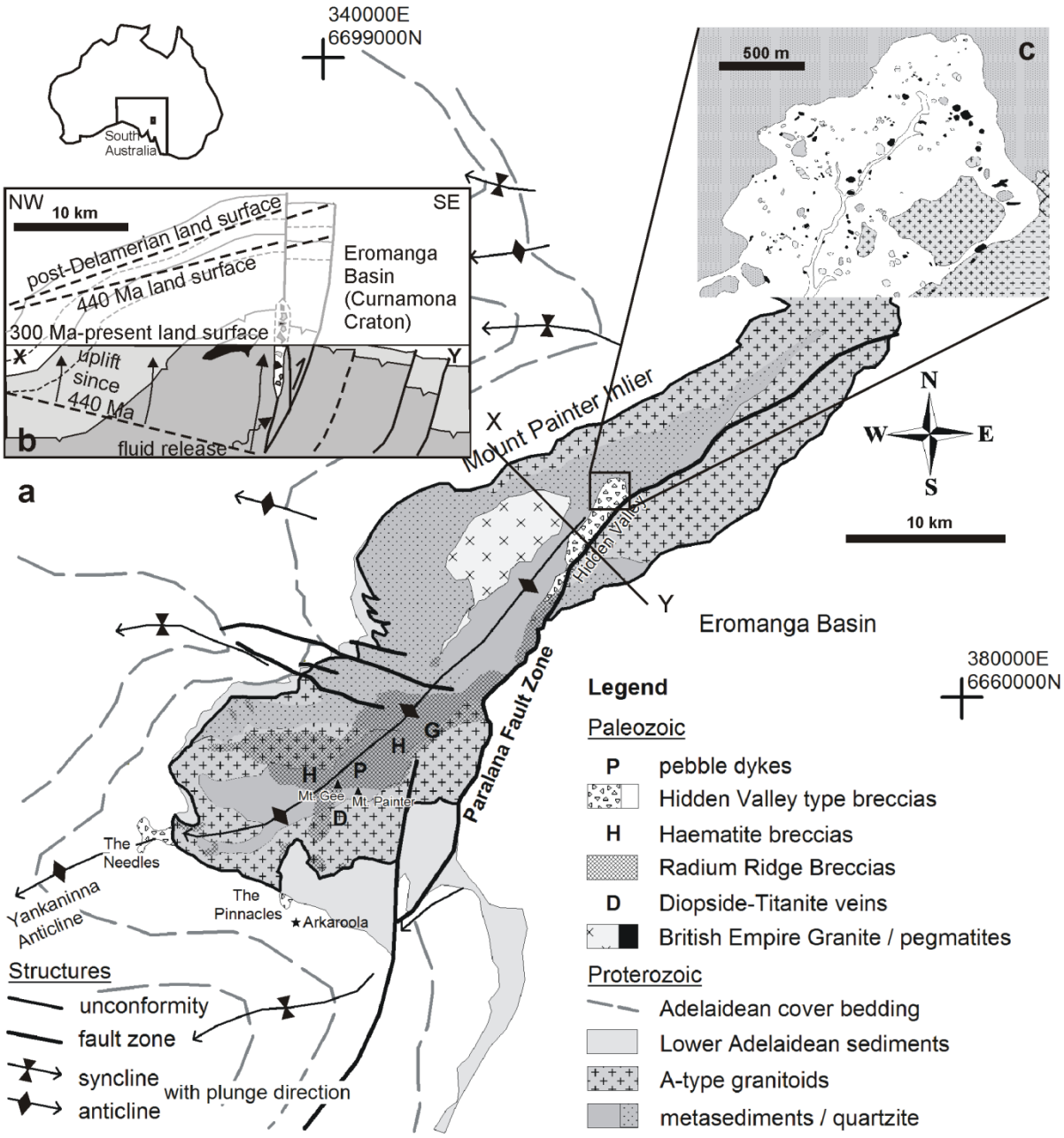

Fig. 1 a) Location and simplified geological map of the Mt. Painter Inlier (MPI) and adjacent Adelaidean Sequence cover (adopted from Coats and Blissett, 1971). The zone of K-feldspar alteration and brecciation (Radium Ridge Breccias) is added to the map. b) Cross section X-Y through the central MPI illustrating the post-Delamerian differential exhumation and the location of the Hidden Valley breccia (based on profiles by Paul et al., 1999). c) Geological map of northern Hidden Valley. The largest clasts reach a diameter of ~300 m.

Fig.2:

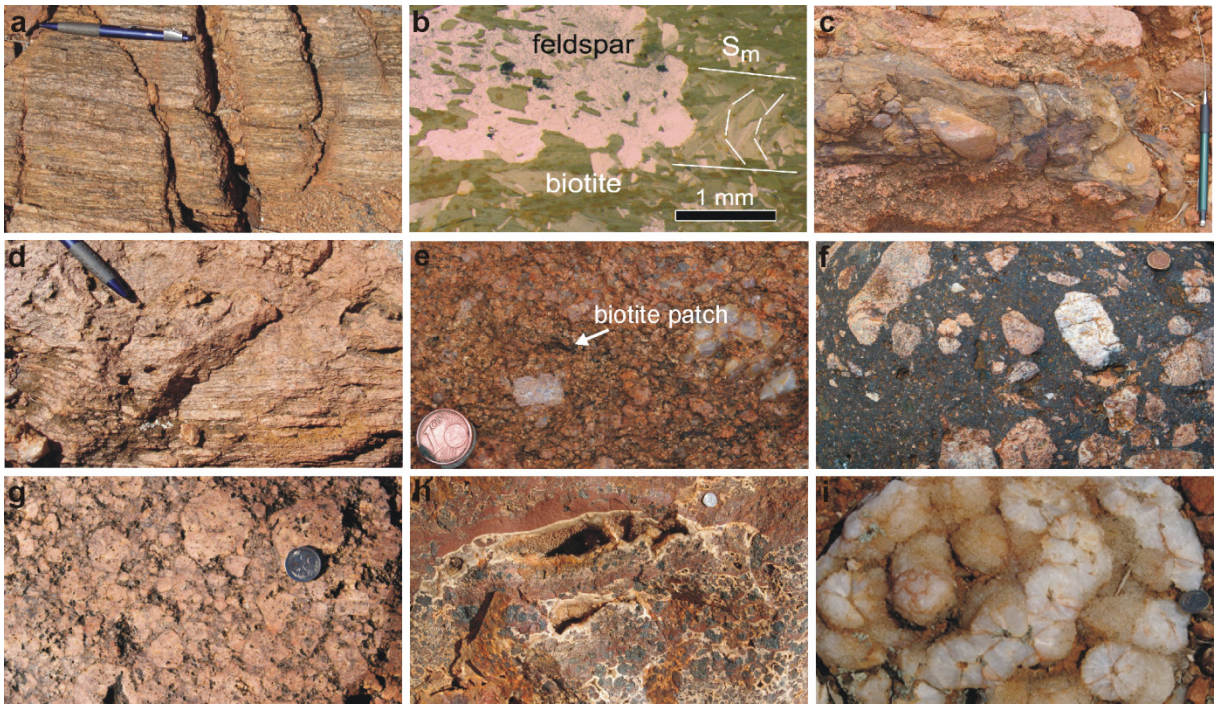

Fig. 2 a) Field photograph of Radium Creek Group gneiss, showing strong schistosity (S_m). b) Micrograph of deformed Mesoproterozoic biotite schist with a main Proterozoic crenulation cleavage (S_m) that is overgrown by post-deformational feldspar neoblasts. c) Thin vertical pebble dyke cutting heavily K-feldspar altered Radium Creek Group. d) Radium Creek Group gneiss that is gradually overprinted by K-feldspar alteration and loses its foliation. e) Strongly K-feldspar-altered Radium Creek Group gneiss. Only very small patches of biotite (arrow) from the biotite-schist precursor remain, still aligned along the Mesotproterozoic main foliation. f) Iron ore breccia with rounded clasts of basement rocks and altered K-feldspar lithologies. g) K-feldspar and quartz cemented breccia of K-feldspar altered rocks (Radium Ridge Breccia). h) Near-surface Mt. Gee-type quartz-haematite sinter from Mt. Gee. i) Nailhole quartz rosettes typical for Mt. Gee Sinter

Fig.3:

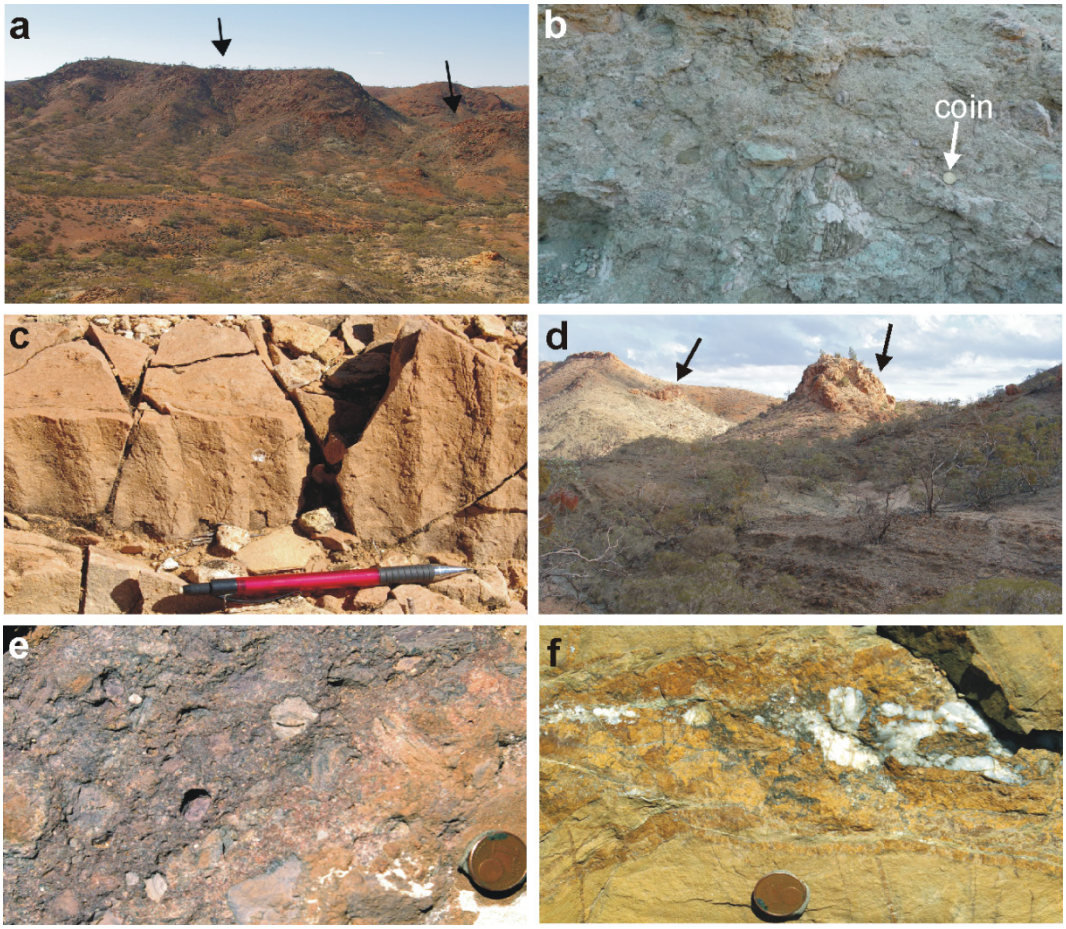

Fig. 3 a) Overview of northern Hidden Valley, looking east. The two hills in the back (arrows) are large clasts in the breccia. Bright patches in the foreground are pegmatite blocks. b) Hidden Valley breccia with rounded to angular clasts of sedimentary and metamorphic rocks. 23 mm coin for scale. c) Wave ripples in a clast of Adelaidean sandstone in the Hidden Valley breccia. d) Overview of the Pinnacles breccia, looking SE. Two large pegmatite clasts (arrows) crop out in the weathered breccia. (e) Breccia from the Oraparinna Diapir in the Flinders Ranges, so far interpreted as formed by salt diapirism, but possibly of hydrothermal origin instead. (f) Hydrothermal dolomite-hematite-barite veins from the same locality as (e) in the Oraparinna Diapir.

Fig.4:

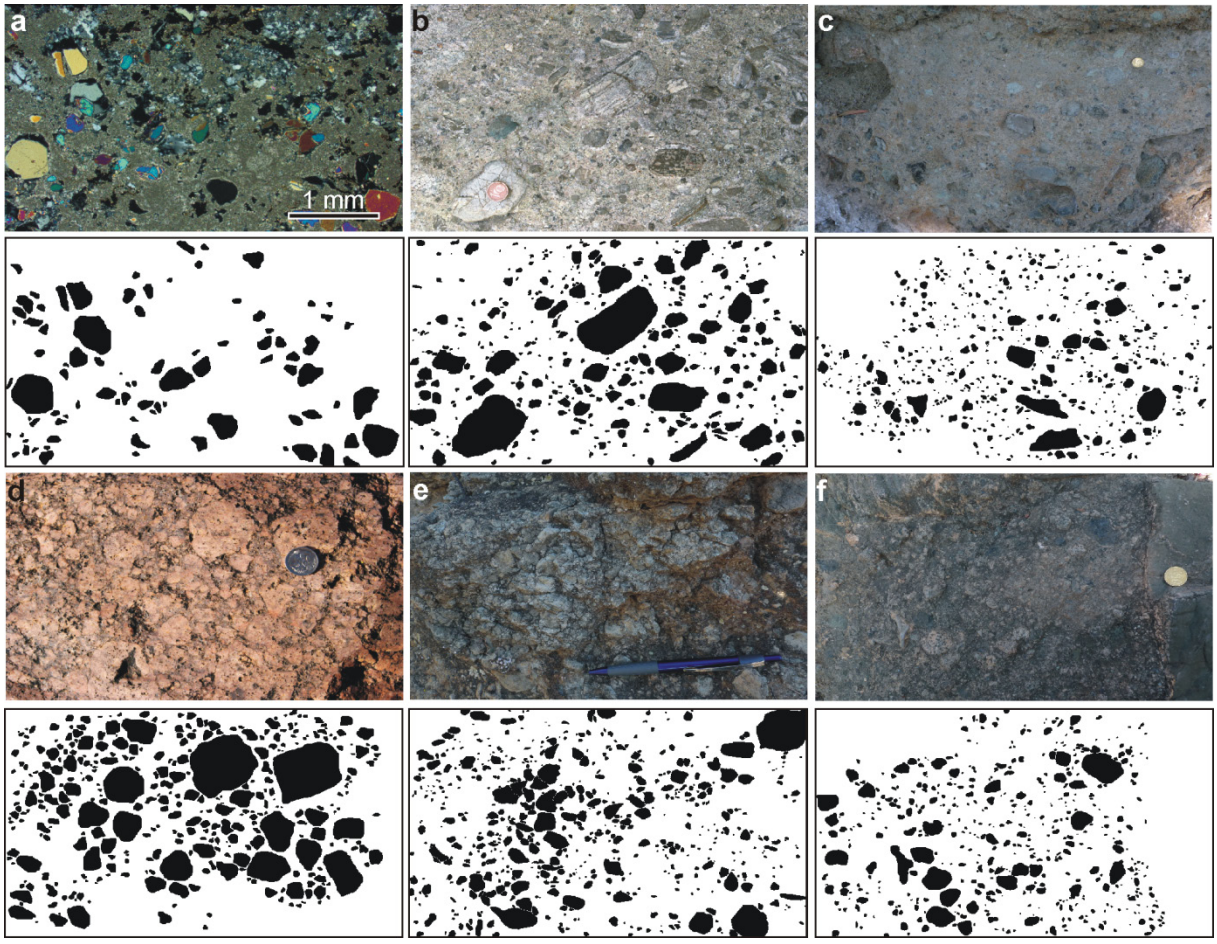

Fig. 4 Selected photographs of analysed breccia samples and the hand-drawings of the clasts. a) Thin section HVTS2 of a soft Hidden Valley breccia, showing 1/8 of the analyzed area. Well visible are the angular to rounded clasts of rock fragments and minerals, as well as a microcrystalline mass of talc, biotite, chlorite and clays in which clasts are difficult to recognize. b-c) Outcrop photographs of typical Hidden Valley-type breccias (HVPH8 and HVPH4, respectively) with a variety of heavily altered rounded clasts. d) Radium Ridge Breccia with rounded clasts of K-feldspar altered host rock (KFSP3). e) Brecciated metasediments at the Needles (NE2). f) Breccia at the Pinnacles with rounded and altered metasedimentary clasts (PI1)

Fig.5:

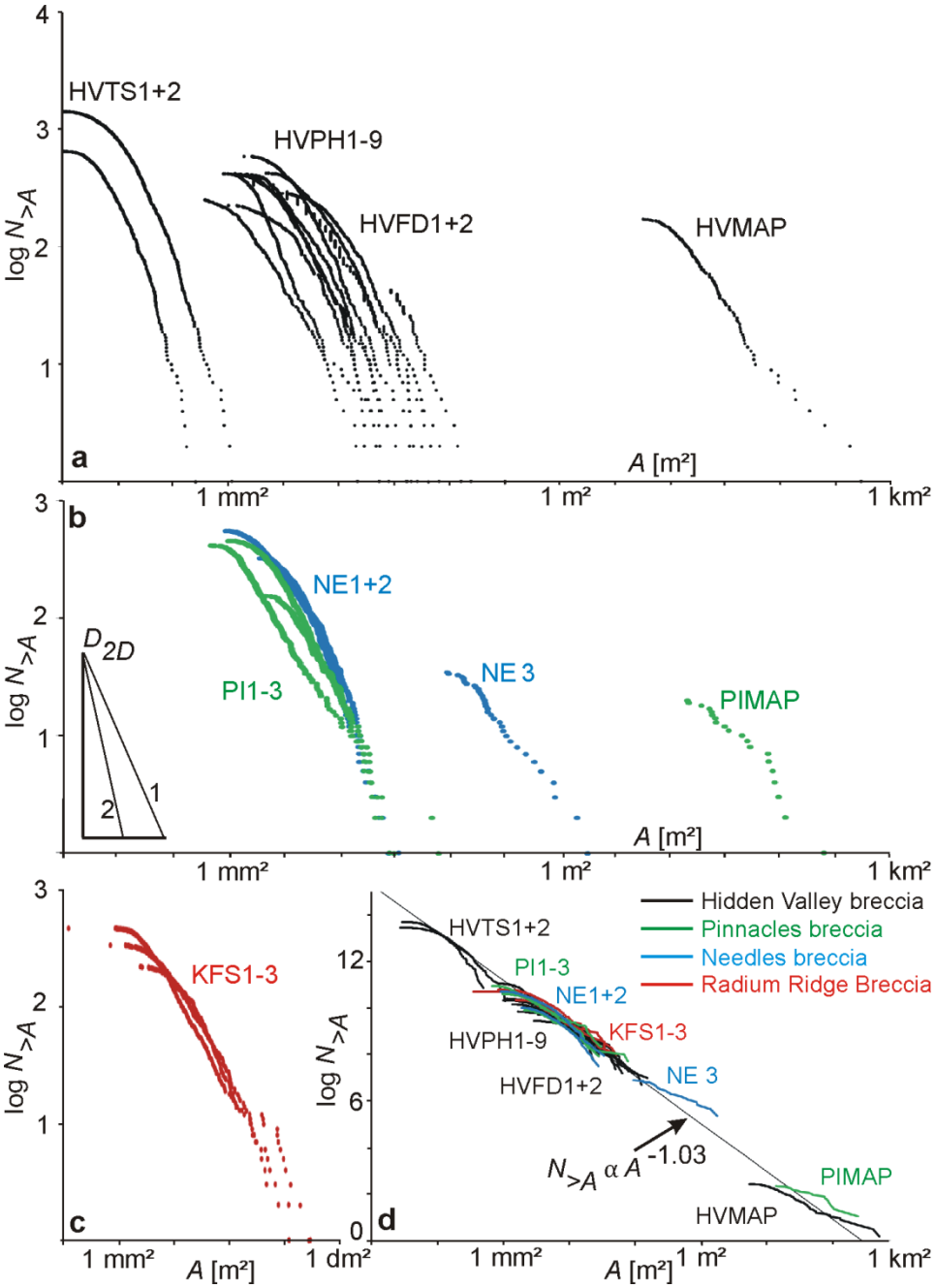

Fig. 5 Results of size analyses on the various breccias, where the number of clasts ($N_{>A}$) larger than a certain area (A) is plotted against that area. The slope of straight sections in these double logarithmic plots is the fractal dimension D_{2D}. a) Hidden Valley. b) The Needles and the Pinnacles and c) Radium Ridge Breccias. d) All analyses plotted together in a single graph, recalculated for an area of 3.2 km^2, which is the area of the map of northern Hidden Valley (Fig.1c). All analyses combined give a fractal dimension of D_{2D}=1.03

Fig.6:

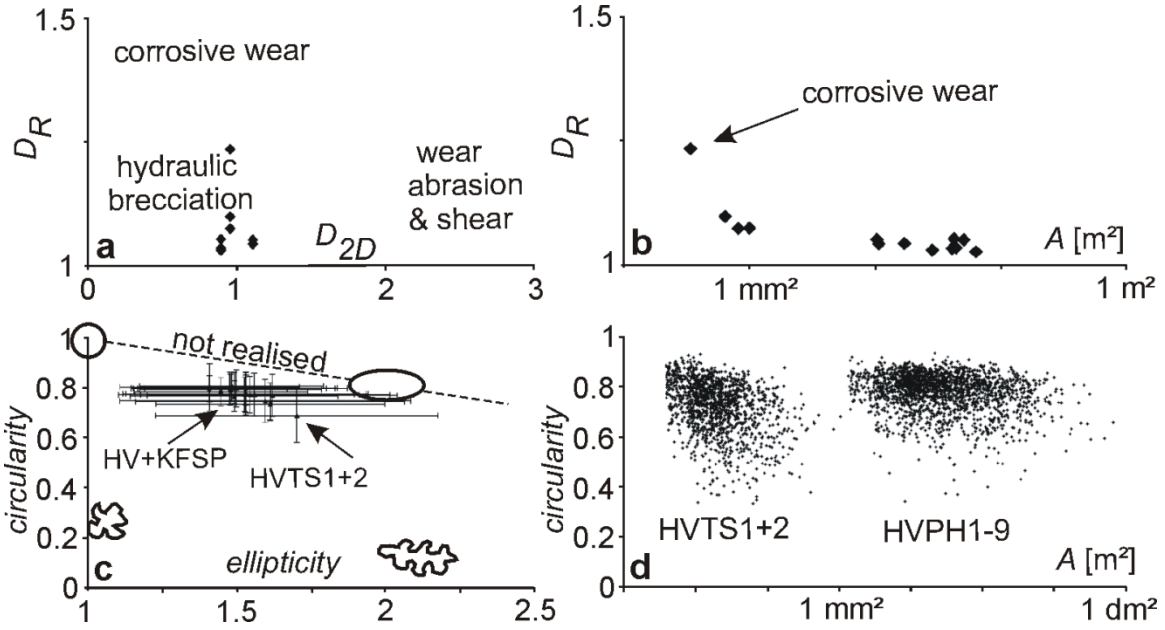

Fig. 6 Results of shape analyses on the various breccias. a) Graph of D_R against D_{2D} with the fields for different brecciation processes of Jébrak (1997). All data, except one for the smallest clasts, plot well in the field for hydraulic brecciation. b) Graph of boundary fractal dimension (D_R) against area. Only the smallest clasts have elevated D_R values indicative of corrosive wear. c) The shape of a clast can be defined with its circularity and its ellipticity. A value for circularity ~1 means well rounded. The mean values of KFSP and HV photographs plot at high circularity, whereas data from the thin sections HVTS1+2 trend towards more irregular shapes, potentially due to corrosive wear. d) Graph of circularity as a function of clast area shows that there is no significant change in circularity with area. Variability in circularity is, however, larger for smaller clasts

Fig.7:

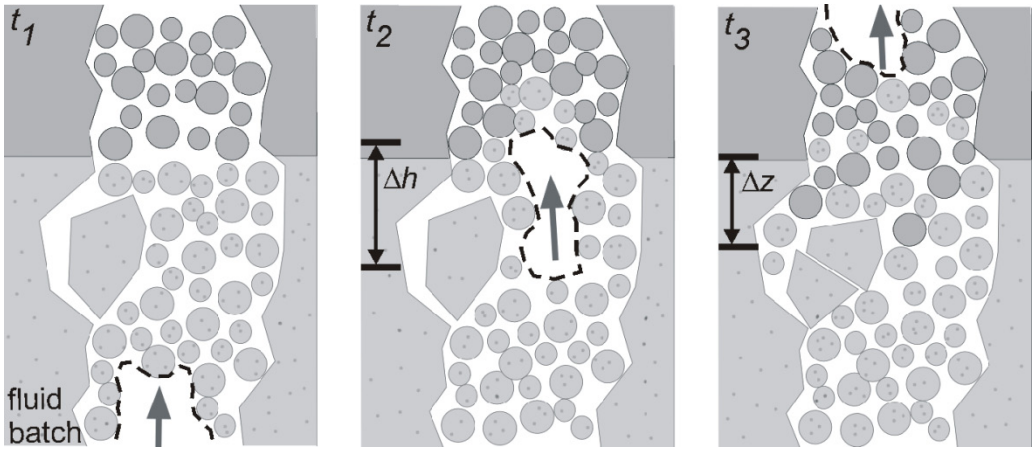

Fig. 7 Schematic sketch of the HV-type brecciation shown at three stages t_1 to t_3. Fluid batches with a height of Δh move upwards if the fluid-rock ratio is high enough. After passage of the fluid batch (t_3), clasts have move down or up a distance Δz. See text for further explanation

Fig.8:

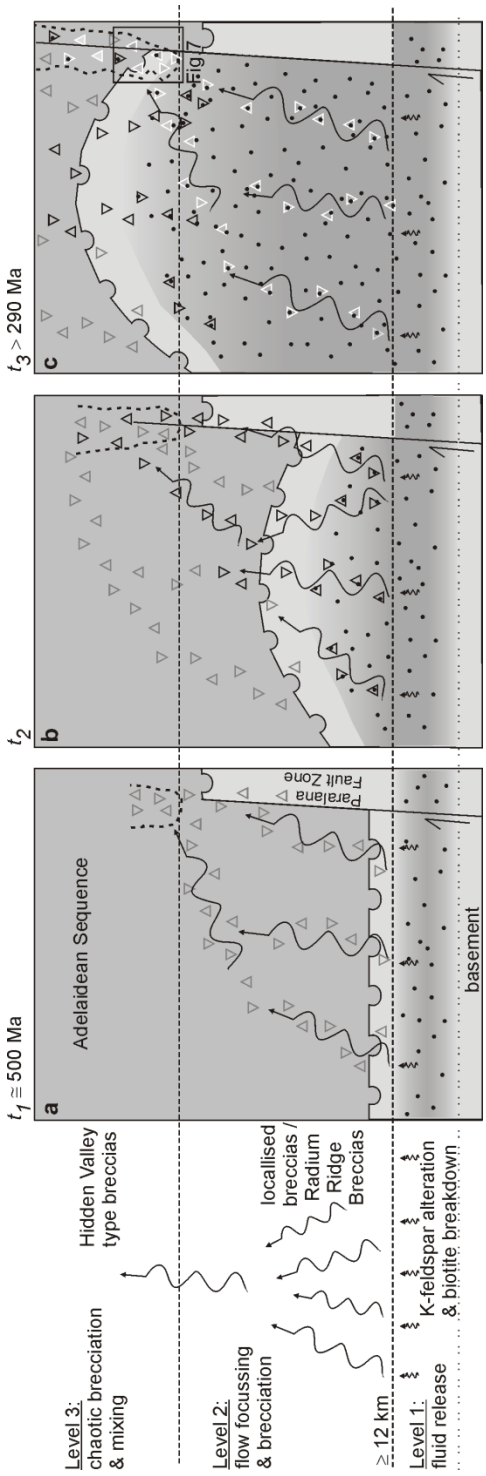

Fig 8 Simplified model of hydrothermal alteration and brecciation levels. During differential exhumation between ~500-300 Ma the MPI moved through these levels. a) Situation after the deposition of the Adelaidean Sequence and at the beginning of the differential exhumation. Fluid focusing results in early Hidden Valley-type brecciation in Adelaidean rocks. b) Basement rocks move through the zone of alteration and brecciation. Hidden Valley-type brecciation continues at zones of maximum fluid-focusing. c) Continuing fluid-release results in multiple overprinting and brecciation. With ongoing exhumation basement rocks move through the zone of Hidden Valley-type brecciation and start to mix with Adelaidean sedimentary rocks (see Fig. 7)

Table 1

type	sample	morphology	*N* total	*N* selection	D_{2D}	mean D_{2D}	mean ellipticity of selection	mean circularity of selection	mean area *A* [mm²]
K-feldspar cemented breccia	KFSP1	corrosion, rounded	478	389	0.837		1.53	0.80	25
	KFSP2	rounded	225	144	0.896		1.41	0.80	123
	KFSP3	rounded	342	215	0.845	1.07	1.45	0.79	52
Hidden Valley - type breccia	HVMAP	rounded	176	94	0.734				2311
	HVFD1	rounded	43	42	1.097				
	HVFD2	rounded	368	189	0.823				
	HVPH1	rounded	289	172	0.936		1.59	0.75	463
	HVPH2	rounded	227	194	0.866		1.61	0.75	63
	HVPH3	rounded	425	289	0.819		1.53	0.78	39
	HVPH4	corrosion, rounded	601	338	1.011		1.48	0.81	89
	HVPH5	rounded	423	265	0.701		1.54	0.77	71
	HVPH6	rounded	253	182	0.757		1.48	0.79	8
	HVPH7	rounded	433	241	0.692		1.50	0.80	127
	HVPH8	rounded	420	277	0.891		1.41	0.80	40
	HVPH9	rounded	424	312	1.105		1.56	0.77	9
thin section	HVTS1	angular-rounded	1448	819	0.943		1.70	0.69	0.05
thin section	HVTS2	angular-rounded	670	500	0.943	1.07	1.62	0.77	0.02
The Needles	NE1	rounded	328	227	0.916		1.48	0.80	61
	NE2	rounded	559	370	0.663		1.53	0.78	23
	NE3	rounded	35	31			1.61	0.74	30
The Pinnacles	PI1	rounded, consolidated	459	264	0.915		1.49	0.80	27
	PI2	rounded, consolidated	423	364	0.775		1.53	0.78	19
	PI3	rounded	157	128	0.77	1.15	1.49	0.77	57
	PIMAP	angular	20	20			1.84	0.77	105000

Table 1 Results of the breccia analysis of all measured samples. Mean D_{2D} values are the mean of the slopes of all straight sections in a log$N$>A vs. log$A$ plot. N total: number of all measured clasts; N selection: number of clasts in a straight section. See text for further description

---------- **APPENDIX 3 (ELBURG ET AL., 2013)** ----------

New constraints on Phanerozoic magmatic and hydrothermal events in the Mt Painter Province, South Australia

Marlina A. Elburg [a,b], Tom Andersen [c], Paul D. Bons [d], Siri L. Simonsen [c], Anett Weisheit [d]

[a] Department of Geology and Soil Science, Ghent University, Belgium

[b] Geology Division, SAEES, University of KwaZulu-Natal, South Africa

[c] Department of Geosciences, University of Oslo, Norway

[d] Department of Geosciences, Eberhard Karls University, Tübingen, Germany

Abstract

Zircon and monazite U–Pb dating show a punctuated history of tectonic, magmatic and hydrothermal activity in the Mt Painter Province (South Australia) that spans most of the Palaeozoic. The Cambro-Ordovician Delamerian Orogeny was characterised by very limited intrusions of sodic pegmatitic leucogranites, for which the Hf isotopic data show influence of an isotopically more primitive source than the local Mesoproterozoic granitoids and metasediments. Another phase of magmatic activity occurred in an intraplate setting around 460–440 Ma, with more extensive met- and peraluminous granitoids and another phase of sodic leucogranites. Both intracrustal reworking and potential mantle input are seen at this stage. Iron-rich uranium ores yielded a monazite U–Pb age of 355±5 Ma, and whole rock Sm–Nd isotope systematic indicate that the ores were sourced from the local Mesoproterozoic granitoids. The Palaeozoic events in the Mt Painter Province span a period of 200 My, and occurred during more than 10 km of exhumation of the Mesoproterozoic basement rocks. This study shows that central South Australia was more strongly affected by large-scale regional tectonics (Alice Springs Orogeny and Lachlan Orogeny) than hitherto known.

1. Introduction

The Mt Painter Province (South Australia), consisting of the Mt Painter and Mt Babbage Inliers, is part of the Curnamona Province; the economically well-endowed Broken Hill Domain also belongs to this Province. The Mt Painter Province is well known for the high heat production of its basement granites (Neumann, 2001) and for its supergene enrichments of uranium that were discovered in the first half of the 20th century (Mawson, 1944). The Mt Painter basement granites are similar in age and geochemistry to those associated with the world-class Olympic Dam Iron Ore–Copper–Gold (–U–REE) deposit, located about 250 km to the west on the Gawler Craton. Iron-rich ore sheets with significant copper and uranium enrichments are also present in the Mt Painter Inlier (Drexel and Major, 1987; Brugger et al., 2011; Elburg et al., 2012). The Olympic Dam ores have been shown to have formed shortly after intrusion of the Mesoproterozoic Hiltaba Suite granites, which are likely to have been the source of the ore-forming elements (Haynes et al., 1995; Johnson and McCulloch, 1995). Field observations (Elburg et al., 2012) suggest that the Mt Painter ores have been formed significantly later than the U-rich Mesoproterozoic granites that host them. They have been tentatively associated with a phase of hydrothermal activity postdating the Delamerian Orogeny around 440 Ma (Elburg et al., 2012) and with a later phase of hydrothermal activity at ~300 Ma (Brugger et al., 2011).

This uncertainty illustrates the fact that the Phanerozoic history of the Mt Painter is relatively poorly known, which contrasts with the recognised importance of Phanerozoic events in the Proterozoic terranes of Central Australia (Hand and Sandiford, 1999; Mawby et al., 1999).

This contribution will redress this omission, by presenting ages and isotopic data for ore formation as well as igneous and metamorphic events in the area. The question whether the different stages of magmatic and hydrothermal activity are a result of purely intracrustal reworking is also addressed. Our new data suggest a multiphase history for the area, with effects from both the approximately 500 Ma Delamerian Orogeny and the long-lived Alice Springs Orogeny, with dates in the range of 440–455 and 355–375 Ma.

2. Regional setting

The Mt Painter Inlier and the more northerly Mt Babbage Inlier form two tectonic windows that expose a basement of Mesoproterozoic metamorphic metasediments and granitoids (Fig. 1). Depositional ages of the metasediments appear to be only marginally older than the intrusive activity (Fanning et al., 2003; Fraser and Neumann, 2010; Elburg et al., 2012). Two phases of Mesoproterozoic magmatic activity have been recognised in the Mt Painter Inlier (Mt Neill Suite: ~1575 Ma; other granites (a.o. Terrapinna, Yerila, ~1545 Ma; Stewart and Foden, 2001). In the proposed revision of the stratigraphic scheme for the Mt Painter and Mt Babbage Inlier (Cowley et al., 2011; Fricke and Hore, 2011) the older phase of magmatism belongs to the Coulthard Suite of the Ninnerie Supersuite, while the slightly younger intrusive form the Moolawatana Suite. Basement rocks were deformed at amphibolite-facies conditions to form a strong and pervasive main foliation (Armit et al., 2012) that overprints at least one older foliation (Elburg et al., 2001, 2012). Formation of the main foliation, and hence main deformation, preceded deposition of the Adelaide Rift Sequence from about 800 Ma onwards (Preiss, 1987). Evidence for this is the truncation of the main foliation by the Adelaidean unconformity (Elburg et al., 2001) and the occurrence of foliated Mt Neill Suite clasts in the lowermost Adelaidean sediments (Shanahan Conglomerate). Deposition of the >10 km thick Adelaide Rift Sequence continued until the onset of the ca. 500 Ma Delamerian Orogeny (Drexel et al., 1993; Foden et al., 2006).

The present-day geometry of the Mt Painter Inlier is a large NE–SW trending anticline, the Yankaninna Anticline, which brought the basement up in its core. It is bounded by the Paralana Fault System to the east, where it ramped up against Adelaidean to Pliocene sediment (Celerier et al., 2005; Hore and Hill, 2009). Formation of the Yankaninna Anticline is classically attributed to Delamerian folding (Coats and Blissett, 1971; Paul et al., 1999). The youngest age of ductile deformation ($T \geq 300$ °C) is 485 Ma for a monazite that grew in a ductile shear zone within the basement (Elburg et al.,

2003). Based on feldspar 40Ar–39Ar dating, McLaren et al. (2002) report temperatures around 400 °C at 430 Ma, 50–100 °C cooling at 400 Ma, and a further 100–200 °C cooling at about 325 Ma. Unmetamorphosed sediments of the "pebble dyke", a diamictite of which the maximum age is 315±9 Ma (Brugger et al., 2011), are evidence that the basement reached the surface at about Permian times. While rocks in the core of the Yankaninna Anticline were exhumed by about 15 km, there is no evidence that rocks in the cores of synclines experienced significant exhumation, with the topmost Adelaidean Rift Sequence units still preserved. Similarly, the Curnamona Craton also appears to have experienced minor exhumation at most. The exhumation history of the anticline core thus reflects the growth of the fold, which not only occurred during the Delamerian Orogeny, but over a >200 My period (Cambrian to Permian) that spans both the Delamerian and Alice Springs orogenies.

By the Cambrian, the Adelaidean unconformity and basement were buried to more than 10 km depth. Lowermost Adelaidean units were metamorphosed at temperatures over 400 °C (Mildren and Sandiford, 1995; McLaren et al., 2002) and small plugs of sodium-rich leucogranites and pegmatites intruded basement and cover (Elburg et al., 2003). Metamorphism of the lower Adelaidean units is associated with high heat production of the basement granites, which raised the geothermal gradient to 40–50 °C/km (Mildren and Sandiford, 1995; Sandiford et al., 1998).

A second phase of Phanerozoic magmatism occurred around 460–440 Ma, with intrusives such as the British Empire Granite and the informally named Paralana Granodiorite (being the metaluminous part of the British Empire Granite; Elburg et al., 2003; McLaren et al., 2006), the Mudnawatana Tonalite (Coats and Blissett, 1971), and the Gordon Springs Granodiorite (Teale, 1979). Considering the geochemical coherence of these granitoids (which were collectively referred to as Paralana Granodiorite by Elburg et al., 2012), they are likely to belong to a single pulse of magmatism. Other features that have been dated at approximately 440–460 Ma are diopside–titanite veins, and a samarskite like Nb–U phase and associated monazite (Elburg et al., 2003). Rims on zircons within hyperaluminous (corundum- and spinel-bearing) lithologies also yielded ages that ranged down to 460 Ma (Elburg et al., 2012).

The core of the Yankaninna Anticline is affected by heavy K–feldspar alteration and brecciation that covers an area of about 60 km2. U-bearing, iron-rich breccias with chlorite alteration halos are found within these massive, pink to orange breccias. The iron ores form flat-lying sheets, several metres thick and tens to hundreds of metres in areal extent. Clasts in strongly K–feldspar altered breccias and iron ores consist of local host rock (Mesoproterozoic granitoids or metamorphics). Soft, chlorite- and clay-bearing breccias with highly variable clast content, including pegmatite bodies, occur at the margin of the inlier within the lowermost Adelaidean units (at e.g. the Needles and the Pinnacles; Fig. 1). The largest occurrence of this type of breccia is, however, found at Hidden Valley, on a splay of the Paralana Fault system, surrounded by Mt Neill Suite rocks. The age of these breccias, and hence

the hydrothermal activity that caused their formation, remains uncertain. Their maximum age is constrained to post-Delamerian by the lack of ductile deformation or metamorphic overprint. The breccias are pre-Permian, as they are truncated by the pebble dyke.

The central Mt Painter Inlier was affected by a second hydrothermal event that post-dated the diamictite. It produced the large quartz and specularitic hematite bodies (known as the Mt Gee Sinter, Drexel and Major, 1987) and locally kaolinised the Radium Ridge Breccias (Drexel and Major, 1987) which today is represented by the topographic highs of Mt Gee and Mt Painter. This very near-surface event is tentatively dated as being Permian by Brugger et al. (2011).

3. Petrography and geochemistry of dated materials

Major and some trace element analyses were performed at Ghent University using an ARCOS Inductively Coupled Plasma-Optical Emission Spectrometer (ICPOES) after flux dissolution, and low-abundance trace elements by ICPMS following techniques described by Elburg et al. (2012), as were the Sm–Nd analyses for the two ore samples (Fig. 3).

Monazite and zircon were analysed using a JEOL JSM-5310LV Scanning Electron Microscope (SEM) with an Oxford Energy Dispersive System (EDS) at the Department of Geology and Soil Sciences, Ghent University.

U–Pb and Lu–Hf isotope compositions were analysed by laser ablation inductively coupled plasma source mass spectrometry using a Nu Plasma HR mass spectrometer and a NewWave LUV213 laser microprobe at the Department of Geosciences, University of Oslo.

Further details of the analytical techniques are given in the electronic Supplementary data.

3.1. Whole rock characteristics

Sample PIN9 (from 'The Pinnacles') was taken as a representative of the sodic leucogranites that appear to pierce the Neoproterozoic cover rocks in breccia zones. The sample consists of quartz and albite, with a small number of relatively large zircons. Its composition is unlikely to represent a true liquid, because of the very high SiO2 content of 79.5 wt.% (Table 1). The sample's agpaitic index (molecular (Na2O+K2O)/Al2O3) is 0.96 and its ASI 1.02 (molecular (Al2O3/ (CaO+Na2O+K2O)). It contains 7% Na2O and only 0.44% K2O (Elburg et al., 2003).

Sample ARK751 of a whitish-yellow microgranite shows mineralogical and chemical similarities to PIN9, but it was sampled within the basement area, close to a large body of pegmatite-like granitoid

called 'The Armchair', of which samples often have K2O/Na2O ratios of >1, contrasting with the ratios in ARK751 and PIN9.

Both PIN9 and ARK751 have low contents of most trace elements (Fig. 2), including Rare Earth Elements (REE). However, they contain appreciable amounts of Nb (>50 ppm), and they are therefore most closely related to the A1 granite type of Eby (1992). This contrasts with the Mesoproterozoic granites of the area, which consistently come up as A2-type (Elburg et al., 2012). Another remarkable feature of these granites is their Th/U ratio of ~0.4, compared to the crustal average of 4, with U concentrations of 9–10 ppm. Their Zr contents are around 80 ppm, which is high compared to other leucogranite samples from this area, which typically contain 10–40 ppm Zr. If the whole rock compositions represent liquids, the zircon saturation temperature (Watson and Harrison, 1983) would be around 740 °C.

Sample ARK674 comes from a small outcrop in the central southern Mt Painter Inlier of fine-grained, undeformed granite that consists of plagioclase, quartz, K–feldspar and biotite, with Fe–Ti-oxide, monazite, apatite and zircon as accessory minerals, in the general area of occurrence of the Gordon Springs Granodiorite (Teale, 1979). It is geochemically similar to the met- to peraluminous granitoids of the British Empire Granite/Paralana Granodiorite, and the Mudnawatana Tonalite in the more northerly Mt Babbage Inlier (Elburg et al., 2012). These samples classify as 'calc-alkalic' in the modified alkali–lime index diagram of Frost et al. (2001). The zircon saturation temperature for ARK674 is 780 °C.

The conventional TIMS monazite U–Pb age data and whole rock analyses for samples BEM4 and BEM5 (Paralana Granodiorite and British Empire Granite respectively) have been reported in Elburg et al. (2003). Both samples are derived from the large undeformed pluton in the middle of the Mt Painter Inlier (Fig. 1). Monazites from these samples were also dated in this study to check for any systematic offset between data from different laboratories (Adelaide versus Oslo) and different techniques (TIMS versus LA–MC–ICPMS). Additionally, spinel-bearing sample ARK445, for which the zircon U–Pb LA–MC–ICPMS data were presented in Elburg et al. (2012), was also subjected to LA–MC–ICPMS dating of its monazites. This sample was interpreted to represent a highly metasomatised Mesoproterozoic mafic dyke.

As described by Elburg et al. (2012) the ores consist largely of iron oxide, with hematite and Mn-(hydr)oxides overgrowing/replacing magnetite. Monazite is an important minor phase. Barite veins crosscut some ores, and fluorite and quartz appear to be late phases too. Apart from iron and manganese, the ores are also enriched in Cu and U, and sometimes in Mo and As as well (Table 1). The dated sample, ARK732 contains more than 2000 ppm U, but has low Th (9 ppm), and very high concentrations of REE and strong LREE enrichment (Ce=2500 ppm), Ba (19,000 ppm) and Cu (1400

ppm). Sample ARK734 (used for Sm–Nd isotope geochemistry) comes from the same area, but is less enriched in U and Cu (Table 1).

3.2. Monazite and zircon geochemistry

Monazite from the British Empire Granite (BEM 5) and informally named Paralana Granodiorite (BEM 4) form a continuous trend (Fig. 3a) from lower Th, U, Y and higher La and Ce (BEM4) to higher Th, U, Y and lower LREE (BEM5). Occasionally, the BEM4 monazites have cores of spongy material, consisting mainly of ThO2 and SiO2, with a stoichiometry close to that expected for huttonite (monoclinic ThSiO4, which is isostructural with monazite). The composition of monazite from spinel-bearing sample ARK445 is roughly similar to that of BEM4, but with somewhat lower levels of Th (and therefore higher LREE), while U is not detectable by EDS. Monazite from ore sample ARK732 contains higher LREE, lower Th and Y. U concentrations are typically detectable by EDS, but are significantly lower than for the granitoid-derived monazites. In short, monazite crystals from the different samples fall in distinct groups, and the most notable feature of these analyses is the paradoxically low U content of the monazites within the U-ore.

The geochemical data for zircon from metaluminous granite ARK674 and sodic leucogranites ARK751 and PIN9 show the expected negative correlation between ZrO2 and HfO2 (Fig. 3b). PIN9 has the highest average HfO2 contents at 3.5 wt.%, followed by 3.0% for ARK751, but the ranges for the two samples overlap. The zircons from ARK674 are clearly distinct at 1.8 wt.% HfO2, with no distinction between cores and rims. UO2 contents are around the 0.5% level, and therefore of little reliability, but some parts of grains of ARK751 show higher values, going up to 2.5%. These areas also contain appreciable P2O5 (up to 10%), sometimes detectable Y2O3 and lower Zr and Hf (these areas were not included in the Hf-concentration averages). As a comparison, we also analysed a set of zircons from a hyperaluminous sample (ARK668), interpreted to have been a metasomatised mafic dyke, which had given higher Hf intensities in rims than in cores during a previous session of LA–MC–ICPMS analysis (Elburg et al., 2012). Overall, the Hf concentrations fall within the same range as those for the metaluminous granite ARK674, but the rims show on average higher concentrations than the cores. The average difference in HfO2 content between rim and core for a given zircon is 0.44±0.37%, whereas for ARK674 this is −0.03±0.4, and therefore not significant.

3.3. Zircon morphology

Zircon crystals in leucogranite sample PIN9 are prismatic and up to 500 μm in length. They have a dull light brown colour and are cloudy. Those from leucogranite ARK751 have a similar colour and

shape, but are no larger than 300 μm in length. For both samples, cathodoluminescence (CL) imaging show a mottled internal structure (Fig. 4a, b), while only rare rims show the oscillatory zoning typically associated with igneous zircons. Micron-sized inclusions of a uranium-bearing phase (likely an oxide or hydroxide) were observed within some of the PIN9 zircons. There is no evidence for any inherited cores in the zircons from either their shape or CL images. We interpret the irregular internal structure seen in CL to reflect post-magmatic metamictisation.

ARK674 contains zircons that are typically 150 μm, and rarely reach lengths of 300 μm. Most of the zircons in this sample consist of a core and a rim that can be distinguished both in CL and backscattered electron (BSE) imaging (Fig. 4c). The core areas typically show better-defined oscillatory zoning than the rims, but more patchily zoned cores also exist. The cores vary from euhedral to more rounded. The rims vary in thickness from a few microns on the prism faces up to 60 μm on the terminations. Rare zircons appear to consist of the 'rim facies' only (Fig. 4d).

4. Results

4.1. U–Pb data

Zircon from leucogranite sample PIN9 contains very high U contents, and the ages vary from discordant through concordant to reversely discordant (Fig. 5a). An unconstrained discordia through all the data points gives a lower intercept of 62±89 and an upper intercept of 511±12 Ma (n=21; Table 2; errors quoted at the 2 sigma level). The seven most concordant analyses yield a 206Pb/238U age of 505±4 Ma (see inset), which is within error of the discordia upper intercept.

The zircons from ARK751 are of significantly poorer quality. When only the analyses with a 206Pb/204Pb ratio of >1000 (10 out of 20) are considered and corrected for common Pb, they yield a discordia with an upper intercept of 492±60 Ma (Fig. 5b). Two out of these ten analyses are close to concordance, and they yield an average 206Pb/238U age of approximately 455 Ma. It is important to notice that these two analyses stem from zircon rims that display oscillatory zoning (Fig. 4b), rather than the patchy zoning, suggestive of post-magmatic disturbance, displayed by the rest of the crystals. On the basis of this evidence, we think that this approximately 455 Ma age is the best estimate for the magmatic age of this leucogranite, even though the discordia could also be interpreted as reflecting an age that is indistinguishable within error from that of PIN9.

The zircon ages in sample ARK674 are clustered in two groups; the cores give ages around 1570 Ma, and the rims around 460 Ma (Fig. 5c). Fifty out of 54 analyses yield a discordia with an upper intercept of 1567±7 Ma, and a lower intercept of 458±8 Ma. Out of the four discarded analyses, two

had very low 206Pb/204Pb ratios (~500). The least discordant rims (n=14) give a weighted average 206Pb/238U age of 462±4 Ma, which is indistinguishable from the lower intercept age.

Monazite from BEM5 yields a Tera–Wasserburg intercept age of 454±4 Ma (2 SD, n=9) when three analyses are left out (Fig. 6a). The three discarded analyses give somewhat older ages, and this could reflect inheritance, as this sample is a peraluminous granite. The 5 least discordant grains give a weighted average 206Pb/238U age of 452±4 Ma (Table 2). For BEM4, ten out of eleven grains yield a Tera–Wasserburg intercept age of 439±8 Ma (Fig. 6b). If the 5 most concordant grains are used, the concordia age is 443±4 Ma. The ages for BEM4 compare very well with the bulk U–Pb TIMS age on the same samples, which were 441–445 Ma (isochron and concordia ages, Elburg et al., 2003), suggesting no systematic offset between the two techniques. The 454 Ma age for BEM5 is slightly older than, but within error of the 449±1 Ma concordia age reported by Elburg et al. (2003).

Monazite from ARK445 gives a concordia age of 440±4 Ma (Fig. 6c), when 6 out of 13 analyses are selected. The discarded analyses yield ages on a Tera–Wasserburg plot that are both higher and lower than 440 Ma. This is somewhat similar to the situation for the zircon rims from this sample (Elburg et al., 2012), which also showed a range of concordant ages between 420 and 480, with an important cluster around 455 Ma. The monazite results are close to being within error of the results from an unpublished a LA–ICPMS (Element II) test run of these same monazites against the GJ-1 zircon standard done at Frankfurt University, Germany, which yielded a 206Pb/238U age of 455±10 Ma (n=16, two points rejected).

Eight analyses were performed on monazite from ore sample ARK732 and six data points yield a concordia age that is undoubtedly younger than the other three monazite ages at 355±5 Ma (Fig. 6d). A weighted average 206Pb/238U age for all analyses yields an indistinguishable age of 355±4 Ma.

4.2. Lu–Hf systematics of zircon

Zircons from leucogranites ARK751 and PIN9, and from metaluminous granite ARK674 were analysed for their Hf isotopic compositions by LA–MC–ICPMS. For sample ARK674, care was taken that the Hf spots were obtained from the same CL-defined areas that were dated. All data can be found in the electronic Supplementary data file. The data for sample PIN9 are very well clustered (Fig. 7a), which is likely to reflect the high intensities of the Hf beam during the analyses (typically 5–6 V compared to values of ~3.5 V for ARK674), combined with relatively low Lu and Yb contents. The 19 analyses give an average of εHf500Ma=−1.7±0.4 (1 SD). The data for ARK751 show a somewhat wider spread, which may be related to the higher Lu and Yb contents. However, there is no correlation between either the present-day or age-corrected 176Hf/177Hf and 176Yb/177Hf ratio, indicating that our correction procedure does not introduce a systematic error. The εHf455 Ma is +0.3±0.6 (1 SD,

n=24); at 500 Ma, this would be +1.2±0.7, showing that the small difference with PIN9 is not an artefact of a potentially incorrect age (see discussion on U–Pb results).

The zircons from the metaluminous granite ARK674 are grouped according to being either Mesoproterozoic cores or Palaeozoic rims, and recalculated to their respective ages. Some of the spread in the data could be related to minor overlap between the different zones, as the rims are quite thin and the CL images only provide information on the surface of the zircon, and not the three-dimensional shape of the zones. The cores give an average age-corrected 176Hf/177Hf ratio of 0.28189±6, which translates to εHf1570 Ma=+3.7±2.2 (1 SD; n=21). The rims give a 176Hf/177Hf ratio of 0.28266±4, which equals εHf460 Ma=+5.7±1.6 (1 SD; n=24). The values for the cores fall within the same range as the zircons from the local Mesoproterozoic granites and their metasomatised equivalents (Elburg et al., 2012), while the rims display significantly higher εHf460 Ma values than other materials of the same age from this area. Apart from the leucogranite data presented here, zircon rims of similar age were also found within metasomatised mafic dykes; these have an average εHf455 Ma of −17 (176Hf/177Hf=0.282013; Elburg et al., 2012), and are therefore significantly more negative than the granitoid data presented here.

4.3. Sm–Nd systematics of whole rock samples

Whole rock ore samples ARK732 and ARK734 were analysed for their Sm–Nd isotope systematics (Table 1). Both samples are highly enriched in LREE, resulting in a low 147Sm/144Nd ratio of 0.06–0.07. At 370 Ma, the 143Nd/144Nd ratio of these two ore samples is 0.51149, which represents an epsilon Nd value of −13.1. The ore samples are in Nd isotopic equilibrium with most of the Mesoproterozoic granites in the area (data from Elburg et al., 2012) around 200–410 Ma (Fig. 7b). Sample PIN9 (data from Elburg et al., 2003) shows Nd isotopic systematics that are indistinguishable from those of the Mesoproterozoic granites, yielding an initial (at 500 Ma) εNd value of −12.3. Data for two samples of the Palaeozoic metaluminous granites, ARK674 and ARK580, were already presented in Elburg et al. (2012; both referred to as Paralana Granodiorite), and they have initial (at 455 Ma) εNd ratios of −4.5. Therefore, the ores only intersect the Nd isotope–time curves for Palaeozoic metaluminous granites such as ARK674 around 1250 Ma, i.e. long before these granitoids were actually formed. Neither the ores nor the leucogranite sample intersect the Nd growth curves for the metasedimentary rocks from the Mt Painter (data from Neumann, 2001; Elburg, unpublished).

5. Discussion

5.1. Timing of events and regional framework

The new zircon and monazite ages both confirm previous age data, and expand the range of published ages for this area. From the ages obtained thus far, it seems that the Mt Painter and Mt Babbage Inliers have been affected by Palaeozoic orogenic and magmatic/hydrothermal events that have been recognised with greater clarity in other parts of Australia. We will discuss these events in the order of decreasing age. A summary of the available ages for the Mt Painter Province is given in Fig. 8.

5.1.1. 514–490 Ma (Delamerian)

The existing age constraints on the sodic leucogranites that pierce the Neoproterozoic cover rocks are a 496±8 Ma Sm/Nd isochron and a 436±17 Ma whole rock errorchron (Elburg et al., 2003) and three Rb–Sr whole rock isochrons (G. Teale, unpublished data, quoted in Wülser, 2009) of 450±4, 418±2 and 372±2 Ma. The older Sm/Nd age is confirmed by the U–Pb zircon data for PIN9 presented here.

The 514–490 Delamerian Orogeny (Foden et al., 2006) was thought to have been responsible for the large-scale folding of the area (Paul et al., 1999). Only one folded Delamerian-age pegmatite dyke in the basement was reported by Elburg et al. (2003). Most sodic leucogranites, however, are found within cover rocks that have undergone brittle deformation, and they show no signs of ductile deformation which would be expected at the local ≥400 °C temperature at Delamerian times. Some doubts have lingered over the validity of the Delamerian age for these leucogranites, considering their undeformed nature and their association with brittle deformation in the cover rocks (Bakker and Elburg, 2006). It is possible that the brecciation occurred at a later stage than the intrusion of the leucogranites. These breccia zones are of limited extent within the southern part of the Mt Painter Inlier where our work has been concentrated, but a large scale version exists in the 'Hidden Valley' area on the northeastern side of the Mt Painter Inlier (Bons et al., 2011). Different leucogranitic bodies within the Hidden Valley breccia also yield ages between 500 and 450 Ma (Wülser, 2009), without showing clear evidence of actual intrusion into the breccia.

It is likely that at least some of the observed metamorphism in the area occurred during the Delamerian Orogeny. Wülser (2009) reports electron microprobe monazite ages at 440–500 Ma from a regional survey and Delamerian ages for U-bearing phases using LA–Q–ICPMS analysis. The spread in zircon ages in the hyperaluminous metasomatised dykes (Elburg et al., 2012) also points towards zircon new-growth starting around 500 Ma. To our knowledge, igneous activity around this time in the

Mt Painter and Mt Babbage Inliers is solely represented by the sodic leucogranites that are found associated with breccia zones in the cover.

On a larger scale, the Delamerian Orogen took place at the active oceanic margin of Gondwana, the Terra Australis Orogen (Cawood, 2005; Pankhurst and Vaughan, 2009), running from South America to South Africa, Antarctica and Australia, and can be considered as an extension of the slightly earlier Ross Orogen in Antarctica (Foden et al., 2006). The effects of the Delamerian Orogeny are most notable in the South Australian Adelaide Fold Belt south of the Mt Painter Province (Foden et al., 1999, 2006), extending to western Victoria (Turner et al., 1993). In these areas, as well as the more northerly Peak and Denison Ranges, magmatism (Turner and Foden, 1996; Foden et al., 2002) was more extensive than in the Mt Painter Province, and metamorphic effects are also well-documented (Jenkins and Sandiford, 1992; Turner et al., 1994). So, despite the high heat production of the Mesoproterozoic granites in the Mt Painter Province, magmatism during the Delamerian was far more limited here than in areas that do not show anomalously high heat flow.

5.1.2. 460–440 Ma

Despite the poor quality of the zircons in leucogranite sample ARK751, derived from an outcrop hosted within the Mesoproterozoic basement, the age is certainly between 455 and 500 Ma, with our preference for the younger age, based on the two analyses of oscillatory zoned material, which is chemically similar to the discordant cores. The small difference in Hf isotopic composition with zircons from PIN9 (see further discussion below) supports the idea that this may be a different phase of magmatism.

The 439–455 Ma LA–MC–ICPMS monazite ages for the met-/peraluminous Palaeozoic magmatism (BEM4 and BEM5) agree with the zircon data for ARK 674, and the previously published bulk ID-TIMS age. The monazite ages of the hyperaluminous sample ARK445 also agree with the zircon data of 455–500 Ma. This shows that there is no systematic offset between different techniques. Magmatism and hydrothermal activity at 440–460 Ma in the Mt Painter Province is documented by undeformed metaluminous to peraluminous granites (Elburg et al., 2003; McLaren et al., 2006), diopside–titanite veins (Bakker and Elburg, 2006), leucogranites within the basement (this contribution) and monazite and zircon growth in the hyperaluminous metasomatised dykes (this contribution; Elburg et al., 2012); and two of the Rb–Sr whole rock iso-/errorchrons for some of the leucogranites (see above). This event is also documented in the Adelaide Fold Belt to the southwest, with a 435±5 Ma K–Ar age for a willemite deposit (Groves et al., 2003); in the Harts Ranges to the northwest (Mawby et al., 1999; Buick et al., 2008; and references therein),with both metamorphic and igneous ages related to the Alice Springs Orogeny; and in the western Lachlan Fold Belt, located to

the southeast (Gray and Foster, 2004), where the approximately 440 Ma Ar–Ar ages represent metamorphism.

Whether all these events are correlated is not clear. It seems likely that the willemite ore deposition took place in the waning stages of the event that is also recorded in the Mt Painter Inlier. The Alice Springs Orogeny happened in an intraplate setting, whereby pre-existing structures were reactivated as a result of far-field stresses (Sandiford and Hand, 1998; Hand and Sandiford, 1999). The Lachlan Fold Belt represents the eastward translation of the same active continental margin that gave rise to the Adelaide Fold Belt during the Delamerian Orogeny (Gray and Foster, 2004). A significant number of the 440–460 Ma Alice Springs ages in the Harts Ranges represent igneous intrusions (Buick et al., 2008), rather than the metamorphism-only ages of the slightly less distant western Lachlan Fold Belt. Since the ages for the Mt Painter Province are also related to igneous activity, it is more tempting to make a connection to the north than to the east.

The current model that folding at Mt Painter only took place during the Delamerian Orogeny and was followed by passive exhumation (McLaren et al., 2002) seems at odds with the fact that there was significant deformation both in the Lachlan and Alice Springs Orogen at around 440 Ma. However, the uplift history of Mt Painter shows that, whereas folding started during the Delamerian, it actually took place over the whole Palaeozoic. The ca. 430 Ma cooling episode reported by McLaren et al. (2002) records a reactivation of the Paralana Fault System. Approximately N–S directed compression caused the thick Adelaide Rift Sequence and underlying basement to obliquely ramp up the rigid Curnamona Craton. The vertical component of movement was a few km during this event, while the horizontal strike–slip component remains unconstrained. Such reactivation of structures is similar to that recorded in the Alice Springs Orogeny (Hand and Sandiford, 1999). The Curnamona Craton thus acted as a rigid block that was skirted by large-scale shear zones that connect the Lachlan Orogen with the Musgrave and Arunta blocks (Gray and Foster, 2004).

5.1.3. 380–350 Ma and younger

The concordance between our laser-ablation monazite ages and previously published analyses for those materials provides credence to the 355 Ma age for the monazite in the Fe–U–Cu–REE ore. This age is similar to the 361–365 Ma Re–Os ages on molybdenite from a drillhole to the south of our sampling location (Skirrow et al., 2011) which was also interpreted as dating the mineralisation. The monazite age of 355 Ma provides evidence for significant mobility of REE at this time, and presumably also for the iron that forms the bulk of the ore, and U. Mobility of the latter element is also implied by the 367±13 Ma brannerite (UTi2O6) LA–Q–ICPMS Pb/Pb age (Wülser, 2009) from Hidden Valley.

Mica and K–feldspar argon–argon and potassium–argon ages that encompass the 355 Ma age reported here were presented by McLaren et al. (2002), but these were interpreted in terms of a cooling history only. In combination with our new data, a punctuated thermal history seems more likely, with thermal spikes superimposed upon the overall cooling history, which can profoundly affect argon age spectra (Lister and Baldwin, 1996). The 355 Ma ages are again similar to those seen for magmatism and metamorphism in the Alice Springs Orogeny (Buick et al., 2008). The effects of this orogeny have now been recognised from the Mt Isa Inlier (Spikings et al., 2006) to the Gawler Craton (Schmidt and Clark, 2011) and the Kimberley region (Lan and Chen, 2012). Within the Mt Painter Province, evidence for this orogeny mainly comes from low temperature geochronology (Mitchell et al., 1996, 2002). At the same time, granitic magmas intruded in western Tasmania, most likely in an extensional setting after the amalgamation of east and west Tasmania (Black et al., 2010). On the eastern side of Australia, magmatism was shifting from the Lachlan Fold Belt (Sircombe and McQueen, 2000) to the extrusive arc sequences of the New England Orogen (Jeon et al., 2012).

As for the Alice Springs Orogen at this stage, and the earlier 440–460 Ma magmatic activity, the hydrothermal activity in the Mt Painter Inlier around 355 Ma must have happened in an intraplate setting.

The ores that were dated at 355 Ma are associated with chlorite alteration and brittle deformation, but they appear to have undergone a multistage history, with primary magnetite-bearing assemblages giving way to hematite, late manganese (hydr)oxide overgrowths and barite veins, and silicification. It is likely that the monazite age of 355 Ma records a relatively early, high-temperature event, and that the brittle behaviour and chloritisation are somewhat later.

Similar brittle overprinting, associated with quartz–hematite growth, has also been observed within the 440 Ma titanite–diopside veins (Bakker and Elburg, 2006). Although these authors suggested that the quartz–hematite epithermal event (Drexel and Major, 1987) represented the waning stages of the 440–460 Ma event (Elburg et al., 2003), we now concur with Brugger et al. (2011) that this must represent a much later event, likely ~300 Ma. This is also suggested by the associated brittle behaviour and our reinterpretation of the Rb–Sr two-point isochron of fluorite and quartz, for which the data was presented in Elburg et al. (2003), yielding an age of 219±25 Ma. However, based on fluid inclusion studies (Bakker and Elburg, 2006) we interpret the ~300 Ma hydrothermal system to be very poor in dissolved solids, and only overprinting an earlier phase of iron–U–REE mineralisation, that we now put at about 355 Ma.

5.2. Crustal reworking versus mantle input

The long thermal history of the Mt Painter Inlier has often been ascribed to the high heat-producing nature of the Mesoproterozoic granites, combined with a blanketing effect of the Neoproterozoic cover rocks (Mildren and Sandiford, 1995; Sandiford et al., 1998; McLaren et al., 2006; Brugger et al., 2011). The zircon Hf and whole rock Sm–Nd data may help to determine whether this is purely intracrustal reworking, or that a chemical and therefore also thermal contribution from the mantle has been involved (Elburg et al., 2003, 2012).

An example of intracrustal reworking in the area has been provided by Elburg et al. (2012); the zircon and Nd data from that study are shown in Fig. 7a to provide a baseline for this scenario. Corundum and spinel-bearing 'hyperaluminous' samples were interpreted to be highly metasomatised mafic dykes, associated with the Mesoproterozoic granites. This was based on a dominant zircon core population with age and Hf isotopic characteristics similar to that of the Mesoproterozoic granites, and whole rock initial Nd isotopic ratios that also fall within the range of those granites. The zircons in these metasomatised dykes have rims with Palaeozoic (approximately 455 Ma) ages, and Hf isotopic ratios that can be generated by 'ageing' the Hf isotopic ratio of the 1570 Ma cores with a typically upper crustal 176Lu/177Hf ratio of 0.010. In a diagram of zircon εHf versus whole rock εNd (Fig. 9), both the Mesoproterozoic granites, back-calculated to 1570 Ma, and the metasomatised dykes, calculated at 455 Ma yield data arrays that lie within the global whole rock εHf–εNd envelope defined by Vervoort and Patchett (1996).

The Nd–Hf isotopic data for metaluminous Palaeozoic granite ARK674, with broadly the same age of zircon rims as the metasomatised mafic dykes, show a different picture. The Nd isotopic data for this sample was already argued to indicate input from a source with a time-integrated Sm/Nd ratio that is higher than that of the Mesoproterozoic granites, and this was interpreted to reflect input from the mantle (Elburg et al., 2012). The new Hf isotope data for the zircon rims confirm this interpretation: the Hf isotopic composition of the rims is significantly higher than that of the zircon rims in the hyperaluminous dykes. Starting from the typical Mesoproterozoic Hf isotopic signature, the rim signature can only be generated if the 176Lu/177Hf ratio is similar to that of the depleted mantle (0.039), which is virtually impossible to achieve during crustal reworking. Within the εHf versus εNd diagram, the array for this sample, calculated at 460 Ma, is of course very wide, as a result of the Hf data from the cores (lower end of the array) and rims (upper end). The combination of the two dissimilar zircon contributions, together with its whole rock εNd value, is likely to fall within the crustal array. Both the Nd and Hf isotope characteristics point towards input from a mantle source, combined with the reworked crustal material, as evidenced by the approximately 1570 Ma zircon cores.

The homogeneity of the inherited zircon core population, and its Hf isotopic composition, suggest that these cores were derived from the Mesoproterozoic A-type granites. However, input of a substantial amount of the local A-type granitoids is difficult to reconcile with the 'calc-alkalic' to 'calcic' (following Frost et al., 2001) and M–I–S-type (following Whalen et al., 1987) character of sample ARK674. This could imply the presence of unexposed Mesoproterozoic granitoids with similar chemical characteristics at depth in the basement, or yet unexplained remelting process to turn A-type protoliths into calc-alkaline granitoids.

For the two leucogranite samples analysed for Hf isotopes, we only have Nd isotope data for PIN9 (Elburg et al., 2003), which suggest that this magma could be formed by remelting of the Mesoproterozoic granitoids, i.e. purely intracrustal reworking. However, the zircon Hf data does not support this interpretation. This relatively high Hf isotopic signature could only be developed from the typical Mesoproterozoic zircon signature if the 176Lu/177Hf ratio was 0.029, which is more typical for basalts than for average upper crust or granite. There is no inherited component in the zircons, and the data cluster very tightly — well outside the crustal array in the εHf versus εNd diagram. The geochemical signature of the zircons, with their high Hf/Zr ratios, is in agreement with crystallisation from a highly fractionated melt (Wang et al., 2010a), such as the leucogranite in which they are found. The chance that the zircons are xenocrysts is therefore minimal.

The discrepancy between the Nd and Hf isotopic data for leucogranite PIN9 can be explained in two ways:

a. The leucogranites were generated by partial melting of the Mesoproterozoic granites, and thereby inherited the Nd isotopic signature from this source. Most of the Hf in the Mesoproterozoic granites would have been contained in zircon, which only entered the melt to a very limited extent, explaining the modest Zr concentration of 80 ppm versus 400–800 ppm in the Mesoproterozoic granites. Therefore, the Lu/Hf ratio of the melt would have been significantly higher than that of the Mesoproterozoic granites themselves, and the Hf more radiogenic (higher 176Hf/177Hf ratio). If this scenario were correct, we would expect to see a high Lu/Hf ratio in the whole rock analyses of the leucogranites. This is not the case, but it is possible that the whole rock compositions do not reflect liquid compositions.

b. The higher Hf isotopic signature (εHf=−2 rather than εHf=−15, which is expected for reworking of the Mesoproterozoic granites) reflects a contribution from a more primitive, mafic source. This is not observed in the Nd isotopic signature because of contamination with material from the Mesoproterozoic granites, which have a Nd/Hf ratio of 6, whereas that of the leucogranites is 0.13. This contrast in Nd/Hf ratio may be augmented by the more mobile behaviour of the REE compared to Hf in this area, as evidenced by the presence of iron ore–U–REE ores. A contribution from the (high-REE) Mesoproterozoic granites has swamped the Nd isotopic signature of the (low-REE)

leucogranites, whereas the Hf isotopic composition of the leucogranite's zircons is more representative of the original liquid composition than the whole rock Nd isotope composition.

We prefer the second scenario on the basis of the chemical differences between the Mesoproterozoic granites (A2-type) and Palaeozoic leucogranites (A1-type). A simple mixing calculation was performed to investigate this possibility (Fig. 10). The high Hf and Nd isotope end member was taken as having the Nd and Hf concentrations of PIN9 (0.6 and 4.6 ppm respectively), as well as its Hf isotopic composition (0.28242, or εHf=−1.7). Its Nd isotopic composition was taken to match its Hf isotopic composition on the crustal evolution line, with εNd=−1.8 (143Nd/144Nd=0.5119). The other end member has a Nd isotopic composition to match the Mesoproterozoic granites at 500 Ma (143Nd/144Nd=0.51135, εNd−12.5), and a similar Nd concentration (120 ppm). Its Hf isotopic composition was calculated by radiogenic ingrowth of the original Hf isotopic signature of the 1570 Ma zircons using an average crustal 176Lu/177Hf ratio of 0.01 (represented by the curve for the metasomatised dykes in Fig. 7a; 176Hf/177Hf= 0.280205, εHf=−15) One of the curves uses a Hf concentration of 23 ppm (Nd/Hf=6), similar to the whole rock composition of the Mesoproterozoic granites, and the other one only 12 ppm (Nd/Hf=10), representing reduced Hf mobility because its being contained in zircon. Both curves illustrate that 1% contamination already has a significant effect on the Nd isotopic composition, while the Hf isotopic composition shows little change. This simplified calculation illustrates the importance of the contrasting Nd/Hf ratios of the two end members for explaining the isotopic discrepancy. The presence of A-type magmas with 143Nd/144Nd ratios around 0.5119 or higher has been documented in other parts of the Adelaide Fold Belt (Turner et al., 1992; Turner and Foden, 1996; Pankhurst et al., 2011), where their isotopic signature has been interpreted as reflecting a mantle signature. So the interpretation of mantle involvement during the Delamerian Orogeny is in keeping with previous work. However, there are two distinctions between the A-type granites described in other parts of the Adelaide Fold Belt, and the leucogranites in the Mt Painter Inlier: the former classify as A2-type following Eby (1992), and have ages of ~495 Ma (Foden et al., 2006), whereas our dated samples gave an age of >495 Ma, and classifies as a (high-Nb) A1-type.

The zircon Hf isotope data from the 455 Ma leucogranite (ARK751), the similarly aged sample of Gordon Springs Granodiorite (ARK674), and the 500 Ma leucogranite (PIN9) all point towards involvement of materials with a relatively high time-integrated Lu/Hf ratio, being either the mantle, or mafic crustal lithologies. One potential mafic crustal lithology is the Neoproterozoic (approximately 825 Ma) basaltic Wooltana Volcanics, which have a 143Nd/144Nd ratio at 500 Ma of 0.5121 and a 176Hf/177Hf of 0.28264 (calculated from data by Wang et al., 2010b); adding a small component of the Mesoproterozoic granites could yield the isotopic composition of PIN9. It is therefore possible to invoke melting intrusive Wooltana-Basalt equivalents and some contribution of the Mesoproterozoic granites to explain the isotopic signature of the Palaeozoic granitoids. The cause for such a melting event is not known, but could be the high heat production of Mesoproterozoic granites that had raised

the geothermal gradient. In case of such purely crustal melting, one would expect mostly melting of felsic material and not of mafic material, of which the presence below the current erosion surface is speculative. It is more likely that the radiogenic Hf and Nd signature is the result of the influx of mantle material, which provided both a thermal and chemical input. Considering that Palaeozoic magmatic activity was associated with growth of the crustal-scale Yankaninna Anticline, a possible source for mafic input could be decompressional melting of the mantle.

On the other hand, the Nd isotope data for the ~355 Ma ores do not necessitate the input of any mantle-derived Nd into the system, since the isotopic signature overlap with those of the Mesoproterozoic granites around this time. However, since the inlier would have been at even shallower depths than around 500–440 Ma and the effect of a heating blanket by the Adelaidean sediments decreases with ongoing uplift, it is even less likely that the radiogenic heat production of the granites was solely responsible for this Carboniferous event.

6. Conclusions

Our new data shows that magmatic–hydrothermal activity occurred in a punctuated fashion within the Mt Painter Province during the Palaeozoic.

The Delamerian Orogeny around 500 Ma, which occurred as a response to subduction along the southern margin of Gondwana, was accompanied by very limited pegmatitic A1-type magmatism in the Mt Painter Inlier. This contrasts with the more extensive magmatism seen in the more southerly part of the Adelaide Fold Belt. Hf isotopic ratios of zircons point towards the involvement of materials with more primitive characteristics than the Mesoproterozoic granitoids or metasediments, and this could point towards mantle input during this time. Remelting of the Mesoproterozoic granitoids with retention of Hf in the (zircon-bearing) residue seems less likely on the basis of the contrasting geochemical characteristics.

Met- to peraluminous magmatism had already been known to occur during a 460–440 Ma event (Elburg et al., 2003; McLaren et al., 2006). Nd isotopic characteristics that are more primitive than the Mesoproterozoic basement characterise the metaluminous granitoids (Elburg et al., 2003; Elburg et al., 2012), and Hf isotopic ratios on Palaeozoic zircon rims confirm the involvement of isotopically more primitive material. Although the U–Pb age date is not highly reliable, leucogranites, broadly similar to those associated with the Delamerian Orogeny, may also have intruded around this time. Igneous activity occurred during growth of the crustal-scale Yankaninna Anticline, which commenced during the Delamerian Orogeny and continued until probably the Permian. The anticline formed as a result of oblique ramping of the Mt Painter rocks onto the Curnamona Craton along the reactivated Paralana Fault System. Much of this activity took place during the Alice Springs Orogeny, indicating that the

effects of this tectonic event are more pronounced in the Northern Flinders Ranges than hitherto assumed.

The date for formation of the iron-rich U ore is given by a monazite U–Pb age of 355±5 Ma, in broad agreement with the 361–365 Re–Os age on molybdenite (Skirrow et al., 2011). Whole rock Sm–Nd systematic show that the source rock for the ore are the Mesoproterozoic A2-type granites. No evidence exists for the involvement of isotopically more primitive materials at this stage. Therefore, the scenario for purely intracrustal reworking (McLaren et al., 2006) only seems to hold for this rather late-stage of the evolution of the Mt Painter Province.

Acknowledgments

We are very grateful to Dr. Seydoux-Guillaume and Dr. Bingen for providing us with monazite standards. Ingrid Smet performed the Sm–Nd analyses for the two ore samples. Axel Gerdes was instrumental in obtaining the first test analyses of the ARK445 monazites. The zircon standard (NMNH 117288) for SEM analysis was provided by the Smithsonian Institution. The constructive comments of two anonymous reviewers have been gratefully accepted. This project was partly funded by the German Research Foundation (DFG, Project BO-1776/8) and by the Research Foundation Flanders (FWO, Project G.A078.11). This is contribution no. 28 from the Department of Geosciences, University of Oslo Isotope Geology Laboratory.

Appendix A. Supplementary data

Supplementary data to this article can be found online at http:// dx.doi.org/10.1016/j.gr.2012.12.017.

References

Armit, R.J., Betts, P.G., Schaefer, B.F., Ailleres, L., 2012. Constraints on long-lived Mesoproterozoic and Palaeozoic deformational events and crustal architecture in the northern Mount Painter Province, Australia. Gondwana Research 22, 207–226.

Bakker, R.J., Elburg, M.A., 2006. From diopside–titanite pegmatites to hematite–quartz growth: the development of a magmatic–hydrothermal system in Arkaroola (northern Flinders Ranges, South Australia). Contributions to Mineralogy and Petrology 152, 541–569.

Black, L.P., Everard, J.L., McClenaghan, M.P., Korsch, R.J., Calver, C.R., Fioretti, A.M., Brown, A.V., Foudoulis, C., 2010. Controls on Devonian–Carboniferous magmatism in Tasmania, based on inherited zircon age patterns, Sr, Nd and Pb isotopes, and major and trace element geochemistry. Australian Journal of Earth Sciences 57, 933–968.

Bons, P.D., Weisheit, A., Elburg, M.A., 2011. A km-scale fluidised breccia in the Mesoproterozoic Mt. Painter Inlier of South Australia. Deformation, Rheology and Tectonics Meeting Abstract volume. Faculty of Geology, Oviedo University, Spain, p. 28. http://www.geol.uniovi.es/drt2011/Programme.html.

Brugger, J., Wülser, P.-A., Foden, J., 2011. Genesis and preservation of a uranium-rich Paleozoic epithermal system with a surface expression (Northern Flinders Ranges, South Australia): radiogenic heat driving regional hydrothermal circulation over geological timescales. Astrobiology 11, 499–508.

Buick, I.S., Storkey, A., Williams, I.S., 2008. Timing relationships between pegmatite emplacement, metamorphism and deformation during the intra-plate Alice Springs Orogeny, central Australia. Journal of Metamorphic Geology 26, 915–936.

Cawood, P.A., 2005. Terra Australis Orogen: Rodinia breakup and development of the Pacific and Iapetus margins of Gondwana during the Neoproterozoic and Paleozoic. Earth-Science Reviews 69, 249–279.

Celerier, J., Sandiford, M., Hansen, D.L., Quigley, M., 2005. Modes of active intraplate deformation, Flinders Ranges, Australia. Tectonics 24, TC6006.

Coats, R.P., Blissett, A.H., 1971. Regional and economic geology of the Mount Painter Province. Geological Survey of South Australia Bulletin 43.

Cowley, W.M., Hore, S.B., Preiss, W.V., Sheard, M.J., Wade, C.E., 2011. A revised stratigraphic scheme for the Mount Painter and Mount Babbage Inliers. In: Forbes, C.J. (Ed.), 6th Sprigg Symposium: Unravelling the northern Flinders and beyond: Geological Society of Australia Abstracts, pp. 1–4.

Drexel, J.F., Major, R.B., 1987. Geology of the uraniferous breccias near Mount Painter, South Australia and revision of rock nomenclature. Quarterly Geological Notes 104, 14–24.

Drexel, J.F., Preiss, W.V., Parker, A.J., 1993. The geology of South Australia, Vol. 1. The Precambrian: South Australia Geological Survey Bulletin, 54. Geological Survey of South Australia, Adelaide.

Eby, G.N., 1992. Chemical subdivision of the A-type granitoids: petrogenetic and tectonic implications. Geology 20, 641–644.

Elburg, M.A., Bons, P.D., Dougherty-Page, J., Janka, C.E., Neumann, N., Schaefer, B., 2001. Age and metasomatic alteration of the Mt Neill Granite at Nooldoonooldoona Waterhole, Mt Painter Inlier, South Australia. Australian Journal of Earth Sciences 48, 721–730.

Elburg, M.A., Bons, P.D., Foden, J., Brugger, J., 2003. A newly defined Late Ordovician magmatic–thermal event in the Mt Painter Province, northern Flinders Ranges, Australia. Australian Journal of Earth Sciences 50, 611–631.

Elburg, M.A., Andersen, T., Bons, P.D., Weisheit, A., Simonsen, S.L., Smet, I., 2012. Metasomatism and metallogeny of A-type granites of the Mt Painter–Mt Babbage Inliers, South Australia. Lithos 151, 83–104.

Fanning, C.M., Teale, G.S., Robertson, R.S., 2003. Is there Willyama Supergroup sequence in the Mount Painter Inlier? In: Peljo, M. (Ed.), Broken Hill Exploration Initiative. Geoscience Australia, Broken Hill, pp. 38–41.

Foden, J., Sandiford, M., Dougherty-Page, J., Williams, I., 1999. Geochemistry and geochronology of the Rathjen Gneiss: implications for the early tectonic evolution of the Delamerian Orogen. Australian Journal of Earth Sciences 46, 377–389.

Foden, J.D., Elburg, M.A., Turner, S.P., Sandiford, M., O'Callaghan, J., Mitchell, S., 2002. Granite production in the Delamerian Orogen, South Australia. Journal of the Geological Society of London 159, 1–19.

Foden, J., Elburg, M.A., Dougherty-Page, J., Burtt, A., Turner, S., 2006. The timing and duration of the Delamerian Orogeny: correlation with the Ross Orogen and implications for Gondwana assembly. Journal of Geology 114, 189–210.

Fraser, G.L., Neumann, N.L., 2010. New SHRIMP U–Pb Zircon Ages from the Gawler Craton and Curnamona Province, South Australia, 2008–2010. Record 2010/16. Geoscience Australia, Canberra, Australia.

Fricke, C.E., Hore, S.B., 2011. Definition of the Mesoproterozoic Ninnerie Supersuite, Curnamona Province, South Australia. South Australia. Department of Primary Industries and Resources. Report Book 2010/00020.

Frost, B.R., Barnes, C.G., Collins, W.J., Arculus, R.J., Ellis, D.J., Frost, C.D., 2001. A geochemical classification for granitic rocks. Journal of Petrology 42, 2033–2048.

Gray, D.R., Foster, D.A., 2004. Tectonic evolution of the Lachlan Orogen, southeast Australia: historical review, data synthesis and modern perspectives. Australian Journal of Earth Sciences 51, 773–817.

Groves, I.M., Carman, C.E., Dunlap, W.J., 2003. Geology of the Beltana Willemite Deposit, Flinders Ranges, South Australia. Economic Geology 98, 797–818.

Hand, M., Sandiford, M., 1999. Intraplate deformation in central Australia, the link between subsidence and fault reactivation. Tectonophysics 305, 121–140.

Haynes, D.W., Cross, K.C., Bills, R.T., Reed, M.H., 1995. Olympic Dam ore genesis — a fluid-mixing model. Economic Geology and the Bulletin of the Society of Economic Geologists 90, 281–307.

Hore, S.B., Hill, S.M., 2009. Palaeoredox fronts: setting and associated alteration exposed within a key section for understanding uranium mineralisation at the Four Mile West deposit. MESA Journal 55, 34–39.

Jenkins, R.J.F., Sandiford,M., 1992. Observations on the tectonic evolution of the southern Adelaide Fold Belt. Tectonophysics 214, 27–36.

Jeon, H., Williams, I.S., Chappell, B.W., 2012. Magma to mud to magma: rapid crustal recycling by Permian granite magmatism near the eastern Gondwana margin. Earth and Planetary Science Letters 319, 104–117.

Johnson, J.P., McCulloch, M.T., 1995. Sources of mineralising fluids for the Olympic Dam deposit (South Australia): Sm–Nd isotopic constraints. Chemical Geology 121, 177–199.

Kretz, R., 1983. Symbols for rock-forming minerals. American Mineralogist 68, 277–279.

Lan, Z.W., Chen, Z.Q., 2012. New xenotime ages obtained from the Paleoproterozoic Kimberley Group, NW Australia: implications for regional hydrothermal events. Australian Journal of Earth Sciences 59, 119–133.

Lister, G.S., Baldwin, S.L., 1996. Modelling the effect of arbitrary P–T–t histories on argon diffusion in minerals using the MacArgon program for the Apple Macintosh. Tectonophysics 253, 83–109.

Mawby, J., Hand, M., Foden, J., 1999. Sm–Nd evidence for high-grade Ordovician metamorphism in the Arunta Block, central Australia. Journal of Metamorphic Geology 17, 653–668.

Mawson, D., 1944. The nature and occurrence of uraniferous mineral deposits in South Australia. Transactions of the Royal Society of South Australia 68, 334–356.

McDonough, W.F., Sun, S.-S., 1995. The composition of the earth. Chemical Geology 120, 223–253.

McLaren, S., Dunlap, W.J., Sandiford, M., McDougall, I., 2002. Thermochronology of high heat-producing crust at Mount Painter, South Australia: implications for tectonic reactivation of continental interiors. Tectonics 21 (article no 1020).

McLaren, S., Sandiford, M., Powell, R., Neumann, N., Woodhead, J., 2006. Palaeozoic intraplate crustal anatexis in the Mount Painter Province, South Australia: timing, thermal budgets and the role of crustal heat production. Journal of Petrology 47, 2281–2302.

Mildren, S., Sandiford, M., 1995. Heat refraction and low-pressure metamorphism in the northern Flinders Ranges, South Australia. Australian Journal of Earth Sciences 42, 241–247.

Mitchell, M.M., Kohn, B.P., Foster, D.A., 1996. Apatite fission track thermochronology of the Mt Painter Inlier & the adjacent Adelaide Geosyncline. AGCRC report, p. 52.

Mitchell, M.M., Kohn, B.P., O'Sullivan, P.B., Hartley, M.J., Foster, D.A., 2002. Low-temperature thermochronology of the Mt Painter Province, South Australia. Australian Journal of Earth Sciences 49, 551–563.

Neumann, N., 2001. Geochemical and isotopic characteristics of South Australian Proterozoic granites: implications for the origin and evolution of high heat-producing terrains. Ph.D. Thesis, University of Adelaide, Adelaide.

Pankhurst, R.J., Vaughan, A.P.M., 2009. The tectonic context of the Early Palaeozoic southern margin of Gondwana. In: Bassett, M.G. (Ed.), Early Palaeozoic Peri-Gondwana Terranes: New Insights from Tectonics and Biogeography. Geological Society Special Publication. Geological Society Publishing House, Bath, pp. 171–176.

Pankhurst, M.J., Vernon, R.H., Turner, S.P., Schaefer, B.F., Foden, J.D., 2011. Contrasting Sr and Nd isotopic behaviour during magma mingling; new insights from the Mannum A-type granite. Lithos 126, 135–146.

Paul, E., Flöttmann, T., Sandiford, M., 1999. Structural geometry and controls on basement-involved deformation in the northern Flinders Ranges, Adelaide Fold Belt, South Australia. Australian Journal of Earth Sciences 46, 343–354.

Preiss,W.V., 1987. The Adelaide Geosyncline: Late Proterozoic stratigraphy, sedimentation, palaeontology and tectonics. Geological Survey of South Australia Bulletin 53, 34–41.

Preiss, W.V., 2000. The Adelaide Geosyncline of South Australia and its significance in Neoproterozoic continental reconstruction. Precambrian Research 100, 21–63.

Sandiford, M., Hand, M., 1998. Controls on the locus of intraplate deformation in central Australia. Earth and Planetary Science Letters 162, 97–110.

Sandiford, M., Hand, M., McLaren, S., 1998. High geothermal gradient metamorphism during thermal subsidence. Earth and Planetary Science Letters 163, 149–165.

Schmidt, P.W., Clark, D.A., 2011. Magnetic characteristics of the Hiltaba Suite Granitoids and Volcanics: Late Devonian overprinting and related thermal history of the Gawler Craton. Australian Journal of Earth Sciences 58, 361–374.

Sircombe, K.N., McQueen, K.G., 2000. Zircon dating of Devonian–Carboniferous rocks from the Bombala area, New South Wales. Australian Journal of Earth Sciences 47, 1041–1051.

Skirrow, R.G., Creaser, R., Hore, S.B., 2011. Mt Gee-Armchair U–REE deposits, South Australia. In: Skirrow, R.G. (Ed.), Uranium Mineralisation Events in Australia: Geochronology of the Nolans Bore, Kintyre, Oasis, Mt Gee-Armchair, and Maureen Deposits. Geoscience Australia Record 2011/12. Geoscience Australia, Canberra, pp. 36–57.

Spikings, R.A., Foster, D.A., Kohn, B.P., 2006. Low-temperature (b110 °C) thermal history of the Mt Isa and Murphy Inliers, northeast Australia: evidence from apatite fission track thermochronology. Australian Journal of Earth Sciences 53, 151–165.

Stewart, K., Foden, J., 2001. Mesoproterozoic Granites of South Australia. University of Adelaide, Adelaide.

Teale, G.S., 1979. Revision of nomenclature for Palaeozoic intrusives of the Mount Painter Province, South Australia. Royal Society of South Australia Transactions 103, 95–100.

Turner, S., Foden, J.D., 1996. Petrogenesis of late-Delamerian A-type granites and granophyre, South Australia: magma mingling in the Mannum granite. Mineralogy and Petrology 56, 147–169.

Turner, S.P., Foden, J.D., Morrison, R.S., 1992. Derivation of an A-type magma by fractionation of basaltic magma: an example from the Padthaway Ridge, South Australia. Lithos 28, 151–179.

Turner, S.P., Adams, C.J., Flottmann, T., Foden, J.D., 1993. Geochemical and geochronological constraints on the Glenelg River Complex, western Victoria. Australian Journal of Earth Sciences 40, 275–292.

Turner, S., Sandiford, M., Flottmann, T., Foden, J., 1994. Rb/Sr dating of differentiated cleavage from the Upper Adelaidean metasediments at Hallett Cove, southern Adelaide Fold Belt. Journal of Structural Geology 16, 1233–1241.

Vervoort, J.D., Patchett, P.J., 1996. Behavior of hafnium and neodymium isotopes in the crust: constraints from Precambrian crustally derived granites. Geochimica et Cosmochimica Acta 60, 3717–3733.

Wang, X., Griffin, W.L., Chen, J., 2010a. Hf contents and Zr/Hf ratios in granitic zircons. Geochemical Journal 44, 65–72.

Wang, X.C., Li, X.H., Li, Z.X., Liu, Y., Yang, Y.H., 2010b. The Willouran basic province of South Australia: its relation to the Guibei large igneous province in South China and the breakup of Rodinia. Lithos 119, 569–584.

Watson, E.B., Harrison, T.M., 1983. Zircon saturation revisited: temperature and composition effects in a variety of crustal magma types. Earth and Planetary Science Letters 64, 295–304.

Whalen, J.B., Currie, K.L., Chappell, B.W., 1987. A-type granites: geochemical characteristics, discrimination and petrogenesis. Contributions to Mineralogy and Petrology 95, 407–419.

Wingate, M.T.D., Campbell, I.H., Compston, W., Gibson, G.M., 1998. Ion microprobe U–Pb ages for Neoproterozoic basaltic magmatism in south-central Australia and implications for the breakup of Rodinia. Precambrian Research 87, 135–159.

Wülser, P.-A., 2009. Uranium metallogeny in the North Flinders Ranges region of South Australia. PhD Thesis, University of Adelaide, Adelaide, 250 pp.

Fig.1:

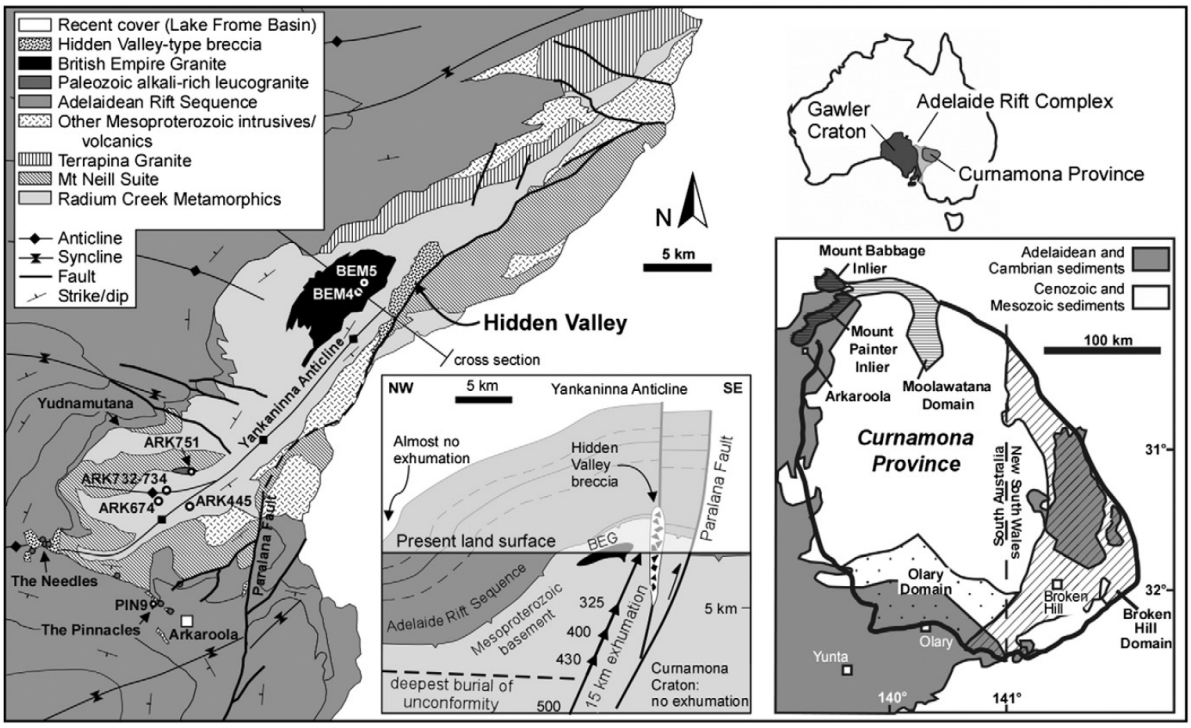

Fig. 1. Map of the Mt Painter Inlier and Neoproterozoic cover rocks, after Coats and Blissett (1971), and Stewart and Foden (2001) for the Mesoproterozoic granitoids. Insets show the location of the area within the Curnamona Province, and in relation to the Gawler Craton, with its world-class IOCG deposit at Olympic Dam. The NW–SE profile illustrates the contrasting uplift histories for the Mt Painter Inlier and the Curnamona Craton.

Fig.2:

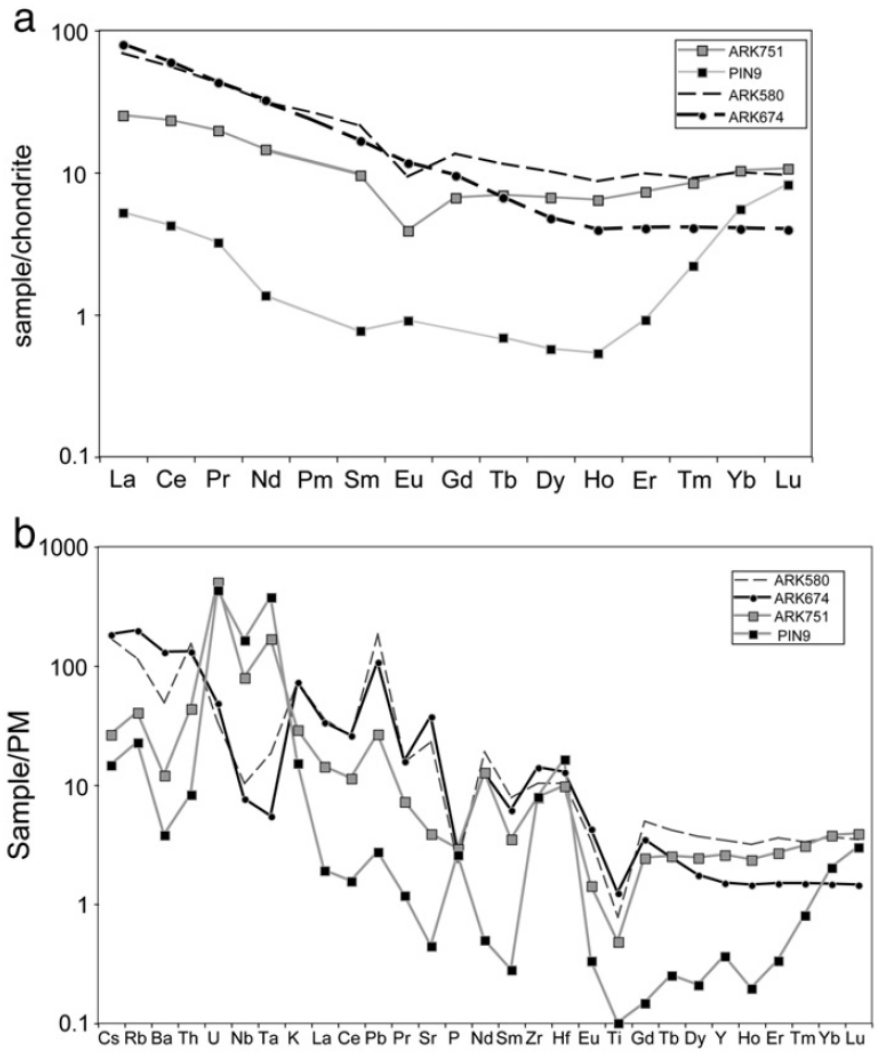

Fig. 2. Normalised trace element patterns for studied igneous samples. Normalising values are from McDonough and Sun (1995). a: Chondrite normalised rare earth element patterns. b: Primitive mantle-normalised trace element patterns.

Fig.3:

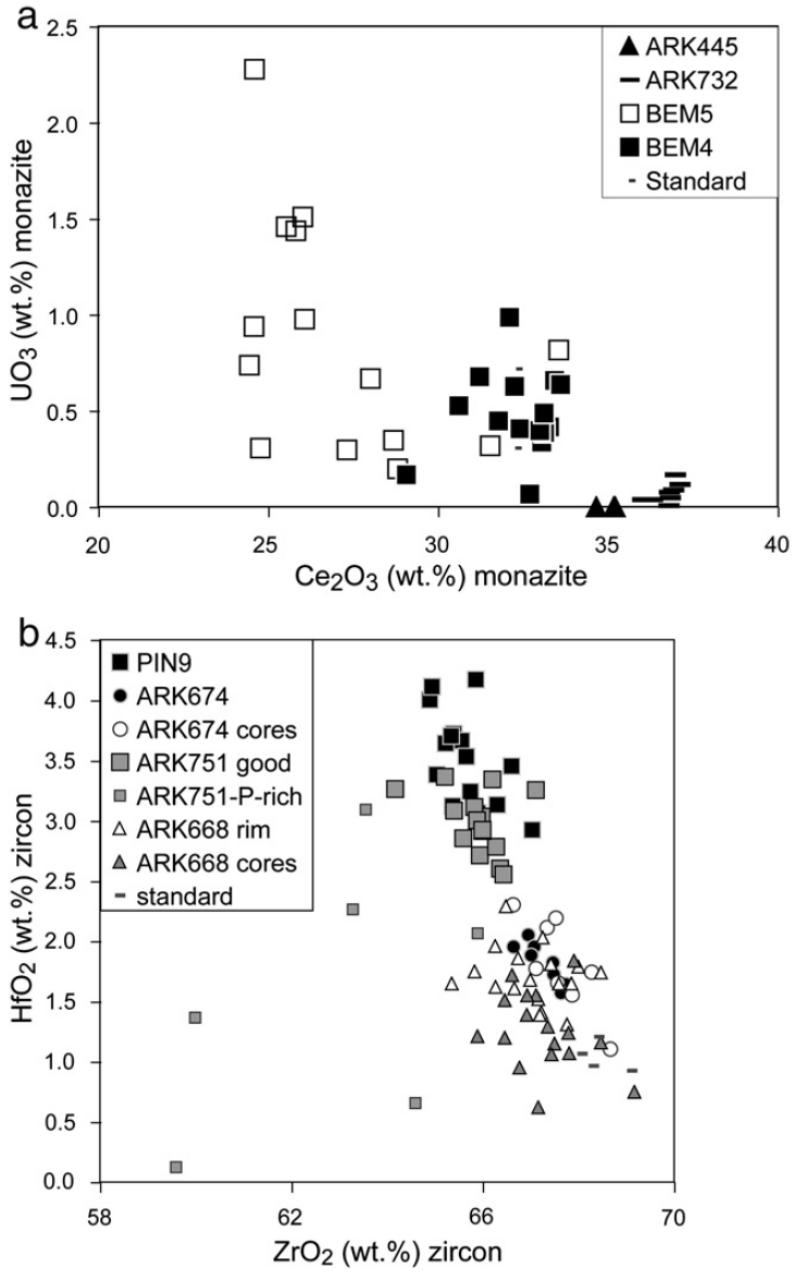

Fig. 3. SEM data for monazite and zircon from dated samples. a: UO3 versus Ce2O3 for monazite from the met-/peraluminous 455 Ma granitoids (BEM4, 5), the metasomatised dyke (ARK445) and the iron–uranium ore (ARK732). Data for Moacir standard are also shown. b: HfO2 versus ZrO2 for zircon from leucogranites PIN9 and ARK751 (including impure domains, labelled 'P-rich'), and cores and rims from metasomatised dyke ARK668, and metaluminous granitoid ARK674. Standard data are shown for comparison (NMNH 117288).

Fig.4:

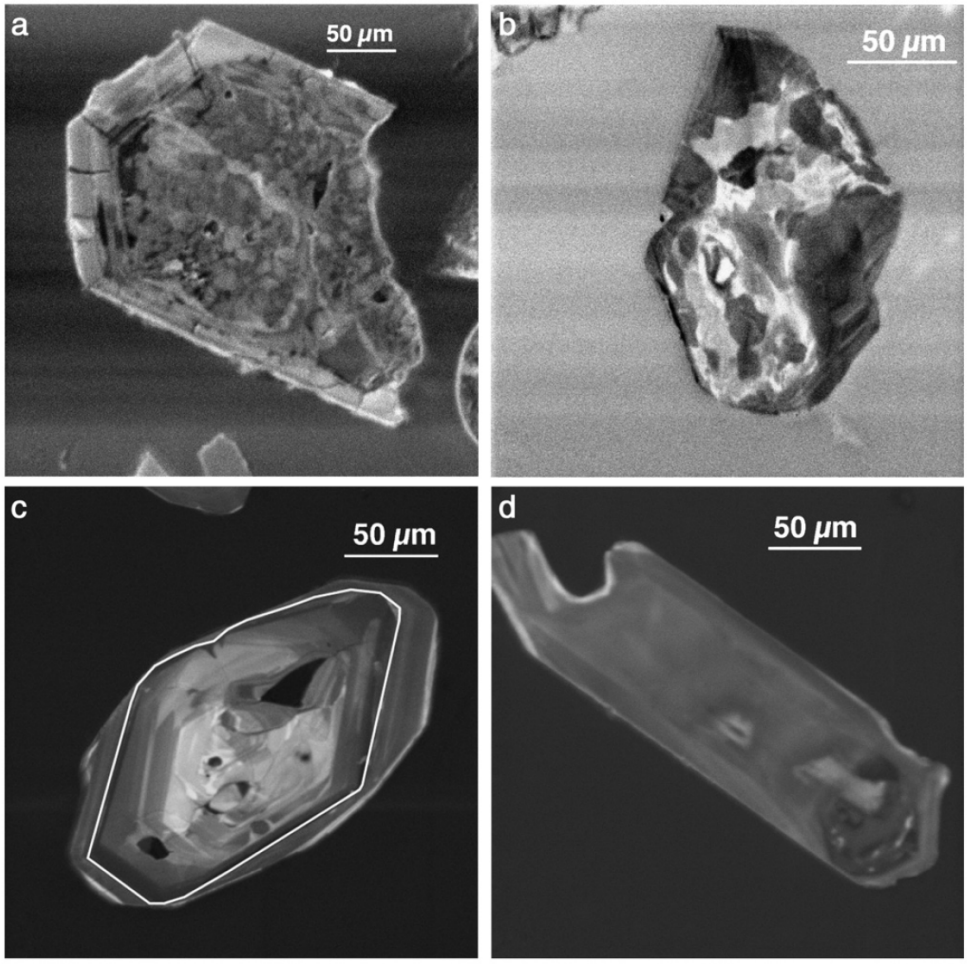

Fig. 4. Cathodoluminescence images of zircons. a. Leucogranite sample PIN9, zircon 20, showing a mottled interior and zoned rim, with perpendicular cracks, interpreted to reflect expansion of the core when it became metamict. Its 206Pb/238U age after common Pb correction is 469±5 Ma (6% discordant), and the εHf at that age −1.8±0.4. b. Leucogranite sample ARK751, zircon 23. The oscillatory zoned part on the right was ablated for U–Pb analysis. This was the only analysis from ARK751 that did not contain common Pb, had ~1000 ppm U and gave a concordant 206Pb/238U age of 453±5 Ma. c. Metaluminous granite ARK674, zircon 7. The boundary between the core and the rim of this zircon has been indicated by a drawn white line. The rim yielded a 206Pb/238U age of 470±6 Ma, with a 176Hf/177Hf ratio of 0.28267 (εHf+6.3±0.7 at 460 Ma). The core yielded a discordant 207Pb/206Pb age of 1507±36 Ma, with a 176Hf/177Hf ratio of 0.28197 (εHf=+6.7±1.1 at 1572 Ma). The discordant age and the relatively high Hf isotopic composition compared to the rest of the population may reflect some mixing between old and young components for the core analysis. d. Metaluminous granite ARK674, zircon 40, consisting of newly grown zircon only. The 206Pb/238U age is 452±2 Ma, εHf=+5.5±0.4 Ma (n=2).

Fig.5:

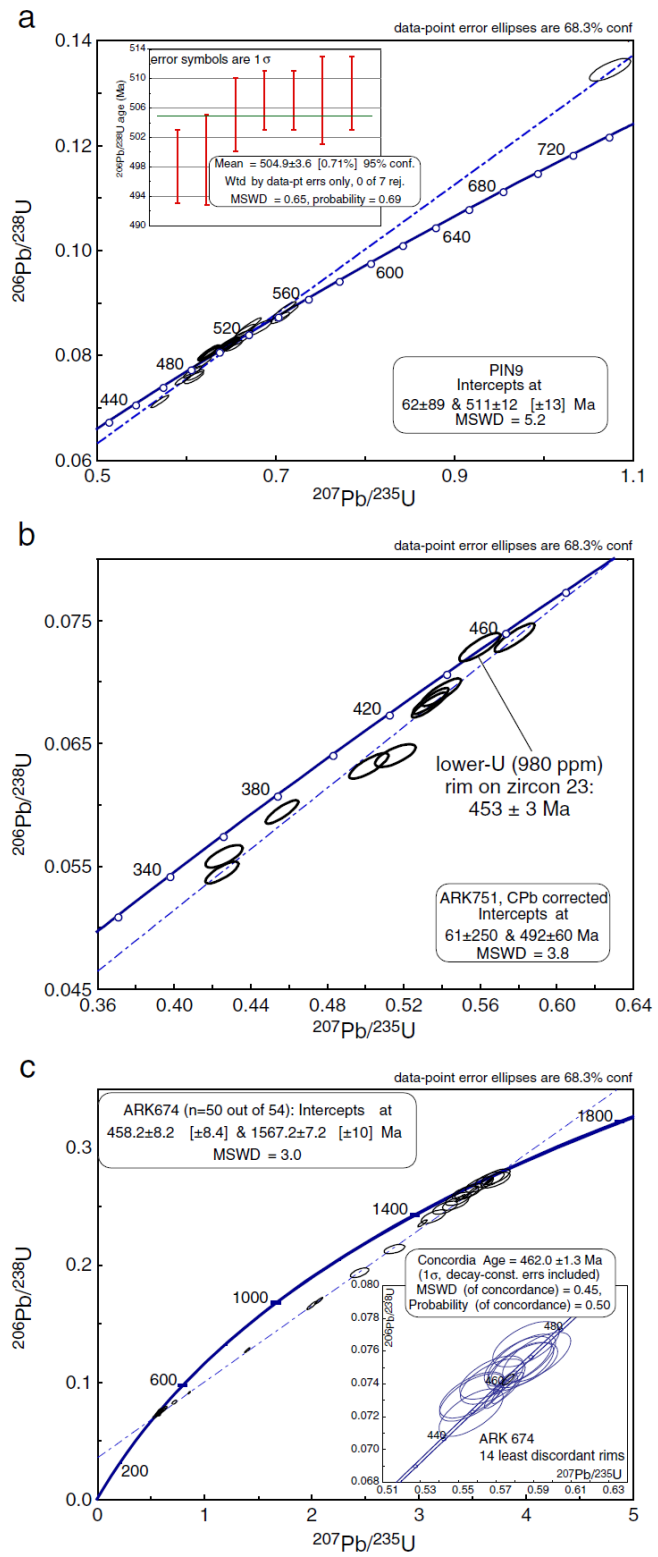

Fig. 5. U–Pb age data for zircons. a: Leucogranite sample PIN9. b: Leucogranite sample ARK751. c: Metaluminous granitoid ARK674.

Fig.6:

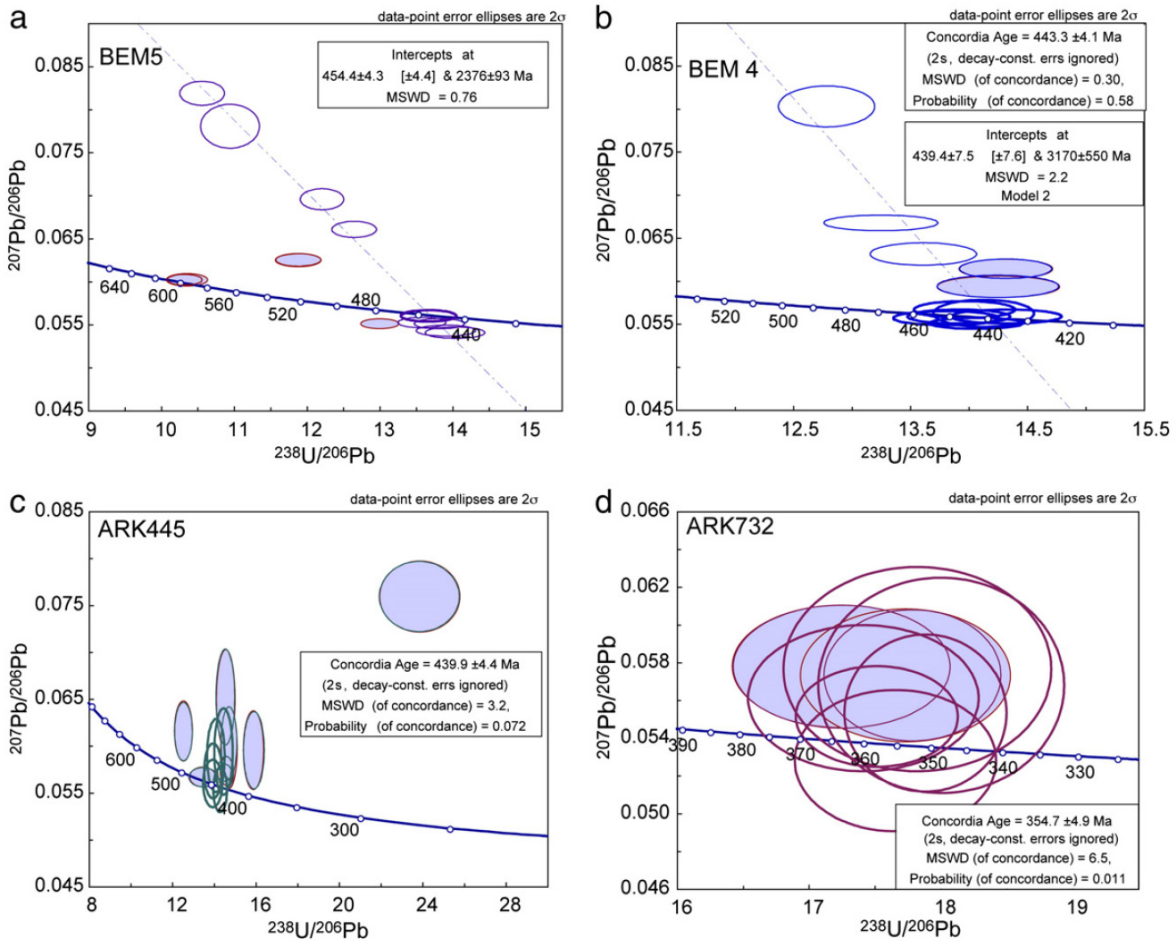

Fig. 6. U–Pb age data for monazite. a: Met-/peraluminous granites BEM4 and 5, which were dated previously by ID-TIMS on bulk monazite. b: Metasomatised dyke sample ARK445, dated previously by LA–MC–ICPMS on zircon. c: Ore sample ARK732.

Fig.7:

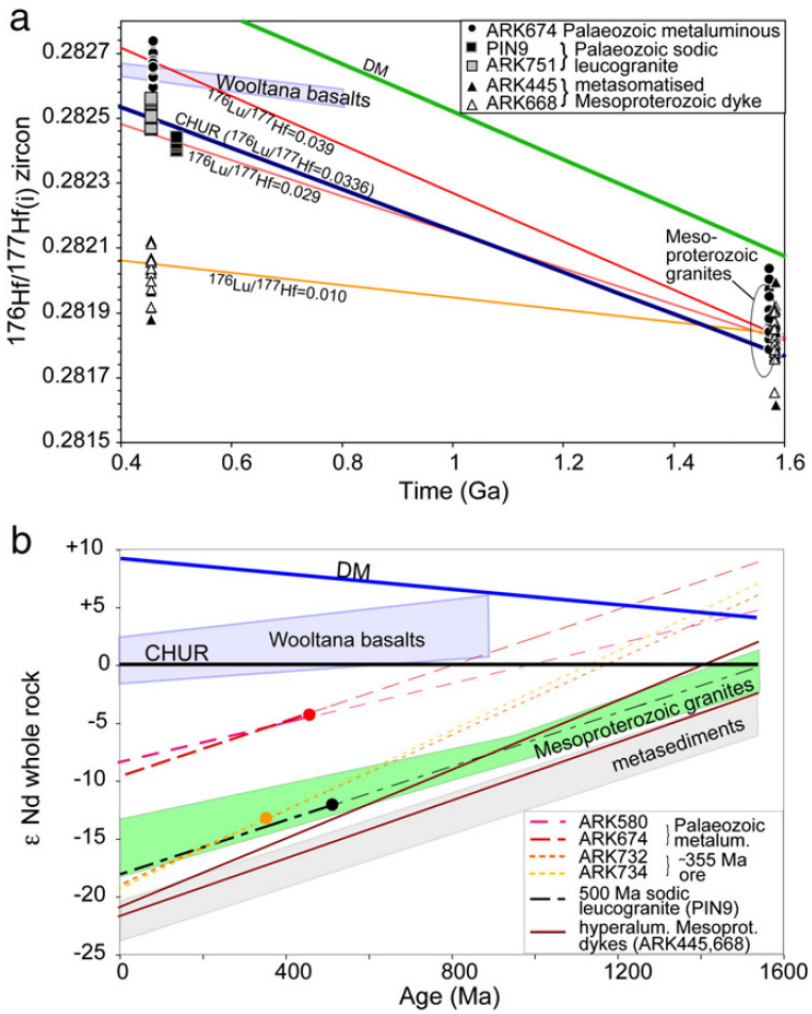

Fig. 7. a: Hf isotopic ratios versus time for analysed zircons. Data for metasomatised dykes are from Elburg et al., 2012. Whole rock data for Wooltana basalts are from Wang et al. (2010b). b: Whole rock Nd isotope data for ore samples. Data for ARK674, ARK580 and fields for Mesoproterozoic granites are from Elburg et al. (2012), for PIN9 from Elburg et al. (2003).

Fig.8:

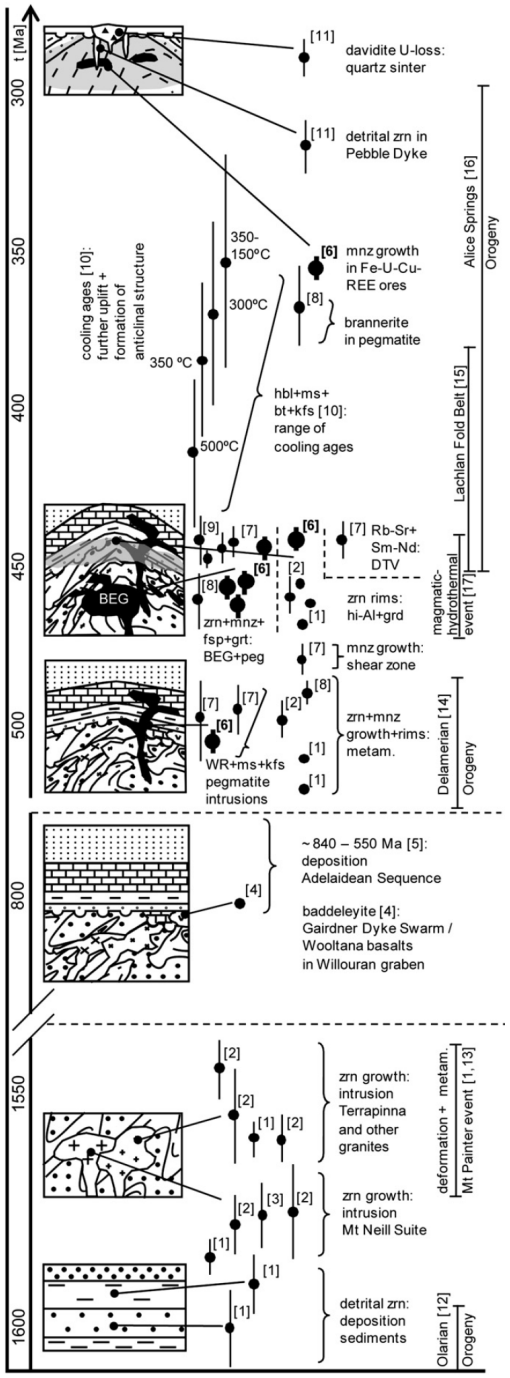

Fig. 8. General overview to the geological evolution of the Mt Painter Province from the Proterozoic to the Palaeozoic. The interpretation is supported by a selection of published geochronology and new age data by this study (bold symbols). A relationship to regional events in Australia is discussed in the text. Mineral abbreviations are after Kretz (1983). Metam.: metamorphism; BEG: British Empire Granite and Granodiorite; hi-Al: hyperaluminous rocks, after Elburg et al. (2012); grd: granodiorite; DTV: diopside–titanite vein ([1] Fraser and Neumann, 2010; [2] Elburg et al., 2012; [3] Elburg et al., 2001; [4] Wingate et al., 1998; [5] Preiss, 2000; [6] this study; [7] Elburg et al., 2003; [8] Wülser, 2009; [9] McLaren et al., 2006; [10] McLaren et al., 2002; [11] Brugger et al., 2011; [12] Drexel et al., 1993; [13] Paul et al., 1999; [14] Foden et al., 2006; [15] Gray and Foster, 2004; [16] Buick et al., 2008).

Fig.9:

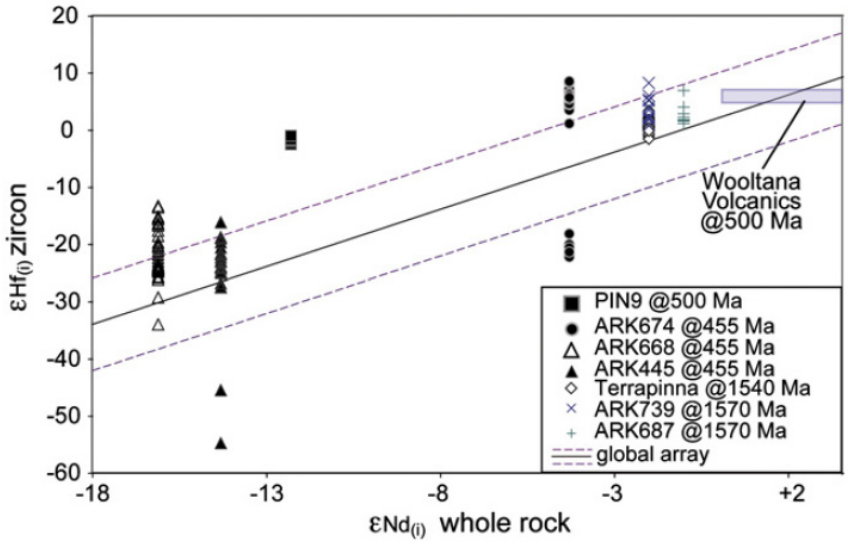

Fig. 9. Diagram of εHf of zircon versus whole rock εNd. Crustal envelope is from Vervoort and Patchett (1996). ARK687 and ARK739 are metasomatised Mesoproterozoic granite samples are from Elburg et al. (2012).

Fig.10:

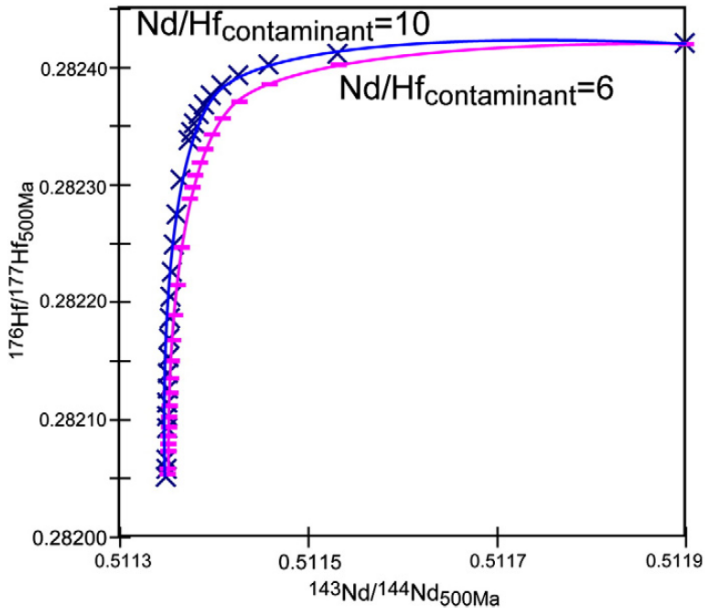

Fig. 10. Simple mixing models for Hf and Nd isotopes. In both cases, the high Hf and Nd isotope end member was taken as having the Nd and Hf concentrations and Hf isotopic composition of PIN9. Its Nd isotopic composition was taken to match its Hf isotopic composition on the crustal evolution line. The other end member has a Nd isotopic composition to match the Mesoproterozoic granites at 500 Ma, and a similar Nd concentration. Its Hf isotopic composition was calculated by radiogenic ingrowth of the original Hf isotopic signature of the 1570 Ma zircons using an average crustal 176Lu/177Hf ratio of 0.01. One of the curves uses an Hf concentration of 23 ppm (Nd/Hf=6), similar to the whole rock composition of the Mesoproterozoic granites, and the other one only 12 ppm (Nd/Hf=10), representing reduced Hf mobility because of its being contained in zircon. Tick marks are 1% contamination for the ten first markers near the top right hand side of the curve, 5% contamination for the following ones.

Tab.1:

Sample no.	ARK674	ARK751	ME00PIN9	ARK732	ARK734
Easting 54	337750	340530	337419	338245	338235
Northing 54	6654328	6656801	6646901	6655654	6655653
SiO_2	71.50	77.83	79.50	10.82	10.30
TiO_2	0.25	0.10	0.02	0.03	0.03
Al_2O_3	16.24	14.09	12.51	1.11	1.28
Fe_2O_3	2.13	0.37	0.13	77.99	85.73
MnO	0.02	0.01	0.00	6.07	0.71
MgO	0.72	0.08	0.08	0.04	0.04
CaO	3.10	0.40	0.15	0.00	2.48
Na_2O	4.43	7.00	6.98	0.01	0.00
K_2O	2.09	0.83	0.44	0.15	0.04
P_2O_5	0.06	0.06	0.05	0.29	0.24
LOI	0.43	0.41	0.13	4.82	5.51
Total	100.55	100.76	99.58	96.51	100.84
ASI	1.07	1.07	1.02		
Rb	118	24	14	1	0
Ba	857	79	25	19,035	3743
Sr	740	77	9	90	32
Zr	146	82	83	22	56
Y	9	14	2	237	199
Sc	3.2	1.0	1.9	5.4	1.5
V	21.4	5.9	3.0	10.4	5.4
Ga	19.2	21.2	34.3	NA	NA
Cu	1	4	2	1434	945
Zn	10	1	1	627	282
Ni	2	0	1	6	16
Li	NA	1.6	1.8	11.3	7.1
Be	1.0	5.6	2.9	4.0	1.8
Cr	6.3	3.3	1.3	4.6	2.7
Ni	2.5	8.1	1.6	8.6	10.1
Ga	19.2	20.4	40.6	NA	NA
Nb	5.0	52.0	107.6	19.8	38.9
Mo	0.8	0.5	0.3	226.0	225.0
Cs	1.4	0.2	0.1	0.1	0.0
La	18.9	6.0	1.2	904.6	810.2
Ce	36.6	14.3	2.6	1939.4	1346.2
Pr	4.0	1.8	0.3	144.7	118.1
Nd	14.8	6.6	0.6	448.1	349.4
Sm	2.5	1.4	0.1	53.3	38.1
Eu	0.7	0.2	0.1	7.2	5.6
Gd	1.9	1.3	0.1	58.3	42.8
Tb	0.24	0.25	0.02	6.88	4.56
Dy	1.2	1.6	0.1	36.7	22.3
Ho	0.21	0.35	0.03	7.37	4.56
Er	0.6	1.2	0.1	23.2	13.9
Tm	0.10	0.21	0.05	3.44	2.05
Yb	0.6	1.7	0.9	23.0	13.3
Lu	0.10	0.26	0.20	3.16	1.83
Hf	3.6	2.8	4.6	0.5	0.6
Ta	0.2	6.2	13.8	0.3	0.4
Pb	7.6	0.8	0.2	100.2	30.1
Th	10.4	3.5	0.7	9.0	6.7
U	1.0	10.2	8.7	2052.0	453.0
T zircon (°C)	777	737	736		
$^{143}Nd/^{144}Nd$	0.512140		0.511707	0.511661	0.511645
$^{147}Sm/^{144}Nd$	0.1029		0.1050	0.0699	0.0635

Table 1
Whole rock data for analysed samples. Oxides in wt.%, elements in ppm. LOI=loss on ignition. ASI=alumina saturation index (molecular Al2O3/(Na2O+K2O+CaO)). PIN9 from Elburg et al. (2003), ARK732 from Elburg et al. (2012).

Tab.2:

Sample	Mineral	Age type	n_{used}/n_{total}	Age (Ma)	2σ (Ma)
PIN9	Zircon	Upper intercept	21/21	511	12
		Weighted average $^{206}Pb/^{238}U$	7/21	505	4
ARK751	Zircon	Upper intercept, CPb corrected	10/20	492	60
		Weighted average $^{206}Pb/^{238}U$	2/20	455	4
ARK674	Zircon	Upper intercept	50/54	1567	7
		Lower intercept	50/54	458	8
		Weighted average $^{206}Pb/^{238}U$	14/54	462	4
BEM5	Monazite	Tera–Wasserburg intercept	9/11	454	4
		Weighted average $^{206}Pb/^{238}U$	5/11	452	4
BEM4	Monazite	Tera–Wasserburg intercept	10/11	439	8
		Concordia	5/11	443	4
ARK445	Monazite	Concordia	6/13	440	4
ARK732	Monazite	Concordia	6/8	355	5
		Weighted average $^{206}Pb/^{238}U$	8/8	355	4

Table 2 Summary of the U–Pb age data.

---------- **APPENDIX 4 (ELBURG ET AL., 2012)** ----------

Metasomatism and metallogeny of A-type granites of the Mt. Painter–Mt. Babbage Inliers, South Australia

Marlina A. Elburg[a,b], Tom Andersen[c], Paul D. Bons[d], Anett Weisheit[d], Siri L. Simonsen[c], Ingrid Smet[a]

[a] Department of Geology and Soil Science, Ghent University, Belgium

[b] School of Geological Sciences, University of KwaZulu-Natal, Durban, South Africa

[c] Department of Geosciences, University of Oslo, Norway

[d] Department of Geosciences, Eberhard Karls University, Tübingen, Germany

Abstract

The Mt. Painter and Mt. Babbage Inliers (South Australia) are largely composed of Mesoproterozoic A-type granitoids that intruded marginally older metasediments. Metasomatic activity has had a pronounced influence on the granites in the southerly Mt. Painter Inlier. U–Pb dating and Hf isotope ratios of zircons from granites and hyperaluminous rocks show the latter to be heavily metasomatised equivalents of the granitoids. Similar metasomatic processes are likely to have been responsible for the formation of Fe-oxide–U–REE ores. These ores formed more than 1100 Ma after intrusion of the Mesoproterozoic A-type granites, and elemental remobilisation may have been associated with a new phase of granitoid magmatism around 455 Ma. The ferroan and incompatible element-rich nature of A-type granites makes them a suitable source for ores that can be tapped whenever thermal and fluid conditions are favourable.

1. Introduction

The most common mineralisation associated with the broad class of granites denoted as 'A-type' (ferroan) is tin, tungsten and beryllium (Haapala et al., 2005). However, iron oxide–copper–gold (IOCG) plus uranium and rare earth elements (REE) constitute another economically important class of ores that show a spatial and temporal relationship to such granites (Haapala, 1995). A prime example of this type of mineralisation is the giant Olympic Dam deposit, located on the South Australian Gawler Craton, associated with ca. 1590 Ma A-type granites (Creaser and Cooper, 1993). The association between A-type granites and IOCG mineralisation is logical as one of the defining characteristics of A-type granites is their iron enrichment (Loiselle and Wones, 1979); it has therefore been suggested that A-type granites should better be called ferroan granites (Frost and Frost, 2011). As ore-forming processes necessitate the mobilisation of elements from their source, followed by their concentration and deposition, ore formation is always associated with changes in whole rock composition. Therefore, the chemical composition of granites affected by ore formation can be unrepresentative of their magmatic signature, hampering efforts to fit them into existing classification schemes. Apart from the well-known occurrence on the Gawler Craton, Mesoproterozoic A-type granites are also found in other parts of South Australia, such as the Curnamona Province (Fig. 1). In this contribution, we provide new data for A-type granites from the Mt. Painter and Mt. Babbage Inliers on the northwestern side of the Curnamona Province, focusing on the metasomatic and metallogenetic processes that have affected the granitoids. Our data indicate that deformation and metasomatism can alter granitoid rocks almost beyond recognition, whereby only resistant minerals such as zircon can potentially give clues to the identity of the protolith. Recognition of the protolith allows quantification of metasomatic processes, which is a prerequisite to investigate a potential link

with ore formation. For the A-type granites described here, a variety of metasomatic processes seem to have played a role, including albitisation and Mg-metasomatism, with concomitant mobilisation of iron. The latter element now makes up the bulk of the U and Cu-bearing ores in the area. The intrusion of Palaeozoic granites, with I–S type affinities, may have acted as the heat source for at least some of the metasomatic activity.

2. Regional setting and field data

The Mt. Painter and Mt. Babbage Inliers belong to the Moolawatana Domain (Conor and Preiss, 2008) of the Curnamona Province, which straddles the boundary between South Australia and New South Wales (Fig. 1). Large parts of the province are covered with (meta)sediments of Neoproterozoic to Recent age; other exposed Meso- to Palaeoproterozoic areas are the Olary and Broken Hill Domains in the south. The first comprehensive work on the geology of the Mt. Painter and Mt. Babbage Inliers, including their Neoproterozoic–Palaeozoic cover, was done by Coats and Blissettt (1971), following on from earlier work by Mawson, Sprigg and others (Mawson, 1923, 1944; Sprigg, 1945). The Inliers constitute tectonic windows into the Mesoproterozoic basement of the Neoproterozoic–Cambrian ("Adelaidean") sediments of the Adelaide Rift Sequence (Fig. 1; Preiss, 1987).

These windows were formed by large-scale folding during the 515–485 Ma (Foden et al., 1999, 2006) Delamerian Orogeny. Interference of NW–SE and subsequent N–S shortening (Drexel et al., 1993) caused ~10 km sized domes and basins, in which the basement is exposed in the cores of anticlinal domes (Fig. 1). Further exhumation and exposure of the inliers was caused by uplift along the Paralana Fault System, which bounds the Mt. Painter Inlier to the east, where it is juxtaposed against Tertiary gravels. Overall shortening of the Delamerian thick-skinned folding was relatively minor, only a few tens of percent (Paul et al., 1999). Within the basement it caused 100 m-scale parasitic folds and crenulations in suitable biotite-rich lithologies. In the Adelaidean cover, which did not experience any other deformation event, cleavage developed in the most pelitic lithologies and growth of andalusite, cordierite and biotite in metapelites of the lowermost Adelaidean units record progressive Delamerian metamorphism (Coats and Blissett, 1971; Mildren and Sandiford, 1995).

Most basement rocks are strongly foliated, and many of the granitoids can therefore be considered to be metagranites. The age of this main foliation was tentatively set at ~1555 Ma by Dipple et al. (2005), which may coincide with the metamorphic overprint described by Fraser and Neumann (2010), which will be discussed later. The deformation event is, however, highly heterogeneous. Strong localisation, especially in granitoids, left behind almost undeformed regions (Elburg et al., 2001). The main tectonic event that affected the basement is, however, certainly older than the Adelaidean Sequence, as the foliation is truncated by the Adelaidean unconformity and strongly-foliated basement clasts can be found in the basal Shanahan Conglomerate.

The oldest rocks in the area are the Radium Creek Metamorphics, which are metasediments that range from quartzites and meta-arkoses to phyllites, schists and migmatites. Their depositional age is likely to be Mesoproterozoic (Fanning et al., 2003), although older publications have suggested a Palaeoproterozoic age (Drexel et al., 1993). Corundum-bearing biotite schists and phlogopitites, which are an important focus of the present work, are traditionally mapped as belonging to the Corundum Creek Schist member of the Radium Creek Metamorphics.

The metamorphic suite has been intruded by granites, which have been subdivided into the older Mt. Neill Suite (approximately 1575 Ma, Elburg et al., 2001), which dominates the Mt. Painter Inlier, and the somewhat younger (1555–1560 Ma) Moolawatana Suite (Stewart and Foden, 2001), to which the Terrapinna and Yerila Granite belong; the Terrapinna is volumetrically the most important member (Fig. 1). The Mesoproterozoic granites vary in texture and geochemistry, and this has been used for the subdivisions defined in previous works (Stewart and Foden, 2001). Within the Mt. Painter Inlier, the area mapped as the Mt. Neill Suite comprises both true granitoids and albitised lithologies (chemically trondhjemites, see below), which have a characteristic grey appearance, while the true granites are pinker in colour. The Mt. Neill Suite rocks are equigranular to porphyritic, and contain quartz crystals with a noticeable bluish colour.

Deformation has turned some granitoids into gneisses and schists, but the colour of the quartz crystals bears witness to the identity of their protolith (Elburg et al., 2001); they will be referred to as quartz–augen gneisses. Mafic igneous lithologies are rare, but mafic enclaves have been found, and one sample was analysed for this study (ARK691; Fig. 2B). The rounded to scalloped shape of this enclave suggests that it was a globule of more mafic magma that mingled with and chilled against the cooler granitic host magma. The Terrapinna Granite is exposed in both the Mt. Painter and Mt. Babbage Inlier. Within the Mt. Painter, it has a pink-orange colour and is equigranular, but it is more porphyritic in the northern Inlier (Fig. 2A). The Yerila occurs in the Mt. Babbage Inlier only, and is a greyish granite with large K-feldspar crystals.

Biotite- or phlogopite-rich corundum-, spinel- and sapphirine-bearing rocks, collectively referred to as hyperaluminous rocks, have only been found in the Mt. Painter Inlier proper, and do not seem to occur in the overlying Neoproterozoic cover sequence. The most conspicuous outcrops, which have been described previously (Coats and Blissett, 1971; Teale, 1980 and references therein) occur within the Corundum Creek Schist member of the Radium Creek Metamorphics, near the #6 uranium mine (locality 1 on Fig. 1) and at the Corundum Mine approximately four kilometres further to the WNW (locality 2). The ‘normal’ metasediments in these areas consist of feldspathic quartzites and arenaceous schists, of which analysed sample ARK661 is an example.

These are, however, not the only occurrences of hyperaluminous rocks in the Mt. Painter Inlier. Fig. 1 shows the location of several other occurrences we found during fieldwork in the past years. Those

discussed in this contribution are numbered. An important observation is that these hyperaluminous lithologies do not occur solely within the Radium Creek Metamorphics, but are also found within the Mesoproterozoic granites (at the Hidden Valley locality 4). The map gives a very broad overview of the lithologies, but more detailed fieldwork has shown that some areas mapped as Radium Creek Metamorphics are mainly heavily deformed granites, as is the case for the Mt. Painter locality 3. The host rocks to localities 1 and 2 consist of true metasediments though.

Attempts to follow the outcrops of these hyperaluminous rocks to see whether they formed a traceable lithology met with little success, apart from those at locality 1. This layer appears to be folded by the Delamerian Orogeny (Fig. 3). The other occurrences have a more discontinuous patchy appearance, with outcrops varying in size between only a metre squared, to several tens of metres across. Unfortunately, outcrops are often scattered and clear contacts with the host rocks are generally not visible.

The inlier was covered by Neoproterozoic to Cambrian sediments of the Adelaide Rift Complex, with various lithologies (sandstones, shales, glacial tillites, carbonates, dolomites). Mafic extrusives, called the Wooltana Basalts, are also found within the lower part of the sequence, and have been correlated with the approximately 827 Ma Gairdner Dyke Swarm (Wingate et al., 1998), associated with the break-up of Rodinia and creation of the Adelaide Rift.

During or after the 515–485 Ma Delamerian Orogeny the area was intruded by small bodies of pegmatitic to leucogranitic sodium-rich granites in the aftermath of the Delamerian Orogeny. These have been dated by Sm–Nd on garnet-whole rock to approximately 500 Ma (Elburg et al., 2003), but this age seems at odds with their undeformed appearance. These bodies will not be discussed further in this paper. Somewhat more extensive metaluminous and peraluminous granites (Fig. 1) intruded during a separate Ordovician event at 440–460 Ma. The age of these granites has been established by ID-TIMS U–Pb dating of bulk monazite (Elburg et al., 2003) and Pb–Pb dating of garnet (McLaren et al., 2006). These granitoids are found in both inliers, either as large bodies or as spatially more restricted outcrops. The peraluminous parts of these bodies have been called the British Empire Granite (restricted to the batholith in the Mt. Painter Inlier), and the metaluminous parts are taken together as the Paralana Granodiorite (Stewart and Foden, 2001). The exact definition of what constitutes the Paralana Granodiorite is not completely clear, and both deformed and undeformed granitoids have been included in this group in some previous studies. All samples of the Paralana Granodiorite discussed in this study have an equigranular, undeformed appearance. Enclosed xenoliths of deformed Mesoproterozoic granitoids display sharp contacts (Fig. 2C) and felsic dykes associated with the Paralana Granodiorite clearly crosscut the Mesoproterozoic granitoids.

Uranium mineralisation associated with massive hematite breccias has been known to exist in the area since 1910 (Coats and Blissettt, 1971), and secondary concentrations (with torbernite as the most

conspicuous U-mineral) have been mined in the first half of the 20th century. The uranium is likely derived from the Mesoproterozoic granites and remobilised several times, from the Ordovician to sub-recent times (Elburg et al., 2003; Wülser, 2009). Several companies have conducted exploration programmes in the area afterwards, concentrating on sheets of hematite-rich breccias in the southern part of the Mt. Painter Inlier. Our samples are derived from one of these approximately 5-metre thick sheets, which dip about 30° to the east (Fig. 2H). The ores are in part dark brown and friable, but have a more solid black appearance in other places, which seems to result from silicification. The friable ores tend to give the higher scintillometer readings.

3. Analytical techniques

Samples selected for zircon studies were crushed and sieved to sub-500 μm grain size. After removing the fines by washing, zircons were separated using the Frantz magnet and bromoform. Zircons were handpicked, mounted in epoxy, photographed and studied in transmitted light to select inclusion-free areas for U–Pb and Hf isotope analyses. The zircons were then imaged by cathodoluminescence at the Department of Geology and Soil Science of Ghent University using a JEOL 6400 scanning electron microscope (20 keV accelerating voltage) and VISTA software, to ascertain that selected spots for U–Pb and Hf analysis were located within the same growth zone of the zircon.

U–Pb and Lu–Hf isotope compositions were analysed by laser-ablation inductively coupled plasma source mass spectrometry using a Nu Plasma HR mass spectrometer and a NewWave LUV213 laser microprobe at the Department of Geosciences, University of Oslo. The analytical protocols described in detail by Rosa et al. (2009) and Andersen et al. (2009) were used for U–Pb geochronology of zircon, and those of Heinonen et al. (2010) for Lu–Hf. The average value for 176Hf/177Hf of the Temora standard during the two sessions of the analyses in the first half of 2010 was 0.282693±22 (1 sd, n=20), and for the Mud Tank zircon 0.282516±20 (1 sd, n=40). The value for the decay constant of 176Lu was taken as 1.867×10– 11 a−1 (Scherer et al., 2007; Söderlund et al., 2004). The calculations of εHf were done using a present-day chondritic 176Hf/177Hf value of 0.282785 and 176Lu/177Hf of 0.0336 (Bouvier et al., 2008). Interferences on mass 176 from 176Lu and 176Yb were corrected using an empirical correction routine based on reference zircons with known 176Hf/177Hf and variable REE/Hf ratio; this method gives accurate results up to 176Yb/177Hf ratios of ca. 0.35 (Heinonen et al., 2010). All isochrons and concordance ages were calculated using the programme Isoplot (Ludwig, 2008), version 3.71-r5.

Whole rock analyses were performed at Ghent University after crushing the rocks in a stainless steel jaw crusher, and powdering representative splits in either an agate or a tungsten carbide mill, with agate milling restricted to spinel- and corundum-free samples. Comparison between the two mills only

showed detectable contamination of Co in the tungsten carbide mill (as we did not analyse W and C), so this element is not reported. Samples underwent Loss on Ignition by heating at 950 °C for 8 h, after pre-drying at 110 °C for 2 h. Two hundred milligrammes of sample was mixed with 1 g of mixed lithium meta-/tetraborate flux (65:35, Breitländer Specflux A1222), fused in graphite crucibles in an oven at 1050 °C for 15 min, after which the melt was poured into and dissolved in 100 ml 2% HNO3. A range of rock standards, bracketing the expected major element compositions of the samples, was dissolved in a similar manner, and used as calibration standards. As the iron-rich ores fell outside the bracketing standards, and did not produce a dissolvable homogenous melt, 0.1 g of the powdered ore was mixed with 0.1 g of pure SiO2 (Fischer S153-3), and this mixture melted with flux; this gave a homogeneous melt and clear solution. Major and some trace elements were analysed with a Spectro ARCOS ICP-OES, housed at the Department of Analytical Chemistry of Ghent University. A four times more dilute version of the same solutions was analysed by Q-ICPMS (PE Elan 5000) for Rare Earth Elements (REE) and other traces that could not be reliably analysed by ICPOES, using BHVO-2 and AGV-2 as calibration standards. Special care was taken to correct for LREE-oxide interferences on the MREE, considering the very LREE-enriched nature of the samples. This was achieved by spiking selected samples with LREE-standards to determine oxide formation relative to Th, and monitoring the ThO+/Th+ ratio for each sample.

Nd isotopes were measured on a ThermoScientific Neptune MC– ICPMS, housed at the Department of Chemistry of Ghent University. All samples were dissolved in high pressure bombs with a mixture of 40% HF and 7N HNO3 at 185 °C for five days, and fluorides broken down with aqua regia at the same conditions for two days. The sample was split for Sm/Nd and Nd isotope ratio measurement. For the isotopic ratio determination, Nd was isolated following procedures similar to those described by Pin and Zalduegui (1997). Nd isotope ratios were analysed in static mode (100 scans) on solutions of approximately 0.5–1 ppm Nd, with mass bias correction using an exponential law (Russell equation) to 146Nd/144Nd=0.7219. Full procedure blanks were as low as instrument background. Solution standard JNdi gave 143Nd/144Nd=0.512110±5 (1 sd, n=13), BHVO-2 0.512989±4 (n=2) and AGV-2 0.512800±3 (n=2). Sm/Nd ratios were measured in low resolution mode on an ElementII SF-ICPMS at Ghent University using sample-standard bracketing, with BHVO-2 as a bracketing standard (147Sm/144Nd=0.1503; Kent et al., 2004). This yielded 147Sm/144Nd ratios for BCR-2 of 0.1385±1 and for AGV-2 0.1070±1.

4. Petrography

All Mesoproterozoic granites are equigranular, but their grain size and microstructure mainly depend on the degree of deformation. They contain quartz, K-feldspar (mainly microcline), plagioclase, biotite, and accessory apatite, zircon and monazite. Titanite was observed within less evolved samples

of the Terrapinna Granite, and garnet in evolved peraluminous samples. Secondary phases are chlorite and muscovite, and occasionally Fe–Ti-oxides and rutile. Fluorite and hornblende are present in the more calcium-rich samples of the Yerila Granite. One sample from the Terrapinna Granite (ARK708B) that had undergone biotitisation showed a marked decrease in the modal percentage of K-feldspar with increasing biotite concentrations. The K-feldspar in samples of the Mt. Neill Suite that have undergone albitisation has a very patchy appearance, consisting of Ab- and Or-rich domains. Deformation has caused alignment of ferromagnesian phases, and often dynamic recrystallisation of quartz and/or feldspars.

The quartz–augen gneisses, which were interpreted as deformed versions of the Mt. Neill Suite, contain quartz augen up to 5 mm in diameter, around which the micas are wrapped. Biotite predates muscovite growth in these samples.

The ~440–460 Ma granites are equigranular and consist of quartz, plagioclase, K-feldspar, with biotite in the less silicic, metaluminous samples (Paralana Granodiorite) and muscovite±garnet in the most evolved and peraluminous samples (British Empire Granite). Zircon, monazite and apatite are accessory phases; the latter often contains growth zones with an almost black appearance, apparently due to submicroscopic solid and fluid inclusions. Micas are not aligned, and evidence for deformation is restricted to undulose extinction of quartz.

The main mineral in most outcrops of the hyperaluminous rocks is a ferromagnesian mica, varying from black to pale brown in colour, as a reflection of varying Fe/Mg ratios. Corundum and spinel are the most common highly aluminous minerals, sometimes occurring as 10-cm diameter ‘eggs’ in which the inner part consists of white corundum and the outer part of blue-grey spinel. However, corundum is more typically blue in colour, with subordinate white and pink varieties. Spinel varies from blue-grey to greenish in hand specimen. Cordierite is a less common phase, occurring at locality 2. Högbomite has been described from locality 1 (Teale, 1980), together with taaffeeite. Sapphirine occurs locally at localities 1 and 2; sillimanite is found at localities 2 and 3. The mutual relationships between these minerals are complex, and will be discussed elsewhere. Essentially, the rock-forming minerals document progressive Mg-metasomatism and desilicification. Common accessory phases are magnetite/hematite, the latter often occurring as exsolution from spinel, rutile/anatase, monazite/xenotime and zircon. Tourmaline occurs occasionally, and appears to have formed relatively late. An overview of the mineralogy of the hyperaluminous samples is given in Electronic Appendix A1.

Deformation of minerals is minor: sapphirine shows signs of brittle behaviour, and the foliation sometimes wraps around the porphyroblasts. Darker-coloured biotite schists can be foliated and crenulated (Fig. 2D), but lighter-coloured phlogopitites generally do not show any shape-preferred

orientation of the minerals. Sillimanite patches in the biotite schist at the Mt. Painter locality (sample ARK739) are randomly oriented (Fig. 2E).

Sample ARK687A from location 4 is the corundum–phlogopite-rich side of a larger (60×15×15 cm) block, which graded from material resembling a mica-rich version of the local granite (ARK687L) into corundum–phlogopite schist (Fig. 2F).

The metasediments of the Radium Creek Metamorphics are phyllites and quartz–feldspar meta-arenites. The latter group, to which analysed sample ARK661 belongs, consists dominantly of quartz and microcline, with biotite and muscovite as minor phases. Quartz has pronounced undulose extinction and forms ribbons, which define the same foliation as the micas.

The main non-opaque phases in the ores are (hydrothermal) quartz, barite and fluorite; monazite is an important accessory phase. The oxides are magnetite and hematite, with hematite overall later than magnetite, and manganese (hydr)oxides, also late. Pyrite is thought to have formed early in the paragenetic sequence, to be replaced by sulphates at a later stage. SEM-investigations identified micron-sized grains of an unidentified uranium-(hydr)oxide mineral. The ores are commonly associated with zones of brecciation and chloritisation (Fig. 3).

5. Results

5.1. Geochemistry

5.1.1. Major and trace elements

Representative analyses are given in Table 1. Occasional low totals are likely related to the presence of fluorine, boron, arsenic and/or sulphur in the sample, which were not analysed for. All Mesoproterozoic granitoids are A-types in the definition of Whalen et al. (1987) (Fig. 4A), and A2 in the classification of Eby (1992). This also holds for the albitised samples (e.g. ARK20) and most of the quartz–augen gneisses that had been interpreted to be deformed and metasomatised equivalents of the Mt. Neill Suite. The Palaeozoic metaluminous granites (Paralana Granodiorite) are clearly distinct, with lower Zr and Ga/Al ratios. In terms of FeO*/(FeO*+MgO) (Frost et al., 2001), the Mesoproterozoic granites range from ferroan to magnesian (Fig. 4B), while all but one (highly evolved) sample of the Palaeozoic granites fall within the magnesian field. The extension to very low iron numbers for especially the Mt. Neill Suite sample is likely to be a result of metasomatic activity. Classification schemes based on even more mobile elements must be viewed with caution, considering the evidence for metasomatic processes. This is for instance shown by the clear negative correlation between Na2O and K2O due to albitisation (Fig. 4C). A very minor increase in SiO2 and a somewhat more noticeable one in MgO accompany albitisation, thereby lowering the FeO*/(FeO*+MgO) ratios

(Fig. 4D). Rb, Ba, Pb and to a lesser extent U and Zn decrease with increasing sodium contents, whereas no obvious changes are noted in the other trace elements.

The Palaeozoic granites, however, fall consistently into the class of 'calc-alkaline' or even 'calcic' granites in the classification of Frost et al. (2001) (not shown). The quartz–augen gneisses have been affected by severe metasomatism and deformation (Dipple et al., 2005), and their geochemistry is unlikely to bear much relation to that of their protolith anymore, apart from the least mobile elements, such as Zr, Ga and Al. As our work has focussed on the metasomatic changes in the granites, our data set is biassed towards altered samples, and the literature data for the Mt. Neill Suite is more representative of their igneous signature.

Within the present data set, there are two Mesoproterozoic samples with significantly lower SiO2 contents (Fig. 4B). The one from the Mt. Neill Suite is mafic enclave ARK691, from which the zircons were analysed. As mafic enclaves are affected by equilibration processes with the host granitic magma during cooling of the pluton (Elburg, 1996b), the whole rock composition of this sample is unlikely to be a true reflection of the mafic magma that mingled with the granite. The low-SiO2 Terrapinna sample (ARK708B) is characterised by very high modal biotite contents. This sample has an unusually high Zn content compared to the other granitoids (250 vs. 60 ppm), an element that has a strong preference for biotite. This suggests that the chemical composition of the sample is dictated by the modal mineralogy, rather than the other way around, and we therefore also interpret this high biotite content as a result of metasomatism. Therefore, although the Terrapinna Granite did not suffer from albitisation, it did suffer from other, presumably later, metasomatic processes.

All Mesoproterozoic samples are characterised by high contents of REE, Y, Th, U and Zr (Fig. 5, 6D, F) compared to the Palaeozoic samples, which in turn show higher Sr concentrations (Fig. 6E). The three Mesoproterozoic granite suites can be distinguished from each other on the basis of certain trace element concentrations. The Terrapinna Granite has higher Ba and lower Nb, Y and HREE, while the Yerila Granite shows the highest Th and U contents (Fig. 5A). All Mesoproterozoic granites show strong enrichments in the LREE (Fig. 5B). The positive Ce-anomalies for one of the samples may be due to secondary processes. Trends against SiO2 are scattered, but most elements tend to decrease with increasing SiO2 (Fig. 6A).

La/Yb ratios decrease with increasing SiO2 content, but mafic enclave ARK691 is an exception (Fig. 5), which is caused by high HREE-values, likely related to high modal abundances of xenotime; this is probably caused by igneous equilibration processes between enclave and granitoid magma.

Although the focus of this paper is on the Mesoproterozoic rather than the Palaeozoic granites, it should be mentioned that the latter fall into two chemical groups, based on Sr contents (Fig. 6E). The samples that underwent a reconnaissance zircon investigation came from the high Sr (ARK579) and

low Sr (BEM4) group. The latter has only been found in the Mt. Painter Inlier, while the high Sr group also occurs in the Mt. Babbage Inlier.

The hyperaluminous rocks are, unsurprisingly, characterised by low SiO2 and high Al2O3 contents (Fig. 6A). MgO is also enriched (up to 25 wt.%; Fig. 6B), reflecting the presence of phlogopite, magnesium-rich spinel, sapphirine and/or cordierite, resulting in very low iron numbers. High K2O contents are coupled with high Rb, reflecting the modal proportions of biotite or phlogopite. Th, REE and Y content can be very high, but trends are scattered (Fig. 6C, F).

A diagram of Zr vs. TiO2 (Fig. 6D) shows that the hyperaluminous rocks define two broad trends, with distinct Zr/TiO2 ratios. The dominant trend is one of large variations in Zr concentrations at low and only moderately variable TiO2 contents (high Zr/TiO2 trend). This is an extension of the trend for the Mesoproterozoic granitoids, on which the biotitised Terrapinna granitoid also falls, plus the hyperaluminous samples from location 4, such as ARK687A-L, the gradational granite-to-corundum block of which the zircons were analysed. The majority of the samples from locality 3 (including zircon sample ARK739) also follow this trend. The samples from localities 1 and 2 lie on the low Zr/TiO2 trend, as does mafic enclave ARK691.

The ores consist mainly of iron-oxide (up to 85 wt.% Fe2O3; Fig. 6F), with smaller amounts of silica and manganese (b10 wt.% MnO), and calcium in the fluorite-bearing samples (Fig. 6E). Occasional very high barium contents are related to the presence of barite. Zr and TiO2 contents are low, but Y and HREE contents fall in the same range as the granites and hyperaluminous samples. Th concentrations are less than 10 ppm. Cu and U contents are broadly correlated and reach 1400 and 2000 ppm respectively (not shown); they are also associated with high LREE concentrations, with Ce contents up to 2000 ppm (Fig. 6F, note log scale). Ore-related samples are enriched in Mo (Table 1), but this enrichment does not correlate with Cu or U. The sample with highest Mo-contents (~400 ppm) also showed a small As peak in its ICP-OES spectrum, despite sample preparation not having been optimised for the retention of the more volatile elements.

Based on the geochemical and field evidence for metasomatic alteration, isocon diagrams (Fig. 7) were constructed to constrain the relative mobilities of the elements during metasomatism. The different panels explore the various metasomatic processes.

The process of albitisation (Fig. 7A) is characterised by gain of Na and loss of K, Sr, Ba and Rb. This appears to happen at constant volume, as the most likely isocon line (immobility of Al, Ti and Zr) coincides with the 1:1 line. ARK687A represents incipient phlogopitisation (Mg-metasomatism; Fig. 7B), and this is shown relative to an already albitised granitoid, which may or may not be the correct ‘original’ rock, so the loss of Na and gain of K and Rb may be overestimated.

The likely isocon runs through Al, Ti, Zr, Hf and Ta, and indicates net mass loss, mainly due to decreasing SiO2-contents. MgO was gained during the process. Hyperaluminous rocks can be produced by continuing loss of silica (Fig. 7C). Fe and U are also lost in this process.

The line through Zr and Hf may be most representative for the true isocon (based on the zircon studies discussed below), in which case Ti was gained and Al lost.

When granites are turned into biotite (rather than phlogopite) schists, as is interpreted to have happened with Terrapinna sample ARK708B, silica and REE are lost, and Mn, Fe, Mg and Zn gained (Fig. 7D). If Zr and Ti were immobile, Al must have been lost, and significant mass loss occurred. If constant Al concentrations are assumed, no mass loss occurred.

Based on the similarity in Zr/TiO2 ratios between the hyperaluminous samples from localities 1 and 2, and mafic enclave ARK691, an isocon plot was constructed with the latter as the potential protolith (Fig. 7E). This is also based on our field impression that these hyperaluminous samples are metasomatised (mafic) dykes, as will be discussed in greater detail below. Immobility of Zr or Ti implies a gain in Al, Ga and Mg. This is surprising, as Al is often assumed to be immobile, but Fig. 7C already showed mobility of Al in the case of the hyperaluminous sample derived from a granitic protolith. Nearly all other elements are lost, with Si, Fe and Ca as the most important major elements.

As the low Zr/TiO2 hyperaluminous samples occur in an area which has been mapped as metasediments by Coats and Blissett (1971), an isocon diagram was constructed in which the local metasediment was supposed to be the protolith (Fig. 7F). As these metasediments are quartzofeldspathic, excessive mass losses of 85–90% should have occurred to accommodate this particular scenario.

5.1.2. Nd isotopes

Nd isotopic ratios have been measured on a selection of granitoids: one sample each from the Mesoproterozoic Mt. Neill Suite, Terrapinna and Yerila Granites, and two from the Palaeozoic Paralana Granodiorite. The four hyperaluminous samples that were subjected to zircon studies, plus the less altered part of the granite-to-corundum block (ARK687L) were also analysed. The data are given in Table 2 and displayed as εNd values versus time in Fig. 8. The accuracy of the age-corrected values is dependent on the Sm/Nd ratio having remained unchanged, which could be questioned for the hyperaluminous samples. However, the isocon diagrams show that mobility of Sm and Nd was limited, so it is likely that the Sm/Nd ratios have not changed appreciably during metasomatism. This is supported by the very similar Nd isotopic values and Sm/Nd ratios of the two sides of the granite-to-corundum block, ARK687A and L. Fig. 8 also gives literature data for the Mt. Neill Suite and the Radium Creek Metamorphics (Neumann, 2001; Stewart and Foden, 2001).

Our one sample from the (relatively unmetasomatised) Mt. Neill Suite yields somewhat higher initial Nd isotopic ratios than the range reported in literature, but the Terrapinna and Yerila Granite are indistinguishable from values reported previously: their εNd at an assumed age of intrusion (see below) of 1540 Ma is −1.8 to −1.9, while Stewart and Foden (2001) report an average initial εNd value of −1.9 for both suites. Four of the five hyperaluminous samples give εNd values at 1575 Ma that fall within the range for the Mt. Neill Suite from literature, whereas one of the low Zr/TiO2 group samples yields an initial value that is slightly higher than our analysed sample of the Mt. Neill Suite at εNd +2.5. Mantle extraction ages are similar for the hyperaluminous samples and the Mesoproterozoic granites.

The two samples of the Paralana Granodiorite have present-day εNd values that are significantly higher than those for the Mesoproterozoic granitoids. Recalculated to either Palaeozoic or Mesoproterozoic times, their values remain more radiogenic than those for the older granite suite, as has been noted before by Elburg et al. (2003). As a consequence, their mantle extraction ages are also significantly younger than those for the Mesoproterozoic granites or hyperaluminous samples. The range of Nd isotopic compositions of the Radium Creek Metamorphics (Neumann, 2001) at 1575 Ma falls below the values for any of the samples that we analysed.

5.2. Zircon chronology and isotopes

5.2.1. Morphology

Zircons from the Mesoproterozoic granitoids were analysed for samples ARK691 (enclave-bearing Mt. Neill Granite), GT2 (deformed Mt. Neill Granite), ARK20 (albitised Mt. Neill Granite, in some publications also referred to as 'trondhjemite'), and Terrapinna Granite samples ARK583 and ARK590. The zircons vary in size between 200 and 50 μm, and typically have a squat morphology. They display well-developed oscillatory zoning in cathodoluminescence imaging (Fig. 9A–E).

The zircons from the quartz–augen gneiss, believed to be a deformed equivalent of the Mt. Neill Suite, look very similar (Fig. 9F).

Zircons from the hyperaluminous samples located within the Radium Creek Metamorphics (ARK445 and 668 from localities 1 and 2 respectively) have a characteristic morphology, consisting of a core and a rim that can be distinguished from each other in thin section. Sizes of the separated zircons vary between 20 and 110 μm. Cores generally display oscillatory zoning, and can display resorption features, with pronounced embayments (Fig. 9M), but in other cases, their shape appears sub- to euhedral (Fig. 9L). An approximately micron-thick irregular zone of CL-bright material often separates core and rim zones (Fig. 9M). SEM-EDS analyses that include this brighter strip show the presence of phosphorus. Considering that xenotime inclusions within the zircons are also CL-bright,

this may indicate presence of significant xenotime substitution within the zircon lattice in this zone. In contrast to the cores, rims are typically unzoned, or show wavy zoning that does not follow crystallographically defined planes (Fig. 9I,J). As a result of this rim formation, the shape of the zircons is typically bipyramidal (Fig. 9M).

Zircons from hyperaluminous samples ARK687A and ARK739 display the prismatic to squarish shapes, relatively large sizes (up to 200 μm) and regular oscillatory zoning patterns (Fig. 9G, H) reminiscent of zircons from the analysed Mesoproterozoic granitoids.

The metasediment sample (ARK661) from the Radium Creek Metamorphics came from the same area as hyperaluminous sample ARK445 and was analysed to constrain a potential contaminant for the granitoid magmas. There is quite a variety of shapes but clearly bipyramidal zircons, such as those in the local hyperaluminous samples, are absent. Many zircons are euhedral to subhedral and display oscillatory zoning (Fig. 9O). Younger rims, overgrowing the oscillatory-zoned parts, are rare and too thin for standard LA-ICPMS analysis. More rounded zircons, with less pronounced or more irregular, patchy, zoning are also present (Fig. 9P).

Zircons within the metaluminous Palaeozoic granites (Paralana Granodiorite) vary in size and shape from prismatic small crystals to substantially larger square crystals. They all display zoning, although this is better developed in the smaller ones than the larger crystals (Fig. 9Q–S).

5.2.2. U–Pb results

Concordia diagrams are shown in 10 and 11, and an overview of the interpreted results is provided in Table 3.

5.2.2.1. Mesoproterozoic granitoids.

Both samples of the Terrapinna Granite (ARK583, 590) from the Mt. Babbage block yield ages that are slightly discordant, with upper intercepts of 1553–1561 Ma, and average 207Pb/206Pb ages of 1545–1555 Ma (Table 3; Fig. 10A, B). One older core was found in ARK590, with a discordant 207Pb/206Pb age of approximately 1850 Ma. Of the Mt. Neill Suite granites, one sample (ARK20) yields a concordant age of 1554±8 Ma. Samples GT2 and ARK691 are discordant with upper intercepts of 1574±10 and 1592±10 Ma respectively, and lower intercepts of 503±13 and 373±13 Ma. The weighted average 207Pb/206Pb ages of the most concordant zircons are 1556±5 and 1579±6.

Sample B61 is one of the quartz–augen gneisses, which have been argued to be deformed and metasomatised equivalents of the Mt. Neill Suite on the basis of Kober technique Pb–Pb dating of the

zircons (Elburg et al., 2001). The 1550–1560 Ma ages obtained in the present study (Table 3, Fig. 10F) confirm this view.

5.2.2.2. Hyperaluminous rocks

The relatively homogeneous zircon populations from sample ARK739 yielded a concordant age of 1552±11 Ma (Fig. 11A), but with a MSWD of 18, as several data points lie slightly below the concordia. An unrestricted Monte Carlo solution yielded an upper intercept age of 1561 Ma, but with a rather wide error (+1500/−3) Ma. Anchoring the lower intercept at 455±2 Ma (see below) gave an upper intercept of 1574±13 Ma with an MSWD of 0.60 (Table 3). This is within error of the weighted average 207Pb/206Pb age of 1564±8 Ma.

ARK687A defines a discordia with intercept ages at 1577 (+30/−16) and 437 (+360/−320) Ma; the upper intercept is 1577±13 Ma (MSWD 0.54) when the lower intercept is anchored at 455±2 Ma (Table 3). This is within error of the weighted average 207Pb/206Pb age of 1565±7 Ma.

Samples ARK445 and ARK668, containing the two-phase zircons, display a complex age pattern (Fig. 11C–F), not helped by the small size of the rims, which caused some analyses to straddle the boundary between the two domains. As wide a variety of zircon cores as possible was targeted in terms of shape and zoning, but as the great majority of cores showed oscillatory zoning, this was the dominant population analysed. For both samples, these cores are strongly clustered with 207Pb/206Pb ages close to 1580Ma. However, especially for the smaller zircons of ARK445, quite a few analyses are discordant, and may represent mixtures of cores and rims. Few cores show older 207Pb/206Pb ages, at approximately 2250 (highly discordant), 2500 and 3050Ma for ARK445, whereas four discordant analyses of cores in ARK668 yield a discordia with an upper intercept at 1703± 19 and lower intercept at 433±59Ma. The two most discordant analyses of these four show patchy zoning, the other two oscillatory zoning.

One of the patchy-zoned cores (ARK668-58C1, Fig. 9N) is mantled by oscillatory-zoned material with a 207Pb/206Pb age of 1585±10. The true rim, consisting of the usual wavily-zoned zircon, was not analysed as it was not wide enough. The rim ages that are concordant range between 445 and 520 Ma for ARK668, and dominantly between 420 and 485 Ma for ARK445. If the older (~1600 Ma) cores are excluded ARK668 yields a dscordia with intercepts at 482±9 Ma and 1599±11 Ma (MSWD=11).

The age spectrum of zircons in ARK445 can only yield a discordia after culling of highly discordant data points, with an upper intercept of approximately 1600 Ma, and a lower one of 463±10 Ma. If the most concordant analyses are used to calculate an upper weighted average 207Pb/206Pb age, ARK668 gives an age of 1582±5 Ma (14 pts) and ARK445 of 1584±4 Ma (n=12). Average 206Pb/238U ages

for the concordant younger rims are 461±9 Ma for ARK445 and 491±12 Ma for ARK668. However, the range of concordant ages is such that they cannot be equivalent (Table 3, Fig. 11D, F). This could indicate zircon growth over a longer period of time, or several pulses of growth. If the 206Pb/238U ages for the young rims are ordered and plotted (Fig. 12), sample ARK668 appears to define three plateaus. The youngest age gives a well-defined weighted average, albeit with only three data points, of 453±5 Ma (95% confidence). Two data points may represent mixtures between the first and second plateau. The next seven points define an age of 489± 4 Ma, with an MSWD of 0.67. Another five points give 508±4, with an MSWD of 0.14.

Plateau ages are less clear for ARK445 (Fig. 12). Three points trail to younger ages and are not used; the main plateau (12 points) yields 463±4 Ma. The first three points of this plateau may define a sub-plateau at 458±7, but this is within error of the age of the remaining five points (466±5). Two older data points yield 483± 8 Ma. The combined concordia age of the first sub-plateau in ARK445 with the three data points from ARK668 gives 455±2 (n=6; MSWD 0.06). This is indistinguishable from an unpublished LA-ICPMS monazite concordia age for ARK445 at 454±4; MSWD=0.23; n=14 (Elburg, unpublished data). Combining all post-Delamerian data points gives an indistinguishable weighted average 206Pb/238U age of 459±6 Ma. The 14 analyses that fall within the range for the Delamerian Orogeny give a weighted average 206Pb/238U age of 498±6 Ma (Fig. 12).

5.2.2.3. Metasediment

The zircons from metasediment sample ARK661 yield a range of ages (Fig. 11G), with a prominent group (14 out of 37) giving near-concordant 1675–1710 Ma ages. They may belong to more than one group (as suggested by the Hf isotope data, see below), but this is difficult to resolve. The four discordant zircons from ARK668 probably belong to this same age group. Five metasedimentary zircons define a discordia with a slightly younger upper intercept at 1629±10 Ma. Six other discordant zircons (e.g. Fig. 9P) yield a discordia with an upper intercept of 2582 +140/−72 Ma and a lower intercept of 1546 +240/−230 Ma. One of the old cores within ARK445 also lies on this discordia. There are 5 zircons that define a discordia with an upper intercept around 1580 Ma. These zircons display square shapes and oscillatory zoning (Fig. 9O), and therefore appear to be igneous. The presence of these zircons, with ages similar to those of the intrusives, is puzzling, but has been reported by other workers for the Radium Creek Metamorphics (Fanning et al., 2003; Neumann et al., 2010).

5.2.2.4. Palaeozoic granites

Zircons within the 440–460 Ma granites are rare and are nearly all inherited (Fig. 11H), also in the metaluminous samples analysed in this study (BEM4 from the Mt. Painter Inlier, ARK579 from the Mt. Babbage Inlier). The upper intercept ages are around 1540 Ma for both samples. Since the present study did not focus on these metaluminous granites, too few analyses were carried out to obtain a relevant Palaeozoic age; only one zircon from each sample gave a younger age between 400 and 500 Ma.

5.2.3. Lu–Hf results

Where possible Lu–Hf analyses were obtained within the same zone as the U–Pb analyses. However, the younger zircon rims in hyperaluminous samples ARK445 and ARK668 were often too small to obtain both a U–Pb age and a Hf isotope analysis, so some Hf isotope analyses were performed on rims that were not dated. As the CL image of the rims was characteristic, we are convinced that these rims would also have yielded ages in the 440–500 Ma range. Potential mixing between Mesoproterozoic cores and younger rims, resulting from drilling down through one zone into the next, could be monitored by the intensity of the Hf signal, which was invariably higher for the rims than for the cores (e.g. for ARK668: average 2.8±0.3 V for the cores and 3.8±0.3 V for the younger rims). Also the border between the two domains gave a very recognisable spiky signal, perhaps stemming from the P-rich brightly luminescent zone. All reported results have been corrected for radiogenic ingrowth of 176Hf from the small amount of 176Lu that was present, using the average 207Pb/206Pb age for the Mesoproterozoic zircons, and the 206Pb/238U age for the Palaeozoic ones. All data can be found in Electronic Appendix A2, and are shown as ordered Hf isotope plots in Electronic Appendix Fig. A3. All but two of the grains analysed gave $176Yb/177Hf \leq 0.11$, i.e. within the range of the Temora-2 standard zircon, the two deviating analyses are still within the validity range of the interference correction method used (Heinonen et al., 2010).

5.2.3.1. Mesoproterozoic granites

The zircons from the two samples of the Terrapinna Granite (ARK583 and 590) from the Mt. Babbage Inlier yielded very similar Hf isotopic compositions corresponding to εHf around+1 (Fig. 13A), with a fairly small spread in the data of one epsilon unit i.e. within analytical error. The mafic enclave within the Mt. Neill Granite (ARK691) gave a comparably small spread in the data, with an average of +2.0. The other Mt. Neill Suite samples show a somewhat larger spread, but there is no clear polymodality in the Hf isotope data. Averages of εHf of +2.3±1.7 for ARK20 and +2.9±2.2 for GT2 are indistinguishable within error from the other samples. This also holds for the quartz–augen

gneiss B61 (+1.3± 1.6), supporting the interpretation that this lithology corresponds to deformed and metasomatised Mt. Neill Suite granitoids.

The hyperaluminous samples ARK 739 and ARK 687A, found within the area of exposed Mt. Neill Suite, fall within the same range of Hf isotopic compositions as the unmetasomatised samples from this Suite, with εHf +3.7±2.1 and +2.7±1.6 (Fig. 13B). Again, the spread is somewhat larger than expected from a homogeneous magma, but there is no evidence for a polymodal distribution.

This also holds for the majority of approximately 1580 Ma zircons from the hyperaluminous samples (ARK445 and 668) found within the area mapped as Radium Creek Metamorphics (+2.2±2.1 and +1.2±1.6). One zircon core from each sample was excluded from this average, as they plotted at a significantly lower εHf value. In the case of zircon ARK445-40 (Fig. 9K), it is clear that this low-epsilon (−5.7) core has a different CL response than the enveloping, oscillatory-zoned material with εHf −0.5. The two low-epsilon zircon cores overlap with zircons within metasediment sample ARK661, which occurs as the host to the hyperaluminous samples in the area where sample ARK445 was taken (see below). Most other zircons with ages > ~1580 Ma from these two samples are also matched by metasedimentary zircons in terms of age and Hf isotopic composition.

The young zircon rims in ARK445 and 668 range from εHf −21 up to −12 at their Palaeozoic age of formation. As most Hf isotope analyses needed to be done on rims that had not been analysed for U–Pb (because of the restricted size of these overgrowths), the Hf isotope compositions cannot be linked to the age sub-groups defined within the Palaeozoic overgrowths.

The approximately 2580 Ma zircons from metasediment ARK661 show εHf values ranging from 0 up to +4, and the one core of this age within ARK445 falls right in the middle of this range with εHf=+1.8. Those with ages in the 1610–1710 range fall within two groups: a slightly older group shows a range of εHf from −10 up to −4, and a group with on average younger ages that ranges from −2 up to +7 (Fig. 13B). Two zircons from ARK668 and one from ARK445 fall close to these groups too. Of the 1580 age group, two zircons fall at low εHf around −5, and thereby out of the range of the typical igneous zircons from the granitoids. However, two zircons not only have ages but also Hf isotopic compositions indistinguishable from those of the granitoids at εHf +1 and +3.

The Hf isotopic composition of the approximately 1540 Ma zircons in the Palaeozoic calcic to calc-alkalic granites BEM4 and ARK579 broadly overlaps with that of the Mesoproterozoic granites, although those for ARK579 extend the range to marginally more positive εHf values (up to +9). The three analyses of the 430–490 Ma zircons from these granites plot around εHf −3. This is significantly higher than the similarly aged zircon rims in the hyperaluminous samples, which do not reach values higher than −12.

6. Discussion

6.1. Interpretation of hyperaluminous samples

There are several lines of evidence that point towards the hyperaluminous samples being metasomatised igneous rocks. The case is most clear-cut for the high Zr/TiO2 samples. There is field evidence, showing an altered, but still K-feldspar-bearing, granitoid (ARK687L) grading into a phlogopite–corundum rock (ARK687A) (Fig. 2F). Zircons from the two high Zr/TiO2 samples analysed are indistinguishable in shape, age and Hf isotopic composition from the zircons in the granites. The εNd value at 1575 Ma for these samples is indistinguishable from the literature range reported for the Mesoproterozoic granites. The idea that their alumina-enriched character may be primary and that they represent biotite-rich cumulates associated with the Mesoproterozoic granites, is not in accordance with the field evidence. The chemistry of biotite-rich samples, such as ARK708B (Table 1, Fig. 7D) is also different from the high Zr/TiO2 hyperaluminous samples, with a significantly higher FeO/MgO ratio and Zn content, and a much lower Alumina Saturation Index. The case for the igneous parentage of the low Zr/TiO2 samples is slightly less obvious, but nevertheless more likely than an interpretation as a metasediment. The whole rock Nd isotopic ratios at 1575 Ma fall within the range for the Mt. Neill Suite from literature, extended with our own new data point. The values are higher than and outside of the range of the metasediments at 1575 Ma. Local metasediments are mainly quartzo-feldspathic, and therefore have high Si/Al ratios, quite unlike the hyperaluminous samples. More importantly, the zircons within the metasediments have a different shape from those in the hyperaluminous samples, and their age and isotopic pattern is also distinct. There is some overlap between older cores within the hyperaluminous samples and those from the surrounding metasediments.

If the protolith of the hyperaluminous samples is thought to be a mafic dyke, in keeping with the low Zr/TiO2 character of the analysed mafic enclave, these older cores would point towards crustal contamination. Their apparent higher abundance in the low Zr/TiO2 samples could be related to the lower incidence of zircon within more mafic magmas (thereby giving more prominence to inherited cores; Elburg, 1996a), combined with the location of these presumed mafic dykes in metasedimentary host rocks. Alternatively, the presumed lower alkali-contents of a mafic magma compared to a felsic one could mean that the mafic dykes were closer to their zircon saturation temperature than the granites (Watson and Harrison, 1983), and therefore the zircons had a higher chance of survival. However, the zircon saturation temperature is also inversely proportional with silica-content, which would have been lower in the mafic dykes, so this seems a less likely option. The zircons within the low Zr/TiO2 samples show pronounced overgrowths, pointing towards local dissolution/precipitation processes, whereas these overgrowths are absent in the high Zr/TiO2 samples analysed. The newly grown zircon rims look similar to those on some of the Palaeozoic granites, but the Hf isotopic

compositions are dissimilar; moreover, the whole rock Nd isotopic composition of the Palaeozoic granites is different from that of the low Zr/TiO2 hyperaluminous samples.

The Hf isotopic composition of the 440–500 Ma zircon rims in the hyperaluminous samples ARK445 and 668 can be explained by radiogenic ingrowth, starting from a Hf isotopic composition similar to that of the Mesoproterozoic granites. If this evolves with 176Lu/177Hf=0.0010 (Fig. 13B), well within the range of Lu/Hf ratios measured for the granitoids, the Hf isotopic signature at 440–500 Ma matches that of the rims measured. Intracrustal reworking is therefore the most likely interpretation for this phase of zircon crystallisation. These zircon rims have higher Hf contents than the cores, and this may reflect lower temperatures of formation (Wang et al., 2010) or higher Hf/Zr ratios of the fluid/melt from which they formed.

The question remains why the low Zr/TiO2 samples analysed have these overgrowths, and the high Zr/TiO2 samples do not. It is unlikely to be related to the degree of metasomatism, reflected by the higher Al2O3/SiO2 (1.6–2.8) of the low Zr/TiO2 samples of which the zircons were analysed; thin section inspection of a low Zr/TiO2 sample (ARK439 from locality 1) with an Al2O3/SiO2 ratio (0.5) comparable to the high Zr/TiO2 samples (ARK739 and ARK687A; Al2O3/ SiO2=0.6) shows that the zircons also have overgrowths, albeit less pronounced than in the two analysed samples. Also the low Zr/TiO2 samples from locality 3 appear to contain either very small one-phase zircons, or two-phase zircons in thin section. We therefore think that the presence of overgrowths is related to differences in the mineralogy of the protolith. For the granitic protoliths, nearly all of the zirconium was probably contained in zircon, while the somewhat more mafic lithologies may have contained amphibole or clinopyroxene in which some of the zirconium may have been accommodated. This zirconium was then more easily mobilised during metasomatic processes, giving rise to the observed newly grown rims.

6.2. Mesoproterozoic granites

6.2.1. Age relationships

The age of the granitoids, as determined by the present study, is in broad agreement with previous work. The granitoids from the Mt. Neill Suite (ARK20, 691, GT2, B61), for which we obtain weighted average 207Pb–206Pb ages of 1557–1579 Ma, have been dated previously at approximately 1572 (zircon 207Pb–206Pb age, Elburg et al., 2001), 1569–1576 (zircon U–Pb ages, Teale, 1993), and 1585±3 Ma (SHRIMP U–Pb zircon, Fraser and Neumann, 2010). Our range of ages thus extends to slightly younger values than reported previously. This may be either real or may be related to metamorphic–metasomatic events, for which Fraser and Neumann (2010) report rather subtle U–Pb zircon evidence from gneisses and migmatites, at approximately 1550– 1560 Ma. In this respect, it

may be relevant that our most pristine sample (ARK691) yields the oldest age, and that deformed and partially albitised samples (GT2, B61, ARK20) yield slightly younger ages.

The age for the Terrapinna Granite (1545–1555) is similar to the 1560±3 Ma age reported by Fraser and Neumann (2010); 1556±4 and 1557±6 Ma quoted by Stewart and Foden (2001); and 1572± 15 reported by Wülser (2009). The slightly younger age of the Terrapinna Granite compared to the Mt. Neill Suite appears to be a consistent feature. As the Terrapinna Granite does not show signs of albitisation, it is tempting to make a connection between this younger stage of magmatism and the albitisation process. The Terrapinna Granite is locally biotitised (e.g. sample ARK708B), so this must have been a younger metasomatic process. In turn, biotitisation is older than the metasomatic process that caused phlogopitisation and hyperaluminosity, as biotitites show an upright crenulation cleavage (Fig. 2D) that can be related to Delamerian (514–485 Ma) deformation, whereas phlogopitites do not show a mineral shape preferred orientation.

The undeformed nature of the hyperaluminous samples agrees with the U–Pb data on zircon rims, which extend down to ages younger than the 485 Ma, which is quoted as the end of the Delamerian Orogeny. The zircon rim age spectrum, however, is complex, and does not seem to define a single population. Although care was taken to only process the signal belonging to the zircon rims, mixing of Mesoproterozoic cores and younger rims cannot be completely excluded to be the cause of this range. It is, however, also possible that zircon new-growth was a protracted process.

The zircons from the high Zr/TiO2, and the majority of the zircon cores from the low Zr/TiO2 hyperaluminous samples yield ages that are indistinguishable from those in the Mt. Neill Suite. This supports the idea that these hyperaluminous rocks represent metasomatised intrusives, as argued above, with the distinction between the two groups mirroring that between the mafic enclaves and the host granite, i.e. more mafic versus more felsic rocks.

The ages recorded in the metasediment hosting the low Zr/TiO2 hyperaluminous samples are, as expected, variable, down to ages that are surprisingly similar to those of the granitoids. This is comparable to previous age data for the Radium Creek Metamorphics (Fraser and Neumann, 2010), where the maximum depositional age was constrained as being 1600±8 and 1591±6, within error of our upper intercept age for the youngest group of zircons.

The Palaeozoic age of the undeformed, calcic to calc-alkalic (in the terminology of Frost et al., 2001) Paralana Granodiorite is poorly constrained from the present dataset, but agrees broadly with the, perhaps slightly discordant, U–Pb monazite age of 441–445 Ma for sample BEM4 (Elburg et al., 2003). Young zircon ages from other granitoids (of which the geochemistry is not reported) vary from 456 to 459 Ma (Wülser, 2009) and approximately 458 and 467 Ma (Fraser and Neumann, 2010). The Mesoproterozoic component reported in the latter study is 1552±6 Ma, similar to our ages, and resembling those of the Terrapinna Granite.

6.3. Magma sources

The Hf isotope data of the Mesoproterozoic zircons in the metagranitoids does not show distinct bimodality that could be taken as unequivocal evidence for input from different sources, such as mantle and crust. The data for the two samples of the Terrapinna Granite (ARK583, 590) are remarkably homogeneous, with a standard deviation that is only slightly larger than those for the Temora standard.

Variation in the Mt. Neill Suite and its metasomatised equivalents is somewhat larger, with tailing towards higher epsilon Hf values. The enclave-bearing sample (ARK691) was thought to have the highest likelihood of containing different zircon populations because of its mixed mafic–felsic lithology, but it is the most homogeneous of this suite. Epsilon Hf values hover around+2, and our own and published (Stewart and Foden, 2001) whole rock epsilon Nd values for the same suites hover around −2. These whole rock εNd values are slightly low for the zircon Hf isotopic compositions compared to the terrestrial array (Bouvier et al., 2008) and suggest that whole rock numbers show a slightly greater influence of crustal contamination compared to the zircon data. Some evidence for crustal contamination can already be observed in the lower Zr/TiO2 (derived from more mafic magmatic rocks) hyperaluminous samples, in the form of occasional zircon cores with older ages and lower Hf isotopic composition.

The Hf isotopic ratios of the Mesoproterozoic metagranitoids could be interpreted as reflecting derivation from a mantle domain less depleted than the upper mantle, such as the subcontinental lithospheric mantle or a plume source; or from a well-homogenised magma with both depleted mantle and crustal components; or from a reworked magmatic source which separated from the depleted mantle at 1.8–2.2 Ga, i.e. 200–600 Ma prior to Mesoproterozoic magmatism (as evidenced by the depleted mantle extraction ages). For any interpretation involving a depleted mantle source to work, degrees of melting need to be very small, in order to explain the significant enrichments in incompatible elements, such as the lanthanides and actinides.

When allowing for a twenty-fold enrichment during differentiation, a more mafic precursor to the granites would have a Th content of 5 ppm. Taking a depleted mantle with a Th concentration of 0.0079 ppm (Workman and Hart, 2005) and assuming a solid/melt distribution coefficient of 0 and equilibrium melting, the depleted mantle would need to be melted to less than 0.2%, which seems an unrealistically low percentage. The exposed metasediments that could act as a crustal contaminant contain relatively low concentrations of these elements (Fig. 5A) and can therefore not be invoked as a source for the enrichments.

As a group, the Mesoproterozoic granitoids are enriched in incompatible elements (also compared to the Palaeozoic granites), but there are significant differences between the individual suites. For instance, the Terrapinna Granite contains lower concentrations of incompatible elements and shows

more pronounced negative Nb–Ta and positive Pb anomalies than samples from the Mt. Neill Suite or Yerila Granite (Fig. 5A). These anomalies are characteristic for subduction-related magmas, sediments (e.g. sample ARK661) and upper continental crust in general. There is, however, no Nd or Hf isotopic evidence for a larger proportion of an older recycled component in the Terrapinna granitoids compared to the Mt. Neill Suite. Although the Terrapinna Granite shows the most pronounced Nb–Ta anomaly, the other Mesoproterozoic granites also show a depletion in Nb and Ta compared to neighbouring elements in a normalised trace element diagram. The levels of incompatible element enrichment also vary between the Mesoproterozoic suites, with the Yerila showing the greatest enrichment and the Terrapinna the least. An apparent continuum exists from granites with a very clear A-type, ferroan signature to granites in which this signature is less pronounced. On top of this variation, that we interpret to be primary igneous, a range of metasomatic processes (see below) have affected the granites and obscured their igneous signature.

The variation seen in the levels of trace element enrichment contrasts with the isotopic signature, which does not show consistent differences between the suites. Literature data (Stewart and Foden, 2001) points towards greater Nd isotope variability in the Mt. Neill Suite, and this is in accordance with our analyses. This variation in Nd isotopic values, together with the range in zircon Hf isotopic compositions that is wider than can be accounted for by analytical uncertainty only, hints at contributions of more than one source to the granites. The question whether this isotopic variability is a result of upper crustal contamination only or also a reflection of deeper-seated processes cannot be answered at this moment.

The absence of clear evidence for an isotopically primitive (depleted mantle) component in the source of the Mesoproterozoic magmas discussed here contrasts with data for the Mesoproterozoic granites of the Gawler Craton that are associated with the Olympic Dam ore deposit. Whole rock Nd (Johnson and McCulloch, 1995) and zircon Hf (Belousova et al., 2009) isotope data point towards a mantle component in magmatism associated with this world-class iron oxide–copper–gold(+REE) deposit. Spatial association of such deposits with magmatism showing evidence for a mantle component has been proposed as one of the defining features of IOCG deposits sensu stricto (Electronic Appendix Table A4; Groves et al., 2010).

The Paralana Granodiorite has been proposed to be a reworked version of the Mesoproterozoic granites (Neumann et al., 2010), based on the predominance of inherited components in their zircons, which this work has shown not only to hold for zircon ages but also for their Hf isotopic signature (Fig. 13B). In terms of trace element concentrations, the closest match to the Paralana Granodiorite is the Terrapinna Granite. In a similar way that Mesoproterozoic granites could be turned into hyperaluminous samples, they might be metasomatised into a different type of granitoid.

However, this scenario seems hard to reconcile with the systematic variations of trace and major elements within the suite, which are very different from those observed for the Terrapinna Granite (Fig. 6D, E). The outcrops of the Paralana Granodiorite that we studied and sampled show sharp contacts between xenoliths of Terrapinna Granite and Paralana Granodiorite (Fig. 2C) and also between Paralana-associated aplites and the Mesoproterozoic granitoids.

Preliminary Hf data on zircon in the Paralana Granodiorite gives an indication for the presence of a more primitive component, and this is supported by the Nd isotope data. We therefore interpret this as a distinct phase of magmatism, involving a mantle component. However, more work needs to be done regarding its exact petrogenesis, as the dominance of inherited components in the zircon population is quite enigmatic.

6.4. Metasomatism and ore formation

Our studies document significant metasomatism of the Mesoproterozoic granitoids, from early-stage albitisation, a later stage of biotitisation, followed by phlogopitisation. The relative timing of these events is constrained by field relations and structural data, but their precise absolute age is less clear. Albitisation does not seem to be associated with new zircon growth. As discussed, albitisation affects the Mt. Neill Suite, but not the younger Mesoproterozoic granitoids (e.g. Terrrapinna), and therefore it seems likely that the second stage of Mesoproterozoic magmatism is responsible for this albitisation. Fraser and Neumann (2010) also report U–Pb SHRIMP ages of gneisses around 1550 Ma, which they interpret as recrystallisation ages. Biotitisation, which also affects the second stage Mesoproterozoic granites, must have happened prior to the Delamerian (ca. 500 Ma) Orogeny, as the biotitites show a crenulation cleavage that conforms to Delamerian deformation patterns. Phlogopitites, on the other hand, do not show a mineral preferred orientation. Three of the hyperaluminous samples analysed for their zircons were phlogopite-bearing, but only two of them showed clear zircon rims yielding younger, Palaeozoic ages, representing more than one phase of zircon growth. The youngest plateau age (~455 Ma) postdates the Delamerian Orogeny, and may therefore represent phlogopitisation. Considering published ages for the Palaeozoic granitoids (Paralana Granodiorite), phlogopitisation and granite intrusion seem to be coeval.

We propose this 455 Ma age as a more accurate reflection of the start of the magmatic–hydrothermal event than the 440 Ma proposed by Elburg et al. (2003) on the basis of bulk mineral U–Pb data. Formation of the iron–uranium–REE ore sheets has not been dated directly, but all available evidence also points towards a post-Delamerian age, and may therefore be associated with the documented metasomatism of the older granitoids.

– The mapped distribution of the ore sheets appears to be unaffected by the Delamerian folding.

– The isocon approach indicates that the hyperaluminous samples are depleted compared to their likely protoliths in the elements that are enriched in the ores (Fe, Mn, U).

– The approximately 455 Ma metasomatic event is associated with significant REE mobility, resulting in documented new-growth of monazite in hyperaluminous sample ARK445. The ores are also significantly enriched in LREE.

– The high manganese, phosphorus and identifiable arsenic contents of the ores correlate with the mineralogy of the "intermediate assemblage" overgrowing 440–465 Ma (bulk ID-TIMS U–Pb dating of titanite, Elburg et al., 2003) diopside–titanite veins (Bakker and Elburg, 2006).

We therefore think that phlogopitisation and ore formation may have been a result of hydrothermal activity, driven by granitic magmatism around 455 Ma. Whole rock Nd isotopic ratios (this study; Elburg et al., 2003; Stewart and Foden, 2001) and preliminary zircon Hf isotope data point towards involvement of a component that is more juvenile than the Mesoproterozoic granites and probably mantle-derived for Palaeozoic magmatism. However, the Palaeozoic granitoids are certainly not bringing in the ore-forming elements, as they are low in iron, REE and U. There is no evidence that these characteristics are anything else than primary magmatic, in view of the good correlation with igneous fractionation indices. Palaeozoic magmatism therefore only provided the extra heat necessary to fire up the hydrothermal system that remobilised materials from the Mesoproterozoic granitoids. Obviously, this metasomatic event was not the only one affecting the area, as albitisation and biotitisation went before, and a phase of K-feldspar alteration and quartz–hematite formation (Bakker and Elburg, 2006; Fig. 3) occurred later (probably in the Permian or Mesozoic; Idnurm and Heinrich, 1993; Elburg, unpublished data).

The relationships established in this study have important implications for the metallogenic potential of A-type granites. It means that the pre-enrichment that A-type granites provide for certain elements (iron, uranium) can be tapped and used as a source for economic mineralisation at any stage, either shortly after the intrusion (in the case of Olympic Dam), or more than a billion years later, as documented here. However, it seems that the high heat production of the granites themselves may perhaps be sufficient to fire up certain metasomatic processes, but those that produce economically valuable deposits need the heat input associated with mantle-derived magmatism.

The size (and thereby value) of the ore deposits that are generated could be related to the magnitude of mantle input, which seems to have been less significant in the case of the Palaeozoic granitoids of the Mt. Painter and Mt. Babbage Inliers than for the granitoids associated with the Olympic Dam deposit. Another distinction between the two areas is that the approximately 455 Ma hydrothermal activity in the Mt. Painter Inlier is not the last event, but was overprinted by a younger phase of low-temperature, low-salinity (and low-REE) fluids that gave rise to quartz–hematite breccias (Bakker and Elburg, 2006). These fluids seem to be responsible for the silicification and remobilisation of some of

the ores, thereby making the area economically less prospective. A comparison of the mineralisation in the Mt. Painter Inlier with typical IOCG deposits (Groves et al., 2010) is given in Electronic Appendix A4.

7. Conclusions

Mesoproterozoic magmatism in the Mt. Painter and Mt. Babbage Inlier gave rise to A-type granites with significant primary enrichment in U, Th and REE, albeit at varying levels. The Hf isotopic composition of the zircons is relatively homogeneous, and does not show unequivocal evidence for the involvement of separate mantle and crustal components, apart from local upper crustal contamination. Hyperaluminous Mg-rich rocks can be divided in high and low Zr/TiO2 groups. The former resemble the Mesoproterozoic granites in terms of immobile elements; the U–Pb ages and Hf isotopic composition of the zircons support this interpretation. The low Zr/TiO2 group is chemically similar to the mafic enclaves within the Mt. Neill Suite. The zircons from the low Zr/TiO2 samples show a small inherited component, which is matched by zircons from the metasedimentary host rocks. The main core population is similar to that of the Mesoproterozoic granitoids. Rims display Palaeozoic ages, ranging from late-Delamerian to a plateau at 455±2, an age also recorded by monazite. Hf isotopes show that this zircon growth can be explained by intracrustal remobilisation. The Palaeozoic age for the hyperaluminous rocks coincides with that for metaluminous granites, for which Nd isotope and preliminary zircon Hf isotope data show a mantle contribution. Structural and chemical evidence suggest that the Fe–Cu–U–REE ore sheets exposed in the area may have been formed during the same magmatic–hydrothermal event. The Mesoproterozoic granites provided the chemical ingredients for these ores, while the Palaeozoic mantle input provided the heat source driving the hydrothermal system. A-type granites, by virtue of their enrichment in elements such as U and REE, can therefore be a valuable source for ores. This source can be tapped at any later stage, provided there is a mantle heat source around to drive the hydrothermal system.

Supplementary materials related to this article can be found online at doi:10.1016/j.lithos.2011.09.009.

Acknowledgements

John Foden is thanked for sharing his unpublished data with us. This research was supported by FWO grant 3GA07811 to ME. Financial support to PDB and AW was by the German Research Foundation (DFG) project BO 1776/8-1 and Marathon Resources Ltd. Financial support to TA was from the Department of Geosciences, University of Oslo through a Småforsk grant. Comments by reviewers Jean-Claire Duchesne and Federico Farina helped to clarify the discussion of the

manuscript. Editor Roberto Dall'Agnol is gratefully acknowledged for both his scientific comments and his efforts spotting the last(?) remaining errors. This is contribution no. 23 from the Department of Geosciences, University of Oslo Isotope Geology Laboratory and publication number A&MS-ADD-02 from the Atomic & Mass Spectrometry Unit of Ghent University.

References

Andersen, T., Andersson, U.B., Graham, S., Aberg, G., Simonsen, S.L., 2009. Granitic magmatism by melting of juvenile continental crust: new constraints on the source of Palaeoproterozoic granitoids in Fennoscandia from Hf isotopes in zircon. Journal of the Geological Society 166, 233–247.

Bakker, R.J., Elburg, M.A., 2006. From diopside–titanite pegmatites to hematite–quartz growth: the development of a magmatic–hydrothermal system in Arkaroola (northern Flinders Ranges, South Australia). Contributions to Mineralogy and Petrology 152, 541–569.

Belousova, E.A., Reid, A.J., Griffin, W.L., O'Reilly, S.Y., 2009. Rejuvenation vs. recycling of Archean crust in the Gawler Craton, South Australia: evidence from U–Pb and Hf isotopes in detrital zircon. Lithos 113, 570–582.

Bouvier, A., Vervoort, J.D., Patchett, P.J., 2008. The Lu–Hf and Sm–Nd isotopic composition of CHUR: constraints from unequilibrated chondrites and implications for the bulk composition of terrestrial planets. Earth and Planetary Science Letters 273 (1–2), 48–57.

Coats, R.P., Blissett, A.H., 1971. Regional and economic geology of the Mount Painter Province. Geological Survey of South Australia Bulletin 43.

Conor, C.H.H., Preiss, W.V., 2008. Understanding the 1720–1640 Ma Palaeoproterozoic Willyama Supergroup, Curnamona Province, Southeastern Australia: implications for tectonics, basin evolution and ore genesis. Precambrian Research 166, 297–317.

Creaser, R.A., Cooper, J.A., 1993. U–Pb geochronology of middle Proterozoic felsic magmatism surrounding the Olympic Dam Cu–U–Au–Ag and Moonta Cu–Au–Ag deposits, South Australia. Economic Geology and the Bulletin of the Society of Economic Geologists 88 (1), 186–197.

DePaolo, D.J., 1981. Neodymium isotopes in the Colorado Plateau Front Range and implications for crust formation and mantle evolution in the Proterozoic. Nature 291, 705–708.

Dipple, G., Bons, P.D., Oliver, N.H.S., 2005. A vector of high-temperature paleo-fluid flow deduced from mass transfer across permeability barriers (quartz veins). Geofluids 5, 67–82.

Drexel, J.F., Preiss, W.V., Parker, A.J., 1993. The geology of South Australia. The Precambrian: South Australia Geological Survey Bulletin 54, Vol. 1. Geological Survey of South Australia, Adelaide.

Eby, G.N., 1992. Chemical subdivision of the A-type granitoids: petrogenetic and tectonic implications. Geology 20, 641–644.

Elburg, M.A., 1996a. U–Pb ages and morphologies of zircon in micrograniteoid enclaves and peraluminous host granite: evidence for magma mingling. Contributions to Mineralogy and Petrology 123, 177–189.

Elburg, M.A., 1996b. Evidence of isotopic equilibration between micrograniteoid enclaves and host granodiorite, Warburton Granodiorite, Lachlan Fold Belt, Australia. Lithos 38, 1–22.

Elburg, M.A., Bons, P.D., Dougherty-Page, J., Janka, C.E., Neumann, N., Schaefer, B., 2001. Age and metasomatic alteration of the Mt. Neill Granite at Nooldoonooldoona Waterhole, Mt. Painter Inlier, South Australia. Australian Journal of Earth Sciences 48, 721–730.

Elburg, M.A., Bons, P.D., Foden, J., Brugger, J., 2003. A newly defined Late Ordovician magmatic–thermal event in the Mt. Painter Province, northern Flinders Ranges, Australia. Australian Journal of Earth Sciences 50, 611–631.

Fanning, C.M., Teale, G.S., Robertson, R.S., 2003. Is there Willyama Supergroup sequence in the Mount Painter Inlier? In: Peljo, M. (Ed.), Broken Hill Exploration Initiative. Geoscience Australia, Broken Hill, pp. 38–41.

Foden, J., Sandiford, M., Dougherty-Page, J., Williams, I., 1999. Geochemistry and geochronology of the Rathjen Gneiss: implications for the early tectonic evolution of the Delamerian Orogen. Australian Journal of Earth Sciences 46, 377–389.

Foden, J., Elburg, M.A., Dougherty-Page, J., Burtt, A., Turner, S., 2006. The timing and duration of the Delamerian Orogeny: correlation with the Ross Orgen and implications for Gondwana assembly. Journal of Geology 114, 189–210.

Fraser, G.L., Neumann, N.L., 2010. New SHRIMP U–Pb zircon ages from the Gawler Craton and Curnamona Province, South Australia, 2008–2010. Record 2010/16, Geoscience Australia, Canberra, Australia.

Frost, C.D., Frost, B.R., 2011. On ferroan (A-type) granitoids: their compositional variability and modes of origin. Journal of Petrology 52 (1), 39–53.

Frost, B.R., Barnes, C.G., Collins, W.J., Arculus, R.J., Ellis, D.J., Frost, C.D., 2001. A geochemical classification for granitic rocks. Journal of Petrology 42 (11), 2033–2048.

Groves, D.I., Bierlein, F.P., Meinert, L.D., Hitzman, M.W., 2010. Iron oxide copper–gold (IOCG) deposits through earth history: implications for origin, lithospheric setting, and distinction from other epigenetic iron oxide deposits. Economic Geology 105, 641–654.

Haapala, I., 1995. Metallogeny of the rapakivi granites. Mineralogy and Petrology 54 (3–4), 149–160.

Haapala, I., Ramo, O.T., Frindt, S., 2005. Comparison of Proterozoic and Phanerozoic riftrelated basaltic–granitic magmatism. Lithos 80 (1–4), 1–32.

Heinonen, A.P., Andersen, T., Rämö, O.T., 2010. Source constraints from the Hf isotope composition of zircon in the rapakivi granites and associated mafic rocks of southern Finland. Journal of Petrology 51, 1687–1709.

Idnurm, M., Heinrich, C., 1993. A palaeomagnetic study of the hydrothermal activity and uranium mineralisation of Mt. Painter, South Australia. Australian Journal of Earth Sciences 40, 87–101.

Johnson, J.P., McCulloch, M.T., 1995. Sources of mineralising fluids for the Olympic Dam deposit (South Australia): Sm–Nd isotopic constraints. Chemical Geology 121, 177–199.

Kent, A.J.R., Jacobsen, B., Peate, D.W., Waight, T.E., Baker, J.A., 2004. Isotope dilution MC–ICP-MS rare earth element analysis of geochemical reference materials NIST SRM 610, NIST SRM 612, NIST SRM 614, BHVO-2G, BHVO-2, BCR-2G, JB-2, WS-E, W-2, AGV-1 and AGV-2. Geostandards and Geoanalytical Research 28 (3), 417–429.

Loiselle, M.C., Wones, D.R., 1979. Characteristics and origin of anorogenic granites. Geological Society of America Abstracts with Programs 11, 468.

Ludwig, K., 2008. User's Manual for Isoplot 3.6, a geochronological toolkit for Microsoft Excel. Special Publication No. 4, Berkeley Geochronology Center. .

Mawson, D., 1923. The igneous rocks of the Mount Painter Belt. Transactions of the Royal Society of South Australia 47, 376–387.

Mawson, D., 1944. The nature and occurrence of uraniferous mineral deposits in South Australia. Transactions of the Royal Society of South Australia 68, 334–356.

McLaren, S., Sandiford, M., Powell, R., Neumann, N., Woodhead, J., 2006. Palaeozoic intraplate crustal anatexis in the Mount Painter Province, South Australia: timing, thermal budgets and the role of crustal heat production. Journal of Petrology 47 (12), 2281–2302.

Mildren, S., Sandiford, M., 1995. Heat refraction and low-pressure metamorphism in the northern Flinders Ranges, South Australia. Australian Journal of Earth Sciences 42, 241–247.

Neumann, N., 2001. Geochemical and isotopic characteristics of South Australian Proterozoic granites: implications for the origin and evolution of high heat-producing terrains. Ph.D. Thesis, University of Adelaide, Adelaide.

Neumann, N., Hore, S., Fraser, G., 2010. New geochronology from the Mount Painter Province. South Australia—Linking the Gawler Craton and Curnamona Province. AESC 2010, Canberra.

Paul, E., Flöttmann, T., Sandiford, M., 1999. Structural geometry and controls on basement-involved deformation in the northern Flinders Ranges, Adelaide Fold Belt, South Australia. Australian Journal of Earth Sciences 46, 343–354.

Pin, C., Zalduegui, J.F.S., 1997. Sequential separation of light rare-earth elements, thorium and uranium by miniaturized extraction chromatography; application to isotopic analyses of silicate rocks. Analytica Chimica Acta 339, 79–89.

Preiss, W.V., 1987. The Adelaide Geosyncline: Late Proterozoic stratigraphy, sedimentation, palaeontology and tectonics. Geological Survey of South Australia Bulletin 53, 34–41.

Rosa, D.R.N., Finch, A.A., Andersen, T., Inverno, C.M.C., 2009. U–Pb geochronology and Hf isotope ratios of magmatic zircons from the Iberian Pyrite Belt. Mineralogy and Petrology 95, 47–69.

Scherer, E.E., Munker, C., Mezger, K., 2007. The Lu–Hf systematics of meteorites: consistent or not? Geochimica et Cosmochimica Acta 71 (15), A888.

Söderlund, U., Patchett, J.P., Vervoort, J.D., Isachsen, C.E., 2004. The Lu-176 decay constant determined by Lu–Hf and U–Pb isotope systematics of Precambrian mafic intrusions. Earth and Planetary Science Letters 219 (3–4), 311–324.

Sprigg, R.C., 1945. Investigation of the Uranium Deposits at Mount Painter, South Australia. Department of Mines. Report Book 45/1. Department of Mines, South Australia.

Stewart, K., Foden, J., 2001. Mesoproterozoic Granites of South Australia. University of Adelaide, Adelaide.

Sun, S.-s., McDonough, W.F., 1989. Chemical and isotopic systematics of oceanic basalts: implications for mantle composition and processes. In: Saunders, A.D., Norry, M.J. (Eds.), Magmatism in the Ocean Basins: Geological Society Special Publication, pp. 313–345.

Teale, G.S., 1980. The occurrence of högbomite and taaffeite in a spinel–phlogopite schist from the Mount Painter Province of South Australia. Mineralogical Magazine 43, 575–577.

Teale, G.S., 1993. Mesoproterozoic: Mount Painter and Mount Babbage Inliers. In: Drexel, J.F., Preiss, W.V., Parker, A.J. (Eds.), The Geology of South Australia. : The Precambrian, 1. South Australia Geological Survey Bulletin. South Australia Geological Survey, Adealaide, pp. 149–156.

Wang, X., Griffin, W.L., Chen, J., 2010. Hf contents and Zr/Hf ratios in granitic zircons. Geochemical Journal 44 (1), 65–72.

Watson, E.B., Harrison, T.M., 1983. Zircon saturation revisited: temperature and composition effects in a variety of crustal magma types. Earth and Planetary Science Letters 64, 295–304.

Whalen, J.B., Currie, K.L., Chappell, B.W., 1987. A-type granites: geochemical characteristics, discrimination and petrogenesis. Contributions to Mineralogy and Petrology 95, 407–419.

Wingate, M.T.D., Campbell, I.H., Compston, W., Gibson, G.M., 1998. Ion microprobe U– Pb ages for Neoproterozoic basaltic magmatism in south-central Australia and implications for the breakup of Rodinia. Precambrian Research 87, 135–159.

Workman, R.K., Hart, S.R., 2005. Major and trace element composition of the depleted MORB mantle (DMM). Earth and Planetary Science Letters 231, 53–72.

Wülser, P.-A., 2009. Uranium metallogeny in the North Flinders Ranges region of South Australia. PhD Thesis, University of Adelaide, Adelaide, 250 pp.

Fig.1:

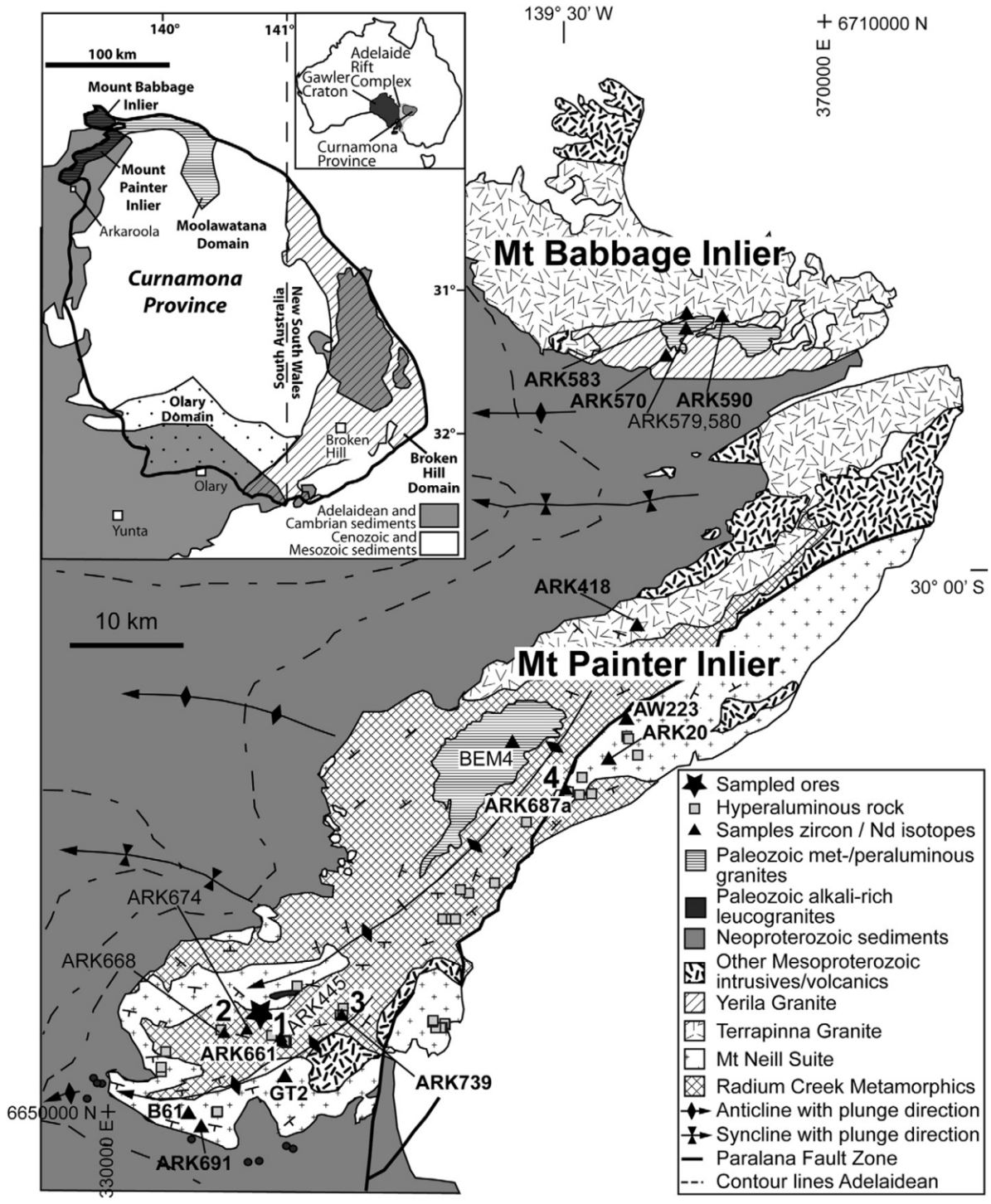

Fig. 1. Lithological map of the Mt. Painter and Mt. Babbage Inliers after Coats and Blissett (1971) and Stewart and Foden (2001). The distribution of the Radium Creek Metamorphics is taken directly from Coats and Blissett (1971), but more detailed mapping shows that some parts represent heavily deformed granitoids. Samples used for zircon studies are indicated with a triangle; samples yielding Precambrian ages only in bold face. Inset: Curnamona Province with discussed Domains, after Conor and Preiss (2008). The Mount Painter and Mount Babbage Inliers belong to the Moolawatana Domain. The overview map of Australia shows the location of the Curnamona Province and Gawler Craton.

Fig.2:

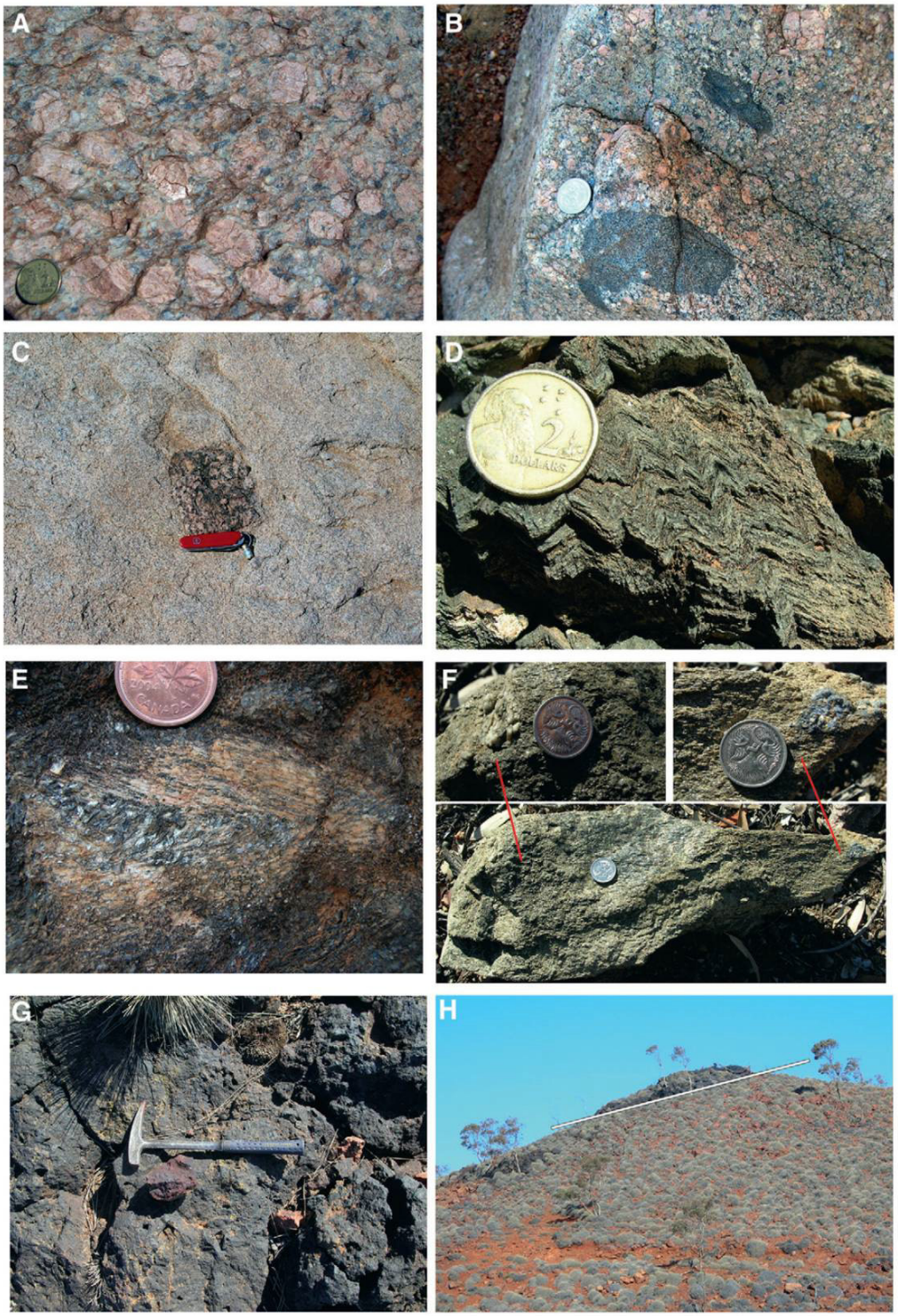

Fig. 2. (A) Terrapinna Granite in the Mt. Babbage Inlier. (B) Enclaves (sample ARK691) in Mt. Neill Suite granite. (C) Xenolith of Terrapinna Granite within the Paralana Granodiorite in the Mt. Babbage Inlier. (D) Crenulations in biotite schists. (E) Hyperaluminous sample with sillimanite. (F) Sample ARK687, which grades from a left-hand part (ARK687L) of metasomatised granite with recognisable feldspar, to a right-hand part of phlogopite plus corundum (ARK687A in Table 1) (G) Iron oxide ore (sample ARK732) (H) Field view of ore sheets, with layering indicated by drawn white line.

Fig.3:

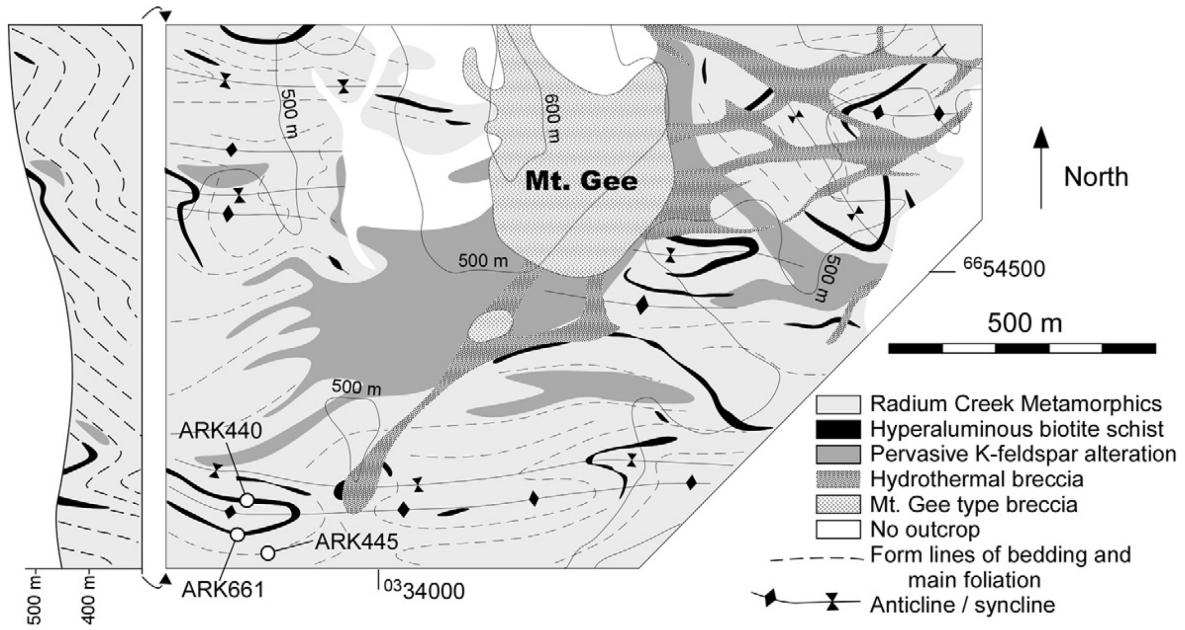

Fig. 3. Geological map of area around Mt. Gee in the centre of the southern MPI, near location 1 in Fig. 1. The area shows heavy overprinting by hydrothermal Palaeozoic K-feldspar alteration and brecciation, as well as younger quartz and hematite breccias of the Mt. Gee hydrothermal system. Mostly E–Wstriking synforms and antiforms can be recognised in the Radium Creek Metamorphics, especially where hyperaluminous biotite/phlogopite schists (black) can be traced across folds.

Fig.4:

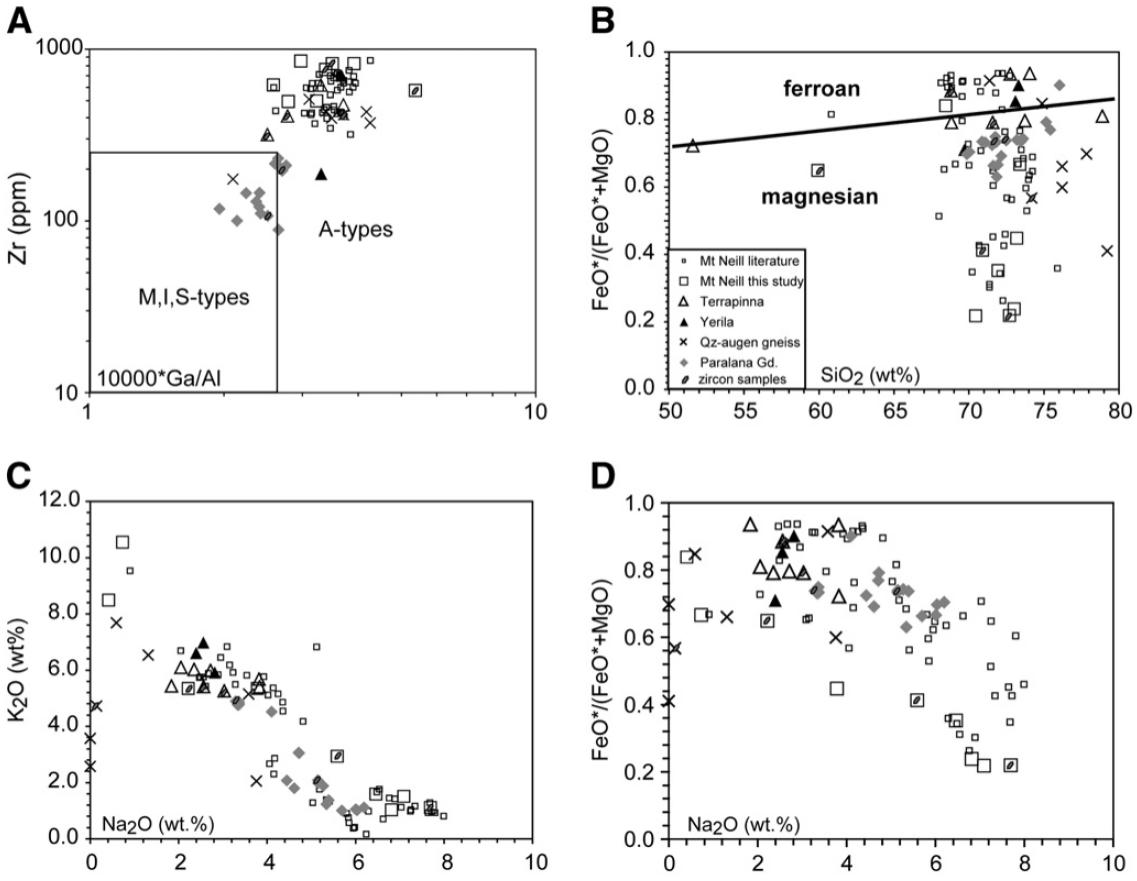

Fig. 4. Whole rock variation diagrams for the Mesoproterozoic (Mt. Neill Suite and its deformed equivalents the quartz–augen gneiss, Terrapinna and Yerila Granite) and Palaeozoic (Paralana Granodiorite) granitoids. Mt. Neill Suite literature data from the database of Stewart and Foden (2001). FeO*=all iron expressed as FeO. (A) Zr versus 1000*Ga/Al after Whalen et al. (1987) showing the distinction between the Mesoproterozoic and Palaeozoic granitoids; (B) FeO*/FeO*+MgO versus SiO2 after Frost et al. (2001) showing the boundaries between ferroan and magnesian granites; the results for this diagram are however influenced by metasomatic alteration; (C) K2O versus Na2O showing the effects of albitisation on the Mt. Neill Suite; (D) FeO*/FeO*+MgO versus Na2O showing the effect of albitisation on the iron/magnesium ratio.

Fig.5:

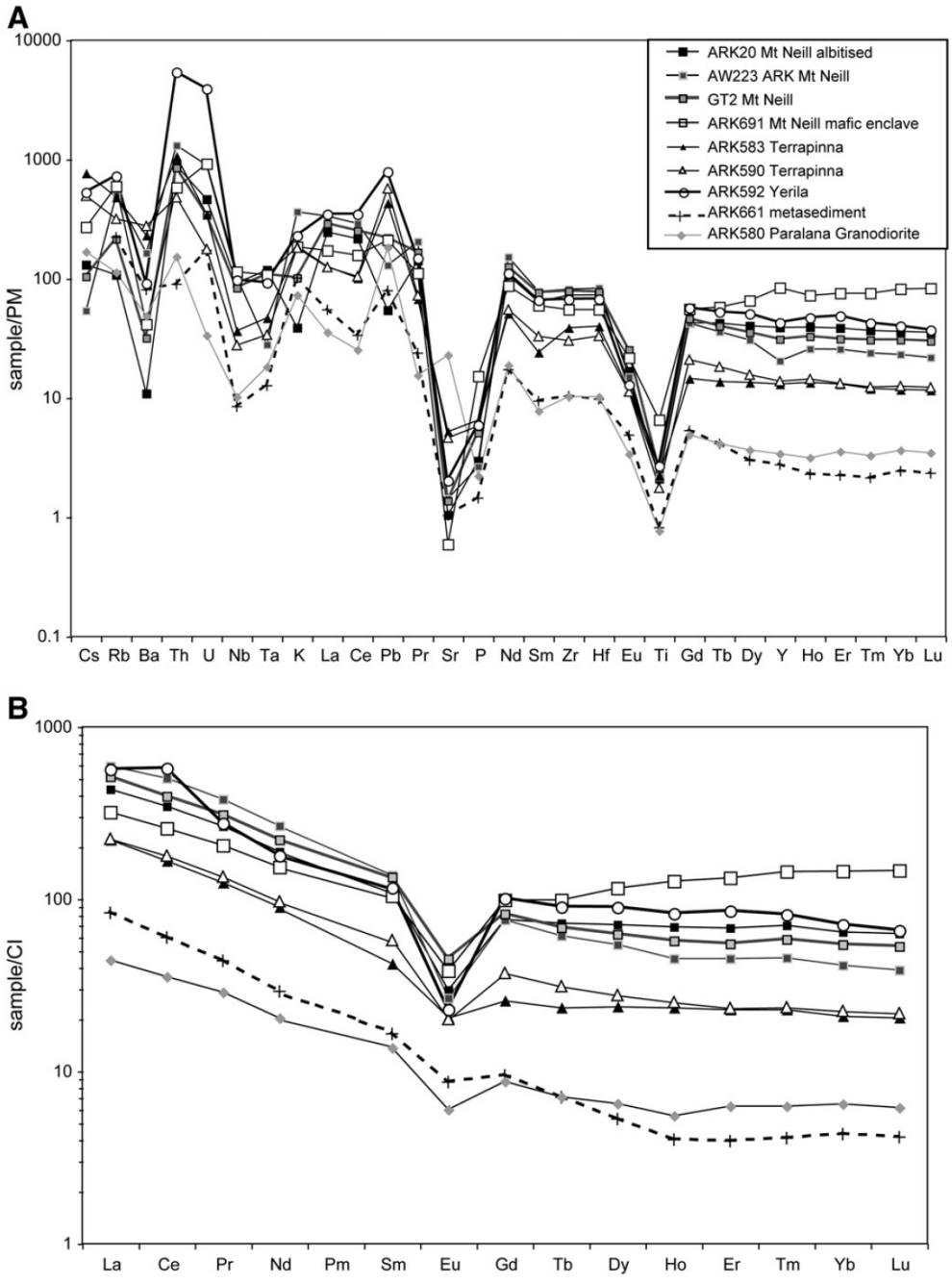

Fig. 5. Normalised trace element diagrams. Normalising values from Sun and McDonough (1989). (A) Primitive mantle-normalised diagram for representative samples of the Mesoproterozoic granitoids, Palaeozoic Paralana Granodiorite and Radium Creek Metamorphics metasediment. (B) Chondrite normalised rare earth element patterns. The positive Ce-anomaly may be the result of alteration.

Fig.6:

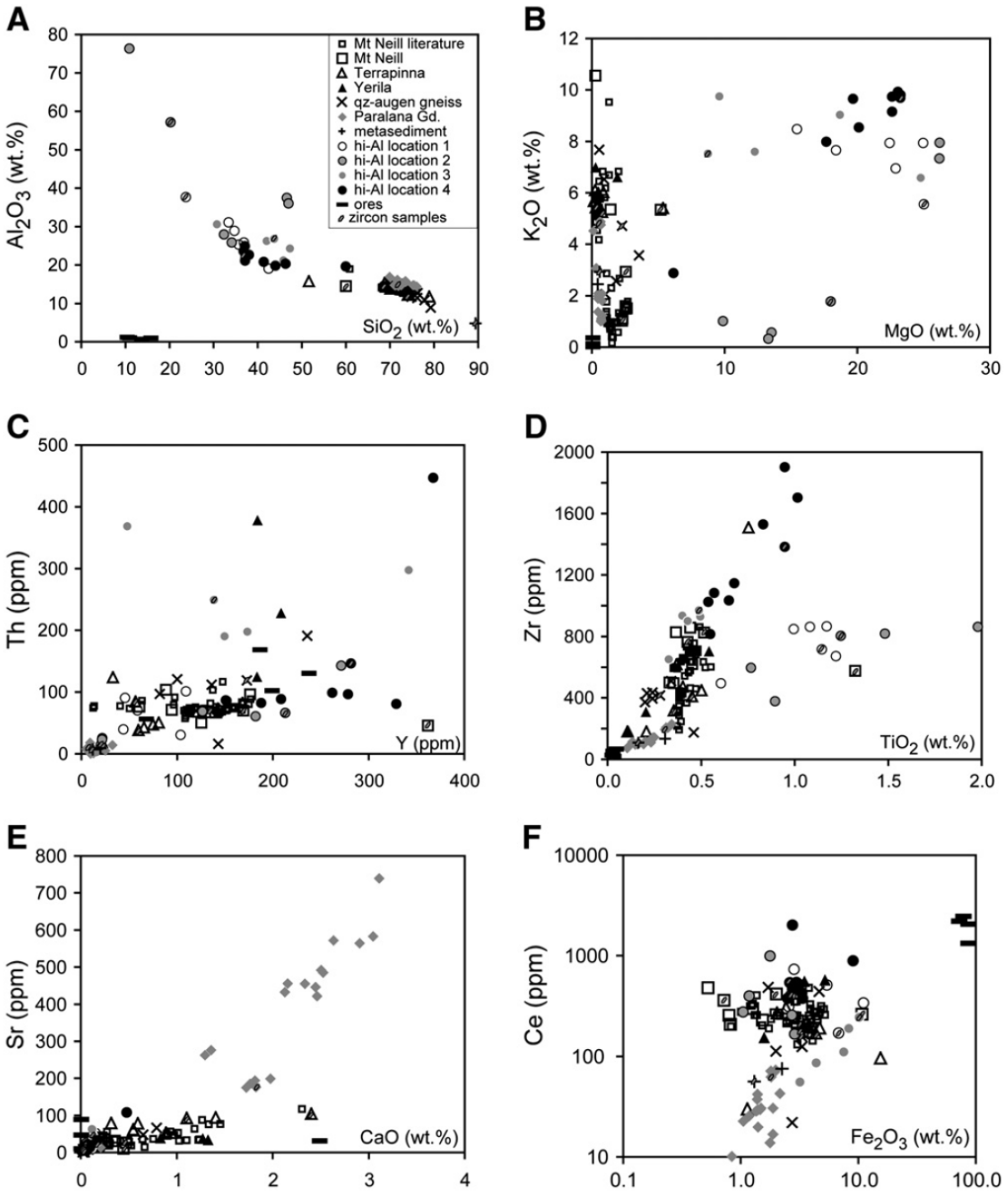

Fig. 6. Whole rock major and trace element data for all rock types. Note logarithmic scale for diagram F.

Fig.7:

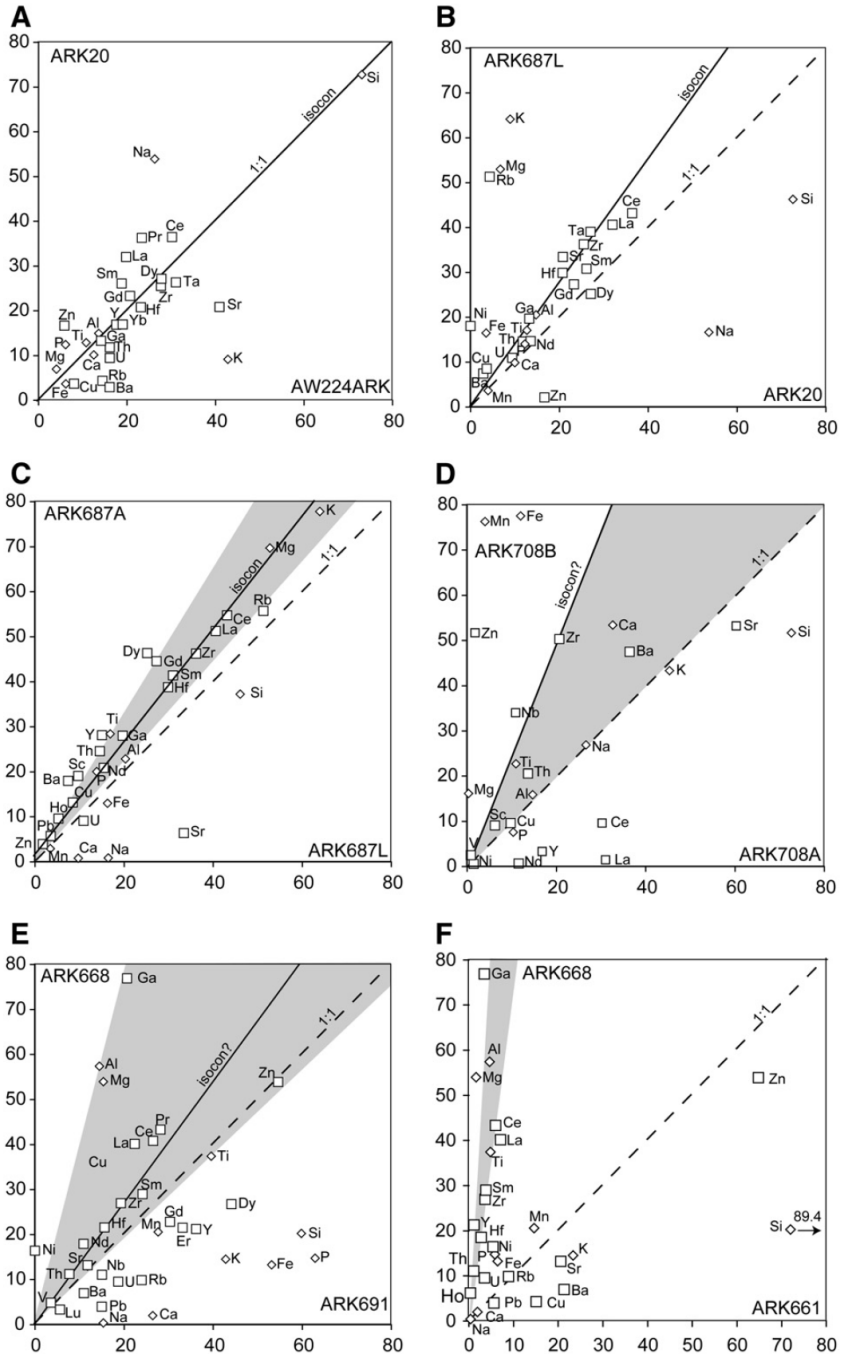

Fig. 7. Isocon diagram for several sets of samples. For ease of representation, the concentrations of oxides (major elements; diamonds) and trace elements (squares) were in some case multiplied by a constant. The grey envelopes indicate the range of elements that are typically assumed to be immobile (Ti, Al, Zr) during metasomatism; the isocon is likely to lie within this envelope. Not all elements are shown on each panel to avoid overcrowding. A: Albitised granite ARK20 versus original Mt. Neill Granite AW224ARK; B: incipiently Mg-metasomatised sample ARK687A versus albitised granite ARK20; C: hyperaluminous sample ARK687A versus more pristine granite ARK687L; D: biotitised sample ARK708B versus unaltered Terrapinna Granite ARK708A; E: hyperaluminous sample ARK668 versus microgranitoid enclave ARK691; F: hyperaluminous sample ARK668 versus metasediment ARK661.

Fig.8:

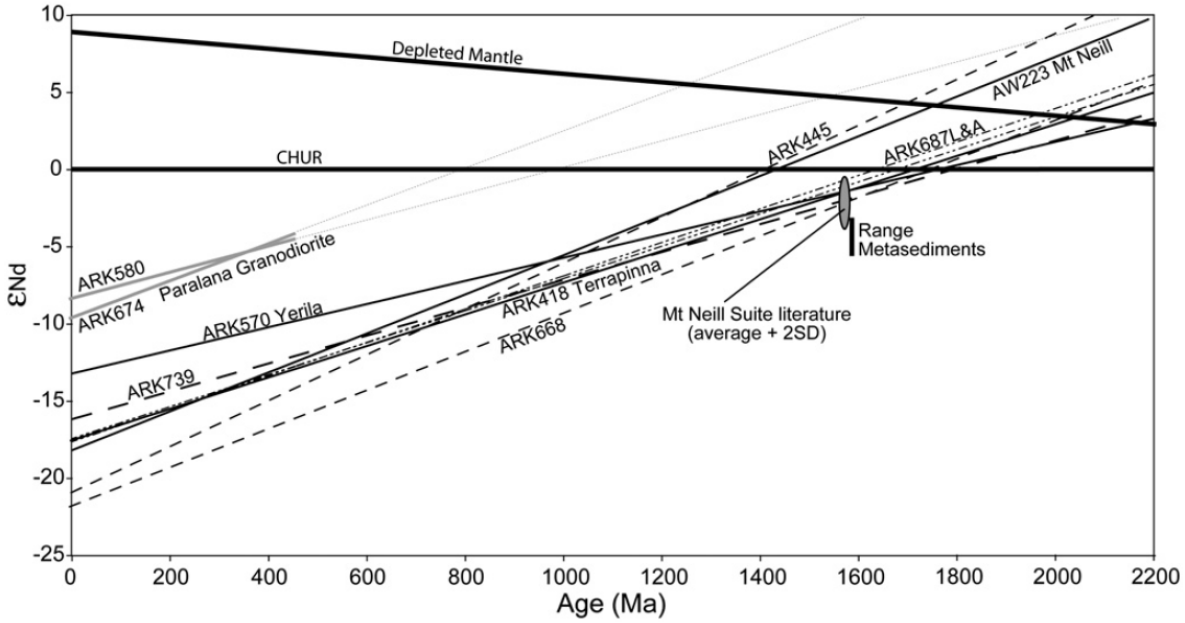

Fig. 8. Epsilon Nd values versus time for the Mesoproterozoic granites (Mt. Neill Suite sample AW223, Terrapinna Granite ARK418, Yerila Granite ARK570; solid black lines), Palaeozoic Paralana Granodiorite (ARK580 from the Mt. Babbage Inlier, ARK674 from the Mt. Painter Inlier; solid grey lines, stippled at ages older than the intrusive age) and hyperaluminous samples (dashed lines). Also indicated is the average Nd isotope ratio for the Mt. Neill Suite (±2 standard deviations) from Stewart and Foden (2001), and the values for four metasediment samples from Neumann (2001).

Fig.9:

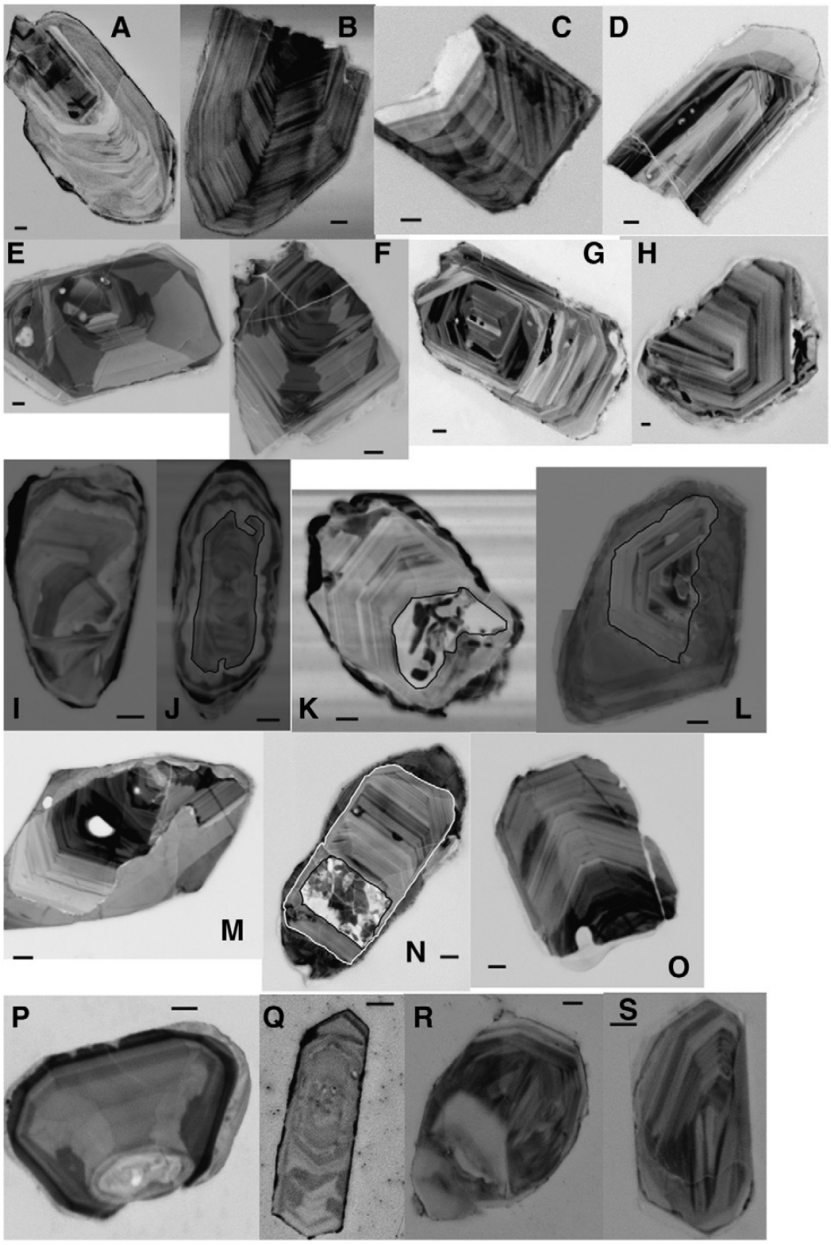

Fig. 9. Cathodoluminescence pictures of typical zircons from the analysed samples; scale bar is 20 μm. Zircon cores in panels j, k, l and n have been traced in black (and white for n) to indicate the border between core and rim zones. (A) Terrapinna Granite ARK583; (B) Terrapinna Granite ARK590; (C) Mt. Neill Suite mafic enclave ARK691; (D) Mt. Neill Suite granite ARK20; (E) Mt. Neill Suite deformed granite GT2; (F) quartz–augen gneiss B61; (G) hyperaluminous biotite–sillimanite schist ARK739; (H) corundum–phlogopitite ARK687A; (I) hyperaluminous spinel–corundum–phlogopitite sample ARK 445, zircon 69 (core 1580 Ma group with εHf +3, rim 464 Ma);(J) ARK445, zircon 37 core (traced in black) 1580 Ma with εHf +2, rim 440 Ma; (K) ARK445, zircon 40, inner core (traced in black) εHf −5 at 1580 Ma, oscillatory zoned outer core −0.5; (L) hyperaluminous spinel–corundum–cordieritite ARK668, zircon 47, core (traced in black) 1580 Ma with εHf +3, rim 460 Ma; (M) ARK668 zircon 2, rim 440 Ma, εHf −20; (N) ARK668, zircon 58 inner core (traced in black) 1700 Ma, outer core (traced in white) 1580 Ma; (O) metasediment ARK661, zircon 35, 1580 Ma εHf−5; (P) ARK661, zircon 50, 2580 Ma; (Q) Palaeozoic Paralana Granodiorite, Mt. Painter Inlier, BEM 4, zircon 1 (493 Ma); (R) BEM4, zircon 4 (discordant 1540 Ma group); (S) Palaeozoic Paralana Granodiorite, Mt. Babbage Inlier, ARK579, zircon 47 (1540 Ma group).

Fig.10:

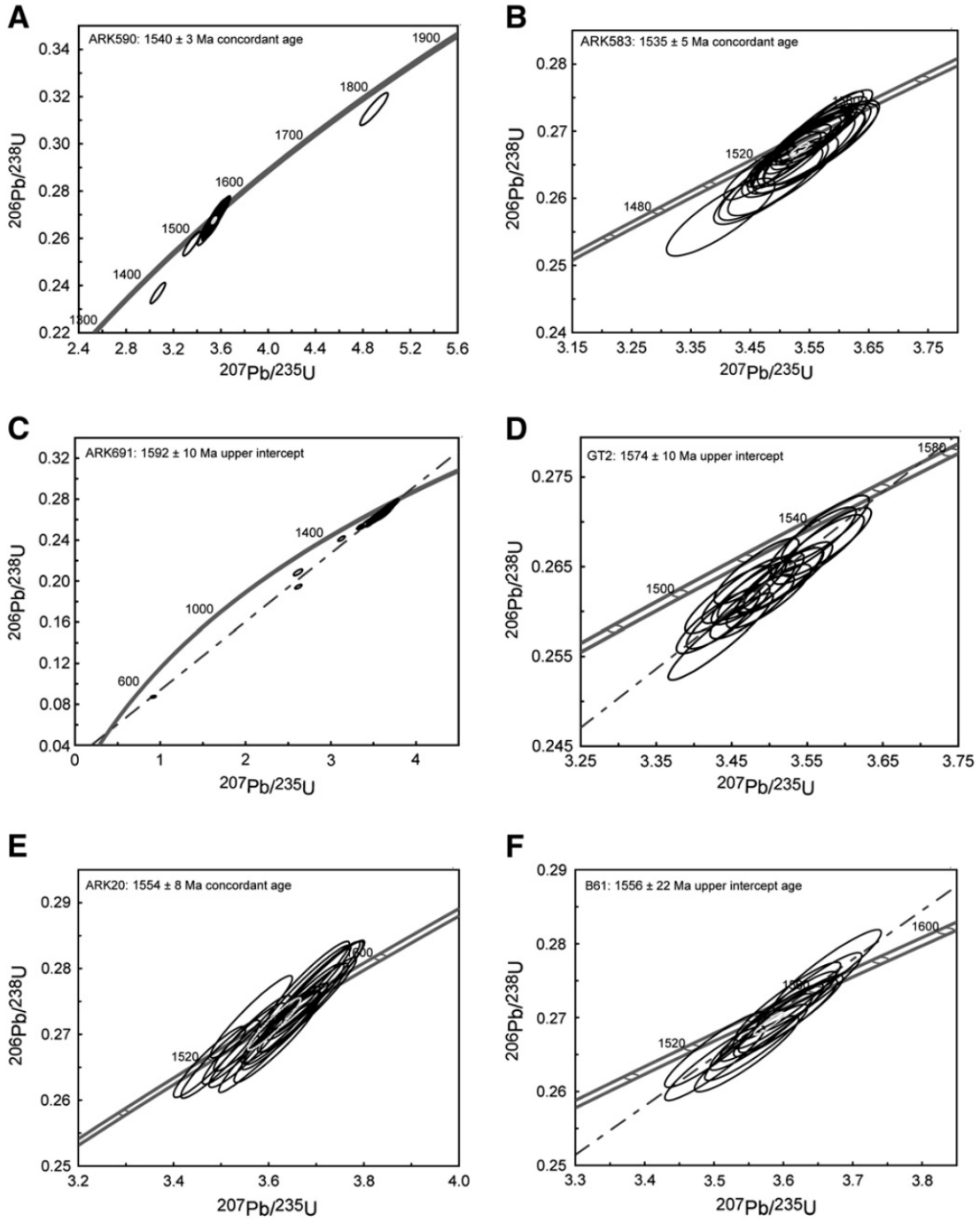

Fig. 10. A–F Concordia diagrams for zircons from the Mesoproterozoic granitoids and quartz–augen gneiss. Size of the error ellipse corresponds to the 68% confidence interval.

Fig.11:

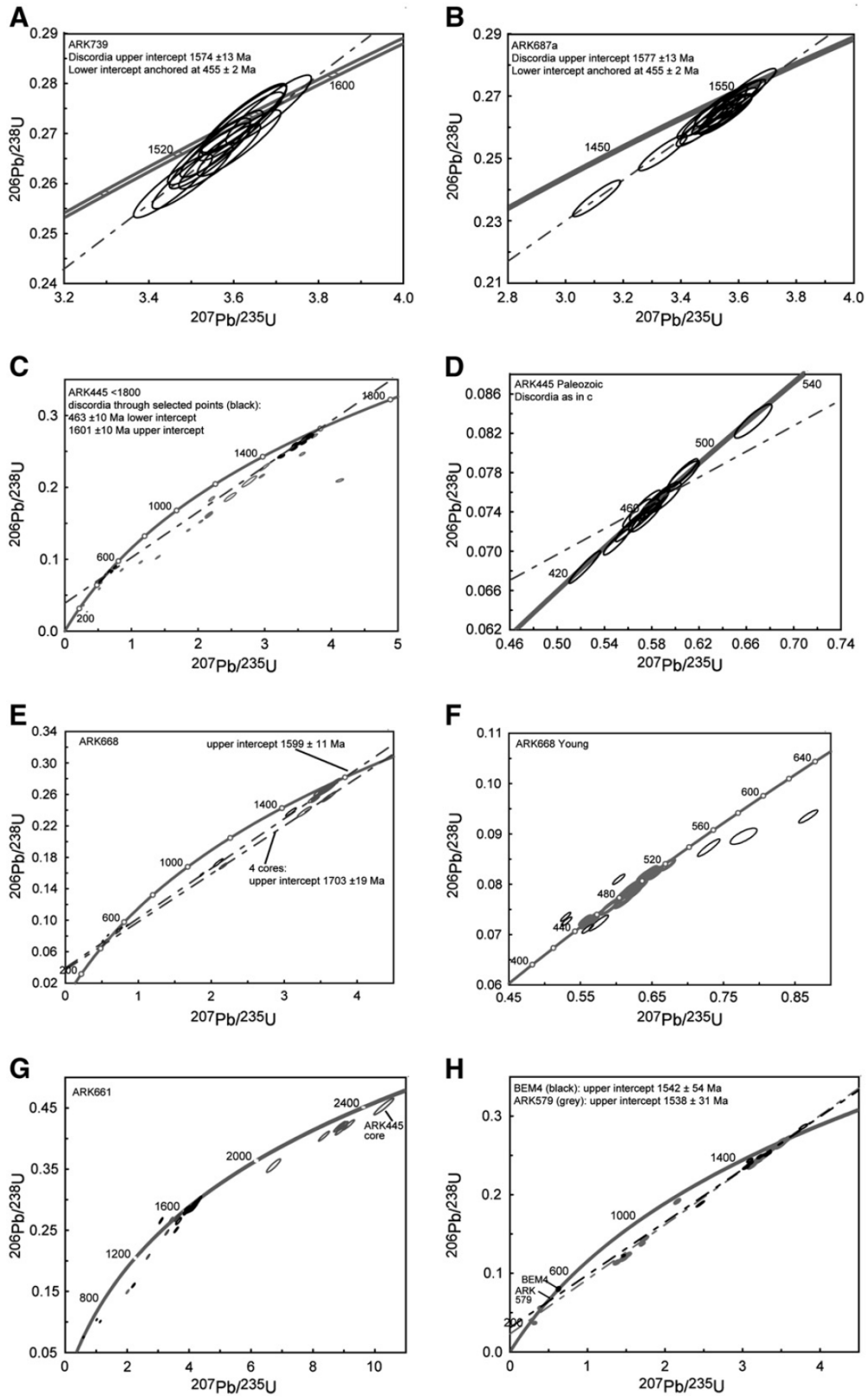

Fig. 11. Concordia diagrams for hyperaluminous rocks (A–F), metasediment (G) and Palaeozoic metaluminous Paralana Granodiorite (H).

Fig.12:

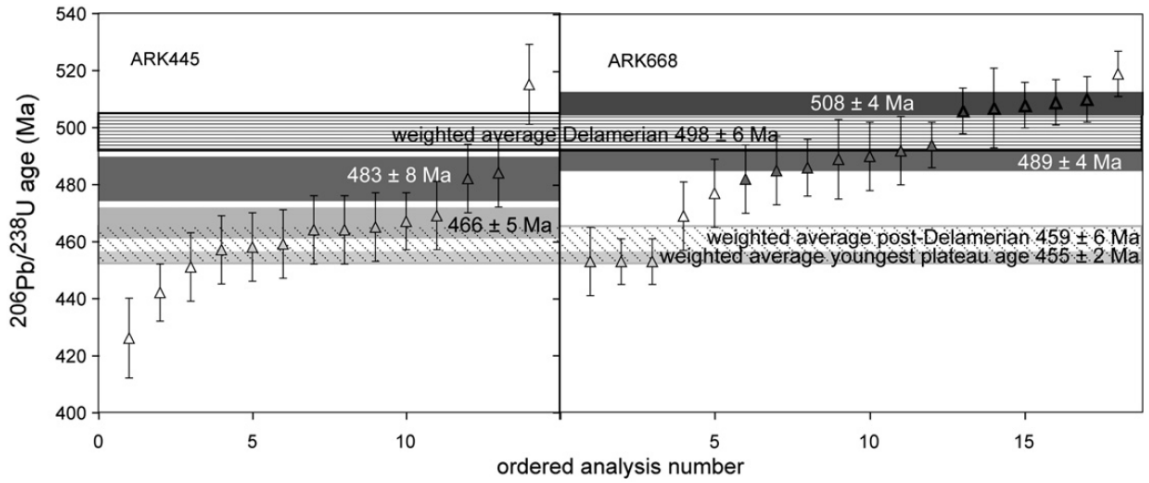

Fig. 12. Concordant Palaeozoic zircon ages from the hyperaluminous samples, ordered according to their age. Error bars are 2 SE. Analyses 1–3 of ARK668 and 4–6 of ARK445 give a combined age of 455±2 Ma, which is indistinguishable of the monazite 206Pb/238U age for ARK445. Horizontal bars indicate weighted average ages and their error for different sub-groups; see text for discussion.

Fig.13:

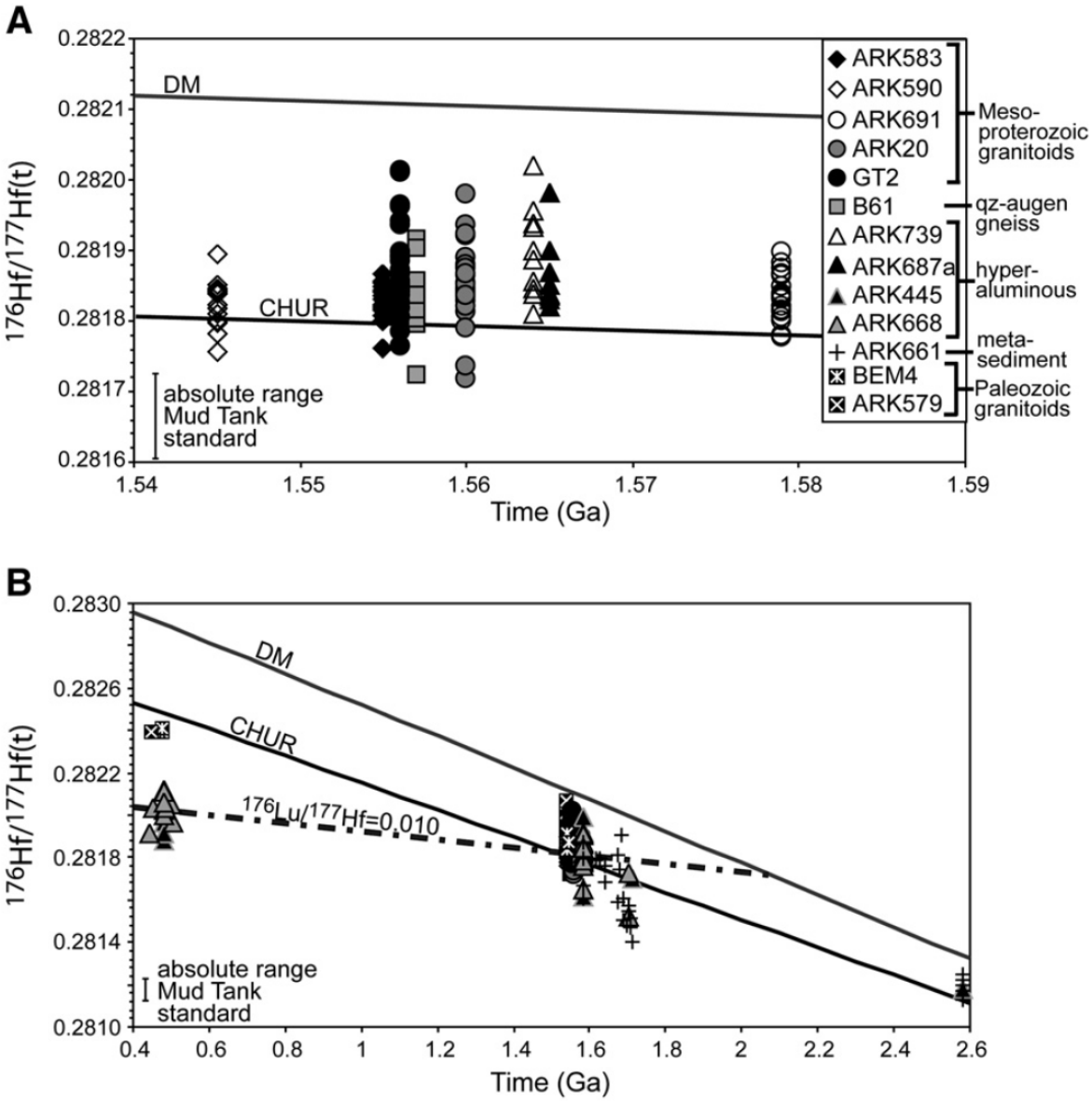

Fig. 13. Initial 176Hf/177Hf ratio versus age for all samples analysed. Also shown is the full range of the Mud Tank zircon standard, as the ideal case for the expected range for a homogeneous sample with analytical method employed. (A) Mesoproterozoic granitoids only; (B) Mesoproterozoic granitoids, hyperaluminous rocks, metasediment and Palaeozoic Paralana Granodiorite.

Tab.1:

	Mt Neill Suite				Qz–augen	Terrapinna				Yerila	Paralana Gd	Meta-sediment	Hyper-aluminous					Fe–U–Cu–REE ore
		Albitised	Deformed	Enclave	Gneiss	Mt Babbage	Mt Babbage	Mt Painter	Biotitised		Mt Babbage	Locality 1	Locality 1	Locality 2	Locality 3	Locality 4	Locality 4	
Sample	AW224	ARK20	GT2	ARK691	B61	ARK583	ARK590	ARK708A	ARK708B	ARK592	ARK580	ARK661	ARK445	ARK668	ARK739	ARK687A	ARK687L	ARK732
SiO_2	73.15	72.68	70.87	59.89	74.18	68.81	71.58	72.75	51.59	69.64	73.42	89.38	23.59	20.15	43.62	37.12	46.20	10.82
TiO_2	0.36	0.43	0.51	1.32	0.28	0.45	0.35	0.37	0.75	0.54	0.16	0.16	1.14	1.24	0.49	0.94	0.57	0.03
Al_2O_3	13.73	14.85	14.99	14.59	13.25	15.33	14.53	14.8	15.79	13.73	15.73	4.78	37.8	57.29	26.92	22.76	20.43	1.11
$Fe_2O_3^*$	1.25	0.72	1.99	10.65	3.29	4.33	3.22	2.42	15.49	5.16	1.37	1.31	6.73	2.63	10.06	2.59	3.28	77.99
MnO	0.01	0.01	0.01	0.07	0.01	0.06	0.04	0.01	0.2	0.05	0.04	0.04	0.04	0.05	0.03	0.01	0.01	6.07
MgO	1.38	2.28	2.53	5.15	2.26	0.5	0.76	0.15	5.35	1.89	0.44	0.58	24.97	17.96	8.7	23.2	17.62	0.04
CaO	0.21	0.17	0.47	0.44	0.02	2.4	1.11	0.55	0.89	0.82	2.33	0.03	0.02	0.03	0.12	0.01	0.16	0
Na_2O	3.77	7.68	5.58	2.21	0.14	2.56	3.03	3.82	3.83	2.38	5.14	0.07	0.12	0.04	1.39	0.11	2.37	0.01
K_2O	5.36	1.13	2.95	5.36	4.72	5.41	5.26	5.68	5.4	6.63	2.11	2.93	5.57	1.8	7.54	9.71	8.01	0.15
P_2O_5	0.03	0.06	0.11	0.32	0.05	0.13	0.12	0.05	0.04	0.12	0.05	0.03	0.03	0.07	0.04	0.1	0.07	0.29
LOI	0.54	0.75	1.05	0.94	1.74	1.03	0.63	0.51	1.06	0.59	0.55	0.73	1.45	7.15	3.57	0.91	1.91	4.82
Total	99.26	99.65	101.45	99.69	99.95	98.75	100.74	100.61	99.34	100.97	100.78	99.32	100.02	101.28	98.9	96.55	98.71	96.51
FeO^*/MgO	0.82	0.28	0.71	1.86	1.31	7.74	3.8	14.24	2.6	2.47	2.79	2.02	0.24	0.13	1.04	0.1	0.17	1610
ASI	1.11	1.05	1.13	1.42	2.46	1.06	1.14	1.1	1.15	1.09	1.05	1.43	6.03	27.62	2.52	2.12	1.59	
$Fe^{\#}$	0.45	0.22	0.41	0.65	0.57	0.89	0.79	0.93	0.72	0.71	0.74	0.67	0.2	0.12	0.51	0.09	0.14	1
Rb	218	65	129	359	365	291	191	308	NA	436	68	133	410	148	598	835	770	1
Ba	403	72	210	274	231	1536	1831	913	1188	603	321	534	309	175	701	449	186	19,035
Sr	41	21	27	12	1	104	93	60	53	40	456	21	7	13	48	6	33	90
Zr	830	766	828	579	416	409	318	618	1510	707	108	109	720	808	973	1387	1086	22
Y	176	169	133	362	173	57	60	168	33	184	11	12	20	212	138	281	150	237
Sc	5	7	9	14	6	5	9	6	9	12	3	3	6	12	9	19	10	5
Cr	5	0	ND	11	14	5	5	4	ND	4	2	14	71	308	5	3	ND	5
V	12	12	12	36	2	22	20	9	25	16	13	16	114	49	23	33	24	10
Ga	28	26	28	41	26	23	19	26	NA	27	21	7	35	154	42	56	39	ND
Cu	8	4	1	3	NA	8	5	10	10	4	1	15	5	4	10	13	9	1434
Zn	6	17	14	55	NA	52	54	9	258	52	35	65	716	54	9	4	2	627
Ni	3	1	ND	2	NA	1	2	1	1	1	0	5	46	16	5	23	18	6
Be	5.8	1.7	1.3	2.9	NA	3.5	3.1	7.9	NA	6.2	3.1	1.4	6.3	37.4	13.4	6	3.0	4
Nb	65	60	55	75	75	24	18	54	NA	64	7	6	36	55	119	141	91	20
Mo	1	3.8	0.6	1.2	NA	2.3	0.3	5.9	NA	3.4	0.9	0.6	1	1.2	0.8	0.4	0.5	226
Cs	NA	1	0.8	2.1	NA	6.1	3.9	NA	NA	4.2	1.3	NA	NA	NA	NA	NA	NA	0.1
La	93	160	189	118	76	82	83	145	7	209	16	31	79	190	97	248	192.0	905
Ce	274	331	379	246	159	160	171	282	96	552	34	57	149	391	211	508	391.0	1939
Pr	23.4	36.3	42.4	28.2	NA	17.2	18.5	30.3	NA	37.9	3.9	6	14.4	43.3	23.5	56	43.5	144.7
Nd	87.3	134.5	157.3	109.3	71	64.4	69	110.4	5.8	127	14.5	20.7	48.4	169.1	85.7	205.1	160.5	448.1
Sm	18.8	26.1	31.1	24.2	NA	9.8	13.4	21.3	NA	26.9	3.2	3.8	6.4	29	18	41.4	31.0	53.3
Eu	1.6	2.6	3.9	3.3	NA	1.8	1.7	2.3	NA	2	0.5	0.8	0.6	3.4	0.9	4.8	3.5	7.2
Gd	20.7	23.3	25.1	30.4	NA	7.9	11.4	22.9	NA	31	2.7	2.9	5	22.8	17.4	44.5	27.3	58.3
Tb	4.1	4.2	4	5.7	NA	1.4	1.8	4.1	NA	5.2	0.4	0.4	0.6	3.7	3.2	7.1	4.4	6.9
Dy	27.8	27.1	23.9	44.1	NA	9.1	10.6	26.4	NA	34.2	2.5	2	3.2	26.7	21.2	46.4	25.2	36.7
Ho	6.2	5.9	4.9	10.8	NA	2	2.1	5.7	NA	7	0.5	0.3	0.6	6.2	4.6	9.6	5.3	7.4
Er	19.1	16.9	13.7	33.2	NA	5.7	5.8	17.7	NA	21.3	1.6	1	2	21.5	15.5	29.9	15.8	23.2
Tm	2.9	2.5	2.1	5.2	NA	0.8	0.8	2.7	NA	2.9	0.2	0.1	0.4	3.4	2.5	4.5	2.5	3.4
Yb	18.7	16	13.5	36.1	NA	5.2	5.6	17.7	NA	17.7	1.6	1.1	2.8	22.6	16.9	28.7	15.8	23
Lu	2.9	2.4	2	5.6	NA	0.8	0.8	2.7	NA	2.5	0.2	0.2	0.5	3.3	2.5	4.3	2.5	3.2
Hf	23.1	20.8	21.9	15.6	NA	11.4	9.4	17.3	NA	19.1	2.9	2.8	19	21.6	31.3	38.8	29.9	0.5
Ta	5.2	4.4	4	4	NA	1.7	1.3	4.4	NA	3.4	0.7	0.5	2.8	3.1	11.1	10.6	6.5	0.3
Pb	8	3.9	15.7	15	1	30.7	40.7	13.4	NA	55.9	13	5.6	1	4	9.3	5.7	3.5	100.2
Th	98.5	70.7	67.8	46.3	119	84.6	38.3	80.2	124	427.7	12.2	7.1	15.4	67.3	250	147.3	87.4	9
U	16.2	9.4	7	18.7	24	7	3.6	22.6	NA	79.6	0.7	3.5	5.2	9.5	29.8	9.1	10.9	2052

LOI = Loss on ignition. $Fe_2O_3^*$ = all iron reported as Fe_2O_3. ASI = Aluminium Saturation Index (molecular $Al_2O_3/(Na_2O + K_2O + CaO)$). Gd = Granodiorite; NA = not analysed; ND = not detected.

Table 1

Representative whole rock analyses. Oxides in weight percent, elements in ppm. XRF analysis for sample B61 from Elburg et al. (2001). All other analyses were done by ICP-OES for major elements plus Ba, Sr, Zr, Y, Cu, Zn; ICP-MS for the other elements, apart from ARK708b, for which all data are ICPOES.

Tab.2:

Unit	Sample	$^{143}Nd/^{144}Nd$	1 SD	1 SE	$^{147}Sm/^{144}Nd$	1 SD	εNd_0	εNd_{455}	εNd_{1575}	T^{DM}	T^{CHUR}
Mt Neill Granite	AW223	0.511704	0.000016	0.000002	0.0978	0.0006	−18.2	−12.49	1.76	1.75	1.43
Terrapinna Granite	ARK418	0.511729	0.000017	0.000002	0.1167	0.0007	−17.7	−13.09	−1.57	2.05	1.72
Yerila Granite	ARK570	0.511957	0.000017	0.000002	0.1386	0.0008	−13.3	−9.92	−1.56	2.19	1.78
Paralana Granodiorite	ARK580	0.512205	0.000022	0.000003	0.1303	0.0008	−8.5	−4.60	4.97	1.52	0.99
Paralana Granodiorite	ARK674	0.512140	0.000023	0.000002	0.1029	0.0006	−9.7	−4.27	9.27	1.23	0.81
Hyperaluminous	ARK445	0.511562	0.000022	0.000002	0.0806	0.0005	−21.0	−14.26	2.46	1.68	1.41
Hyperaluminous	ARK668	0.511522	0.000016	0.000002	0.0990	0.0006	−21.8	−16.10	−2.04	2.01	1.73
Hyperaluminous	ARK687A	0.511743	0.000016	0.000002	0.1155	0.0007	−17.5	−12.75	−1.06	2.00	1.67
Hyperaluminous	ARK687L	0.511733	0.000014	0.000001	0.1126	0.0007	−17.7	−12.79	−0.68	1.96	1.63
Hyperaluminous	ARK739	0.511810	0.000018	0.000002	0.1260	0.0008	−16.2	−12.06	−1.88	2.13	1.78

T^{DM} = Depleted Mantle extraction age (in Ga) following DePaolo (1981). T^{CHUR}=Mantle extraction age (Ga) for the Chondrite Uniform Reservoir.
Present-day CHUR values were taken as $^{143}Nd/^{144}Nd = 0.512638$ and $^{147}Sm/^{144}Nd = 0.1967$.

Table 2
Nd isotope data for Mesoproterozoic and Palaeozoic granites, and hyperaluminous samples.

Tab.3:

Sample	Lithology	Discordia upper intercept (Ma)	Discordia lower intercept (Ma)	MSWD discordia	Concordia age ± 1 sd (Ma)	MSWD concordia age	Ratios used/ ratios measured for concordia	Weighted average $^{207}Pb/^{206}Pb$ age ($^{238}U/^{206}Pb$ Paleozoic)	MSWD	Ratios used/ratios measured for weighted average age
ARK583	Terra	1561 +1500/−12	301 +1200/−260	0.033	1535 ± 5	20	10/10	**1555 ± 11**	0.048	10/10
ARK590	Terra	1553 +14/−11	467 +280/−270	0.54	1540 ± 3	11.5	17/19	**1545 ± 6**	1.3	19/19
GT2	Mt Neill	**1574 ± 10**	503 ± 13		Discordant			1556 ± 5	0.87	17/19
ARK20	Mt Neill	Concordant			1554 ± 8	1.7	19/19	**1560 ± 5**	2.2	18/19
ARK691	Mt Neill	1592 ± 10	373 ± 70	2.6	Discordant			**1579 ± 6**	1.7	25/28
B61	qz–aug.	1556 ± 22	467 ± 520	5.6	1549 ± 3	9.2	12/14	**1557 ± 5**	0.66	12/14
ARK739	hi–Al	**1574 ± 13**	Anchored 455 ± 2	0.60	1552 ± 11	18	11/11	1564 ± 8	0.43	11/11
ARK687A	hi–Al	**1578 ± 12**	Anchored 455 ± 2	0.44	Discordant			1565 ± 7	0.53	12/14
ARK445-old	hi–Al	1601 ± 10		3.8	Discordant			**1584 ± 4**	1.04	12/13*
ARK445-young	hi–Al		463 ± 10		Not equivalent			*461 ± 9*$	6.2	13/14*
" – 1st plateau								458 ± 7	0.03	3/14
" – 2nd plateau								466 ± 5	0.13	5/14
" – 3rd plateau								483 ± 8	0.06	2/14
ARK668-old	hi–Al	1599 ± 11		11.7	Discordant			**1582 ± 5**	1.2	14/14*
ARK668-young	hi–Al		483 ± 10		Not equivalent			*491 ± 12*$	10.4	11/11*
" – 1st plateau								453 ± 5	0	3/18
" – 2nd plateau								489 ± 4	0.67	7/18
" – 3rd plateau								508 ± 4	0.14	5/18
ARK668-4 cores	hi–Al	**1703 ± 19**	433 ± 59	0.28	Discordant					
ARK445 + 668 youngest								**455 ± 2**	0.06	6/26
ARK661 ~ 1580	Metased	1578 +19/−14	244 ± 310	1.08	Discordant					
ARK661 ~ 1700	Metased	1675–1711 Ma			Not equivalent					
ARK661 ~ 1625	Metased	1629 ± 10	13 ± 50	2.0	Discordant					
ARK661 >1800	metased	2582 +140/−72	1546 +240/−230	1.14	Discordant					
BEM4	PG	1542 ± 54	*355 ± 150*	74	*493 ± 2*		1			
ARK579	PG	1538 ± 31	*286 ± 78*	56	*426 ± 5*		1			

Italics: information value only (no statistical significance).
Terra = Terrapinna Granite; qz–aug. = Quartz–augen gneiss; hi–Al = hyperaluminous; metased = metasediment; PG = Paralana Granodiorite. Preferred ages are indicated in bold.
* selected analyses only (as indicated on discordia diagram, see text for discussion).
$ $^{238}U/^{206}Pb$ age for concordant analyses < 1550 Ma.

Table 3
Zircon U–Pb age data.